

ECPMG 2020

4th European Conference on
**Physical Modelling
in Geotechnics**

Editors: Jan Laue & Tarun Bansal



LULEÅ
UNIVERSITY
OF TECHNOLOGY

PROCEEDINGS OF THE 4th EUROPEAN CONFERENCE ON PHYSICAL
MODELLING IN GEOTECHNICS
~~LULEÅ, SWEDEN, 15-17 MARCH 2020~~
HYBRID LULEÅ/ZOOM, 7-8 SEPTEMBER 2020

**4th European Conference on
Physical Modelling
in Geotechnics**

Edited by:

Jan Laue & Tarun Bansal

Luleå University of Technology, Sweden



This work is licensed under the Creative Commons Attribution- NonCommercial-NoDerivatives 4.0 International License. To view a copy of this license, visit <http://creativecommons.org/licenses/by-nc-nd/4.0/>

ISBN (print): 978-91-7790-542-4

ISBN (pdf): 978-91-7790-543-1

Table of contents

Preface	VII
1 <i>Back to basics</i>	
Identification of scaling laws for the friction in centrifuge models of reinforced soil <i>Jean de Sauvage & Thierry Dubreucq</i>	3
Silty sand characterization in the geotechnical centrifuge <i>Varvara Zania, Sine Maria Christensen & Irene Rocchi</i>	9
The effects of sand grading on the bearing capacity of surface foundations <i>Mathias R. Jensen, Varvara Zania & Barry M. Lehane</i>	17
Tests of varied sample preparation methods for centrifuge modelling <i>Eric Ritchie, Leonardo Lalicata, Sam Divall & Richard Goodey</i>	25
Accelerations in dynamic centrifuge modelling of seismic liquefaction problems <i>Andreia Marques, Paulo Coelho, Stuart Haigh & Gopal Madabhushi</i>	31
Boundary effects in centrifuge modelling of soil liquefaction <i>Zheng Li & Sandra Escoffier</i>	39
Centrifuge model studies on dry granular soils subjected to dynamic compaction induced tamping <i>Saptarshi Kundu & B.V.S. Viswanadham</i>	43
Model preparation for unsaturated soil testing in a centrifuge environment <i>Leonardo Maria Lalicata, Luc Thorel, Augusto Desideri, G.M. Rotisciani & Francesca Casini</i>	49
Effect of Crushed Particles on Soil-Structure Interface Behaviour <i>Angus Pettey & Charles Heron</i>	57
Carboxymethylcellulose as a Newtonian viscous fluid for centrifuge modelling <i>Jarno Terwindt, Wouter van der Star & Dirk de Lange</i>	65
2 <i>Physical modelling techniques and facilities</i>	
A new geotechnical centrifuge at Deltares, Delft, the Netherlands <i>Rob Zwaan, Jarno Terwindt, Dirk de Lange & Adam Bezuijen</i>	75
A Novel Small-Scale Model Testing Device for Laterally Loaded Piles <i>Hendrik Sturm & Andrea Støren</i>	83
Development of a Hammer to drive monopiles of offshore wind turbines in Centrifuge <i>Semaan Maatouk, Matthieu Blanc & Luc Thorel</i>	89
Experimental testing and ring polygons for the rolling stock – track infrastructure interaction and subgrade analysis <i>Alexander Savin, Andrey Zaytsev, Alexander Abrashitov, Andrey Sidrakov & Alexander Gorlov</i>	95

Pneumatic load frame for long-term in-situ application of moderate tension loads on foundation elements <i>Jorge Yannie, Claes Alén & Jelke Dijkstra</i>	103
Chromatic aberration when using white LEDs for PIV: issues and remedies <i>Mir Amid Hashemi, Jingmin Xu, Charles M. Heron & Alec M. Marshall</i>	109
Physical Model of Rainfall Induced Landslide in Flume Test: Preliminary Results <i>Željko Arbanas, Vedran Jagodnik, Josip Peranić, Sara Pajalić, Martina Vivoda Prodan & Nina Čeh</i>	115
3 Piles: installation and capacity	
Soil plug investigation with respect to pile geometry and installation method <i>Sascha Henke</i>	125
Pile group effects on installation and capacity of jacked piles in sand tested in the centrifuge <i>Dirk de Lange & Jarno Terwindt</i>	133
Centrifuge modelling of shaft resistance of a rough rock-socketed pile <i>José Gregorio Gutiérrez-Ch, Geyang Song, Charles Heron, Alec Marshall & Rafael Jimenez</i>	139
Physical modelling of single-helix piles in sand using calibration chamber tests <i>Diego Moreira da Silva & Cristina de Hollanda Cavalcanti Tsuha</i>	143
Study on the installation effect of helical piles in very dense sand <i>José Antonio Schiavon, Cristina de Hollanda Cavalcanti Tsuha & Luc Thorel</i>	151
Experimental technique for creating enhanced capacity piles in a centrifuge environment <i>Leonardo Lalicata, Andrew McNamara & Sarah Stallebrass</i>	157
Model tests of grouted piles in gravel esker and fill soils <i>Wik Breure & Anders B Lundberg</i>	163
4 Infrastructures	
Geotechnical instrumentation of an experimental embankment dam <i>Jasmina Toromanovic, Johan Lagerlund, Peter Viklander & Jan Laue</i>	171
Surface wave propagation in centrifuge testing using Electromagnetic Drop-Projectile system <i>Vipul Kumar & S.P.G. Madabhushi</i>	177
Centrifuge modelling of train passage over clay subgrades <i>Scott Robinson, Andrew Brennan, Cameron Munro, Peter Woodward, David Connolly, Omar Lagrouche & Ahmet Esen</i>	185
Centrifuge modelling of tunnel-soil-pile interaction considering the presence of rigid caps <i>Jingmin Xu, Andrea Franza & Alec M. Marshall</i>	193
Centrifuge Modelling of the Reverse Faulting-Tunnel Interaction in Granular Alluvial Soil considering Tunnel Flexible Joints <i>Hamid Tohidifar, Mojtaba Moosavi & Mohammad Kazem Jafari</i>	201
Soil Improvement of a Subway Station Excavated by an Earth Pressure Balance Machine <i>Mohammad Zamani Ahmad Mahmoudi, Ali Entezari Zarandi, Milad Naghbi & Ali Azad</i>	205

Performance of Geogrid reinforced soil walls with low permeable backfill: Centrifuge Study <i>B.V.S. Viswanadham, Midhula Jayanandan, Dipankana Bhattacharjee & Prince Kumar</i>	213
Centrifuge model studies on geogrid and hybrid geosynthetic reinforced slopes subjected to rainfall <i>Dipankana Bhattacharjee & B.V.S Viswanadham</i>	221
Effect of fiber soil reinforcement on the bearing capacity of a surface strip foundation <i>Maria Diakoumi, Kevin Stone & David Roddy</i>	227
 5 Offshore geotechnics	
Centrifuge tests of monopile foundations under one-way cyclic lateral loading <i>Kunkun Cheng, Charles M. Heron, Luke J. Prendergast & Alec M. Marshall</i>	235
Use of optical fibres to measure pore water pressure development during impact pile driving: a geotechnical centrifuge study <i>Amin Askarinejad, Tristan O. Quinten, Mario Alvarez Grima, Cornelis van 't Hof & Ken Gavin</i>	243
The modelling of piles under multidirectional loading <i>Christophe Gaudin, Conleth O'Loughlin & Manuel Herduin</i>	247
Suction caisson response under tensile and compressional vertical cyclic loading in sand over clay <i>Marc Stapelfeldt & Jürgen Grabe</i>	255
Centrifuge Modelling of Suction Caissons Subjected to Cyclic Loading in Tension <i>Yuen Zhang, Kamaleshwar Sudhakaran & Amin Askarinejad</i>	263
An investigation into the performance of helical piles with fins under lateral loading <i>Kevin Stone, Maria Diakoumi & Oliver Jeffcock</i>	269
Pile test database on centrifuged models: tension loading for floating wind turbine anchor <i>Luc Thorel, Ismat El Haffar & Matthieu Blanc</i>	275
 6 Extended Abstracts	
Experimental study of the interaction of shallow foundations with an emerging strike-slip fault rupture <i>Athanasios Agalianos, Evangelia Korre, Tarek H. Abdoun & Ioannis Anastasopoulos</i>	281
Investigation of the dynamic behavior of gravity-type quay wall under saturated condition <i>Yeon-Sam Kim, Kil-Wan Ko & Dong-Soo Kim</i>	283
Design of a Miniature Cone Penetrometer for the Geotechnical Centrifuge of Delft University of Technology <i>Dirk de Lange, Siavash Honardar & Amin Askarinejad</i>	285
Behaviour of prefabricated concrete screw piles under axial loading <i>André Arnold & Amin Askarinejad</i>	287
Validation of ESB Box and Estimation of Shear Wave Velocity in Partially Saturated Soil <i>Yoon-Ah Kim, Hae-In Lee, Satish Manandhar & Dong-Soo Kim</i>	289
Retrofit, redesign, and restructuring of a large geotechnical centrifuge research center <i>April J. Bowman, Anthony F. Tessari & Christopher Price</i>	291

Using Fibre Bragg Grating sensors to estimate the horizontal monopile behaviour in centrifuge <i>Matthieu Blanc, Zhong-Sen Li & Luc Thorel</i>	293
High density soil instrumentation for a thermal pile test <i>Anders Bergström, Saqib Javed & Jelke Dijkstra</i>	295
Physical Modelling of Geotechnical structure subjected to Hydraulic Scour <i>Liam Jones & Ioannis Anastasopoulos</i>	297
Distribution of temperature in culverts in cold climate <i>Karina Tommik, Jan Laue, Sven Knutsson & Nina Lintzén</i>	299
Geosynthetic reinforcement in lightly piled embankments: Laboratory model development <i>Per Gunnvard, Jan Laue & Qi Jia</i>	301
Co-seismic response of a mat-founded structure on deposits with silty-sand layers <i>April J. Bowman, Orestis Adamidis, Shideh Dashti & Ioannis Anastasopoulos</i>	303
Author Index	305

Preface

Exchange of Knowledge and experience by means of written contributions, presentations and lively discussions among researchers involved in Physical Modelling in Geotechnics is an essential part in further developing our profession. The series of European Conferences on Physical Modelling sponsored by the Technical committee (TC) 104 of the International Society of Soil Mechanics and Geotechnical Engineering (ISSMGE) fills the gap between the International Conferences on Physical Modelling in Geotechnics taking place every four years. This series has started as Conference Series on Centrifuge Modelling (Centrifuge 1988) and the scope has later been widened to geotechnical physical modelling in general. This conference series reaches its 10th event in 2022. Regional conferences were established in Europe (2008) and Asia (2012) alternating in the middle of the four year period of the international conferences.

The 4th European conference on physical modelling in Geotechnics taking place in Luleå in the north of Sweden follows its preceding ones held in London (2008), Delft (2012) and Nantes (2016). It is the first of all international and regional conferences taking place in Scandinavia and also the first taking place at a facility which does not have a geotechnical centrifuge yet. Contributions have been received from Europe but also from both Americas, Asia and Australia.

The proceedings consists of 40-reviewed full paper and 12 extended abstracts. Extended abstracts have been chosen to be a second option of contributions to allow discussion of new topics and results. Selected contributions will be invited to be published in a special edition of the International Journal on Physical Modelling. The extended abstracts are presented in a 3-minute pitch format to enhance discussion. After an inspirational talk given by Prof Malcom Bolton and a motivational talk presented by Prof Michael Davies, the other contributions are presented in 7 sessions under the heading of “Back to the basics”, “Physical modelling techniques and facilities”, “Piles installation and capacities”, “Infrastructure” and “Offshore Geotechnics”.

The participants were also supposed to enjoy the Vårvinter (Springwinter) in Luleå including self-load tests on the frozen harbour. This had to be cancelled due to the COVID 19 pandemic and the conference has to be transferred to be hybrid. We hope that everyone will take the chance to visit Luleå in winter and we promise the delegates are very welcome.

Dr.-Ing. Jan Laue
Chair of the 4th European Conference on Physical Modelling in Geotechnics
Professor in Geotechnical Engineering
Head of the Division of Mining and Geotechnical Engineering
Luleå University of Technology, Luleå, Sweden

1. Back to basics

Identification of scaling laws for the friction in centrifuge models of reinforced soil

Jean de Sauvage¹, Thierry Dubreucq¹

¹Geotechnical Engineering, Environment, Natural Hazards and Earth Sciences Department, IFSTTAR, Université Gustave Eiffel, France

Corresponding author: Jean de Sauvage (jean.de-sauvage@ifsttar.fr)

ABSTRACT: Centrifuge modelling requires the respect of scaling laws. For many phenomena, these scaling laws have been studied and described but some of them are still unresolved. For example, the scaling laws concerning the friction between the soil and an inclusion such as a nail have been only partly characterised. As long as the size of the grains is small enough in comparison with the size of the inclusion, the peak shear strength is the same as in the prototype but the scaling of the displacement needed to mobilize this strength is unknown yet. This raises issues for the modelling of reinforced soil structures.

The influence of the grains size and the roughness of the inclusion on the friction law at the soil-inclusion interface have been characterised experimentally. Mini-pull out tests have been carried out in an adapted simple shear box. These tests have been carried out in Hostun sand and with inclusions presenting various diameters and roughness. Discrete Element numerical simulations realised with the open source software Yade-DEM completed this experimental study. It allowed to study the local mobilization of the shear strength along the inclusion and to understand the micromechanical processes involved. The comparison of experimental and numerical results allows to explain the principles governing the mobilisation of shear strength in the centrifuge models of reinforced soil structures and to set the first steps towards scaling laws.

Keywords: Friction; Scaling Law; Centrifuge Modelling; Reinforced Soil.

1 INTRODUCTION

Centrifuge modelling is a cost effective way to study the behaviour of geotechnical structures. In particular, it is often used for the modelling of reinforced soil (*e.g.* Dubreucq 1999, de Sauvage 2018). However, it requires the respect of scaling laws and the ones concerning the friction between the soil and an inclusion such as a nail have been only partly characterised. As long as the size of the grains is small enough in comparison with the size of the inclusion, the peak shear strength is the same as in the prototype but the scaling of the relative displacement needed between soil and inclusion to mobilize this strength is unknown yet (Garnier *et al* 2007). The question whether the friction depends on the relative displacement or on the distortion is not sorted out. This raises issues for the modelling of reinforced soil structure. For example, the tip displacement of a soil-nailed wall is a consequence of the soil mass movement needed to mobilize shear strength along the inclusions.

Milligan and Tei (1998) have carried out a study of these scaling laws for nails in sand. They mentioned that the peak displacement did not depend on the nail diameter or length and did not depend on the vertical stress. However they noticed that the peak displacement for smooth nails was less than the half of the one measured for rough ones.

In order to confirm these observations and to observe the influence of roughness, mini-pull out

tests were carried out as well as numerical simulations using Discrete Element Method.

2 MINI PULL OUT TESTS

A simple shear test apparatus has been adapted by drilling a hole in the side of the box and fixing the load cell to a mandrel instead of the upper half box. This way, the pull out force and the nail's head displacement can be monitored under different vertical loads. The inside dimensions of the box are 139 mm x 145 mm and its height is 48.5 mm. The friction length of the rods is 144 mm and its horizontal speed is equal to 1 mm/min.

Three different surface roughness types were considered: smooth rods, threaded rods and coated rods. The last ones intended to model the grouting of prototype nails and arc-welding rods were used. They are composed of a steel core and a granular coating of 0.8 mm thickness. The roughness index R_n is defined by R_{max}/d_{50} where R_{max} is the maximal distance between peaks and valleys. Then, the measured roughness index were:

- clean smooth rods: $R_n = 0.11$
- coated rods: $R_n = 0.43$
- threaded rods: $2.40 < R_n < 4.23$

It is difficult to study the influence of the grains size without changing the behaviour of the soil. In order to investigate the size effect, it was decided to use different nail sizes. The diameters of the threaded rods were 1.89 mm, 2.86 mm and

3.83 mm. The diameters of the smooth ones were 1.98 mm, 3.01 mm and 3.97 mm and the coated ones were only found in two diameters: 3.42 mm and 4.05 mm. The coating was intact after the pull out tests. To simplify notations the rods will be named “2 mm”, “3 mm”, “3.5 mm” and “4 mm” later on.

The first experiments showed that even a very small roughness had an influence on the pull out force. The peak shear strength was higher with a lightly oxidized rod than with the same rod after cleaning through phosphorous acid even though the roughness of the oxidised one is not sensible by hand.

The surrounding soil is Hostun sand (HN38 type, $d_{50} = 109 \mu\text{m}$). A grease clog prevents the sand to pour out of the box without disturbing the rod displacement. Density is dynamically adjusted using a rubber hammer and the target volumic weight for all tests is 1480 kg/m^3 , corresponding to an 80% density index. The same person operated all the tests and the total volume of sand used allows neglecting the creation of fine particles by breakage during the successive tests. For every configuration, three different vertical stresses have been imposed: 51 kPa, 101 kPa and 153 kPa.

3 RESULTS

For each tests, the lateral friction, computed as the pull out force divided by the friction surface, was plotted against the displacement of the rod (reduced by the rod diameter). The figure 1 gives an example of such a plot.

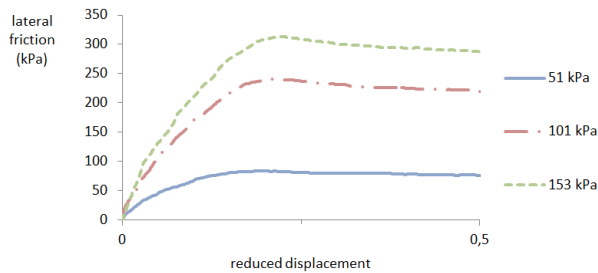


Figure 1. Lateral friction against the reduced displacement for the “4 mm” threaded rod under different vertical stresses.

The peak shear strength, q_s , is defined as the maximum of these curves. Using penetrometer tests realised by Schiavon (2016) on HN38 sand, the point resistance q_c was estimated and, for the rough rods, the relation between q_s and q_c was found to be similar to the one mentioned in the French recommendations on tiebacks (CFMS 1995).

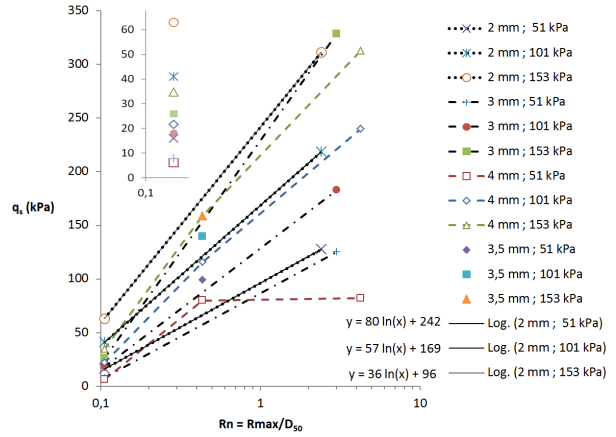


Figure 2. Lateral friction against the normalized roughness (on a logarithmic scale).

Figure 2 shows the lateral friction against the normalized roughness for all the tests performed. It can be noticed that the most significant parameter is the roughness since q_s increases linearly with the logarithm of the normalized roughness. The slope of the “ q_s against $\log(R_n)$ ” line is proportional to the vertical stress. For 2 mm rods this slope is equal to $2.3\sigma_v - 32$ with a regression coefficient $R^2=0.99$.

The diameter of rods has a relatively small influence on q_s for the rough ones but for the smooth ones, q_s is almost doubled when the diameter drops from 4 mm to 2 mm under the maximum stress 153 kPa. Furthermore, for every vertical stress, the shear strength is divided by 10 for smooth rods in comparison with the rough ones.

As mentioned before, a specific attention was dedicated to peak displacement u_p , defined as the rod displacement needed to mobilize the maximum shear strength at the interface between soil and inclusion. The figure 3 plots, for three different vertical stresses, the peak displacement reduced by the rod diameter and corrected by the elastic stretching. This correction is necessary to investigate the scaling laws ruling the sole interface friction.

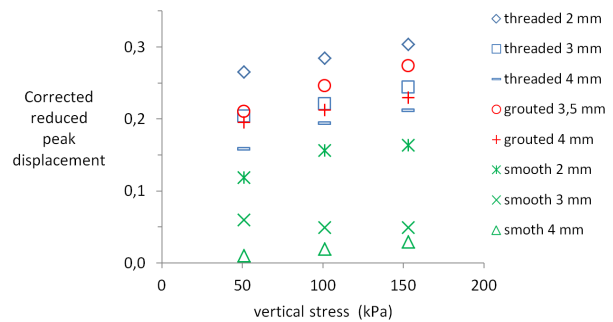


Figure 3. Corrected reduced peak displacement against the vertical stress for different rods.

For rough or coated rods, u_p increases slightly with the vertical stress imposed. The rate of this increase does not depend on the rod diameter. However, for the smooth rods, the peak displacement does not depend on the vertical stress.

Under a constant vertical stress, the reduced peak displacement increases when the diameter decreases. For example, under 101 kPa and with a threaded rod, it goes from 0.19 (4 mm) to 0.28 (2 mm). It also shows that the absolute peak displacement is not really constant as in the experiments carried out by Milligan. For the smooth rods, the influence of diameter is much more significant.

To consider the scaling laws, one must keep in mind that, with prototype nails (diameter ≈ 10 cm) in sand, the order of magnitude of the peak displacement in pull-out tests is 1 cm (Schlosser *et al* 1993).

Eventually, the vertical displacement of the actuator imposing the vertical load has been also monitored but the values were extremely small, *i.e.* less than 0.05 mm.

4 NUMERICAL SIMULATIONS

To extend the numerical study and to understand the micromechanical processes underlying the friction behaviour of the soil-inclusion interface, it was decided to use the Discrete Element Method, called DEM later on, and described by Cundall and Strack (1979). The open-source framework Yade (Šmilauer *et al* 2015) provided a powerful tool. This method gives access to data that are difficult to obtain in an experimental work such as the rotation of particles.

Yade offers a great choice of grains shapes and size distributions as well as a big variety of mechanical behaviours. In order to limit the computation time, the first model was realised with spheres and their behaviour was supposed elastic-frictional. The Young modulus of the grains was chosen to be 80 GPa. This value is an average of the values used in the literature, ranging from 56 GPa to 113 GPa. Their friction angle is 30° .

The setting of the initial state is a critical step in every DEM simulation since the arrangement and interlocking of the granular assembly can deeply affect the final measures. In this case, a box was formed of fix rigid facets to contain the grains, a *wall* type element was placed on the top to impose a vertical stress later on and the nail was realised with *Pfacet* type elements. The size of the box was chosen to be 1 cm x 1 cm x 1 cm. Then the pack of grains was set up using the *randomDensePacking* function. The target void ratio was then obtained

with a Radius-Expansion Friction-Decrease approach (Chareyre and Villard 2002).

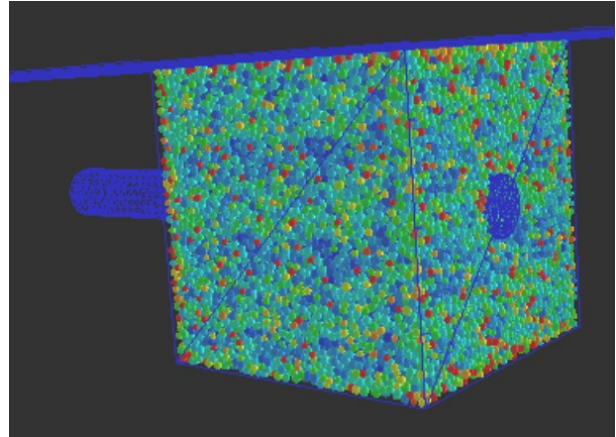


Figure 4. View of the initial step of the DEM simulation

The choice made to realise the initial state does not model the sand pouring usually used for the preparation of samples in centrifuge modelling but is a good way to create a random pack with a desired density index.

When the sample is ready, a downward velocity is prescribed to the *wall* type element until the desired vertical stress is reached. Eventually a prescribed horizontal velocity is prescribed to the nail. At each step, the sum of forces and moments acting on each grain is computed based respectively on relative displacement or overlapping with respect to the contact point and relative rotations and their acceleration is deduced. In a schematic way, on contact points, the contact normal forces are due to the elasticity of the grains and the tangential ones are related to the normal ones by the friction law. For more details, one can see the documentation on the contact formulation *Law2_ScGeom_FrictPhys_CundallStrack*.

The nail geometry was designed on GMSH (Geuzaine and Remacle 2009) and imported as an STL file. It allowed assigning a geometrical roughness. There is no interaction between the nail and the box and, therefore, the only force exerted on the nail is due to the grains. Note that there is no friction between the grains and the box or the *wall*.

The figure 5 is an example of plotting the pull out force against the displacement for a test carried out with a rough rod. The values cannot be compared to the ones in the experimental tests, partly because of the simple assumptions made on the shape and size distribution of grains. It can also be noticed that no decrease in the pull out force is observed after the peak strength is reached. On the example presented, the decrease is only due to the finite length of the nail: after 4 mm, the tail of the nail enters in the volume observed.

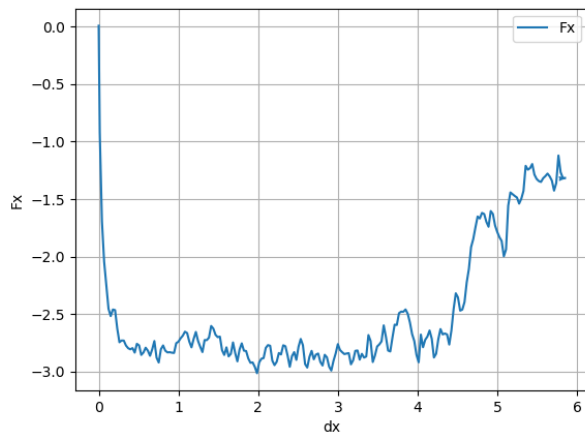


Figure 5. Pull out force (N) against the nail displacement (mm) for a rough rod.

However, the tendencies observed in the experimental tests are confirmed and the peak displacement increases with the roughness.

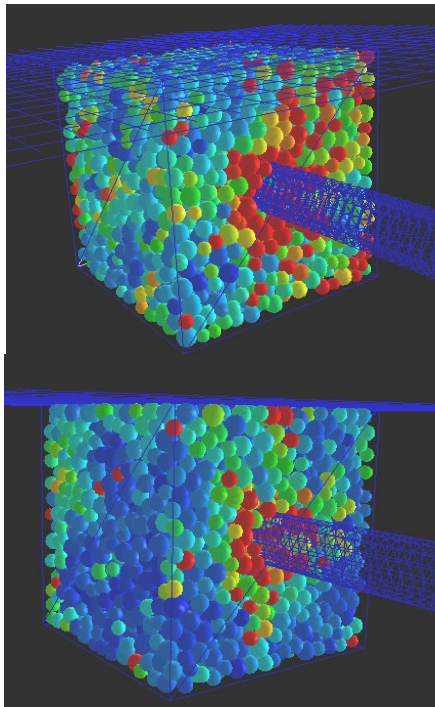


Figure 6. Visualization of rotated particles (in red) for a rough rod (top) and a smooth one (bottom)

The figure 6 presents the two simulations realized with a smooth rod and a rough one. The particles are coloured according to their rotations: the red ones are the most disturbed ones. This visualization suggests that the rough rod mobilizes a bigger volume of sand. This could explain the differences observed regarding the peak displacements.

5 CONCLUSION

The experimental tests here presented need to be confirmed with other soils or particle size

distribution cuts-off. However, they already show a minor divergence with the results of Milligan and Tei. More important, they clearly point the strong influence of the roughness on the peak displacement value. In order to find the scaling laws ruling the friction at the interface between soil and inclusion, a careful study of roughness has to be carried on.

The DEM simulations presented are quite simple and cannot pretend to highlight all the phenomena underlying the friction behaviour but they already show their potential to explain the scaling of interface friction.

6 ACKNOWLEDGEMENTS

The authors want to acknowledge Christophe Roppert and Minh-Tan Do from the Materials and structures Department in IFSTTAR, University Gustave Eiffel. They did the roughness measurements.

7 REFERENCES

- CFMS. 1995. *Recommandations Tirants d’Ancrage TA 95 (Ground Anchor Recommendations)*. Eyrolles, Paris, France.
- Chareyre, B. and Villard, P. 2002. Discrete element modeling of curved geosynthetic anchorages with known macro-properties. *In Proceedings of the First International PFC Symposium*, pp 197-203.
- Cundall, P. A. and Strack, O. D. L. 1979. A discrete numerical model for granular assemblies. *Geotechnique* **29**(1) : 47-65.
- Dubreucq, T. 1999. *Renforcement des fondations superficielles par inclusions planes horizontales extensibles quelques effets de taille dans le frottement sable-inclusion*. PhD thesis, École Nationale des Ponts et Chaussées.
- Garnier, J. *et al* 2007. Catalogue of scaling laws and similitude questions in geotechnical centrifuge modelling, *International Journal of Physical Modelling in Geotechnics*, **7**(3) : 01-23.
- Geuzaine, C. and Remacle, J.-F. 2009. Gmsh: a three-dimensional finite element mesh generator with built-in pre- and post-processing facilities. *International Journal for Numerical Methods in Engineering* **79**(11) : 1309-1331
- Milligan, G. W. E. and Tei K. 1998. The pull-out resistance of model soil nails. *Soils and Foundations*, **38**(2) : 179-190.
- de Sauvage, J. 2018. *Étude du comportement des murs de soutènement par clouage des sols en place : application au dimensionnement du parement*. PhD thesis, ENTPE.

Schiavon, J.A. 2016. Behaviour of helical anchors subjected to cyclic loadings. PhD thesis. École centrale de Nantes, Universidade de São Paulo.

Šmilauer, V. *et al*, 2015. Yade documentation 2nd ed (The Yade Project), <http://yade-dem.org/doc/>

Schlosser, F. *et al*, 1993. Recommendations Clouterre 1991, French national research project Clouterre (English translation), Presses de l'ENPC, Paris.

Silty sand characterization in the geotechnical centrifuge

Varvara Zania¹, Sine Maria Christensen¹, Irene Rocchi¹

¹*Civil Engineering Department, Technical University of Denmark, Denmark*

Corresponding author: Varvara Zania (vaza@byg.dtu.dk)

ABSTRACT: The geotechnical characterization of soil deposits from piezocone data can be quite challenging when it comes to intermediate soils, like silty sand. There are well established and widely used empirical correlations for the characterization of cohesionless and cohesive soils, however there are still open questions when it comes to the interpretation of piezocone measurements for silty sand deposits. This study aims at improving the understanding of the mechanical behavior of silty sand. In order to do so cone penetration tests with pore pressure measurement at the shoulder of the penetrometer were performed on silty sand samples in the geotechnical centrifuge. After a literature review on the current sample preparation methods, the moist tamping method with under compaction has been employed to ensure a homogeneous silty sand sample. Three samples have been prepared at 23%, 33% and 55% fine content (non plastic). The stress level effect has been studied by performing CPTUs at different g levels. In addition, the CPTU results were interpreted to evaluate strength parameters of the soil. Element triaxial tests were carried out and the results were compared with the interpretations of the CPTU data. Sieve analysis indicate that the reconstituted samples were homogeneous and uniform, except from the low fine content sample which was over compacted at larger depths. The interpretation methods are capturing the classification of soil type but underestimate the fine content for the silty sand with non plastic fines. The results indicate higher peak angle of friction at higher fine content, which is consistent in both empirical correlations and triaxial test results.

Keywords: Silty Sand; CPTU Interpretation; Soil Classification; Fine Content; Peak Friction Angle.

1 INTRODUCTION

Cone penetration testing (CPT) is one of the most common methods for ground profiling and soil characterization. In the past decades, several publications have contributed to the interpretation of CPTs, while the main categorization with respect to the mechanical behaviour has been to coarse-grained and fine-grained soils (Robertson, 1990). A unified approach has been suggested lately based on integrated contours on the normalized soil behaviour charts (Robertson, 2009). There are well-established and widely used empirical correlations for the characterization of cohesionless and cohesive soils (Robertson and Cabal, 2015, Lunne et al. 1997). Nevertheless, the interpretation of piezocone measurements for silty sand deposits can be quite challenging, as for the transitional soils it depends on the penetration rate, the fine content and the plastic behaviour (Martinez et al, 2018). This has led to approximate conservative suggestions for the angle of friction of silty sands, like a decrease by 3° of the equivalent angle of friction of the clean sand (EN1997-2, 2007) or even a value of 32° is suggested for low-risk projects (Robertson and Cabal, 2015).

Due to the wide application of CPTs in field testing, design methods for geotechnical problems like bearing capacity of foundations and liquefaction assessment have been developed on the basis of the normalized tip resistance (Kulhawy and

Mayne,1990, and Robertson and Cabal, 2015). As silty sand deposits can be vulnerable to earthquake loading, their characterization is very important (Han et al, 2016).

The aim of this study is to provide further insight into the mechanical behaviour of silty sand. A laboratory investigation would require the reconstitution of silty sand samples; hence it is pertinent to first describe the available sample preparation methods, their applicability in the centrifuge and other relevant drawbacks. After the identification of an appropriate reconstitution method, silty sand samples have been prepared at different fine contents and CPTUs have been performed in the geotechnical centrifuge. The effect of the stress levels was examined by the application of different centrifugal acceleration. Samples were retrieved from the strongbox, and sieve analysis and triaxial tests at similar confinement stresses were carried out in order to compare and evaluate the interpretation methods for silty sand characterization.

2 SAMPLE PREPARATION METHODS

The reconstitution of a soil sample in the laboratory is expected to provide specimens with densities ranging from loose to dense as found at its natural deposit. A homogeneous sample, without particle segregation must also be uniform, which can be assessed by the void ratio throughout the sample

(Huang et al. 2015). Hereafter an overview of the available methods for preparation of silty sand samples is provided, and then the adopted procedure in the current study is described.

2.1. Literature review

Reconstituted silty sand samples can be prepared in the laboratory by one of the following methods: (a) dry or moist tamping (Amini & Qi, 2000, Kim et al. 2014, Ladd, 1978), (b) dry/wet/mist pluviation (Lo Presti et al., 1992, Huang et al., 2015), and (c) slurry deposition (Silva, 2009, Suzuki, 2015).

Dry or moist tamping is carried out by sequential compaction of layers of given thickness with a specified force and frequency of tamping. A sample prepared with the use of moist tamping method is partially saturated, and can be loose to dense. The capillary tension forces, which are present during the process allow the construction of a much looser sample, than other methods, such as pluviation, (Kuerbis & Vaid 1988). A modification of the tamping method was reported by Ladd (1978) named the under compaction method, which minimised the particle segregation for samples with a wide range of particle sizes and produced homogeneous samples. The principle of under compaction is to increase the compaction for each new layer applied i.e. the first layer is lightly tamped, and the tamping is gradually increased with increasing number of layers.

Dry (or air) pluviation and wet (or water) pluviation are similar techniques. The material is poured dry into a sample container and either deposited dry or in water. In the dry pluviation, the fall height of the particles affects the relative density of the sample. This is due to the energy at which the particles are deposited. Furthermore, the void ratio and thereby density of the sample is also influenced by the funnel size used for pluviation. A homogeneous specimen of well-graded soil without particle segregation is difficult to obtain with the dry pluviation method. This is attributed to both the pluviation of sediments and the following saturation (Kuerbis & Vaid 1988). Lo Presti et al. (1992) reported also particle segregation by assessing the particle size distribution of subspecimens from a constructed specimen. It was observed, that the finest particles were concentrated in the bottom of the specimen after vibration, which was applied to obtain a denser specimen.

The mist pluviation method is carried out like the air pluviation, but the soil material falls through a mist zone, where the soil particles are mixed with water droplets. The mist pluviation method was evaluated by a series of triaxial tests and the determination of water content and spatial variation

of fines content by slicing the specimen into five equal layers. It was concluded that the method of mist pluviation is able to produce homogeneous silty sand specimens, as described by Huang et al. (2015).

Kuerbis & Vaid (1988) evaluated how to prepare well graded or silty sand samples, such that particle segregation is avoided. They proposed the slurry deposition method, which was further developed by Carraro & Prezzi (2008). In the first version of the slurry deposition method by Kuerbis & Vaid (1988), the fines and sand are prepared as two separate slurries and poured into a mixing tube. In the newer version by Carraro & Prezzi (2008) the fines and sand are mixed dry in a closed container until the mass is homogeneous, before pouring it into a tube half filled with deaired water through a funnel, afterwards making it a slurry by shaking and rotating the closed tube for at least 20 minutes, removing air bubbles and topping up with deaired water when necessary. The mixing tube is placed in the triaxial apparatus allowing the particles to settle for around 20 minutes, before the tube is moved up.

Silva (2009) studied the rate effect of silica silt when conducting miniature CPT in the centrifuge. The silica flour samples were prepared by mixing it as a slurry having a water content of 120%. The slurry was poured into the sample container, but it was observed that the finest silt particles were deposited at the surface of the sample due to particle segregation.

2.2. Soil samples

The literature review has indicated that the moist tamping and the mist pluviation methods can reportedly produce homogeneous silty sand reconstituted samples without particle segregation. In the current study, due to the limitations regarding the application of the mist pluviation method in the centrifuge, the moist tamping method with under compaction was employed.

The soil sample was prepared sequentially in 4 layers, with a target thickness of approximately 4cm each, according to the procedure described hereafter. Fontainebleau sand and silica flour, which have reportedly 2% and 84% fine content respectively (according to their particle size distribution curves), were mixed firstly in dry state in pre-calculated ratios to provide different values of target fine content. The homogeneous soil mass was then mixed again thoroughly with water corresponding to 12% water content. The silty sand mixture was placed in the strongbox, on top of a pre compacted saturated coarse sand layer 145mm thick, which was covered by a geotextile filter. The coarse sand layer was placed in the bottom of the

sample container to allow a uniform flow of water through the sample during the saturation phase. The thickness of the coarse sand layer was measured before each sample preparation, and there was no further compaction observed.

Each layer of silty sand was compacted by placing a steel circular plate on the soil surface and using a proctor hammer. The weight block on the hammer had a mass of 2.5kg and the fall height was 30cm, this is equal to a potential energy of 7.36J. The steel plate was placed on top of the sample to distribute the compaction force evenly on the entire surface of the soil. After the layer was compacted the surface was scarified, before applying the next layer, to ensure continuity in the interface between layers. The layers were tamped according to the under compaction method, which means that the tamping of the layers was gradually increased. All samples were saturated with deaired water. The water flow was induced from the bottom of the container, while the hydraulic gradient was controlled through a standpipe. The duration of the saturation increased with the fine content from 5h to 24h. A water level of 2cm above the soil surface was maintained after the sample was prepared. The water level ensured that the cone tip would be submerged in water and therefore the pore pressure transducer would be kept fully saturated during the acceleration of the centrifuge.

After the centrifuge testing, samples were taken from the undisturbed part of the container for both sieve analysis and triaxial testing. The sieve analysis of samples from the top and the bottom of the silty sand and from the triaxial samples after testing were consistent indicating a homogeneous sample. The fine content was estimated based on both ISO 17892-4 (2016) and ASTM D2487 (2017) standards. The properties of the prepared silty sand samples are reported in Table 1.

Table 1. Properties of the silty sand samples prepared for the centrifuge CPTUs.

Sample	MT1	MT2	MT3
Bulk unit weight, γ_1 (kN/m ³)	19,7	19,5	19,9
Bulk unit weight, γ_2 (kN/m ³)	19,8	19,5	19,7
Fine content (ISO 17892-4)	23,4	32,8	54,8
Fine content (ASTM D2487)	22,9	31,8	54,5
Layer thickness (mm)	162	170	175
Layer thickness end (mm)	147	165	165

The bulk unit weight has been calculated based on both overall measurements of mass and volume in the strongbox (γ_1) and from the samples for triaxial testing (γ_2), and the two values are very close and indicate a dense silty sand sample. It has to be noted that the thickness of the silty sand layer decreased

during the spinning of the centrifuge. The consolidation was not monitored, only the final thickness was measured at the end of the test. Table 1 reports the thickness of the silty sand sample before the centrifuge tests and after the end of testing. The overall settlement was between 5% and 10% of the layers thickness depending on the fine content.

3 CENTRIFUGE TESTING

All the centrifuge tests were conducted in the 2.5m radius geotechnical beam centrifuge at DTU. A load frame was mounted on top of the strongbox with four bolts. Afterwards, the centrifuge was accelerated and a constant rotational speed was maintained equivalent to 50g and 70g. The mini penetrometer used for the centrifuge CPTUs has an apex angle equal to 60°, a diameter (B) of 11.3mm and a net cone area ratio equal to 0.55. In flight CPTUs were carried out at two locations for each g level, keeping a distance of at least 6B between them. The piezocone was installed at a velocity of 1.33mm/s to a penetration depth of about 120 to 140mm in order to avoid any boundary effects arising from the proximity to the geotextile. To minimise boundary effects, the CPTUs were undertaken at a minimum distance of 150mm from the strongbox boundaries. The pore pressure transducer of the mini penetrometer was calibrated after inflight penetration tests on clean water. The tip resistance and sleeve friction is measured by strain gauges on a full bridge connection, which were calibrated on axial loading against a reference calibrated load cell on the data logging system of the centrifuge.

4 RESULTS AND DISCUSSION

The tip resistance, sleeve friction and pore pressure measurements are presented hereafter. At first one g level is discussed and then normalized responses for both examined stress levels.

The tip resistance for the three samples is shown in Figure 1. It can be noticed, that the tip resistance of the sample with the lower fine content indicates increasing strength with depth, with a clear indication of change of slope at the interface of the two intermediate compaction layers (80mm depth). This highlights that the all the layers beyond the uppermost one were overcompacted. On the other hand, the tip resistance of the samples with higher fine content shows that the silty layer is homogeneous without any variations or contrasts around the interfaces of the compaction layers. Furthermore, any effect of the fine content on the tip resistance is hardly noticed at shallow depth;

however beyond 40mm penetration the tip resistance increases with higher fine content.

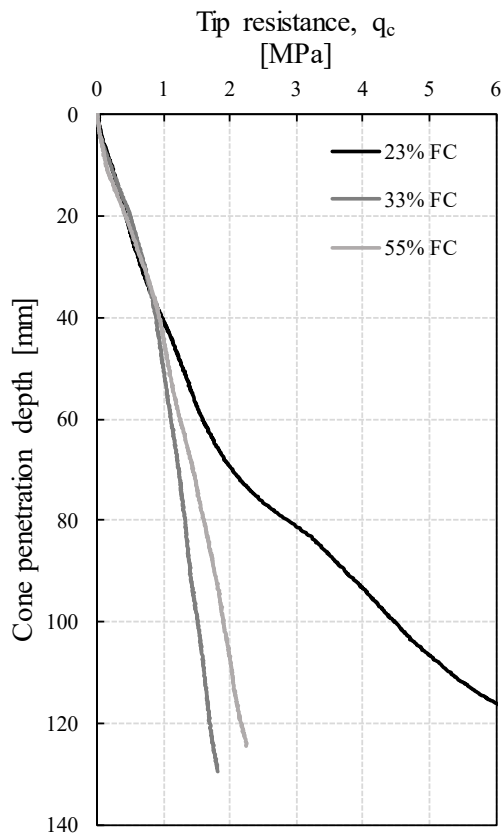


Figure 1. Tip resistance variation with depth at 50g for three silty sand samples.

pressure measurement was zeroed along with all the sensor readings before each cone penetration.

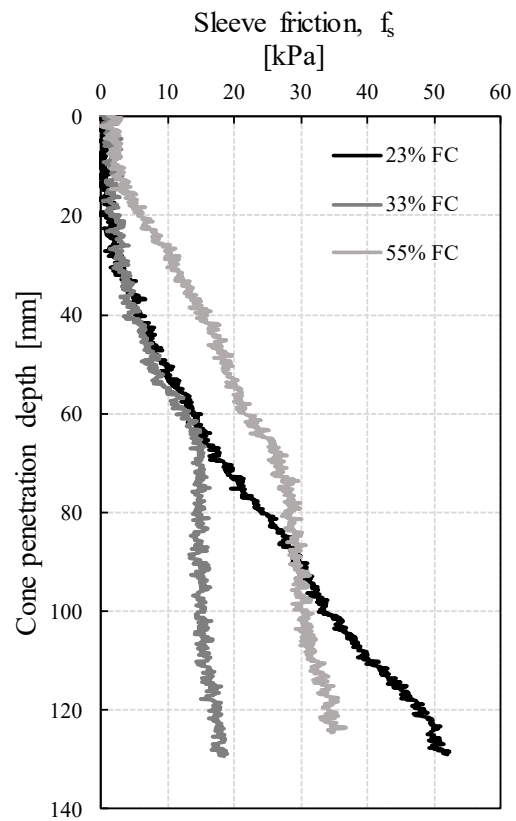


Figure 2. Sleeve friction variation with depth at 50g for three silty sand samples.

The sleeve friction for the three samples is presented in Figure 2. The sleeve friction is gradually mobilized as the sleeve of the cone penetrates into the soil layer, providing reliable estimates beyond 55mm depth. It is observed that the sleeve friction for the samples with 23% and 33% fine content are in agreement at shallow depths (up to approximately 40mm which corresponds to the uppermost and last compacted layer), while only the sample with 55% fine content attains higher sleeve friction. Nevertheless, the sleeve friction at deep penetration in the silty sand with 23% fine content is also showing higher resistance indicating a non homogeneous sample, denser at larger depths. The sleeve friction for both samples at 33% and 55% fine content has a similar trend of increase with depth and a change in slope at about 65mm penetration depth. The sleeve friction attains always higher values at the higher fine content.

The pore pressure measurements show initially a very low response, which can be explained by the fact that the pore pressure transducer is located at the shoulder of the cone, hence reliable pore pressure measurements are obtained at a penetration depth greater than the width of the cone. The pore

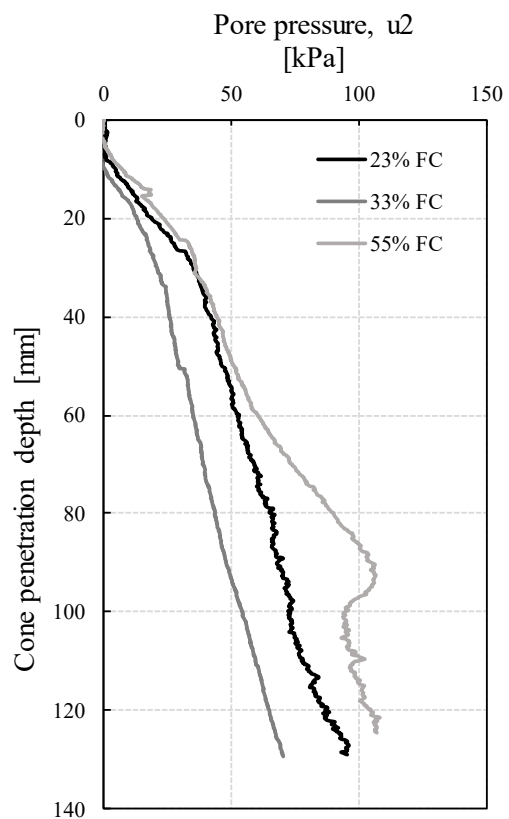


Figure 3. Pore pressure variation with depth at 50g for three silty sand samples.

Higher pore pressure are recorded at the 55% fine content sample, presumably as a result of the increased fine content. There is not consistent increase of pore pressure with fine content as the sample with the lowest fine content exhibits higher pore pressures than the sample with 33% fine content. The variation with depth of the pore pressure is similar for all three tests presented here, except from a slight change of slope between 70mm and 100mm for the higher fine content. This was not recorded in any other CPTU carried out in the same sample.

During the retraction of the cone pore pressures were measured and were equal to the hydrostatic for all the tests presented here. It is concluded that the reconstituted silty sand samples were homogeneous and uniform, apart from the sample with the lowest fine content, which is deemed comparable with the remaining samples only up to a depth equal to 40mm.

4.1. Effect of stress level

The effect of the stress on the cone penetration has been evaluated by comparing the normalised tip resistance with the vertical effective stress at two different g levels as shown in Figure 4. It is noticed that the trends of the variation of the normalized tip resistance, are not influenced significantly by the stress level. On the other hand, the low fine content sample appears to have a continuously increasing resistance as a result of the overcompaction of the deeper layers.

The critical depth, which is defined as the penetration where the normalised tip resistance becomes constant (Bolton et al, 1999), appears to be slightly influenced by the stress level. On the other hand it is affected by the fine content, increasing from $z/B=2$ to $z/B=4$ for 33% and 55% fine content respectively. Considering that the penetration up to 40mm depth, can be reliable for the sample with 23% fine content, the effect of the fine content on the peak response can be evaluated. It is observed that the peak normalized cone resistance is not monotonically related to the fine content. The peak normalized tip resistance is lower at the higher g level regardless of the fine content. It also appears that the stress exponent is dependent on the g level for the silty sands with 33% and 55% fine content, and more specifically it is expected to be higher at 70g compared to 50g.

The excess pore pressure normalized with the vertical effective stress is plotted with the

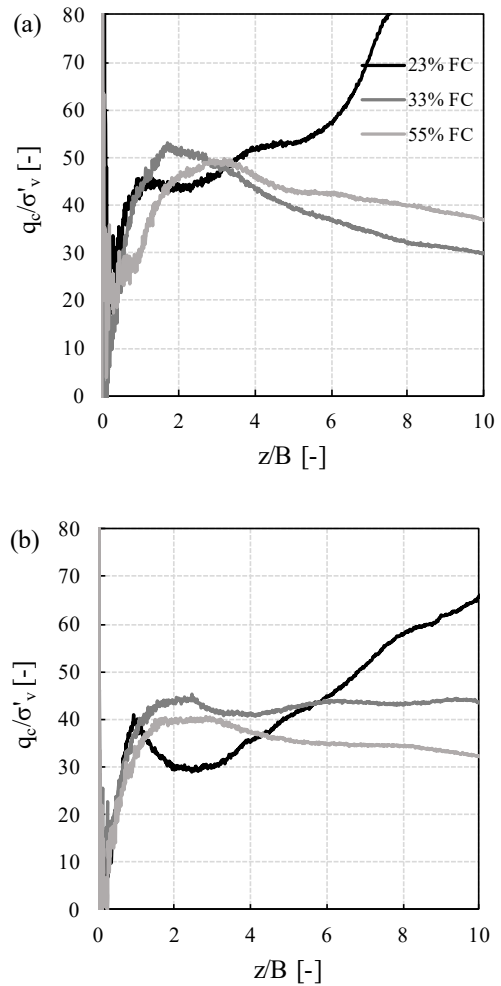


Figure 4. Normalized tip resistance with normalized depth at (a) 50g and (b) 70g for three silty sand samples.

normalized depth in Figure 5 for the three silty sand samples at two g levels. Pore pressure built up develops for all the experiments after the cone was fully embedded in the silty sand, observed as change in slope at about $z/B=1$. The variation appears to keep increasing up to a depth of $z/B=2$ for most tests and exhibit a fairly constant value thereafter. The slight inclination at greater depths can be related with the different stress normalization exponent as also in the case for the normalized tip resistance (see Figure 4). Irrespectively of the g level the normalized excess pore pressure decreases with decreasing fine content. Moreover, it seems that the silty sand with 33% fine content has an almost drained response at z/B greater than 4 with the excess pore pressure being less than 10% of the vertical effective stresses. On the other hand, the silty sand sample at 55% fine content exhibits excess pore pressure larger than 50% of the vertical effective stresses.

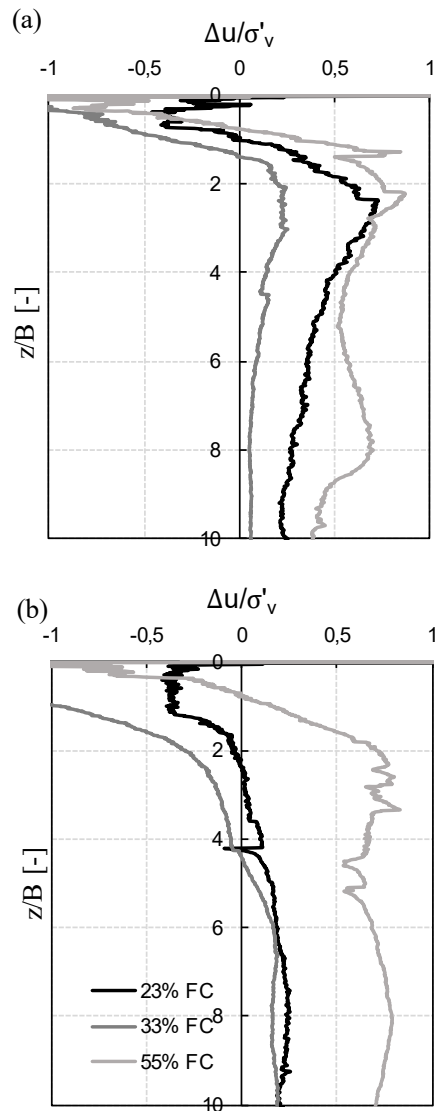


Figure 5. Normalized excess pore pressure with normalized depth at (a) 50g and (b) 70g for three silty sand samples.

4.2. CPT based soil characterization

The centrifuge CPTUs were interpreted based on existing soil classification and characterization schemes. In Figure 6 normalized cone resistance is plotted with respect to the normalized friction ratio for all samples at 50g and 70g. The soil classification according to the unified soil behaviour type approach suggested by Robertson (2009) is also shown. It is evident that the results of the sample with the low fine content are unreliable especially at 70g. This is due to the high sleeve friction recorded in this particular test. The recorded sleeve friction in this experiment showed an erratic response with an increase for every subsequent penetration of the cone. The results of the low fine content at 50g show an increase of the normalised tip resistance as the penetration progressed to the deeper more compacted layers. Overall all the samples are characterized as ‘Sand mixtures: silty sand to sandy silt’ in regards with the soil behaviour

type, which is in agreement with the soil sample composition.

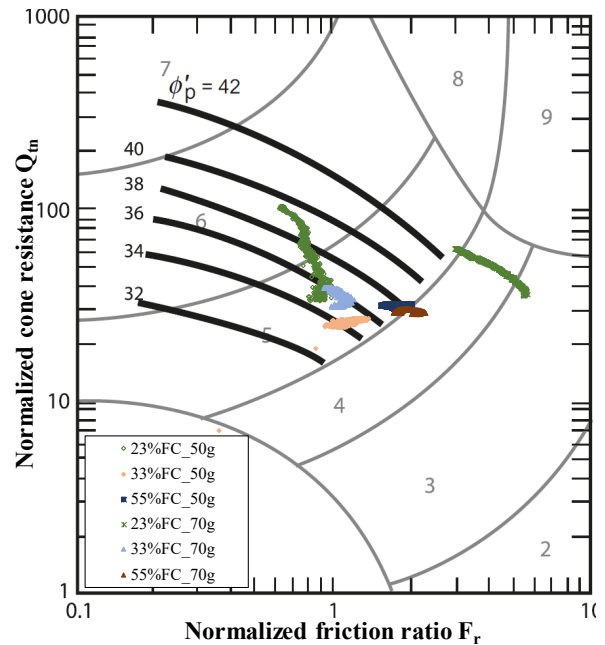


Figure 6. Normalized tip resistance with normalized friction ratio for three silty sand samples. Classification scheme with soil behaviour type zones based on Robertson 2009.

The soil behaviour type index I_c which is essentially the radius of concentric circles that define the boundaries of the soil type was defined by Robertson (2009) as:

$$I_c = [(3,47 - \log Q_t)^2 + (\log F_r + 1,22)^2]^{0,5} \quad (1)$$

where Q_t is dimensionless cone resistance, and F_r is the friction ratio.

Table 2 presents a summary of estimated parameters for soil classification and characterization. The I_c obtained for each one of the tests are also reported. It is noticed that the CPTU of the sample with 33% fine content exhibits a slight decrease of the I_c with the increase of the stress level. It has been suggested that there is a link between the compressibility of soil and the I_c , which would indicate a less compressible silty sand at higher stress levels. The stress dependency is also represented by the stress normalization exponent, which was defined by Robertson (2009) as:

$$n = 0,38I_c + 0,05 \left(\frac{\sigma'_{v0}}{p_a} \right) - 0,15 \quad (2)$$

where σ'_{v0} is the vertical effective stress, and p_a is the atmospheric pressure. This expression predicts decrease of the exponent with the increase of the g level for the sample with 33% fine content and the opposite for the sample with the higher fine content. Nevertheless, the centrifuge CPTUs have provided

a trend of increasing exponent with fine content at low stresses and higher stress exponents at higher stress level. The stress exponent provided by Equation 2 is in agreement with the centrifuge CPTUs only for the higher fine content.

The fine content can also be estimated based on I_c according to the following expression:

$$FC = 1,75I_c^{3,25} - 3,7 \quad (3)$$

where I_c is the soil behaviour type index. Recent studies suggest that current correlations appear to underestimate the fines contents (Yi, 2014). This is in accordance to the findings of the centrifuge CPTUs. As seen in Table 2 the calculated fine content is lower than the resulting of the sieve analysis reported in Table 1.

The drained peak friction angle was estimated based on four different methods:

(a) the expression by Robertson and Campanella (1983):

$$\tan\phi' = \frac{1}{2,68} \left[\log \left(\frac{q_c}{\sigma'_{v0}} \right) + 0,29 \right] \quad (4)$$

where q_c is the cone tip resistance and σ'_{v0} is the vertical effective stress.

(b) the expression by Kulhawy and Mayne (1990):

$$\phi' = 17,6 + 11 \log \left[\left(\frac{q_c}{p_a} \right) / \left(\frac{\sigma'_{v0}}{p_a} \right)^{0,5} \right] \quad (5)$$

where σ'_{v0} is the vertical effective stress, q_c is the cone tip resistance and p_a is the atmospheric pressure.

(c) the NTH method as suggested by Senneset et al. (1989) and Mayne and Ouyang (2018)

and (d) the peak friction angle contours on the normalized soil behaviour type chart by Robertson (2009).

Table 2. Interpretation of mechanical properties of the silty sand samples.

Sample	MT1 50g	MT2 50g	MT2 70g	MT3 50g	MT3 70g
I_c (eq.1)	1,7-2,1	2,4	2,2	2,4	2,5
n (eq.2)	0,58- 0,66	0,75- 0,78	0,73- 0,74	0,77- 0,79	0,82- 0,83
n (Fig.4)		0,55	0,95	0,77	0,85
FC (eq.3)	6-12	18-20	15-16	19-21	22-23
ϕ' (eq.4)	37-42	33-35	35	35	34
ϕ' (eq.5)	33-40	32	33-35	33	33
ϕ' NTH	>40	34-36	36-37	36-37	37
ϕ' TRX	34	30	-	39	39

Triaxial tests were carried out at confinement stress equal to 60kPa corresponding to the vertical effective stress at the middle of the silty sand layer. The shearing rate was slow enough to ensure fully drained conditions. The estimated values of the angle of friction from the CPTU interpretation and those derived from the triaxial tests are reported in Table 2. The range of friction angles provided for the sample with the low fine content is quite wide as expected from the increase of the normalized tip resistance which resulted from the over compaction of the deeper layers. The NTH method provides consistently higher values compared to those by Eq. 4 and 5. It should be mentioned that the normalised excess pore pressure (B_q) has a very low value ranging from 0,01 to 0,04 at 33% and 55% fine content respectively. These three methods do not appear to capture any effect of the fine content on the peak friction angle. However, an increase of the peak friction angle with the increase of the fine content was obtained in the triaxial tests, which was related to change from contractive (33% fine content) to dilative (55% fine content) behaviour. The sample with 55% fine content had a dilation angle equal to 13°. The increase of the peak friction angle with the higher fine content is also captured in the last method (Robertson, 2009) as shown in the contour plots in Figure 6.

5 CONCLUSION

An experimental study in the geotechnical centrifuge was performed aiming to provide some insight into the mechanical behaviour of silty sands. Homogeneous samples were reconstituted with the wet tamping method using under compaction, however only the samples with higher fine contents were uniform. The classification of the samples was in accordance to the anticipated soil behaviour. However, the fine content was underestimated by current methods. The peak friction angle was found to increase with the increase of the fine content.

6 ACKNOWLEDGEMENTS

The assistance of MSc student Efthymios Panagiotis in the centrifuge and triaxial experiments and the support of the technical personnel at DTU is gratefully acknowledged.

7 REFERENCES

Amini, F., & Qi, G. Z. 2000. Liquefaction testing of stratified silty sands. *Journal of Geotechnical and Geoenvironmental Engineering*, **126**(3): 208–217.

- ASTM D2487-17 2017. Standard Practice for Classification of Soils for Engineering Purposes (Unified Soil Classification System), ASTM International, West Conshohocken, PA.
- Bolton, M. D., Gui, M. W., Garnier, J., Corté, J. F., Bagge, G., Laue, J. & Renzi, R. 1999. Centrifuge cone penetration tests in sand. *Géotechnique*, **49**: 543–552.
- Carraro, J. A. H. & Prezzi, M. 2008. A New Slurry-Based Method of Preparation of Specimens of Sand Containing Fines. *Geotechnical Testing Journal*, **31**(1).
- DS/EN ISO 17892-4 (2016), Geotechnical investigation and testing - laboratory testing of soil - part 4: Determination of particle size distribution.
- EN 1997, 2007, Eurocode 7: Geotechnical design - Part 2: Ground investigation and testing, Danish Standards.
- Han, J.-T., Kim, T. & Cho, W. 2016. Centrifuge modeling of seismic response of normally consolidated deep silt deposit. *Acta Geotechnica*, **11**(1): 71–81.
- Huang, A.-B., Chang, W.-J., Hsu, H.-H. & Huang, Y.-J. 2015. A mist pluviation method for reconstituting silty sand specimens. *Engineering Geology*, **188**: 1–9.
- Kim, J. H., Kim, S. R., Lee, H. Y., Choo, Y. W., Kim, D. S. & Kim, D. J. 2014. Miniature cone tip resistance on silty sand in centrifuge model tests. *Physical Modelling in Geotechnics*, 1301–1306.
- Kuerbis, R. & Vaid, Y. P. 1988. Sand Sample Preparation - The Slurry Deposition Method. *Soils and Foundations*, **28**(4): 107–118.
- Kulhawy, F. & Mayne, P. 1990. Manual on estimating soil properties for foundation design.
- Ladd, R. S. 1978. Preparing test specimens using undercompaction. *Geotechnical Testing Journal*, **1**(1): 16–23.
- Lo Presti, D., Pedroni, S. & Crippa, V. 1992. Maximum dry density of cohesionless soils by pluviation and by ASTM d 4253-83: A comparative study. *Geotechnical Testing Journal*, **15**(2): 180–189.
- Lunne, T., Robertson, P.K., & Powell, J.J.M., 1997. Cone penetration testing in geotechnical practice. Blackie Academic, EF Spon/Routledge Publ., New York.
- Martínez, M., Tonni, L., Gottardi, G. & Rocchi, I. 2018. Analysis of CPTU data for the geotechnical characterization of intermediate sediments. *In Cone Penetration Testing 2018 : Proceedings of the 4th International Symposium on Cone Penetration Testing*, CRC Press, pp. 281–287.
- Mayne, P. & Ouyang, Z. 2018. Calibrating NTH method for -' in clayey soils using centrifuge CPTu, in 'Proceedings of the 4th International Symposium on Cone Penetration Testing'.
- Robertson, P.K. & Campanella, R.G. 1983. Interpretation of cone penetration tests. Part I: sand. *Canadian Geotechnical Journal*, **20**(4): 719–733.
- Robertson, P. K. 1990. Soil classification using the cone penetration test. *Canadian Geotechnical Journal*, **4**, 151–158.
- Robertson, P. K. 2009. Interpretation of cone penetration tests – a unified approach. *Canadian Geotechnical Journal*, **46**, 1337–1355.
- Robertson, P. K. & Cabal, K. 2015. Guide to Cone Penetration Testing for Geotechnical Engineering, 6th edn, Gregg Drilling & Testing, Inc.
- Senneset, K., Sandven, R. & Janbu, N. 1989. Evaluation of soil parameters from piezocone tests, *Transportation Research Record*, No. 1235, 24–37.
- Silva, M. 2009. Rate effects in centrifuge piezocone penetration on dilatant silica silt and subsequent dissipation. *Australian Geomechanics Journal*, **44**, 19–28.
- Suzuki, Y. 2015. Investigation and interpretation of cone penetration rate effects, PhD thesis, The University of Western Australia.
- Yi, F. 2014. Estimating soil fines contents from CPT data. *In Proc. 3rd International Symposium on Cone Penetration Testing*, Huntington Beach, Las Vegas, Nevada, USA, pp. 949-955.

The effects of sand grading on the bearing capacity of surface foundations

Mathias R. Jensen¹, Varvara Zania¹, Barry M. Lehane²

¹*Civil Engineering Department, Technical University of Denmark, Denmark*

²*Civil Engineering Department, University of Western Australia, Australia*

Corresponding author: Varvara Zania (vaza@byg.dtu.dk)

ABSTRACT: The bearing capacity of surface foundations in cohesionless soil has been studied extensively in the past decades. Experimental investigations have shown that particle size effects in the bearing capacity problem are associated not only with strength mobilization but also with the shear band thickness. Centrifuge testing can provide useful insights, especially when taking into consideration the scale effects, by using a modelling of models approach. This paper describes the results of a systematic study examining the effects of sand grading on the responses of surface footings. Four different sands, including two commercially sourced silica sands and two mixed silica sands, were deposited by air pluviation and tested under controlled conditions in the geotechnical centrifuge at Technical University of Denmark (DTU). To examine correlations often employed in the field between tip resistance (q_c) of Cone Penetration Tests (CPTs) and footing bearing pressure (q_f), a series of CPTs were conducted in samples prepared at similar conditions to the samples of the footing tests. The results indicate that the bearing capacity is controlled by a general shear failure mechanism and that further research is required to assess the range of applicability of direct relationships between bearing capacity and q_c for surface footings.

Keywords: Footings; CPT; Centrifuge Modelling; Sands; Sand Grading.

1 INTRODUCTION

The traditional bearing capacity approach first proposed by Terzaghi in 1943 has been widely investigated since its formulation and new insights on the bearing resistance of footings have been obtained. These include the influence of (a) the progressive failure as strain localization can lead to hardening and softening at critical states, (b) anisotropy, (c) shear band thickness and (d) nonlinear peak strength envelope (Lau and Bolton, 2011). The effect of the particle size has been associated with the relative thickness of the shear band (Tatsuoka et al, 1997). In current practice, a direct correlation with the CPT tip resistance (q_c) is employed, where the reference “capacity” is defined by the well-known 0.1B Method corresponding to the bearing pressure (q) required to cause a footing to settle by 10% of its width $s/B = 10\%$ (Amar et al. 1998). The bearing capacity (q_f) calculated using the standard bearing capacity equation is usually much larger than the one determined from a direct CPT method at $s/B = 10\%$ ($q_{0.1}$), as it requires settlements well in excess of 10% of the foundation width to develop, especially in the case of a local shear failure (Lau and Bolton, 2011).

Briaud and Gibbens (1999) observed that the response of footing load tests conducted in the field can be unified via a “characteristic load-displacement curve” when the data are presented in terms of bearing pressure versus normalised displacement:

$$q = r_s \cdot \sqrt{s/B} \quad (1)$$

where r_s is a soil parameter. In the case of sands, many researchers have examined correlations between r_s with the tip resistance q_c , e.g. Mayne and Illingworth (2010) Mayne et al. (2012), Lehane (2013), Mayne and Woeller (2014) and Mayne & Dasenbrock (2018). Mayne and Illingworth (2010) analysed a database of field tests and derived a mean trend for footings on sand that indicates $r_s = 0.585q_c$. When using this value in Eq. 1 for the capacity criterion of $s/B = 10\%$, the bearing pressure ($q_{0.1}$) is equal to $0.18q_c$; this value is very similar to the value of $0.16q_c$ determined independently by Lehane (2013).

However, experimental and numerical studies have shown that footing tests on dense sand are controlled by a general shear failure mechanism (Kimura et al. 1985; Cerato and Lutenecker 2007; Mase and Hishiguchi 2009). On the other hand, the mechanism reported for the footing tests conducted in the field (up to $s/B=10\%$) is analogous to expansion of a spherical cavity (e.g. Lehane 2013). The direct CPT method relies on a similarity between the failure mechanism of the footing and the deep penetration CPTs.

The aim of this study was to investigate the effect of sand grading on the bearing capacity and to evaluate the uniqueness of the relationship between deep penetration q_c and $q_{0.1}$ for different sand types. A centrifuge study was undertaken, where soil

conditions are controlled. Four silica sands with similar particle regularity, including two uniformly graded sands and two mixed sands with a wider grading variation, were therefore tested. To confirm expectations of modelling of models in centrifuge testing of footings (e.g. Ovesen 1975), two surface footings of different diameters (40mm and 60mm) were tested at two different g levels (40g and 60g) for each sand. These models both represent a circular footing of 2.4m diameter at the prototype scale. Furthermore, two centrifuge CPTs were carried out for each sand at two different g levels (ranging from 32.2g to 64.5g) in new samples prepared at a similar relative density (D_r).

2 SOIL PROPERTIES

The uniformly distributed fractions C and D of Leighton Buzzard sand (referred to as LB-C and LB-D in this study) were tested. In addition, two sands were mixed from the LB-C and LB-D sands and a third Leighton Buzzard fraction (fraction B, LB-B). Mix 1 comprises 1/3 of each of the three fractions, and Mix 2 comprises 1/5 of fractions B and C and 3/5 of fraction D. The two mixed sands were mixed with a concrete mixer. Several sieve analyses were carried out for each mixed sand to ensure that the sands were mixed homogeneously and the particle distribution curves are presented in Figure 1.

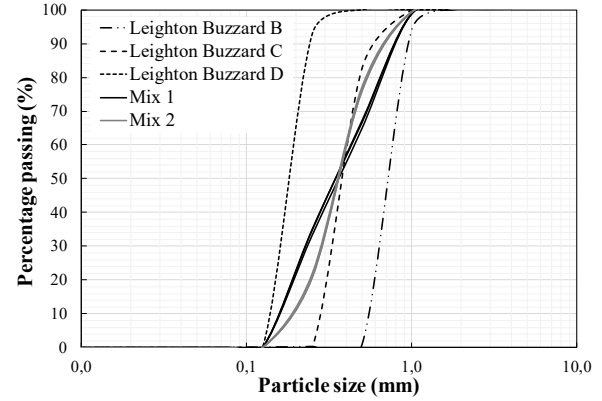


Figure 1. Particle size distribution curves for the sands in this study.

2.1. Basic indices

The basic classification indices of the four sands investigated are summarised in Table 1. All sands have very similar particle shapes, but a slight variance in uniformity coefficient ($C_u = d_{60}/d_{10}$ of 1.49 to 2.80 (where d_{60} and d_{10} are the mesh sizes through which 60 percent and 10 percent of the sand particles pass, respectively). LB-C and LB-D are commercially sourced silica sands with distinctly different mean effective particle size (d_{50}). In order to specifically investigate the effect of C_u in this study, the two mixed sands were mixed to have a similar d_{50} to the LB-C sand. A long series of direct shear tests indicated that the two mixed sands have slightly higher critical state friction angles (ϕ'_{cs}) than LB-C and LB-D (Jensen, 2019). The void ratio limits were determined following Danish Geotechnical Society Guidelines (DGF 2001).

Table 1. Index properties of sands investigated

Sand	Gradation		Void ratio limits		Particle shape			G_s	ϕ'_{cs} : degrees
	d_{50} : mm	C_u	e_{max}	e_{min}	R	S	ρ		
Leighton Buzzard C (LB-C)	0.40	1.54	0.78	0.53	0.51	0.75	0.63	2.66	31.4
Leighton Buzzard D (LB-D)	0.19	1.49	0.87	0.59	0.46	0.70	0.58	2.66	30.7
Mix 1	0.37	2.80	0.71	0.43	0.49	0.73	0.61	2.66	32.6
Mix 2	0.38	2.31	0.74	0.47	0.50	0.74	0.62	2.66	32.7

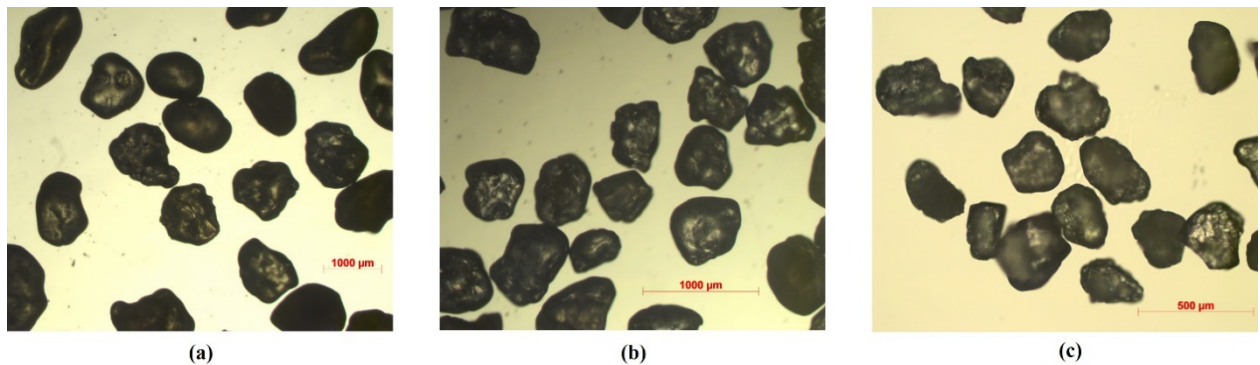


Figure 2. Microscope images of sand particles: (a) LB-B; (b) LB-C; (c) LB-D.

2.2. Particle shape quantification

Representative optical microscope images for the sands are provided in Figure 2 (including Leighton Buzzard fraction B which is used for the mixed sands), where the sands are shown to have very similar particle shapes. Visual observations were used to derive the roundness (R), mean sphericity (S) and regularity (ρ) provided in Table 1 using the methodology described by Jensen et al. (2019).

3 CENTRIFUGE TESTS

3.1. Sample preparation and test programme

The sand was pluviated into the strongbox (having an internal diameter of 527mm and an internal height of 498mm) to give a final height of 317mm when levelled off. The sand pluviation was performed at 1g and manoeuvred manually in a circular motion at a constant drop height above the sand surface. In order to control the density of the sample, the sand flow and the drop height were adjusted (with increasing flow and decreasing drop height leading to a lower density). All tests were performed in a dry condition.

The footings were 16mm thick and made of aluminium. The testing programme of the footing tests is shown in Table 2 (including D_r , g level and footing diameter B). The smallest B/d_{50} ratio is 100, which ensures that centrifuge scale effects are negligible (Ovesen 1979). Furthermore, two centrifuge CPTs were carried out for each type of sand at two different g levels ranging from 32.2g to 64.5g. The CPTs were performed in different samples to the footing tests, however, these were prepared at nearly the same relative density; with the largest deviation being the CPTs performed in the Mix 2 sand at $D_r = 85\%$.

Table 2. Footing testing programme

Test no.	Sand	D_r (%)	g level	B (mm)	B/d_{50}
1	LB-C	81	40	60	150
2	LB-C	82	60	40	100
3	LB-D	82	40	60	316
4	LB-D	82	60	40	211
5	Mix 1	84	40	60	162
6	Mix 1	82	60	40	108
7	Mix 2	80	40	60	158
8	Mix 2	80	60	40	105

All footing tests were conducted under displacement control in the 2.5m radius geotechnical beam centrifuge at DTU. A load frame was secured on top of the strongbox with four bolts. For the footing tests, a piston was installed with a

hinge above it to allow free rotation. This piston was then used in-flight to apply load to the footings. A stiff plastic beam was screwed onto the piston and was functioning as a reference point for the LVDT mounted on the side of the loading frame. The vertical displacement of the footings during penetration was therefore monitored with better precision than the one obtained from the control of the linear actuator. The LVDT was regrettably not mounted for Test 1 and therefore the load-displacement curve for this test is not deemed reliable at small displacements. All footings were placed on the sand surface in the centre of the strongbox to avoid boundary effects. The cone used for the centrifuge CPTs has a diameter (d_c) of 11.3mm and was installed at a velocity of 1.33mm/s to a penetration of about 200 to 240mm. To minimise boundary effects, the CPTs were undertaken at a minimum distance of 150mm to the nearest boundary.

3.2. Footing test results

The variation of bearing stress (q) with the settlements normalised by the respective footing diameters (s/B) are provided in Figure 3. In accordance with modelling of models in centrifuge testing of footings (e.g. Ovesen 1975), the responses up to $s/B = 10\%$ of the 40mm diameter footings (60g) are nearly the same as those of the 60mm diameter footings (40g). Test 1 deviates from this trend as a result of the low accuracy of the measured displacement. The footing responses seem to differ at footing penetrations in excess of $s/B = 10\%$ for LB-C and Mix 2, whereas excellent agreement appears for the entire footing penetrations for the LB-D and Mix 1 sands.

Experimental centrifuge work and numerical simulation studies have shown that bearing capacity factors are size-dependent for footings on sand, with the bearing capacity (q_f) decreasing with footing width (or diameter) (Kimura et al. 1985; Cerato and Lutenegeger 2007; Mase and Hishiguchi 2009). These studies show that a footing placed on a dense sand is expected to fail in a general shear failure. One characteristic of this failure mode is heaving of the soil surface adjacent to the footing. This characteristic was observed after every footing test in this study; see an example in Figure 4. The bearing pressure of a footing in general shear rapidly reaches a peak and a subsequent plateau, after which the surcharge around the footing (N_q -term in Terzaghi's bearing capacity formula) makes the bearing pressure increase to very large depths. The footing responses plotted in Figure 3 indicate that the footings in this study failed in general shear.

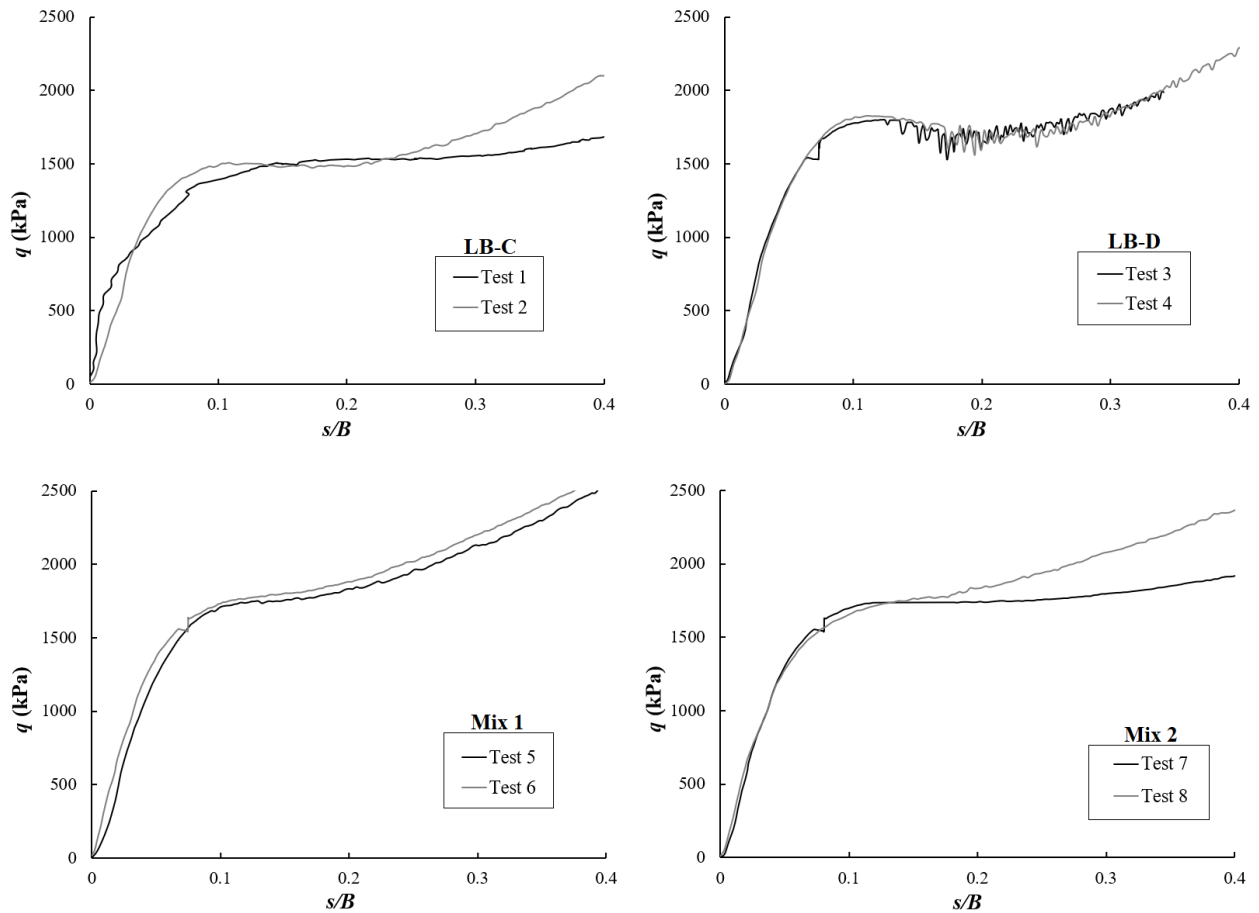


Figure 3. Bearing stress versus normalised settlement for footings on the four investigated sands.



Figure 4. Example of a general shear failure observed after one of the footing tests.

When following a procedure proposed by Lau and Bolton (2011) with Terzaghi's bearing capacity formula superimposed for different friction angles, it is seen that the maximum mobilized friction angles of the footing tests occur at or close to $s/B = 10\%$. This is illustrated in Figure 5, where Test 3 and 4 are plotted (note that γ' is the effective unit weight of the sand). Therefore, it can be inferred that $q_{0.1}$ approximately coincides with the maximum mobilized friction angle when the sand fails in general shear. It is also noticed that the equivalent friction angle at $s/B = 10\%$ is higher than the critical state angle shown in Table 1.

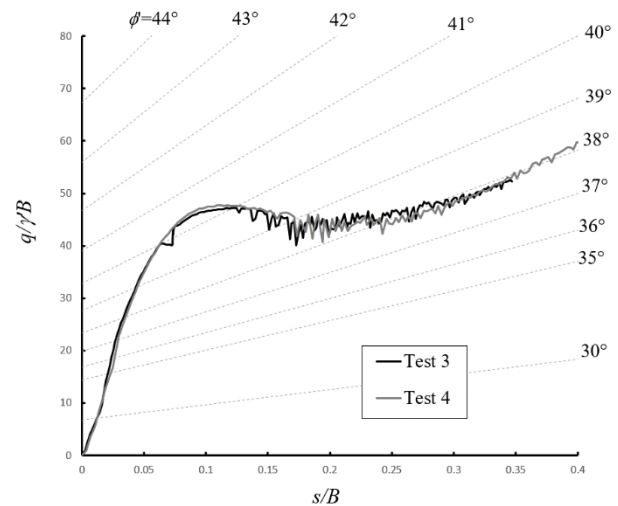


Figure 5. Footing results of Test 3 and 4; with Terzaghi's bearing capacity formula superimposed for different friction angles.

However, in field tests, where footings are generally embedded in the sand, a sudden collapse (or failure) is rarely seen. Therefore, the most common response shows no clear peak or plateau, and the bearing pressure increases to very large depths. The same type of response was observed from embedded footing tests conducted in the centrifuge by Liu and Lehane (2019). In fact, these tests have shown that the mode of deformation at

$s/B = 10\%$ is similar to that of cavity expansion without failure planes extending to ground level (e.g. see Lehane 2013). It follows from this failure mechanism that $q_{0.1}$ vs. s/B characteristics are largely independent of footing width (or diameter).

3.3. Effects of sand grading on $q_{0.1}$

The bearing stresses measured at normalized settlements $s/B = 10\%$ ($q_{0.1}$) are generally very similar between all four sands (1600 ± 200 kPa), with the highest and lowest measured $q_{0.1}$ for LB-D and LB-C, respectively (see Figure 3). Slightly higher values of $q_{0.1}$ ($\approx 12\text{-}15\%$ higher) were obtained for the two mixed sands in comparison to LB-C sand (all three sands having approximately the same d_{50}). Hence, some effect of the sand uniformity is observed. Furthermore, an effect of the mean particle size d_{50} appears on $q_{0.1}$. This is seen with the LB-D sand (having a smaller d_{50} than the other three sands) taking $\approx 22\%$ higher values of $q_{0.1}$ when compared to LB-C sand and $\approx 5\text{-}8\%$ higher values than the mixed sands. The peak friction angles found from direct shear tests for the different sands, have been higher for the mixed sands following a 1:1 association with C_u (Jensen, 2019). This indicates that besides the friction angle the bearing capacity is strongly associated with the d_{50} , which could be attributed to the shear band thickness developed in the general shear failure.

4 RELATING q_c WITH (CENTRIFUGE) FOOTING RESPONSE

In the generalised direct CPT method for evaluation of footing response, which is often used in the field, the load-displacement curves are normalised by the cone tip resistance (q_c). The bearing capacity (evaluated at $s/B = 10\%$) can be capped at stresses corresponding to a percentage of the average measured q_c ($q_{c,avg}$), determined over a depth interval which according to Mayne and Woeller (2014) can be taken from founding level to $1.5B$ depth below. For this purpose the centrifuge CPTs (of which some are shown in Figure 6) were corrected following the procedure described below.

4.1. Correction for shallow depth effect on q_c

For a 2.4m diameter footing, a CPT conducted in the field will have penetrated a depth of more than 100 cone diameters before the tip reaches a depth of $1.5B$. However, the centrifuge CPTs in this study had penetrated $5.3d_c$ (40g) and $8.0d_c$ (60g) at $1.5B$ depth. Therefore, in order to draw parallels to a field situation, the CPT q_c values were corrected in the upper soil horizon due to shallow depth effects (e.g. see Gui and Bolton 1998).

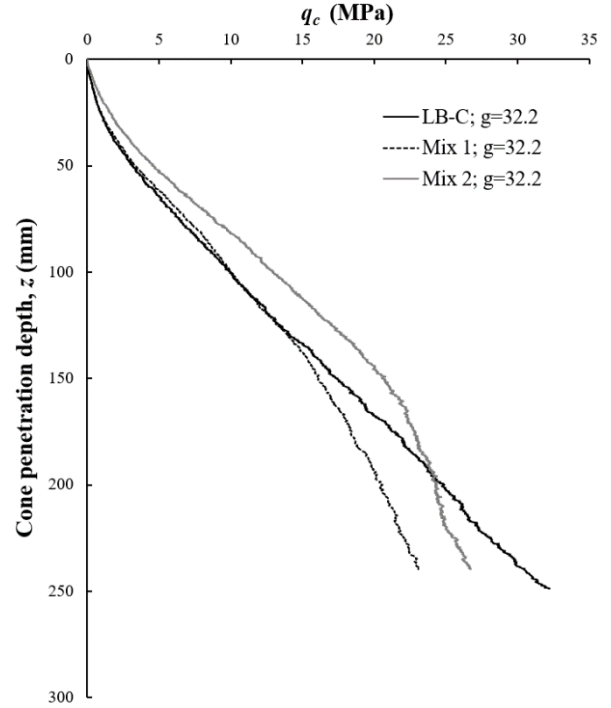


Figure 6. Evidence of upward concavity in the CPT profiles.

The tip resistance in the shallow depth phase is associated with upward movements of the surface around the cone rod, which is similar to a general shear failure of a footing. At a certain depth (deep penetration) a localised mechanism in the vicinity of the cone tip takes over, and q_c can be predicted using spherical cavity expansion theory (e.g. Yu and Mitchell 1998; Suryasentana and Lehane 2016). In this phase the increase in normalised tip resistance slows down rapidly and enters a quasi-stationary regime. At deep penetration in a homogeneous normally consolidated sand, q_c increases as a constant function of vertical effective stress (σ'_v). An ideal correction method should therefore produce an equal normalised tip resistance at different depths in the same soil at the same relative density (D_r).

The tip resistance can be normalised (or corrected) to a common $\sigma'_{v,ref}$:

$$q_{c,ref} = q_c \cdot \left(\frac{\sigma'_{v,ref}}{\sigma'_v} \right)^c \quad (2)$$

where $\sigma'_{v,ref}$ is a reference vertical effective stress, $q_{c,ref}$ is q_c at $\sigma'_{v,ref}$ and c is a stress normalisation exponent.

As evident in Figure 6, the shallow penetration phase is characterised by a parabolic increase (upward concavity) of q_c with depth; this trend was noted by Puech and Foray (2002), Senders (2010) and Bolton et al. (1999). This upward concavity means that the stress exponent (c) in Eq. 2 decreases with depth until at a critical depth (d_{cr}) when the tip

resistance enters the quasi-stationary regime and c takes on a nearly constant value (steady state). In order to evaluate c with depth, Eq. 2 can be rearranged:

$$c = \frac{\ln\left(\frac{q_{c,ref}}{q_c}\right)}{\ln\left(\frac{\sigma_{v,ref}}{\sigma_v}\right)} \quad (3)$$

The variations of Eq. 3 with the normalised penetration depth (z/d_c) for the LB-C and Mix 2 sands are plotted in Figure 7, where the transition between shallow and deep penetration is illustrated with a critical ratio of penetration depth to cone diameter, $(z/d_c)_{cr}$. The “steady state” value of c and $(z/d_c)_{cr}$ for all four sands are listed in Table 3.

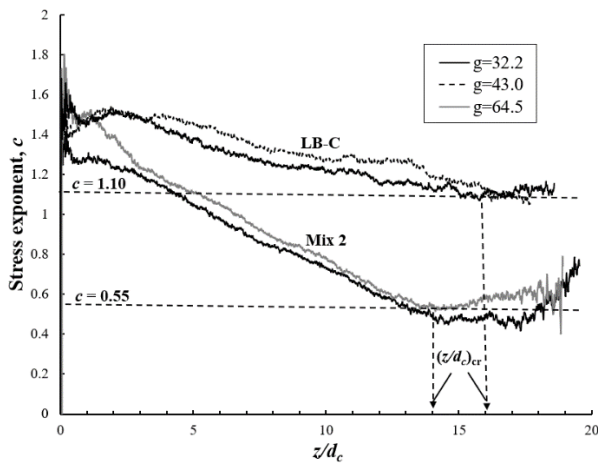


Figure 7. Variation of stress exponent (c) with normalized penetration depth (z/d_c)

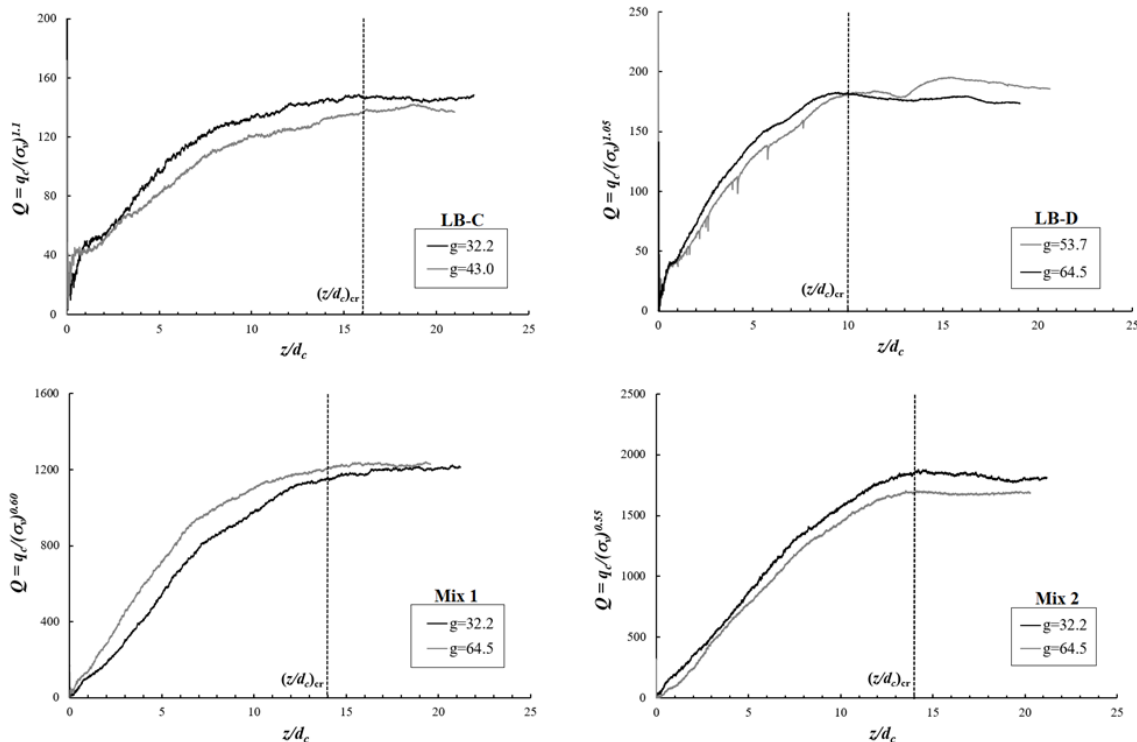


Figure 8. Normalized tip resistance (Q) versus normalized penetration depth (z/d_c) for all centrifuge CPTs.

Table 3. Estimations for all the centrifuge CPTs.

Sand	$(z/d_c)_{cr}$	c (steady state)	Q	$q_{c,avg}$ (MPa)
LB-C	16	1.10	140	5.89
LB-D	10	1.05	185	6.27
Mix 1	15	0.60	1220	9.53
Mix 2	14	0.55	1750	11.52

It is noticeable that relatively high values of ‘ c ’ are reported in this study when compared with values reported in calibration chamber tests (e.g. see Moss et al. 2006). However, values of ‘ c ’ tend to be closer to unity in centrifuge tests (Bolton et al. 1999), which may be an artefact of the ratio of the lower cone diameter to the stress gradient. The ‘ c ’ values greater than unity seen for LB-C and LB-D sands are not credible, since values of $c > 1$ indicate an upward concavity of q_c even at deep penetration. ‘ c ’ values less than one should generally be expected in sands with uniform relative densities due to the reducing tendency for dilation at higher stress levels.

Jensen et al. (2019) observed that increasing values of uniformity coefficient (C_u) leads to sands, which are more dilatant at small stress levels and require smaller stress levels for the sand behaviour to become contractive. Therefore, given that the tip resistance is influenced by these two factors, some variations in the steady state c could be expected. It is possible that the uniformity of the sands (the

mixed sands having higher C_u values than the LB-C and LB-D sands) contributes to some extent to the observed variations of the c exponent, although the magnitude of differences seen in Table 3 indicate that further research is required.

With the estimated “steady state” c values (in Table 3), the normalised tip resistance (Q) is determined by:

$$Q = q_c / (\sigma'_v)^c \quad (4)$$

The variations of Eq. 4 with z/d_c for all four sands are shown in Figure 8 where Q is seen to develop a near constant value after the critical ratio of penetration to cone diameter $(z/d_c)_{cr}$. The best-fit values of the near constant Q are listed in Table 3. Note that the significantly higher values of Q for the mixed sands compared with LB-C and LB-D sands are due to the lower values of c (see Eq. 4). In order to correct the centrifuge CPT data for shallow penetration effects (which are negligible in the field), the near constant values of Q are assumed to extend all the way to the soil surface ($z/d_c = 0$).

4.2. Normalisation of (centrifuge) surface footing response with $q_{c,avg}$

The corrected q_c values averaged to a depth of $1.5B$ below founding level ($q_{c,avg}$) are determined for each sand and listed in Table 3. The bearing pressures (q) measured in each footing test are then normalised by the corresponding $q_{c,avg}$ and plotted against s/B in Figure 9. It can be inferred that the $q/q_{c,avg}$ vs. s/B characteristic changes with the uniformity of the sand. The $q_{0.1}/q_{c,avg}$ ratios range from 0.25 to 0.29 for LB-C and LB-D sands and 0.15 to 0.18 for Mix 1 and Mix 2. This is mainly due to the large variation in $q_{c,avg}$ between the mixed sands and the LB-C and LB-D sands (which is primarily due to the very different stress exponents; see Table 3). Further research is required to firstly establish how the stress exponent ‘ c ’ varies with the sand properties so that the appropriate $q_{c,avg}$ value can be obtained. It is noteworthy that Liu and Lehane (2020) showed relatively unique $q/q_{c,avg}$ vs s/B characteristics for embedded footings in four different sand types and with a range of mean particle sizes, mineralogies and uniformity coefficients. The Liu & Lehane (2020) results are comparable to those of LB-C and LB-D on Figure 9, which have ‘ c ’ values close to unity.

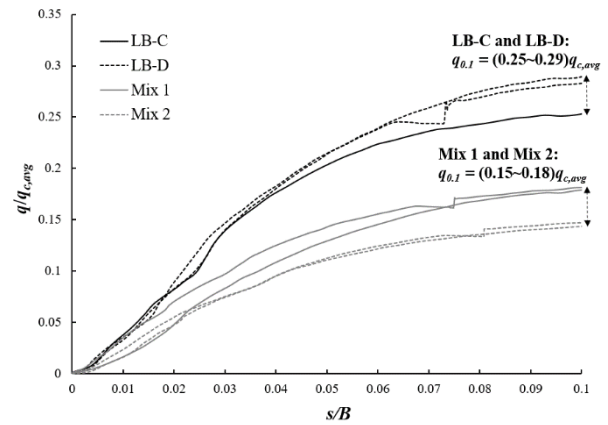


Figure 9. Variation of normalised bearing stress ($q/q_{c,avg}$) with normalised settlement (s/B) for all footing tests.

5 CONCLUSIONS

A centrifuge surface footing and CPT investigation conducted on four sands at the same relative density but with different particle size distributions has shown:

- Approximately 12-15% higher values of $q_{0.1}$ was observed with a slight increase in uniformity coefficient (C_u).
- An apparent increase by about 20% in $q_{0.1}$ values when the mean particle size (d_{50}) was lowered by 50%.

The trends and the normalisation using CPT q_c of centrifuge test load displacement data are the subject of an on-going study at the Technical University of Denmark.

6 ACKNOWLEDGMENTS

The authors appreciate the support of technical personnel at DTU in the experimental study.

7 REFERENCES

- Amar, S., Baguelin, F., Canepa, Y., & Frank, R. 1998. New design rules for the bearing capacity of shallow foundations based on Menard pressuremeter tests. *Geotechnical Site Characterization, Vols 1 and 2*, 727–733.
- Bolton, M. D., Gui, M. W., Garnier, J., Corte, J. F., Bagge, G., Laue, J., & Renzi, R. 1999. Centrifuge cone penetration tests in sand. *Geotechnique*, **49**(4): 543–552.
- Briaud, J. L., & Gibbens, R. 1999. Behavior of five large spread footings in sand. *Journal of Geotechnical and Geoenvironmental Engineering*, **125**(9): 787–796.

- Cerato, A. B., & Lutenegeger, A. J. 2007. Scale effects of shallow foundation bearing capacity on granular material. *Journal of Geotechnical and Geoenvironmental Engineering*, **133**(10): 1192–1202.
- DGF 2001. *Laboratoriehåndbogen - DGF Bulletin 15*. Dansk Geoteknisk Forening, Lyngby, Denmark.
- Gui, M. W., & Bolton, M. D. 1998. Geometry and scale effects in CPT and pile design. *Geotechnical Site Characterization*, Vols 1 and 2, pp. 1063–1068.
- Jensen, M.R., Zania, V., Lehane, B.M., Liu, Q., & Butterworth, C. 2019. The strength of Perth sands in direct shear. In: *Proc. of the 13th ANZ Geomechanics Conference*, 1-3 April, Perth, Australia, pp. 185-190.
- Jensen, M.R. 2019. Effects of Particle Size, Uniformity, and Particle Shape on the Strength and Bearing Capacity of Sands. MSc Thesis, Technical University of Denmark.
- Kimura, T., Kusakabe, O., & Saitoh, K. 1985. Geotechnical model tests of bearing capacity problems in a centrifuge. *Géotechnique*, **35**(1): 33–45.
- Lau, C.K., and Bolton, M.D. 2011. The bearing capacity of footings on granular soils. II: Experimental evidence. *Géotechnique* **61**(8): 639-650.
- Lehane, B. M. 2013. Relating foundation capacity in sands to CPT qc. *Geotechnical and Geophysical Site Characterization 4 - Proceedings of the 4th International Conference on Site Characterization 4, ISC-4*, 1, pp. 63–81.
- Liu & Lehane (2020). A systematic investigation of the load-displacement response of shallow footings on sand. *Geotechnique*, //doi.org/10.1680/jgeot.19.P.253
- Mase, T., & Hashiguchi, K. 2009. Numerical analysis of footing settlement problem by subloading surface model. *Soils and Foundations*, **49**(2), 207–220.
- Mayne, P. W. & Illingworth, F. 2010. Direct CPT method for footings on sand using a database approach. *Proceedings, 2nd Intl. Symposium on Cone Penetration Testing*, Vol. 3, pp. 315-322.
- Mayne, P. W., Uzielli, M., & Illingworth, F. 2012. Shallow footing response on sands using a direct method based on cone penetration tests. *Geotechnical Special Publication*, (227), pp. 664–679.
- Mayne, P. W., & Woeller, D. J. 2014. Generalized direct CPT method for evaluating footing deformation response and capacity on sands, silts, and clays. *Geotechnical Special Publication*, (234), pp. 1983–1997.
- Mayne, P. W., & Dasenbrock, D. 2018. Direct CPT Method for 130 Footings on Sands. *Geotechnical Special Publication*, pp. 135–146.
- Moss, R. E. S., Seed, R. B., & Olsen, R. S. 2006. Normalizing the CPT for overburden stress. *Journal of Geotechnical and Geoenvironmental Engineering*, **132**(3): 378–387.
- Ovesen, N. K. 1975. Centrifugal testing applied to bearing capacity problems of footings on sand. *Géotechnique*, **25**(2): 394–401.
- Ovesen, N. K. 1979. Panel discussion: The scaling law relationship. *Proc. 7th Eur. Conf. Soil Mech. and Found. Engng*, Brighton, 4, pp. 319–323.
- Puech, A., & Foray, P. 2002. Refined Model for Interpreting Shallow Penetration CPTs in Sands. *Proceedings of the Annual Offshore Technology Conference*, pp. 2441–2449.
- Robertson, P. K., 2009. Interpretation of cone penetration tests – a unified approach. *Can. Geotech. J.* **46** (11), 1337–1355.
- Senders, M. 2010. Cone resistance profiles for laboratory tests in sand. *Proc. 2nd Int. Conf. on Cone Penetration Testing*, Huntington Beach, CA, paper no. 2-08.
- Suryasentana, S. K., & Lehane, B. M. 2016. Updated CPT-based p–y formulation for laterally loaded piles in cohesionless soil under static loading. *Geotechnique*, **66**(6): 445–453.
- Tatsuoka, F., Goto, S., Tanaka, T., Tani, K., Kimura, Y., 1997. Particle size effects on bearing capacity of footing on granular material. *Proc. of IS-NAGOYA*, pp. 133–138.
- Yu, H. S., & Mitchell, J. K. 1998. Analysis of cone resistance: Review of methods. *Journal of Geotechnical and Geoenvironmental Engineering*, **124**(2): 140–149.

Tests of varied sample preparation methods for centrifuge modelling

Eric Ritchie¹, Leonardo Lalicata¹, Sam Divall¹, Richard Goodey¹

¹*Department of Civil Engineering, City, University of London, London, United Kingdom*

Corresponding author: Eric Ritchie (eric.ritchie.1@city.ac.uk)

ABSTRACT: Centrifuge modelling is an established technique capable of investigating the ground's response to complex geotechnical events. Centrifuge models are often created from reconstituted soil, with well-defined boundary conditions and known soil parameters. Clay soil models may be prepared by mixing clay powder with distilled water to form a slurry. This slurry is placed within a soil container and subjected to a vertical stress (usually in a consolidation press or consolidated inflight). This creates an isotropic model but there is a fundamental difference between this soil model and naturally occurring soil deposits. The structure and fabric present within a naturally occurring clay is not reproduced by this preparation process. It is well-established that structure and fabric in naturally deposited soils are as significant in their effect on soil behaviour as, for instance, the stress history. Inherent structure and fabric within clay soils creates anisotropy which can vary with depth, this is particularly apparent when considering the permeability. Creating a soil model for centrifuge modelling with representative permeability anisotropy would allow for a better representation of consolidation driven events and the ability to observe long-term behaviour of complex geotechnical events. Currently, there are limited methods of doing so, leading to a considerable gap in knowledge associated with the behaviour of layered ground. This paper describes the development of the equipment and experimental procedure for quantifying the structure developed by different sample preparation techniques for centrifuge modelling.

Keywords: Laboratory Testing; Centrifuge Modelling; Soil Structure.

1 INTRODUCTION

Centrifuge modelling has enabled researchers and engineers to investigate construction and geotechnical events. Most commonly centrifuge modelling has been utilised to determine mechanisms and patterns of movement. Predominantly these patterns are as a result of the deformations experienced due to a construction event i.e. the short-term movements. However, in a clay soil there can be continuing movements that occur years after the construction event has finished as excess pore pressure dissipate. These long-term movements can be significant as reported in Hill and Staerk (2016). Long-term settlement between construction stages and after construction has nearly doubled the settlement induced by tunnelling. Hill & Staerk (2016) also highlight the difference between two observation points at Whitechapel Crossrail station, Vallance Road and Kempton Court buildings where no settlement mitigation could be used. Due to the differing invert levels at the two locations the ground conditions subsequently varied. The rate of consolidation at Vallance Road decayed nearly twice as fast as that at Kempton Court, due to the presence of sand beds near the invert at Vallance Road.

Current centrifuge models are idealised and conducted in homogenous blocks of clay, such that there are well known properties and well-defined boundary conditions. However, there is a

fundamental disparity between this and a site such as Whitechapel station. London like many other cities is a sedimentary clay which has been deposited in layers creating inherent anisotropy. A homogenous clay model cannot simulate the different dissipation rates of excess pore pressures as seen at Whitechapel station.

There have been efforts to conduct centrifuge tests in layered ground conditions such as Grant (1998), Hird (2006) and Hossain and Randolph (2010), in which the interaction between different stiffness layers were the primary objective. However, these models are not representative of a sedimentary structure. Laboratory sedimentation is not a new procedure and has been used previously to create laboratory samples. Stallebrass et al. (2007) split open a sedimented sample and a reconstituted sample and the difference in structure is evident (Figure 1). Structure can be defined as the difference in interpedicular bonding and the different arrangement of particles (fabric).

Divall et al. (2018) created layered models within a geotechnical centrifuge by sedimenting high water content slurries in flight. Further developing this preliminary method could create a model in which permeability anisotropies could be designed. Such that representative dissipation of pore pressures could be observed and the long-term patterns of movements can be investigated through centrifuge modelling.

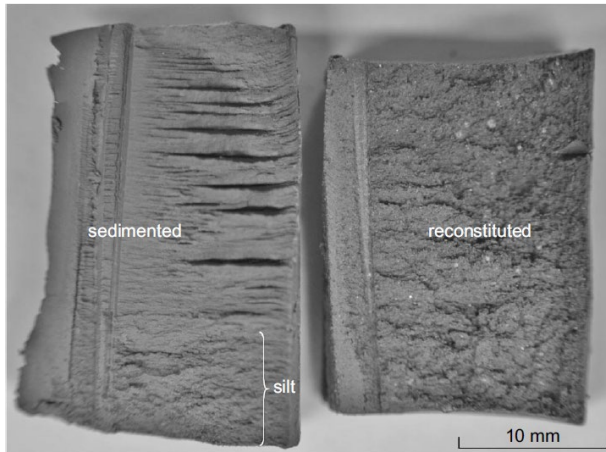


Figure 1. Photographs of split sedimented and reconstituted London Clay samples Stallebrass et al. (2007).

The properties of any sedimented samples within a centrifuge need to be quantified, the permeability anisotropy needs to be measured. The compression behaviour needs to be understood such that a desired height of centrifuge model can be achieved. Triaxial tests also need to be completed such that they can be used for numerical analyses. These parameters measured will be compared to the standard techniques of making centrifuge modelling to assess the difference in behaviour. This highlighted a further question, there is no single way that centrifuge models are created, and does the method of sample preparation effect the resulting model properties.

This paper details the preliminary testing of the difference between centrifuge sample preparation techniques. Oedometer tests are presented on a variety of slurries prepared in different ways representing the different sample preparation procedures commonly used in centrifuge modelling.

2 MODEL MAKING PROCEDURES

2.1 Kaolin clay powder and distilled water

Cairncross (1973) was cited in Mair (1979) as the earliest example of a method of creating homogenous clay models consisting of powdered clay and distilled water to twice its liquid limit (120% water content). Once fully mixed the slurry is carefully placed into a strongbox container to avoid entrapping air. The clay is agitated to remove any possible air bubbles created during pouring. The slurry is then consolidated in stages to achieve a desired stress history. This is done through either a hydraulic or a pneumatic press, in a series of loading stages arriving at a homogenous sample.

2.2 Recycling previous tests in Kaolin clay

Tests previously performed in kaolin clay models created as described above, can be recycled to make another centrifuge model. By cutting the remainder

away any part of the clay that has been in contact with grease or contaminants and cutting the remainder into small pieces. These are then soaked in distilled water and mixed to form a second slurry with a water content of 120%. The slurry is then consolidated as described previously.

Work undertaken by Phillips (2016) found that when natural and reconstituted clay cuttings are agitated in water they do not break down to the particulate size. They will disaggregate into slurries that contain a higher percentage of silt size agglomerates of clay particles also referred to as 'clay peds'. This effectively changes the particle size distribution of the material.

The fabric of a sample consolidated from a slurry consisting of recycled material may be noticeably different from a sample consolidated from clay powder. As soil behaviour is partly governed by the influence of structure (Leroueil & Vaughan, 1990), the difference in structure may be significant enough to change its engineering properties compared to a sample prepared from powder and distilled water.

2.3 Mixing under a vacuum

Slurries prepared from powder or recycled material can be subjected to vacuum to de-air the mixture. Slurries can be mixed under a vacuum and then pumped directly into a strongbox container reducing air being introduced to the sample. Alternatively, the slurry can be mixed as previously described but before being poured into the strongbox it is subjected to a vacuum (Hossain & Randolph, 2010). The slurry is then carefully placed into the strongbox container and consolidated as described previously.

The use of a vacuum to de-air the sample may change the compressibility of the sample as well as increase the consistency of the sample preparation technique. Reducing the chance of air pockets being trapped in the sample, which if in contact with a structure being modelled, could be significant. This method removes variability from researcher to researcher, as it does not require any manual agitation.

2.4 Consolidating models in flight

Alternatively, from consolidating a sample within a press, a slurry can be consolidated under self-weight within a centrifuge. A slurry prepared by any of the methods above is poured into a strongbox and then placed onto a centrifuge swing. Alternatively, the slurry can be pumped into the strongbox in flight. In both cases, typically the slurry is placed on top of a geofabric mat or porous plastic sheet to allow for drainage at the base of the sample. The slurry is then

accelerated in stages to consolidate under self-weight at varying g-levels. This creates a stress profile that increases with depth. To create a uniform stress distribution or an overconsolidated sample a surcharge can be applied to the surface of the sample.

To avoid generation of high excess pore pressures that creates pipping and preferential drainage paths during consolidation, the model is accelerated slowly to the desired g-level. Subsequently, consolidation of samples can be a lengthy procedure and the total model preparation length is comparable to that of a hydraulic or pneumatic press.

Work completed by Mikasa & Takada (1986) recognised segregation caused when consolidating soft soils within the centrifuge, when using a soil consistency (water content) that did not allow for particle segregation. Using post-test investigation techniques, it was determined that segregation occurred from a marked drop off in the effective stress void-ratio curve. The authors suggested using a water content equal or less than twice the liquid limit of the clay to avoid segregation. Townsend et al. (1986) also recognised the issue of segregation in centrifuge modelling and combined with other researchers have proposed to avoid segregation by using low initial water content samples and staged consolidation procedures.

Sorta et al. (2012) investigated the effect of an increased acceleration field to the segregation characteristics of a variety of clay-sand mixtures. Samples were left to consolidate under their own self-weight at 1g for a month, then the segregation index was calculated as defined in Donahue et al. (2018). The same slurries were then consolidated in flight for the equivalent of a month at relevant g-levels. The segregation index was calculated and the segregating boundaries was plotted on a ternary diagram to categorise different properties.

This concluded that the segregation boundaries are significantly shifted at elevated g-levels (i.e. a sample may not segregate under normal conditions but may during consolidation in flight). The boundary is also dependent on the source of the material. If the resulting structure of the sample consolidated in flight is different from that of sample prepared in a mechanical press then the sample behaviour may also differ. From existing literature, it is inconclusive if consolidating a sample on a centrifuge would yield different material properties.

To investigate the influence of different sample preparation techniques a series of one-dimensional compression tests were completed to compare coefficients of compression and swelling, as well as the reputability of results.

3 EXPERIMENTAL PROCEDURE

3.1 Sample preparation

3.1.1 Preparation of slurry from powder

To create the first slurry speswhite kaolin clay was used, the same as what is used for centrifuge models at City, University of London. The clay powder was mixed to approximately twice the liquid limit or 120% water content, in a 9-litre Hobart paddle mixer, for approximately 2 hours until the clay was a smooth slurry.

3.1.2 Preparation of slurry from recycled material

To create a slurry from recycled material, a 6-inch California bearing ratio mould (CBR mould) of kaolin clay which had been prepared as described in section 3.1.1, was consolidated to a stress of 500 kPa to create a triaxial sample. The remainder of the clay was trimmed removing any parts in contact with the CBR mould. The sections were cut into small cubes approximately 40-50mm³. The cubes were soaked in distilled water and mixed to a water content of 120% in the same Hobart mixer.

To create a different slurry using recycled material a CBR mould was filled with clay slurry mixed from powder and loaded to a maximum stress of 200 kPa. The sample was then removed from the press and cut into small cubes of 40-50 mm³ and mixed with distilled water to a target water content of 120%. Both slurries had been mixed for a minimum of 5 hours, it was sometimes necessary to stop the mixer to break the larger lumps by hand.

3.1.3 Preparation of a slurry using a vacuum

The samples subjected to a vacuum were prepared in the same way as that from Speswhite kaolin powder in section 3.1.1. Once the slurry was mixed it was transferred to a vacuum chamber where it was subjected to a vacuum and agitated for 30 minutes. After which the sample was removed from the chamber further agitated by hand and subjected to the vacuum for a second time for a further 30 minutes. The sample was then ready for testing in an oedometer.

3.1.4 Consolidating samples within a centrifuge

To consolidate samples in flight for testing in an oedometer or a standard element test, clay is poured into a sedimentation column designed to be used within the centrifuge as shown in Figures 2 and 3. These sedimentation columns will be used for a future test series to create sedimented samples similar to Stallebrass et al. (2007) but using a

centrifuge. In which the resulting samples permeability and mechanical properties will be measured. These sedimented samples will be compared to the aforementioned standard techniques of creating centrifuge models to assess any differences.

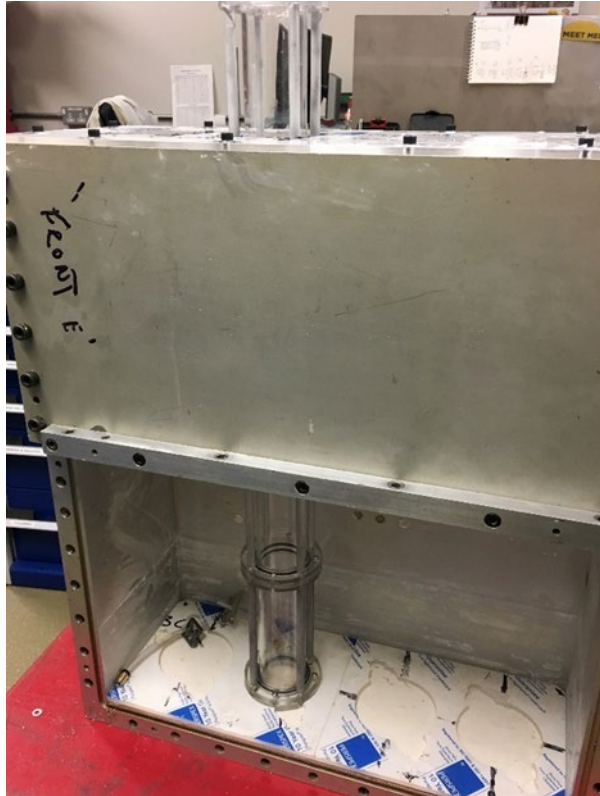


Figure 2. Sedimentation column arrangement



Figure 3. Sedimentation columns on centrifuge swing during commissioning tests.

The sedimentation columns are manufactured from 3mm thick, 54mm internal diameter PMMA tubing that has a total height of 800mm. The column can be split into two sections the lower section being 180mm tall allowing for the samples to be extracted or converted to a permeameter cell

by attaching a top cap. 100mm of clay slurry prepared from a powder was poured into the tube. The column was then accelerated to 10g and allowed to consolidate under self-weight for 24 hours, after every 24 hours the g-level was doubled to a maximum g level of 100g is achieved. The effective radius is set to two thirds of the slurry height within the columns for all tests as per Taylor (1995). After allowing for consolidation at maximum acceleration the centrifuge was decelerated and the columns removed for further testing.

3.2 Summary of tests completed

Table 1 summarises the slurries created, that were tested within the oedometer. All tests were prepared using distilled water.

Table 1. Summary of tests undertaken

Test Number	Kaolin powder	Recycled material	Subjected to a vacuum
T1	✓		
T2	✓		
T3	✓		✓
T4	✓		✓
T5		✓	
T6		✓	
T7		✓	

3.3 Oedometer testing

Once the samples were created they were then tested within a standard 75mm oedometer. The loading platen and the bottom porous stone were saturated within a vacuum chamber. The slurry was placed carefully in the centre of the oedometer cell then spread to create an even layer. The clay was then agitated manually prior to testing to remove any air introduced when pouring the clay samples.

The samples created using the centrifuge, are extruded into a custom made oedometer with an oedometer ring diameter the same as the internal diameter of the sedimentation columns. This is to minimise disturbance caused by trimming samples. The oedometer ring initially sits inside a recess within a PMMA holder. Once the base has been removed from the sedimentation column it is secured to PMMA holder and the clay sample was extruded into the oedometer ring. The sedimentation column is removed and resealed for future testing. The oedometer ring fits into an adapter such that it can be used in a standard 75mm

cell. A custom piston has also been manufactured and applies a stress of 1.5kPa.

The samples were then one-dimensionally compressed and swelled within the oedometer to determine the compression and swelling indexes. Samples were subjected to a maximum vertical effective stress of 400 kPa, unloaded to a range of different stress then reloaded back to a maximum stress of 400 kPa. The displacement was measured continuously with a linear variable displacement transducer (LVDT) resting on the arm of the loading frame with a reading taken at one a second.

4 RESULTS

For this paper, the results for samples consolidated in flight have been omitted due to insufficient data. The one-dimensional compression data for the other sample preparation techniques are compared in Figure 4. It can be seen there is a 5% difference in compression indexes between the samples consolidated from a powder versus those that have been subjected to a vacuum prior to testing. The samples subjected to the vacuum are always less compressible, this is thought to be due to the volume of air being expelled from the sample during the consolidation stages. Thus, creating a higher compression index. The samples prepared using a vacuum had a greater consistency with the difference in compression index being less than 1%. The samples prepared from powder and mixing with distilled water are consistent within a 5% bracket, thought to be due to the varying amount of air present within the sample.

The slurries consisting of recycled material as opposed to powder were around 20% less compressible than the other sample preparation techniques. The results of the tests are also more varied than the others and fall within a 10% bracket. The reason for this is thought to be due to the different grading curve achieved after recycling the clay cuttings (after Phillips, 2016). The silt agglomerates within the slurry are not broken-down during mixing and once loaded in the oedometer it creates a less compressible sample.

Phillips (2016) noted that when disaggregating kaolin clay cuttings after 30 minutes of mixing there was an increase in sub 63µm particles. However, after a further 30 minutes of mixing there was a reduction in sub 63µm particles.

Oedometer test 1 and 2 with recycled material were from the same batch of slurry. The slurry was sealed and then remixed prior to testing. The second oedometer test conducted of recycled material is less compressible than the first, this could be variation within the sample or as the second sample

is mixed for a longer period of time there was more ‘peds’ present creating a less compressible sample.

Oedometer test number 3 with recycled material is very similar to test number 1. These were both the first samples to be prepared from the slurry directly after initial mixing. From these preliminary tests it is inconclusive to what effect stress history had on of the cuttings. There could be a more complex interaction between cuttings, mixing duration, mixing speed and waiting and remixing a slurry.

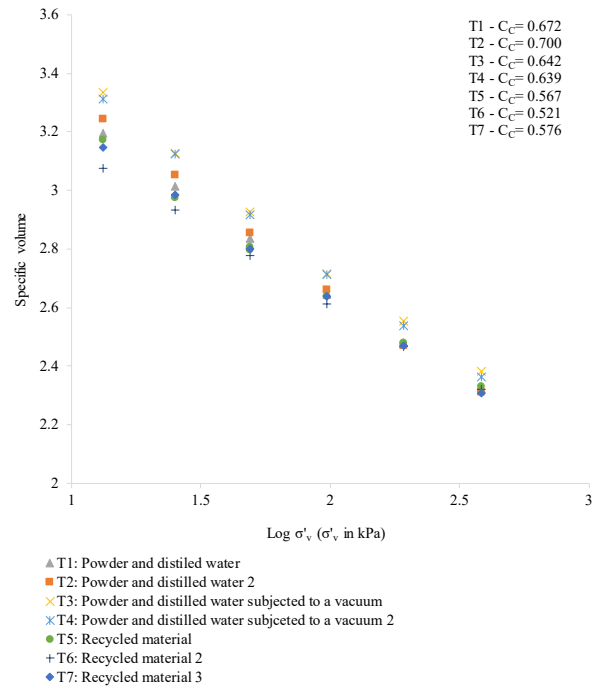


Figure 4. One-dimensional compression curves for different sample preparation techniques

The average swelling index for each of the sample preparation techniques was 0.11. There is no obvious trend and all results sit within a 10% bracket of the average value. There is the smallest variation in swelling index with the samples prepared from recycled material, the reason for this trend is not clear and requires further testing.

5 CONCLUSIONS

The compression test results show there is a significant difference between the sample preparation procedures that deserves further investigation. From the preliminary tests it can be determined that;

1. Samples consisting of kaolin powder and distilled water become slightly less compressible after being subjected to a vacuum

2. Slurries consisting of recycled clay cuttings are significantly less compressible than samples prepared from powder thought to be due to presence of peds.
3. The swell indexes fall within a similar range for all preparation techniques.

The difference between clay properties are potentially significant for centrifuge modelling if within a series of tests there are some models prepared from powder and some prepared from recycled material. The response of any test may differ producing a variation in results. This also influences numerical modelling, models are often compared to centrifuge test data. If the soil model properties do not reflect the test parameters this could affect the results for such models.

There needs to be further testing on samples consolidated in flight to see where this fits within the other sample preparation techniques. Further testing on samples consisting of recycled material that have also been subjected to a vacuum should be investigated. It is predicted that this will further reduce the compressibility as seen with the samples prepared from powder.

6 ACKNOWLEDGEMENTS

This research was supported by the George Daniels scholarship at City, University of London. Additional thanks should also go to the members of the research centre for Multi-Scale Geotechnical Engineering London for their support during the project.

7 REFERENCES

- Cairncross, A.M. (1973). Deformations around tunnels in stiff clay. PhD thesis, University of Cambridge.
- Divall, S., Stallebrass, S.E. Goodey, R.J, & Ritchie. E.P. (2018). Development of layered models for geotechnical centrifuge tests. *Physical Modelling in Geotechnics – McNamara et al. (Eds) 2018* Taylor & Francis Group, London, ISBN 978-1-138-34419-8.
- Grant, R. J. (1998). Movements around a tunnel in two-layer ground. Doctoral thesis, Department of Civil Engineering Geotechnical Engineering Research Centre. The City University, London.
- Hill, N., & Staerk, A. (2016). Long-term settlement following SCL-tunnel excavation. *Crossrail project Infrastructure design and construction- 3*, pp 227-248.
- Hird, C.C., Emmett, K.B.& Davies, G. 2006. Piling in layered ground: risks to groundwater and archaeology. Science Report SC020074/SR. Environment Agency: Bristol.
- Hossain, M. S. & Randolph, M. F. (2010). Deep-penetrating spudcan foundations on layered clays centrifuge tests. *Géotechnique* 60, No. 3, 157-170.
- Mair, R. J. (1979), Centrifugal modelling of tunnel construction in soft clay. PhD thesis, University of Cambridge.
- Mikasa, M, & Takada, N, (1984). Self-weight consolidation of very soft clay by centrifuge. In *Sedimentation Consolidation Models—Predictions and Validation* (Yong RN and Townsend FC (eds)). ASCE, New York, NY, USA, pp. 121–140.
- Philips, N. S. (2016). Disaggregation of soil during slurry pipe jacking. PhD thesis, City University of London, Geotechnical Engineering Research Group, School of Mathematics, Computer Science and Engineering
- Sorta, A. R., Sego, D. C. & Wilson, W. (2012). Effect of Thixotropy and Segregation on centrifuge modelling. *International journal of Physical Modelling Geotechnics*, 2012, 12(4), 143-161.
- Stallebrass, S. E., Atkinson, J. H. & Mašín, D. (2007). Manufacture of samples of overconsolidated clay by laboratory sedimentation. *Géotechnique* 57, No. 2, 249–253.
- Taylor, R. (1995). *Geotechnical centrifuge technology*. London: Blackie Academic & Professional.
- Townsend FC, McVay MC, Bloomquist DG and McClimans SA (1986) Reclamation of Phosphatic Clay Waste Ponds by Capping. Volume 1: Centrifugal Model Evaluation of Reclamation Schemes for Phosphatic Waste Clay Ponds. Florida Institute of Phosphate Research, Florida, Bartow, FL, USA, FIPR publication no. 02-030-056.

Accelerations in dynamic centrifuge modelling of seismic liquefaction problems

Andreia Marques¹, Paulo Coelho¹, Stuart Haigh², Gopal Madabhushi²

¹*Dep. of Civil Engineering, University of Coimbra, Portugal*

²*Dep. of Engineering, University of Cambridge, UK*

Corresponding author: Andreia Marques (as.silvamarques@gmail.com)

ABSTRACT: Earthquake-induced soil liquefaction continues to be a major subject of continuing research over the last decades. In fact, despite the recent advances on the comprehension of this phenomenon, it is repeatedly observed in recent earthquakes and have devastating effects in modern societies increasingly dependent on liquefaction-susceptible infrastructures. Earthquake-induced liquefaction effects are particularly important in shallow foundations built in seismically active areas on saturated deposits of granular soils, being quite complex to model, as significant loss of the soil's strength and stiffness due to excess pore pressure build-up, complex soil-structure interaction (SSI) mechanisms and very large deformations are typically observed. Dynamic centrifuge modelling is accepted as a powerful research tool to experimentally shed light on these problems, as it can effectively mimic the soil's effective stress during and after the seismic motion and realistically capture SSI effects. This paper discuss the ability of this experimental research tool to accurately assess the mechanisms governing the behaviour of shallow foundations built on liquefiable ground, focussing mostly on the mechanisms governing the propagation of horizontal and vertical accelerations in the ground and foundations observed in centrifuge test performed on a model built inside an ESB container and representing neighbouring shallow foundations built on ground undergoing liquefaction due to a seismic simulation generated by the Stored Angular Momentum (SAM) actuator. Several instruments were place through the model to understand in detail the mechanisms, including acceleration MEMS placed on the footings and accelerometers placed in the ground and model boundaries. It was observed that boundary effects may affect the performance of the model and that footings exhibit non-planned vertical accelerations that may not result from individual rocking mechanisms but rather from some rocking of the all centrifuge model. Overall, the unique value of centrifuge modelling in liquefaction research is demonstrated, especially if the testing conditions are fully understood.

Keywords: Liquefaction; Centrifuge Modelling; Shallow Foundations; ESB Container; SAM Actuator.

1 INTRODUCTION

Earthquake induced soil liquefaction is a complex problem that has been continuously affecting modern society. Even if it is seldom responsible for a significant number of human fatalities, this catastrophic phenomenon seriously affects human life as it can cause severe damage to buildings, bridges and other structures and infrastructures, causing significant and prolonged economic losses and social disruption.

This phenomenon is commonly observed in loose saturated deposits of sandy soil, under structures resting on shallow foundations. In fact, settlement and tilting of shallow foundations on saturated sandy/silty soils has been repeatedly observed throughout the world as a consequence of liquefaction or softening of the foundation soil – for instance in Mexico City during Michoacan earthquake of 1985 (Mendoza and Avunit 1988), in the city of Adapazari due to 1999 Kocaeli earthquake (Karaca 2001; Bakir et al. 2002; Yılmaz et al. 2004), during the 2010 Maule (Chile) Earthquake (Bray and Frost 2010), in 2011 Tohoku (Japan) Earthquake (Ashford et al. 2011), and in the

more recent 2010-11 New Zealand earthquakes (Cubrinovski et al. 2011) or the 2018 Indonesia Sulawesi earthquake (Sassa and Takagawa 2019). Figure 1 shows some recent examples of liquefaction induced effects on buildings resting on shallow foundations, highlighting the need for further research into the complex behaviour of shallow foundations built on liquefiable soils, including studying efficient techniques to ensure foundation safety through ground improvement. This is only possible through advanced physical modelling or properly-calibrated numerical modelling, which usually requires the use of dynamic centrifuge modelling.



Figure 1. Seismic-liquefaction damage on buildings resting on shallow foundations. (adapted from Cubrinovski, 2013)

The effects of seismic liquefaction are indeed a very complex phenomenon to model, as significant loss of the soil's strength and stiffness due to excess pore pressure build-up, complex soil-structure interaction (SSI) mechanisms and very large deformations are typically observed. In the physical modelling of engineering problems, scaled models of field prototypes are normally used to simulate field conditions. The reliability of such scale models in geotechnical engineering may be undermined by the reduced stress level they might be subjected to, resulting in a noticeably different response with respect to prototype geotechnical models. This particular limitation of 1g testing of scaled models may be overcome if the stresses and strains at homologous points in the prototype and model structures could be identical. This can be achieved by spinning the model built at 1:N scale on a geotechnical centrifuge to increase the gravitational field by a factor of N, so that the prototype stresses are matched (Muir Wood, 2004).

Centrifuge modelling is based on the principle of creating scaled-down models of geotechnical structures in order to depict the behaviour of a prototype model, which corresponds to a non-scale simplified representation of the real problem. The behaviour of soils has been established to be highly non-linear and hence true prototype behaviour can only be observed in a model under stress and strain conditions similar to the prototype. A geotechnical centrifuge enables us to recreate the same stress and strain level within the scaled model by testing a 1:N scale model at N times earth's gravity, created by centrifugal force. The similarity of stress, strain and material behaviour ensures the realism of model behaviour as long as the boundary conditions are correctly implemented. However, despite centrifuge modelling being a very attractive tool to model such complex problems, it still may carry some unexpected phenomenon during its performance.

2 CHARACTERISTICS OF THE DYNAMIC CENTRIFUGE MODEL

To highlight the behaviour of neighbouring shallow foundations under liquefaction effects, a dynamic centrifuge test was performed at Cambridge University's Schofield Centre. The centrifuge model represented an 18 m deep liquefiable deposit with two nearby shallow foundations placed on loose deposits of fully saturated sandy soil, as schematically shown in Figure 2.

The test was conducted using the 10-m diameter Turner Beam Centrifuge (Schofield, 1980). The centrifuge model was prepared inside an ESB container (Zeng and Schofield, 1992), in order to minimise undesirable boundary effects. The actuator used in the centrifuge test to generate seismic simulations was the SAM actuator (Madabhushi et al., 1998), which is a simple and reliable mechanical actuator that uses the energy stored in a pair of flywheels to generate the input motion. Despite not being able to reproduce real seismic actions, it generates nearly sinusoidal horizontal acceleration motions of chosen duration and amplitude, which is considered valuable for fundamental research on earthquake effects, as it avoids the difficulties introduced by more complex dynamic loading.

Hostun sand, whose properties are summarized in Table 1 and described in detail by Flavigny et al. (1990), was selected to create the model. It is a fine-grained, clean and uniform silica sand typically very susceptible to liquefaction as it lies well within the boundaries for most liquefiable soil (Figure 3).

Table 1. Properties of Hostun sand (Stringer, 2008).

Angle of repose (°)	D ₁₀ (mm)	D ₅₀ (mm)	C _u =D ₆₀ /D ₁₀	e _{max}	e _{min}	G _s
33	0.286	0.424	1.59	1.067	0.555	2.65

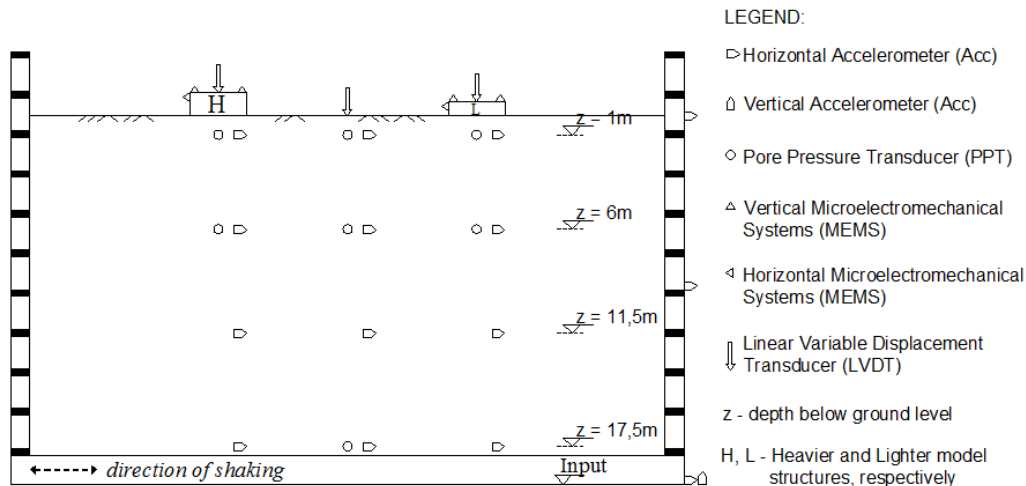


Figure 2. Model layout with the type, position and identification of the instruments used during the test (prototype scale).

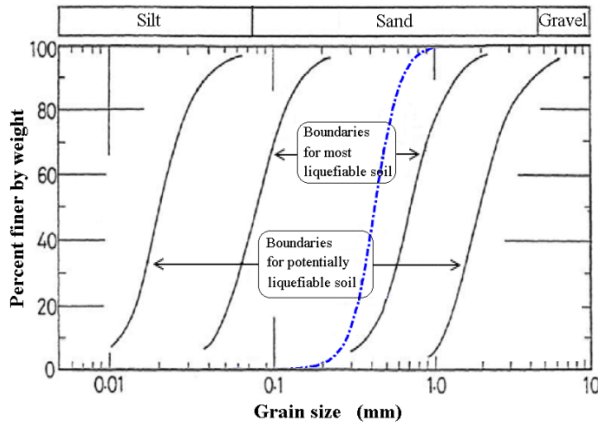


Figure 3. Particle size distribution curve for Hostun sand superimposed on liquefaction susceptibility curves proposed by Tsuchida (1970) – adapted from Stringer (2008).

Considering the aim of the test, structural models had a simple design, consisting of solid steel blocks with prototype dimensions (length x width x height) of $3 \times 3 \times 0.75 \text{ m}^3$, in the case of the lighter structure (L), and $3 \times 3 \times 1.225 \text{ m}^3$, in the case of the heavier structure (H). The pressure transmitted through the foundations basis equals 58 and 95 kPa, for the heavier and lighter structures, respectively.

A series of pore-pressure transducers (PPTs), accelerometers (accs) and linear variable displacement transducers (LVDTs) were installed in the model to assess the soil behaviour during the centrifuge test (Figure 2). A series of microelectromechanical system accelerometers (MEMS) were carefully attached to the footing to measure the vertical and horizontal accelerations induced in the footings during the earthquake. Several accs were attached to the bottom and lateral walls of the container to measure the vertical and horizontal input motions and to evaluate the horizontal motion propagation through the ESB walls.

Full saturation of the model ground is an essential part of the model preparation in centrifuge-based liquefaction research, as liquefaction is strongly affected by the degree of saturation. The saturation process requires time and strict control to avoid model disturbance and thus yield superior results. A viscous solution of hydroxypropyl methylcellulose in water was used as the pore fluid (Madabhushi, 1994), in order to achieve the so-called viscosity scaling (Lambe and Whitman 1982) and overcome the conflict between time scaling in flow and dynamic phenomena that occur simultaneously during liquefaction. The fluid used had a viscosity 50 times that of water to match the centrifuge acceleration used in the centrifuge test (50-g). This saturation procedure was processed with a novel automatic saturation system (Cam-Sat), available at Cambridge. The design and application of this

system are described fully by Stringer and Madabhushi (2009), subsequent improvements to the system being discussed by Stringer and Madabhushi (2010). With this system the saturation procedure is automated, not requiring a constant human presence through the entire process.

3 RESULTS AND DISCUSSION

The data presented in this work focuses mostly on the discussion of the acceleration motions measured on the footings through the MEMS installed in both structures.

3.1. Input motions

The centrifuge model was subjected to an input seismic motion at the base, applied parallel to the long side of the model and designed to replicate a relatively strong real earthquake, planned to last about 25 seconds, have a predominant frequency of 1 Hz and impose maximum peak horizontal accelerations close to 0.3-g. The long earthquake duration planned aimed at intensifying liquefaction effects and facilitating model behaviour analysis.

The actual time history of the horizontal seismic loading applied to the base of the model container is depicted in Figure 4a, showing that the planned earthquake simulation was successfully imposed to the model. The seismic simulation applied is not purely single-frequency, although the predominant frequency matches the desired value of 1Hz.

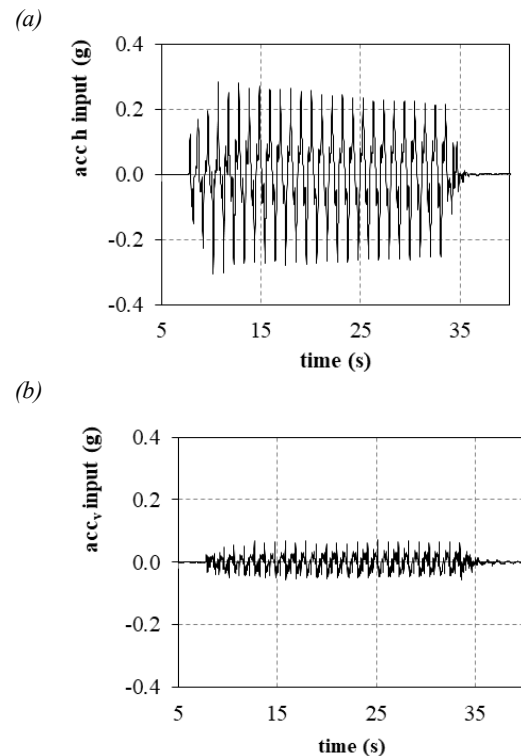


Figure 4. Time history of the seismic motion applied to the model: (a) horizontal accelerations, (b) vertical accelerations.

An accelerometer was also placed at the base of the model, in the vertical direction, to assess a possible unplanned vertical motion imposed to the model (Figure 4b). The measurements confirm that the total input motion applied to the base of the model also includes a vertical component. Still, this component is significantly smaller than the horizontal input motion and should not affect meaningfully the overall model behaviour.

3.2. Excess-pore-pressure generation and settlements

The measurements of the excess-pore-pressure in the ground at different locations and the settlements of the footings during and after the earthquake undoubtedly prove that the ground liquefied due to the seismic loading and that the settlements of the footings are compatible with the performance of real structures in the field when affected by liquefaction effects. More detail on the data obtained is shown in Marques et al (2012).

3.3. Accelerations in the footings

The values of the horizontal accelerations measured in each footing and in the soil under each footing axis at different depths are depicted in Figure 5. The first major conclusion is that the transmission to the soil of the horizontal shaking applied to the base of the model is quite successful, as the horizontal accelerations recorded at the bottom of the soil model are very similar to those measured at the base of the container. Contrarily, the upward propagation

of the horizontal accelerations is considerably different in the soil and in the lateral boundary formed by the ESB vertical walls. This is certainly due to the fact that the container walls, designed to match the stiffness of the sand used in the design, maintain a similar response during the earthquake. In contrast, as the sand liquefies, the stiffness degradation caused by the large effective stress reduction strongly affects the propagation of the accelerations through the deposit. In fact, it is clear that large attenuation of the horizontal accelerations occur as the waves travel upward within the liquefied soil. Therefore, the different response of the soil and the container walls, which is a logical result of the differences in the stiffness of the materials once the sand liquefies, may induce boundary effects that should be avoided by placing the model footings sufficiently away from the container walls. It should be emphasised, however, that soil softening due to excess pore pressure generation is believed to strongly mitigate boundary effects by reducing the soil's ability to transmit reflected seismic waves from the model box boundaries toward the footing models. Therefore, no significant amplification of the acceleration records should be expected once the soil starts to liquefy, namely at a reasonable distance from the walls. In this test, as suggested by Figure 5, no apparent increase is visible in the soil response under the footings, where the boundary effects would be more relevant. Consequently, the footings seem to be placed as far from the walls as necessary to prevent unrealistic accelerations.

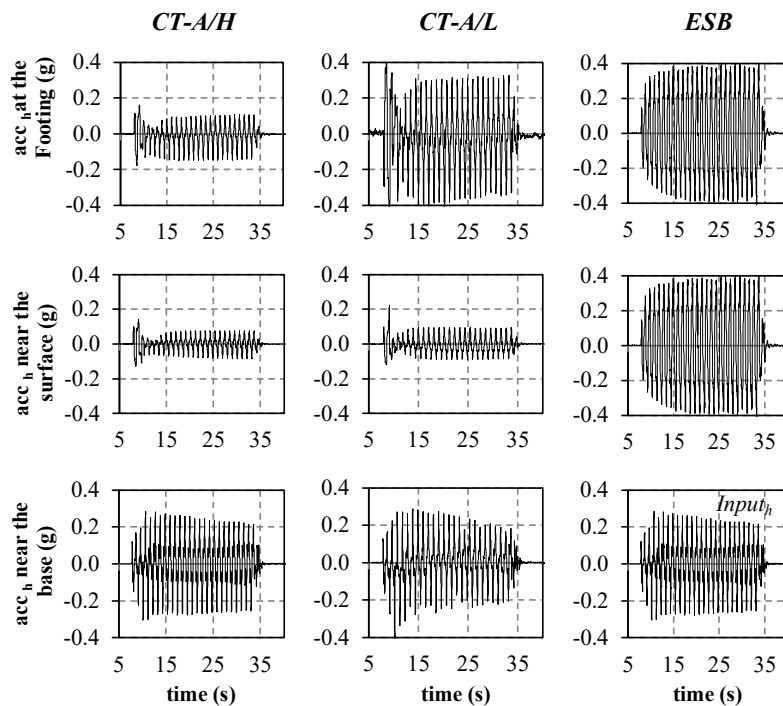


Figure 5. Analyses of the time histories of horizontal accelerations at the footings and at different positions between the centre of each footing and the walls of the ESB container in model.

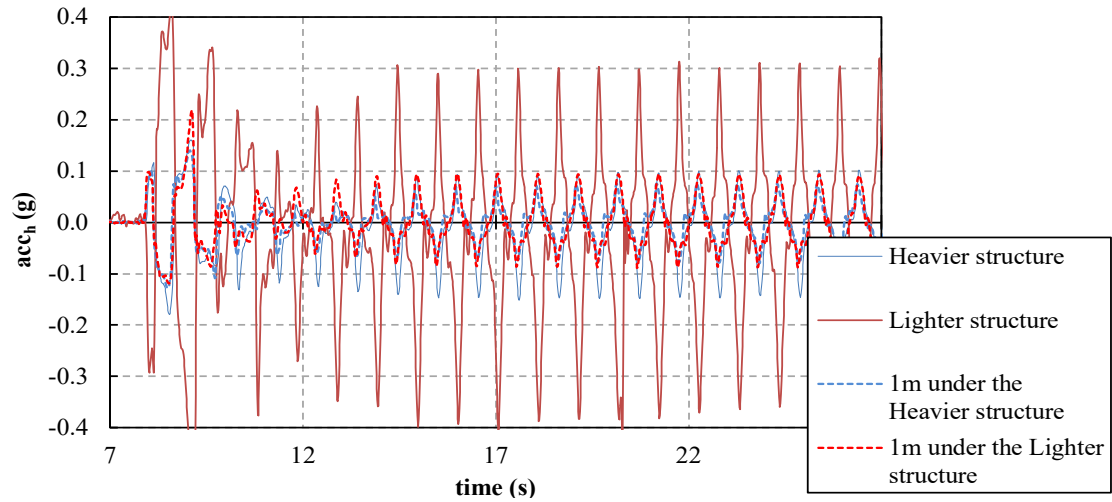


Figure 6. Horizontal motions measured in both footings and in the soil underneath.

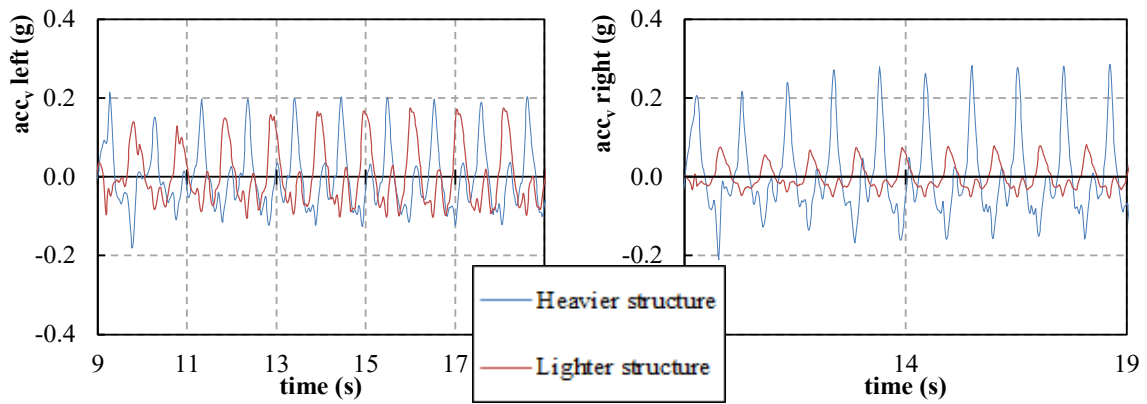


Figure 7. Comparison of the vertical motions measured at each structure during a short duration of time.

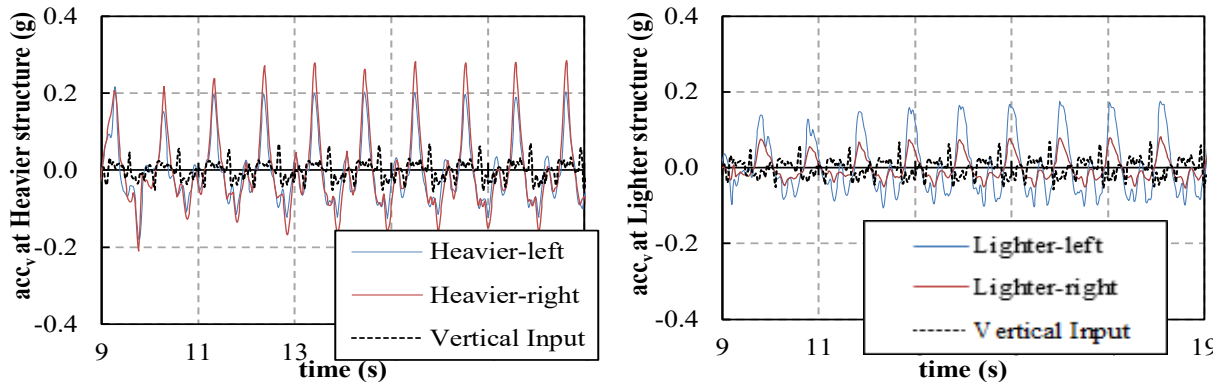


Figure 8. Comparison of the vertical motions measured at the left and right sides of both structures during a short period.

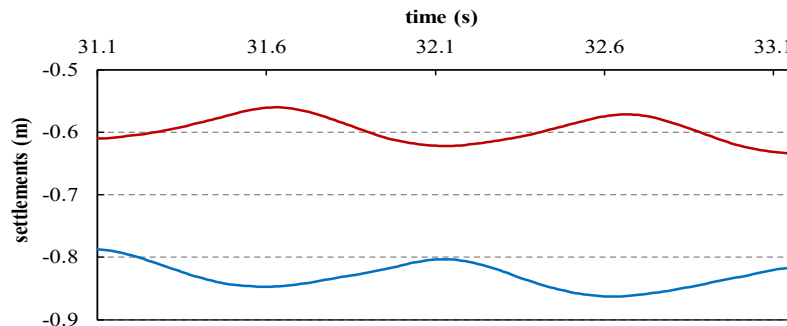


Figure 9. Oscillation in the LVDT readings during a short period due to possible shaking induced by model rocking.

For a more detailed and perceptible analyses of the horizontal accelerations measured in the test, a zoom of the data measured in each footing and near the surface are presented in Figure 6 corresponding to a relatively short period of time. Figure 6 clearly shows that the horizontal motions measured in each footing are not in phase with each other. Furthermore, the horizontal motions that reach the heavier structure (H) are in phase with the ground motion propagation, while the motions that reach the lighter footing (L) are not in phase with the rest of the horizontal data (soil and heavier structure). This observation is certainly unexpected, suggesting that the lighter structure might be experiencing some individual mechanism governing its motion that diverges from the motion of the ground and heavier structure.

On the other hand, soil softening due to seismic liquefaction may facilitate rocking of the soil model in the vertical plane under horizontal base shaking. Although this is not visible in the soil data, as vertical accelerometers were not installed throughout the soil deposit, experimental results on the footing's vertical motions emphasizes the occurrence of significant rocking motion. For a clearer observation of this phenomenon, Figure 7 shows the comparison of the left and right vertical motions measured at both sides in each footing, while Figure 8 compares the vertical motions measured in both sides of the same footing and compares these with the measured vertical input. Analysing each of these figures, it is clear that the vertical accelerations measured in the footings are not a mere consequence of the vertical input, suggesting also that a rocking mechanism causing the vertical accelerations in the footings does not seem to occur in each footing individually, as it is visible in Figure 8. Instead, the rocking mechanism seems a result of a global rocking mechanism affecting all the model (Figure 7). In fact, both sides of each footing show vertical motion that are in phase, the footing's motions being completely out of phase with each other. This disturbs the response of the footing models, being also visible when comparing the vertical oscillations obtained in both shallow foundations during typical cycles of shaking, through LVDT's placed on top of the footings (Figure 9). Footing oscillation may be assumed to be equal to the ground surface oscillation at that location. At the time represented by the analysed cycle of base shaking (~31.1-33.1s), the soil has already been fully softened by the generation of epp, resulting in a fluid-like ground surface oscillation. These results highlight the fact that both footings have similar levels of vertical oscillations but are not in phase. This unexpected

global rocking of the model may result from an unplanned rocking motion introduced in the model during the simulation of the earthquake or from a response of the soil model caused by the low-friction interface between the soil and the container. Nevertheless, the overall performance of the results measured should not be significantly affected by this unexpected behaviour, especially if it is properly understood.

4 CONCLUSIONS

The experimental data obtained in a dynamic centrifuge model representing two neighbouring shallow foundations built on liquefiable ground show the unique value of this powerful experimental research tool in assessing the mechanisms governing the performance of the structures during and after a seismic event. In fact, the stiffness degradation of the soil induced by large excess-pore-pressure degradation and its effects on the motion upward propagation is clearly captured by the model, as are the excess-pore pressure generation and the footing and ground vertical settlements.

However, as the stiffness of the ESB container remains the same during the earthquake, significant unrealistic boundary effects may occur in the ground near the physical limits of the model ground. In order to avoid these possible boundary effects and the negative consequences on the behaviour exhibited by the footings, it is important to place the structures sufficiently distant from the container walls, namely when using a ESB container. It should be noticed that using other containers, such as laminar containers, may reduce this problem but create other challenges in centrifuge modelling.

Last but not the least, the analysis of the rocking mechanisms observed in the models should take into consideration that unexpected components of acceleration, which are often not even measured, may be applied to the models. Furthermore, additional vertical accelerations in the footings may result from complex rocking mechanisms that may not be totally realistic, as they result from global rocking of the model instead of a realistic response of the footing to the dynamic loading. This unforeseen response, only observed because of the unusual number and position of the accelerometers used in the test, may result from an unplanned rocking motion introduced in the model during the simulation of the earthquake or from a response of the soil model caused by the low-friction interface between the soil and the container. In any case, the consequences of this problem should not affect the overall value of the data obtained.

Considering the validated ability of centrifuge modelling to model problems as complex as the one considered and the large limitations of potential alternatives, progress in the understanding of the behaviour of shallow foundations built in liquefiable ground and improvements in the development of more efficient liquefaction mitigation measures strongly depends on the use of centrifuge modelling as a research tool, especially if some limitations are appropriately dealt with in the design of the model and analysis of the data.

5 ACKNOWLEDGEMENTS

This research was funded by the European Community's 7th Framework Programme [FP7/2007-2013] for access to the Turner Beam Centrifuge, Cambridge, UK, under Grant Agreement n° 227887. The first author would also like to thank FCT – Fundação para a Ciência e a Tecnologia, Portugal – for sponsoring her PhD programme (grant no. SFRH/BD/73170/2010). The kind and skilled support of the technicians and researchers involved in the experimental work carried out in the Schofield Centre is also acknowledged.

6 REFERENCES

- Ashford, A. S., Boulanger, R., and Brandenberg, S. 2011. Recommended design practice for pile foundations in laterally spreading ground. Report PEER 2011/04, Pacific Earthquake Engineering Research Center (PEER), Berkeley, CA.
- Bakir, B.S., Sucuoglu, H. and Yilmaz, T. 2002. An Overview of Local Site Effects and the Associated Building Damage during 17 August 1999 Izmit Earthquake. *Bulletin of seismological Society of America*, **92**(1): 509-526.
- Bray, J. D. and Frost, D. 2010. Geo-engineering Reconnaissance of the 2010 Maule, Chile Earthquake. *Geotechnical Extreme Events Reconnaissance (GEER) Association report No. GEER-022*, Chapter 7.
- Cubrinovski, M., Bradley, B., Wotherspoon, L., Green, R.A., Bray, J.D., Wood, C., Pender, M., Allen, J., Bradshaw, A., Rix, G., Taylor, M., Robinson, K., Henderson, D., Giorgini, S., Ma, K., Winkely, A., Zupan, J., O'Rourke, T., DePascale, G., Wells, D. 2011. Geotechnical Aspects of the 22 February 2011 Christchurch Earthquake, *Bulletin of the New Zealand Society for Earthquake Engineering*, **44**(4): 205-226.
- Cubrinovski, M. 2013. Liquefaction-Induced Damage in the 2010-2011 Christchurch (New Zealand) Earthquakes. 7th Int. Conf. on Case Histories in Geotechnical Engineering, Chicago, USA.
- Flavigny, E., Desrues, J. and Palayer, B. 1990. Le sable d'Hostun «RF». *Revue Française de Géotechnique*, **53**, 67-69.
- Karaca, G. 2001. An Investigation into Large Vertical Displacement Experienced by the Structures in Adapazari during 17 August 1999 Earthquake. MS thesis, Middle East Technical University, Ankara, Turkey.
- Lambe, P.C. and Whitman, R.V. 1982. Scaling for earthquake shaking tests on a centrifuge. *Proceedings International Conference on Soil Dynamics and Earthquake Engineering*, Vol. 1, Southampton, England, July 1982: 367-378.
- Madabhushi, S.P.G. 1994a. Scaling laws in Dynamic Centrifuge Modelling. *Proc. VIIIth Int. Conf. of the Association for Computer Methods and Advances in Geomechanics*, West Virginia University, Morgantown, USA.
- Madabhushi, S.P.G., Schofield, A.N. and Lesley, S. 1998. A new Stored Angular Momentum (SAM) based Earthquake Actuator. *Proc. Centrifuge'98, Int. Conf. on Centrifuge Modelling*, Tokyo, Japan:111-116.
- Marques, A.S., Coelho, P.A.L.F., Cilingir, U., Haigh, S.K. & Madabhushi, S.P.G. 2012. Centrifuge modeling of liquefaction-induced effects on shallow foundations with different bearing pressures. 2nd Eurofuge conference on Physical Modelling in Geotechnics. Delf.
- Mendoza, M.J. and Avunit, G. 1988. The Mexico Earthquake of September 19, 1985-Behavior of Building Foundations in Mexico City", *Earthquake Spectra*, **4**(4): 835-853.
- Muir Wood, D. 2004. *Geotechnical modelling*, Volume 1. Taylor & Francis.
- Sassa, S., Takagawa, T. 2019. Liquefied gravity flow-induced tsunamis: first evidence and comparison from the 2018 Indonesia Sulawesi earthquake and tsunami disasters. *Landslides* **16**, 195-200. <https://doi.org/10.1007/s10346-018-1114-x>
- Schofield, A.N. 1980. Cambridge geotechnical centrifuge operations, 20th Rankine Lecture. *Geotechnique*, **30**(3):227-268.
- Stringer, M.E. 2008. *Pile Shaft Friction in Liquefaction*. First Year Report, University of Cambridge, UK.
- Stringer, M.E. and Madabhushi, S.P.G. 2009. Novel Computer Controlled Saturation of Dynamic Centrifuge Models using High Viscosity Fluids. *ASTM Geotechnical Testing Journal*, **32** (6), 53-59.
- Stringer, M.E. and Madabhushi S.P.G. 2010. Improving Model Quality in Dynamic Centrifuge Modelling through Computer Controlled Saturation. In: *Proc. International Conference on Physical Modelling in*

Geotechnics S. M. Springman, J. Laue, and L. Seawards, eds., Zurich, Switzerland: Balkema.

Yılmaz, M. T., Pekcan, O., Bakır B. S. 2004. Undrained cyclic shear and deformation behavior of silt-clay mixtures of Adapazarı, Turkey. *Soil Dynamics and Earthquake Engineering*, **24**(7), 497-507.

Zeng, X., and Schofield, A. N. 1992. Design and performance of an Equivalent Shear Beam (ESB) model container for earthquake centrifuge modelling. *Geotechnique*, **46**(1), 83-102.

Boundary effects in centrifuge modelling of soil liquefaction

Zheng Li¹, Sandra Escoffier¹

¹*Université Gustave Eiffel, Département Géotechnique, Environnement, Risques naturels et Sciences de la terre (GERS), Geomaterials & Models in Geotechnics Laboratory (GMG), France*

Corresponding author: Sandra Escoffier (sandra.escoffier@ifsttar.fr)

ABSTRACT: Centrifuge modelling is commonly regarded as a valuable tool for seismic analysis of geotechnical problems. However, the correct recovery the loading condition under seismic loadings greatly depends on the boundary of the container, whereas the soil was placed. This issue is of great importance especially for soil liquefaction. The issue of significant soil stiffness and shear strength degradation with increasing strain, which should ideally be reproduced by the physical boundaries of the centrifuge model, becomes very important. Recently a new laminar container was designed at Université Gustave Eiffel centrifuge laboratory, which advances the correct modelling of boundary condition under seismic/dynamic loadings. The newly designed laminar box composes metal frames and rollers trying to have almost zero lateral stiffness, which minimizes greatly the boundary effects. This paper presents a series of centrifuge tests on soil liquefaction problem using this newly designed laminar container. Loose and dense Hostun HN31 sand with relative density of 50% and 80% were used. The influence of boundary effects induced by laminar container on the liquefaction of sand with different relative densities was highlighted and quantified.

Keywords: Liquefaction; Centrifuge Modelling; Boundary Effects; Laminar.

1 INTRODUCTION

As a very effective approach, centrifuge modelling has played a very important role in improving the understanding not only of phenomena's, but also the mechanism of many geotechnical problems. For the simulation of seismic effects, dynamic centrifuge modelling has been used for nearly two decades to investigate the seismic behaviour of various soil-structure systems. The artificial boundary of a model container may cause distortion in the stress and strain field in the model compared with those in the prototype modelled (Teymur & Madabhushi, 2003).

In order to enhance the value of the experimental results resulting from centrifuge tests, proper simulation of boundary conditions is required. This issue remains one of the most controversial aspects of centrifuge modelling of soil's dynamic behaviour, especially if the seismic event leads to liquefaction, since the dramatic reduction of soil stiffness and shear strength caused by liquefaction should ideally be reproduced by the model boundaries (Coelho, Haigh, & Madabhushi, 2003).

In this paper, the boundary effects induced by a newly designed laminar container at Université Gustave Eiffel are evaluated. A series of 1D centrifuge shaking table tests on saturated sand model were conducted to simulate level deposits subjected to base shaking with different magnitude and frequencies. The boundary effects are evaluated mainly in terms of maximum

displacement profiles and phase-lag between the laminar container and soil column.

2 EXPERIMENTAL SET-UP

In this section, the experimental set-up of the centrifuge test will be introduced. In this study, the test was carried out under the gravity level 60g. All the units will be presented in prototype scale otherwise mentioned.

2.1. Centrifuge models

2.1.1 Laminar container

Recently, a new laminar container was developed in the centrifuge team of Université Gustave Eiffel in Nantes. Figure 1 shows the 3D model of the laminar container. The inner dimensions of the container are 719*379 mm. Each ring in the laminar container has a height of 10mm with weight of 1.025 kg. The number of rings can be adjusted according to the height of the soil model. In this study, 22 rings were in the laminar container. The aim of the laminar container is to have a 'zero' lateral stiffness container. Rollers were installed between rings. Therefore, the rings can move freely in the horizontal direction. A very thin rubber film with 1 mm was installed inside the container to minimize as much as possible the constraints of rubber film. Two buffer stops were placed at the side of the container to limit the extreme unwanted lateral displacement. A rigid frame is also installed on the side of the container to ensure the 1D shear deformation.

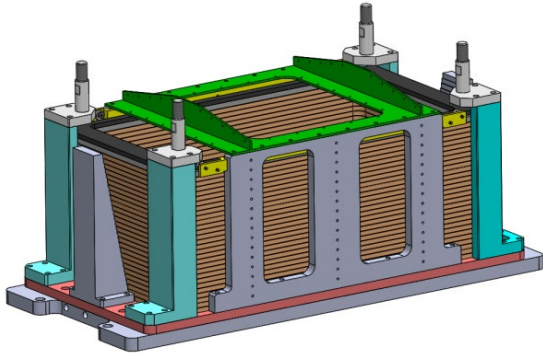


Figure 1. Laminar container recently developed in Université Gustave Eiffel centrifuge laboratory

2.1.2 Material properties

Hostun HN31 sand was used in the soil model, the properties of the sand are summarized in Table. 1.

Table 1. Characteristics of Hostun HN31 sand.

Sand	D_{50} (mm)	C_u	e_{min}	e_{max}	ρ_s (g/cm^3)
HN31	0.35	1.57	0.656	1	1.60

2.1.3 Model preparation

Instead of the normally used air pluviation preparation technique, moisture tamping method was used to prepare the sand sample. In order to achieve a homogenous sand model, under-compaction method (Ladd, 1978) was adopted. This method was originally used for preparation small scale triaxial laboratory tests which considers the influence of the tamping of upper layers to the under layers. The initial water content of the moist sand is 3.3%, loose sand model with relative density of 50% was then prepared following the under-compaction method.

The method proposed by Ueno (1998) was utilized to saturate the sand model at 1g. HPMC viscous fluid was prepared and the viscosity was around 60 cSt. The degree of saturation was determined by the method proposed by Okamura and Inoue (2012). The final degree of saturation was estimated around 92.0%.

2.1.4 Sensor plan and experimental program

Figure 2. shows the sensor plan in the dynamic centrifuge tests. Three arrays of accelerometers marker with red triangles were instrumented. In each sensor array, there are 5 accelerometers. The depths of these 5 accelerometers from bottom to top in prototype are 13.5, 10.5, 7.5, 4.5 and 1.5m. The base shaking was input at the bottom of the soil column at the depth 15.0 m. By comparing the lateral responses of the central, middle and side array, the boundary effect of the laminar container

in dynamic test can be evaluated. Pore pressure sensors were also used to monitor the built-up of excessive pore pressures.

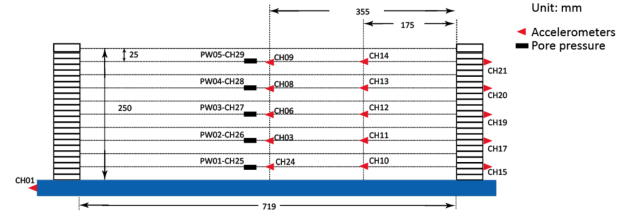


Figure 2. Sensor plan of the centrifuge model (model scale)

A large number (totally 50 shaking events) of simple sine base input signals with different frequencies and amplitudes were used in the test. The input sequence of the shaking events is shown in Figure 3. where the input frequency and amplitude are also noted.

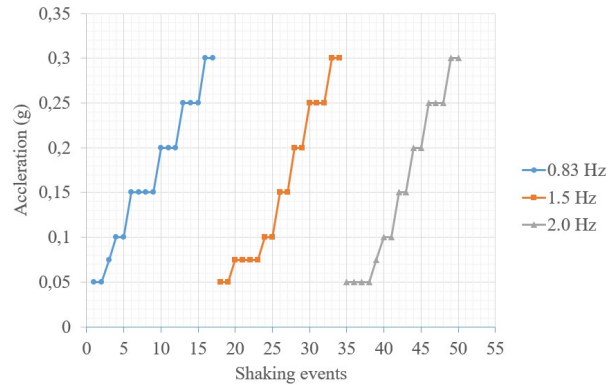


Figure 3. Shaking events (Acceleration and frequency are in prototype scale)

3 RESULTS AND DISCUSSION

As it was explained in section 2.1.4, large number of base shakings were input to the model. As a result, the initially loose sand became denser and denser. The initial relative density is around 50% and nearly 2.0 cm settlement was observed on the surface of the sand. The final relative density is estimated around 98%. The data from pore pressure sensor confirms this. After the 30th shaking event, instead of the built-up of pore pressure, a suction behaviour of water was observed in the sand, which corresponds to the dilatancy of sand under shear loading. Therefore, the boundary effects of the laminar container should be evaluated according to different state of the sand model, i.e., loose, medium dense and dense states.

The boundary effects of the laminar container are first analysed for the sand model in loose state. Take the 6th shaking event (0.1 g) as an example, the maximum displacement profiles of central, middle and side array are shown in Figure 4. The profiles of central and middle array are almost identical. Different behaviour is observed for the side array.

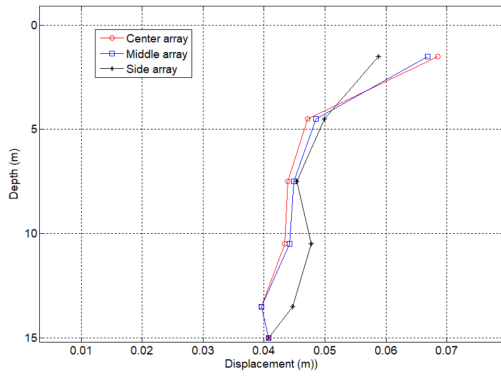


Figure 4. Maximum displacement profiles of central, middle and side array, 6th shaking event (0.1 g input)

By analysing the time history of displacements near the soil surface (depth 1.5m, prototype scale, CH09, CH14 and CH21), the displacement amplitudes are different. In addition, the displacement on the container is lag behind to the displacement in the soil.

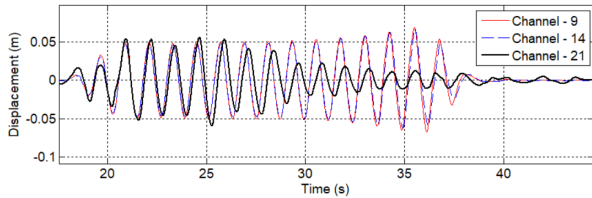


Figure 5. Displacement time-history of CH09, CH14 and CH21, depth 1.5m, prototype scale. 6th shaking event (0.1 g input)

However, with the increase of depth, the phase-lag between the side wall and soil column decreases. Only very small phase-lag can be found. The differences mainly come from the displacement amplitudes, see Figure 6.

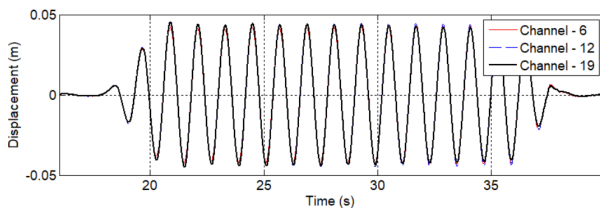


Figure 6. Displacement time-history of CH06, CH12 and CH19, depth 7.5m, prototype scale. 6th shaking event (0.1 g input)

For the sand model in medium dense state (shaking event 26), the maximum displacement profiles of central, middle and side array are shown in Figure 7. Similar as the sand in loose state, the profiles of central and middle array are almost identical. Different behaviour is observed for the side array.

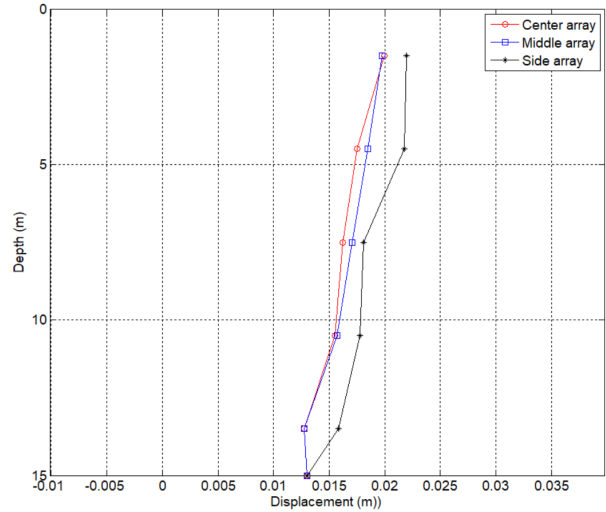


Figure 7. Maximum displacement profiles of central, middle and side array, 26th shaking event (0.1 g input)

At the shallow depth 1.5 m under the soil surface, the displacement time-history is shown in Figure 8. The displacements of central and middle in the soil are identical. However, great phase-lag is observed between the soil and container.

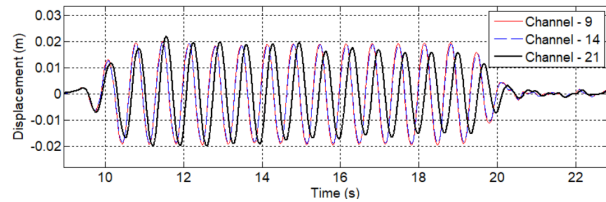


Figure 8. Displacement time-history of CH09, CH14 and CH21, depth 1.5m, prototype scale. 26th shaking event (0.1 g input)

Even in deeper depth, phase-lag can be observed. For example, at depth 7.5m, the side wall is always lagged behind the soil.

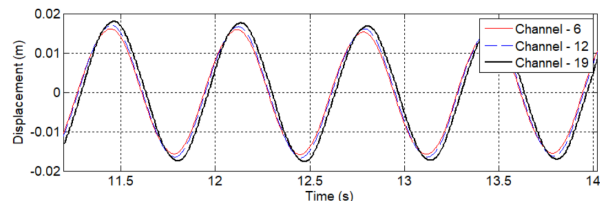


Figure 9. Displacement time-history of CH06, CH12 and CH19, depth 7.5m, prototype scale. 26th shaking event (0.1 g input)

Comparing with the sand model in medium dense state, similar boundary effects of model with very dense sand are observed. The behaviour of the central and middle array is identical; however, great phase-lag was observed between the side wall and the soil. The results are shown in Figures 10, 11 and 12.

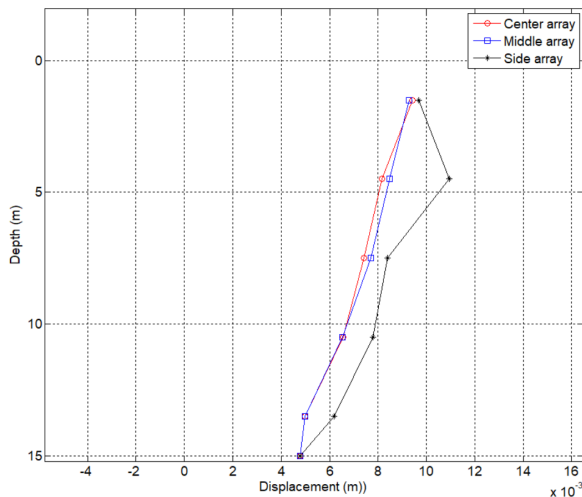


Figure 10. Maximum displacement profiles of central, middle and side array, 42th shaking event (0.1 g input)

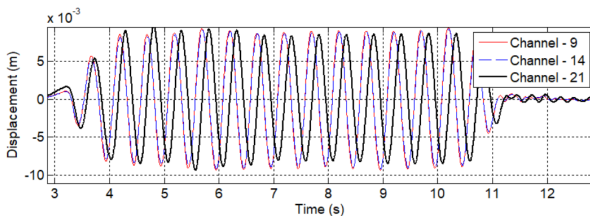


Figure 11. Displacement time-history of CH09, CH14 and CH21, depth 1.5m, prototype scale. 42th shaking event (0.1 g input)

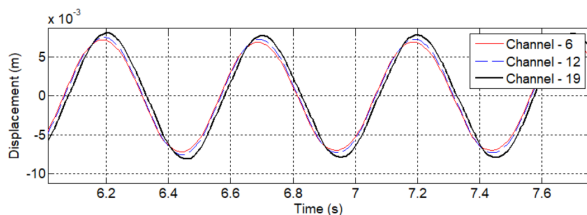


Figure 12. Displacement time-history of CH06, CH12 and CH19, depth 7.5m, prototype scale. 42th shaking event (0.1 g input)

4 CONCLUSIONS

In this paper, the boundary effects of a new laminar container designed and built in centrifuge team in Université Gustave Eiffel were evaluated. In general, the behaviour of the soil columns in the center and in quarter of the container are almost identical. However, great phase-lag was observed of the side-wall of the laminar container, especially for medium and very dense sand model. At the same depth, the ring of the laminar container is lagged behind the motion of the soil column.

5 ACKNOWLEDGEMENTS

The authors would like also to thank the valuable support and help of the technical staff of the Université Gustave Eiffel centrifuge team.

6 REFERENCES

- Coelho, P. A. L. F., Haigh, S. K., & Madabhushi, S. P. G. 2003. Boundary effects in dynamic centrifuge modelling of liquefaction in sand deposits. 16th ASCE Engineering Mechanics Conference, 1–12. Seattle.
- Ladd, R. S. 1978. Preparing test specimens using undercompaction. *Geotechnical Testing Journal*, **1**(1), 16–23.
- Okamura, M., & Inoue, T. 2012. Preparation of fully saturated models for liquefaction study. *International Journal of Physical Modelling in Geotechnics*, **12**(1), 39–46. <https://doi.org/10.1680/ijpmsg.2012.12.1.39>
- Teymur, B., & Madabhushi, S. P. G. 2003. Experimental study of boundary effects in dynamic centrifuge modelling. *Géotechnique*, **53**(7), 655–663.
- Ueno, K. 1998. Methods of preparation of sand samples. *Proceedings of the International Conference Centrifuge 98*, 1047–1056. Tokyo.

Centrifuge model studies on dry granular soils subjected to dynamic compaction induced tamping

Saptarshi Kundu¹, B.V.S. Viswanadham²

¹Research Scholar, Department of Civil Engineering, Indian Institute of Technology Bombay, INDIA

²Professor, Department of Civil Engineering, Indian Institute of Technology Bombay, INDIA

Corresponding author: *B.V.S. Viswanadham* (viswam@civil.iitb.ac.in)

ABSTRACT: The objective of this paper is to present centrifuge model studies on dry granular soils subjected to dynamic compaction (DC) induced tamping. A custom developed and designed inflight DC actuator was used. The developed actuator is equipped with a motorized lifting and dropping mechanism to induce repeated drops on the soil surface at high gravities, with prototype energies varying from 50 ton-meter to 400 ton-meter. The actuator can thus simulate both low-energy blows and high-energy DC processes adopted in the field. The present paper discusses the results of two centrifuge model tests performed on dry loose granular soil deposit using the 4.5 m radius large-beam centrifuge facility available at IIT Bombay, India. The analysis of data captured by accelerometers, coupled with GeoPIV based Image Analysis was employed to demonstrate the effectiveness of DC in granular soils using the developed actuator for various tamper energies. The results are interpreted in terms of crater depth, induced ground velocities and peak accelerations and increase in relative density of the soil post DC.

Keywords: Centrifuge; Dynamic Compaction; Scaling Laws; Ground Improvement.

1 INTRODUCTION

In recent times, rapid industrialization and infrastructure developments have created acute scarcity of suitable construction sites. This has led to renewed interest in finding means of improving the geotechnical characteristics of sites with deficient subsoil types (like loose soil deposits, collapsible soils, reclaimed fills, coal ash deposits, waste dump sites, etc.). Among the available ground improvement techniques, Dynamic compaction (DC) has gained popularity in view of its simplicity, low-environmental impact and cost-effectiveness. The method transmits kinetic energy onto the soil/material by repeatedly dropping heavy tamper from a significant height at regularly spaced intervals (square pattern with print spacing of the order of 4 m - 6 m). This eventually leads to optimization of foundations for structures, thereby economizing the project. The current practice for evaluating the feasibility of DC and choosing the operational parameters at the site are not well established. The decisions have to be made depending mainly on field trials, past experience, and empirical equations derived from field case studies. The above factors necessitate a detailed investigation of DC process for establishing design parameters governing its efficiency.

Field testing and related case studies on the effectiveness of DC were documented by various researchers including Mayne et al. (1984), Zou et al. (2005), Bo et al. (2009) and Feng et al. (2011). However, the results presented were extremely site-specific, and limited information on the

improvement depth and degree of compaction can be gathered from the above due to soil heterogeneity and problems related to instrumentation and data acquisition. Further, the results of low-energy DC tests by Feng et al. (2000), Arslan et al. (2007), Bonab and Rezaei (2009), Bonab and Zare (2014), Kundu and Viswanadham (2016) and Kundu and Viswanadham (2018) lack field validation owing to dissimilar stress conditions in the model and full-scale prototype. Limited centrifuge model simulations on dry soil conducted by Oshima and Takada (1998) and Merrifield and Davies (2000) also exhibited major restrictions in modelling the time interval between successive tamper drops. Hence, there arises the necessity of developing a robust actuator for studying DC induced ground improvement and factors influencing its efficiency.

The present study aims at investigating the response of dry, loose sand deposit subjected to DC. Centrifuge-based physical modelling technique was adopted in this regard to replicate identical stress-strain response in model and prototype soil deposits. Tests were conducted at high gravities on a typical dry, loose sand using a custom-developed in-flight actuator. Design details of the actuator are discussed in subsequent sections. The influence of tamping energy during DC was also investigated. Data interpretation was done through data captured by accelerometers, coupled with GeoPIV based Image Analysis on photographs captured during centrifuge tests. The results have been presented in terms of crater depths, effective depth of improvement and ground vibrations induced during DC.

2 IN-FLIGHT DC ACTUATOR

An actuator was custom designed and developed for simulating DC within a centrifuge. In case of centrifuge modelling, the body forces of model geomaterials are increased by inducing centripetal acceleration N times that of earth's gravity (g) so as to replicate full-scale stresses in the centrifuge model reduced by N times at homologous points. Accordingly, appropriate scaling laws need to be established for linking the model behaviour to that of the prototype. The relevant scaling laws adopted in this study related to simulation of DC in centrifuge are presented in Table 1, based on which the present actuator has been designed.

The various components of the actuator include the support system, impactor assembly, tamper-hook arrangement and guiding rod-assembly. Essential components of the actuator are shown in Figure 1 along with instrumentation details. The support system consists of beam, columns and flanges, and carries the weight of the whole actuator. The impactor assembly as shown in Figure 2 consisting of drive shaft, sheave, follower, steel hoist rope and stopper for hook arrangement controls the lifting and dropping of tamper. Three distinctive components, namely base plate, guide shafts and collar are integrated to constitute the tamper used for DC (Figure 3). The hook arrangement (Figure 4) is used for engaging and disengaging tamper in-flight during DC. In addition, guiding rod-assembly (Figure 5) consisting of central and peripheral rods enable linear guidance of tamper and nullify the effects of Coriolis force generated at high gravities respectively.

A brief explanation of the mechanism involved in lifting and dropping of tamper is provided here. Activation of motor facilitates rotation of drive shaft in clockwise direction which causes the cam mounted on drive shaft to engage the follower of sheave. This results in simultaneous and equiangular rotation of sheave and subsequent lifting of tamper using hoist rope. Further rotation of driving shaft causes hook arrangement to reach a position where hook comes in contact with hook stopper and rotates anticlockwise about the hinge. The above process results in release of the tamper, thereby initiating free-fall on the soil surface. Rotation of the drive shaft beyond this point creates a situation when the cam rotates out of contact with the follower. Subsequently, the hook arrangement descends under the influence of gravity and slides over tamper collar to reach the initial position. The afore-mentioned sequences are repeated to facilitate subsequent blows on the soil surface, and the process can be terminated at any point of time

during centrifuge tests by de-activating the motor. Thus, the present actuator has been designed to enable variation of tamper striking frequency through control of motor rotational speed, which is advantageous while modeling DC in saturated soils. Detailed description of the in-flight actuator is presented in Kundu and Viswanadham (2020).

Table 1 Scaling laws for simulating DC in centrifuge

Parameters	S.F.
Angle of internal friction (ϕ) ($^\circ$)	1
Unit weight of soil (γ) (kN/m^3)	N
Relative density of soil (RD) (%)	1
Mass of tamper (m) (t)	$1/N^3$
Radius of tamper (r) (m)	$1/N$
Drop height (H) (m)	$1/N$
Time interval between successive blows (t_i) (min)	$1/N$
Tamper velocity (v) (m/s)	1
Ground acceleration (A) (m/s^2)	N^a
Ground velocity (V) (m/s)	1
Crater depth (d_c) (m)	$1/N$
Depth of improvement (d_i) (m)	$1/N$
Energy of tamper (E) (t-m)	$1/N^3$

N : Gravity level or scale factor; S.F.: Scale factor; ^aFor example, $A_m/A_p = N$; m: model; p: prototype.

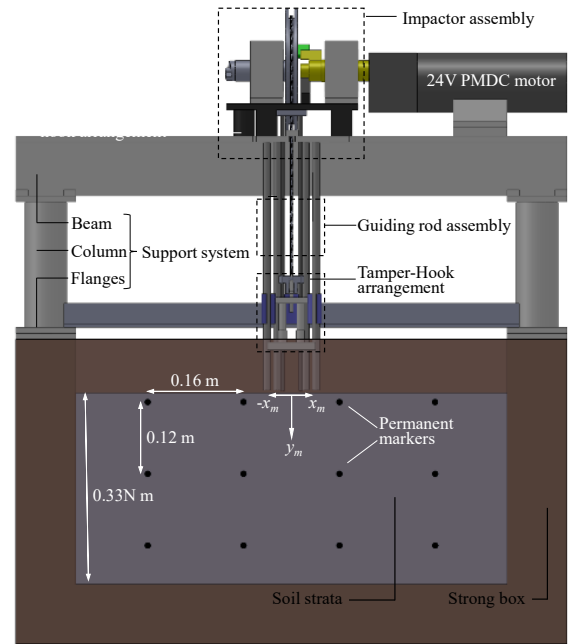


Figure 1. Schematic representation of DC simulator assembly

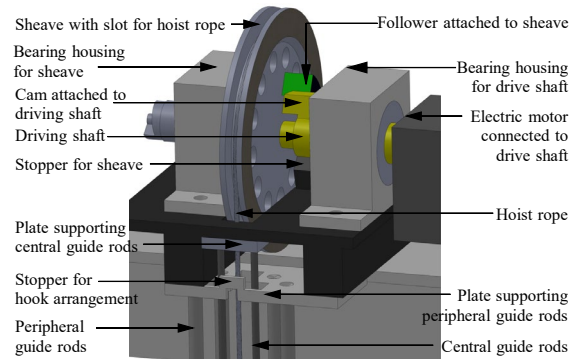


Figure 2. Schematic representation of impactor assembly

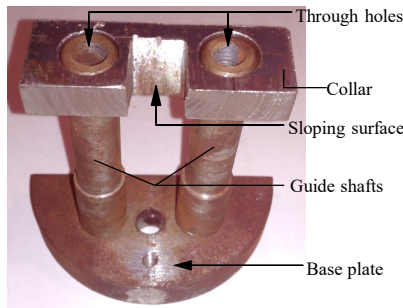


Figure 3. Details of tamper

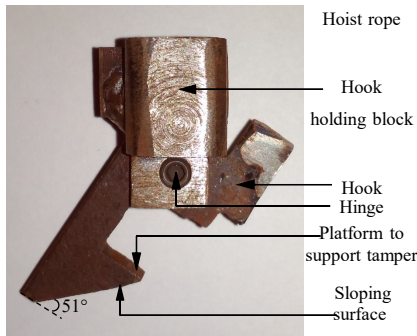


Figure 4. Hook arrangement and associated components

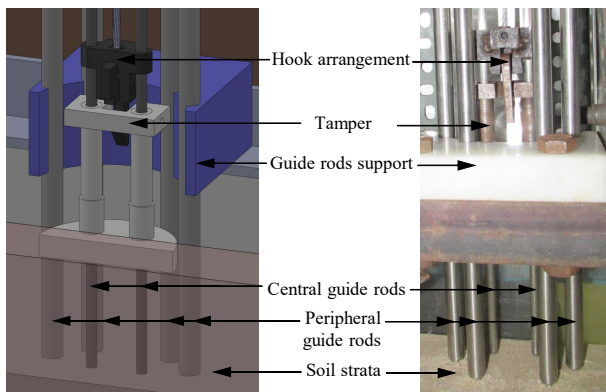


Figure 5. Guiding-rod assembly

3 MODEL MATERIAL AND METHODOLOGY ADOPTED

The model soil used in the study is Goa sand having a specific gravity of 2.654 with $e_{max} = 0.94$ and $e_{min} = 0.63$. The sand is poorly graded with negligible fines, and can be classified as SP [$C_u = 2.065$; $C_c = 1.117$] according to the Unified Soil Classification System (USCS). The model soil thus represents a typical granular material existing in loose state in the field, and exhibits characteristics of soils typically selected for DC projects.

The present paper discusses the results of two centrifuge model tests performed at 30 gravities using the developed in-flight DC actuator. The first test was performed on dry sand with 56 t-m (ton-meter) energy, while the second test involved 208 t-m energy. A rigid container with internal dimensions of 720 mm in length, 450 mm in breadth and 410 mm in depth was used for model

preparation. The front side of the container was provided with a transparent perspex sheet of 50 mm thickness for enabling view of front elevation of the model during testing. The plane of the perspex sheet served as a plane of symmetry, on account of which, only half of the soil mass and cylindrical tamper were modelled. With this, axial symmetry of DC on the soil surface was modelled. A set of twelve permanent markers made of thin transparency sheets were pasted along inner side of perspex sheet, thereby constituting a series of quadrants consisting of four markers along the corners, as shown in Figure 1. These markers serve as reference points for carrying out GeoPIV analysis on images captured during centrifuge tests. Further, in order to simulate homogeneous field conditions in the small-scale centrifuge model, the sand models were prepared in a loose dry state by adopting the air-pluviation technique and placed at a relative density (RD) of 35%. During model preparation accelerometers were placed on the soil surface at desired locations.

A large beam centrifuge of 4.5 m radius and capacity of 2,500 g-kN at the National Geotechnical Centrifuge Facility (NGCF), Indian Institute of Technology Bombay, INDIA was used to conduct centrifuge tests. Details of the centrifuge equipment and associated specifications are available in Chandrasekaran (2001). After completion of various stages involved in model preparation, the model container was mounted on the swing basket of centrifuge. The in-flight DC actuator along with other accessories were subsequently assembled and fixed thoroughly. In addition, the front elevation of model was illuminated to enable clear visualization of the model at all stages of centrifuge testing.

After taking Ig readings, centrifuge was started and the desired g-level was attained. Then motor was activated remotely for raising and dropping semi-cylindrical steel tamper (mass and radius of tamper scaled as per modelling considerations in centrifuge) 16 times on the surface of the soil deposit from a prefixed drop height. Selection of 16 number of blows was made considering standard field observations. After imparting the 16th blow to the soil surface, the motor was deactivated and stopping of centrifuge equipment was initiated.

Peak ground accelerations and velocity induced during tamper drops were analysed with the help of recorded accelerometer data. A GoPro digital camera (Hero 5 Black, USA), having a resolution of 12 megapixels was used to record proceedings of the experiment in-flight condition by capturing one image in every two seconds. Geo-PIV based image analysis [White et al. (2003)] on images captured during flight was used to plot crater formations,

displacement contours, volumetric strain contours and increase in relative density post DC.

4 RESULTS AND DISCUSSION

The results of centrifuge tests on dry sand are discussed briefly in this section. All values are reported in prototype scale. The variation of crater depths (d_c) and crater radius (r_c) corresponding to 16 blows are shown in Figure 6 for both the models. Crater depth and radius increased progressively with successive blows. The maximum crater depth and radius are observed to be about 0.49 m and 1.8 m respectively in Model TC1 at 56 t-m energy level. Upon increasing the energy level to 208 t-m, the maximum crater depth and crater radius increased to 1.16 m and 2.8 m respectively in Model TC2.

In addition, the displacement contours of Models TC1 and TC2 in radial and vertical directions at the end of 16 blows are presented in Figure 7 and Figure 8 respectively. In general, the contours depict considerable displacement of soil owing to densification, which gradually reduced with depth and radial distance from the center of tamper. It can be inferred that the vertical and radial boundaries of the displaced zone substantially increased on account of higher energy levels simulated in Model TC2 as compared to Model TC1.

Further, to study the depth of improvement induced by DC, the increase in relative density (RD) or volumetric strain (ϵ_v) contours post DC are presented in Figure 9 for Models TC1 and TC2. In the present study, depth of improvement (d_i) for models prepared with sand is considered as the thickness of soil strata measured from initial ground surface to a depth below which ΔRD is less than 10%. (ϵ_v) corresponding to ΔRD of 10% is 1.7%. The corresponding variation of $d_{i,e}$ with all 16 blows are shown in Figure 10. The effective depth of improvement ($d_{i,e}$) is defined as the depth of improvement measured from the base of crater. This is denoted as $d_{i,e}$, which is equal to difference of depth of improvement and depth of crater ($d_i - d_c$). The value of $d_{i,e}$ in dry sand increased from 4.1 m for low energy DC in Model TC1 to 5.59 m for high energy DC in Model TC2. Further, the average radial width of improvement (r_i) increased from 2 m to 4 m with increase in blow energy. Thus the approximate volume of soil ($\pi r_i^2 d_{i,e}$) improved by DC increased from 51 m³ to 281 m³ corresponding to an increase in energy from 56 t-m to 208 t-m. Thus, an increase in DC energy in the order of 3.71 times resulted in increased soil volume by about 5.5 times. Further, increase in r_i value by 2 times with increasing energy signifies that for higher energy levels, double the tamping spacing can be adopted in the field. In order to gain insight into the

centrifuge test results, d_i and $d_{i,e}$ obtained herein are compared to the standard formula [Equation (1)] suggested by Menard and Broise (1975).

$$d_i \text{ or } d_{i,e} = n(mH)^{0.5} \quad (1)$$

where, m is mass of tamper and H is height of fall.

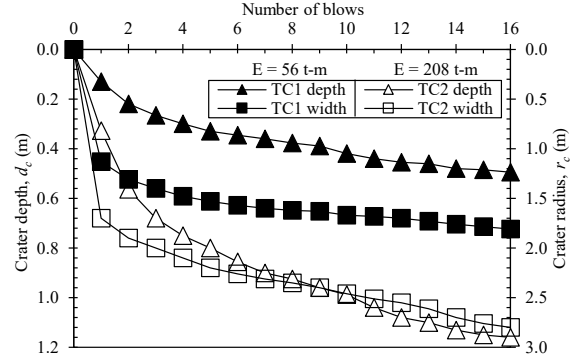


Figure 6. Effect of energy level on crater depth

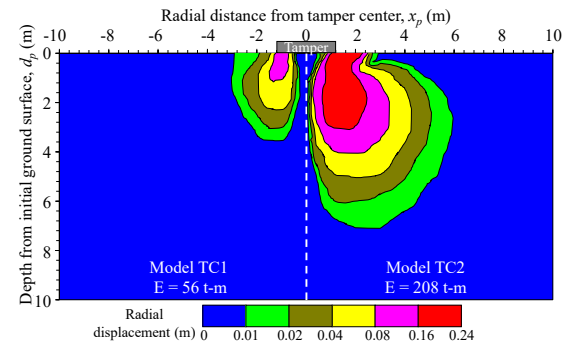


Figure 7. Effect of energy level on radial displacement of soil

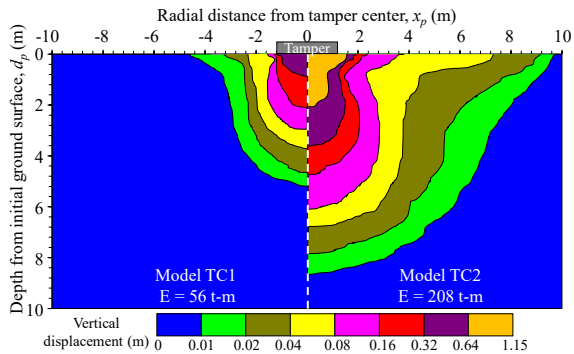


Figure 8. Effect of energy level on vertical displacement

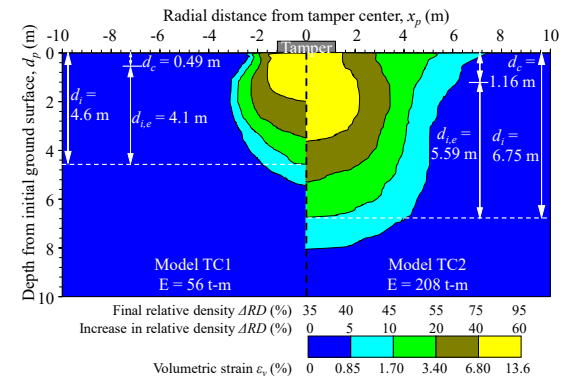


Figure 9. Effect of energy level on contours of relative density

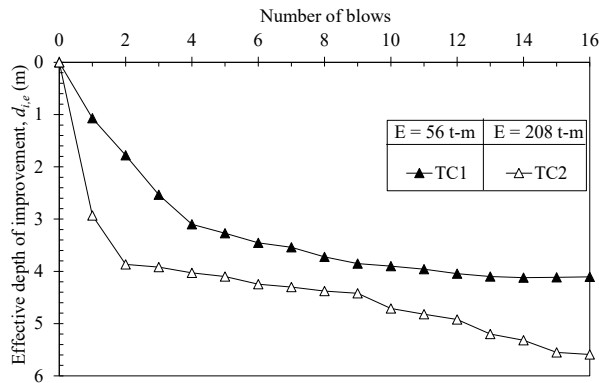


Figure 10. Effect of energy level on $(d_{i,e})$ with blows

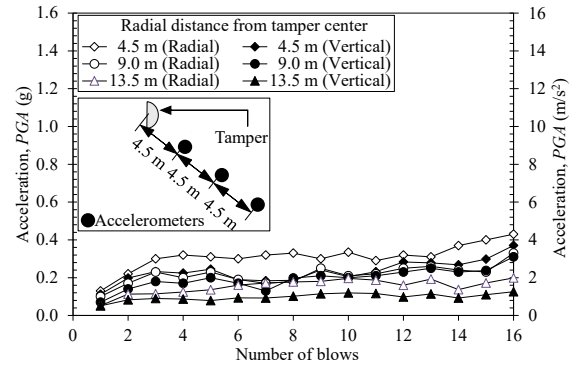
In the present study, the value of the empirical constant n is computed for both (d_i) and $(d_{i,e})$. For Model TC1 $n(d_i) = 0.61$ and $n(d_{i,e}) = 0.55$ and for Model TC2 $n(d_i) = 0.47$ and $n(d_{i,e}) = 0.39$. This indicates that with increasing energy level the n value decreases.

In addition, the PGA and PGV values along radial and vertical directions induced during DC in soils for energy levels of 56 t-m and 208 t-m after the 1st, 4th, 8th and 16th blow are presented in Figs. 11(a) - 11(b) to Figs. 12(a) - 12(b). Figs. 11(a) - 11(b) indicate that the PGA values after 16th blow are 0.44g [radial] and 0.38g [vertical] for Model TC1, which increased to 1.5g [radial] and 1.23g [vertical] respectively in Model TC2 upon increasing the tamper energy. Based on Figs. 12(a) - 12(b) the peak radial velocity near tamper after 16th blow is observed to be about 40 mm/s in Model TC1, and about 211 mm/s in Model TC2. The corresponding peak vertical velocity is about 25 mm/s in Model TC1 and about 112 mm/s in Model TC2. Hence, as evident from the PGA and PGV plots, an increase in energy level from 56 t-m in Model TC1 to 208 t-m in Model TC2 resulted in substantial increase in PGA and PGV values monitored at the same blow number. The test results in terms of crater depth, effective depth of improvement, PGA and PGV values are summarized in Table 2. The specifications of FHWA [Lukas (1995)] restricts PGV to 76 mm/s to avoid hazards to adjacent structures. In the present study, the PGV at 13.5 m distance from tamper center are 17.32 mm/s and 32.8 mm/s for Model TC1 and TC2 respectively.

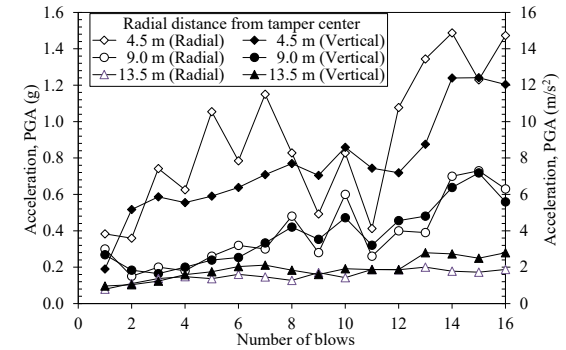
Table 2 Summary of centrifuge test results

Test legend	E (t-m)	$d_{i,e}$ (m)		PGA (g)		PGV (mm/s)	
		$(d_c)_{max}$	(m)	Radial	Vertical	Radial	Vertical
TC1	56	4.10	0.49	0.202	0.128	17.32	10.9
TC2	208	5.59	1.16	0.191	0.284	32.8	18.2

All values are reported in prototype scale; ^aReported after 16th blow at 13.5 m from tamper center; E: Tamper energy in each blow; $(d_c)_{max}$: Maximum crater depth;



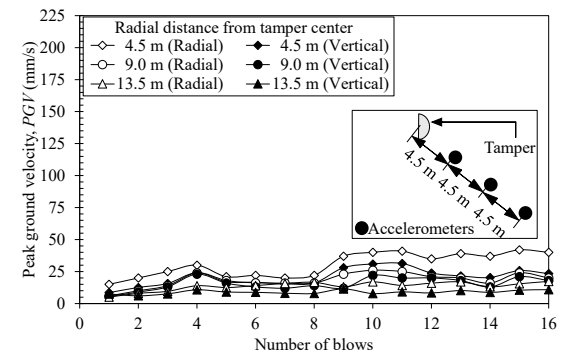
(a) Model TC1 [Dry sand; E = 56 t-m]



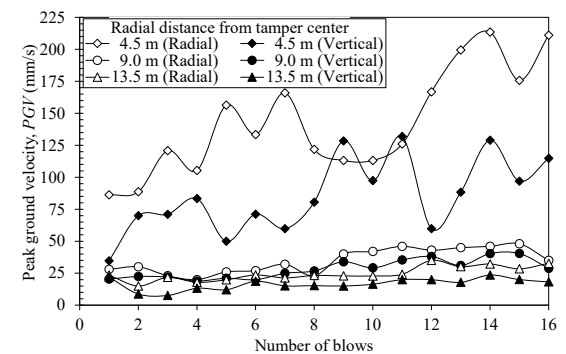
(b) Model TC2 [Dry sand; E = 208 t-m]

Figure 11. Variation of peak ground acceleration (PGA) with successive blows

Hence, the observed PGV induced during DC are well within the maximum magnitude of 76 mm/s at a radial distance of 13.5 m away from tamper, thereby indicating relevance of the technique.



(a) Model TC1 [Dry sand; E = 56 t-m]



(b) Model TC2 [Dry sand; E = 208 t-m]

Figure 12. Variation of peak ground velocity (PGV) with successive blows

5 CONCLUSIONS

The present study was intended to investigate the response of dry, loose granular soil deposits subjected to DC within a geotechnical centrifuge. A custom-designed actuator was developed in this regard, design details of which are presented. The actuator is found to be capable of replicating low-energy as well as high-energy DC processes in-flight within a geotechnical centrifuge. The results obtained in the course of the present study indicated the effectiveness of both low-energy and high-energy DC processes in improving the characteristics of loose granular soils. The crater depths, effective depth of improvement and ground vibrations induced during DC were found to increase with higher tamping energy. Further, the close correlation of depth of improvement obtained during centrifuge tests using the developed actuator with corresponding data reported in the field indicated the robustness and sound performance characteristics of the actuator.

6 ACKNOWLEDGEMENTS

The authors would like to thank the staff of the National Geotechnical Centrifuge Facility and of Geotechnical Engineering Laboratory at the Indian Institute of Technology Bombay, Mumbai, INDIA, for their support throughout the present study.

7 REFERENCES

- Arslan, H., Baykal, G. and Ertas, O. 2007. Influence of tamper weight shape on dynamic compaction. *Ground Improvement*, **11**(2): 61-66.
- Bo, M.W., Na, Y.M., Arulrajah, A. and Chang, M.F. 2009. Densification of granular soil by dynamic compaction. *Ground Improvement*, **162**(3): 121-132.
- Chandrasekaran, V. S. 2001. Numerical and centrifuge modelling in soil structure interaction. *Indian Geotechnical Journal*, **31**(1): 30-59.
- Feng, S. J., Shui, W. H., Tan, K., Gao, L. Y. and He L.J. 2011. Field evaluation of dynamic compaction on granular deposits. *Journal of Performance of Constructed Facilities*, ASCE, **25**(3): 241-249.
- Feng, T.W., Chen, K.H., Su, Y.T. and Shi, Y.C. 2000. Laboratory investigation of efficiency of conical-based pounders for dynamic compaction. *Géotechnique*, **50**(6): 667-674.
- Hajjalilue-Bonab, M. and Rezaei, A.H. 2009. Physical modelling of low-energy dynamic compaction. *International Journal of Physical Modelling in Geotechnics*, **9**(3): 21-32.
- Hajjalilue-Bonab, M. and Zare, F.S. 2014. Investigation on tamping spacing in dynamic compaction using model tests. *Ground Improvement*, **167**(3): 219-231.
- Kundu, S. and Viswanadham, B.V.S. 2016. Studies to evaluate the impact of tamper on the depth of improvement in dynamic compaction. *Japanese Geotechnical Society Special Publication*, **2**(59): 2033-2037.
- Kundu, S. and Viswanadham, B.V.S. 2018. Influence of tamper shape on dynamic compaction of granular soil. *Proceedings of the 9th International Conference on Physical Modelling in Geotechnics*, London, UK, 17-20 July 2018, Andrew McNamara, Sam Divall, Richard Goodey, Neil Taylor, Sarah Stallebrass, Jignasha Panchal (Eds), Taylor & Francis Group (Pubs.), Vol. 2, pp. 1205-1209.
- Kundu, S. and Viswanadham, B.V.S. 2020. Design and development of an in-flight actuator for modelling dynamic compaction in a geotechnical centrifuge. *Geotechnical Testing Journal*, ASTM, Manuscript number: GTJ-2019-0169R2
- Lukas, R.G. 1995. *Geotechnical Engineering Circular No. 1 - Dynamic compaction*. Federal Highway Administration Report No. - FHWA-SA-95-037, Washington D.C.
- Mayne, P.W., Jones, J.S. and E'Dinas, D.C. 1984. Ground response to dynamic compaction. *Journal of Geotechnical Engineering*, ASCE, **110**(6): 757-774.
- Menard, L. and Broise, Y. 1975. Theoretical and practical aspect of dynamic consolidation. *Géotechnique*, **25**(1): 3-18.
- Merrifield, C.M. and Davies, M.C.R. 2000. A study of low-energy dynamic compaction: field trials and centrifuge modelling. *Géotechnique*, **50**(6): 675-681.
- Oshima, A. and Takada, N. 1998. Evaluation of compacted area of heavy tamping by cone point resistance. *Proceedings of the Centrifuge'98*, Tokyo, T. Kimura, O. Kusakabe and J. Takemura (eds), Rotterdam: Balkema (pubs.), Vol. 1, pp. 813-818.
- White, D.J., Take, W.A. and Bolton, M.D. 2003. Soil deformation measurement using particle image velocimetry (PIV) and photogrammetry. *Géotechnique*, **53**(7): 619-631.
- Zou, W. L., Wang, Z., Yao and Z. F. 2005. Effect of dynamic compaction on placement of high-road embankment. *Journal of Performance of Constructed Facilities*, ASCE, **19**(4): 316-323.

Model preparation for unsaturated soil testing in a centrifuge environment

Leonardo Maria Lalicata¹, Luc Thorel², Augusto Desideri³, G.M. Rotisciani³, Francesca Casini⁴

¹*School of Engineering and Mathematical Sciences, City, University of London, London, UK*

²*GERS Department, Geomaterials and Modelling in Geotechnics Laboratory, Univ. Gustave Eiffel, Nantes Campus, Bouguenais, France*

³*Department of Structural & Geotechnical Engineering, University of Rome La Sapienza, Rome, Italy*

⁴*Dipartimento di Ingegneria Civile e Ingegneria Informatica, Università degli Studi di Roma "Tor Vergata", Rome, Italy*

Corresponding author: Leonardo Maria Lalicata (leonardo.lalicata@city.ac.uk)

ABSTRACT: This paper presents selected aspects of the model preparation and the experimental procedures used for testing the unsaturated soil behaviour in centrifuge environment. The study is based on the results of centrifuge tests carried out to investigate the influence of partial saturation on the behaviour of laterally loaded piles. The soil used in the experimentation is a high permeability silty clay soil, named B-grade kaolin. The models were statically compacted at two different densities with the same water content. In order to reduce the after compaction suction, the samples were subjected to an imbibition process at $1 \times g$ connecting the bottom of the model with the water reservoir. The influence of the compaction process and the imbibition stage on the subsequent inflight soil conditions are discussed and analysed. The centrifuge tests were realised at the centrifuge centre of the University Gustave Eiffel, in Nantes, France, in the framework of the GEOTRANSALP project.

Keywords: Unsaturated Soils; Static Compaction; Water Retention Curve; Centrifuge Modelling; Hydro-Mechanical Stress Paths.

1 INTRODUCTION

Centrifuge modelling represents a valid methodology to investigate the performance of different types of geotechnical works such as shallow and deep foundations, tunnels, slopes and embankments. Traditionally, studies have been conducted on fully saturated or completely dry soil models. However, in some cases the variation of the water content in the soil due to the water table oscillation, rainfall events, interaction with the atmosphere and exceptional events (i.e. pipe rupture etc...) may be crucial for the geotechnical works behaviour. These and other problems have been recently investigated by centrifuge modelling (Casini *et al.*, 2009; Soranzo *et al.*, 2015; Thorel *et al.*, 2011). Scaling laws for unsaturated soils have been experimentally investigated, among others, by Depountis *et al.* (2001) and Caicedo *et al.* (2006) under different soil condition and g -levels. The authors found that capillary rise and diffusion time in the centrifuge could be scaled by $1/N$ and $1/N^2$, respectively. Details of the analytical formulations can be found in Caicedo and Thorel (2014).

Compaction is the most common technique to prepare unsaturated soil samples (Caicedo and Thorel, 2014). Dynamic compaction allows to control the density but not the compaction stress. On the other hand, with the uniaxial static compaction procedure both density and compaction stress can

be measured although the horizontal stresses are in general unknown.

This paper presents the details of the model preparation of the experimental investigation conducted by Lalicata *et al.* (2019). The study aimed at assessing the influence of partial saturation on the response of laterally loaded piles installed in fine-grained soils. The centrifuge tests ($N = 100 \times g$) were carried out using the centrifuge facilities of the University Gustave Eiffel, located close to Nantes (France) in the framework of the GEOTRANSALP-PILE-UNSAT agreement.

2 MATERIALS

2.1. The soil used

The material used is a commercial soil named B-Grade kaolin (90% fine silt and 10% clay). This soil has a low plasticity index ($IP=14\%$) and a low liquid limits ($w_L=42\%$), the plastic limit is $w_P=28\%$. A complete hydro-mechanical characterisation was conducted in the geotechnical laboratory using standard apparatus for unsaturated and saturated soils. Results are reported in Lalicata (2018) and Lalicata *et al.* (2020). For the sake of brevity, only the flooding oedometer tests and the suction controlled oedometer tests are presented here. The hydro-mechanical parameters of the soil are listed in Table 1.

Table 1. Hydro-mechanical properties of B-Grade kaolin.

ρ_s (g/cm ³)	C_c	C_s	N_0^*	ϕ' (°)	c_v (mm ² /s)
2.66	0.26	0.078	1.36	22	1.0

* N_0 is the voids ratio at $\sigma'_v=1$ kPa under oedometric conditions.

Several imbibition tests in the oedometer apparatus were undertaken to define the after compaction conditions (w , e) for centrifuge models. The samples (18 mm thick and 70 mm in diameter) were prepared with different compaction features and subjected to different total vertical stresses σ_v applied before the wetting stage. In the main series of the tests, the vertical stress was 150 kPa corresponding to the vertical stress active at half of the pile embedded length ($z=8$ m). Samples were left equalise under the external load before filling the oedometer cell with water.

The soil powder was dried at 105 °C for 24 hours before adding the demineralized water to reach the target water content. The moisture was manually mixed and then it was kept in sealed bags for 24-48 hours to homogenise in a temperature-controlled environment. The specimens were statically compacted ($v=1.5$ mm/min) directly in the oedometric ring.

Three voids ratio are taken into account ($e_0 = 0.77$, 0.92 and 1.12), for water content ranging from 10% to 26%, with steps of 4%. For each grid point, at least two samples were tested.

Figure 1a shows the wetting induced deformation under $\sigma_v = 150$ kPa in function of the compaction void ratios. Water content measurements at the end of the test have shown that all the samples reached degrees of saturation closed to one ($S_{r,min}=0.95$). Results are grouped for the initial water content. For the material, the latter does not have a significant influence on the wetting deformation while the results strongly depends on the initial void ratios. The deformations reduce approximately linearly as the voids ratio decrease. Little swelling was observed for the more compacted samples ($e_0=0.77$).

The influence of the applied external load during samples inundation is depicted in Figure 1b, for stresses ranging from 0 to 600 kPa. Samples were prepared at $e_0=1.12$ and $w=14\%$. Soil swelling occurs only in absence of external load applied, while since from $\sigma_v= 50$ kPa the soil experience positive deformations that increase up to $\sigma_v= 300$ kPa and then they slightly reduce in magnitude. Thus, in the centrifuge, this soil would have experienced modest swelling in the shallower layer and volume reductions increasing with depth.

In order to explore the influence of the compaction conditions of soil in the centrifuge tests, two void

ratios are selected (0.93 and 0.75) prepared with the same water content $w=15\%$. The two densities are considered representative, respectively, of a collapsible soil and a swelling soil under wetting processes. The higher void ratios of 1.12 was discarded as showed deformation too elevated, Figure 1b.

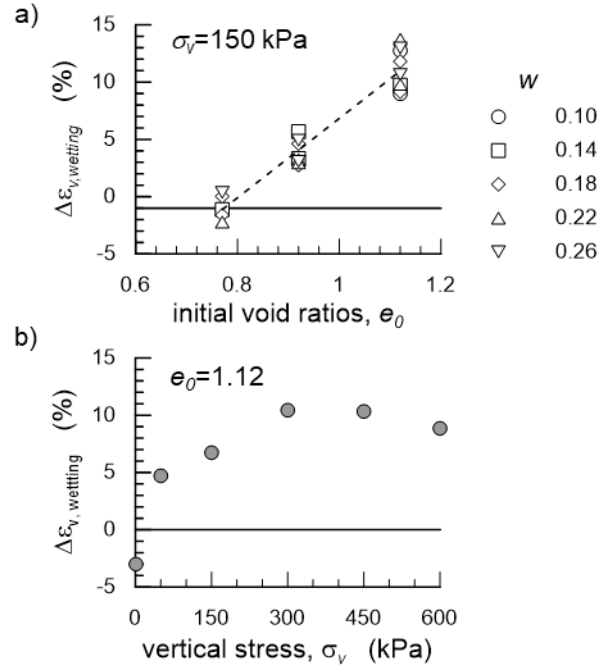


Figure 1. Wetting induced deformation versus: a) initial void ratios, b) total vertical stress.

The soil water retention curve (SWRC) was obtained by means of the suction controlled oedometer (Romero et al. 1995). The data corresponding to the main wetting curve a two different void ratios, 0.93 and 0.75, are presented in Figure 2 in terms of suction s (in log scale) versus the degree of saturation S_r . In the suction range experimentally studied, the data exhibit a marked influence of porosity in the retention behaviour. In fact, as porosity decreases, air entry value increases and the slope of the transition zone reduces in the S_r-s plane. The Van Genuchten (1980) equation was used to fit the data:

$$S_r = S_{r,res} + (S_{r,sat} - S_{r,res}) \cdot \left(\frac{1}{1 + (\alpha s)^n} \right)^m \quad (1)$$

Where $S_{r,res}$ and $S_{r,sat}$ are respectively the residual and saturated degree of saturation; α is the inverse of the air entry value, n governs the slope of the transition zone and m controls the inflection point at the residual values of suction. The values of the parameters are listed in Table 2. Neglecting the hysteresis of the SWRC, eq (1) can be used to

estimate the as-compacted suction and thus the initial effective stress in the model according to the Bishop effective stresses definition: $\sigma' = \sigma + S_r \cdot s$ (Bishop and Blight, 1963). As the total stress is zero after the compaction the effective stresses in the soil reduces to the product $S_r \cdot s$, and are 387 kPa for $e_0=0.93$ ($S_{r0}=0.43$) and 1768 kPa for $e_0=0.75$ ($S_{r0}=0.52$) respectively.

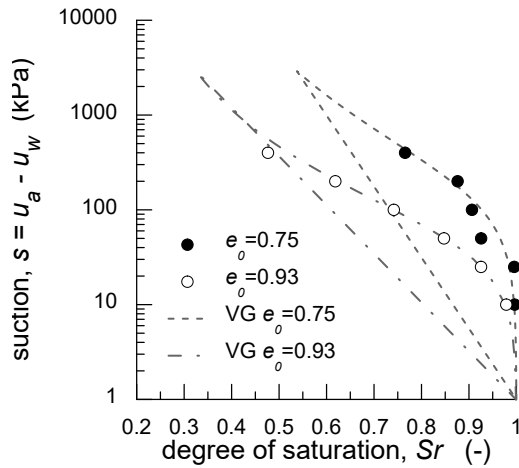


Figure 2. Soil water retention curves, SWRC, for the two densities used in the centrifuge tests.

Table 2. Van Genuchten parameters for different void ratios.

e_0	$S_{r,sat}$	$S_{r,res}$	α (1/kPa)	n	m
0.93	1.0	0.16	0.02	1.4	0.25
0.75	1.0	0.16	0.006	1.3	0.23

2.2. The model pile

The model pile (scale 1/100) is a close-ended aluminium tube (external diameter $D=12$ mm, thickness $t=1$ mm) embedded into the soil for 150 mm. The pile was instrumented with 10 pairs of strain gauges arranged every 15 mm, providing the bending moment profile along the pile length. The strain gauges were calibrated in the laboratory adopting the cantilever scheme with point load. The experimental arrangement for the calibration is presented in Figure 3.

2.3. The experimental apparatus

The axial symmetric models 180 mm deep were prepared in 300 mm diameter rigid tub. As shown in Figure 4, two twin containers were spin up at the same time: one was used for CPT measurement before, during and after the test. The other was used for the load test on the pile that was bored in the centre of the model, at $1 \times g$, by means of a manual screwing system. The screw was mounted into a rigid frame to maintain position and verticality.

The model was extensively instrumented in order to follow both the equalisation phases and pile loading (Figure 5).



Figure 3. Model pile and calibration set-up.

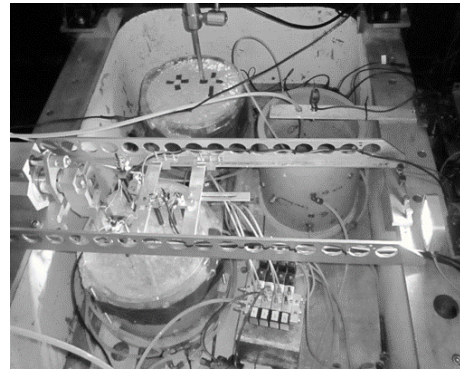


Figure 4. Model assembled in the strongbox

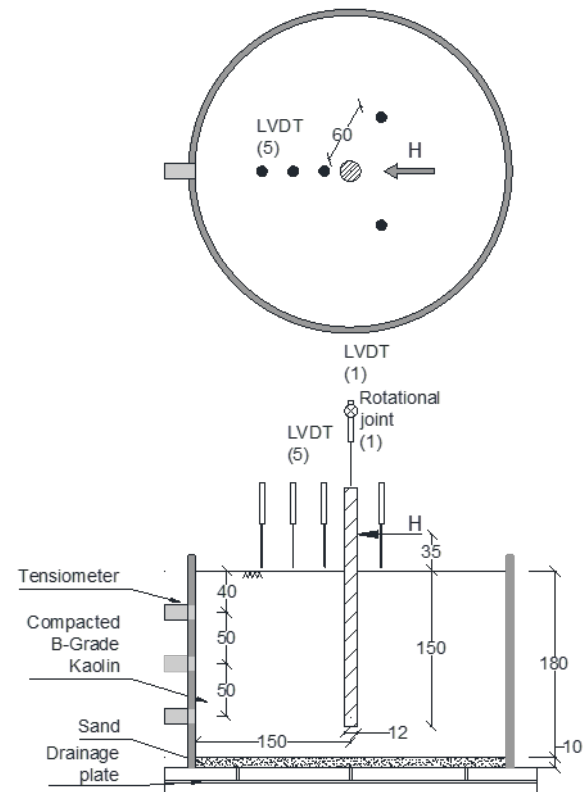


Figure 5. Model instrumentation.

The bottom of the model was connected to a water reservoir, the level of which was governed by an electro-pneumatic valve system remotely controlled by the operator from the centrifuge control room. A laser sensor measured the water height in the tank. Five LVDT sensors measured soil settlements, three tensiometers, installed on the side of the container, measured the pore water pressure (negative and positive) in the soil. The lateral load was applied at 35 mm from ground level by a hydraulic actuator. The loading phase was displacement-controlled ($v=0.003$ mm/s at model scale), and a load cell measured the lateral load. One LVDT built in on a rotational joint gave the pile's vertical displacement and rotation.

3 CENTRIFUGE TEST PROCEDURE

In total four centrifuge tests were undertaken, varying both the elevation of the water table, z_w , and the initial void ratio of the soil, e_0 (Table 3). In the two tests where the water table was 70 mm from the ground level the pile was loaded until a lateral displacement, y , of 30-40% of the diameter, D , was reached. In the following step, the water table level was raised to ground level keeping the load constant. For the sake of comparison, two additional tests were conducted up to soil failure in fully saturated condition ($z_w=0$) on soil samples prepared at the same voids ratio of the main tests. Measurements of pile displacements, lateral load and bending moments were recorded.

In order to reduce the as compacted suction, the samples were subjected to an imbibition process at 1g, connecting the bottom of the model with the water reservoir.

Before pile loading, equalisation of pore pressures in the soil was allowed. The load was applied with a very slow displacement rate to avoid the creation of excess pore pressures. At the end of each test, undisturbed specimen were sampled to obtain the water content and voids ratio distribution with depth.

Table 3. Initial conditions of the centrifuge tests.

Test ID	e_0	z_w (mm)	w_0	σ_{vc} (kPa)	Sr_0
T 05	0.93	0	15.03	580	42.02
T 06	0.93	70	14.67	559	42.01
T 08	0.75	70	14.72	1395	51.03
T 09	0.75	0	14.72	1395	51.03

3.1. Model preparation

Samples were prepared by static compaction at two different voids ratios ($e_0=0.93$ and 0.75) and the same water content ($w=15\%$).

The moisture was prepared following the same procedure used for the flooding tests. After the moisture homogenisation, the soil was then passed in a mechanical mixer to size down the aggregates and stored again in sealed plastic bags.

3.2. Compaction

The soil models were statically compacted, in a rigid tub of 300 mm in diameter. An extension is required to compact the soil to the target density. A 10 mm thick sand layer, surrounded by geotextile, allowed the drainage at the bottom of the model. A 2 mm thick plastic sheet coated the inner side to reduce skin friction during model preparation and during the test.

The soil is compacted in six layers of final height 30 mm with a displacement rate of 1.5 mm/min. The compaction is a displacement-controlled process: the press stops when the target displacement was reached. In Figure 6 typical results of the compaction process are presented for one loose soil sample ($e_0=0.93$).

After the compaction of each layer, its surface was scarified to achieve a good connection with the sequent one.

The soil surface was covered with a plastic film to prevent water evaporation in the upper part of the model.

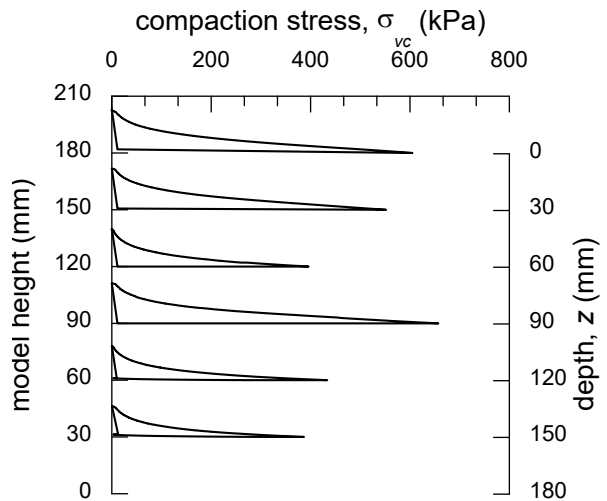


Figure 6. Typical results of the compaction process for one of the low density models.

The reasonable homogeneity of the distribution of vertical compaction stresses, Figure 7, and the good repeatability of the results in the different tests confirm the validity of the procedure used. It has to be noticed, however, that the dispersion increases with the soil density. The compaction stress increases with dry density from a mean value of 500 kPa for the loose soil ($e_0 = 0.93$) to 1400 kPa for the dense soil ($e_0 = 0.75$).

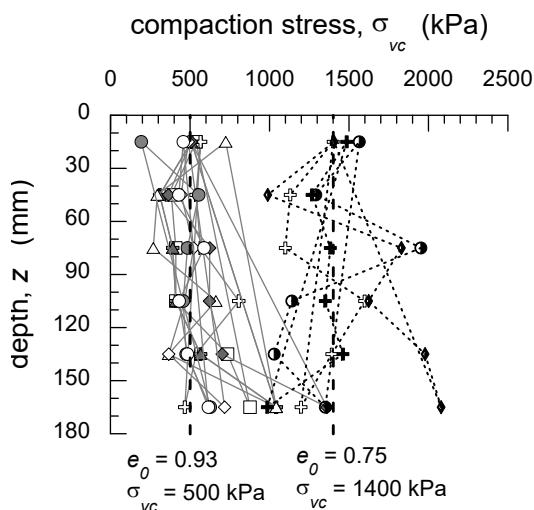


Figure 7. Compaction stress profiles in the tests.

4 ANALYSIS OF THE RESULTS

In this section, selected results are presented to illustrate first the influence of the centrifuge test procedure on the soil behaviour. The complete results are presented in Lalicata et al. (2019) and Lalicata (2018).

4.1. 1g imbibition

The absorbed water volume in this stage is presented in Figure 8a. Figure 8b shows the temporal evolution of the vertical displacements at the soil surface for the two densities considered. The wetting process induces the development of vertical displacements directed upwards attaining a final values of approximately 3 mm for the loose soil and ~6 mm for the dense soil. The water infiltration into the soil layer entails an increase in water volume by around 2 lt in both cases.

The vertical displacements increase as the wetting front advances. Despite the absorbed water volume is approximately coincident in the two cases, the wetting-induced swelling in the dense soil is roughly the double of that found in the loose soil. This outcome reflects the relevant difference in the as-compacted suction and the degree of saturation (see Table 8). Because of the different shape of the SWRC, (see Figure 2), the same approximate variation in S_r leads to a suction decrease and, thus to a stress unloading, greater in the dense than in the loose soils.

The overall imbibition process induced by capillary rise at 1g with zero pore pressure at base had not still reached stationary conditions, because the main aim of this phase was to increase the suction to speed-up the equilibrium in the following in-flight phase.

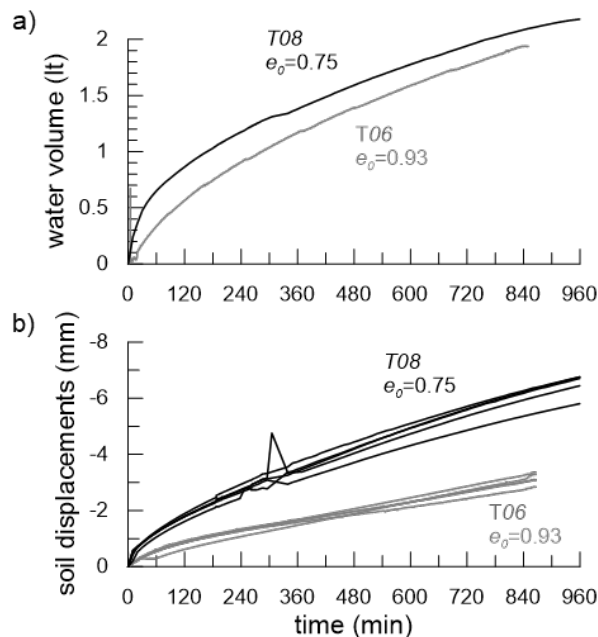


Figure 8. 1g imbibition: a) adsorbed volume, b) vertical displacement of soil.

4.2. In flight phases

Figure 9 shows the temporal evolution of the vertical displacements at the ground surface during the in-flight phase for T06 ($e_0=0.93$) and T08 ($e_0=0.75$). The increase in the gravity loading, together with the hydraulic boundary condition imposed at the base, leads to an instantaneous settlement of about 3 mm and 7 mm for the dense and the loose soil respectively. The vertical displacements increase in time up to 3.5 mm and 10 mm in the two cases.

After the pile loading, the water table was raised up of 70 mm saturating the whole model. The loose sample globally settles as the volumetric collapse of the unsaturated part is greater than the volumetric swelling of the deeper soil layer. On the other hand, the LVDTs measured very little increase in soil volume in the dense sample.

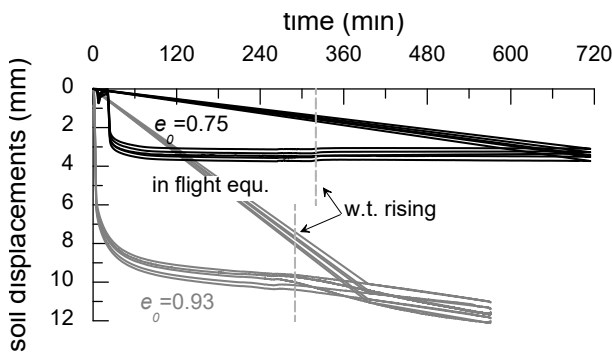


Figure 9. Soil vertical displacements versus time in test T06 ($e_0=0.93$) and T08 ($e_0=0.75$).

The instantaneous soil volume reduction observed as g increases is possible because the soil is not fully saturated. Indeed, the increment of total stresses is taken all by the effective stresses, as the presence of air in pores allows for a soil skeleton compression. According to the previous imbibition stage, the soil degree of saturation is not uniform in the soil but reduces moving towards the ground surface (far from the bottom boundary condition). Thus, the initial settlement is likely to be related to the compression of the upper part of the model. Conversely, the consolidation settlement has to be attributed to the excess pore pressures dissipation in the lower part of the model.

The pore pressure evolution for the test T06 shown in Figure 10 qualitatively confirms these findings. In fact, in the lower part of the model ($z=140\text{mm}$), the pore pressure rises as g increases and then reduces with time. In the upper part ($z=40\text{mm}$), it reduces slightly at the beginnings. After four hours of consolidation the trends seem to be stabilised but the absolute values are different from those expected. The tensiometers correctly capture the pore pressure variation during the rising of the water table; they measured approximately +70 kPa at the end of the test. Since the instruments worked well at 1g environment both before and after each test, further investigations are needed to understand the validity of these tools in high gravitational fields.

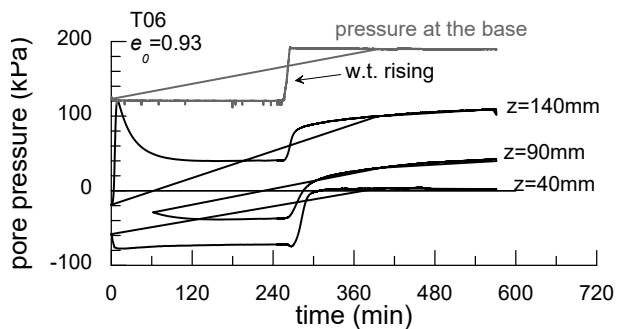


Figure 10. Pore pressures versus time in T06 ($e_0=0.93$).

The pile head displacement and force evolution versus time are presented in Figure 11 a-b for the two soil densities. During the saturation at constant load, the pile head displacements increased more for the sample with $e_0=0.93$ than the one with $e_0=0.75$. In both cases, the inundation event provoked the collapse of the pile. In fact, the displacements keep growing even if the pore pressures tend to the equilibrium (Figure 10).

4.3. End of test measurements

The voids ratio profiles with depth, at the end of the tests, in Figure 12 allows drawing some general

considerations about the soil state at the end of the tests. The reference test on saturated soil conditions for the dense soil, T09 ($e_0=0.75$), shows a profile of voids ratio approximately constant with depth to a value of ~ 0.75 . For the loose soil (T05) the voids ratio decreases with depth from a value of ~ 0.9 at the ground surface to a value of 0.76 for a depth of 170 mm. The latter distribution well fits the oedometric normal consolidation line, NCL, below 40 mm of depth, while the denser ones intercept it at $z=120$ mm. The models were subjected to the same experimental procedure (1g imbibition, increase of total stress and in-flight equalisation). Thus, these differences are related both to the different initial void ratio and the different shape of the SWRC that controls the variation of mean effective stress and the preconsolidation pressure during hydro-mechanical stress paths.

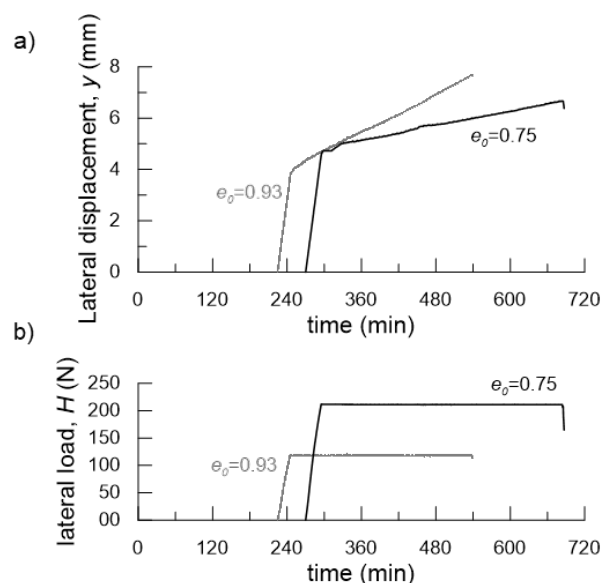


Figure 11. Pile loading and rising of the water table stages: a) lateral displacement versus time, b) lateral load versus time.

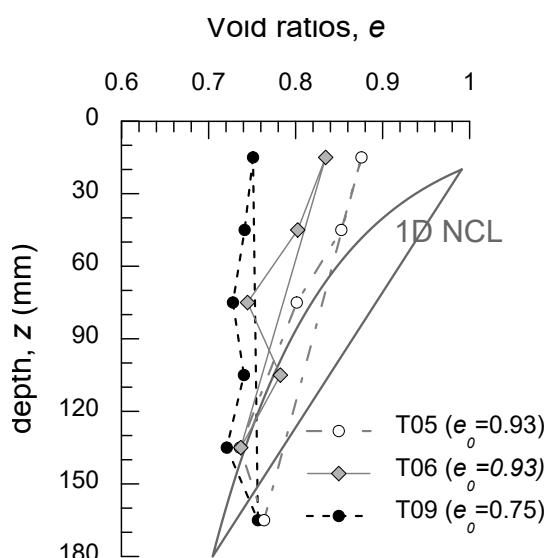


Figure 12. Voids ratios profiles with depth at the end of the tests.

In test T06, after the water table rising, below $z=90$ mm, the voids ratio is the same of T05 (saturated reference test). From 40 to 90 mm of depth the effects of the volumetric collapse upon wetting are very significant while this has a small influence in the shallower part of the model ($z<40$ mm).

5 CONCLUDING REMARKS

The paper presents the experimental details of the centrifuge testing on an unsaturated fine graded soil focusing on the soil behaviour from the model preparation to the end of the test.

The study demonstrate the feasibility of centrifuge modelling in unsaturated soils highlighting the influence of the initial density on the soil response during the flight:

- Low compacted soils experience significant positive deformations during both flight and the rising of the water table.
- Dense soils show a moderate compression during the g-level increase and the application of the hydraulic boundary condition at the bottom. Moderate swelling was observed during the water table rising.

Useful insights on the soil response in flight can be collected from simple flooding oedometer tests. On the other hand, the knowledge of the SWRC, and its dependence from void ratios, is crucial to analyse the hydraulic behaviour of the soil during the centrifuge tests.

The 1g imbibition phase prior testing efficiently reduces the soil suction and speed up the in-flight consolidation time. Some attention is required to not over saturate the material before the centrifuge test beginning.

The tensiometers correctly reproduced the pore pressures variations in-flight but more work must be done to investigate the shift observed from the expected values.

To date, the procedure for the model preparation requires a significant effort from the researcher that limits the applicability to large experimental campaigns. Further reflections on possible improvements of the experimental procedures are needed.

However, the findings of this study encourage the use of centrifuge modelling to investigate the soil structure interaction in unsaturated soils.

6 REFERENCES

Bishop, A. and Blight, G. 1963. Some aspects of effective stress in saturated and partly saturated soils. *Géotechnique*, **13**(3): 177–197.

Caicedo, B. and Thorel, L. 2014. Centrifuge Modelling of Unsaturated soils. *Advances in the Mechanics of Unsaturated soils. Journal of Geoenvironmental Sciences*, **2**(1-2): 83-103. doi:10.3233/JGS-130013.

Caicedo, B., Medina, C., and Cacique, A. 2006. Validation of time scale factor of expansive soils in centrifuge modeling. *In Proceedings of the International Conference on the Physical Modelling in Geotechnics*, Hong Kong, 4-6 August 2006. Balkema, Rotterdam, pp. 273–277.

Casini, F., Munoz, J., Lorenzo, S., Thorel, L., Vaunat, J., Delage, P. and Gallipoli, D. 2009. Centrifuge modelling of an unsaturated collapsible soil. *In Between theory and practice in unsaturated soil mechanics*. Rotterdam: Millpress.

Depountis, N., Davies, M.C.R., Harris, C., Burkhart, S., Thorel, L., Rezzoug, A., Konig, D., Merrifield, C. and Craig, W.H 2001. Centrifuge modelling of capillary rise. *Engineering Geology*, **60**(1-4): 95-106.

Lalicata L.M., Rotisciani G.M., Desideri A., Casini F., Thorel L. 2020. Numerical Study of Laterally Loaded Pile in Unsaturated Soils. *In Geotechnical Research for Land Protection and Development*. Springer, Cham. doi.:10.1007/978-3-030-21359-6_76

Lalicata, L. 2018. Effect of saturation degree on the mechanical behaviour of a single pile subjected to lateral forces (in Italian). Ph.D. thesis, Department of Structural and Geotechnical Engineering, Sapienza Università di Roma, Rome.

Lalicata, L., Desideri, A., Casini, F. and Thorel, L. 2019. Experimental observation on a laterally loaded pile in unsaturated silty soil. *Canadian Geotechnical Journal* **56**(11): 1545-1556. doi.:10.1139/cgj-2018-0322.

Romero, E., Lloret, A. and Gens, A. 1995. Development of a new suction temperature controlled oedometer cell. *In Proceedings of the first International Conference on Unsaturated Soils*, Paris, France, 6-8 September 1995. Balkema, Rotterdam, pp 533-539.

Soranzo, E., Tamagnini, R. and Wu, W. 2015. Face stability of shallow tunnels in partially saturated soil: centrifuge testing and numerical analysis. *Géotechnique*, **65**(6): 454–467.

Thorel, L., Ferber, V., Caicedo, B. and Khokhar, I. 2011. Physical modelling of wetting-induced collapse in embankment base. *Géotechnique*, **61**(5), 409–420.

Van Genuchten, M. T. 1980. A closed-form equation for predicting the hydraulic conductivity of unsaturated soils. *Soil Science Society of America Journal*, **44**(1): 892–898.

Effect of Crushed Particles on Soil-Structure Interface Behaviour

Angus Pettey¹, Charles Heron¹

¹Nottingham Centre for Geomechanics, University of Nottingham, UK

Corresponding author: Angus Pettey (angus.pettey@nottingham.ac.uk)

ABSTRACT: When shear is induced at a soil-structure interface fines will be generated either by particle crushing or the breakage of asperities. In a standard monotonic interface test these fines will have a negligible impact upon the interface behaviour. However, during cyclic loading the volume of fines generated can become significant and hence the long-term effect on the interface behaviour needs to be investigated. Traditionally interface tests are designed such that the soil sits above the interface (an ‘upright’ test) and hence gravity and segregation would lead to the fines migrating towards the interface thus amplifying their impact on the observed behaviour. However not all prototype interfaces are orientated in this upright direction; for example a pipeline will have an ‘upright’ interface at the crown of the pipe, an ‘inverted’ orientated interface at the invert of the pipe (where fines will migrate away from the interface) and an interface orientated at ninety degrees at the spring-line (side) of the pipe (where fines will migrate along the interface). As such, it is important to consider every potential prototype case when developing, for example, constitutive models. The development of such models to predict interface behaviour is becoming more commonplace, though consideration of the issues from the perspective of real engineering problems will enhance the utility of any models developed.

A bespoke cyclic interface shearing device has been adapted to facilitate testing of interfaces in a variety of orientations. This equipment is also capable of providing visual observation of the movement and crushing of the soil particles during shearing using transparent model containers and high-resolution imaging. A series of interface tests conducted using this apparatus will be presented in this paper and the impact of fines, and fines migration, on the interface behaviour will be discussed.

Keywords: Soil-Structure Interface; Granular Mechanics; Particle Crushing.

1 INTRODUCTION

The physical changes in soil-structure interfaces occur in the *interface layer*. This is a distinct band of soil that is in contact with the structural interface and far-field soil. The layer has been defined by various studies as five to ten times the mean particle diameter (DeJong et al. 2006; DeJong and Westgate 2009).

The confinement condition of a soil-structure interface has been widely studied. Three distinct conditions are found to affect the response of the interface: Constant Normal Load (CNL), $K = 0$; Constant Normal Stiffness (CNS), $K = \text{constant}$; Constant Volume (CV), $K = \infty$ (DeJong and Westgate 2009; Evgin and Fakharian 1996). The condition that occurs at the interface can vary for different applications. For example, a piled foundation, will experience an approximately constant stiffness boundary condition in the radial direction.

One major shortcoming in the published literature regarding interface behaviour, is that cyclic behaviour of the interface has only been considered up to 45 cycles by DeJong et al. (2006). Other studies have considered cyclical behaviour, albeit at lower cycle number. In ‘live’ engineering problems such as the thermal cycling of pipelines or pile

driving, interfaces may be sheared hundreds or thousands of times. The mechanism underlying this shearing is yet to be fully understood at cumulative displacements in the order of tens of millimetres, let alone thousands. It has been shown by experimentation on soil-soil interfaces, that cyclical shearing gives rise to crushing of granular matter.

For this study, Leighton Buzzard Sand (LBS) Fraction B is used as the testing medium due to the wealth of published research into its particle characteristics. Cavarretta et al. (2010, 2016); Senetakis et al. (2013), detail the particle crushing characteristics of LBS Fraction B in particle-particle contact. Such research provides a good reference point for developing the more complex model of soil deformation at the interface.

Another shortcoming of interface research thus far, is that there has only been consideration of the *upright* condition of the interface, that is, where fine material migrates towards the interface layer due to gravity. An alternate case to model would be the *inverted* interface, where fine material developed falls away from the interface. This case is of importance when considering the boundary conditions of the interface, a buried pipeline for example, will have both an upright and inverted interface at the top and bottom of its circumference.

A third case also exists, where an interface is orientated at ninety degrees at the spring-line of the pipe, where fines propagate parallel to the interface. A diagram of the three principal orientations is shown in Figure 1.

For the purposes of this study, only the upright and inverted cases will be considered.

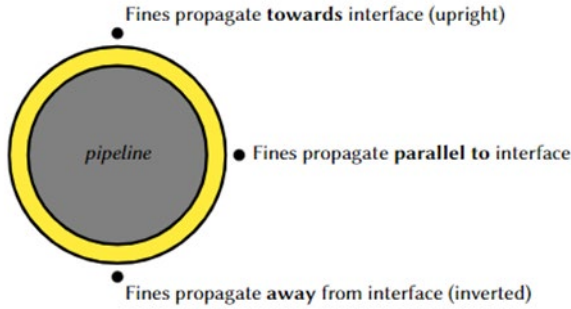


Figure 1. Diagram of the three principal interface orientation conditions.

2 METHODOLOGY

2.1. Test apparatus

To identify the impacts of large cumulative displacements on interfaces, testing is carried out using a bespoke interface shear-testing device, developed within the Nottingham Centre for Geomechanics (Hashemi and Heron 2017).

Since the first uses of this apparatus, several improvements have been made. Firstly, imaging of the soil sample during testing is now possible, using a transparent sample container. Imaging of the soil sample allows for mechanical changes, identified in the interface layer, to be matched to recorded changes in sample stress and volumetric behaviour. Such an approach gives more context to trends identified in results data.

Secondly, the entire assembly can be rotated through 180° for the testing of the inverted condition. Thirdly, the vertical load motor has been replaced by a pneumatic actuator and pressure controller. The controller has a much faster response time than the previously used motor and encoder control loop. Proportional–Integral–Derivative control is used to set a target pressure in the actuator, to apply a constant normal load on the sample. This improvement allows for a greater stiffness in the far-field soil, giving a closer approximation of the CNL condition than previously published. A schematic of the Toton Shear apparatus, in its upright configuration, with the described improvements is displayed in Figure 2.

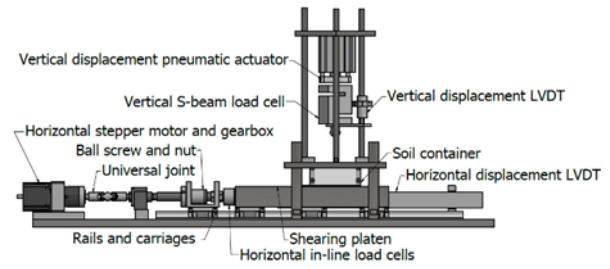


Figure 2. Schematic of updated Toton Shear apparatus

2.2. Test plan

A basic test plan was used to simulate the interface condition at large cumulative shear displacements. The test plan is shown in Table 1. Each test consists of 4000 shear reversals of 10 mm displacements, peak to peak (2000 full cycles). Although numerous previously published studies have used the cycle number to denote the length of a test, this can disguise the true amount of shearing a sample has experienced. For example, a shallow pipeline experiencing thermal cycling will not undergo repeated cycling at a constant displacement for its entire lifespan. It would be more accurate to consider the cumulative displacement and number of shearing reversals.

The normal stress, σ_n , and shear displacement magnitude, $|u_x|$, are constants throughout testing, to isolate the effect of a change in interface orientation angle, θ . The shear rate, v , is also constant throughout testing at 1 mm/s. Each test is repeated, for validation of results, and the identification of trends. Note that subsequent use of ‘upright’ and ‘inverted’ will refer to an interface orientation angle of 0° and 180° respectively, relative to the horizontal.

Table 1. Test Plan

Test Code	σ_n (kPa)	$ u_x $ (mm)	θ ($^\circ$)
100-10-000-1	100	10	0
100-10-000-2	100	10	0
100-10-180-1	100	10	180
100-10-180-2	100	10	180

2.3. Testing medium

2.3.1 Soil

Prior to testing, the Fraction B LBS was washed and dried, with a particle size distribution analysis carried out in accordance with BS 1377-1:2016 (British Standards Institution 2016). It is found that 90% of material passes between 2 mm and 1.18 mm.

Samples are poured from the same height, through a sieve of size 3 mm, to limit the rate of each pour and ensure samples have equivalent relative density prior to testing. Each test sample is of mass 300 g, with a cross-sectional area of 80×80 mm. At the

end of testing, the sample is collected by spatula. The same particle size distribution analysis is then carried out, to assess the change in sample constitution.

Hutchings and Shipway (2017), show that silica sand, such as the LBS used in this study, has a Vickers hardness value of 700-1200 HV. This is of key importance when considering the tribological implications of the shearing of the interface.

2.3.2 Structural interface plate

A 3 mm stainless steel plate is used to simulate the structural interface for the tests presented in this study. Vickers hardness tests have been conducted upon the material used, and an average hardness value of 188 HV has been found across three separate plates.

Each plate of dimension 300 x 108 mm has two tests conducted upon it, in virgin areas.

2.4. Data collection and processing

2.4.1 Rolling resistance

The Toton Shear apparatus utilises two parallel 1 kN capacity load cells, to transfer rotational force from the ball screw and nut, applied by a stepper motor, to linear force upon the shear platen.

The shear platen is mounted upon rails that incur a rolling resistance. Prior to testing the samples, this rolling resistance is quantified by a series of 20 calibration shear displacements of 12 mm. A 0.001 inch feeler gauge is passed below the soil container before calibration, to ensure that the soil container does not impart any resistance upon the shear platen and has a consistent offset from the platen, outside of the cross section of the sample. When processing the raw data, acquired by a National Instruments Data Acquisition (DAQ) unit, the horizontal loads for forward – load cells in compression – and backward – load cells in tension – movement are treated separately, with calibration loads calculated for each. Across all four tests, the average forward and backwards rolling resistances were found to be 42.74 N, and -42.58 N respectively. The corresponding resistance is subtracted, as appropriate, from all load data in subsequent calculations and plots.

2.4.2 Image data

Image data is captured by a Teledyne DALSA Genie Nano camera unit and 16 mm lens, mounted adjacent to the sample container. Due to the long focal length, an exposure time of 0.08 s is used to capture each frame. Images of resolution 4112 x 3008 pixels are recorded every 2.5 mm of travel during shearing, giving an equivalent

frequency of 0.4 Hz. Whilst during initial loading of the sample, images are recorded with a 1 Hz frequency. A high refresh rate is used as it is hoped in future studies to utilise the recorded image data in the use of advanced Particle Image Velocimetry.

Each frame of image data can be matched to controller data by the indexing of each frame in the recorded data. As such, the micromechanisms that take place at the interface, can be identified with added context of the volumetric and stress response of the sample. One drawback of this analysis is that the image data only represents a 2D plane of the sample. An assumption must be made that the mechanism witnessed in this plane, must also exist throughout the depth of the sample.

During post-processing, the raw Portable Network Graphics (.png) files are cropped to the size of the sample in the frame, and the frame number is added to the image. An example of the recorded image data is shown in Figure 3. The individual frames are stitched together as a video file that can be used to examine the evolution of the micromechanisms present at the interface.

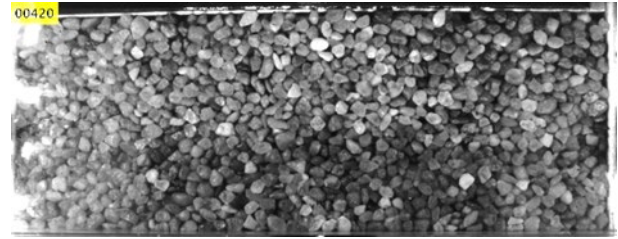


Figure 3. Sample image after post-processing

2.5. Data smoothing

The data gathered by the DAQ unit has an acquisition loop length of 0.1 s. As such, load data, particularly the horizontal data, is required to be smoothed by an appropriate method to remove the noise in the recorded data.

Firstly, the average load, across the two parallel load cells, for each shear displacement (half cycle) is calculated. Hence, for the tests conducted in this study, 4000 average loads are presented. The same method has been carried out for the vertical load data, to allow the calculation of stress ratio, μ , for each cycle, shown in Equation 1,

$$\mu = \frac{H_L}{Z_L} \quad (1)$$

where H_L is the average horizontal load of a single shear displacement, and Z_L is the average vertical load of a single shear displacement. The unprocessed data is retained to allow for closer analysis of response in each displacement.

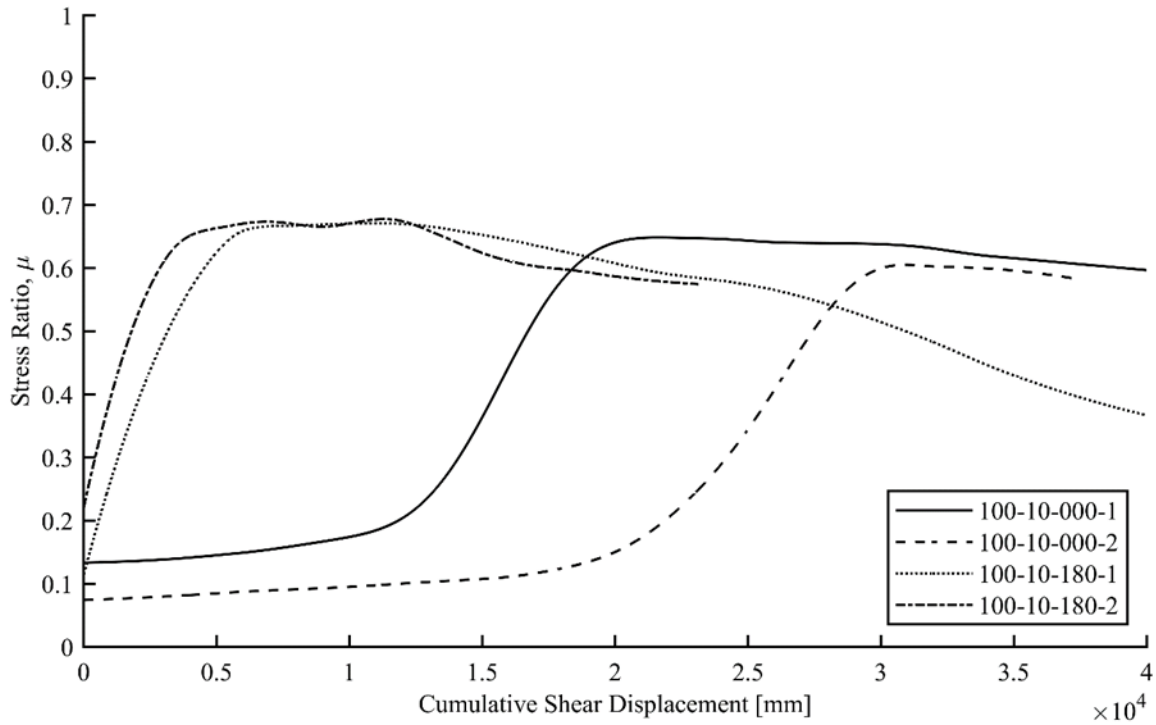


Figure 4. Plot of the stress ratio, μ , vs cumulative shear displacement

Secondly, a local regression smoothing method (loess) (MATLAB 2019) is used to remove noise in the data. Smoothing is carried out upon load data in addition to vertical displacement data, recorded by the vertical Linear Variable Differential Transformer (LVDT), as to increase the clarity of general trends across test data.

3 RESULTS AND DISCUSSION

3.1. Stress response

Figure 4 displays a plot of the evolution of the stress ratio throughout each of the four tests, up to a maximum cumulative shear displacement of 40,000 mm. It should be noted that due to a safety limit within the controller software, tests 100-10-000-2 and 100-10-180-2 did not complete the full 4000 shear displacements. The safety limit exists as to prevent damage to the apparatus. Tests that fail in this manner are unable to be restarted as the sample will have travelled outside of the tested area of the interface plate. Hence, unexpected rotations of particles at the interface may occur. Furthermore, when the test is stopped for a prolonged period, shear stress degradation occurs as the linear driving force on the shear platen is released by the stepper motor. As such, data for these tests has been cut at their relevant end points of 37,410 mm and 23,150 mm of displacement respectively. Fortunately, the data from these tests shows good similarity to the repeated tests.

An immediate observation that can be made is that at large displacements, there is a steep increase in

the stress ratio of each specimen, which has previously been unrecorded in published work. For the test pressure of 100 kPa and cyclic displacement of 10 mm, an upper limit exists at a stress ratio of 0.7. This value seems independent of the orientation of the interface, with inverted tests reaching no higher value than upright tests. However, the inverted tests seem to show a more pronounced peak in stress ratio before steadily falling.

It is evident that there is a similar trend in the rate of change in stress ratio during the rapid increase. The similarity in the rate of change in stress can be better shown by plotting the derivative of stress ratio against itself- shown in Figure 5. It is shown that the

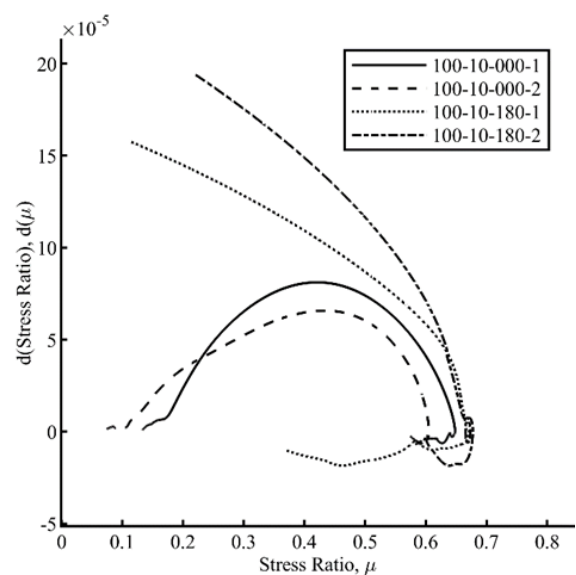


Figure 5. Plot of first derivative of stress ratio, $d(\mu)$, vs stress ratio, μ

earlier the onset of an increase in stress ratio, the greater the peak rate of increase. Interestingly, once the peak stress ratio has been reached, regardless of the stress path taken, the residual stress ratio is very similar for a test of the same type. This could suggest the existence of a critical state style condition. Note also, the inverted tests display a clear negative gradient after the peak stress ratio has been reached.

3.2. Volumetric response

The eventual increase in stress ratio may be explained by the volumetric response of the sample over large shear displacements. The samples all contract over the duration of the test in a similar way to that presented in DeJong et al. (2003). On each reversal of shear displacement, the sample experiences a small dilation before steadily contracting for the rest of the displacement, as the soil skeleton rearranges to its lowest energy state. The volumetric data recorded by the vertical LVDT is shown in Figure 6.

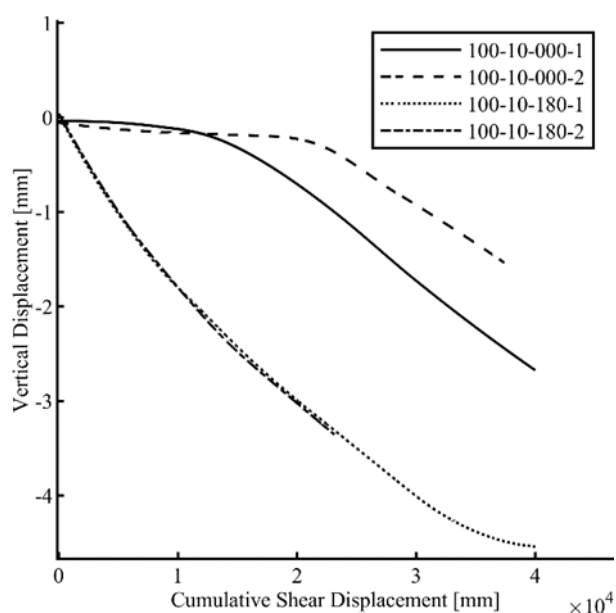


Figure 6. Plot of vertical displacement against cumulative shear displacement

Similar to the stress response, there seems to exist a steady state where the rate of contraction of the sample remains constant after a point. During testing, the samples all experienced a plastic contraction due to crushing of the grains in the interface layer, confirmed by an audible crushing sound.

The crushing experienced can be witnessed in the image data. For example, in test 100-10-000-1 where the gradient becomes almost constant, at a cumulative shear displacement of 15000 mm and 1500 reversals, the stress ratio begins to increase

rapidly at the same point, and crushing is also seen to begin to occur.

The crushing of the sample can also be confirmed by grain size distribution analysis. Figure 7 shows a plot of grain size analysis on each of the four tested samples and a baseline of the clean, untested Fraction B. With consideration of the vertical displacement data in Figure 6, samples with a greater total contraction, have a greater proportion of fine particles at the end of the test.

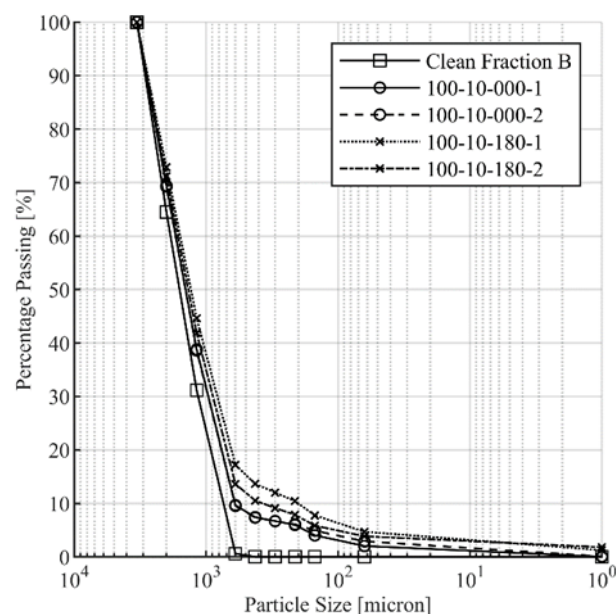


Figure 7. Grain size distribution analysis for each test and a clean, untested sample

Test 100-10-180-1 experienced the greatest total contraction. The gradient of its vertical displacement seems to fall close to zero as a cumulative displacement of 40,000 mm is reached. Figure 8 shows a frame of image data taken at the end of the 100-10-180-1 test, with a cumulative displacement of 40,000 mm. When compared with the sample image in Figure 3, it can be seen that the interface layer, shown at the bottom of the images, is saturated with fine material. It could be hypothesised that when the interface layer is fully saturated with fine material, an ultimate contraction is reached, where a sliding mechanism occurs again, and unbroken particles in the far-field soil do not contact the interface. The stress state at this point may reflect a standard direct shear test, comprised

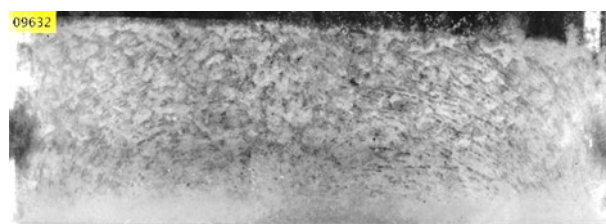


Figure 8. Frame taken from test 100-10-180-1 at 40,000 mm displacement

of the fine material. Further investigation into the stress state in the interface layer when saturated with fines, will need to take place.

It was observed during the upright tests that a period of sliding occurred, prior to the crushing. It is believed that any sample will experience crushing after an amount of interface shearing. Although the increase in stress ratio and plastic contraction occurred at smaller cumulative displacements for the inverted tests, it should not be assumed that all inverted tests will act in a similar manner. Future testing will seek to clarify if this immediate response is a function of orientation angle.

3.3. Damage to interface

After each test is conducted, surface fine material is cleaned from the plates. An image showing the plates of the one upright and one inverted test area is shown in Figure 9. The tested area is clearly identified, with micro abrasions and ploughing wear on the interface plate. Plastic flow occurs via third-body abrasion when a normal load is applied to an abrasive particle with hardness $1.2\times$ greater than the first (damaged) body (Hutchings and Shipway 2017). As demonstrated in Section 2.3.1, the hardness of silica sand far exceeds the value given for the structural interface plate. When the silica particles are forced into the relatively soft steel interface repeatedly, ploughing of troughs and abrasion occurs. Further study should be given to the relative hardness of the interface, and what effect that has on shear behaviour.

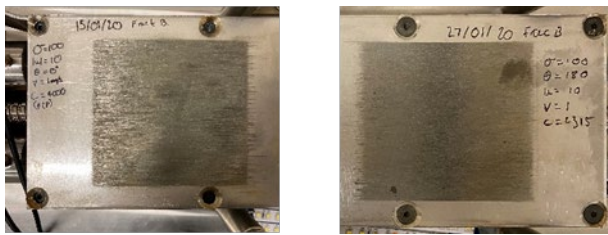


Figure 9. Image of damaged interface plate after tests 100-10-000-1 (left), 100-180-10-2 (right)

One could hypothesise that the increase in stress ratio occurs due to fine particles falling into the abrasions on the interface plate. As the fine material, some of which has a diameter $<63\ \mu\text{m}$, is worked into the abrasions, the fine soil skeleton transfers more normal stress into shear stress.

The damage upon the interface plate is worse in the middle of the sample area, note the darker band of wear in the middle of the sample area, caused by deeper grooves that reflect less light. This observation is key in validating that the

experimental response is not caused by boundary effects. As the sample cycles through a stroke of 10 mm, the leftmost and rightmost 10 mm of interface plate boundaries of the interface plate are only worn for half of the amount of travel, as soil particles travel over this area. Hence, it would be expected for the boundaries to experience a smaller amount of wear than central areas.

3.4. Micromechanical response

Using the image data, the micromechanisms that occur during interface shearing at high cumulative displacements, can be identified. For the first time, a distinct micromechanism has been identified for interface shearing. After many shear reversals, a random translation of a single particle within the interface layer occurs, causing a cascading rearrangement of particles in the remainder of the interface layer, and in the far field soil. This mechanism has not been previously described, and is likened to popcorn cooking, as the translation of one particle causes the translation of many more. This *popcorning* can be easily identified within the image data when viewed as a video, though is more difficult to identify in discrete frames, and therefore is omitted from this paper.

The effect of inversion upon the fine material generated at the interface, can more easily be shown by comparison of the upright and inverted tests after crushing has begun. Figure 10 displays a comparison of the samples from the 100-000-10-4000 and 100-180-10-4000 tests, after the crushing mechanisms have begun, and near to the end of the tests. The fine material in the upright test, Figure 10 (a), has formed a clear band of packed fine material, with a peak quantity of fines in the centre of the sample. This is to be expected as fines tend towards the interface under the effect of gravity. In contrast, in the inverted sample (b), fines have fallen throughout the sample, coating particles in the far-field soil. However, a concentration does exist in the interface layer.

The absence of fine material in the far-field soil of the upright sample, and the concentration of fines in the interface layer of the inverted test, suggests that crushing only occurs in the interface layer. If crushing was to occur in the far-field soil, fines would be seen to coat the particles throughout the upright sample, with a greater concentration in the interface layer; this does not occur. Further work will be conducted to determine the origins of the fine/crushed material.

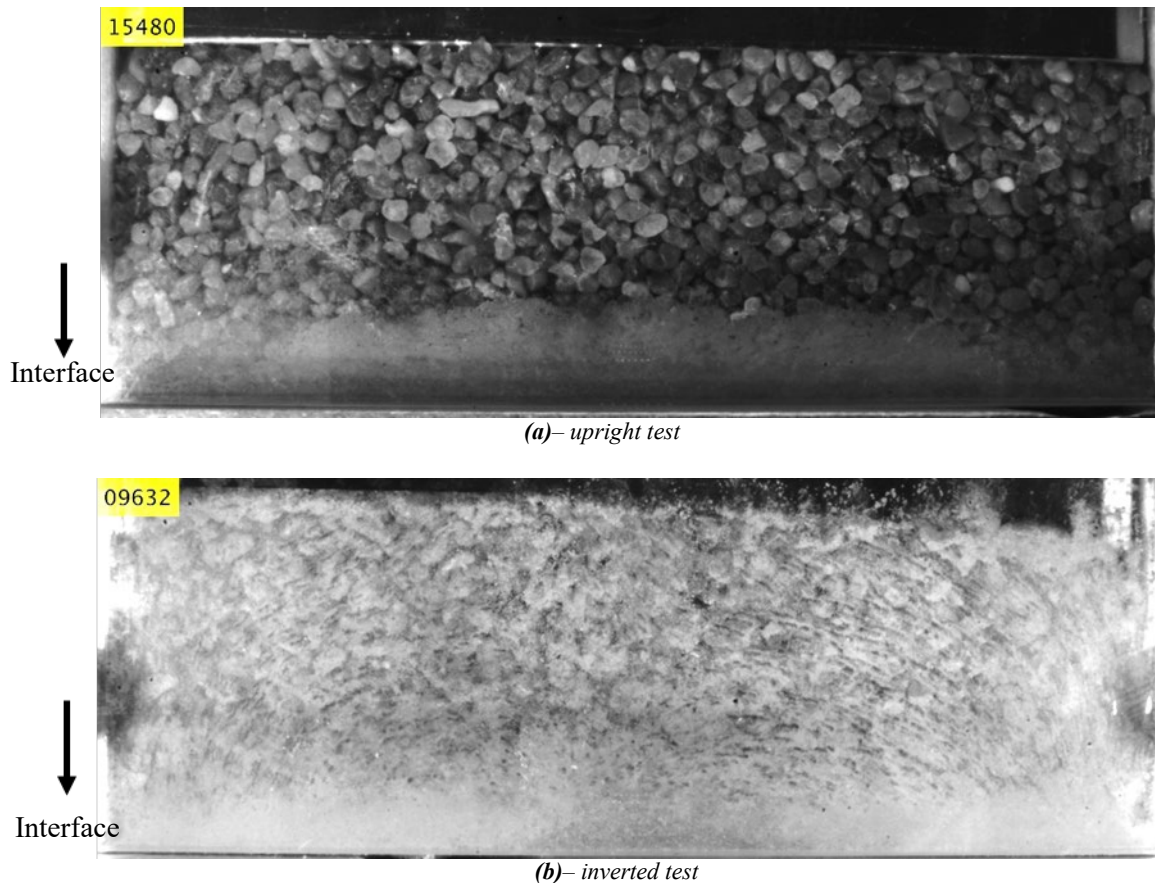


Figure 10. Comparison of crushing mechanisms for inverted and upright testing

4 CONCLUSION

The experimental work presented in this study represents the first insight into interface shear behaviour at large cumulative displacements in the order of thousands of millimetres of travel and shear reversals. The existence of non-linear shear behaviour at large displacements is described and analysed with respect to the volumetric and stress responses of the test samples. Future work conducted will seek to specifically identify the cause of the steep rise in stress ratio, as well as the crushing of grains in the interface layer.

5 ACKNOWLEDGEMENTS

This research is funded with an Engineering and Physical Sciences Research Council grant in addition to funding from the Nottingham Centre for Geomechanics, University of Nottingham.

With thanks to Mir Hashemi Afrapoli, Luke Bedford, Steve Lawton, for their efforts to fabricate and assemble the testing apparatus and control systems.

6 REFERENCES

British Standards Institution, 2016. Methods of test for soils for civil engineering purposes. Part 1.

Cavarretta, I., Coop, M., O'Sullivan, C., 2010. The influence of particle characteristics on the behaviour of coarse grained soils. *Géotechnique* **60**, 413–423.

Cavarretta, I., O'Sullivan, C., Coop, M.R., 2016. The relevance of roundness to the crushing strength of granular materials. *Géotechnique* **67**, 301–312.

DeJong, J., White, D., Randolph, M., 2006. Microscale observation and modeling of soil-structure interface behavior using particle image velocimetry. *Soils and Foundations* **46**, 15–28.

DeJong, J.T., Randolph, M.F., White, D.J., 2003. Interface load transfer degradation during cyclic loading: a microscale investigation. *Soils and foundations* **43**, 81–93.

DeJong, J.T., Westgate, Z.J., 2009. Role of Initial State, Material Properties, and Confinement Condition on Local and Global Soil-Structure Interface Behavior. *J. Geotech. Geoenviron. Eng.* **135**, 1646–1660.

Evgin, E., Fakharian, K., 1996. Effect of stress paths on the behavior of sand-steel interfaces. *Canadian Geotechnical Journal* **33**, 191–199.

Hashemi, M.A., Heron, C.M., 2017. Development of a soil-interface device for cyclic and large deformation shearing, in: *Proc. 19th ICSMGE*.

Hutchings, I.M., Shipway, P., 2017. Tribology: friction and wear of engineering materials. Elsevier Science & Technology. London, UK

MATLAB, 2019. MATLAB Documentation 9.7.0.1190202 (r2019a). The MathWorks Inc., Natick, Massachusetts.

Senetakis, K., Coop, M.R., Todisco, M.C., 2013. The inter-particle coefficient of friction at the contacts of Leighton Buzzard sand quartz minerals. Soils and Foundations **53**, 746–755.

Carboxymethylcellulose as a Newtonian viscous fluid for centrifuge modelling

Jarno Terwindt¹, Wouter van der Star², Dirk de Lange¹

¹*Geo-engineering, Deltares, the Netherlands*

²*Subsurface and groundwater quality, Deltares, the Netherlands*

Corresponding author: *Jarno Terwindt (jarno.terwindt@deltares.nl)*

ABSTRACT: In geotechnical centrifuge modelling, the unification of time-scaling factors is particularly important for studies regarding coupling consolidation and dynamic phenomena, for example pile installation problems and earthquake loading. A common method to achieve this unification is the use of a substitute pore fluid, which has a viscosity which is larger than that of the prototype pore fluid (generally water). Aqueous methyl celluloses have proven very valuable for this purpose, mainly because the viscosity can be increased while the density remains relatively unaffected and the solution can be characterised as near-Newtonian. In this paper we describe the use of a low molecular weight sodium carboxymethylcellulose (designated ICMC) in 1% to 4% solutions as an alternative to methyl celluloses through physical chemical, (density, temperature dependence) and geotechnical (permeability in sand and friction angle) analyses and describe the experience with this pore fluid at the Delft Geotechnics centrifuge over the past 20 years.

The ICMC was characterized as a near-Newtonian fluid up to the limit of the rheometer of 2000 s⁻¹, for a 1% solution. The fluid was density varied from 1.004 to 1.007 kg/L at concentration from 1.5% to 3.5%. Temperature dependence of viscosity was relevant (a change in dynamic viscosity of 25 mPa·s to 20 mPa·s at a temperature change from 20°C to 25°C, for a 1.5% solution) and should thus be taken into account during interpretation. Colouring with biodegradable dyes from the food industry (red E124, blue E132) at concentrations of 10 g/L enabled tracking of flow patterns through regular film and photography in various sand types with a negligible effect on density and viscosity. Prepared solutions were stable for over 180 days when stored at 10 °C. These characteristics are compared to other methyl cellulose solutions used in geotechnical testing such as metholose. The characteristics of these pore fluids turn out to be similar to the extent that they have been reported in literature. The study is concluded with a testing program for new pore fluids and proposals for additional recording of fluid characteristics during experiments.

Keywords: Viscous Pore Fluid; Newtonian Behaviour; Centrifuge Modelling.

1 INTRODUCTION

The geotechnical centrifuge is a valuable modelling tool, as it allows cost-effective examination of real scale problems (Leung et al., 1994, Timkura et al., 1998). However, it is well documented that not all relevant quantities scale in the same manner. Garnier et al. (2007) provides an overview with respect to scaling factors. In coupled consolidation and dynamic phenomena, the unification of time-scaling factors is particularly important. A common method to achieve this is the use of a substitute pore fluid, which has a viscosity of n-times the viscosity of the prototype pore fluid, where n refers to the geometrical scaling factor (i.e. applied g-level). Several substitute pore fluids have been used by different studies, such as silicone oil (Ko, 1994), proprietary fluids (Allard & Schenkeveld, 1994), aqueous solutions of glycerol (Whitman et al., 1981) or methylcellulose (Dewoolkar et al., 1999, Adamis & Gopal, 2015). This paper presents the chemical and physical properties and the application of a variation on the latter substitute pore fluid.

2 VISCOUS PORE FLUID REQUIREMENTS

The requirements of an ideal substitute pore fluid are, amongst others, discussed by Allard & Schenkeveld (1994). The primary requirement is that the overall constitutive behaviour (e.g. stress strain behaviour, pore pressure generation and shear strength) at n-g testing must be the same as the prototype soil and pore fluid at 1-g testing. When the prototype pore fluid is water, the substitute pore fluid should have:

- a density close to water. This is important for correct reproduction of hydrostatic pore pressure, effective stress and inertia and seepage forces;
- the same rheological behaviour as water. The dynamic viscosity should be constant for all shear stress levels (i.e. Newtonian behaviour). This ensures that the soil-fluid interaction is the same in the model as in the prototype;
- the same compressibility as water. This ensures comparable behaviour between the

model and prototype with regard to the soil skeleton during (dynamic) loading and unloading;

- a dynamic viscosity proportionally n times greater than water, where n is the applied g -level. This allows the model soil permeability to be comparable to the prototype soil permeability, following Darcy's law.

The pore fluid must also be chemically polar in order to enable its use with silts and clays, in addition to sands. To the authors' knowledge no viscous pore fluids have been applied in silts of clays in geotechnical centrifuge testing.

Apart from these primary requirements, there are also practical considerations, as discussed by Allard & Schenkeveld (1994), Kutter et al., (1998) and Dewoolkar et al. (1999). These are as follows:

- the substitute pore fluid should be available in a range of viscosities to suit geotechnical centrifuge testing. Typically, g -levels vary between 10 g and 150 g . Therefore, dynamic viscosities of 10 $\text{mPa}\cdot\text{s}$ to 150 $\text{mPa}\cdot\text{s}$ are of interest;
- preparation of the model with the substitute pore fluid should not take excessively more time when compared to preparing a soil model with water, although it is recognized that preparation times will always increase to a certain extent using a substitute pore fluid;
- production times should be acceptable and fluid properties between batches should be consistent;
- fluid properties should not change significantly over time, particularly in-between fluid preparation and test execution;
- the substitute pore fluid should be non-toxic, bio-degradable and inert towards equipment and sensors for safe handling and disposal.

3 FLUID PROPERTIES

3.1. Selection of CMC

The original Delft Geotechnics (Deltares' predecessor) pore fluid (Allard & Schenkeveld, 1994) fulfilled the geotechnical requirements described above and was successfully used in several modelling studies (e.g. Allard et al., 1994). However, it was composed of various volatile and flammable chemicals, and soon the need for a fluid which would be less hazardous and bio-degradable became apparent. High costs were associated with the disposal of soil models and the procedures in

place to minimize health risk to personnel hampered efficient operation.

Following this, an evaluation of possible solutions started and in 1999, Deltares developed a pore fluid based on sodium carboxymethylcellulose (*ICMC*¹). The selected product (AF0305, Akzo Nobel) has a degree of substitution of 0.7-0.95 three available cellulose-groups in each cellulose subunit has been replaced by the functional group carboxymethyl (Figure 1).

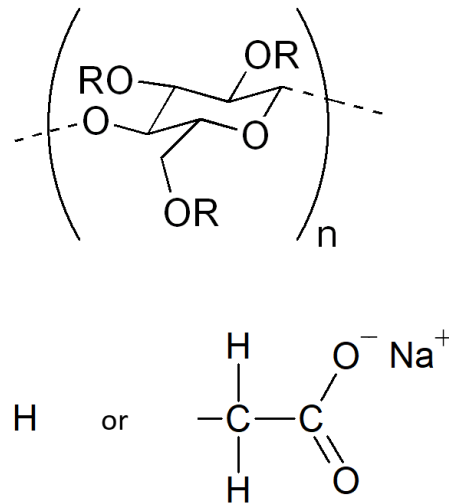


Figure 1. Functional unit of cellulose with 3 locations (-R), where the -H end group is replaced by carboxymethyl.

Other types of *ICMC*, with a higher chain length, were also investigated but proved to exhibit non-Newtonian behaviour at low shear stress and were causing clogging of pore volumes. *ICMC* comes in an odourless, off white, free flowing white powder and is widely used in the food industry as a thickening agent.

Although this was -back in 1999- the first use of a carboxymethylcellulose, the use of modified celluloses as a pore fluid had been coined already in 1998 by Kutter et al. through using methylcellulose (which is chemically similar). In the past years another modified (methyl)cellulose has been heavily used: hydroxypropyl methylcellulose (*HPMC*).

3.2. Physical Properties

A number of different variations of *ICMC* solutions were tested on basic physical properties. Different concentrations were prepared by mixing *ICMC* in hot water and agitating the mixture while permitting the solution to cool. In this paper, the employed

¹ We designate the used CMC in the remainder of this paper as *ICMC*, as it is on the lower end of the viscosity-application range due to a lower molecular weight.

definition of concentration for ICMC solution is dry mass of ICMC over mass water. An elevated temperature prohibits the ICMC particles to dissolve in water, allowing optimal wetting of particles. Upon cooling, the suspended fully wetted particles dissolve into the aqueous solution. This is a common method for preparing methylcellulose type solutions and is, amongst others, described by Dewoolkar et al. (1999) and Adamidis & Gopal (2015).

Although temperature variations are typically limited, say $20^{\circ}\text{C} \pm 2^{\circ}\text{C}$, during geotechnical centrifuge testing, it is still desirable that temperature related variations in model pore fluid viscosity follow the same trend as the prototype pore fluid. In order to validate temperature stability both the specific gravity and the viscosity were measured at different temperatures and concentrations. Temperatures ranged from 5°C to 30°C and concentrations were varied from 0 % (water) to 3.5 %. The specific gravity was measured using a hydrometer and the viscosity was measured using an Ubbelohde viscometer.

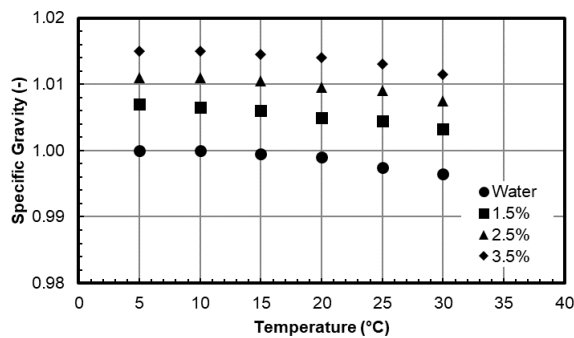


Figure 2. Specific gravity versus temperature for water (0.0% ICMC) and various concentrations of ICMC.

Figure 2 and Figure 3 show that the specific gravity and the viscosity decrease with temperature. To allow for correct interpretation of results it is important to monitor the model temperature during centrifuge testing.

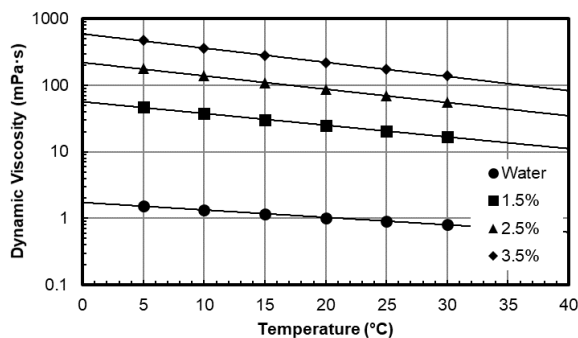


Figure 3. Dynamic viscosity temperature for water (and various concentrations of ICMC). Exponential fits are applied to the data in order to guide the eye.

In order to validate if the ICMC solutions behave like a Newtonian fluid, four different concentrations were prepared and tested using a HAAKE MARS rheometer (Thermo Fisher, Karlsruhe, DE). The shear stress was measured with shear rates varying from approximately 1 s^{-1} to 2000 s^{-1} , where equipment limitations so permitted. The results are presented in Figure 4, and show that, although fluid behaviour is not fully Newtonian over the tested shear rate range, it can be assumed to be Newtonian in the range of interest for (dynamic) centrifuge testing. The range of dynamic centrifuge testing has adopted from Adamidis & Gopal (2015). Additionally, Figure 4 shows that a substitute pore fluid with a viscosity up to $300\text{ mPa}\cdot\text{s}$ can easily be prepared, thus allowing centrifuge testing up to 300 g.

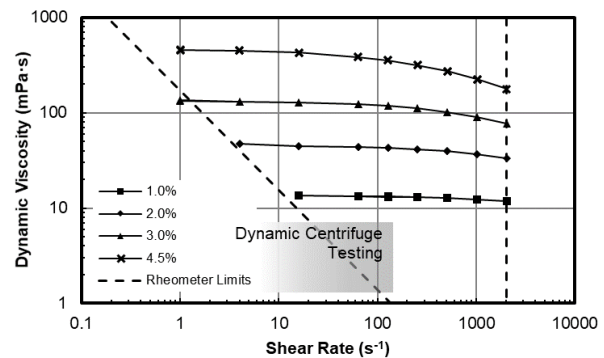


Figure 4. Dynamic viscosity at varying shear rate for various concentrations. Dashed lines indicate measurement limits of the rheometer. Exponential fits are applied to the data in order to guide the eye.

The long-term stability of the solution was also evaluated. During a period of 11 months, the viscosity of a single 2.0 % solution stored at 10°C was periodically measured using an Ubbelohde viscometer at 20°C . Results are shown in Figure 5. The viscosity over almost 1 year was stable, consistent with observations of Dewoolkar et al. (1999) for 1-3% solutions of hydroxypropyl methyl cellulose (HPMC: Metolose 90SH-100).

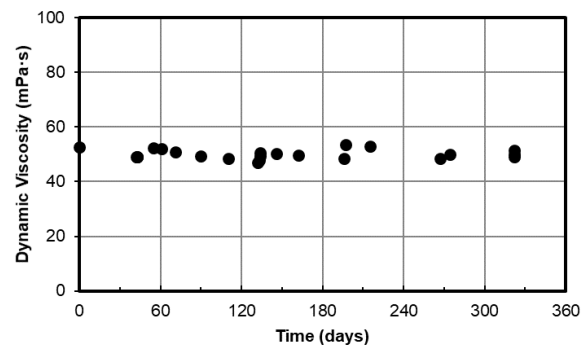


Figure 5. Viscosity versus time for a 2.0% solution. The viscosity was monitored for a period of about 11 months and shows no significant change over time.

Figure 6 shows the effect of the *ICMC*-concentration on the solution viscosity at different temperatures. The results vary for the same product per batch differ in the order of about 10% (data not shown) and thus batch-by-batch adjustment of the used *ICMC*-concentration may be necessary through addition or evaporation of water.

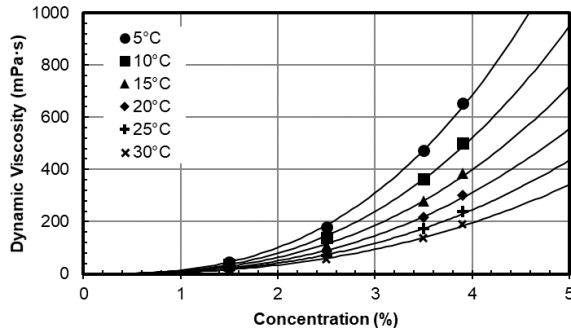


Figure 6. Viscosity versus concentration, at different temperatures. Depending on the batch found viscosities may vary slightly, in the order of about 10 %. Viscosity has been determined using and Ubbelohde viscometer. Exponential fits are applied to the data in order to guide the eye.

Pigments have been added to *ICMC* fluid on several occasions in order to show flow patterns. Adding colour to the pore fluid facilitates visualization of ground water flows, as shown in Figure 7. Such pigments should be well visible on the sands concerned and change the physical characteristics of the fluid as little as possible. The colours red and blue, as shown in Table 1, have been added for visualization with the *ICMC* and showed good visibility at long term (2 months) stability.

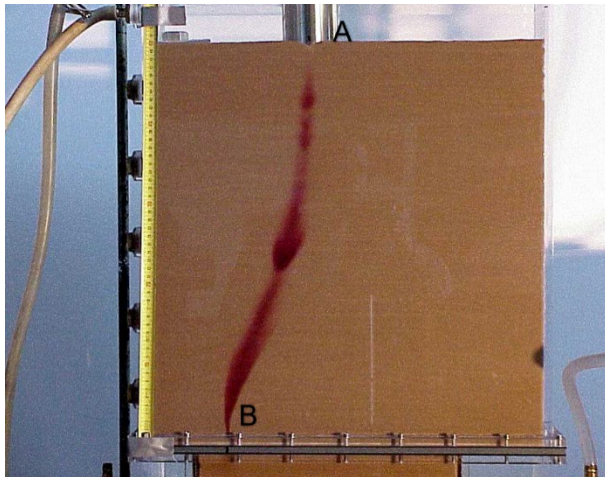


Figure 7. Example of visualization of ground water flow using E132 (in water). Red dyed pore fluid is introduced at point A, while an under-pressure is introduced at point B (Image F.M. Schenkeveld, 2000).

Table 1. Sand Colorants in Water, measured at 20°C.

Parameter	Unit	RED	BLUE
Colourant	-	E124	E132
Name	-	Ponceau 4R	Indigo carmine
Concentration	(g/L)	10	10
Density at 20°C	(kg/L)	1.005	1.003
Viscosity	(mPa·s)	1.053	1.048

3.3. Geotechnical Properties

Constant head permeability tests were conducted on Baskarp B15 Sand (Baskarp sand properties are summarized in Table 2) using a standard constant head set up (ISO 17892-11:2004) and sand samples saturated with water and samples saturated with three different *ICMC* solutions.

Following Darcy's law, the permeability should increase linearly in a 1:1 relation with increasing pore fluid viscosity. Figure 8 shows the ratio of the permeability of water saturated samples to the permeability of *ICMC* solution saturated samples. Results follow a 1:1 slope, thus satisfying the scaling requirement.

Table 2. Soil Properties of Baskarp B15 Sand.

Parameter	Unit	B15
Particle density, γ_s	kN/m ³	2.65
Minimum void ratio, e_{min}	-	0.52
Maximum void ratio, e_{max}	-	0.89
Mean mass diameter, d_{50}	mm	0.13
Coefficient of uniformity, d_{60}/d_{10}	-	1.4

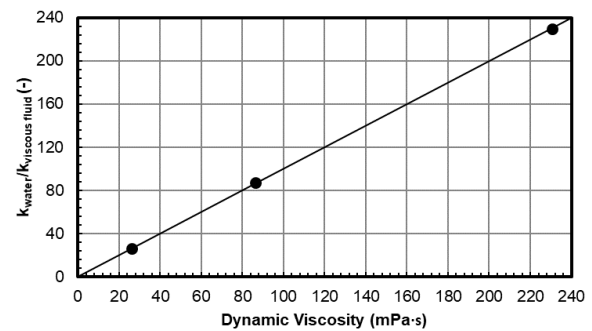


Figure 8. Ratio between vertical hydraulic conductivity of water and *ICMC* viscous substitute pore fluid versus dynamic viscosity. Three different concentrations were prepared, and the hydraulic conductivity was determined at 1-g using a standard constant head permeability test on Baskarp B15 sand. The straight line indicates a 1:1 relation.

Additionally, consolidated anisotropic drained triaxial tests were conducted on Baskarp B15 sand. The aim was to investigate any possible change in friction angle due to the different pore fluid. Samples were prepared in both loose and dense state and saturated with water and *ICMC* solution.

Results are presented in Table 3 and show no significant difference in friction angle between the water saturated and ICMC solution saturated samples.

Table 3. Summarized Consolidated Drained Triaxial Test Results on Baskarp B15 Sand. Vertical and horizontal stress was 300 kPa and 162.5 kPa, respectively.

Pore Fluid	e (-)	μ (mPa·s)	ϕ (°)
Water	0.57	1.0	43.7
Water (coloured)	0.57	1.0	42.8
CMC 3.5%	0.57	299.5	44.0
CMC 3.5% (coloured)	0.57	297.4	42.9
Water	0.71	1.0	40.0
Water (coloured)	0.70	1.0	40.9
CMC 3.5%	0.71	299.5	40.0
CMC 3.5% (coloured)	0.70	297.4	40.1

4 SOIL MODEL PREPERATION

This section describes best practices regarding ICMC. A batch of substitute pore fluid is prepared at the desired viscosity using guidelines on concentration presented in Figure 6. As described earlier, the ICMC is added to de-aired water (heated to about 60°C) while being agitated. When all ICMC particles are fully suspended, the solution is allowed to cool to room temperature. This may be achieved by starting at a high concentration and adding cold (5-10°C) water later as is shown for HPMC (Adamidis & Gopal, 2015). Additional tweaking is sometimes used in order to fine tune the viscosity. When using food grade ICMC, insoluble impurities are still present in the aqueous solution and prohibit infiltration of the ICMC solution into the sand model due to clogging. Therefore, the ICMC solution requires to be filtered before in can be applied as a substitute pore fluid. Such filtering may also reduce the encountered reduction in permeability reported in methyl celluloses (Tobita, 2020). The authors' experience is that glass-fibre filters with a pore opening of 0.5 μm work well.

After filtration, the model can be saturated with the substitute pore fluid. The starting point for obtaining a sand model saturated with viscous fluid is a fully water saturated sand model. A fully saturated sand model can be prepared using techniques described by Poel & Schenkeveld (1998). The phreatic level of the water saturated sand model should be equal to the top of the sand model. A volume of viscous fluid in excess of the amount required to replace the water in the pore volume should now be placed on the surface. The excess volume is required to avoid air entrapment. By applying an under pressure to the sand model the

water will start to flow out of the model and will be replaced by the viscous fluid. Viscosity measurements of the fluid exiting the model can provide indications whether saturation with viscous fluid is complete. Great care should be taken to apply a small enough under pressure in order to allow for homogeneous saturation and avoid preferential flow path in the sand.

5 APPLICATION IN GEOTECHNICAL CENTRIFUGE TESTING

The ICMC-based substitute pore fluid has been developed by Deltares in 1999 under a research project and has been mainly applied in commercial projects of which the results cannot be disclosed. As such no data was published. However, publicly available applications also exist.

Hölscher et al. (2012) and Nguyen (2019) applied this pore fluid in several series of rapid pile load tests and static pile load tests in the geotechnical centrifuge at Deltares at 40 g. The rapid load tests were carried out with several loading rates. Pore pressures were measured at different distances from the pile tip. The tests confirm that a rapid load test can overestimate static capacity due to pore water pressure when testing piles in medium to fine sands. The results were compared with field measurement and it has been concluded that the centrifuge tests represent realistic behaviour.

More recently, Askarinejad et al. (2017) compared the ICMC based pore fluid with a glycerine solution and normal water in pore pressure development of laterally loaded offshore piles. It was concluded, that although the problem was assessed to be a drained situation, the density of the pore fluid played a major role in the development of pore pressure. It was observed that it directly affects the state of the soil and the stiffness and lateral capacity of the pile.

6 COMPARISON OF PORE FLUIDS

Roughly four different pore fluids have been used for centrifuge modelling to properly scale the result: silicon oil-water mixtures (Zeng et al., 1998), water-silicon oil mixtures, xanthan as well as various substituted celluloses. Especially the latter is showing behaviour corresponding with the requirements stated in the introduction. The effect of a pore fluid is however not only determined by the substituent of the cellulose (carboxymethyl in case of ICMC, and methyl in case of methyl cellulose), but is also determined by the % of available spots which is substituted. In general, a higher degree of substitution with oxygen containing substituent (e.g. carboxymethyl in ICMC

Table 4. Overview of modified methyl celluloses as viscous fluids.

Abbreviation	Name	Type (brand)	Substituent(s)	Viscosity of 2% solution (mPa·s)	Degree of substitution ²	Source
HPMC	hydroxypropyl methyl cellulose	Metolose 90SH-100	1) hydroxyproxy 2) methoxy	80-120	1) 47% 2) 6%	Dewoolkar et al. 1999, Shin-Etsu 2018.
HPMC	hydroxypropyl methyl cellulose	Methocel F50	1) hydroxypropoxyl 2) methoxy	40-60	1) 27-30% 2) 4-7.5%	Adamidis et al. 2015, Steward, 1998. Dupont 2019.
/CMC	carboxymethyl cellulose (sodium)	Akucell AF0305	carboxymethoxy	40-60	21-30%	This study, Akzo 2010
MC	methyl cellulose	Metolose SM100	methoxy	80-120	26-33%	Tobita et al. 2008, Shin-Etsu 2018.

and hydroxymethyl in HPMC) will increase the viscosity because there will be more interaction between individual /CMC chains through hydrogen bridges, which leads to a cross-linking characteristic.

Furthermore, cellulose polymers are available in several chain lengths, which has a very strong effect on viscosity. An overview of characteristics of pore fluids used in centrifuge modelling (as far as can be inferred from the paper in combination with publicly available characteristics of the used products) is shown in Table 4.

Table 4 shows that a full comparison of characteristics is complicated, as they are generally not consistently described and supplier information is needed to obtain all available information. We propose therefore to systematically analyse and describe pore fluids in order to aid the reproducibility of experiments in the future. In addition to the characteristics for pore fluids described above it is therefore recommended to also describe:

- chemical characteristics;
- degree of substitution;
- average molecular mass;
- density and viscosity of a 2% solution at the temperature employed.

7 CONCLUSION

Deltares developed a viscous pore fluid for geotechnical centrifuge modelling based on sodium carboxymethylcellulose. The effects of concentration, temperature, ageing and shear rate on these aqueous /CMC solutions were examined. The rheological behaviour is also investigated. Viscosities suitable for centrifuge testing up to 300 g proved to be achievable. The solutions are stable over time and the change in characteristics due to temperature changes is limited, and similar to water.

The /CMC solution shows Newtonian behaviour in the shear rate region of interest for dynamic centrifuge testing. Homogeneous fully saturated soil samples containing the viscous pore fluid were prepared and recommendations for soil model preparation are given in this article. Also, the influence of the viscous pore fluid on the shear strength of the soil model compared with water is not significant. Three cases of successful application of the pore fluid in dynamic geotechnical centrifuge testing are cited. The Deltares geotechnical centrifuge that is under construction (Zwaan et al., 2020) will therefore likely also use this pore fluid in many of its experiments.

8 ACKNOWLEDGEMENTS

The authors would like to thank F.M. Schenkeveld for his efforts on the development of the /CMC pore fluid.

9 REFERENCES

- Adamidis, O. and Madabhushi, G. 2015. On preparation of viscous pore fluids for dynamic centrifuge modelling. *International Journal of Physical Modelling in Geotechnics*, **15**(3): 141-149.
- Akzo Nobel. 2010. Product Specification Akucell AF0305.
- Allard, M.A. and Schenkeveld, F.M. 1994. The Delft Geotechnics model pore fluid for centrifuge tests. *Centrifuge 94*, 133-136.
- Allard, M.A., Andersen, K.H., and Hermstad, J. 1994. Centrifuge Model Tests of a Gravity Platform on Very Dense Sand; 1: Testing Technique and Results. *In Proceedings of the 7th International Conference on the Behaviour of Offshore Structures*, Cambridge Massachusetts, USA, July 1994, pp. 231-254.

² Calculated on a mass-basis

- Askarinejad, A., Philia Boru Sitanggang, A., and Schenkeveld, F. 2017. Effect of pore fluid on the cyclic behavior of laterally loaded offshore piles modelled in centrifuge. *In Proceedings of the 19th International Conference on Soil Mechanics and Geotechnical Engineering*, Seoul, South Korea, 17-21 September 2017, pp. 897-900. DuPont, 2019. Methocel™ Brochure.
- Dewoolkar, M., Ko, H., Stadler, A., and Astaneh, S. 1999. A Substitute Pore Fluid for Seismic Centrifuge Modeling. *Geotechnical Testing Journal*, **22**(3): 196-210.
- Garnier, J., Gaudin, C., Springman, S.M., Culligan, P.J., Goodings, D., Konig, D., Kutter, B., Phillips, R., Randolph M.F. and Thorel. L. 2007. *International Journal of Physical Modelling in Geotechnics*, **7**(3): pp 01-23.
- Hölscher, P., van Tol., A.F., Huy, N.Q. 2012. Rapid pile load tests in the geotechnical centrifuge. *Soils and Foundations*, **52**(6): 1102-1117.
- ISO/TS 17892-11:2004(en), Geotechnical investigation and testing — Laboratory testing of soil — Part 11: Determination of permeability by constant and falling head.
- Ko, H. Y. 1994. Modeling Seismic Problems in Centrifuges. *Centrifuge 94*, pp. 03–12.
- Kutter, B.L., Stewart, D.P. and Chen, Y.R. 1998. Experience with the use of methylcellulose as a viscous pore fluid in centrifuge models. *Geotechnical Testing Journal*, **21**(4): 65-369.
- Nguyen, T.C. 2017. Modelling of pile load tests in granular soils: Loading rate effects. Doctoral thesis. Delft University of Technology.
- Poel, J.T., & Schenkeveld, F.M. 1998. A preparation technique for very homogeneous sand models and CPT research. *In Proceedings of the International Conference Centrifuge 98*, Tokyo, Japan, 23-25 September 1998. Taylor & Francis Group, London, pp. 149–154. Shin-Etsu. 2010. Metolose®. Metolose® SR. Brochure.
- Tobita, T. 2018. Permeability of sand with a methylcellulose solution. *In Proceedings of the International Conference on Physical Modelling in Geotechnics*, London, UK, 17–20 July 2018. Taylor & Francis Group, London, pp. 271–276.
- Tobita, T. 2020. Variation of Permeability of Viscous Fluid During Liquefaction Model Testing. *In Model Tests and Numerical Simulations of Liquefaction and Lateral Spreading*. Kutter, B. Manzari, M.T., Zeghal, M. pp. 649-652.
- Whitman, R. V., Lambe, P. C., and Kutter, B. L. 1981. Initial Results from a Stacked Ring Apparatus for Simulation of a Soil Profile. *In Proceedings of the International Conference on Recent Advances in Geotechnical Earthquake Engineering and Soil Dynamics*, Missouri-Rolla, US, 26 April – 3 May 1981. pp. 1105–1110.
- Zeng, X., Wu J., and Young B. 1998. Influence of viscous fluids on properties of sand. *Geotechnical Testing Journal* **21**(1): 45-51.
- Zwaan, R., Terwindt, J., de Lange., D.A., Bezuijen, A. 2020. A New Geotechnical Centrifuge at Deltares, Delft, the Netherlands. *In Proceedings of the 4th European Conference on Physical Modelling in Geotechnics*, Luleå, Sweden, 15–17 March 2020.

2. Physical modelling techniques and facilities

A new geotechnical centrifuge at Deltares, Delft, the Netherlands

Rob Zwaan, Jarno Terwindt, Dirk de Lange, Adam Bezuijen

Geo-engineering, Infra and Structures, Deltares, The Netherlands

Corresponding author: Rob Zwaan (rob.zwaan@deltares.nl)

ABSTRACT: A new geotechnical centrifuge has been commissioned by Deltares, Delft, The Netherlands, as a replacement of the previous facility, which has expended its serviceable life. The new centrifuge is an Actidyn C72-31 beam type centrifuge, and has a 260 g-tonne capacity and a platform radius of 5.0 m. The platform can house test set-ups with dimensions up to 1.2 m × 1.2 m × 1.2 m (length × width × height). The data-acquisition system is supplied by HBM and has 40 channels with a sampling rate of up to 100 kHz. Two high speed cameras and four monitoring cameras are available for imaging. A 4-axis robotic system allows in-flight excavation and installation operations. The centrifuge is fully prepared for later installation of an earthquake simulator. Supporting facilities consist of a clay mixer and a consolidation frame. This paper details the choices made leading to this centrifuge, the specifications of the centrifuge and supporting facilities.

Keywords: GeoCentrifuge; Deltares; Geotechnical; Centrifuge; C72.

1 INTRODUCTION

From 1987 until 2017 Deltares has been operating a geotechnical centrifuge for research on soil mechanics, the interaction between soil and structures and other related research topics. In 2017 this centrifuge with a beam of 6 m and a capacity of 1050 g-tonne was closed after relocation of the complete soil mechanical department of Deltares to a new location in Delft, the Netherlands. This relocation was part of an infrastructural reorganization in which all the departments of Deltares are located together as much as possible on one location in order to combine forces on the use of facilities, experts and knowledge.

Before the forming of Deltares in 2008 the centrifuge was part of “Delft Geotechnics” and from 1999 “GeoDelft”. The four walled shape of the centrifuge basket, the large size of the basket (2 m × 1 m × 1 m, l × w × h) and payload capacity of the centrifuge made it possible to create very large soil samples inside the basket itself without using a strongbox. It was also possible to create relatively big test set-ups with large strongboxes and/or an extensive amount of utilities for use during centrifuge flights.

The centrifuge contributed to a large amount of geotechnical research projects. During these projects the centrifuge was one of the steps between small scale tests up to field scale tests and had an important role in optimizing and the reducing of risks in designs where the interaction between soil and structures was of importance. It contributed for example to validate improved calculation methods for dike stability and the fact finding when a canal dike failed near the village of Wilnis. It helped to understand the tunneling processes and the pile-

tunnel interaction when the first TBM tunnels were constructed in The Netherlands. It was used to check the influence of ship impact on bridge foundations in Hongkong and Incheon. It has been used to study pile capacity, rapid pile load testing and pile group effects. Furthermore, numerous offshore projects were performed (dragging of anchors, jack-up-seabed interaction etc.).

After the relocation of the soil mechanical department to the new location the centrifuge became a “remote” location. This fact combined with increasing difficulties to find spare parts for the almost thirty-year-old machine, an increasing amount of (ir)regular maintenance work and the partially outdated test control, data- and video acquisition systems has led to the decision to close the centrifuge in April 2017. The centrifuge was dismantled, the large underground centrifuge chamber became a rain water storage and on top a new seventeen floors high building was constructed to accommodate students from the Delft University of Technology.

In 2010 the first plans to acquire a new centrifuge were discussed and up until 2017 these plans were elaborated to a detailed list of demands for the new centrifuge. This list was based on the thirty years of experience with the old centrifuge combined with the possibilities needed for the expanding scope of work since GeoDelft became a part of Deltares. With the detailed list of demands a public tender was started after which it was decided to choose the C72-3 beam centrifuge with a capacity of 260 g-tonne manufactured by Actidyn Systems.

The funding for the new centrifuge is split between the Ministry of Economic Affairs of the Netherlands and Deltares. This funding also

included the construction of the new centrifuge building, new data- and video acquisition system, new test control system, controlled tool system, soil consolidation frame, hydraulic power pack and a new clay mixer with a 500 l capacity.

2 GENERAL CONSIDERATIONS

The previous in-house designed geotechnical centrifuge was one of the biggest geotechnical centrifuges worldwide. However, in daily use that appeared not only advantageous. The centrifuge could only operate under vacuum, which made starting and stopping a relatively long-time procedure since the vacuum had to be created before spinning-up and had to be released before stopping. For this vacuum and for safety, the centrifuge was built in a cellar which decreased the accessibility. Analysing the projects that were run, it appeared that the full capacity in payload nor g-level was hardly ever used. Therefore, it was decided that the new centrifuge could be smaller than the old one but should allow easier access and a shorter turn-around time for one test. Furthermore, maintenance should be simpler and less costly. This is realized by using 'standard equipment' instead of an in-house design, a centrifuge on the same floor level as the Soil Mechanical Laboratory and a centrifuge that can run at atmospheric pressure.

Since it can be expected that soft soil (peat and clay) will be used quite frequently, a stand-alone mode during re-consolidation of that soil was essential.

3 THE C72-3 CENTRIFUGE

The chosen C72-3 is a modified version of the previously manufactured C72 centrifuges. The C72-3 is for a large part comparable with the centrifuges delivered to the Centre for Offshore Foundation systems at the University of Western Australia (Gaudin et al., 2018) and the Korea Advanced Institute of Science and Technology (Kim et al., 2006). The main difference is that the C72-3 is developed to make future installation of the Actidyn Earthquake simulator possible. For this purpose, the C72-3 is equipped with an earthquake simulator prepared platform, extra high-pressure hydraulic sliprings to power the simulator and the whole centrifuge construction is re-designed to a higher payload which increased the capacity to 260 g-tonne instead of 240 g-tonne.

The C72-3 has opted for a gearbox to connect the electric motors with the rotor drive shaft instead of a drive-belt. This choice is made because of the higher payload capacity and larger g-level range. The platform radius is 5 m with platform

dimensions of 1.2 m × 1.2 m × 1.2 m designed for a payload of 2600 kg at 100 g or 1000 kg at 150 g.

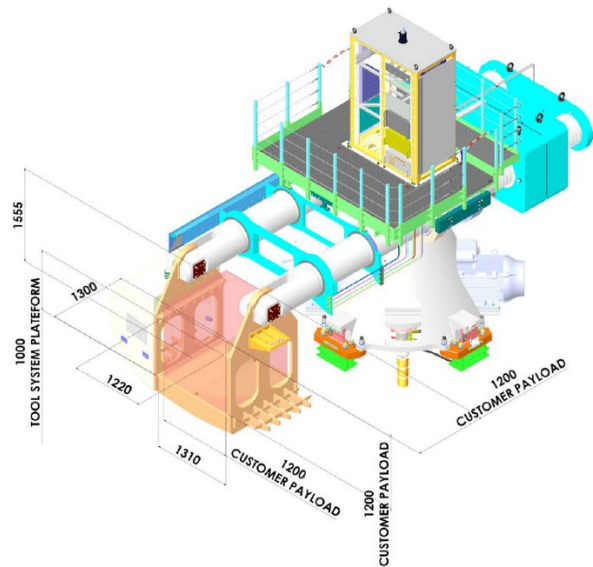


Figure 1. The new C72-3 centrifuge at Deltares.

To maintain the balance of the centrifuge an automatic unbalance detection system is integrated consisting of four detection strain gauges in the floor connection of the pedestal, a counterweight with a mass of 14,896 kg and two hydraulically actuated small weights of 367 kg each inside the two centrifuge beams for fine adjusting purposes. The hydraulic system and the controlling PLC (Programmable Logic Controller), both needed for the automatic balance system, are completely integrated on board of the centrifuge.

When the centrifuge starts, up to a level of 10 g, the position of the large counterweight will be adjusted until the desired position has been reached for coarse balancing. Then when the centrifuge g-level increases to the level needed for the centrifuge experiments, the small counterweights are deployed for fine balancing purposes. The small counterweights also maintain the balance of the centrifuge during flight, when during an experiment the weight or the balance of the payload changes.

On top of the centrifuge beams, a user platform is constructed that provides easy access to the two 19" racks that provide housing for on-board equipment. Besides the centrifuge related equipment such as the unbalance control PLC, (there is enough space for additional equipment such as the test control system, NAS (network attached storage) units, patch panels and power supplies. The 19" racks are situated above the heart of the rotation axis to minimize the g-level on the equipment within the racks.

The centrifuge is driven by two frequency controlled electric motors that drive the gearbox which is coupled to the central axis of the

centrifuge. The total installed main power supply for driving the centrifuge is 270 kW. In addition to this, 70 kW is reserved for on-board systems and experiment power supply and 170 kW for the hydraulic power unit to charge the earthquake simulator and drive hydraulic devices during experiments. To deliver the power needed for the complete centrifuge and surrounding utilities, a new separate high voltage line from the public energy grid is laid out to a designated transformer in the centrifuge building.

4 THE CENTRIFUGE BUILDING

4.1. General Situation

For the new centrifuge a new building had to be created on the Deltares location at the Boussinesqweg in Delft.

To get a good connection with the already existing Soil Mechanical Laboratory and the 1g geotechnical model facilities, it was decided to attach the new centrifuge building to this laboratory. In this way facilities, staff and materials can easily be shared since the centrifuge is a logical addition to the facilities of this lab. It also decreased the amount of space needed for the new building since test set-up construction and model preparation for the centrifuge can be combined with the already existing activities in the lab. In this way only a centrifuge chamber with a second floor for the air conditioning unit and hydraulic power pack, a control chamber and a connecting hallway had to be built. Although this seems not too comprehensive, it still was a challenge to construct this on the soft soils of the Netherlands. For the foundation of this additional building of 255 m² it was necessary to drive 77 piles (see Figure 2) into the ground to a depth of 19 metres. The huge amount of piles was needed on this location to keep the building stabilized, even in case of a fatal unbalance of the centrifuge (loss of payload).

The ground floor of the centrifuge building is attached to the floor of the Soil Mechanical Laboratory and is wide enough to drive a forklift in to the centrifuge chamber when necessary. The only interruptions in the floor surface from the Soil Mechanical Laboratory to the centrifuge room are two narrow expansion and/or vibration joints of 2 cm each. These joints are filled with flexible synthetic spacers to maintain a flat surface. This flat floor surface from the preparation area to the centrifuge chamber is for instance essential for the shockless transport of vulnerable soil samples with low density sand beds.

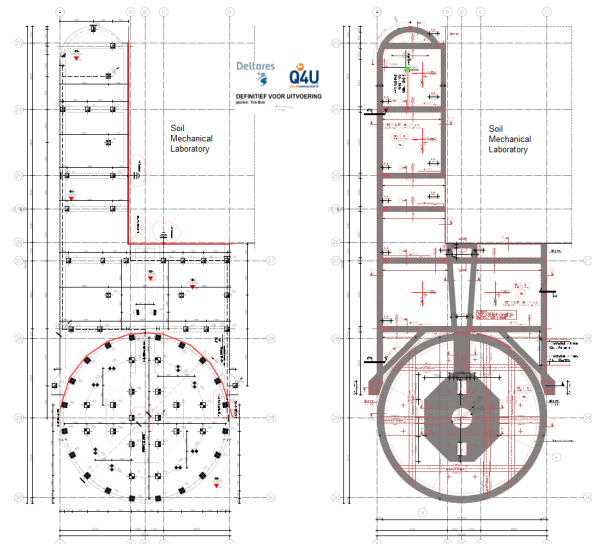


Figure 2. Layout of the centrifuge building foundation.

The centrifuge chamber wall and ceiling are constructed on top of this floor, the steel reinforcement of the floor concrete is thoroughly connected to the four-layered steel reinforcement of the 40 cm thick wall and ceiling. Throughout the whole foundation, floor, wall and ceiling, the steel reinforcement was designed to the maximum possible density to ensure a firm centrifuge base and chamber that can resist a fatal unbalance. As a further precaution a highly reinforced wall of 40 cm thick is placed outside the steel centrifuge chamber door. If the door fails to resist an impact due to fatal unbalance, this wall is the final measure needed in this safety chain.

The rest of the centrifuge building will be a normal steel structure with construction-, glass- and isolation panes.

In Figure 3 a rectangular hatch is visible on top of the centrifuge building. This hatch is also present in the centrifuge chamber ceiling and enables the hoisting of the centrifuge in- and out of the chamber.



Figure 3. Artist-impression of the new centrifuge building.

4.2. Control chamber

The centrifuge control chamber is situated in the rounded end of the hallway opposite of the centrifuge chamber. This ensures a safe distance from the centrifuge chamber while having a clear view on the hallway leading to the centrifuge chamber. The control chamber houses the centrifuge operating desk, the test control desk (including video and data acquisition), 19" racks for NAS, test control modules and other relevant equipment and additional desks for project leaders and/or clients that want to attend during centrifuge tests.

The centrifuge operating desk with a stand-alone computer and designated software enables the operator to control and monitor the centrifuge. Parameters such as desired g-level and rate of acceleration to reach this g-level can be controlled. The real-time monitoring and registration of centrifuge parameters such as temperature and unbalance are also integrated in this system. This system also incorporates safety systems such as an automatic centrifuge stop when unbalance reaches threshold limits or when doors providing access to the centrifuge chamber or utility room are opened. LCD screens display video images of the four safety cameras in the centrifuge building provide real-time sight on what is happening in the several areas.

The test control desk houses everything that is necessary to perform a centrifuge experiment such as real-time controlling of valves, hydraulic actuators, lighting, etc. during flight. The controlling and monitoring of the data- and video acquisition providing real-time test information are also integrated in the test control desk. The test control desk and the centrifuge operating desk are situated next to each other.

4.3. The utility room

The centrifuge building is partially equipped with a second floor above the centrifuge chamber. This houses the utility room with the centrifuge power cabinets, the climate installation for the centrifuge chamber and the hydraulic pressure unit. This utility room is part of the air conditioning loop that keeps the temperature in the centrifuge chamber below 30 °C. The air conditioning loop consists of the utility room, the centrifuge chamber and large airducts in the floor and wall of the centrifuge chamber. This creates a closed loop system in which the air is conditioned and recirculated to ensure proper temperature conditions during centrifuge flights. The air flows from the conditioning unit into the utility room, then down through a square hole of 2 m × 2 m in the ground into the centrifuge chamber and then through the airducts back to the

conditioning unit. This circulating airflow also provides cooling for the hydraulic power unit and the centrifuge power cabinet.

The utility room is connected to the second floor of the Soil Mechanical Laboratory with a small hallway enabling easy access when necessary.

5 CENTRIFUGE CONNECTIONS

To connect the centrifuge with the surrounding utilities and mains power the centrifuge is equipped with rotary joints. On top of the two 19" racks a Fiber Optic Rotary Joint is installed to connect the on-board network with the network in the centrifuge. This provides two 10 Gbps fiber optic connections from the two on-board ethernet switches to the two ethernet switches in the control room. From these Juniper EX2300-C switches cat6 ethernet cables are used to create the necessary network connections to further equipment on both sides. This network is used for data- and video acquisition, centrifuge control purposes, the test control system, the 4-D robot and other equipment that requires network connections. From the control room switch the centrifuge network is also connected to the Deltares network through fiber optic cables to provide remote control and monitoring possibilities and access to the Deltares data storage building.

On top of the 19" racks also signal slip rings are available for copper connection of 3 BNC fitted video lines and 32 signal lines each capable of 150 Vdc/1 A. The signal lines are used to copper-connect I/O ports of the on-board test control systems with the control room.

The power sliprings and fluid rotary joints are mounted below the central axis of the centrifuge. The power sliprings provide mains power to the on-board equipment and experiments in the centrifuge basket up to 220 V/ 100 A. The fluid rotary joints provide connection of two hydraulic lines up to 200 bar, one hydraulic line up to 300 bar, pressurized air up to 10 bar, water and de-aired water up to 20 bar and vacuum down to -0.8 bar. The fact that 3 hydraulic lines are installed is caused by the decision to make the centrifuge ready for possible future installation of an earthquake simulator

6 CENTRIFUGE EQUIPMENT

The centrifuge is equipped with several systems necessary to perform experiments. These systems are partially designed and manufactured by Deltares and partially bought from third parties. The systems are designed and purchased based on 30 years of experience with the previous centrifuge and adapted to modern standards.

6.1. Test control system

The test control system is designed to perform any remote action that could be needed during centrifuge experiments. The system is completely designed and built by Deltares and uses CompactRIO hardware and software from National Instruments as heart of the system. The CompactRIO system consists of a controller with a processor and user-programmable FPGA (field-programmable gate array) that is equipped with conditioned I/O modules. These modules provide a wide range of functions and come in a rugged industrial form suitable for use in harsh environments.

For the centrifuge two CompactRIO systems are designed and coupled over an ethernet connection with each other. One system is built in the 19" racks of the centrifuge and the other one in the centrifuge test basket. Both systems are fitted with a wide range of I/O ports ensuring flexible use of this system to enable centrifuge testing. Partially the I/O ports from the on-board systems are copper wired over the signal slip rings to terminations in the 19" rack in the centrifuge control room. These wires can be used to exchange signals between the centrifuge and the control room. This could occur when for instance read-out equipment that is not able to withstand the g-level in the centrifuge needs to be hard-wired with a test running in the centrifuge.

The software user interface enables full control of the whole system from the control room. This system will be used to switch valves, control lighting, steer plungers, provide and switch power, transfer digital and analogue I/O signals between the basket, the 19" rack and the control room.

The versatility of the system enables easy modifications if other functions that are yet unforeseen are needed in the future.

6.2. Data acquisition system

For the centrifuge data acquisition system HBM QuantumX modules are chosen in combination with CatMan AP software. After this decision, the Soil Mechanical Laboratory also switched to this system since the centrifuge is part of the facilities in this lab and therefore it is logical to choose one system to align the data-acquisition process, output files and sensor connectors. The data-acquisition hardware is divided into a system in the control room and a system in the centrifuge basket.

The control room system consists of a BPX002 19" backplane that houses two MX840B 8-channel universal amplifier units, one MX879B multi-I/O module and one CX27C ethernet gateway.

The system on board of the centrifuge basket consists of a BPX002 19" backplane that houses

eight MX410B 4-channel high-dynamic universal amplifiers, one MX879B multi-I/O module and 1 CX27C ethernet gateway. For flexible purposes during centrifuge testing two additional MX840B and one MX879B modules are available. The MX410B can handle data rates up to 100 kS/s (maximum 38 kHz signal bandwidth) and the MX840B can handle 40kS/s (maximum 7.2 kHz signal bandwidth). These sample rates are expected to be more than enough, even for possible future earthquake simulator experiments. The MX879B module provides 8 real-time math possibilities, output of calculated input signals, signal generator features and 32 digital I/O ports. The CX27C module provides 1 Gb/s transmission and PTP (Precision Time Protocol) functionality for the modules in the backplane.

The systems are connected to each other and the control room through ethernet cables and the fiber optic rotary joint. The modular system ensures flexible addition of extra modules for data-acquisition purposes and easy maintenance or repair work. The CatMan AP software ensures easy set-up of data-acquisition sessions, flexible real-time monitoring during tests and extensive data-processing possibilities.

6.3. Video acquisition system

Since computing capacity and processing speed have developed strongly in the past years more possibilities for video-based data gathering became available. This now has become a strong addition on the conventional data-acquisition and increased the need for images with better resolution, high-definition video and high-speed video. For these purposes four 4K color cameras and two high-speed color cameras have been added to the centrifuge equipment. The 4K cameras are manufactured by Flir Systems Inc. and are of the type ORYX 31Mpix with a resolution of 31 MP (megapixel) at 26 fps frame rate. These cameras can be monitored real-time on the test control desk in the control room and the images are also stored on a NAS in the on-board 19" racks for later analysis purposes. When performing dynamic centrifuge experiments, it occurs that events in centrifuge experiments happen extremely fast. To capture these events high-speed cameras are essential. Two cameras manufactured by AOS Technologies AG of the type L-VIT 2500 are available to capture images with a resolution of 2 MP at 2500 fps frame rate for a period of 4 s. These images cause a data stream that is way too large to transmit real-time to the control room, so the storage of these images is done in NAS units in the on-board 19" racks of the centrifuge. After the

experiment is finished the images are downloaded to the control room NAS for further analysis.

Besides the cameras for video acquisition, the centrifuge has two additional fixed on-board cameras with a resolution of 5 MP and a frame rate of 26 fps to monitor the centrifuge itself. These cameras are mounted on the centrifuge beam near the hinges. One camera overlooks the whole centrifuge basket and the other camera is pointed at the 19" racks and the platform on-board. The images can be monitored in the control room on a separate screen.

6.4. The 4-D Controlled Tool System

The new Deltares centrifuge has the possibility of using hydraulic or electric actuators as in the previous centrifuge. In the old centrifuge, the actuators had to be fixed on the locations where actions were required: actions at different locations required several actuators. For the new centrifuge, the 4-D ACTS (Actidyn Controlled Tool System) is acquired. This system provides actuator and tool flexibility during flight up to a g-level of 100 g.

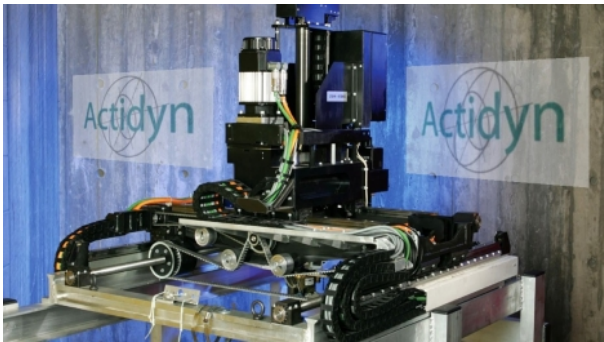


Figure 4. The 4-D controlled tool system.

The ACTS creates the possibility to use 4 different tools on any location covering almost the whole surface of the centrifuge basket during flight. The system is placed on brackets on the centrifuge container side walls at a height of 1.2 m from the floor of the basket.

The system is fitted with two perpendicular electric displacement axes in a plane parallel to the bottom of the centrifuge basket and a dual electric axis of displacement and/or rotation perpendicular to the previous mentioned plane. The axis can be used to maneuver tools and are able to produce a force of up to 5 kN, a torque of up to 5 N·m and a speed of up to 50 mm/s with a positioning accuracy within 1 mm on each axis and 1° on the rotation axis. The tool holder can move along all four axes simultaneously and can pick up or place back the different available tools during flight enabling flexible use of different functionalities.

The tool head of the robot can pick up tools that are fitted with a universal baseplate that enables throughput between the ACTS and the tool of two hydraulic ports, two pneumatic or water ports and power and data lines. This makes it possible to develop, build and use specific tools that can perform a wide array of actions using these provided utilities.

The ACTS is controlled by a Rockwell Automation RSLogix 5000 PLC that is situated in the on-board 19" racks of the centrifuge and a dedicated PC on the test control desk in the control room.

The software of the ACTS gives full control on the functions. It is possible to upload the three-dimensional drawing of the centrifuge test set-up and let the software calculate the most efficient routing to the different points in the model where actions are required during flight while avoiding collisions with the model using no-go zones.

The robot was initially designed, built and used at IFSTTAR (former LCPC, Derkx et al., 1988), and is now identical to that used at the Centre for Offshore Foundation systems at the University of Western Australia (Gaudin et al., 2018) and the Korea Advanced Institute of Science and Technology (Kim et al., 2006).

7 UTILITIES

For the new centrifuge, several utilities are available to facilitate soil model preparation and testing.

7.1. Strongboxes and consolidation cells

The strongboxes are structurally reinforced to minimize mechanical deformation during flight and can also be used as consolidation cell using the consolidation frame or during centrifuge flight.

The platform of the C72 centrifuge is 1.2 m × 1.2 m, which is large enough to use the rectangular and cylindrical strongboxes that were already available from the previous centrifuge. The cylindrical cells are available in 30 cm, 60 cm and 90 cm internal diameter and can be stacked up to the desired height. The rectangular strongbox can hold a model of 80 cm × 20 cm × 40 cm (l × w × h) and has one transparent wall. The strongboxes are fitted with a drainage system in the bottom and have feed-through options in the bottom and walls for water and/or air hoses, these can also be used as entry for sensor cables.

7.2. Clay slurry mixer

On the previous centrifuge location, a Nauta clay slurry mixer with a capacity of 200 l was used to create clay slurry. Since this mixer slowly started to

show more and more signs of wear, the costs for moving the mixer to the new location should be considerable and the fact that the capacity was lower than desired, it was decided to acquire a new clay mixer.

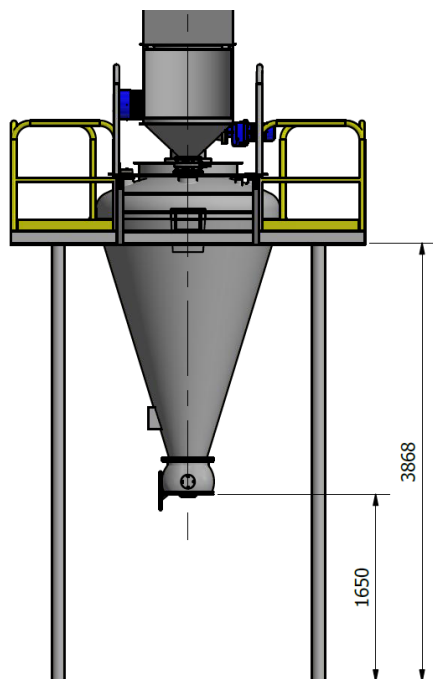


Figure 5. The Heilig 500 l clay mixer.

The new clay mixer is manufactured by Heilig BV from Heerhugowaard (NL) and is delivered completely with the steel construction and platform giving access to the top of the mixer. The mixer has a work volume of 500 l, can handle grains up to 3 mm and can be vacuumed down to 50 mbar(a) in order to create a slurry that is free of air bubbles.

The conical mixer has a sanitary open mixing screw to avoid lump formation while mixing and is provided with a CIP (clean-in-place) system that ensures easy and thorough cleaning after use. The outlet of the mixer on the bottom is provided with a ball valve and a flange of 125 cm diameter. Below this flange, a table with a hydraulic jack can be placed. A clay consolidation cell will be placed on top of this table. The hydraulic jack function pushes the consolidation cell firmly to the flange ensuring an airtight connection. After this, the consolidation cell will be vacuumed to the same pressure level as inside the clay mixer. In this way the air free slurry from the clay mixer will flow air free into the consolidation cell when the ball valve is opened. Then the consolidation cell can slowly be brought to atmospheric pressure again and installed into the consolidation frame.

7.3. Consolidation frame

To consolidate the clay slurries from the clay mixer an Actidyn soil consolidation frame was acquired. This frame consists of a highly reinforced and stiff frame, a hydraulic actuator with a stroke of 1.5 m, a hydraulic power supply up to 15 MPa and a control system. The frame can be used for uniform consolidation or a depth variable consolidation based on the hydraulic gradient method.

During consolidation, parameters such as pressure, flow, temperature, are independently controlled and monitored. The control system also incorporates safety circuitry that are essential to the safe operation of the system. After the user has programmed the desired consolidation path, the system operates fully automatic until consolidation is finished.

Besides the option of using this consolidation frame, it is also possible to consolidate samples during flight using the increased g-force of the centrifuge.

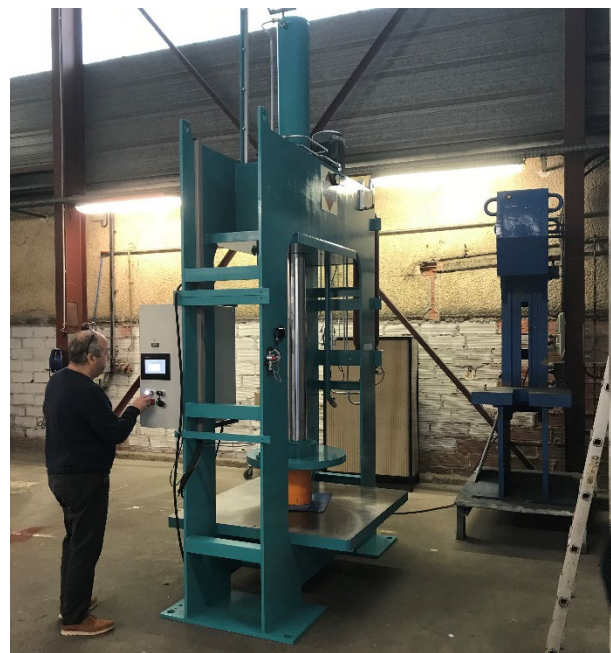


Figure 6. The Actidyn consolidation frame under test.

7.4. Additional equipment

For the centrifuge experiments a wide array of additional equipment is available. Several hydraulic 50 kN hydraulic actuators with strokes of 10 cm up to 70 cm, hydraulic and electric pumps, pneumatic and electric valves and penetrometers in several diameters, lengths and fitted with or without T-bar and/or pore pressure transducers. Besides this an extensive range of sensors is available such as soil pressure transducers, displacement sensors (LVDT and laser), temperature sensors and force transducers.

8 ACKNOWLEDGEMENTS

The realization of the new geotechnical centrifuge is made possible with funding from the Dutch Ministry of Economic Affairs and Deltares. The effort of the management and the Department of Real Estate & Construction Matters of Deltares, the members of the Centrifuge Construction Team and the perseverance and enthusiastic commitment of all the people involved in this, is gratefully acknowledged.

9 REFERENCES

Derx, F., Merliot, E., Cottineau, L.M., Garnier J. 1998. On-board remote-controlled centrifuge robot. *Centrifuge* **98**, pp. 97–102.

Gaudin, C., O'Loughlin, C.D., Breen, J. 2018. A new 240 g-tonne geotechnical centrifuge at the University of Western Australia. *In* Proceedings of the International Conference on Physical Modelling in Geotechnics, London, UK, 17–20 July 2018. Taylor & Francis Group, London, pp. 501-506.

Kim, D.S., Cho, G.C., Kim, N.R. 2006. Development of KOCED geotechnical centrifuge facility at KAIST. *In* Proceedings of the 9th International Conference on Physical Modelling in Geotechnics, Hong-Kong, pp. 147–150.

A Novel Small-Scale Model Testing Device for Laterally Loaded Piles

Hendrik Sturm¹, Andrea Støren²

¹Norwegian Geotechnical Institute (NGI), Oslo, Norway

²Norconsult, Sandvika, Norway

Corresponding author: Hendrik Sturm (hendrik.sturm@ngi.no)

ABSTRACT: In 2014, NGI and BP America Inc. developed and built a novel model testing device for measuring the response of cyclic lateral loaded piles. Objective of this device is to assess site-specific cyclic p-y backbone curves on intact soil specimens under in-situ stress and density conditions. Primary application of these curves is in structural fatigue analysis. For that purpose, the model pile is subjected to sequences with symmetric cyclic displacement amplitudes, where the load level is well below the pile capacity limit. The performance of the p-y apparatus, as the device is called, has been demonstrated by means of an extensive testing program on different soil types. The results were compared with centrifuge test data. It was found that the measurements made in the p-y apparatus agreed very well with both the centrifuge test results and the numerical framework, which was proposed some years prior to the development of the device. Despite the simplicity of the cyclic load history used in these tests, the actuation system is capable to apply more complex cyclic load histories allowing both asymmetric loading, force-controlled testing, and even random load histories. This enables to study the pile response under general monotonic and cyclic loading. An important design aspect, in particular for renewable offshore energy structures, is the Serviceability Limit State (SLS). The general suitability of the p-y apparatus for that application case was investigated recently and the plausibility of the measurement was checked. This article introduces this novel model testing device, shows the performance for its original purpose, and presents preliminary results of the recently conducted more complex cyclic load histories.

Keywords: 1G Pile Model Testing; Cyclic P-Y Curves; Fatigue; Serviceability.

1 INTRODUCTION

Soil structure interaction has become in the recent years increasingly important in offshore geotechnical engineering, particularly with the rise of offshore wind energy turbines. But also, the development of very deep and remote oil and gas reservoirs demands more advanced design approaches to reduce the risk of failures.

Foundation capacity requires information of only the soil strength, while strains are only relevant for compatibility reasons at failure of the soil body. However, soil-structure interaction design requires information of the complete stress-strain response of the soil. Even more complicated is the description of the soil response under cyclic loading, as it depends on the load amplitude and mean value, load frequency, duration and drainage conditions.

In order to cope with this complexity in the design, dedicated engineering models are required. One such model has been developed by BP for the structural well conductor fatigue design (Zakeri et al., 2019). The model proposes a framework for cyclic p-y backbone curves. The basic assumption is the existence of a cyclic attractor of the secant stiffness for a given symmetric and constant displacement amplitude. A pile segment subjected to a constant cyclic displacement amplitude Δy will

respond with a cyclic resistance amplitude Δp , which gradually decreases with number of applied load cycles N . The existence of the cyclic attractor postulates that Δp will approach a constant value; denoted in the BP design framework *steady-state*. At steady state can be calculated a secant stiffness viz.

$$K_{Sec,ss} = \frac{\Delta p}{\Delta y} \quad (1)$$

A cyclic p-y backbone curve can be constructed from the secant stiffness values for different displacement amplitudes.

This framework has been developed based on a series of centrifuge tests. The results of these tests were normalized with the respective static shear strength of the intact specimen. This allows to apply the framework to all type of soils, given that the static shear strength is known. However, since only a limited number of soil types have been tested so far, an application in real projects requires laboratory testing to increase confidence in the framework. For that purpose, NGI developed the so-called p-y apparatus shown in Figure 1 (Zakeri et al., 2017).

2 THE P-Y APPARATUS AND TYPICAL TEST RESULTS

The underlying idea of this apparatus is to assess the steady state secant stiffness on intact specimens taken with standard piston samplers. That means that the soil specimen has an outside diameter of 68mm and a length of 100mm or 200mm, respectively. The specimen is fully confined by means of a rigid cylinder and two special designed endcaps. Through these endcaps is installed a model pile with $D=10\text{mm}$ in diameter, which goes through the whole specimen.

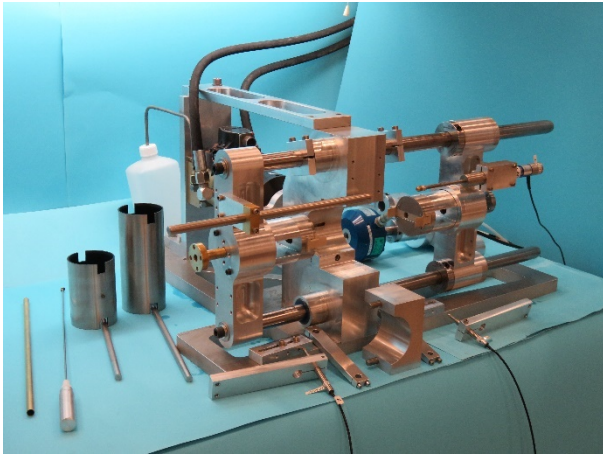


Figure 1. *p-y* apparatus including 2 different sized specimen cylinders and model piles.

After installation of the model pile, the specimen is consolidated to in-situ stress level. At end of the consolidation, the model pile will be attached to a loading frame and a hydraulic actuator applies packages with constant cyclic displacement amplitudes. The number of cycles per package depends on the soil type and behaviour, but typically ranges between 500 and 2500. The cyclic displacement amplitude y/D varies between 0.125% and 8%, where the amplitude is doubled from package to package. Typical loading frequencies are between 0.1Hz and 1Hz.

Although only the response in the last cycle is required in the BP design framework, the complete development of the secant stiffness with number of cycles is reported. In addition, the corresponding hysteretic damping is evaluated and reported, which is of importance for structural fatigue damage analysis. Example results of the normalized steady-state secant stiffness and corresponding damping ratio are presented on Figure 2 and Figure 3.

Figure 2 shows in addition two trend lines based on the BP design framework, which was established based on best fit of centrifuge data.

The measured secant stiffness values agree well with the trend line, but seem to underestimate the

stiffness for low displacement amplitudes. However, a closer inspection of the trend lines in this area reveal an unrealistic shape of the *p-y* curve where the pressure does not start from zero at zero displacement, but rather approaches a constant value. The measurements, however, predict a consistent and realistic *p-y* curve.

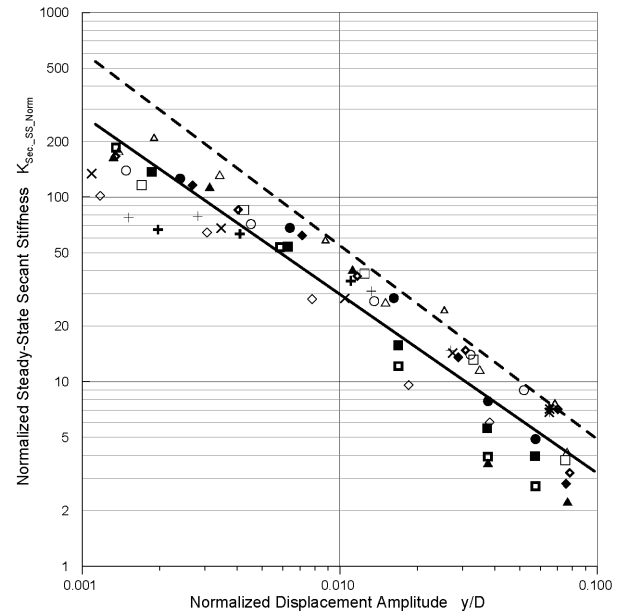


Figure 2. Normalized secant stiffness and trendlines developed based on a comprehensive series of centrifuge tests (caption shown in Figure 3)

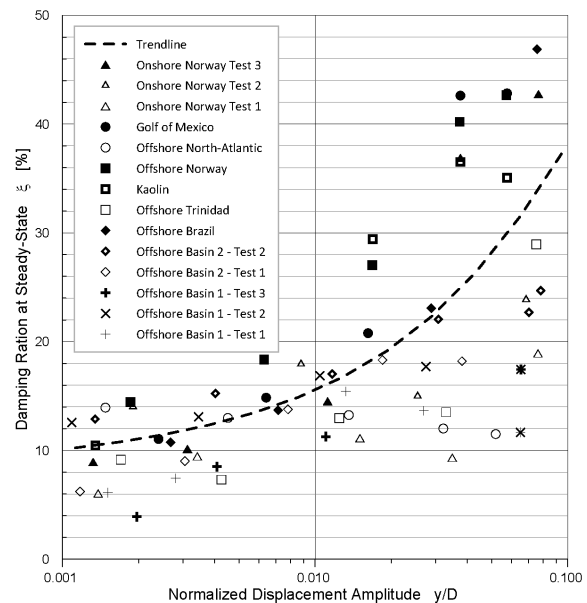


Figure 3. Equivalent damping ratio at steady state and trendline based on the shown data points

The damping values show a plausible trend, but with a large scatter. The dashed line in Figure 3 represents a best fit with a large standard deviation for increasing cyclic displacement amplitudes.

3 SERVICEABILITY TESTING

The p-y apparatus uses an MTS hydraulic actuation system for applying monotonic and cyclic loading. This opens the possibility to test the pile response to generalized cyclic loading. Of particular interest for designers is the foundation serviceability, that means the accumulated displacement due to repeated cyclic loading.

Table 1. Index properties of Kaolin

Parameter	Unit	Value
Specific density	ρ_s [g/cm ³]	2.59
Clay content	[%]	55.7
Grain size	D ₆₀ [mm]	0.003
Plastic limit	w _P [%]	28
Liquid limit	w _L [%]	56.1
Plasticity index	I _P [%]	28.1

In 2018/19, a series of tests has been conducted to study the general suitability of the p-y apparatus for the application to serviceability problems. For that purpose, the first-time load-controlled tests were performed. To ensure repeatability and consistency of the tests, two bins with re-constituted Kaolin clay were prepared. The properties are summarized in Table 1. After consolidation to 80kPa, the blocks of Kaolin were divided into 9 square samples (see Figure 4). Only one specimen can be obtained from each sample.

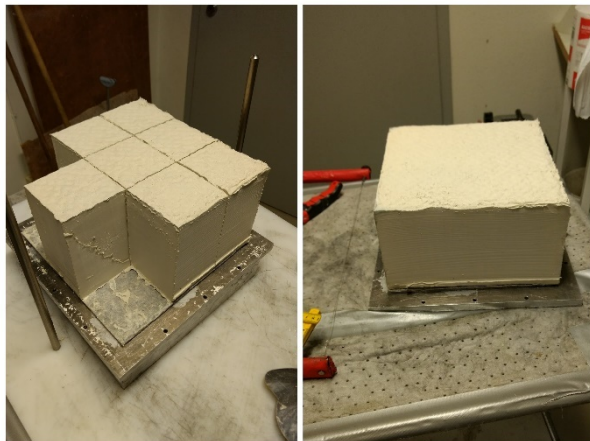


Figure 4. Reconstituted blocks of Kaolin for p-y testing

The sample was then trimmed to fit into the specimen cylinder and built in into the p-y apparatus. After installation of the model pile, the specimen was consolidated in three steps to a final consolidation pressure of 120kPa. The DSS shear strength of this material is approximately 25.5kPa.

The series comprises tests with different cyclic load histories, all performed at the same material with the same initial stress and density state. The tests were conducted such that the specimen height was kept constant during cyclic loading. Due to constructional reasons, the specimen is not water tight and could drain through the endcaps. A back pressure cannot be applied.

4 TEST RESULTS

Figure 5 shows a test with a constant average load of 40kPa and 5 packages with cyclic load amplitudes of 40kPa, 60kPa, 80kPa, 60kPa and 40kPa. 500 cycles per package were applied except for the largest amplitude where 1000 cycles were applied. The loading frequency was 0.25Hz.

It can be seen, that the accumulated average displacement increases continuously, and the accumulation rate becomes larger for larger load amplitudes. When decreasing the load amplitude again, the accumulation rate also decreases and is eventually smaller than in the corresponding package with same load amplitude applied prior to the peak phase.

The cyclic displacement amplitude is small(er) and almost constant for the two first load packages but increases continuously in the third package with the 80kPa load cycles. The specimen shows a softening behaviour. When decreasing the load amplitude again, the corresponding displacement amplitude becomes continuously smaller. The specimen shows a hardening or setup behaviour and seems to regain resistance. But the cyclic amplitude remains larger than measured in the corresponding package prior to the peak phase.

A second test is shown on Figure 6 where a constant cyclic amplitude of 40kPa is applied but the average load is varied in 8 packages from 40kPa, 80kPa, 40kPa, 0kPa, -40kPa, -80kPa, -40kPa and 0kPa. Again, 500 cycles per package with a frequency of 0.25Hz was applied.

It can be seen, that the accumulated average displacement follows the average load and seems to be completely reversible when changing the loading direction. As for Test 4, shown on Figure 5, the accumulation rate is a function of the load intensity.

The cyclic displacement amplitude, however, seems to be almost constant and independent on the average load. An exception are the packages without an average load (i.e. $p_{av}=0kPa$), where significant larger displacement amplitudes are observed.

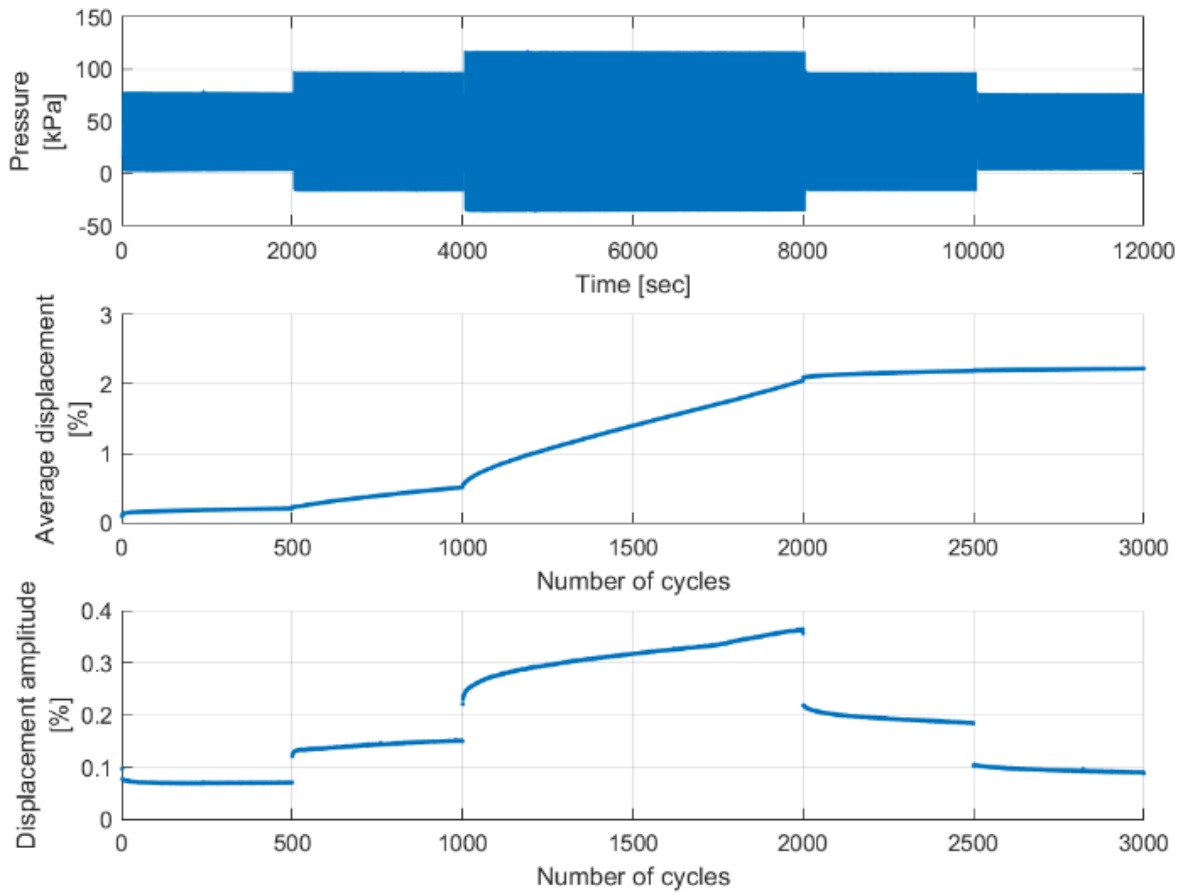


Figure 5. Test 4 with constant average and variable cyclic loading

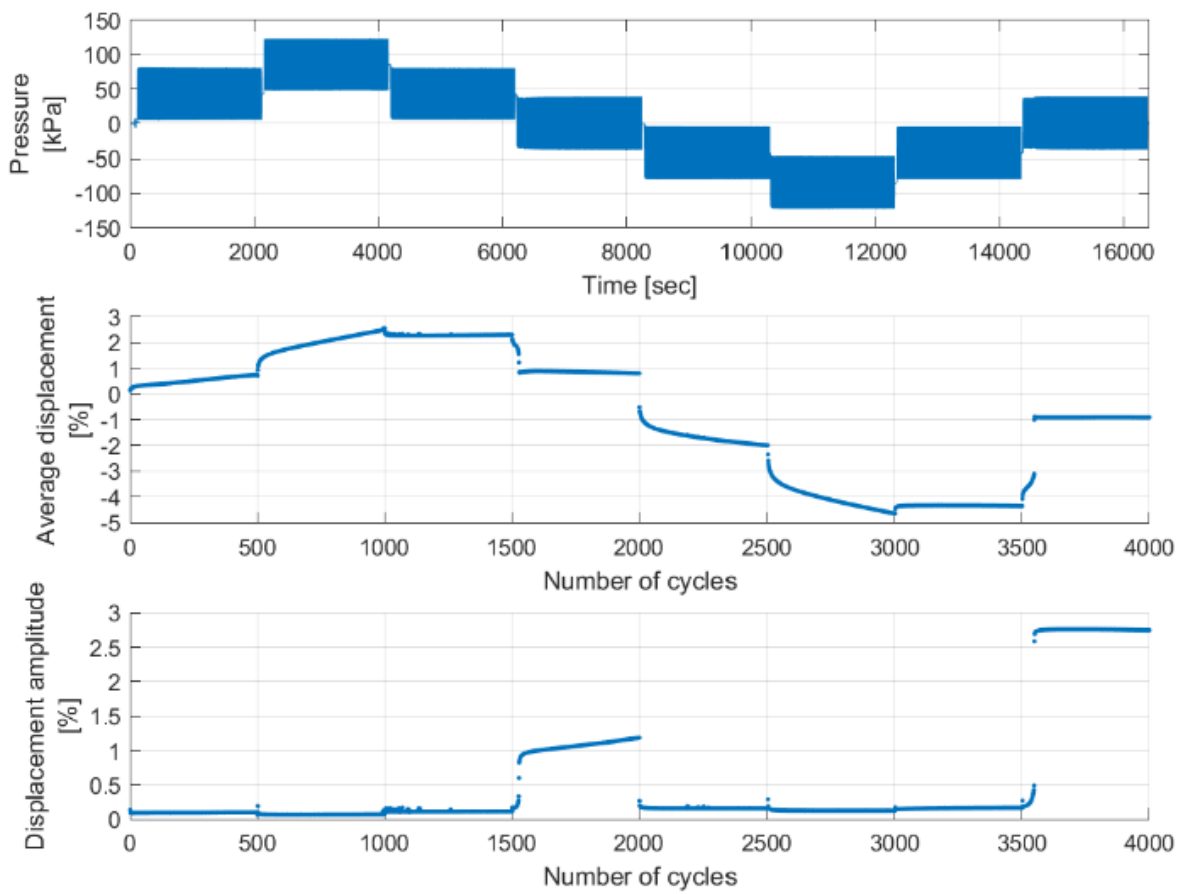


Figure 6. Test 5 with variable average and constant cyclic loading

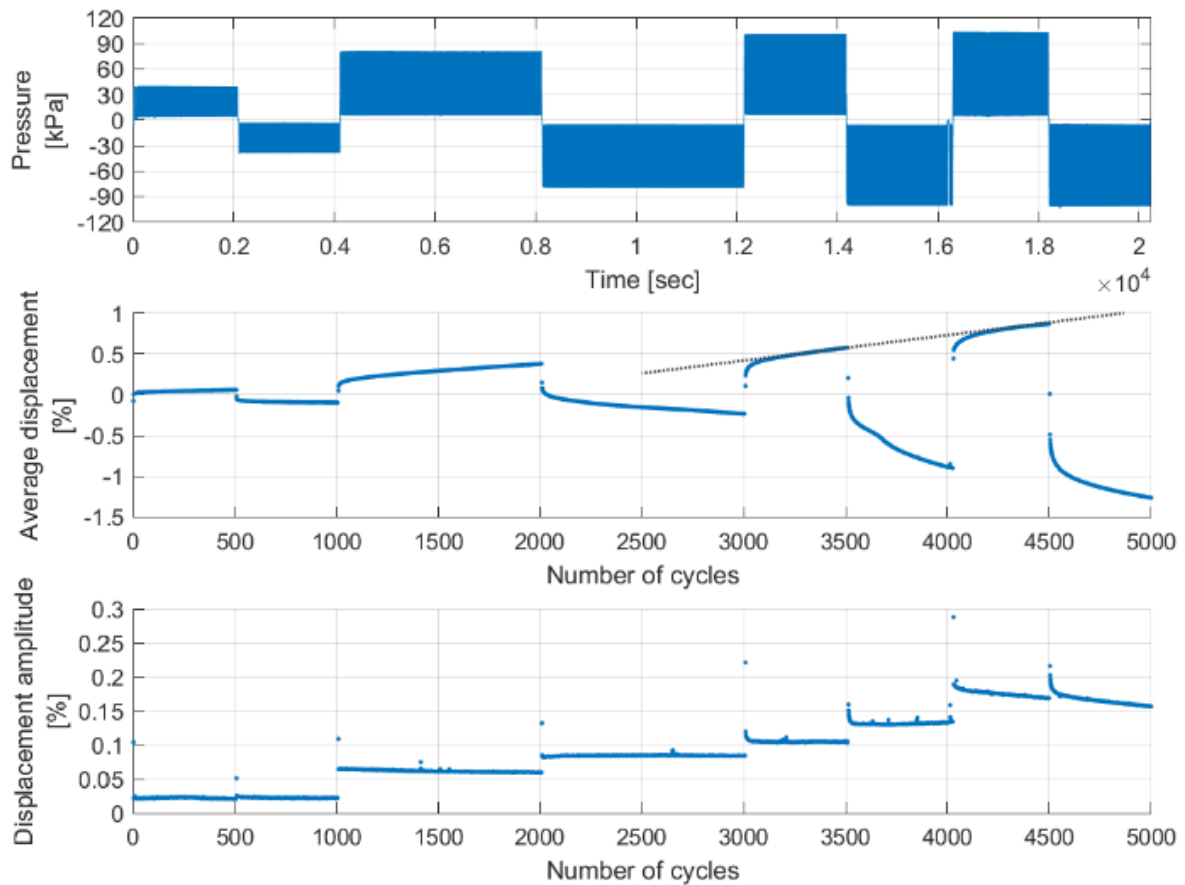


Figure 7. Test 2 with constant cyclic to average load ratio but alternating direction of average load and increasing cyclic loading

The last test presented is Test 2 shown on Figure 7. Like test 5 shown on Figure 6, the direction of the average load was changed. In addition, though, also the value of both the average and the cyclic amplitude changed such that the ratio between cyclic and average load was equal 1 or -1, respectively. The number of load cycles varied between 500 and 1000, all at a frequency of 0.25Hz.

Like for the other two examples, an increase of the average accumulated displacement can be seen for increasing load intensity. Furthermore, the average displacement seems to follow the average load level and even changes the direction accordingly. However, after each reversal, the specimen seems to be "softer", following the previous tendencies independent of the reversal. On Figure 7 is shown a trend line over the fourth and second last package. The reversal in the third last package seems to not affect the accumulation rate nor the absolute value. In fact, it seems that the direction did not matter, and it may be expected that the accumulation rate and absolute value of the average displacement would be the same in the second last package if no load reversal would have been made in the third last package.

Also, the cyclic displacement amplitude gets larger for increasing load amplitude. However, there seems to be a tendency for an increased cyclic

resistance, since the amplitude slightly decreases within each package at constant cyclic load amplitudes.

5 DISCUSSION

The three examples presented in the previous section show, that plausible test results can be obtained using the p-y apparatus. Comparing the results qualitatively with laboratory tests (Wichtmann, 2016) and numerical models (Niemunis et al., 2005), reveal a quite consistent behaviour. The cyclic flow rule proposed by Niemunis et al. (2005), postulates an increased accumulation rate (i.e. the average strain per load cycle) depending on the cyclic amplitude and the ratio of cyclic to average load. This agrees with the observations in Test 4 and test 5 shown on Figure 5 or Figure 6, respectively.

Very limited literature is found on laboratory or model tests with reversals, which could explain the decrease in accumulated displacements as seen in Test 5 (Figure 5). Also, the setup effects, that means the increase in cyclic resistance during loading, as observed in Test 2 (Figure 6), has not been explicitly reported in the literature. However, setup effects in laboratory tests are known and have been reported by Andersen (1988) at the example of undrained cyclic DSS tests with consolidation

periods between the cyclic load packages. The cyclic resistance increased in each package due to re-consolidation and compaction in the resting periods. Although, the specimen height was kept constant in the p-y apparatus, local consolidation effects are still plausible to happen; the largest pore pressure will be generated around the pile, but due to the high consolidation coefficient of Kaolin clay, it is likely that the pore pressure dissipated radially (and axially through the endplates). Specimens of natural clay tested in the p-y apparatus showed after dismounting a zone around the pile which seemed to have a different water content than the rest of the specimen (Zakeri et al., 2017). Kaolin clay, however, is white and such a zone can hardly be identified.

The soft response in Test 5 at zero average load may indicate a gap around the pile. However, since the displacement amplitude was very small, the observation may be also caused by a highly disturbed zone in the vicinity of the pile. The fact that the amplitude in the last package is almost twice the amplitude of that in the fourth package supports this assumption. Only the soil at the side of the pile to which an average load was applied in the previous packages is softer, whereas the soil at the other side is not significantly affected. When applying an average load also in the opposite direction, the soil at both sides become equally soft, hence the cyclic amplitude in the 8th and last package is almost twice as large.

6 CONCLUSION

The results show the general suitability of the p-y apparatus for serviceability testing. Using reconstituted Kaolin allowed to compare the results. But the drainage coefficient of Kaolin is high, and it is believed that water drained out through the endcaps.

It is planned to perform further tests varying more systematically the cyclic load histories. Furthermore, it is considered to perform the tests under constant axial loading allowing the soil

specimen to consolidate continuously. Such tests are currently conducted, but with focus on the secant stiffness. For that purpose, symmetric cyclic load amplitudes are applied. The first tests showed promising results and agreed qualitatively well with numerical predictions. It is thus expected, that the same configuration can be used for serviceability testing as well.

7 ACKNOWLEDGEMENTS

The authors gratefully acknowledge the support from the *Wave Loads and Soil Support* for Extra-Large Monopiles (WAS-XL) project (NFR grant 268182) and from the reducing cost of offshore wind by integrated structural and geotechnical design 2 (REDWIN 2) project (NFR grant 296511).

8 REFERENCES

- Andersen, K.H., 1988. Properties of soft clay under static and cyclic loading. Presented at the International Conference on Engineering Problems of Regional Soils, Beijing, China, pp. 11–26.
- Niemunis, A., Wichtmann, T., Triantafyllidis, Th., 2005. A high-cycle accumulation model for sand. *Computers and Geotechnics* **32**, 245–263. <https://doi.org/10.1016/j.compgeo.2005.03.002>
- Wichtmann, T., 2016. Soil behaviour under cyclic loading - experimental observations, constitutive description and applications (PhD Thesis).
- Zakeri, A., Sturm, H., Dyvik, R., Jeanjean, P., 2017. Development of novel apparatus to obtain soil resistance–displacement relationship for well conductor fatigue analysis. *Can. Geotech. J.* **54**, 1435–1446. <https://doi.org/10.1139/cgj-2016-0528>
- Zakeri, A., Sturm, H., Jeanjean, P., 2019. Validation and Extension of Soil Response Framework for Fatigue Analysis of Offshore Wells and Piles, in: *Offshore Technology Conference*. Presented at the Offshore Technology Conference, Offshore Technology Conference, Houston, Texas. <https://doi.org/10.4043/29236-MS>

Development of a Hammer to drive monopiles of offshore wind turbines in Centrifuge

Semaan Maatouk¹, Matthieu Blanc¹, Luc Thorel¹

¹*GERS-GMG, Gustave Eiffel University, Nantes, France*

Corresponding author: Semaan Maatouk (Semaan.maatouk@ifsttar.fr)

ABSTRACT: A new in-flight hammer has been especially designed at the Gustave Eiffel University to drive in centrifuge at 100×g a model monopile for offshore wind turbine. The model pile driving device uses an electro-mechanical lift system to drive open ended aluminium piles into saturated dense sand. A recap of centrifuge pile drivers are presented. Then the paper describes the development of a powerful pile driving hammer. At the end, the driving curve of a 5 m diameter prototype pile is presented.

Keywords: Centrifuge; Hammer; Open-Ended Monopile; Offshore Wind Turbine; Sand.

1 INTRODUCTION

Offshore wind farms are gradually beginning to flourish since 1991 to produce clean and renewable energy. In shallow coastal waters, where the seabed is beneath 35 m, monopile supports are to this day the preferred foundation solution for offshore wind turbines. These piles are single large-diameter steel tubes, often installed in dense sands, typically 8 to 10 m in diameter, 30 to 50 m long and weighing up to 1000 tonnes (Byrne and al., 2019).

Monopile foundations are commonly installed using dynamic method so called “Impact pile driving”. Offshore pile driving can last up to several hours depending upon pile dimensions, soil conditions and input energy of the hammer. This process usually involves thousands of hammer blows at the pile head. Each of the three majoring characteristics of hammering, i.e. frequency, ram mass and drop height can be adjusted to accommodate different prototype hammers. A recap of the different in flight hammers developed in centrifuge for driving piles are presented in table 1.

In fact, the increase in the turbines capacity reduces the cost of the renewable energy. Thus, a powerful hammer is necessary to drive large diameter monopile. However, there is still limited

systems that studies the impact driving method installation for large diameter pile (Heins and al., 2018, Fan and al., 2019). Therefore, the present paper describes the development of a new in-flight electro-mechanical hammer with blow energy of 3.2 J to drive in centrifuge at 100×g a model monopile of 50 mm large into a saturated dense sand. Hammer blow count is studied against the penetration depth of the monopile.

2 MATERIALS AND METHODS

2.1. Centrifuge modelling

Centrifuge modelling is used here on small scale models installed in a macro gravity allowing for the replication of stress state occurring with prototype soil. The Gustave Eiffel University’s geotechnical centrifuge (Figure 1) has a radius of 5.5 m and its swinging basket permits the installation of a container with embanked mass of 2000 kg at 100×g.

The test presented is carried out on 1/100 scale model piles at 100 times the earth’s gravity (100×g). In this case, the main scaling laws (Garnier and al. 2007) used to link the full scale to the small scale model are listed in Table 2: for instance $x^* = x^{model}/x^{prototype}$.

Concerning the flow of water it follows the Darcy law. Since diffusion processes take place in

Table 1. Recap of centrifuge pile drivers.

Type of pile driver	g-level	Ram mass (g)	Drop height (mm)	Frequency (Hz)	References
Pneumatic	100	95	62 Double acting hammer	2.5	Nunez, and al., 1988
Pneumatic	100	Max. value : 70	0 – 20 Free fall	0 – 20	De Nicola, and al., 1994
Electro-magnetic	31.2	163.8	0 – 32 Free fall	0.6	Levacher, D. and Cottineau, L.M.1996
Electro-mechanical	50	Max. value : 240	40 – 55 Free fall	35	Van Zeban and al., 2018

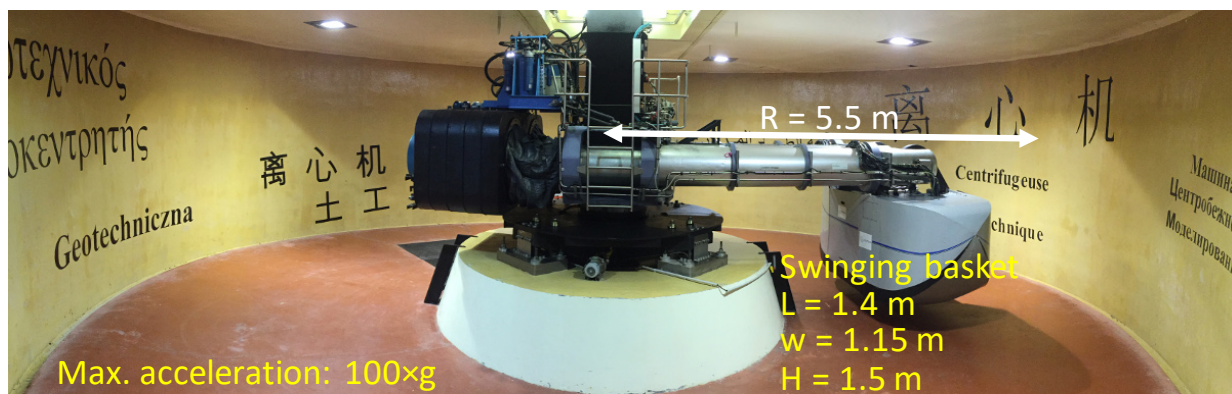


Figure 1. Gustave Eiffel University's geotechnical centrifuge.

Table 2. Scaling law for different parameters (with $N = 100$).

Parameter	Notation	Unit	Scaling factor
Distance	x^*	L	$1/N$
Stress	σ^*	M/LT^2	1
Density	ρ^*	M/L^3	1
Gravity	g^*	L/T^2	N
Deformation	ε^*	-	1
Velocity	v^*	L/T	1
Acceleration	a^*	L/T^2	N
Frequency	f^*	$1/T$	N
Force	F^*	ML/T^2	$1/N^2$
Mass	m^*	M	$1/N^3$
Energy	E^*	ML^2/T^2	$1/N^3$
Blow count	n^*	-	1

centrifuge tests N^2 times faster than at the prototype test, and the hammer is operated at N times the prototype rate, the rate of fluid diffusion should be reduced by a factor of N in the model. This may be achieved either by reducing the particle size of the soil or by using a viscous pore fluid (Kutter B.L. 1994). In contrast, in this study, the soil sample is saturated with water instead of a viscous fluid. Thus, excess of pore water pressure cannot be generated during the hammering process which can induce drained fluid response and therefore changing in the driving curve.

2.2. Model soil

The model soil consists of a poorly graded NE34 Fontainebleau sand (Table 3) with a relative density of 80% obtained by air pluviation into a rectangular strongbox of internal dimensions 1200 mm \times 800 mm \times 360 mm (length \times width \times height).

Once the sand level reaches the top of the strongbox, the sand pluviation is stopped. Then, a raiser with a height of 120 mm (Figure 2(a)) is

placed over the sand sample reconstitution to be saturated by a vertical rising flow through four draining channels located at the bottom part of the strongbox. The attained water table is about 40 mm above the sand surface.

2.3. Model pile

The model pile is a 525 mm (length) by 50 mm (outside diameter) by 2.5 mm (thickness) open-ended circular aluminium tube. This corresponds to a prototype monopile with a length of 52.5 m and an outside diameter of 5 m and a wall thickness of 0.25 m when tested at $100\times g$.

2.4. Hammer description

The experimental set-up presented in Figure 2(a) permits in-flight installation of the monopile by impact driving. The deliver energy chosen to drive the model pile up to an embedment depth of 210 mm is 3.2 J (3200 kJ in prototype scale). This set-up consists of a hollow hydraulic jack fixed over the raiser. An electric motor is placed over the vertical actuator to rotate a rod inside the jack. The end of this rod is attached to a fork which allows the vertical translation of the rotating ram (Figure 2(b)). On this ram, there exist two diametrically opposed cylinder bearings which are rested on a fixed wave-shaped support. It permits the ram free fall until 25 mm to impact driving the pile followed by a ride up of this ram thanks to an electric motor.

During the pile installation, the vertical jack follows the penetrating pile maintaining a specified impact drop height thanks to a laser that detects a target object fixed on the monopile (Figure 2(a)).

The input driving energy into the system can be varied depending on the drop height and on the

Table 3. Characteristics of Fontainebleau NE34 sand (Li and al., 2020).

Sand	d_{60}/d_{10}	d_{50} (μm)	ρ_{d-min} (kg/m^3)	ρ_{d-max} (kg/m^3)
Fontainebleau NE34	1.53	210	1434	1746

ram mass of the hammer. The ram used weighs 160 grams, which cannot be changeable during the pile installation. Therefore, a drop height of 20 mm is chosen to drive the pile with a model blow energy of 3.2 J.

The rotational speed of the motor chosen is 150 round per minute which corresponds to a blow rate of 5 blows per second. By modifying this speed, the number of blows per minute can be adjusted until 33 Hz which corresponds to 20 blows per minute in the prototype.

3 RESULT

On field (at full scale), the most common dynamic method of offshore pile installation is the impact pile driving. Using this installation method, a model monopile is hammered in flight at $100\times g$. Figure 3 shows the cumulative hammer blows recorded during the installation. The ordinate at the origin axis represents the pile penetration under its self-weight at $100\times g$. Thus, the pile penetrated to a depth of around 2.8 m (56% of the pile diameter) in prototype scale before being driven. 4932 blows are necessary to drive the pile to the

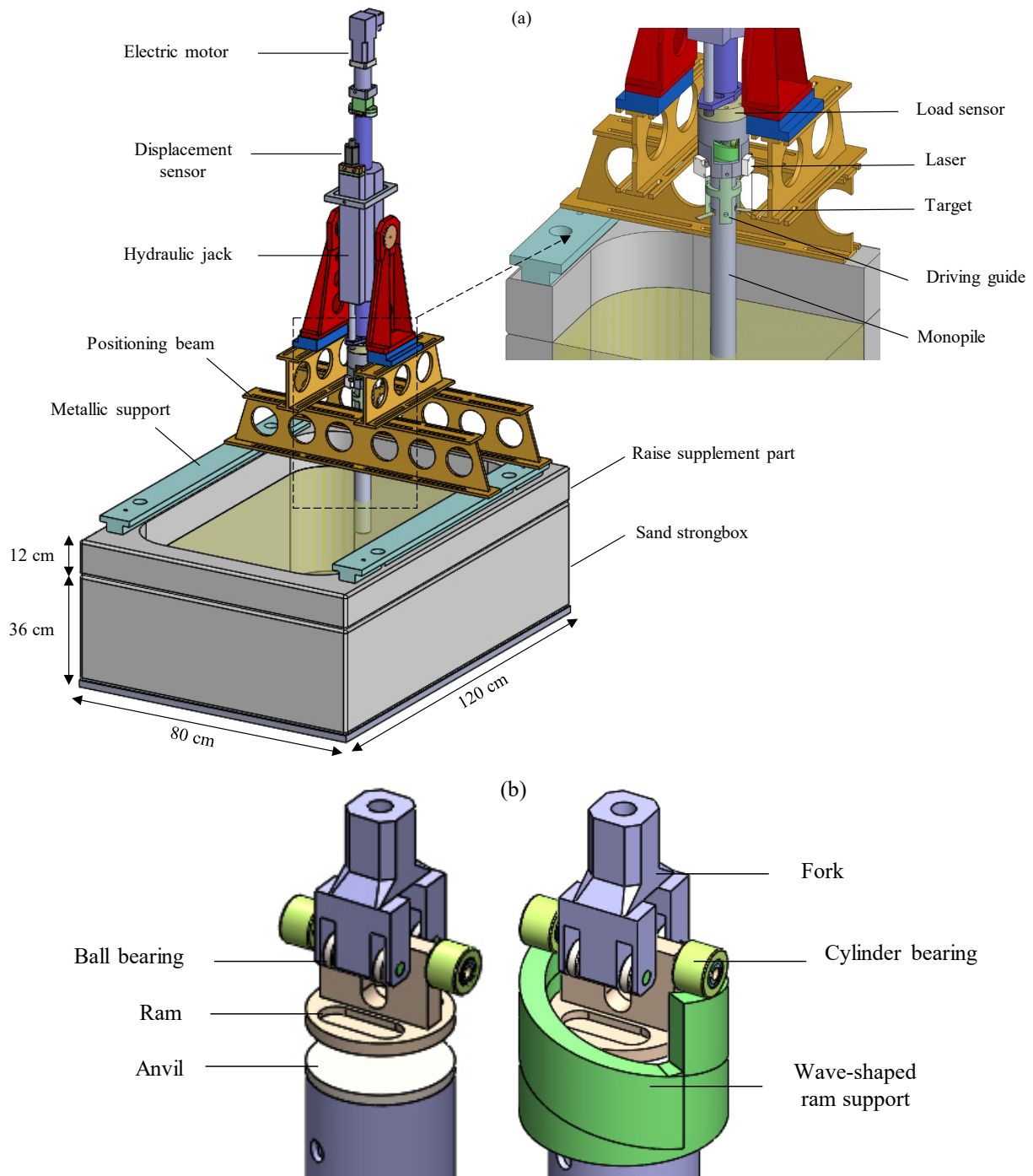


Figure 2. (a) Experimental set-up of pile driving hammer (inner dimensions), (b) Details of the hammering process.

embedment depth of 21 m. As expected, the number of blows required per unit meter penetration increases exponentially with the penetration depth (Figure 4).

4 CONCLUSION

A new in-flight hammer has been designed to drive in centrifuge a 1/100 scale model open-ended monopile of 50 mm diameter. This hammer enables the free fall on 20 mm of a 160 grams ram. Thus, the deliver energy necessary to drive the model monopile into a dense saturated with water

Fontainebleau sand is 3.2 J. Pile driven takes 4932 blows to penetrate the pile to the embedment length of 21 m.

5 PERSPECTIVES

In order to well understand the hammering process, an instrumented monopile with optical Fiber Bragg Grating sensors (Li and al., 2020) and an accelerometer under the anvil would be necessary. Moreover, sand sample should be saturated by viscous fluid in order to achieve “scaling law”. Once the pile is installed, without

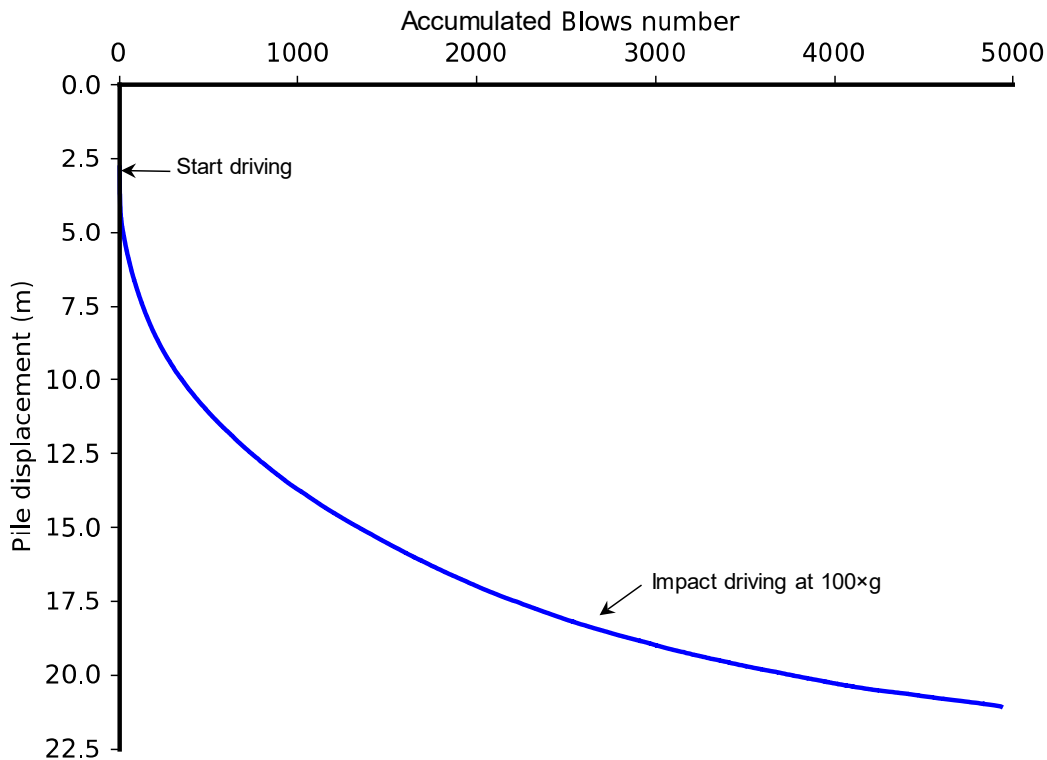


Figure 3. Prototype data driving curve

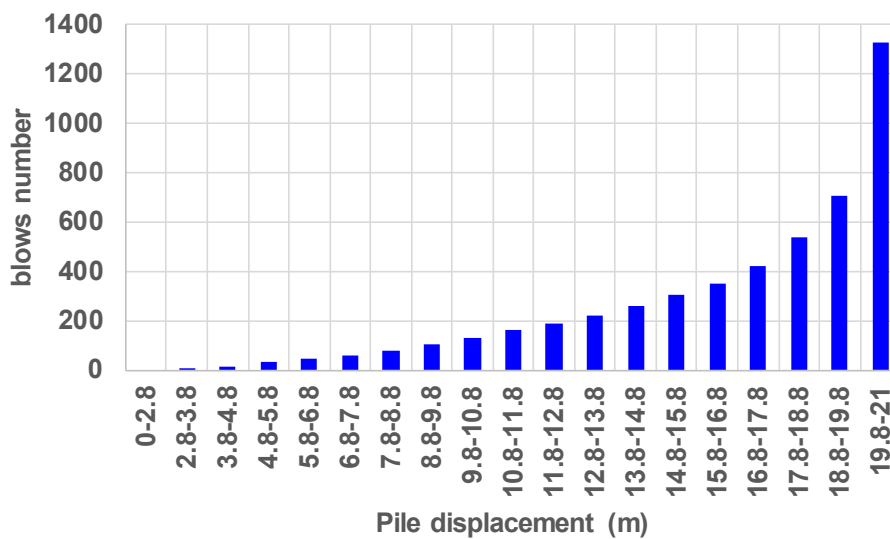


Figure 4. Hammer blow count plotted against the penetration depth

stopping the centrifuge, an electromechanical jack positioned horizontally could be launched to load the pile horizontally either monotonically or cyclically.

6 ACKNOWLEDGEMENTS

The first author wish to thank the Gustave Eiffel University and the Région pays de Loire for his PhD grant.

This work was supported by France Energies Marines and State finance managed by the National Research Agency under the Investments for the Future program bearing the reference SOLCYP+ANR-10-IEED-0006-18.

Assistances and discussions from the technical staff of the centrifuge group are highly acknowledged.

7 REFERENCES

- Byrne, B.W., Burd, H.J., Zdravkovic, L., McAdam, R.A., Taborda, D.M.G., Houlsby, G.T., Jardine, R.J., Martin, C.M., Potts, D.M., Gavin, K.G. 2019. PISA: new design methods for offshore wind turbine monopiles. *Revue Française de Géotechnique*, **158**(3). <https://doi.org/10.1051/geotech/2019009>.
- De Nicola, A. and Randolph, M.F. 1996. Development of a miniature pile driving actuator. *Proceedings Centrifuge 94*, Editor Leung, Lee and Tan, Rotterdam: A.A. Balkema, 473-478.
- Fan, S., Bienen B. and Randolph, M.F. 2019. Centrifuge study on effect of installation method on lateral response of monopiles in sand. *International Journal of physical modelling in Geotechnics*. <https://doi.org/10.1680/jphmg.19.00013>.
- Garnier, J., Gaudin, C., Springman, S.M., Culligan, P.J., Goodings, D., Konig, D., Kutter, B., Phillips, R., Randolph, M.F., Thorel, L. 2007. *Catalogue of scaling laws and similitude questions in geotechnical centrifuge modelling*. *International Journal of physical modelling in Geotechnics*, **17**(3), 1-24.
- Heins, E., Bienen, B., Randolph, M.F., Grabe, J. 2018. Effect of installation method on static and dynamic load test response for piles in sand. *International Journal of physical modelling in Geotechnics*. <https://doi.org/10.1680/jphmg.18.00028>.
- Kutter, B.L. 1994. "Recent advances in centrifuge modelling of seismic shaking," state-of -the-Art Paper. *Proceedings 3rd International Conference on recent advances in Geotechnical Earthquake Engineering and Soil dynamics*, St. Louis, **2**, pp. 927-942.
- Levacher, D., Cottineau, L.M. 1996. Pile driving hammers in centrifuge modelling, 6th *International Conference and Exhibition on Piling and deep foundations*, Bombay, India, 15 – 17 January, 8p.
- Li Z. S., Blanc, M., Thorel, L. 2020. Using FBGS to estimate the horizontal response of a monopile in a geotechnical centrifuge. *International Journal of physical modelling in Geotechnics*. <https://doi.org/10.1680/jphmg.19.00022>.
- Nunez, I.L., Hoadley, P.J., Randolph, M.F., Hullet, J.M. 1998. Driving and tension loading of piles in sand on a centrifuge. *Proceeding Centrifuge 88*, Editor Kimura, Rotterdam: A.A. Balkema, pp. 353-362.
- Van Zeban J.C.B, Azua-Gonzalez C., Alvarez Grima M., Van't Hof C., Askarinejad A., 2018. Design and performance of an electro-mechanical pile driving hammer for geo-centrifuge. *Proceedings of the International Conference on Physical modelling in Geotechnics*, London, UK, **1**, pp. 469-473

Experimental testing and ring polygons for the rolling stock – track infrastructure interaction and subgrade analysis

Alexander Savin¹, Andrey Zaytsev², Alexander Abrashitov², Andrey Sidrakov³, Alexander Gorlov⁴

¹Administration Russian University of Transport, vice-rector for science, Russia

²Track and track facilities Department Russian University of Transport, Russia

³Institute of Track, Construction and Structures of Russian University of Transport, Deputy of Director, Russia

⁴High-speed train moving Department JSC MOSGIPROTRANS, leading engineer, Russia

Corresponding author: Andrey Zaytsev (andrei.zaitsev2010@yandex.ru)

ABSTRACT: This paper presents the calculation and the results of experimental testing of events that compensate for the local subsurface sleepers of the ballast of the railway track and influence of the junction of the rail on lower substructure. The measures were developed with the aim of improving the work to reduce the rate of local subsidence of the ballast prism leading to the appearance of local splashes, which in turn leads to an increase in the probability of failure of the railway structure as a whole. Modelling was carried out on the experimental ring railway track of the Experimental Testing Ring polygon (Sherbinka station). The development of local under-sleeper subsidence of the ballast bed (Kosmin, A and Kosmin, V. 2006) of the railway track from crushed granite, with the formation of splashes and modelling of measures that reduce the rate of development of these processes on the experimental ring railway track of the JSC VNIIZhT (Railway Research Institute) training ground (Sherbinka station). The new tests on the experimental ring are part of the general complex of tests of the ballastless track and its elements (laboratory tests, testing grounds on the ring, operational tests on the operating line). The results of tests on the Experimental ring should be the basis for the continuation of tests on the high-speed test site at speeds up to 400 km / h. This test site will be the first stage of the high-speed highway from Moscow to Kazan and heavy haul operation (freight trains with high axle load). Three tasks solving at this Polygon are presented in this paper.

Keywords: Field Testing; Experimental Polygon Ring; Stone Blowing Technique; Anchors; Ballastless Track.

1 INTRODUCTION

During the railway exploitation, engineers and scientists provided a wide range of researches on the exploitation sections of the railways, especially in the part of rail – wheel interaction, rolling stock – railway track interaction. Approximately, in the same period, the 80-90s years of the XIX century important experiments were performed by Zimmerman on the Eltzas – Lotqaringia railways, by Eng. Stetsevich on the Tambov – Saratov and Baltic railways and Eng. Vasyutinsky on the Warsaw – Wien railway (MIIT Report. 1958, Zaytsev, A. 2015.).

Thus during 1897–1898 an Engineer A.Vasyutinsky did some researches for the permanent way on an experimental site nearby Warsaw: a railway gauge 1435 mm, the rails with weight 31.45 and 38 kg per meters, wooden sleepers with length 2.7 meters and two variants of the ballast prism: from coarse sand in mixture with gravel and rock stones.

Before the Russian Revolution in 1917, the scientific developments and research in the field of railway transport and railway infrastructure were

concentrated in educational institutions, mainly in the Saint-Petersburg and Moscow institutes of railway engineers.

The first branch research center in Russia, the Experimental Institute of Railways, was established by a resolution of the Board of the People's Commissariat of Railways on April 18, 1918. At that time, the country's Railways were acutely concerned about the reconstruction of the traction of rolling stock. To study this issue, the Institute needed to organize a special polygon in the form of a regular circle on an absolutely flat site, for the construction of which a significant territory was required.

A proposal to build a "Special Railway Circle Polygon" for experiments with railway rolling stock and infrastructure was put forward by Alexey Dolinzhev, an employee of the Institute for traction reconstruction, this idea was put into practice in 1932 when creating an Experimental Ring Polygon that was built on the Sherbinka (Butovo) station of the Moscow Railway, the design and construction of which was supervised by Nikolai Belokon' (Stepov, V. and Savin, A. 2017).

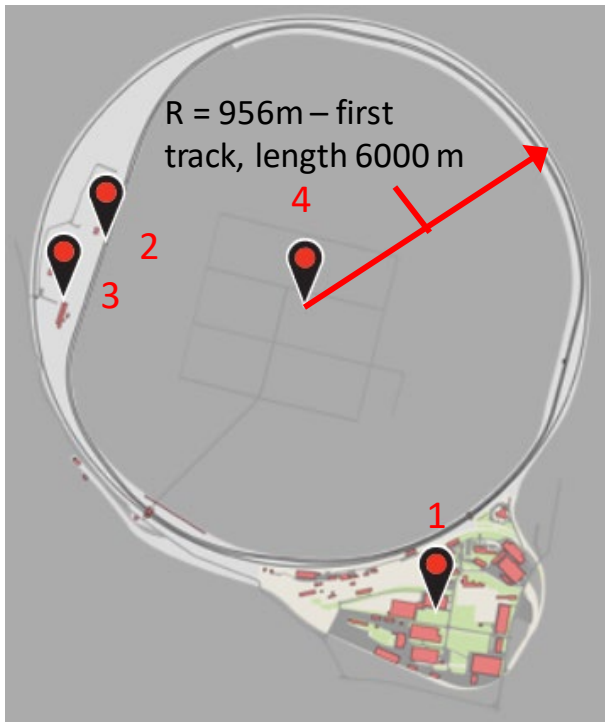


Figure 1. Part of interactive view of the Sherbinka Ring Polygon (1-station track Park 2-ballastless track polygon, 3-contact network laboratory 4-Experimental Ring centre, Interactive Presentation. 2016, Savin, A. and Matveeva, E. 2017, Stepov, V. and Savin, A. 2017).

The Experimental Ring (Figure 1) has: the 1st ring track with a length of 6000 m with a constant curve radius of 956 m without slopes; the 2nd and 3rd ring tracks with a length of 5700 m with curves with a radius of 390 to 1200 m and a longitudinal slope of track - 12‰ (GOST R 57076-2016).

According to the analysis of engineering, geological elements of typical soils and construction materials: on the Experimental ring laid (Figure 2a): 1 - gravel ballast; 2 - embankment soil: dark fine sand, medium density with a high content of crushed stone; 3 – embankment soil: dark fine sand, medium density, with a high content of crushed stone; 4 – embankment soil: sand gravel, moistened, medium density, with grass and gravel; 5 - clay; 6 – loam; 7,8 - clay (Morozova 2013).

This paper presents the results of solving several problems using the capabilities of the test site, depending on their importance for Russian Railways:

- (1) is the development of modern technical solutions to reduce the dynamic impact in the rail joint zone
- (2) is testing the structures of anchors for the subgrade infrastructure at the testing site: including as braces for contact network supports and as structures for strengthening the subgrade slopes,
- (3) is the testing of existing and promising ballastless upper structures for the permanent way of the track for the movement of heavy trains and

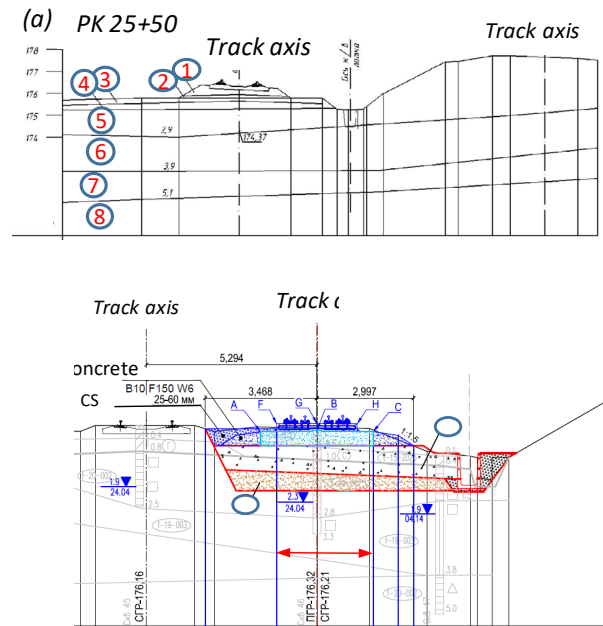


Figure 2. Cross-sections of the railway track a) section of zero place subgrade type (Morozova A. 2013); b) the section with ballastless construction in the tests of A. Savin (1-a mixture of soils treated with polyphilizers; 2 – a crushed stone-gravel-sand mixture)

high-speed traffic (the solution of the last task is not yet completed and is planned to be carried out during large-scale experimental work in 2020).

2 THE PROBLEMS SOLVED AT THE TEST RING POLYGON IN SHCHERBINKA

2.1. Elimination of splashes by stone-blowing technique

The traditional bearing of ballast in the plan and profile tamping violates the established under the sleeper bottom (compacted ballast under the action of dynamic forces the surface of the ballast), resulting in re-packing the ballast under the sleeper granules and the formation of broken and worn particles of the ballast, reducing the drainage properties of under-sleeper ballast foundation and the settlements of the track (Esveld, C. 1989, Peych, Y. 2003.).

The settlements of the track lead to an increase in the number of track linings, which, in turn, leads to a deterioration in the quality of the ballast under the sleeper. In addition, with small lifts, there is a so-called edge or false padding (non-falling of the ballast stone along the edge of the raised 10-15 mm sleeper).

The method of adding ballast under a sleeper was first used before 1910 and became common on the London and North-West Railway (UK), and then it

was quickly extended to other British Railways. Since 1934, the Great southern railway in Ireland has introduced a method of filling the butt end of the sleeper with long-handled shovels.

In the USSR, the souflage was first used in 1936 on crushed stone ballast, in 1937, already on two Railroads souflage was applied, with the pouring of material from butt end of the sleeper.

In the 70s XX century, in the USSR, souflage was prohibited completely for two reasons: the need to the digging up the ends of sleepers, which could lead to a loss of cross-stability of the rail-sleeper grid, and with a rapid increase in the laying of the unjointed track.

Mechanization of the souflage was proposed by John Waters (Waters, J.1981, McMichael, P and McNaughton, A. 2003.), the essence of the new proposal was the introduction of a new rubble "air blowing of stone" (the fascination of the rubble with the flow of air in the working tube), thus the technology of stone-blowing was developed and implemented.

At first stage, the comparative analysis was performed for stone blowing and tamping techniques by 1G physical modelling of recovered ballast. The focus on contamination levels and lateral resistance values and preliminary tests were performed to develop correct physical models (Zaytsev, A., Abrashitov, A., Sydrakov, A. 2018.). The results of the laboratory experiments clearly demonstrated that the ballast adjusted by stone blowing possesses has better mechanical characteristics in comparison to ballast adjusted by tamping. To prove the advantages of the stone blowing technique, experiments are being carried out in the real-world environment.

In parallel, the field tests were carried out on the track alignment technology using stone blowing technic on the 4th section of the Zhilevskaya distance of the Moscow railway (not cycle Polygon). The load capacity of the section is 113 million tons, the passed tonnage is more than 500 million tons, and the set speed of freight trains is 80 km/h. Capital repair has been done five years before the experiments. The construction of the track is an unjointed track on reinforced concrete sleepers, crushed stone ballast, anchoring the rails to the sleepers with an anchored ARS-type of rail fastenings.

As an experiment object, an uncut wet splash was selected in an insulating joint nearby the road crossing. At the rail-joint zone, there was a non-attachment of the sleeper to the ballast at a length of 4 sleepers with subsidence of the second degree. There were sleepers on either side of the joint that

did not fit tightly with the ballast material, two on each side of the joint.

The ballast excavation showed that the bottom bed of the sleepers was strong (damped). Between the sleepers, there were dried traces of a splash of dirty - white pulp that covered the space of eight sleepers: three on the outgoing side of the rail joint and five on the receiving side (Figure 3).



Figure 3. The uncut wet splash, Zhilevo, Moscow Railways

These tests revealed that when using the technology of pneumatic stone blowing on a wet splash, the time between adjacent alignments increased by almost six times. In general, these field tests have shown a possible advantage of straightening with a souflage (stone blowing) over straightening with mechanical and pneumatic tipping of sleepers in the area of small wet splashes in the presence of a strong sleeper bottom bed.

The settlements growth up 20 millimeters for 6 million tons of rolling stock tonnage, and up to 80 percent of the settlements after straightening with pneumatic stone blowing during the first 25 thousand loading cycles (Figure 4).

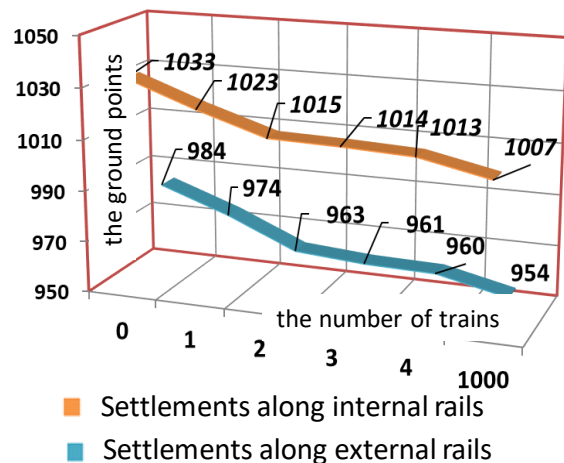


Figure 4. The average rail settlements under train loading after straightening with pneumatic stone blowing at the site

For further research of pneumatic stone blowing technology in autumn of 2018, a special site was prepared on the Experimental Polygon Ring (see Figure 1).

On the curve adjacent to the experimental section, there were numerous wet splashes of up to 8 sleepers at the joints in the plan of the railway track on the section directly, a dry splash was recorded, which manifested itself in the absence of a clear fit of the sleepers to the ballast.

On the curve adjacent to the experimental section, there were numerous wet splashes of up to 8 sleepers in the rail joints in the plan of the railway track, on the experimental section, a dry splash was founded, which manifested itself in the absence of a clear fit of the sleepers to the ballast. The all-gross weight of trains which passed through section was 2 billion 200 million tons.

Pieces of a flat square geogrid measuring 75 by 30 cm with 32 mm mesh were placed under the two sleepers close to the joint on both sides, covered with a plastic mesh with 5 mm mesh (masonry mesh). These geogrids were laid on both sides of the sleepers under the supporting parts of the sleepers (four in total). In the joint numbered 293-294, a mixture of crushed stone and rubber was used as a soufflage (stone blowing) material, in a ratio of 4 to 1, respectively. The rubble was painted blue color (Figure 5).

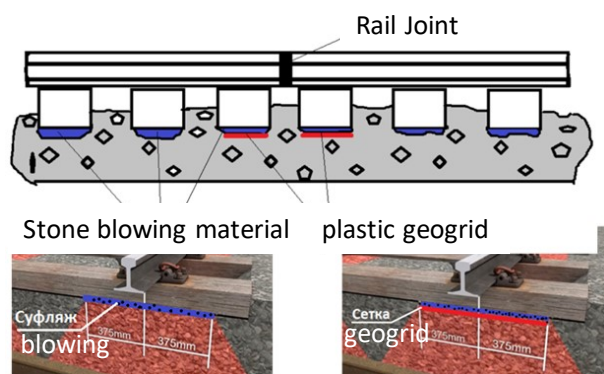


Figure 5. The design scheme of test sites

During the tests, compact blower equipment was used, and the sleeper boxes were partially unearthed and staggared.

According to the results of profile measurements in combination with leveling data and values of rail deflection measurement by flexometers (LVDTs), power longitude profiles of the rail head under the rolling stock were obtained. The most characteristic power profile was obtained on the left thread of the rail joint 293-294 (Figures 6, 7).

The blowing crushed stone of the 5-10 mm fraction was completely embedded in the pores of the ballast particles in the absence of a plastic mesh,

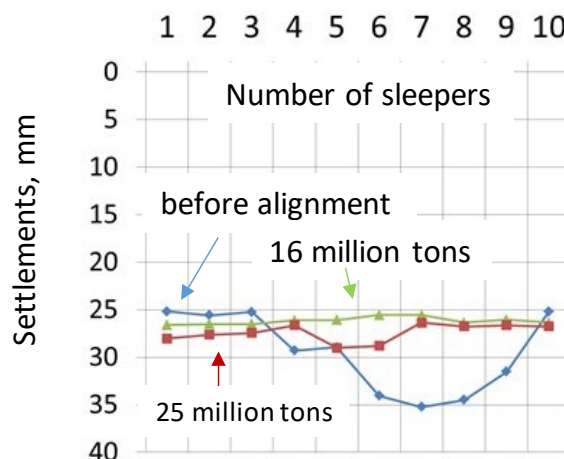


Figure 6. Power profile of the left joint rail line 291-292

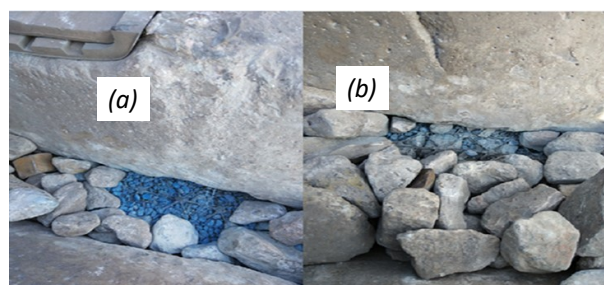


Figure 7. The state of the browning layer after passing 25 million tons of traffic: a) crushed stone with the addition of fine particles b) crushed stone without the addition of rubber crumb

the subsequent use of cut rubber of the 5-8 mm fraction helped prevent the ballast material from being worn under the sleeper for 25 million tons of missed traffic. These Polygon tests have confirmed the high efficiency of the stone blowing technology for straightening the track even in particularly difficult operating conditions with low labor and material costs for carrying out the straightening operation.

The possible application of pneumatic stone blowing technology in some cases include: alignment of a long-used track on ballast, including on dry and wet splashes, preventing the formation of splashes; alignment of the track on overpasses with driving on ballast; alignment of the track in problem areas (crossbars of switches, joints of equalizing spans; alignment of a ballastless tracks.

2.2. Checking the effectiveness of using ground self-opening anchors on Ring Polygon

On the 3rd kilometer of the 3rd track of the Experimental Ring of JSC "VNIIZHT" at the Sherbinka station, tests were conducted of prototypes of "self-opening anchors of the AS-railway series" and sets of equipment for their installation.

A line of self-opening ground anchors, the most popular models are shown in figure 8. These anchors have a load-bearing capacity of up to 12 tons, they use the same anchor rods, as well as nuts with rings or end fittings.

On figure 8b the installation of the anchors is shown. This document describes methods for installing the most common anchor models: both manually and using power equipment. The process of installing anchors to a greater depth differs from the one described only in that longer steel pushers and anchor rods are required.

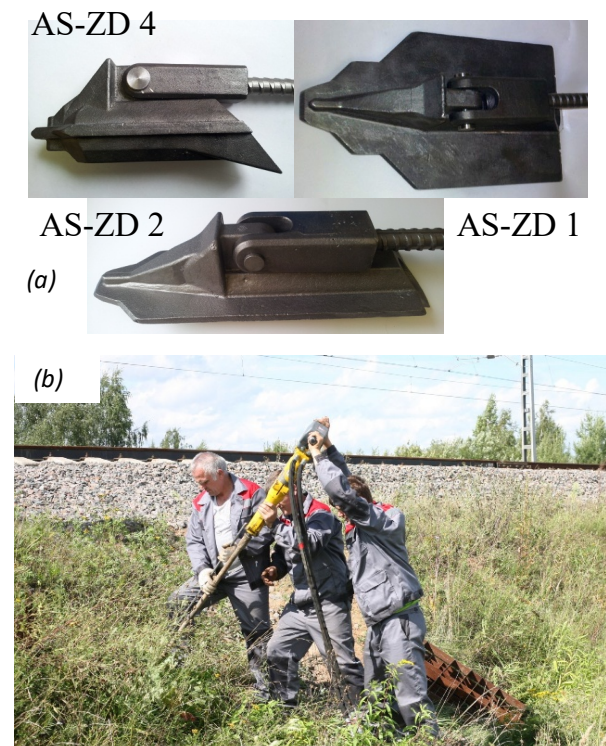


Figure 8. Three types of ground self-opening anchors

The anchors are designed for installation using a hydraulic jackhammer of a weight class of 41 kg. After the anchor is submerged to a depth corresponding to the length of the anchor rod, the installation tool ("steel pusher") is removed. Then the anchor turns from the longitudinal position to the perpendicular, so-called "anchor lock" position.

The direct indication measuring device involving the hydraulic jack, which is equipped with a locking mechanism, allows easy and quick check of the anchor load. If the soil resistance is not hard enough, the operator will immediately determine that additional measures are needed: installing a second anchor, increasing the depth of the dive, or using a larger anchor model.

The placement of the supports and the drawback of the contact network support is shown in Figure 9.

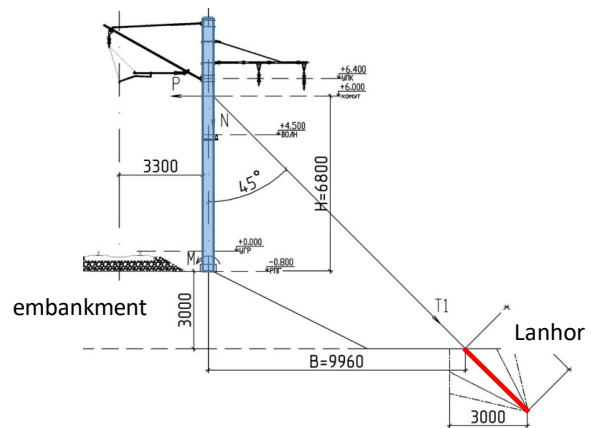


Figure 9. The placement of the anchor to hold the contact network support

Defective support with a bearing capacity of 98 kNm, on an embankment with a size of 3 m. Ground conditions: single-layer soils, loam soft-plastic, watered, with one experimental drawback with an anchor AS-ZHD-2, the size of 360x100 mm, the area of the bearing surface $S=330 \text{ mm}^2$ (Figure 9).

Screw rod with a diameter of 20 mm, length 4 m. The required forces in the cables of the braces (in the traction of the ground anchor) are 11.77 kN for temporary fastening of defective concrete supports.

As a result, the AS-ZHD2 anchor was installed during the installation time of 45 minutes, the depth of the anchor is 3.5 meters.

The anchor was loaded to a maximum load of 15kN, and the working load on the anchor was 13 kN (after holding and stabilizing the indicators). A temporary drawback is fixed on the anchor, the force in which is 2 kN.

Another example will be shown with the placement of an anchor and a plate to protect the slope of the embankment on the polygon. Embankment with a steep slope with a height of 3 meters. Ground conditions: medium-density gravel with sand, used AS-ZHD-4 anchor, size 205x65 mm, bearing surface area $S=110 \text{ mm}^2$. Screw rod with a diameter of 16 mm and a length of 2 m.

As a result of the work, the AS-ZHD4 anchor was installed, with an installation time of 20 minutes, and an anchor depth of 1.5 meters. Testing was performed with an anchor loading up to a maximum load of 13 kN.

Load on the anchor working 11 kN (after exposure and stabilization of indicators). The plate with dimensions 1x1 m is fixed on the anchor (Figure 10).

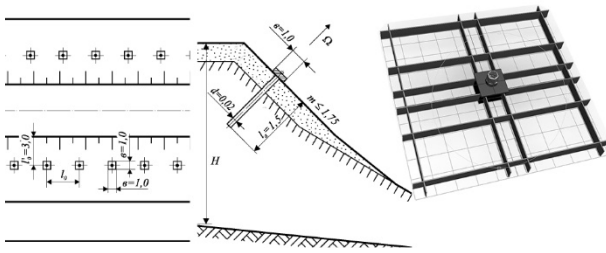


Figure 10. Anchor and plate for the strengthening fill slope

2.3. Using a polygon to check the structures of a ballastless upper structure of a track

Before laying the experimental structures of the ballastless upper structure of the track, special attention was paid to the construction of the base (subgrade), which had the same type of device for all commercially available structures on Russian railway industry: LVT, MaxBögl, Alstom, Tines and was built by a single contractor (Savin, A. 2015, Savin, A. 2017, Ulanov, I. and Gorlov, A. 2019.).

The device of the reinforced layer is standardized on Russian Railways for strengthening, liquid and powder additives are added to the soil mixture (Technical conditions N 2640r of JSC RZD. 2012).

Concentrate number 1 is mixed with water. Concentrate number 2-a mixture of surfactants, cement, lime, slags and other components, added to the soil in the form of a finished powder.

At the base of the four designs of ballastless track (LVT, MaxBögl, Alstom and Tines), arranged on the 2nd path of the Pilot ring, laid politicization reinforced layer and a layer of gravel-sand mixture (SGPS), see Figure 2b.

The thickness of these layers is 0.5 and 0.7 m, respectively. their width is 7 m, the slope of the surface in the cross section is 0.04. The thickness of these layers is 0.5 and 0.7 m, respectively. their width is 7 m, the slope of the surface in the cross section is 0.04.

At the end of strengthening the soil with polyphilizers, the strength for uniaxial compression was determined in the laboratory dry samples, which amounted to 2.08 MPa, water saturation at the same time 1.47 %, from the mass of dry soil. The strength of water-saturated samples was 1.32 MPa.

A new structure is currently being prepared for installation on the ring. When constructing a section of the interface of the roadbed, two protective layers with layer-by-layer compaction are poured with vibro-rollers (RSRS, 2019).

The thickness of the second layer with layer-by-layer compaction with vibratory thickness shall be not less than 1.8 m. The Thickness of the first protective first protective layer should be 0.4 m with ballastless construction of the top structure assuming the presence of a hydraulically bound base layer under the condition of the presence of a hydraulically bound base layer at least 30 cm and 0.7 m at ballast construction of the permanent way.

When dumping of the upper protective layer of the subgrade to form a recess in the form of "wedge" and the ballastless structures form a recess in the form of a "wedge". The length of the interface section is assumed to be 20m.

Then the resulting recess is filled with the material of the protective layer with geogrid reinforcement.

4 CONCLUSION

The results of solving several problems using the capabilities of the test site, depending on their importance: task number (1) is the development of modern technical solutions to reduce the dynamic impact in the rail joint zone.

The possible application of pneumatic stone blowing technology in some cases include: alignment of a long-used track on ballast, including on dry and wet splashes, preventing the formation of splashes; alignment of the track on overpasses with driving on ballast; alignment of the track in problem areas (crossbars of switches, joints of equalizing spans; alignment of a ballastless tracks.

Task number (2) is testing the structures of anchors for the subgrade infrastructure at the testing site: including as braces for contact network supports and as structures for strengthening the subgrade slopes. The anchors are designed for installation using a hydraulic jackhammer of a weight class of 41 kg. After the anchor is submerged to a depth corresponding to the length of the anchor rod, the installation tool ("steel pusher") is removed.

Two examples for current net pole and for reinforcing of subgrade slope are presented.

Task number (3) is the testing of existing and promising ballastless upper structures for the permanent way of the track for the movement of heavy trains and high-speed traffic (the solution of the last task is not yet completed and is planned to be carried out during large-scale experimental work in 2020).

On the Experimental Ring, six types of UAVS from different manufacturers (Rheda, LVT,

MaxBögl, Alstom, Tines) were tested to determine more than 30 parameters (track geometry, track draft, etc.).

The values of deflections and stresses experimentally obtained during heavy traffic with a load of 235 kN on the axis for all types are approximately two times lower than the critical values, 294 which allowed us to conclude that one of the areas of application is cargo traffic (Savin, A. 2017).

Analysis of rainfall intensity paths on the gravel bottom and the intensity of the sediment showed that the sediment of ballastless track occurs 4.8 times slower than the ballast, with the exception of the transitional areas. However, the precipitation is uneven. On a section of 75 m after passing 600 million tons of gross precipitation varies from 2 to 11 mm.

The reason for such roughness slopes is the uneven deformation modulus of the chemically fortified soil and the layer of crushed stone-sand-gravel mixture along the length of the test site.

5 REFERENCES

- Esveld, C. 1989. Track Geometry and Vehicle Reactions. Rail Engineering International Edition. 4: 13.
- GOST R 57076-2016 Field test centres for the railway rolling stock and the infrastructure elements. Technical requirements, Russia, Moscow: Standartinform, 2016 (in Russian). <http://docs.cntd.ru/document/1200139389>
- Interactive Presentation. 2016. Interactive presentation of the Experimental Ring of VNIIZHT JSC 11.11.2016. <http://vniizht.ru/3d/new/>
- Kosmin, A and Kosmin, V. 2006. English-Russian railway dictionary, Marshrut, Moscow, Russia: 960 ISBN 5-89035-084-6
- McMichael, P and McNaughton, A. 2003. The Stoneblower-Delivering the Promise: Development, Testing and Operation of a New Track Maintenance System. TRB Annual Meeting CD-ROM.
- Morozova (Konon), A. 2013 The bearing capacity of the railway track foundation, Candidate of Science Degree Thesis, PGUPS, Saint-Petersburg, Russia: 184.
- MIIT Report. 1958. The report and materials of the experiments on the Oshmyany-Gudogay Belarusian railways. Typescript, Moscow Institute of Transport Engineers (MIIT), Moscow, (in Russian).
- Peych, Y. 2003. Interaction of path elements in the conditions of clogging, ballast dampening, and subluxation of the ground base, Doctor of Science Degree Thesis, Russia, Moscow: 312.
- RSRS, 2019. Temporary railway track of ballast-free construction. track structures on the section of the 3rd track Experimental ring of the Shcherbinka station of the Moscow railway Branch of a LLC "RSRS GmbH Railway Infrastructure projects» "The Railway Tracks» documentation, Russia, Moscow: 28.
- Savin, A. 2015. Combined Method of Ballastless Track Examination. VNIIZhT Bulletin. Railway Research Institute Bulletin. – 2015. – No. 2: 33-36.
- Savin, A. 2017. The conditions for using the ballastless Track, Doctor of Science Degree Thesis, VNIIZT, Moscow, Russia: 444 (in Russian).
- Savin, A. and Matveeva, E. 2017. For the First time in Russia. Experimental ring – 85 years old. Railway engineering (Technika zeleznih dorog). No. 3: 79-86. (in Russian).
- Stepov, V. and Savin, A. 2017. Experimental ring of JSC "VNIIZHT": history, advantages, prospects. Bulletin of the JSC RZD, Moscow. (in Russian).
- Technical conditions N 2640r of JSC RZD. 2012. Technical conditions of for crushed stone-gravel-sand mixture, used for the laying as a sub-ballast protective layers at the railway track infrastructure. Edition 20.12.2012.
- Ulanov, I. and Gorlov, A. 2019. Estimation of structural deformations of the transition section rigidity of the subgrade and artificial structures of the high-speed highway. Eurasian Union of Scientists (ESU). No. 3 (60): 46-55.
- Waters, J. 1981. Pneumatic Ballast Injection a means of adjusting track level. 4th International Rail and Sleeper, conference Adelaide, Australia.
- Zaytsev, A. 2015. Heavy Train Traffic Conditions and Peculiarities. Technology and Art, 6, Vilnius, Litwania, ISSN 2029-400X: 14-19.
- Zaytsev, A., Abrashitov, A., Sydrakov, A. 2018. 1g physical modelling of the stoneblowing technique for the improvement of railway track maintenance Physical Modelling in Geotechnics – McNamara et al. (Eds), Taylor & Francis Group, UK, London, ISBN 978-1-138-34419-8: 203-206.

Pneumatic load frame for long-term in-situ application of moderate tension loads on foundation elements

Jorge Yannie¹, Claes Alén², Jelke Dijkstra²

¹Infrastructure, NCC, Sweden

²Architecture and Civil Engineering, Chalmers University of Technology, Sweden

Corresponding author: Jelke Dijkstra (jelke.dijkstra@chalmers.se)

ABSTRACT: A cost-effective load frame is developed in order to study pile setup or creep of foundations elements under sustained loading in natural soil deposits in a controlled manner. The load frame is specifically designed for long-term in-situ loading of foundation elements in tension up to loads of 500 kN. The novelty is the use of pneumatic springs, actually commercially available pneumatic lifting bags that are demonstrated to function in two modes of operation. In the first constant gas mass application, a control precision of $\pm 10\%$ is easily attainable with few manual adjustments over the course of weeks. In the second regulated application, the addition of an electrical air compressor with accumulator tank increases the precision to $<1\%$ without manual intervention.

Keywords: Load Frame; Pile Load Test; Tension Loads; Long-Term Loading.

1 INTRODUCTION

Field tests are not frequently performed due to the considerable amount of time, work and resources required. In some cases, custom-made load frames need to be developed in order to test the pile response, and sometimes the test equipment is lost with each test. Furthermore, the level of control and consistency is limited, as opposed to physical model tests at 1-g using a calibration chamber (e.g. Brown et al. 2004, Jardine et al. 2009) or at elevated stress levels in the centrifuge (e.g. Nicola et al. 1999, Zhang et al. 2010). Another issue is that in-situ pile load tests cannot be easily generalised, as the results depend on the test site, pile type, testing procedures and experimenter. Nevertheless, field tests are the final step in validation especially when the local soils are difficult to replicate in the laboratory, such as the sensitive clay in the current case.

Common loading methods used in the field are kentledge (dead weight) or complex hydraulic loading systems, (e.g. Fellenius 1972, Karlsrud et al 2014). Dead weight loading requires strict safety measures and large support structures while regulated hydraulic systems are costly and prone to control failure. Furthermore, for reliable studies on pile-setup or pile-creep displacement, the load needs to be applied for long periods of time (Karlsrud et al 2014).

In the current research, a new loading method based on pneumatic lifting bags was developed to overcome some of the aforementioned limitations. This new approach is designed to apply long-term moderate loads (<500 kN) in a robust and simple manner, while being cost-effective and safe. It is a flexible solution that can be easily adopted on

multiple testing sites or for large 1-g test pits, giving repeatability under well controlled procedures. It is based on utilising the potential energy of a (gas) spring system with a very low spring constant so that any additional displacement will only result in a small load variation. This potentially will open up more well controlled pile testing to be performed by research groups with modest means, such as for example universities.

2 PNEUMATIC LIFTING BAGS

The main criterion for long-term testing is to have a constant load within the target accuracy over the test duration. In case the potential energy of a spring system is considered, this translates to having a sufficiently small spring constant so that any change in the displacement range of interest does not significantly change the applied load. Many solutions exist for conventional spring elements with several geometries and materials. For example, typical spring types are compression/tension/torsion coils, flat-rolled, flat-stacked and disc springs. These traditional mechanical springs made out of steel are not easily designed to the specific constant target stiffness over a large displacement range. Hence, the somewhat unconventional solution considered here: the gas (air) spring. The use of gas springs is not new to pile load application, as the controlled combustion of a gas is the standard method used for pile driving, dynamic testing or even quasi-static testing (Rausch et al. 1985, Janes et al. 1991). In the current application, however, the load duration are orders of magnitude longer than in previous studies. Gas springs are available in multiple geometries and materials, however, the

pneumatic lifting bag type provided the most economical solution for the air pressures and contact surface areas considered.

2.1. Configuration

The lifting bags used in this research were sourced from Trelleborg AB (Figure 1). These bags are made of high-quality rubber reinforced with layers of aramid fibre, making them robust and safe to work with in the field. The bags are square shaped with dimensions 658 X 658 X 25 mm³ under deflated state and provide a maximum 380 mm lifting height. These are designed for max 800 kPa (8 bars) of gas pressure and provide different load capacities depending on their contact area. The bags are found to be the optimal solution for the long-term load application based on their simplicity, versatility and low cost. Two bags with model number TLB-32 were used in the current application, with a maximum capacity of 320 kN/bag for the largest contact area.

A frame with a minimum of two bags is required for applying a tension load on the pile head or anchor. The loading capacity of the frame is proportional to the number of bags and the configuration of the bag (i.e. pressure and contact area). The actual configuration used and other options to scale the load are shown in Figure 2. Two bags balance in their common axis (y axis in Figure 2), keeping the frame aligned. However, if the tension loading rod is not centred, the frame can tilt. The latter is not a problem in the case of three or four bags, as these balance in all directions to keep the same internal gas pressure, since all bags are interconnected to the same supply line.

Finally, it is important that the bags are able to redistribute the load on the ground surface without inducing excessive settlements. The latter need is site specific, however, shallow foundation pressures up to 50 kPa did not prove any issues in the trial tests.



Figure 1. Pneumatic lifting bag model TLB32 from Trelleborg AB.

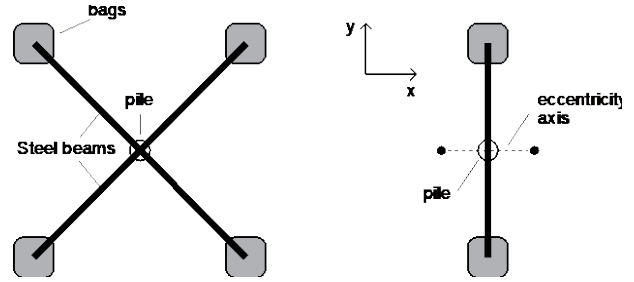


Figure 2. Illustration of possible bag configurations. Four bags gives increased stability against eccentricity as compared to two bags.

2.2. Analytical model

The reaction load from the bags is a function of the lifting height H that governs the contact area A , the applied gas pressure and the gas temperature. Three possible loading scenarios are considered:

- *Constant pressure*: using a constant pressure source, e.g. air compressor with a mechanical regulator valve.
- *Constant gas mass*: the bags are pre-loaded until the target load and subsequently sealed to retain the air mass.
- *Constant load*: using an automatically regulated pressure source that is adjusted as function of the pile head load, e.g. solenoid valves and electrical air compressor.

In the first case, temperature effects will not play any role since the pressure is held constant. Therefore, the bags can be modelled using simple equilibrium equations that are based on volume change only (Equation 1). In the second case, however, the load capacity becomes more complex since changes in volume and temperature can take place simultaneously. For this case, Boyle's law is used to account for volume and temperature changes as shown in Equation 2. The third case will keep the load constant by automatically regulating the pressure in the bags as function of a sensor reading. Therefore, changes in temperature or volume will be compensated for by the control equipment.

The generated load Q depends on the contact length L of the bag and the gas pressure p :

$$Q = \frac{\pi L^2}{4} p \quad (1)$$

Changes in gas pressure caused by volume and/or temperature variations are estimated using Boyle's law:

$$p = \frac{nRT}{V} \quad (2)$$

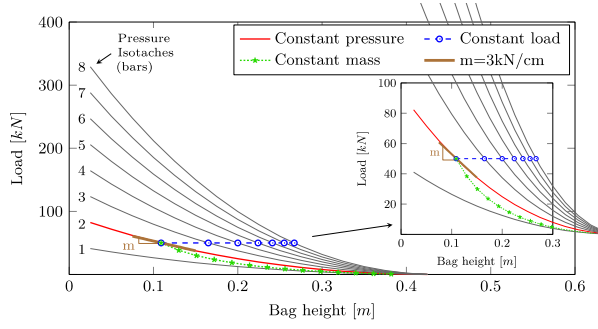


Figure 3. TBL32 load versus displacement curves for different pressure and loading conditions.

where p is the gas pressure, n is the gas mass, R the gas constant, T the gas temperature and V the volume occupied. For a fixed mass of gas with constant temperature T , the volume V occupied by the gas is inversely proportional to the pressure. The gas mass n and the gas constant R are combined in a single constant \underline{k} :

$$p = \frac{kT}{V} \quad (3)$$

These three different scenarios are elaborated in Figure 3 for an initial load of 50 kN using 200 kPa of gas pressure. In all cases, the equilibrium equations are required to calculate the resulting load from the applied gas pressure. These equations require the contact area between the bags and the reaction points, which is approximated by modelling the bag geometry under two conditions, as illustrated in Figure 4. In the first condition, the bags have a complex shape when fully inflated with free boundaries and low gas pressure; with a maximum lifting height based on the bag model. This complex form is approximated using a sphere geometry with a modified radius in order to account for the difference in volume from the true bag shape. In the second condition, the bags are placed between two plywood sheets and compressed, resulting in a shape similar to a merged cylinder and a half-circle ring. Again, this shape is an approximation and the contact surface diameter (cylinder base) is modified to account for the difference in contact from the true bag shape. Finally, the additional assumption of a rigid membrane is required to impose that both geometrical models maintain the same surface area. After making these simplifications the contact surface diameter L is then derived from Equations 4 and 5.

$$A_{sp} = 4\pi R^2 \quad (4)$$

$$A_{sp}^* = \int_0^\pi 2\pi \left(\frac{L}{2} + \frac{H}{2} \sin\alpha \right) \frac{H}{2} d\alpha + \frac{2\pi L^2}{4} \quad (5)$$

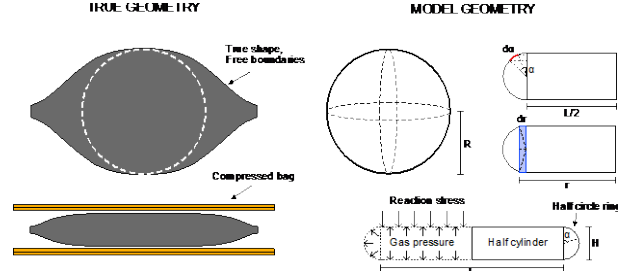


Figure 4. Geometrical model for the lifting bag.

$$L = \sqrt{\frac{\pi^2 H^2}{4} - 2H^2 + 8R^2} - \frac{\pi H}{2} \quad (6)$$

where A_{sp} is the surface area of the sphere representing the free inflated bag, A_{sp}^* is the surface area of the compressed sphere, R is the radius of the sphere, L is the contact surface diameter, H is the maximum lifting height of the bag and α is the angle of the half ring radius to the vertical axis.

The correction factors for the sphere radius $R = \chi R$ and the diameter of the contact surface $L = \eta L$ are calibrated using the load curves provided by the manufacturer. The values for the TLB-32 bag are approximately 1.15 and 1.25, for χ and η respectively, see Figure 5. Having the contact area calculated using L in Equation 6, the volume of the compressed sphere is determined using Equation 7.

$$V = \int_{\frac{L}{2}}^{\frac{L+H}{2}} 4\pi r \sqrt{\left(\frac{H}{2}\right)^2 - \left(r - \frac{L}{2}\right)^2} dr + \frac{\pi H L^2}{4} \quad (7)$$

where V is the volume of the lifting bag when compressed and r is the radius until the side edge. The effect of changes in temperature and height on the bag's behaviour is estimated by combining Boyle's law and Equation 7. First, the constant k is obtained for a given gas pressure, bag volume and gas temperature. Then any changes in temperature and/or volume must be compensated by the gas pressure to keep k constant.

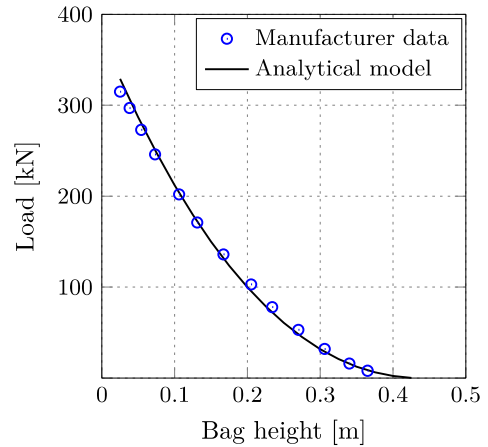


Figure 5. Fit of analytical model against manufacturer data for bag TLB-32.

The basic characteristics of the model pile (or anchor) and relevant soil conditions need to be known in advance in order to design the most appropriate loading system. For the field test reported here, two bags were used per pile in order to have more flexibility in the maximum load and allowable displacement.

3 IMPLEMENTATION

The pneumatic load frame was tested in the field by applying a tension load on 4.20 m long and 0.235 x 0.235 m² square pile elements embedded 13 m below the ground surface. At this depth, the soil comprises of sensitive clays with an undrained shear strength in the range of 30 - 40 kPa leading to a maximum expected short-term failure load of about 138 kN. A tension loading rod fixed at the pile toe guided the load back to surface level. Hence, the shallow load from the reaction frame did not affect the tested pile sections and the pile element was loaded in compression. The latter prevents tension cracks in the concrete.

The load frame consisted of two parallel HEB260 steel beams resting on top of two lifting bags and connected to the tension-loading rod as shown in Figure 6. The bags were located between two double-layered waterproof plywood sheets and rested on top of a 0.30 m thick timber mat. The pressure in the bags pushed the steel beams upward, pulling the pile section and creating a reaction load against the timber mat at the ground surface. Care was taken in centering the tension loading rod and the frame in order to avoid load eccentricities. In the current application a working pressure of 100 - 200 kPa and an initial lifting height of 8 - 10 cm in each bag conservatively leads to up to 150 kN load capacity with a spring stiffness of 3 kN/cm for constant pressure loading (see Figures 3 and 7).

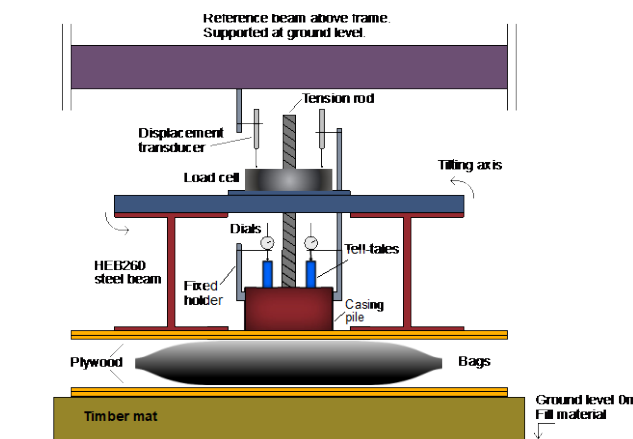


Figure 6. Loading frame components at ground level.

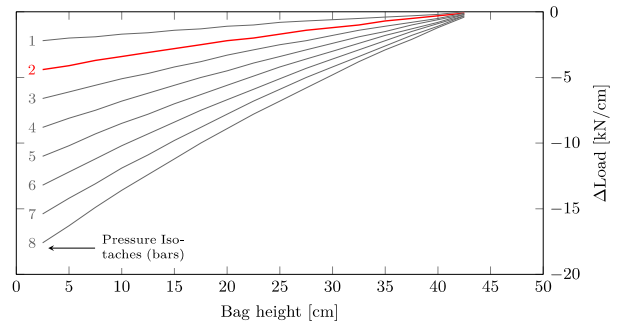


Figure 7. Change in load due to lifting height variations for constant pressure case.

3.1. Constant gas mass

After load application the bags were sealed and left unattended whilst monitoring the load with a load cell (Anyload 363YH; 30 tons) located at the connection joint of the tension loading rod and the HEB beams. This configuration was already satisfactory for quick maintained load testing (where a constant air mass was applied at the beginning of each load step for < 30 min) and for long-term testing (where for an allowed regulation precision of $\pm 10\%$ change in applied Q , manual adjustments were only needed every couple of weeks).

3.2. Constant load

A simple control system using solenoid valves, an electrical air compressor with an accumulator tank of 22 litres and a control computer was developed to obtain more accurate load regulation. The air compressor and accumulator tank were mechanically limited to a constant target pressure. Based on the load cell measurements the control loop implemented in LabView sent a digital signal to a relay that controlled the solenoid valves between the compressor and the lifting bags. The system was designed to adjust any arbitrary load variation resulting from the pile head displacement or changes in ambient temperature. Furthermore, it is protected against power loss since the solenoid valves are of the normally-closed type, with zero differential pressure and very low internal leakage. Consequently, during a potential power interruption, the system temporarily converts to a constant mass system that maintains the load. The total system cost of compressor, two lifting bags, valves, load cell, data acquisition (National instruments NI-cDAQ9178 equipped with two NI9219 and two NI9237 modules) and control computer is below €3000.- at 2017 price level. All parts can be re-used afterwards.

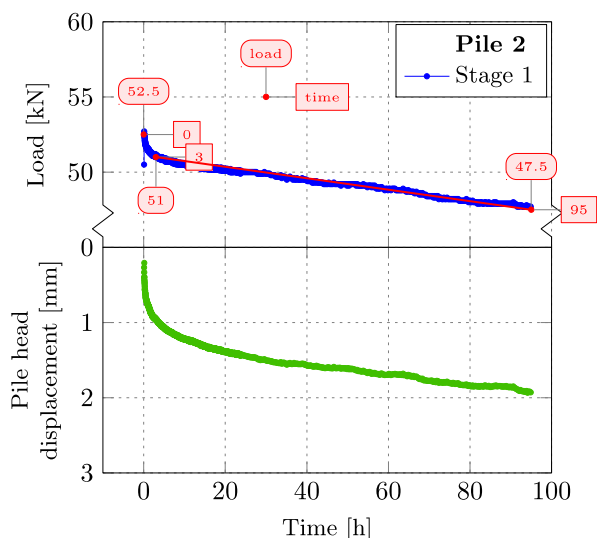


Figure 8. Constant gas mass loading. Stage 1 for test Pile 2.

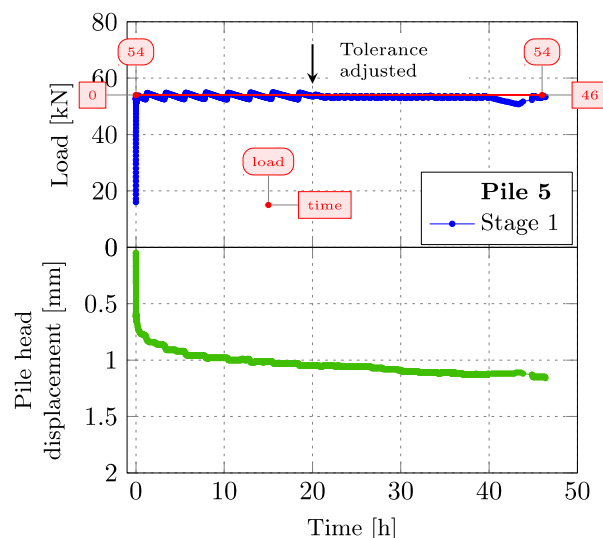


Figure 9. Constant load scenario. Stage 1 for test Pile 5.

4 RESULTS

Two long-term tests were performed to evaluate the lifting bags performance for pile testing. One test used the constant mass (CM) loading scheme while the other utilised the constant load (CL) control. The total duration of the CM and CL test was approximately 3000 hours and 1200 hours respectively. Complete details of these tests can be found in Yannie (2016). Here the most relevant load stages are compared to demonstrate the effectiveness of the loading rig.

For the CM test, the pile was initially loaded to 52.5 kN. The load variation was approximately $\Delta Q = 5$ kN (9.5% of the initial loading) after 100 hours as shown in Figure 8. Figure 9 shows the CL pile test, which was initially loaded to 54 kN. This load was applied for approximately 45 hours before the next load stage. The initial tolerance of the control system allowed a load variation of ± 1 kN, which was further adjusted to ± 0.5 kN by decreasing the allowed tolerances in the control system.

5 CONCLUSIONS

A new non-standard mechanical loading framework has been developed for in-situ testing of pile elements in tension up to 500 kN (4 lifting bags). This setup proves to be robust, cost-effective and easy to adapt to different loading regimes and anticipated pile head displacements. The variation of the applied load in time for the constant mass solution ($\pm 10\% Q$) has been further improved ($< \pm 1\% Q$) with the addition of a simple control system composed of solenoid valves, a portable electric air compressor and an electronic control system.

6 ACKNOWLEDGEMENTS

The kind provision of the test site by PEAB AB and the financial support from Trafikverket in the framework Branch samverkan i Grund (BIG) is greatly acknowledged.

7 REFERENCES

- Brown, M., Anderson, W., & Hyde, A. 2004. Statnamic testing of model piles in a clay calibration chamber. *Int. Journal of Phys. Modelling in Geot.*, **4**(1), 11-24.
- Fellenius, B.H. 1972. Down-drag on piles in clay due to negative skin friction. *Can. Geot. Jnl.*, **9**(4), 323-337.
- Janes, M.C., Horvath, R.C., & Bermingham, P.D. 1991. An innovative dynamic test method for piles. *In Intl. Conf. on recent advances in geotechnical earthquake engineering and soil dynamics*, paper 2.
- Jardine, R.J., Zhu, B., Foray, P., & Dalton, C. P. 2009. Experimental arrangements for investigation of soil stresses developed around a displacement pile. *Soils and foundations*, **49**(5), 661-673.
- Karlsrud, K., Jensen, T.G., Lied, E. K.W., Nowacki, F., & Simonsen, A. S. 2014. Significant ageing effects for axially loaded piles in sand and clay verified by new field load tests. *In Offshore Technology Conference*, Paper number OTC-25197-MS.
- Rausche, F., Goble, G.G., & Likins Jr, G.E. 1985. Dynamic determination of pile capacity. *Journal of Geotechnical Engineering*, **111**(3), 367-383.
- Nicola, A.D., & Randolph, M. F. (1999). Centrifuge modelling of pipe piles in sand under axial loads. *Géotechnique*, **49**(3), 295-318.

Yannie, J. On the long-term behaviour of tension loaded piles in natural soft soils. PhD Thesis Chalmers University of Technology, Gothenburg, Sweden

Zhang, C., White, D., & Randolph, M. (2010). Centrifuge modeling of the cyclic lateral response of a rigid pile in soft clay. *Journal of Geotechnical and Geoenvironmental Engineering*, **137**(7), 717-729.

Chromatic aberration when using white LEDs for PIV: issues and remedies

Mir Amid Hashemi¹, Jingmin Xu¹, Charles M. Heron¹, Alec M. Marshall¹

¹*Department of Civil Engineering, University of Nottingham, UK*

Corresponding author: Mir Amid Hashemi (eazzmh2@nottingham.ac.uk)

ABSTRACT: Particle Image Velocimetry (PIV) is a powerful tool used in geotechnical centrifuge modelling to measure displacement and deformation fields in a 2D plane of a model container. Usually, this plane is a lateral wall of the model held by a relatively thick block of transparent acrylic. Consequently, light passing through the acrylic wall undergoes refraction at an angle that is dependent on the wavelength of the light. The varying levels of refraction, which are of greatest impact near the corners of images where incident angles are largest, can result in images suffering from something similar to a radial blur, which affects image quality and PIV analysis performance. Common practice in centrifuge testing is the use of white light emitting diodes (LEDs), which are a combination of red, green and blue LEDs, hence containing light of a variety of wavelengths. This paper examines the issues related to the use of white LEDs and provides an assessment of PIV performance when using white and monochromatic LEDs. Two experiments were carried out using dry sand; the first with a rigid body movement simulating a no shear strain displacement field, and a second test with sub-surface ground displacements from a greenfield tunnel volume loss test. PIV performance is quantified using the variation of local shear strain in both experiments and a comparison of displacements in the second experiment. Results show a higher level of noise error on the images taken with white LEDs compared with those taken with the monochromatic amber LEDs. It is recommended that LEDs with a single-wavelength colour that closely matches the colour of the medium (i.e. soil) should be used as this will be the wavelength that will be reflected the most by the medium.

Keywords: Particle Image Velocimetry; Chromatic Aberration.

1 INTRODUCTION

Particle Image Velocimetry (PIV) is a widely used tool to measure the displacement field between two images of a deforming object. The geotechnical centrifuge research community has benefitted from the GeoPIV tools described by White et al. (2003), which was later improved by Stanier et al. (2016) under the name GeoPIV-RG.

The methodology used is to allow light to pass through one side of the centrifuge model by means of a transparent material usually made of acrylic. To maintain a rigid boundary condition and keep structural integrity, the thickness of the acrylic wall is usually relatively thick (usually 50 to 100 mm).

A side effect of such thickness is the impact on quality of the image resulting from refraction of light for different wavelengths. It is well known that light refracts when it enters into different media. However, the index of refraction depends on the wavelength of the light. This dependency is known as the dispersion curve. For acrylic (PMMA) the relationship between the refraction index and the wavelength is described by Eq. 1 (Sultanova et al. 2009), with the relationship also presented in Figure 1.

$$n^2 - 1 = \frac{1.1819\lambda^2}{\lambda^2 - 0.011313} \quad (1)$$

where n is the refraction index between air and PMMA acrylic and λ is the wavelength expressed in μm .

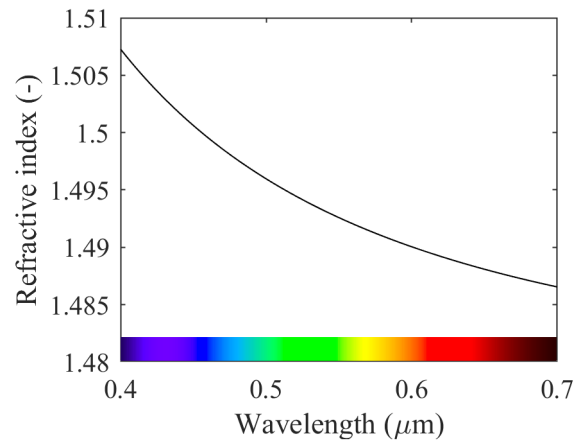


Figure 1. Dispersion curve for PMMA acrylic.

This dispersion affects the quality of the images through the effect of chromatic aberration. An illustration is shown in Figure 2 where an object behind a thick acrylic wall is seen by the camera as if it is in different locations for different colours. The resulting image suffers from an effect similar to radial blur and the sharpness and quality of the soil texture is reduced. Moreover, control markers (especially in the corners) show the same effect and

the accuracy of the detection of their centroid is diminished. An example of such an effect is shown in Figure 3 where the same corner region of an image is compared between lighting with white LEDs (Figure 3a) and monochromatic LEDs (Figure 3b); the image in Figure 3a is visually more blurry than that in Figure 3b.

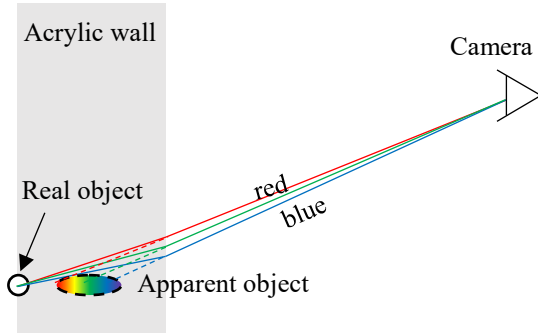


Figure 2. Chromatic aberration effect (exaggerated) of a white object and its appearance on the camera.

To improve the image quality, it is therefore beneficial to use lighting that outputs a sharp spectral response, such as monochromatic LEDs, to decrease chromatic aberration. This paper provides an assessment of the impact of using white LEDs versus monochromatic LEDs on the PIV performance for a relatively standard geotechnical centrifuge test setup.

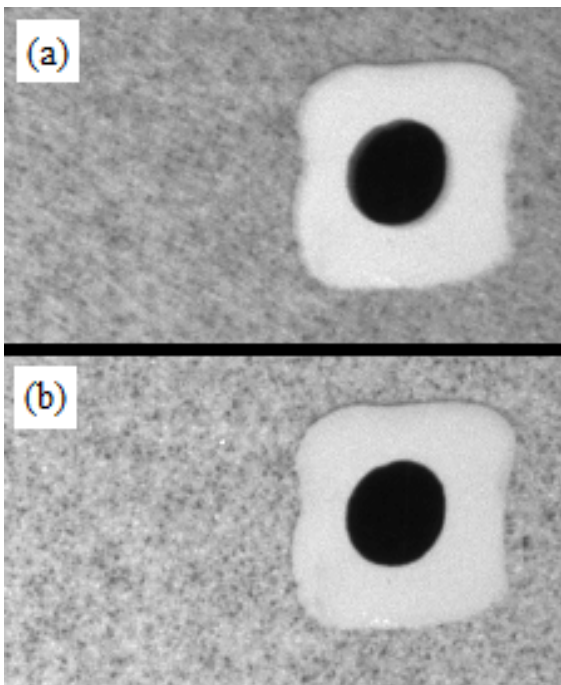


Figure 3. Example of the same picture taken with (a) white LEDs, and (b) monochromatic amber LEDs.

2 METHODOLOGY

Two series of tests were carried out. The first test involved a rigid body movement of a textured plate, whereas the second test included a typical greenfield tunnelling volume loss scenario, both of which were carried out at 1g (i.e. not in the centrifuge).

A 100mm thick acrylic wall was used for both tests. The camera was placed perpendicular to the wall at a distance of 200mm. The camera was a Teledyne DALSA Nano M4020 with a resolution of 4112 x 3008 and a Tamron 1.1" 8mm F1.8 lens. The acrylic wall coordinate system was fixed using control markers (black dots over white squares; see Figure 4), with control marker locations determined using a sheet of photogrammetric targets. The images were saved in the lossless TIFF format.

For both experiments, PIV analyses were carried out on specific areas using an in-house MATLAB code based on Ncorr (Blaber et al. 2015) that uses the inverse compositional Gauss-Newton method for subpixel correlation similar to GeoPIV-RG (Stanier et al. 2016). The analyses used patches measuring 41×41 pixels and spaced 10 pixels apart both horizontally and vertically.

3 RIGID BODY MOVEMENT

The first experiment was made using fine sand (Leighton Buzzard Fraction E sand with an average grains size of $d_{50} = 0.122\text{mm}$) glued on an aluminium plate. The plate was placed against the acrylic wall and moved using a sub-micron precision actuator. The plate was moved in a rectangular pattern, as shown in Figure 4, starting from the bottom right, moving anti-clockwise, with 20 steps (images) taken at the locations indicated by an '*' in Figure 4 and detailed in Table 1, with the coordinate system indicated in Figure 4.

For this study, the main region of interest is where the effects of chromatic aberration are prevalent (near the outer edges of the image), hence the area denoted by the dashed white line in Figure 4 was considered.

Since the plate moves as a rigid body, it does not undergo deformation. Any deviation from zero deformation comes from measurement errors and is a good indicator for quantifying the quality of the PIV analysis.

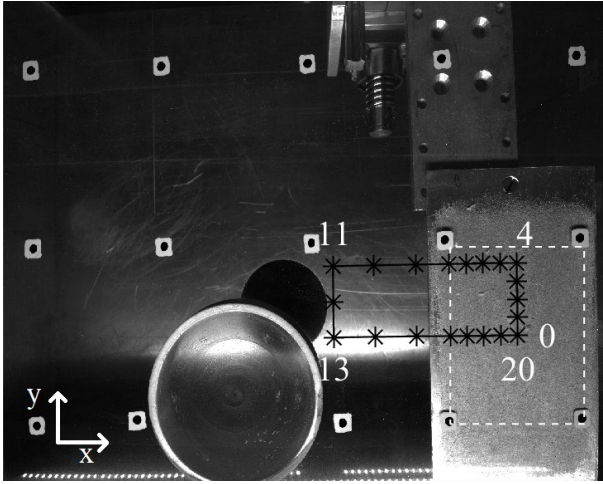


Figure 4. Rigid body movement of a plate following the path drawn in black; the region of interest for PIV tracking is shown with the dashed white line. Images are taken in locations indicated by a '*'.

Table 1. Displacement path of the rectangular plate.

Step number	x-displacement (mm)	y-displacement (mm)
0	0	0
1	0	10
2	0	20
3	0	30
4	0	40
5	-10	40
6	-20	40
7	-30	40
8	-40	40
9	-60	40
10	-85	40
11	-110	40
12	-110	20
13	-110	0
14	-85	0
15	-60	0
16	-40	0
17	-30	0
18	-20	0
19	-10	0
20	0	0

Figure 5 shows the shear strain calculated from the displacement field between step 0 (initial image) and step 4. Results show that, on average for all displacement fields, a higher variability of shear strain for the white LEDs than for the monochromatic amber LEDs.

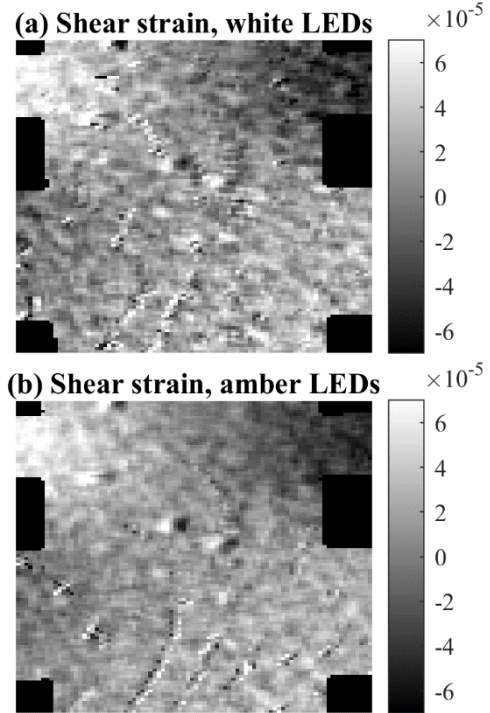


Figure 5. Shear strain comparison between white LEDs (a) and amber LEDs (b).

To quantify the level of variability in shear strain, a variance filter with a 3x3 square was applied on the shear strain field. This calculates how much every patch varies from its neighbouring patches. A histogram of local variances is shown in Figure 6, where it is shown that variability in the shear strain is higher in the case of white LEDs compared to the amber LEDs.

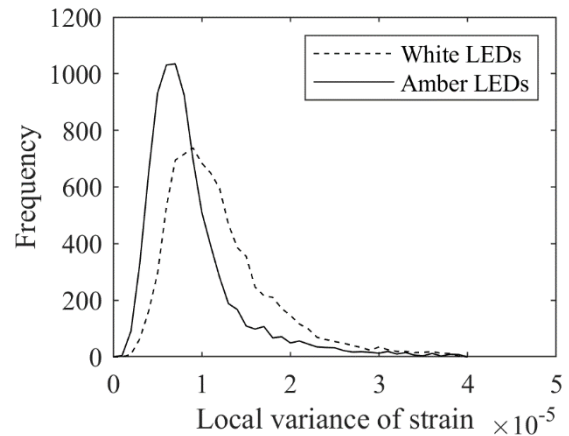


Figure 6. Histogram of local variance of strain for white LEDs (dashed line) and amber LEDs (solid line).

The average of this variance filtered field is then taken to quantify the variability level into a scalar value for each image. This scalar is shown in Figure 7 for each image and for both white LEDs and amber LEDs. Results demonstrate that images lit with monochromatic amber LEDs performed better than those lit with white LEDs, with 30% less variance on average.

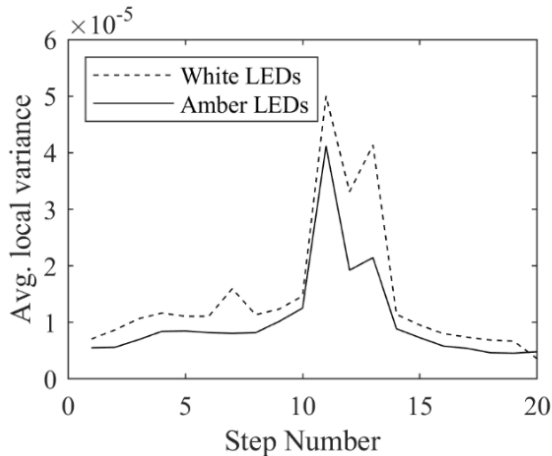


Figure 7. Average of local variance of shear strain for all images compared between white LEDs and amber LEDs.

4 TUNNEL VOLUME LOSS

A typical greenfield tunnel volume loss experiment conducted at 1g was also carried out to determine the effect of white versus monochromatic LEDs. The greenfield tunnelling experiment consisted of a plane-strain strongbox with a 100mm thick acrylic front wall and a cylindrical model tunnel running from the front wall through the soil to the back wall of the container. The model tunnel consisted of a water-filled latex membrane sealed onto a rigid aluminium shaft with enlarged ends that were fixed within the front and back walls of the strongbox (see Zhou et al. 2014 for full details). Tunnel volume loss was imposed by extracting a known volume of water from the model tunnel, and is defined as the volume of water (per unit length) extracted from the tunnel divided by the initial cross-sectional area of the tunnel. The same fine sand from the rigid body movement test was used and was prepared to a loose state (relative density of approximately 30%). Two regions were compared, as shown in Figure 8. The top region is located over the tunnel where maximum displacement occurs. The side region is located where a minimal amount of displacement occurs. A series of tunnel volume losses of 0.1%, 0.2%, 0.3%, 0.4%, 0.5%, 0.6%, 0.8% and 1% were imposed. For each volume loss, two images were taken, one with white LEDs and another with amber LEDs.

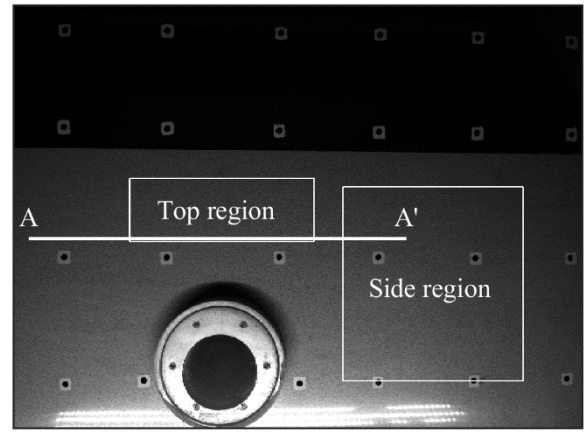


Figure 8. Tunnel volume loss experiment with two regions chosen for comparison. A-A' is the section used for displacement measurement shown in Figure 10.

The same process of shear strain variability quantification as with the rigid body movement test was carried out. Results of local variance are shown in Figure 9a for the Top region and Figure 9b for the side region. Figure 9 shows that there is a consistent reduction of shear strain variability using amber LEDs as opposed of white LEDs.

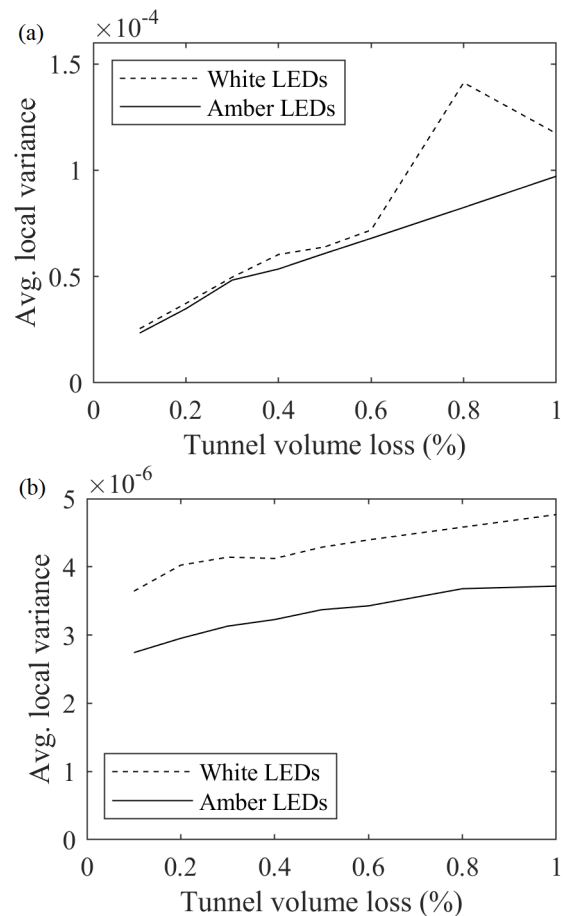


Figure 9. Average local variance of shear strain for tunnel volume loss experiment for (a) top region, and (b) side region.

In order to assess the difference in PIV performance in terms of displacements, a comparison of vertical displacement is shown in Figure 10 for the soil along a horizontal line 100mm above the tunnel centre (see section A-A' in Figure 8). The x axis is the horizontal distance from the centre of the tunnel. It can be seen that the two curves closely match each other when the measurements are made around the centre of the camera. However, there is a small difference between -150mm and -100mm where the data is close to the edge of the camera (see Figure 8). This difference, which is approximately 0.01mm, is very small, however it still may be important when attempting to determine displacements or strains with great accuracy.

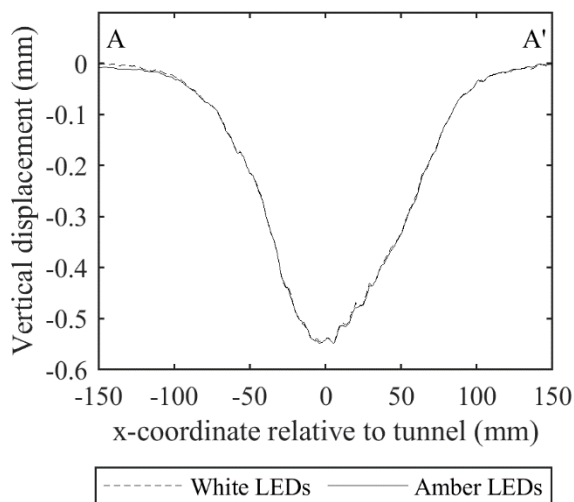


Figure 10. Vertical displacement along horizontal line (section A-A' in Figure 8) 100mm above tunnel axis at 0.3% tunnel volume loss.

5 CONCLUSIONS

This paper demonstrated the effect of chromatic aberration on the quality of images used for particle image velocimetry analysis under relatively typical conditions for geotechnical centrifuge testing. Results showed that using a light source that has a wide colour spectrum range (e.g. white light) affects the sharpness of images and that a monochromatic

light source can provide better images. Two tests were carried out with images taken through a 100mm thick acrylic wall and using either white light LEDs or monochromatic amber LEDs. The first test included a sand-coated plate that was moved as a rigid body along a rectangular pattern near the edge of the image. The second test was a typical greenfield tunnel volume loss experiment. Both experiments showed a lower level of variability on the shear strain measurement when using monochromatic LEDs rather than white LEDs. The difference in measured displacements was found to be small, however it may be important in tests where displacements or strains are needed to be measured with high levels of accuracy.

6 REFERENCES

- Blaber, J., Adair, B. and Antoniou, A. 2015. Ncorr: Open-Source 2D Digital Image Correlation Matlab Software. [online] *Experimental Mechanics*, **55**(6): 1105–1122. Available from <http://doi:10.1007/s11340-015-0009-1>.
- Stanier, S.A., Blaber, J., Take, W.A. and White, D.J. 2015. Improved image-based deformation measurement for geotechnical applications. [online] *Canadian Geotechnical Journal*, **53**: 727–739. Available from <http://doi:10.1139/cgj-2015-0253>.
- Sultanova N.G., Kasarova S.N. and Nikolov, I.D. 2013. Characterization of optical properties of optical polymers. [online] *Optical and Quantum Electronics*, **45**: 221–232. Available from <http://doi:10.1007/s11082-012-9616-6>.
- White, D.J., Take, W.A. and Bolton, M.D. 2003. Soil deformation measurement using particle image velocimetry (PIV) and photogrammetry. *Geotechnique*, **53**(7): 619–631.
- Zhou, B., Marshall, A. M. and Yu, H. S. 2014. The effect of relative density on greenfield settlements above tunnels in sands. In *Geoshanghai 2014 - International conference on geotechnical engineering*, Shanghai: ASCE. 96–105.

Physical Model of Rainfall Induced Landslide in Flume Test: Preliminary Results

Željko Arbanas¹, Vedran Jagodnik¹, Josip Peranić¹, Sara Pajalić¹, Martina Vivoda Prodan¹,
Nina Čeh¹

¹ Faculty of Civil Engineering, University of Rijeka, Croatia

Corresponding author: Željko Arbanas (zeljko.arbanas@gradri.uniri.hr)

ABSTRACT: Physical modelling of landslides using scaled landslide models behavior began in 1970s in Japan at a scaled natural slope physical model. The laboratory experiments of landslide behavior in a scaled physical model (also called flume or flume test) started in 1980s and 1990s in Canada, Japan and Australia under 1g conditions. The main purpose of the landslide physical modelling in the last 25 years was research of initiation, motion and accumulation of fast flow like landslides caused by infiltration of water in a slope. In October 2018, at the Faculty of Civil Engineering University of Rijeka, started a four-year research Project Physical modelling of landslide remediation constructions behavior under static and seismic actions, funded by the Croatian Science Foundation. The main Project aim is the modelling of landslide remedial constructions' behavior in physical models of scaled landslides in static (rainfall triggered landslides) and seismic conditions (earthquake triggered landslides) and their combination under 1g conditions. In this manuscript we will present the preliminary results obtained in landslide initiation test of a sandy slope (constructed of 0-1.0 mm the Drava River sand) exposed to an artificial rain typical for local conditions in Croatia by rainfall simulator. The results of landslide development were monitored by observation of volumetric water content and pore water pressure as well as by of surface displacement by *structure from motion* (SfM) surface observation displacement monitoring inside the model displaced mass. In this paper the preliminary results of provided test will be presented related to initiation and development of the observed instability of the sandy slope model.

Keywords: Landslide; Flume Test; Sandy Slope; Artificial Rainfall; Monitoring.

1 INTRODUCTION

Landslides are one of the major geohazards that threaten vulnerable areas in mountains, cities, along riverbanks, coasts and islands causing severe consequences expressed in lost human lives and economic losses all around the world. Due to climate change we are witnesses of an increase in the frequency and/or intensity of heavy rainfall, as well as shift of locations and periodicity of rainfall, which significantly increase landslide risk in landslide prone areas. Urban expansion due to population growth, development of coastal and mountain areas, construction of roads and railways increase exposure to the landslide hazard. Strong earthquakes are the second triggering factor for numerous rapid and long runout landslides in seismically active areas.

The answers of scientists, engineers, and all others included in landslide risk reduction is in significant developing of landslide science. Some of the answers are in different types of modelling of landslide related researches especially in landslide triggering and landslide process evolution. Landslide modelling for a long time was based on only numerical modelling techniques. Physical modelling of landslide analysing small scale landslide models behaviour was started in 1970s and 1980s in Japan (Oka 1972; Kutara and Ishizuka

1982; Yagi et al. 1985; Yamaguchi et al. 1989) on natural slopes exposed to artificial rainfall. The laboratory experiments of landslide behaviour in a scaled physical model (also called flume or flume test) started in 1980s and 1990s in Canada (Hunger and Morgenstern 1984), Japan (Yagi et al. 1985) and Australia (Eckersley 1990) under 1g conditions.

The research Project Physical modelling of landslide remediation constructions' behaviour under static and seismic actions, funded by the Croatian Science Foundation, started in October 2018 at the Faculty of Civil Engineering, University of Rijeka, Croatia. The main Project aim is modelling behaviour of landslide remedial constructions in physical models of scaled landslides in static and seismic conditions (Arbanas et al. 2019). In this manuscript we will present the initial results obtained in landslide initiation test of a sandy slope exposed to an artificial rain typical for local conditions in Croatia by rainfall simulator. The results of landslide development were monitored by observation of surface displacement by *structure from motion* (SfM), terrestrial laser scanner (TLS) and a pair of high speed cameras, as well as by pore water pressure and displacement monitoring inside the model displaced mass. While analyzes of the observed small scale landslide movements are still ongoing, in this paper we will describe the surface

observations of landslide movements and conclusions that followed from movement analyses.

2 MATERIALS AND METHODS

Physical model of a scaled landslide under static actions caused by artificial rainfall was designed to enable initiation of a landslide caused by controlled artificial rainfall and equipped with adequate photogrammetric equipment and complex sensor network with ability to measure displacements, soil moisture, pore pressures and soil pressures within a landslide body (Figure 1a). The flume is constructed as a steel base construction with transparent Plexiglas sides in layout dimensions of 2.30 x 1.00 m that lies on the working table (Figure 1b). It was provided that the maximal height of the soil material in the slope model is to 30 cm. An inclination of the flume slope can be adjusted for a type of used soil material from 10° to 45°. To prevent a sliding of soil mass at the contact of the flume base, the geogrid is fixed to the flume base.

2.1. Slope construction

For the first test in the constructed flume, the fine sandy material was chosen to be built-in in the flume slope at an inclination of 30°. Fine graded 0-1.0 mm (Figure 2) the Drava River Sand ($D_{60} = 0.37$ mm, $D_{10} = 0.19$ mm, $C_u = 1.947$) was built-in in the flume in 6 cm height 5 layers, 30 cm in total, at relative density $D_r = 0.5$ and reached void ratio of $e = 0.78$. Each layer was compacted by a manual

compactor at the water content of $w = 2\%$. The specific gravity of sand is $G_s = 2.7$.

The strength properties of the Drava River Sand was determined in direct shear apparatus at the same relative density as it is in the flume of $D_r = 0.5$ and low normal stresses appropriate to the stresses present in the flume slope. The average friction angle is $\phi = 34.9^\circ$.

The hydraulic conductivity of the Drava River Sand at the same relative density as it is in the flume of $D_r = 0.5$ determined in oedometer at low normal stresses appropriate to the stresses present in the flume slope is $k = 5 \times 10^{-5}$ m/s. Measured matric suction at the water content of $w = 2\%$ varies from 6 to 8 kPa.

2.2. Monitoring and observations

Monitoring system established at the flume test followed the principles used in observation of real landslides; it was consisted of geotechnical monitoring systems and geodetic monitoring systems (Mihalić Arbanas and Arbanas 2015).

Geodetic monitoring is based on innovative photogrammetric equipment for multi-temporal landslide analysis (Zanuta et al. 2006) from stereo image sequences obtained by a pair of high speed cameras (Feng et al. 2016). The high speed cameras have characteristics of max 2000 fps, resolution of 1280 x 1024 pixel and ISO: 6000 ISO Mono 2000 ISO Color.

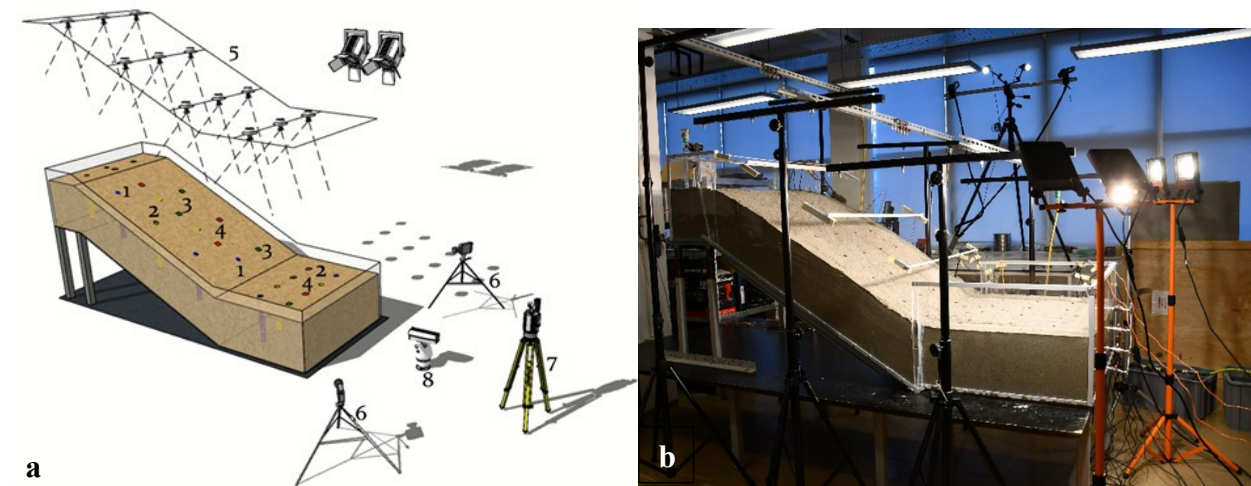


Figure 1. a Schematic view of physical model: 1-tensiometers, 2-pore pressure transducers, 3-strain gauges, 4-accelerometers, 5-rainfall simulator (sprinkler system), 6-high speed cameras, 7-terrestrial laser scanner (TLS), 8-infrared camera (Arbanas et al. 2019); b Photo of physical model.

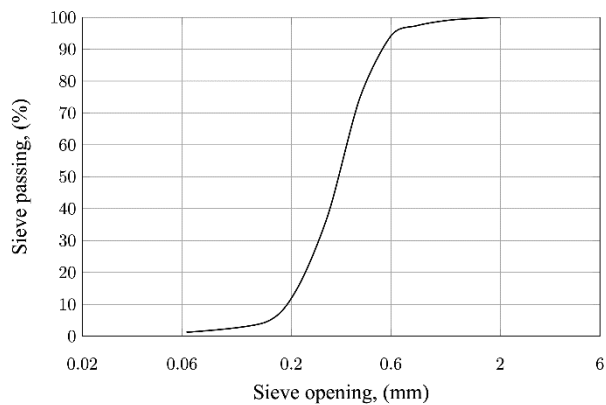


Figure 2. Grain size distribution curve of the Drava Sand built-in in the slope.

Terrestrial laser scanner (TLS) as well as *structure from motion* (SfM) photogrammetry surveys enabled determination of reached 3D landslide surface or high resolution digital model of a landslide model before and after sliding very precisely (Bitelli et al. 2004). The TLS Faro Focus HD 130 with the range of 0.6 – 130 m and resolution of 70 Mpixel as employed for the model slope surface scanning.

Geotechnical monitoring is consisted of a complex network of miniature sensors equivalent to those used in geotechnical monitoring in the field (Mihalić Arbanas and Arbanas 2015). Built-in sensors have ability to measure displacements MEMS (Ooi and Wang 2014), moisture and pore water pressures (pore pressure and moisture transducers), soil pressures and contact forces (load cells, strain gauges) and soil suction (tensiometers) (De Dios et al. 2010; Ooi et al. 2014; Scaioni et al. 2013; Lu et al. 2015). All sensors used in the test are connected to data loggers for continuous data collection during the test.

2.3. Rainfall simulator

One of the most important issues in physical models to simulate landslide initiation and motion caused by rainfall infiltration is full controlled intensities of artificial rainfall. Although it is possible to use some of the already developed rainfall simulators (Iserloh et al. 2012, 2013; Lora et al. 2016), there was necessity for developing of a rainfall simulator that can be adjusted to reach the rainfall intensities characteristic for precipitation events in Croatia. Construction of rainfall simulator includes ordinary elements usually used for watering plants and has an ability to control intensity, flow, and uniformity of wetting as well as the time of rainfall simulation. Rainfall simulator is consisted of a system of tree sprinkler branches with four different axial-flow full-cone nozzles (Figure 3). The supply of the system is controlled by flow meters and water



Figure 3. Photo of one branch with four axial-flow full-cone spraying nozzles.

pressure valve. The minimal intensity that can be achieved with only one nozzle at each branch is 10 mm/hour while a maximal intensity can reach more than 600 mm/hour using 4 nozzles at each branch.

Before the use, the rainfall simulator system was tested and calibrated in different regimes to enable adequate simulation of real precipitations applied to the model slope.

3 RESULTS AND DISCUSSION

After the model slope construction and installation of the monitoring equipment in the slope, the test was conducted by exposing the slope to the artificial rain from three nozzles, one in the upper part of the slope (H), one in the middle of the slope (M), and one in the foot of the slope (L) reaching an uniform artificial rainfall intensity of 58.23 mm/hour. The same intensity was maintained during the test 121 min, when the intensity was increased on 121.52 mm/hour and after 7 minutes (necessary for intensity adjustment using water pressure valve) reduced on 81.01 mm/hour that as maintained to the end of the test, Figure 4.

The first movements in the model slope were registered after 141 minute (126 minutes after the rainfall started) Figure 5a. The landslide initiation was started 11 minutes after complete saturation of the slope foot (115 min after the rainfall started), and landslide occurrence was presented in complete loss of soil strength in the slope toe and development of main scarp in the slope material, Figure 5a. It was noted that after the movement, the ground water started to run out through the sliding mass.

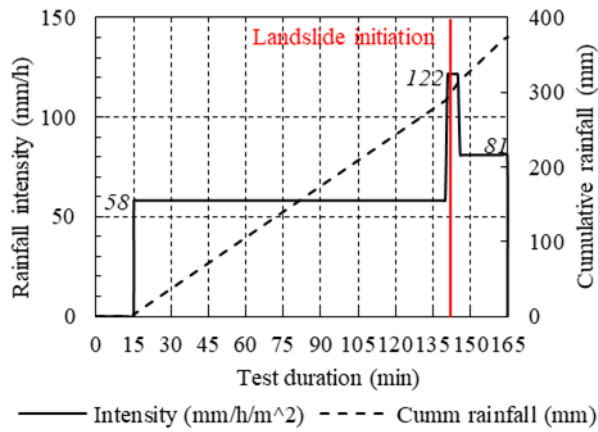


Figure 4. Diagram of rainfall intensity during the test. The rainfall started after 15 minutes of sensors adjustment.

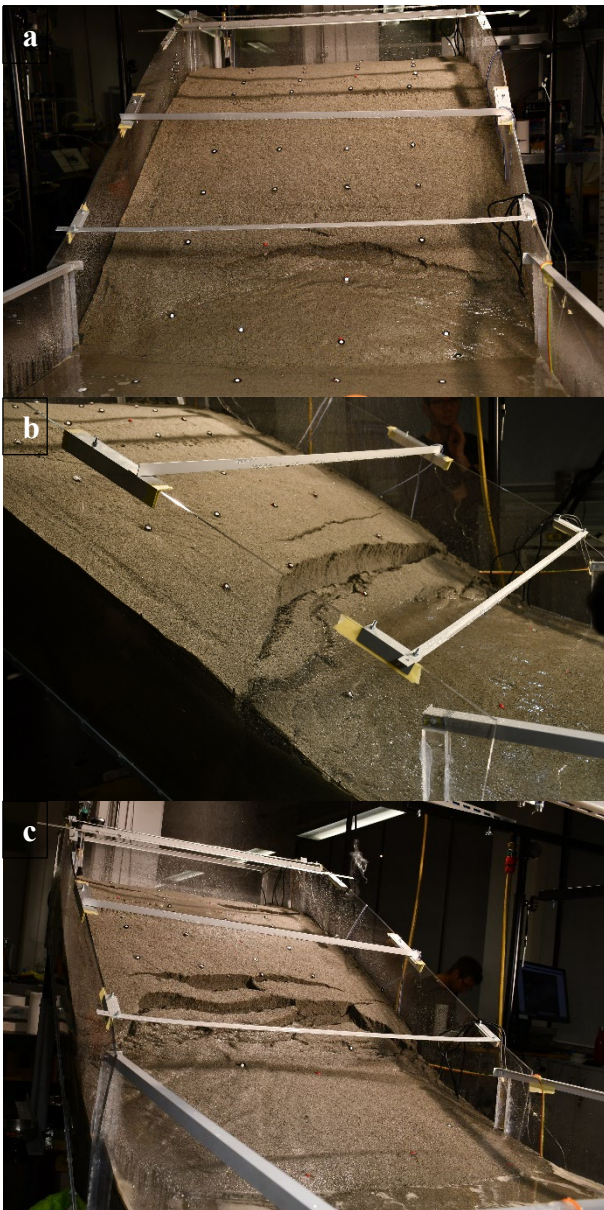


Figure 5. Photos of landslide initiation and retrogressive landslide development. a Landslide initiation (126 minutes after the rainfall started); b Development of the third and fourth main cracks (139 minutes after the rainfall started); c Development of the fifth main crack (48 minutes after the rainfall started).

After the landslide initiation, the further instability distribution was retrogressive with developing of new scarps 135, 139 (Figure 5b), and 148 (Figure 5c) minutes after rainfall started.

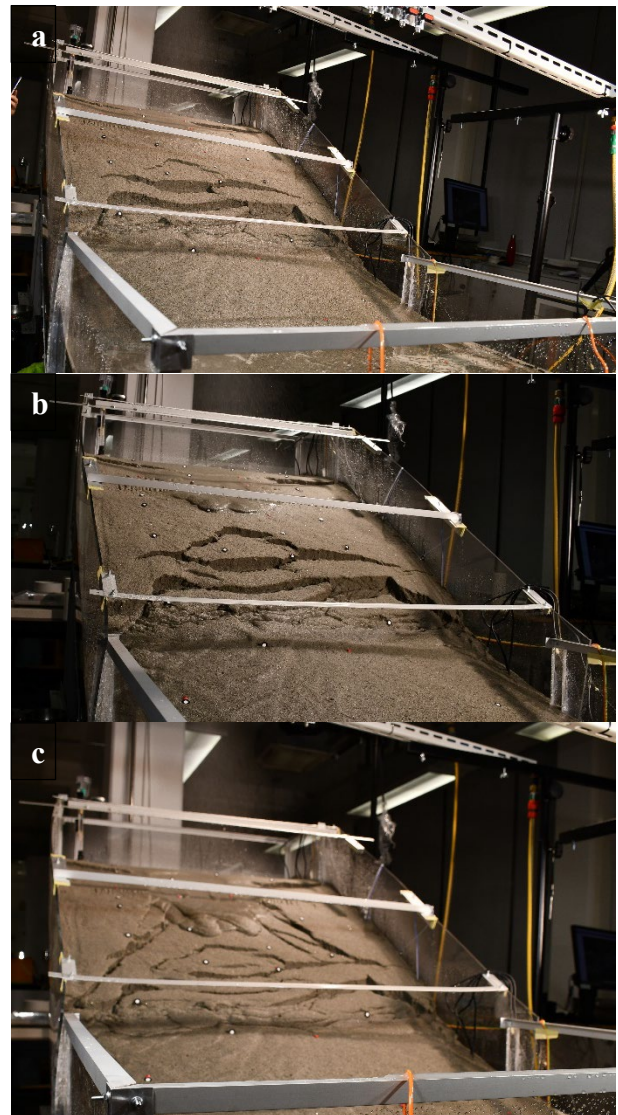


Figure 6. Photos of landslide final retrogressive development. a Landslide retrogressive development (149 minutes after the rainfall started); b Initiation of the debris flow from the top of the slope (149 minutes after the rainfall started); c Final landslide development to the top of the slope (150 minutes after the rainfall started).

After developing of the fifth crack, the rapid spread of the landslide to the top of the slope as occurred in next two minutes including an initiation of a debris flow originated from the crest of the slope (Figure 6 a,b,c). In this moment (150 minutes after the rainfall started), the rainfall was suspended that affected stopping of landslide activity. While this test was conducted with the task to identify conditions of a landslide initiation and mechanism and type of landslide occurrence through the reached level of landslide development, final collapse of the slope was not enabled.

Analysis of measured data of the volumetric water content during the test in the upper (H), middle (M), and lower (L) part of the slope enables the reconstruction of the landslide development, Figure 7 a, b and c.

In the first stage of the test the water infiltration in the slope started and the rise of volumetric water content was faster in shallower layers of the slope in all three parts of the slope (Figure 7 a, b and c). In the lowest and middle part of the slope it is clearly noticeable that the upper layers reached constant values of volumetric water content around 0.2 m³/m³ from 5 to 30 min after rainfall starting in the foot of the slope and from 10 to 40 min in the middle part of the slope. In the top of the slope, the same values of volumetric water content around 0.2 m³/m³ form 5 to 20 min and stayed almost constant to the end of the test. In the same time, the initial suction in the top of the slope took the constant value of 11.5 kPa (Figure 7c). The difference in these volumetric water contents is caused by establishing of a seepage trough the slope, and by increasing of hydraulic conductivity caused by suction decreasing and saturation of the slope from bottom layers to the surface.

An increased inflow and rising of the ground water level in the foot of the slope begun 30 min after rainfall started that is evident at the deepest sensor (L at -24 cm), and this process was continued till the ground water level flooded the surface of the slope foot (117 min after the rainfall started), Figure 8a, maintaining through the test. The rising of the ground water level in the middle of the slope begun 30 minutes later, Figure 7b. A ground water level was not identified at the top of the slope; infiltrated water was drained to the lower slope parts.

The failure of the slope was occurred immediately after the ground water level flooded the surface of the slope foot when that caused decreasing of soil strength and sliding (Figure 5a) and further retrogressive landslide development to the top of the slope. Finally, in the moment when the slope was completely saturated, the rain intensity was too high for further water infiltration and forming of the debris flow from the top of the slope, Figure 8.

Although the analyses of spatial and temporal movements data is still ongoing in the moment of the manuscript preparation, and the results of these analyses are not a subject of this paper, it should be noted that applied methods for model surface observations using photogrammetric equipment for multi-temporal landslide analysis from stereo image sequences obtained by pair of high speed cameras, terrestrial laser scanner (TLS) as well as *structure from motion* (SfM) photogrammetry surveys have

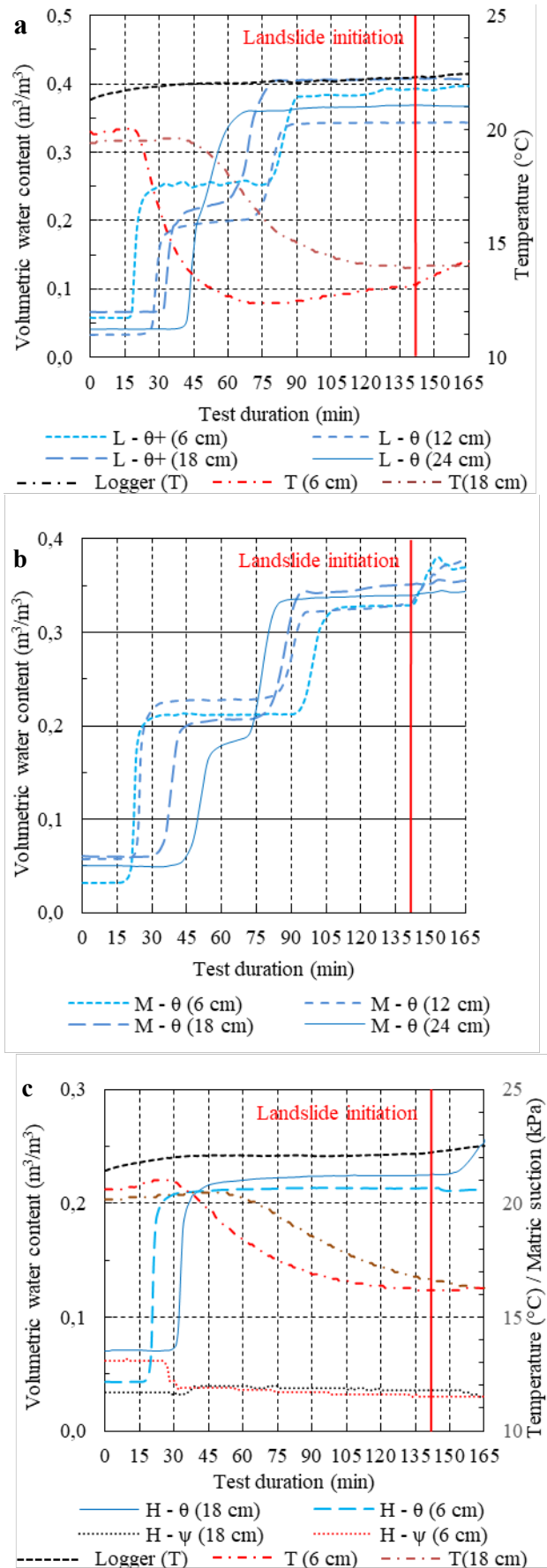


Figure 7. Diagrams of measured values of volumetric water content, suction and temperature during the test. (a) In the foot of the slope; (b) In the middle of the slope; (c) In the top of the slope. Numbers in parentheses designate depth of a sensor.



Figure 8. Debris flow occurred at the end of the test.

an important role in understanding and explanation of landslide initiation in a slope model.

The sliding process in the sandy slope model in previously presented conditions was slower than expected, excepting the debris flow process at the end of the test. The preliminary analyses have shown that an integrated approach using all three surface observation methods would give an optimal

result of landslide model surface motions. Stereo image sequences obtained by pair of high speed cameras enable a base for very precise temporal analysis of surface displacements but the method is depended on surface grid mark point density. Terrestrial laser scanner (TLS) survey can ensure the most precise 3D point cloud of model slope surface, but restrictions are related to time period necessary to complete a survey. An extended time necessary for scanning of about 30 min per scan, points on possibility to use TLS in extremely slow sliding processes or at the start and end of a test. *Structure from motion* (SfM) photogrammetry surveys is less precise than TLS survey, but using the high resolution cameras on small slope models, the obtained point clouds are not of significantly less quality. In a relatively not so fast sliding processes, a series of from a handmade high resolution photos would provide a high quality temporal 3D point cloud. As an example of the TLS and SfM 3D point clouds at the end of described test, without of detailed analyses of their differences, are presented in Figure 9.

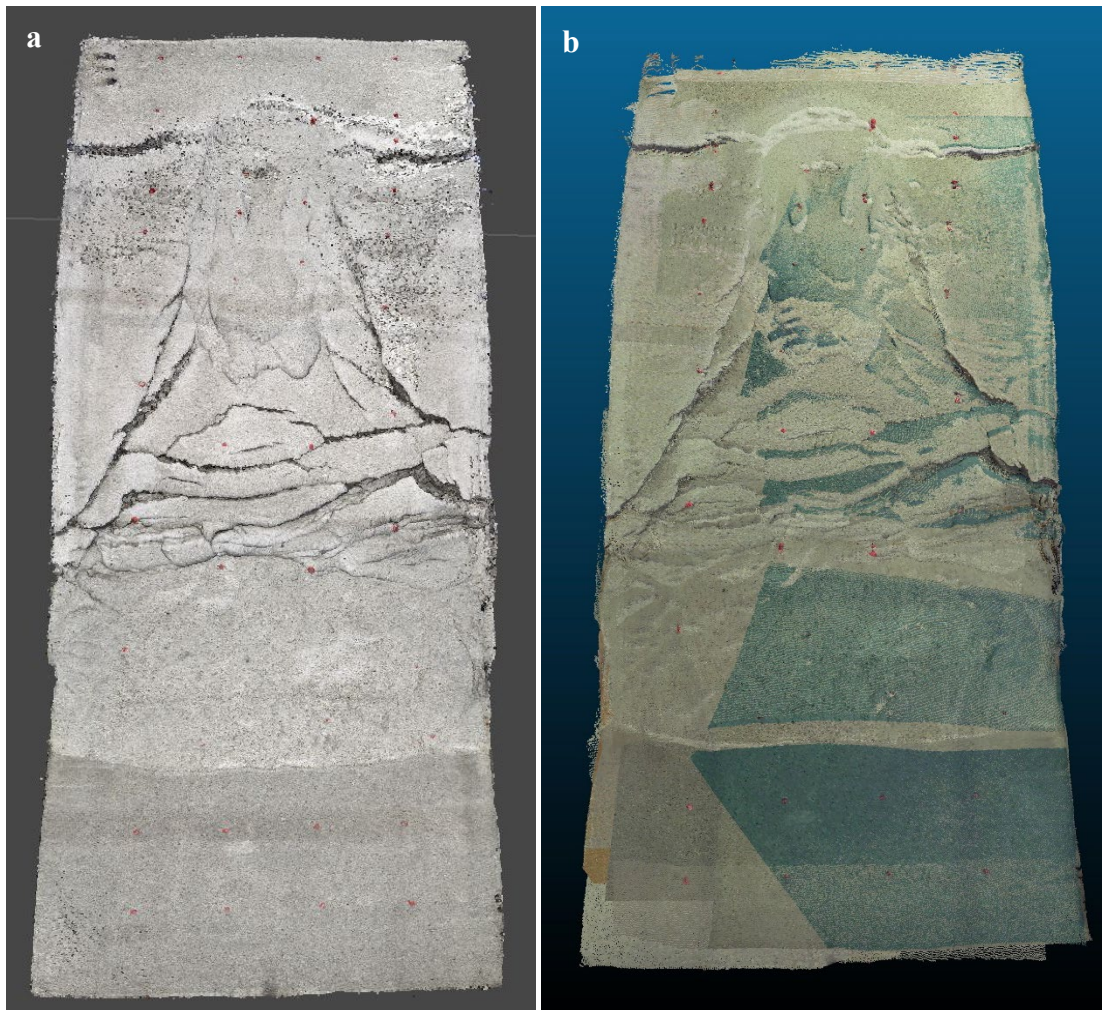


Figure 9. A view at the 3D point cloud provided form a Terrestrial laser scanner (TLS) survey; b Structure from motion (SfM) photogrammetry at the end of the sliding process.

4 CONCLUSION

In this manuscript we presented the preliminary results obtained in landslide initiation test of a sandy slope (constructed of 0-1.0 mm the Drava River sand) exposed to an artificial rain typical for local conditions in Croatia by rainfall simulator. The results of landslide development were monitored by observation of volumetric water content, soil suction and displacement monitoring within the displaced mass model.

Under artificial rainfall the model slope built-in in sandy slope started to slide after 126 minutes, after the ground water level flooded the surface of the slope foot 117 min after the rainfall started, and the landslide as developed to the top of the slope. Finally, in the moment when the whole slope was completely saturated, the rain intensity was too high for further water infiltration and forming of the debris flow from the top of the slope.

The landslide initiation in the foot of the model slope, as well as further developing of landslide to the top of the model slope was explained based on results of the volumetric water content and soil suction observation during the test.

Although the analyses of spatial and temporal movements data is still ongoing in the moment of the manuscript preparation, it should be noted that applied methods for model surface observations using photogrammetric equipment for multi-temporal landslide analysis from stereo image sequences obtained by pair of high speed cameras, terrestrial laser scanner (TLS) as well as *structure from motion* (SfM) photogrammetry surveys have an important role in understanding and explanation of landslide initiation in a slope model. The preliminary analyses have shown that an integrated approach using all three surface observation methods would give an optimal result of landslide model surface motions.

Further analyses of data provided by conducted test as well as results of further test conducted in different slope conditions under different rainfall regimes will give better insights in landslides initiation of sandy slopes exposed to an artificial rainfall.

5 ACKNOWLEDGEMENTS

The research presented in this paper was supported by Croatian Science Foundation under the Project IP-2018-01-1503 Physical modelling of landslide remediation constructions behaviour under static and seismic actions (ModLandRemSS), and University of Rijeka under the Project Uniri-Tehnic-18-113 Laboratory research of static and cyclic behaviour at landslide activation. These supports are gratefully acknowledged. The part of

laboratory equipment used for laboratory testing was provided in the frame of Project Research Infrastructure for Campus based Laboratories at the University of Rijeka, co-funded in a part by the Ministry of Science, Education and Sports of the Republic of Croatia and the European Fund for Regional Development (ERDF). The authors also want to thank to laboratory technicians Juraj Stella and Duje Kalajžić and their help in test conducting, and TLS and SfM surveys.

6 REFERENCES

- Arbanas, Ž., Pajalić, S., Jagodnik, V., Peranić, J., Vivoda Prodan, M., Đomlija, P., Dugonjić Jovančević, S., Čeh, N. 2019. Development of physical model of landslide remedial constructions' behaviour. *In: Proceedings of the Proceedings of 4th Regional Symposium on Landslides in Adriatic Balkan Region, Sarajevo, Bosnia and Herzegovina, 23-25 October 2019.* Geotechnical Society of Bosnia and Herzegovina, Sarajevo, pp. 103-108.
- Bitelli, G., Dubbini, M., Zanutta, A. 2004. Terrestrial laser scanning and digital photogrammetry techniques to monitor landslide bodies. *In: Proceedin of XXth ISPRS Congress: Geo-Imagery Bridging Continents, Istanbul, Turkey, 12–23 July 2004.* International Archives of the Photogrammetry, Remote Sensing and Spatial Information Sciences, Vol. XXXV, Part 5, pp. 246–251.
- De Dios, R.J., Enriquez, J., Victorino, F.G., Mendoza, E.A., Talampas, M.C., Marciano, J.J.S.Jr. 2010. A tilt, soil moisture, and pore water pressure sensor system for slope monitoring applications. *Science Diliman, 21:* 15-27.
- Eckersley, D. 1990. Instrumented laboratory flowslides. *Géotechnique, 40:*489–502.
- Feng, T., Mi, H., Scaioni, M., Qiao, G., Lu, P., Wang, W., Tong, X., Li, R. 2016. Measurement of Surface Changes in a Scaled-Down Landslide Model Using High-Speed Stereo Image Sequences. *Photogrammetry Engineering and Remote Sensing, 82(7):* 547-557.
- Hunger, O., Morgenstern, N.R. 1984. Experiments on the flow behaviour of granular materials at high velocity in an open channel. *Géotechnique, 34:*405–413.
- Iserloh, T., Fister, W., Seeger, M., Willger, H., Ries, J.B. 2012. A small portable rainfall simulator for reproducible experiments on soil erosion. *Soil & Tillage Research, 124:* 131–137.
- Iserloh, T., Ries, J.B., Arnaez, J., Boix-Fayos, C., Butzen, V., Cerda, A., Echeverria, M.T., Fernandez- Galvez, J., Fister, W., Geissler, C., Gomez, J.A., Gomez-Macpherson, H., Kuhn, N.J., Lazaro, R., Leon, F.J., Martinez-Mena, M., Martinez-Murillo, J.F., Marzen,

- M., Mingorance, M.D., Ortigosa, L., Peters, P., Reguees, D., Ruiz-Sinoga, J.D., Scholten, T., Seeger, M., Sole-Benet, A., Wengel, R., Wirtz, S. 2013. European small portable rainfall simulators: a comparison of rainfall characteristics. *Catena*, **110**: 100–112.
- Kutara, K., Ishizuka, H. 1982. Seepage flow in the embankment and stability of slope during rain (in Japanese). Tsuchi--Kiso Paper No 1330, Japan.
- Lora, M., Camporese, M., Salandin, P. 2016. Design and performance of a nozzle-type rainfall simulator for landslide triggering experiments. *Catena*, **140**: 77-89.
- Lu, P., Wu, H., Qiao, G., Li, W., Scaioni, M., Feng, T., Liu, S., Chen, W., Li, N., Liu, C., Tong, X., Hong, Y., Li, R. 2015. Model test study on monitoring dynamic process of slope failure through spatial sensor network. *Environmental Earth Sciences*, **74**(4):3315–3332.
- Mihalić Arbanas, S., Arbanas, Ž. 2015. Landslides: A guide to researching landslide phenomena and processes. *In: Handbook of Research on Advancements in Environmental Engineering*. Gaurina-Međimurac, N. (ed.). IGI Global, Hershey, pp. 474-510.
- Oka, H. 1972. Impacts by the “artificial landslide”: re-examine the rage of nature (in Japanese). *Kagaku Asahi*, **32**:152–153.
- Ooi, G.L., Wang, Y.H. 2014. Applying MEMS Accelerometers to Measure Ground Vibration and Characterize Landslide Initiation Features in Laboratory Flume Test. *In: Proceedings of Geo-Congress 2014, Atlanta, Georgia, February 2014, ASCE*, pp. 2019-2028.
- Ooi, G. L., Wang, Y-H., Tan, P. S., So, C. F., Leung, M. L., Li, X., Lok, K. H. 2014. An Instrumented Flume to Characterize the Initiation Features of Flow Landslides. *Geotechnical Testing Journal*, **37**(5): 1-21.
- Scaioni, M., Lu, P., Feng, T., Chen, W., Qiao, G., Wu, H., Tong, X., Wang, W., Li, R. 2013. Analysis of spatial sensor network observations during landslide simulation experiments. *European Journal of Environmental and Civil Engineering*, **17**(9): 802-825.
- Yagi, N., Yatabe, R., Enoki, M. 1985. Laboratory and Field Experiments on Prediction Method of Occurring Time of Slope Failure due to Rainfall. *Journal of Japan Landslide Society*, **22**:1-7_1.
- Yamaguchi, I., Nishio, K., Kawabe, H., Sibano, H., Lida, C. 1989. Initiation and fluidization of an artificial landslide: Field experiment in Yui Shizuoka Prefecture, Japan (in Japanese). *Shinrin Kosoku Areal Survey*, **158**:3–9.
- Zanutta, A., Baldi P., Bitelli, G., Cardinali, M., Carrara, A. 2006. Qualitative and quantitative photogrammetric techniques for multi-temporal landslide analysis. *Annual Geophysics*, **49**:1067-1080.

3. Piles: installation and capacity

Soil plug investigation with respect to pile geometry and installation method

Sascha Henke

Department of geotechnics, Helmut Schmidt University, Hamburg, Germany

ABSTRACT: Soil plug formation in open-ended piles depends on several factors like installation method, installation depth and pile geometry as well as soil density. To investigate the influence of these factors on soil plug formation an extensive centrifuge testing programme has been carried out. During these tests, piles with different geometry (tubular piles, U-piles and sheet-piles) were installed by quasi-static jacking, cyclic jacking and impact driving. All tests were carried out in silica sand with different soil density. During installation the reaction force as well as stress development inside and outside the piles were measured. In the present paper, the centrifuge testing programme is discussed. Furthermore, exemplary results are presented in detail. The focus lies on stress development inside the piles as an indicator for soil plugging tendency. The results are used to develop a simplified approach to predict stress development inside open-ended piles with respect to the parameters investigated throughout the centrifuge testing programme.

Keywords: Soil Plugging; Centrifuge Testing; Beam Centrifuge; Silica Sand; Pile Installation.

1 INTRODUCTION

Soil plugging in open-ended piles like tubular piles as well as sheet-piles and H-piles is of special geotechnical interest as it on the one hand might increase bearing capacity but on the other might also increase driving resistance. Therefore, research was carried out over the last decades to predict the soil plugging tendency with respect to different influencing parameters like pile diameter, installation method, soil conditions etc., see Kishida (1997), Paikowsky and Whitman (1990), Bruzy et al. (1991), Gavin and Lehane (2003), Jardine et al. (2005) and Lüking (2010) for example.

It has to be stated that the above mentioned papers are only exemplary and many other researchers also focused on different aspects regarding soil plugging and identified many influencing factors like pile diameter, penetration depth, pile geometry, soil conditions etc.

To gain deeper insight into all the above mentioned factors related to soil plug formation an extensive centrifuge testing programme was carried out which is presented in this paper focusing on the influence of pile geometry, installation method as well as soil density. In special, the soil plugging process is measured directly by means of total pressure measurement inside and outside the piles.

2 TESTING PROGRAMME

In the following section the centrifuge testing programme is described.

2.1. General information

All tests were carried out in the geotechnical beam centrifuge at the *University of Western Australia*, see Figure 1.

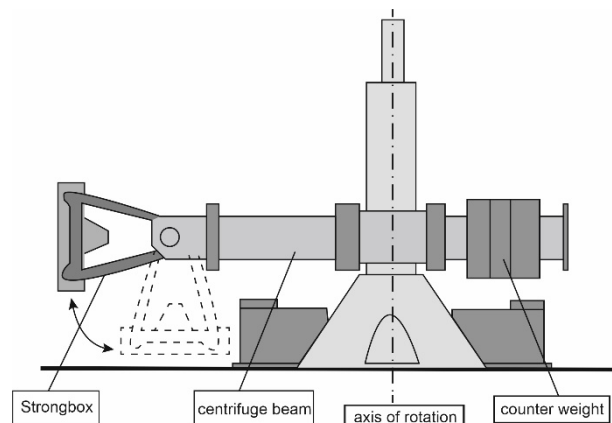


Figure 1. Schematic setup of the beam centrifuge

All tests were executed at an acceleration level of $50g$. Thus, the conversion from model to prototype scale is done using a factor of $N = 50$.

The acceleration field was adjusted that the acceleration of $50g$ acted at $1/3$ of the pile's final penetration depth.

2.2. Silica Sand

All tests were carried out in very fine dry silica sand, a pure sand with a mean grain diameter of $d_{50} = 0.19$ mm. The maximum and minimum void ratios are determined as $e_{max} = 0.79$ and $e_{min} = 0.49$.

2.3 Piles

Piles with different cross-section were investigated:

- Four tubular piles with different diameter,
- three U-profiles (U) with different height and
- three sheet-piles (SW) with different opening angles.

The different piles are shown in Figure 2.

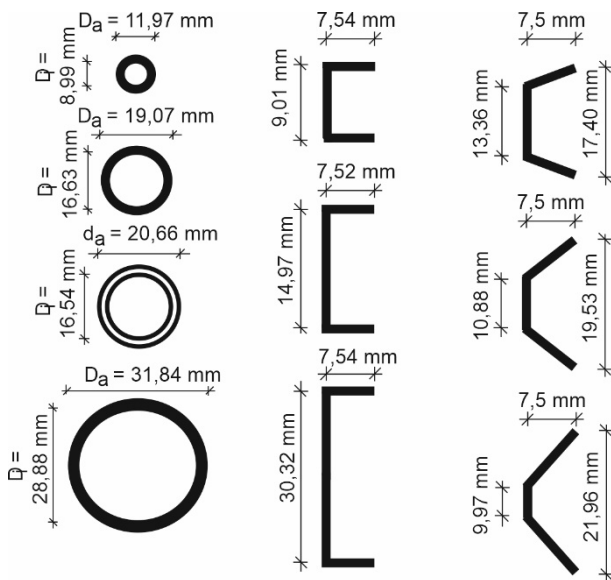


Figure 2. Piles tested in the geotechnical centrifuge

2.4 Installation methods

All piles are installed by quasi-static jacking with constant velocity. Furthermore, the tubular pile with 0.83 m diameter in prototype scale as well as the U-pile with a 0.45 m height in prototype scale are installed by cyclic jacking as well as impact driving.

2.4.1 Pile jacking

The piles were installed displacement controlled with constant velocity of 0.2 mm/s (1 cm/s in prototype scale). The final depth was defined as 150 mm. At 75 mm, 100 mm and 150 mm depth the installation process was stopped to carry out a static load test.

2.4.2 Cyclic jacking

Idealising vibratory pile driving the piles were installed with 0.2 mm/s velocity and an additional sinusoidal movement of the actuator until 150 mm depth was reached. The frequency of the sinusoidal movement was set to $f = 0.25$ Hz with an amplitude of 1 mm.

In these tests, the installation process was also stopped at 75 mm, 100 mm as well as 150 mm depth for static load testing.

2.4.3 Impact driving

Impact driving was carried out using the pile driving hammer developed in de Nicola and Randolph (1994). For a detailed description of the pile driving hammer refer to the above-mentioned paper.

As installation parameters a driving frequency of 10 Hz with a constant falling height of 10 mm (in loose soil) or 20 mm (in dense soil). Thus, the

installation was modelled force-controlled. The mass of the driving weight is 50 g. Maximum penetration depth was set to 150 mm.

2.5 Instrumentation

Main focus laid of the development of total stresses inside and outside the piles. Stress sensors were located inside and outside the piles 5 mm and 40 mm above the pile toe. The maximum capacity of the sensors was approx. 1 MPa. Only the small tubular pile was not instrumented due to space reasons.

Furthermore, the penetration resistance was continuously measured at the pile head during installation (jacking, cyclic jacking). As impact driving was modelled force-controlled the penetration resistance was only measured during the static pile load tests. The general sensor layout for a tubular pile is depicted in Figure 3.

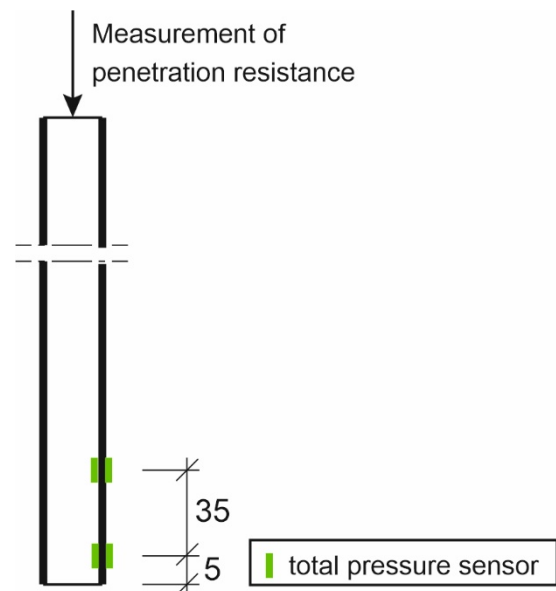


Figure 3. Measurement layout.

2.6 Test preparation

In one test box in general six or seven piles were installed. The distance between two piles was set to at least six times the pile diameter to avoid influence between different piles.

The tests were carried out in loose as well as dense silica sand. The resulting void ratio was calculated out of the soil volume and the weight. To verify homogenous soil conditions cone penetration tests were carried out in advance of the tests.

The relative soil density I_D for loose packings ranged between 0.25 and 0.35. The dense soil showed relative densities I_D between 0.92 and 0.95.

3 RESULTS

3.1 Influence of installation method

Exemplary, the penetration resistance of a U-profile with a prototype height of 0.45 m during jacking as well as cyclic jacking is compared in Figure 4.

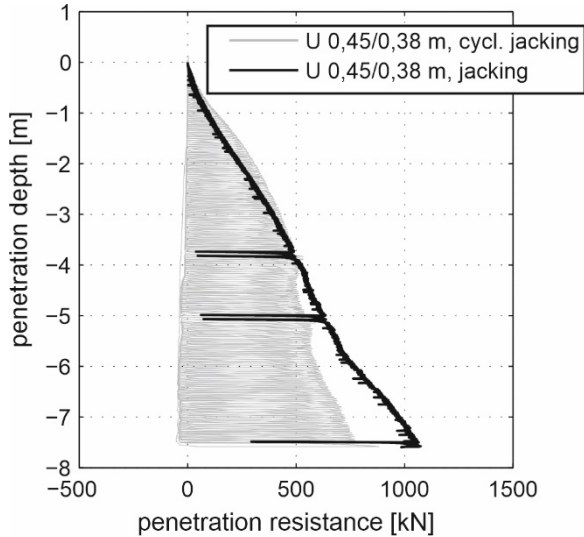


Figure 4. Penetration resistance of a U-profile during jacking and cyclic jacking (loose soil $I_D \approx 0.3$).

It is evident that the penetration resistance is higher during jacking. Furthermore, it can be seen that due to the cyclic motion of the U-profile the penetration resistance continuously changes during cyclic jacking.

As the pile resistance does not directly indicates the tendency of soil plugging, in Figure 5 the total pressures at the pile toe inside and outside the U-pile are depicted with respect to installation depth.

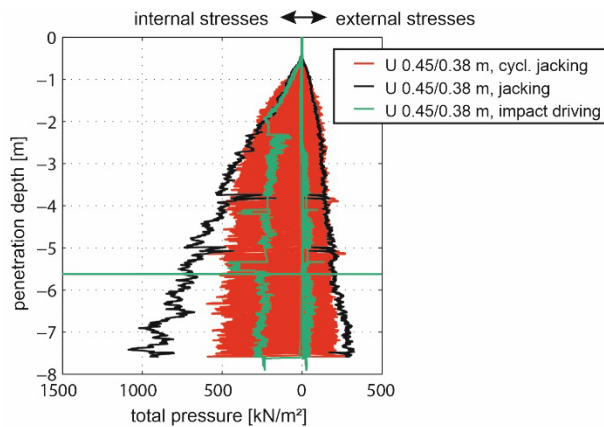


Figure 5. Total pressure development at the toe of a U-profile during jacking, cyclic jacking and impact driving (loose soil $I_D \approx 0.3$)

First, it can be seen that in all cases the total pressures inside the pile are significantly higher compared to the outer side of the U-profile. This indicates that in all cases arching occurs which might lead to soil plug development. Furthermore,

it is evident that during jacking the stress increase inside the pile is much higher compared to impact driving. This is due to dynamic effects during impact driving which leads to soil compaction as well as inertia effects such that total stresses inside the pile decrease.

For better comparison, the total stresses are normalized with the initial vertical stress state in the relevant depth such that a dimensionless factor K_{Pf} is calculated, see Figure 6.

K_{Pf} can be interpreted as effective earth pressure coefficient which indicates soil plugging inside the profile. If K_{Pf} inside a pile is significantly higher compared to the external value arching inside the profile leads to soil plugging.

In the present case, it can be seen that after approx. 2 m penetration, a constant K_{Pf} between 9 to 10 is measured inside the jacked U-profile. For the impact driven pile the development of K_{Pf} is similar during the first 2 m but afterwards significantly decreases. This is due to dynamic effects as the plug which starts to form continuously is loosened due to the dynamic forces.

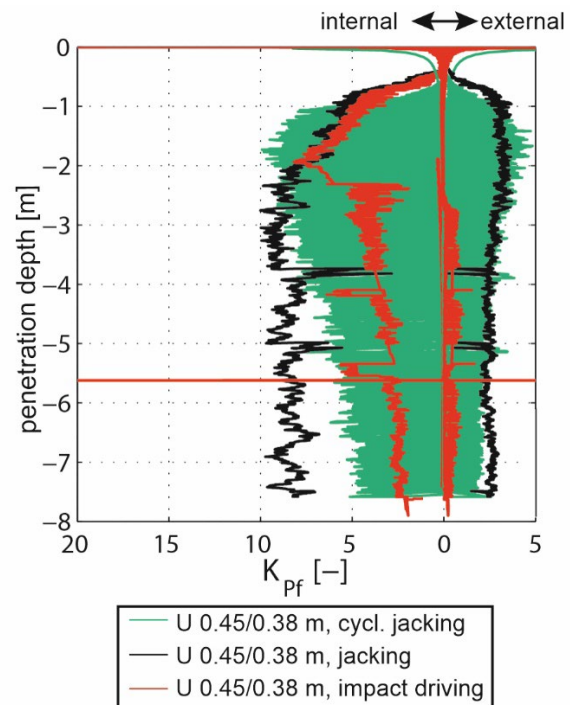


Figure 6. Normalized total pressure K_{Pf} at the toe of a U-profile during jacking, cyclic jacking and impact driving (loose soil $I_D \approx 0.3$)

3.2 Influence of pile geometry

3.2.1 Tubular piles

The main influencing factor regarding the geometry of tubular piles is the pile diameter. Thus, the normalized resistance ($s_{gr} = 0.05D$) during the static load tests after 50 mm, 100 mm and 150 mm (3.5 m, 5 m, 7.5 m in prototype scale) is compared for

jacked piles with different pile diameter, see Figure 7.

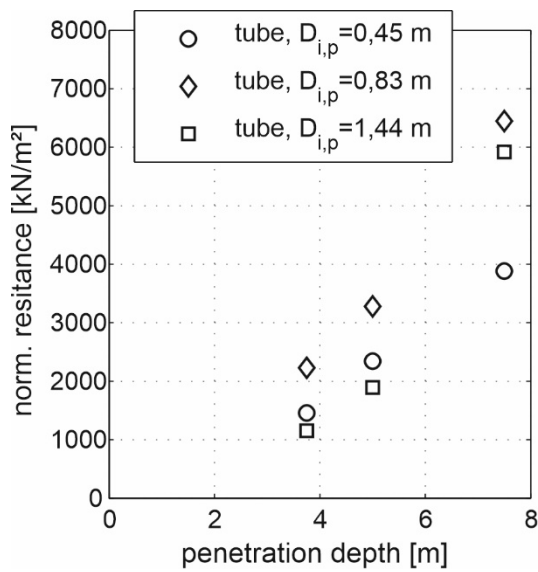


Figure 7. Normalized resistance of jacked tubular piles with different diameter at different penetration depths (loose soil $I_D \approx 0.3$)

It can be seen in Figure 7 that the normalized resistance is the highest for the pile with diameter $D_{i,p} = 0.83$ m whereas the bigger pile ($D_{i,p} = 1.44$ m) has significantly lower normalized resistance at 3.5 m and 5 m depth. At 7.5 m depth the normalized resistance of the biggest pile increases over-proportionally. This indicates that soil plugging starts to develop at this depth for the biggest pile whereas the other piles developed a soil plug at shallower penetration depths.

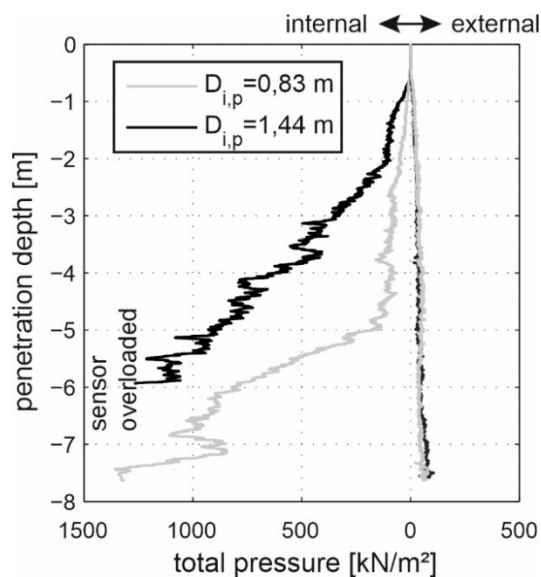


Figure 8. Total stress at the pile toe over penetration depth for different tubular piles during jacking (loose soil $I_D \approx 0.3$)

To justify this assumption, the total stresses at the pile toe for the piles with 0.83 m as well as 1.44 m diameter in prototype scale are compared in Figure 8. In Figure 8, a sudden increase of total internal stresses becomes evident for the 1.44 m diameter pile at a penetration depth of about 5 m. This indicates soil plug formation at this depth.

3.2.2 Sheet-piles

Furthermore, the influence of the opening angle α of sheet piles on soil plugging is investigated. For the definition of the relevant geometric values of a sheet pile, refer to Figure 9.

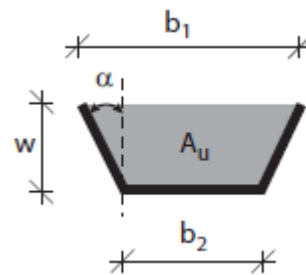


Figure 9. Relevant geometric values of a sheet pile

As already investigated by Radomski (1968) α is an important influencing factor regarding soil plugging tendency inside sheet piles. In the present study, sheet piles with the geometric values depicted in Table 1 are investigated.

Table 1. Geometric values for the different sheet piles investigated in the present study

name	width b_1	width b_2	opening angle α
SW 0.50/1.10 m	1.10 m	0.59 m	38.29°
SW 0.54/0.98 m	0.98 m	0.54 m	30.07°
U 0.75/0.38 m	0.75 m	0.75 m	0°

Summarizing, all piles described in Table 1 have a similar outlined area A_u . The penetration resistance for all sheet piles during jacking into loose silica sand is plotted in Figure 10.

It can be seen that the penetration resistance for all sheet piles is similar during the first 3 m of penetration. Afterwards, differences in penetration resistance are obvious. The U-pile with $\alpha = 0^\circ$ develops higher resistance compared to the other investigated piles. It is obvious that the penetration resistance increases with decreasing opening angle from this depth on.

This can be explained as arching is supported by lower opening angles such that the tendency of soil plug formation decreases with increasing value of α , see Figure 11.

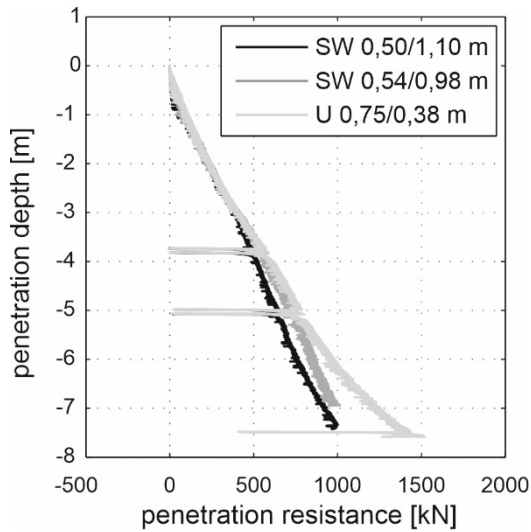


Figure 10. Penetration resistance for different sheet piles during jacking (loose soil $I_D = 0.35$)

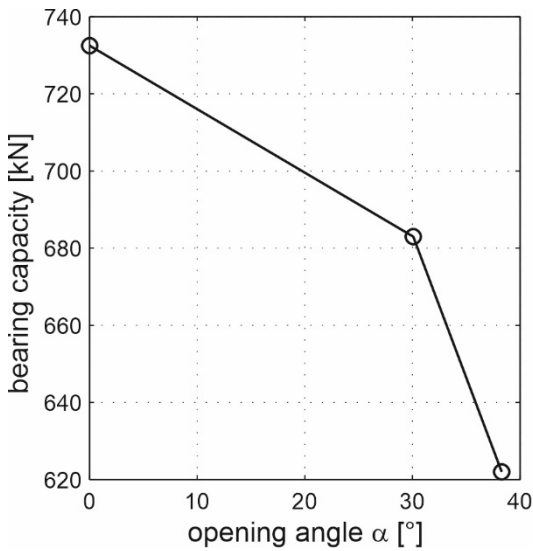


Figure 11. Bearing capacity with respect to the sheet pile's opening angle after 5 m of jacking (loose soil $I_D = 0.35$)

3.3 Influence of soil density

As expected, soil density mainly influences penetration resistance as well as internal stress development inside open-ended piles. The denser the sand the higher is the penetration resistance as well as the total stress development.

Figure 12 shows the penetration resistance development for the tubular pile with prototype diameter of 0.83 m during jacking as well as cyclic jacking into loose sand and dense sand respectively.

Furthermore, the total stress development at the pile toe inside and outside the 0.83 m as well as the 1.44 m diameter tubular pile is shown in Figure 13. It is evident that in both cases total stresses are significantly higher if the piles are installed into dense sand. Regarding the 1.44 m diameter pile it is

also evident that the depth at which the internal stresses increase over-proportionally is much shallower in dense soil (approx. 2 m compared to 5 m in loose sand).

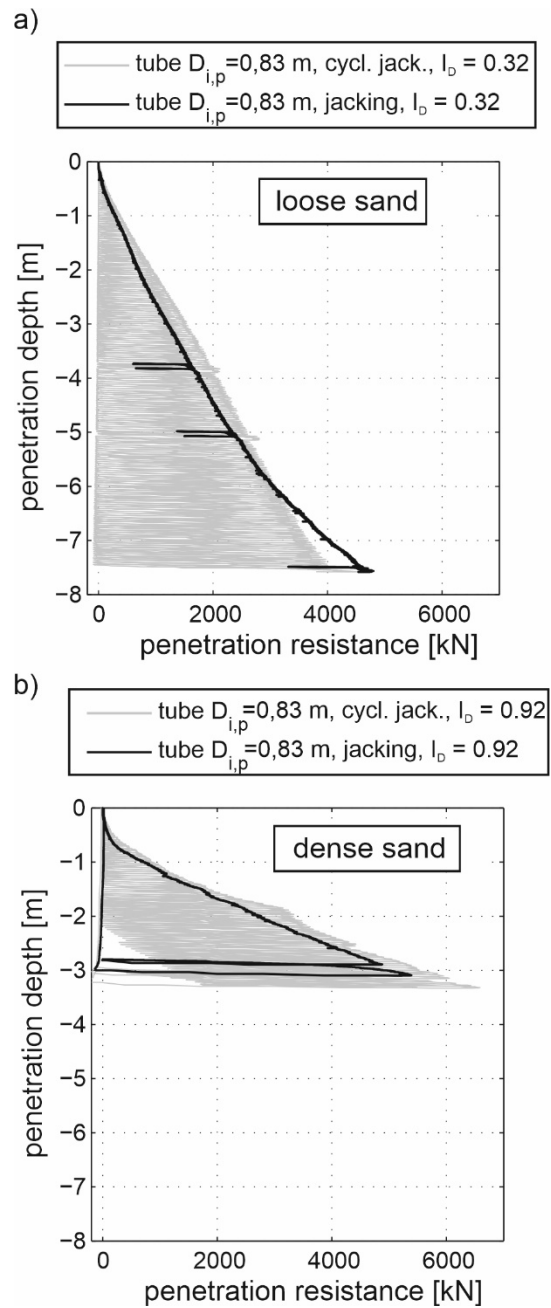


Figure 12. Penetration resistance of a 0.83 m diameter tubular pile during jacking and cyclic jacking into a) loose silica sand and b) dense silica sand

Regarding all test data, the quotient of the depths at which the over-proportional stress increase for different soil densities was identified is calculated as

$$\omega = \frac{z_{v,I_D=0,32}}{z_{v,I_D=0,92}} \quad (1)$$

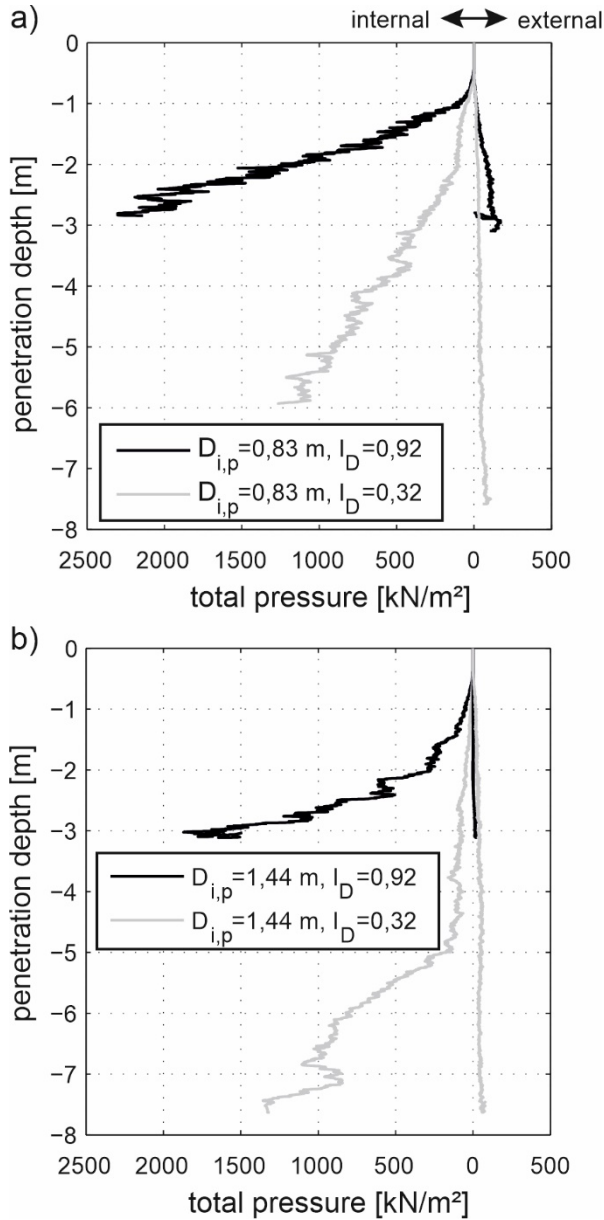


Figure 13. Total pressure development for the a) 0.83 m and b) 1.44 m diameter tubular pile during jacking into loose and dense silica sand

With respect to the present tests, this quotient ω lies between 2.6 and 3.7 which more or less corresponds to the quotient of investigated relative soil densities which is about 2.9. Thus, it can be assumed that a rather simple mathematical correlation exists between these two values which has to be investigated in further research as the present data basis is too small.

4 SIMPLIFIED CALCULATION MODEL

Using the centrifuge test results numerical modelling of pile installation processes was

validated such that additional data could be produced using numerical simulations. Due to lack of space these numerical simulations are not discussed in the present paper. For further information regarding the numerical simulations, refer to Henke (2013).

Resulting out of numerical and experimental data a simplified approach to calculate K_{pf} with respect to pile diameter and soil density could be established.

Regarding jacking of tubular piles the following mechanical model is considered, see Figure 14.

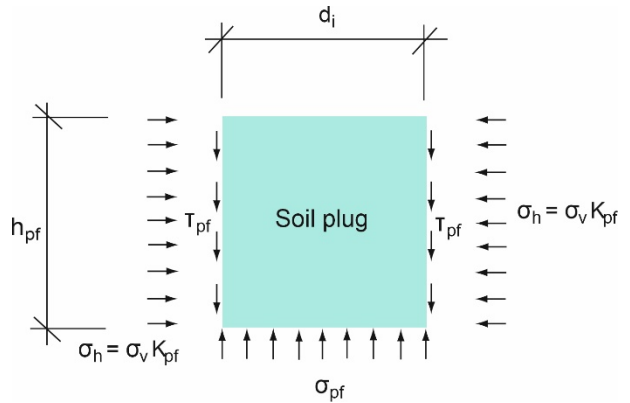


Figure 14. Mechanical model to calculate soil plug resistance inside tubular piles

Mainly, two parameters are unknown. On the one hand K_{pf} and on the other hand the plug height h_{pf} .

First, the work of Randolph et al. (1991) is considered to estimate the plug height as 10 % to 20 % of the penetration depth such that only K_{pf} has to be determined.

For estimation of K_{pf} with respect to pile diameter and soil density the following correlations are evaluated using numerical and experimental data:

$$K_{pf}(D_i) = 506.1e^{-3.564D_i} - 11.63 \quad (2)$$

and

$$K_{pf}(I_D, D_i) = K_{pf}(D_i) + 0.6894e^{6.42I_D} - 8.99 \quad (3)$$

These formulae are valid for $I_D > 0.40$ and $D_i \in [0.40; 0.90]$.

The above mentioned results are graphically visualized in Figure 15 and 16.

It has to be stated that these correlations are evaluated out of a rather small amount of data available such that they have to be detailed in further research work.

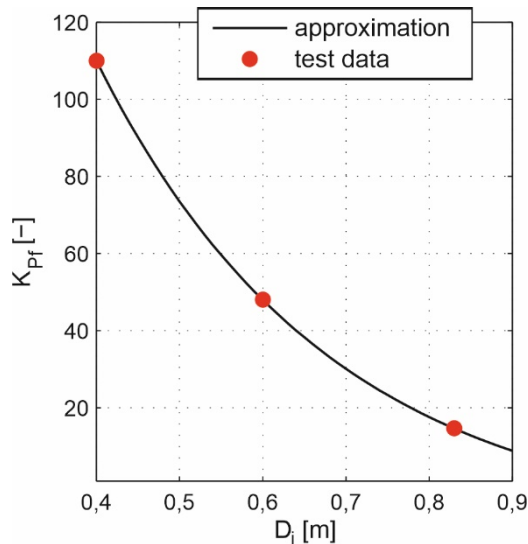


Figure 15. Correlation between K_{Pf} and D_i compared with exemplary test data ($I_D \approx 0.30$)

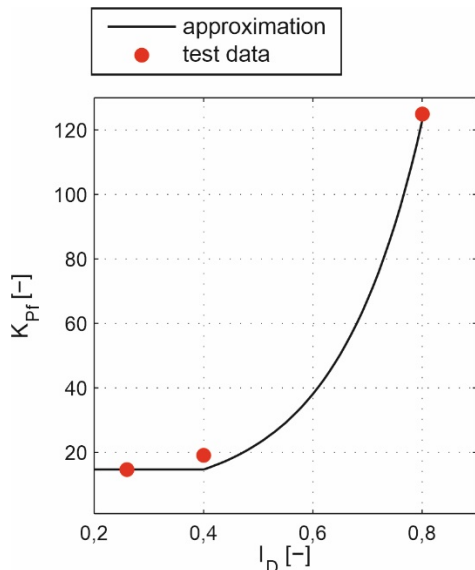


Figure 16. Correlation between K_{Pf} and I_D compared with exemplary test data ($D_i = 0.83$ m)

5 CONCLUSIONS

In the present paper an extensive centrifuge testing programme was presented. In the geotechnical beam centrifuge piles with different geometry were installed on-flight by means of pile jacking, cyclic jacking as well as impact driving.

As all tests were carried out in dry silica sand with different soil density such that it was possible to investigate the influence of soil density on soil plugging tendency, too.

During the pile installation process different values like penetration resistance and total stress development inside and outside the piles were continuously recorded.

Out of all these tests, the following general findings regarding soil plug formation can be summarized.

- Pile geometry significantly influences soil plugging:
 - In tubular piles a decreasing pile diameter increases soil plugging tendency
 - For U-piles the profile's height mainly influences soil plugging. This means, that the smaller the height, the higher is the arching effect inside the pile.
 - The opening angle α of a sheet pile influences soil plugging. Higher opening angle reduces the internal stress development.
- The installation method significantly influences the soil plug formation process. During quasi-static jacking the internal stresses are much higher compared to dynamic installation methods. This leads to the conclusion that dynamic effects like soil densification and inertia effects act against soil plugging.
- As expected, the denser the soil packing the higher is the internal stress build-up which acts as an indicator for soil plug formation.

Summarizing, the centrifuge test results provide valuable data to better understand the mechanism of soil plugging.

Furthermore, the data was used to validate numerical simulations of pile installation processes.

Finally, a simplified approach to predict the soil plug's capacity is presented which has to be detailed in further research.

6 ACKNOWLEDGEMENTS

The author thanks the German Research Foundation (DFG) for funding this project under the number HE 5445/2-1. Furthermore, special thanks belongs to the Centre for Offshore Foundation Systems at UWA in Perth for their valuable support.

7 REFERENCES

- Brucy F., Meinier J., Nauroy J.-F. 1991. Behaviour of Pile Plug in Sandy Soils During and After Driving. 23rd Annual Offshore Technology Conference in Houston, Texas, pp. 145-154.
- de Nicola A., Randolph M.F. 1997. The plugging behaviour of driven and jacked piles in sand. *Géotechnique* 47(4):841-856.
- Gavin K.G., Lehane B. 2003. The shaft capacity of pipe piles in sand. *Canadian Geotechnical Journal*, 40:36-45.

- Henke S. 2013. Untersuchungen zur Pfropfenbildung infolge der Installation offener Profile in granularen Böden. Veröffentlichungen des Instituts für Geotechnik und Baubetrieb der TU Hamburg-Harburg, Heft 29.
- Jardine R., Chow F., Overy R., Standing J. (2005). ICP design methods for driven piles in sand and clays. Thomas Telford, London.
- Kishida H. 1967. The ultimate bearing capacity of pipe piles in sand. Proceedings of the 3rd Asian regional Conference, SMFE, 1:196199.
- Lüking J. 2010. Tragverhalten von offenen Verdrängungspfählen unter Berücksichtigung der Pfropfenbildung in nichtbindigen Böden (German). Schriftenreihe Geotechnik, Universität Kassel, Heft 23.
- Paikowski S.G., Whitman V.R. 1990. The effects of plugging on pile performance and design. Canadian Geotechnical Journal, **27**:429-440.
- Radomski H. 1968. Untersuchungen über den Einfluss der Querschnittsform wellenförmiger Spundwände auf die statischen und rammtechnischen Eigenschaften (German). Mitteilungen des Instituts für Wasserwirtschaft, Grundbau und Wasserbau der Universität Stuttgart, Heft 10.
- Randolph M.F., Leong E.C., Houlsby G.T. 1991. One dimensional analysis of soil plugs in pipe piles. Géotechnique, **41**(4):587-598.

Pile group effects on installation and capacity of jacked piles in sand tested in the centrifuge

Dirk de Lange¹, Jarno Terwindt¹

¹*Geo-engineering, Deltares, the Netherlands*

Corresponding author: Dirk de Lange (Dirk.deLange@deltares.nl)

ABSTRACT: During installation of a foundation pile the surrounding soil state (stress level and void ratio) in the vicinity of the pile will be affected. In which way and to what extent will depend on the installation method, pile dimensions and soil properties. When piles are installed relatively close to each other, the behaviour of a pile within such a group might therefore differ from a single pile. Two centrifuge tests were performed in order to investigate the effects of pile installation on an adjacent pile. Three piles were installed in-line, with a pile to pile spacing of four diameters. The central pile was instrumented such that the resistance and pore water pressure at the tip could be measured. In addition, also the force acting on a friction sleeve and the head of the pile could be measured. During installation of the piles all these parameters were recorded. The capacity of the central pile was measured before and after the installation of the neighbouring piles. The results of these tests are presented and discussed in this paper.

Keywords: Pile-Group; Centrifuge Testing; Pile Installation Order.

1 INTRODUCTION

A good understanding of the behaviour of a pile group and of individual piles in a pile group is important, depending on the stiffness of the superstructure, since many constructions are built upon it. However, existing pile group models and measurements are still subject of discussion (Le Kouby et al., 2016). In general, it can be stated that the behaviour of a pile group differs from the behaviour of a single pile multiplied by the number of piles. This is often expressed by an efficiency coefficient and will generally depend on the pile configuration (spacing and number), the pile properties (dimensions), the installation order and method, and the soil conditions. Le Kouby et al. (2016) give an overview of performed research in this field and present results of calibration chamber tests on the installation order effects on the response of a pile group in silica sand. They also conclude that pile spacing and installation order are important parameters. The local pile responses differ from those of the other piles in the group. Further, they concluded that installing the central pile lastly will lead to the “best” group effect and a stiffer response (both for tip resistance and shaft friction). They also observed a negative group effect for the tip resistance and a positive group effect for the shaft friction.

In 2013, two tests were run in the Deltares beam centrifuge (arm length of 5.5 m). The tests were run at 40g. During these tests, both a single pile and a group of three piles were installed (in flight) in a single sand sample and have been load tested regarding *pile set-up*. The centrifuge continued spinning from the start of the installation until the

final load test. The results regarding *pile set-up* were published in De Lange et al. (2014). This paper discusses the effects of pile installation on an adjacent pile similar to the publication of Le Kouby et al. (2016). A different installation sequence was applied for the pile group during the two tests.

2 MATERIALS AND METHODS

2.1. Test set-up

The test set-up existed of a steel cylindrical sample container, hydraulic cylinders mounted on a stiff steel frame, for pile installation and testing, and the model piles, see Figure 1. The frame was placed on top of the container.

2.2. Dimensions and layout

Closed-ended piles with a diameter, D , of 16 mm were used. The pile group existed of one instrumented pile in the centre and two non-instrumented piles at a (centre-to-centre) distance of 64 mm. These three piles were installed in a line, see Figure 2. The inner diameter of the container was 0.9 m and the height of the sand sample was 0.6 m. The distance from a pile to the wall was 300 mm. The (centre-to-centre) distance from the single pile to the pile group was also 300 mm. The piles were installed to a penetration level of approximately 0.32 m.

2.3. Soil material and preparation method

The tests were performed in fully water saturated Baskarp B15 sand. The main characteristics are given in Table 1. The sand was prepared by dynamic compaction of a fully saturated sample (Rietdijk et

al., 2010). Relative densities of respectively 66.3% and 66.8% were achieved for test 1 and 2.

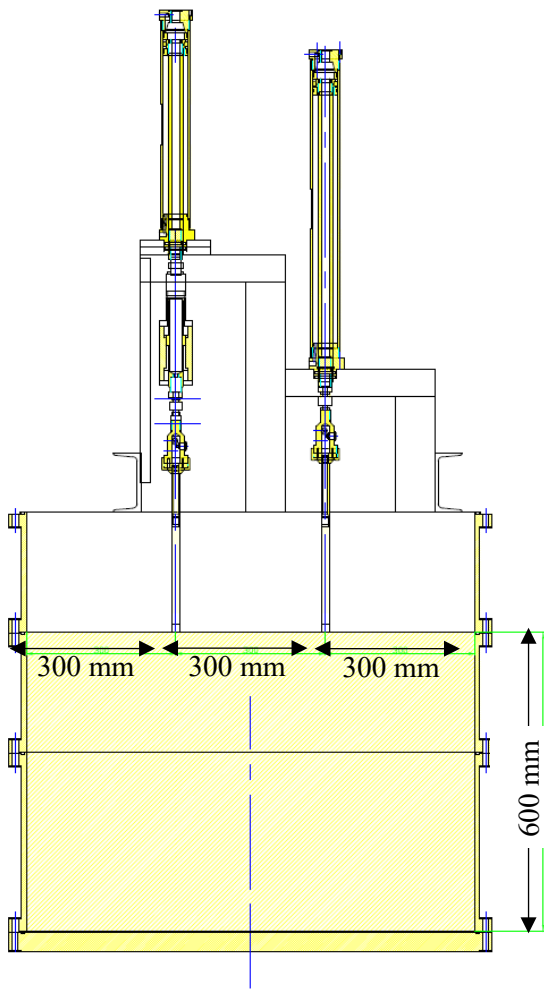


Figure 1. Drawing of test set-up: soil model container together with the hydraulic cylinders and reaction frame.

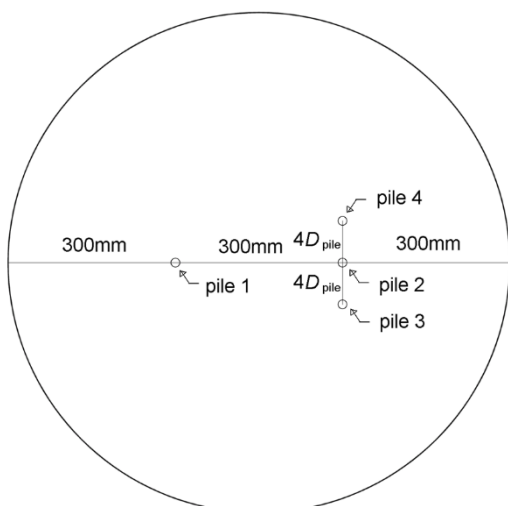


Figure 2. Top view of the pile layout: 16 mm diameter in a 0.9 m diameter container. Pile 1 and 2 were instrumented piles; pile 3 and 4 were dummy piles.

Table 1. Baskarp B15 sand characteristics.

Parameter	Unit	B15
Particle density, ρ_s	kg/m ³	2.65
Mean mass diameter, d_{50}	μm	118
Coefficient of uniformity, d_{60}/d_{10}	-	1.4
Minimum porosity, n_{min}	%	35.2
Maximum porosity, n_{max}	%	47.6

2.3. Model piles and instrumentation

The forces acting on the pile head, the pile base and the friction element could be measured separately for the instrumented piles. Also, the pore water pressure at the base could be measured, see Figure 3. For all piles the displacement of the hydraulic cylinders, which were connected to the piles, was measured.

A rough pile surface was created to pronounce the interaction between the pile shaft and the sand. According to Garnier and König (1988), the piles had totally rough interfaces, since the normalized roughness, R_n , was equal to 0.27 ($R_{max} = 32 \mu\text{m}$), see Figure 4. The suitable roughness was obtained by machining a continuous profile of notches over the entire shaft surface, see Figure 3.

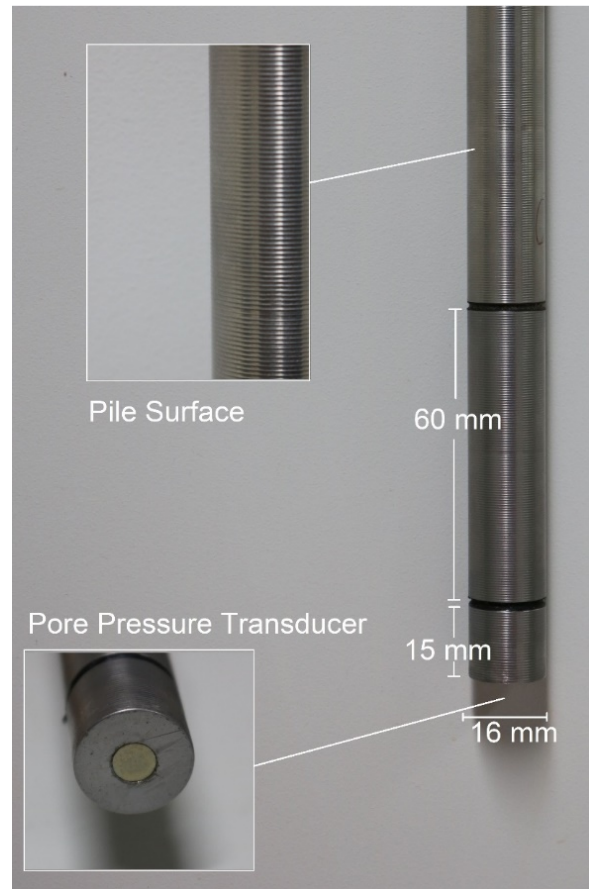


Figure 3. Geometry, surface and sensor locations of the instrumented piles.

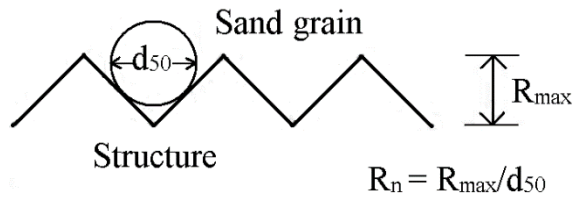


Figure 4. Definition of normalized roughness (Garnier and König 1998).

2.4. Test program and procedure

To study possible ageing effects, the instrumented piles were jacked into the soil over a certain distance to mobilize the axial capacity (compression), multiple times after installation, see Table 2 and 3. During test 1, pile 2 was installed and load tested several times, before pile 3 and 4 were installed. After installation of pile 3 and 4, which were installed simultaneously, pile 2 was again load tested several times. During test 2, pile 3 was installed first. After installation of pile 2, pile 2 was load tested several times before pile 4 was installed. After installation of pile 4, pile 2 was load tested again several times.

Some other differences between test 1 and test 2 should be noticed as well. First, for test 2, the load test at 10 minutes after a prior load test was cancelled. Second, due to operational constraints with the centrifuge during test 2, pile 2 could not be tested at 1000 min after installation of pile 4. And third, the piles were not unloaded by pulling in between installation and load testing during test 1.

Table 2. Test scheme of pile in group, test 1

Step	Activity
1	Installation of pile 2
2	Waiting for 1 min
3	1 st capacity test (10%D)
4	Waiting for 10 min
5	2 nd capacity test (10%D)
6	Waiting for 100 min
7	3 rd capacity test (10%D)
8	Installation of pile 3 and 4
9	Waiting for 1 min
10	4 th capacity test (10%D)
11	Waiting for 10 min
12	5 th capacity test (10%D)
13	Waiting for 100 min
14	6 th capacity test (10%D)
15	Waiting for 1000 min
16	7 th capacity test (10%D)
17	Cyclic displacements of 0.1mm at 50% of capacity measured during prior step
18	8 th capacity test (10%D _p)

Table 3. Test scheme of pile in group, test 2

Step	Activity
1	Installation pile 3
2	Installation pile 2
3	Waiting for 1 min
4	1 st capacity test (20%D)
5	Waiting for 100 min
6	2 nd capacity test (20%D)
7	Waiting for 1000 min
8	3 rd capacity test (20%D)
9	Installation of pile 4
10	Waiting for 1 min
11	4 th capacity test (20%D)
12	Waiting for 100 min
13	5 th capacity test (20%D)

The installation of and the tests on the piles were done displacement controlled. The installations of the piles were performed at a displacement rate of 1 mm/s. The pile load tests were performed at a displacement rate of 0.002 mm/s up to a pile head displacement of 10% (test 1) or 20% (test 2) of the pile diameter, D_p . After each load test, the piles were unloaded by pulling the piles upwards.

3 RESULTS AND DISCUSSION

3.1. Correction and normalization of data

All measured forces are corrected by subtracting the initial values, measured just before installation. In this way, the own weight of the piles has been eliminated. The influence of the increasing acceleration field with depth on the weight of the piles is negligible (also due to opposite buoyant forces). The total friction is defined as the difference between the forces at the pile head and the pile tip.

Further, all presented results are normalized. The displacements are normalized by the pile diameter, D_p . The measured stresses at the pile tip are normalized by the calculated vertical effective stress level at the pile tip. The mean shear stresses at the shaft are normalized by the calculated vertical effective stress at half the height of that part of the shaft, what carries the load.

3.2. Pile installation

During test 1, pile 2 was installed before pile 3 and 4, while during test 2, pile 2 was installed after pile 3. Figure 5 shows the normalized tip resistance during installation of pile 2 in test 1 and 2. Initially, a stiffer tip response was observed for pile 2 during test 1 (“first pile”). However, a higher tip resistance was observed at larger penetration levels during test 2 (“second pile”).

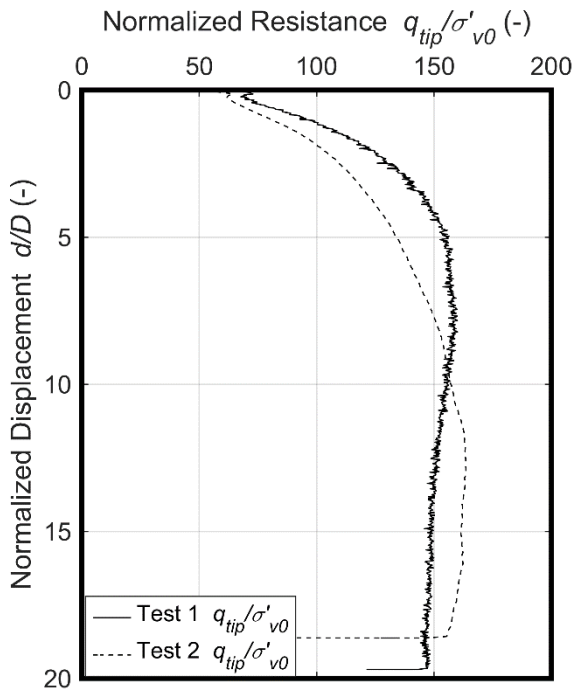


Figure 5. Normalized tip resistance during installation of pile 2.

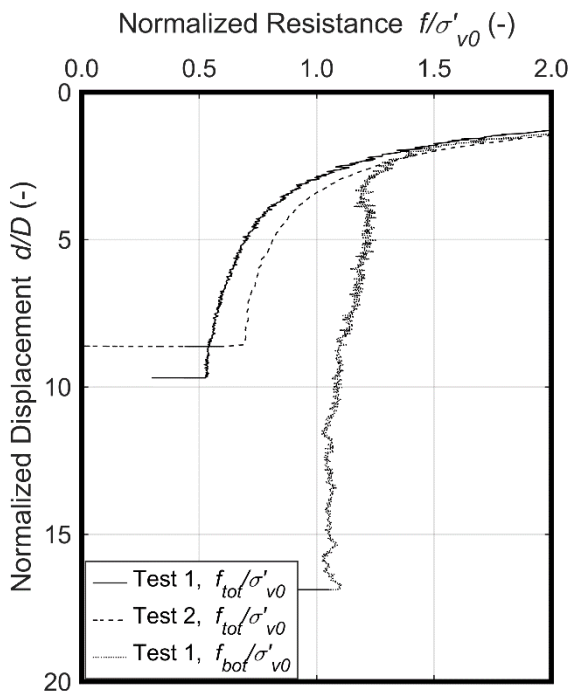


Figure 6. Normalized shaft friction, total and at friction element, during installation of pile 2.

Figure 6 shows the normalized shaft friction during installation of pile 2 in test 1 and 2. The displacement halfway the pile shaft of interest has been taken for the normalized displacement in this figure. The total friction was higher during test 2 compared to test 1. These observed tip and shaft responses are in line with the finding of Le Kouby et al. (2016). The normalized friction at the friction sleeve is substantially larger than the normalized total friction, which can be explained by friction

fatigue (Lehane, 1992). The measured resistance at the friction sleeve was not reliable during test 2. Therefore, this data is not presented in this paper.

3.3. Installation of adjacent piles

During the installation of adjacent piles, all gauges of the instrumented central pile were recorded, and the displacement of the central pile was controlled to be zero, see Figure 7. During test 1, pile 3 and 4 were installed simultaneously, while during test 2, only pile 4 was installed after installation of the central pile (pile 2).

Figure 8 shows the normalized total stress at the tip of pile 2 during installation of the adjacent pile(s) as function of the penetration of the adjacent pile(s). During test 1, the total pressure acting against the tip of pile 2 started to decrease immediately when the adjacent two piles started penetrating the sand. However, after a penetration of about $14D$ the pressure acting on the tip of pile 2 increased to a similar level as before the installation of the adjacent piles. During test 2, a decrease was observed after a penetration of the adjacent pile of about $10D$. The total pressures became more or less constant after a penetration of about $14D$. Figure 9 shows the normalized total pore water pressure at the tip of pile 2 during installation of pile 4 in test 2 as function of the penetration of pile 4. Initially, the pore water pressure increased, after $9D$ penetration of pile 4, it decreased, after $14D$ penetration it increased again and after $17D$ it became stable. It is thought that the soil around the tip of pile 2 initially is being pushed away from the pile (downwards) by the installation of the adjacent pile(s), however, for deeper penetration of the adjacent pile(s), soil displacement around the tip of pile 2 becomes mainly sideward, see Figure 10.

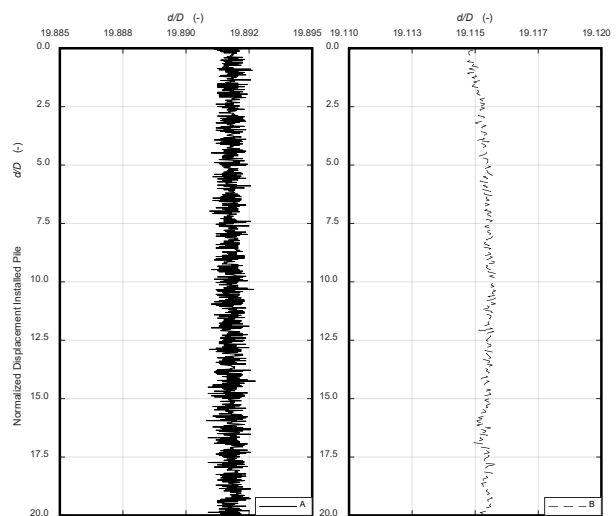


Figure 7. Vertical displacement of pile 2 during installation of the adjacent pile(s) during test 1 (left) and test 2 (right). The vertical axis is the displacement of the pile being installed.

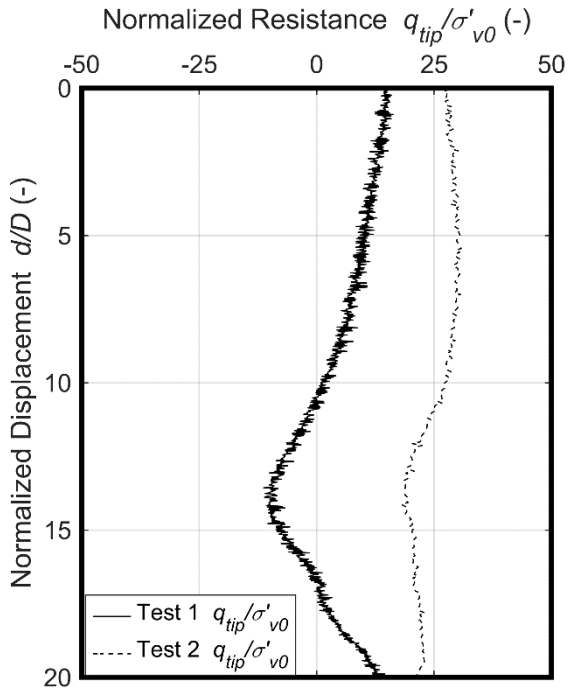


Figure 8. Normalized stress at the tip of pile 2 during installation of the adjacent pile (s). The vertical axis is the displacement of the pile being installed.

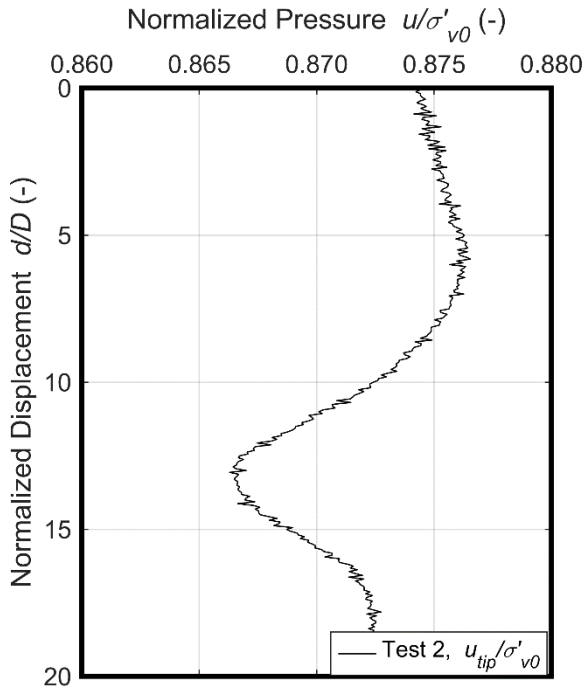


Figure 9. Normalized pore water pressure at the tip of pile 2 during installation of the adjacent pile (s). The vertical axis is the displacement of the pile being installed.

A similar trend has been observed for the friction at the friction sleeve during test, see Figure 11. However, the total friction showed the opposite trend. Initially, the total shaft friction decreased (test 1) or was stable (test 2), after a penetration of the adjacent pile(s) of about $9D_p$, the total friction

increased, and after a penetration of the adjacent pile of about $14D_p$, the total friction decreased.

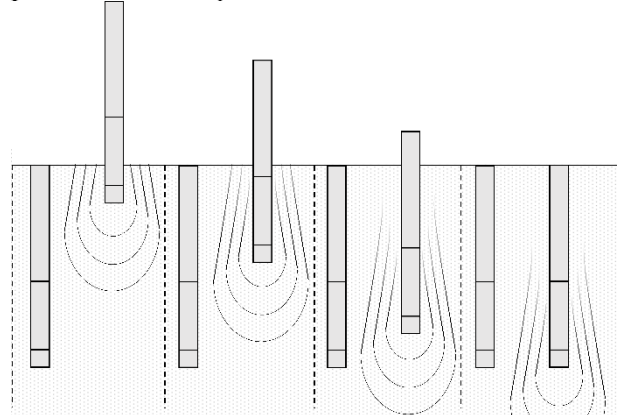


Figure 10. Different mechanisms during installation (adopted from Le Kouby et al. 2016).

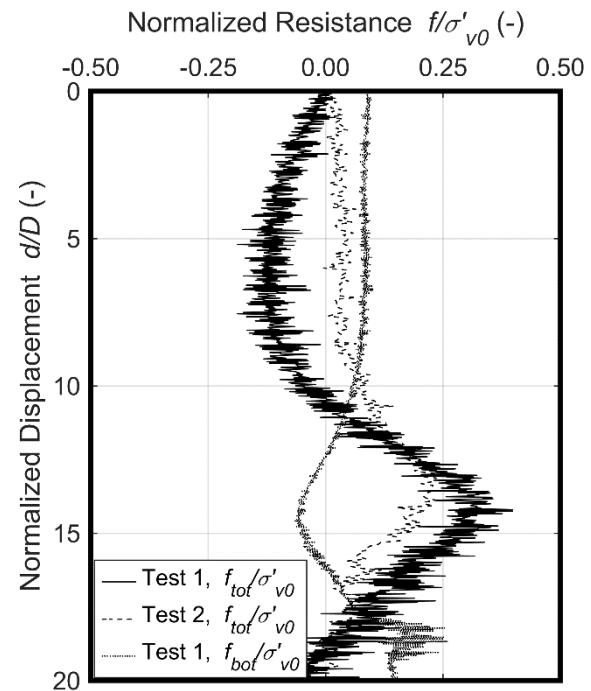


Figure 11. Normalized stress acting on (a part of) the shaft of pile 2 during installation of the adjacent pile (s). The vertical axis is the displacement of the pile being installed.

Positive shaft friction is acting as an upwards force and negative shaft friction as a downwards force. An increase in shaft friction can only be explained by upward soil movement relative to the pile, while a decrease can be explained by downward soil movement. Therefore, it can be concluded that between $9D$ and $14D$ penetration of the adjacent pile(s), the soil movement along the friction sleeve of pile 2 (bottom $5D$) was mainly downwards, while the soil movement along the upper part of the pile shaft ($15D$) was mainly upwards. Movements in the opposite direction can be argued for penetration levels of the adjacent pile(s) between $14D$ and $20D$.

All observed trends were more pronounced during test 1, since two piles were installed simultaneously.

3.4. Influence on single pile capacity

Before and after installation of the adjacent pile(s), the central pile has been load tested several times regarding *pile set-up*. The results are given in Figure 12 (tip resistance) and Figure 13 (shaft friction) as function of normalized tip displacement. Before installation of the adjacent pile(s), during test 1 and 2, the central pile has been load tested three times. Higher tip resistance and total friction were mobilized during the first load tests during test 2, which could be explained by the installation sequence. The results from the first load test during test 1 are not comparable to the results from the other load tests, since no unloading had been applied before the first load test of test 1. After installation of the adjacent pile(s), a weaker tip response and an increase in shaft friction, during the fourth load tests, can be clearly observed.

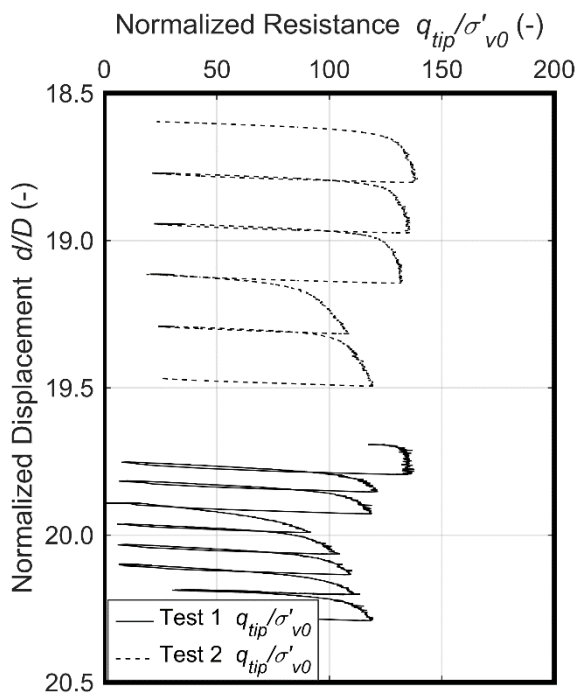


Figure 12. Measured parameters for the instrumented piles during capacity testing.

4 CONCLUSIONS

Results from centrifuge tests on the effects of pile installation (jacking) on an adjacent (instrumented) pile are presented in this paper. The results indicate directions of soil movement along the adjacent pile during pile installation. The results also indicate the effect of the installation sequence and clearly show a weaker tip response and an increase in shaft friction of a single pile after installation of (an) adjacent pile(s). These findings are in line with the findings of Le Kouby et al. (2016) and these are especially important for non-stiff superstructures, which are founded on pile groups.

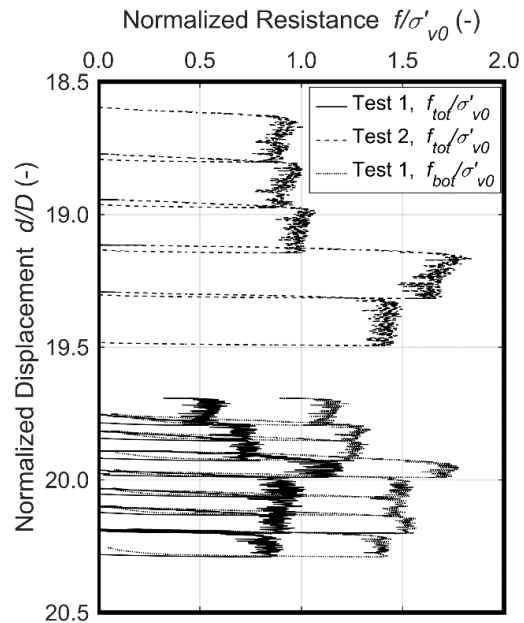


Figure 13. Measured parameters for the instrumented piles during capacity testing.

5 ACKNOWLEDGEMENTS

The authors would like to acknowledge Frans Kop, Rob Zwaan, Ferry Schenkeveld, Thijs van Dijk, Jack van der Vegt and Ruud van der Berg for their contribution to the preparation and performing of the presented tests. Further, Ruud Stoevelaar, Jelke Dijkstra, Frits van Tol and Bert Everts are acknowledged for their guidance. The tests were funded by CURNET and Deltares.

6 REFERENCES

- Garnier, J., and König, D. 1998. Scale effects in piles and nails loading tests in sand. *In Proceedings of the International Conference Centrifuge 98, Tokyo, Japan, Vol. 1, pp. 205–210.*
- Le Kouby, A., Dupla, J.C., Canou, J., Francis, R. 2016. The effects of installation order on the response of a pile group in silica sand. *Soils and Foundations, 56(2): 174-188. doi: 10.1016/j.sandf.2016.02.002*
- De Lange D.A., Van Tol, A.F., Dijkstra, J., Bezuijen A. & Stoevelaar, R. 2010. Set-up effects of piles in sand tested in the centrifuge. *In Proceedings 8th Int. Conf. Phys. Model. Geo., Perth, Australia, 14 – 17 January 2014, Taylor & Francis Group, London, pp. 721-727.*
- Lehane, B.M. 1992. Experimental investigations of pile behaviour using instrumented field piles. PhD thesis, University of London (Imperial College).
- Rietdijk J., Schenkeveld F.M., Schaminee P.E.L. and Bezuijen A. 2010. The drizzle method for sand sample preparation. *In Proceedings 8th Int. Conf. Phys. Model. Geo., Zürich, Switzerland, 28 June – 1 July 2010, Taylor & Francis group, pp. 267-272.*

Centrifuge modelling of shaft resistance of a rough rock-socketed pile

José Gregorio Gutiérrez-Ch¹, Geyang Song², Charles Heron², Alec Marshall², Rafael Jimenez¹

¹*ETSI Caminos, Canales y Puertos, Universidad Politécnica de Madrid, Spain*

²*Nottingham Centre for Geomechanics, University of Nottingham, United Kingdom*

Corresponding author: José Gregorio Gutiérrez-Ch (jg.gutierrez@upm.es)

ABSTRACT: Previous research and field experience have demonstrated that socket roughness is a crucial factor that affects the shaft resistance of rock-socketed piles. This research aims to present a methodology to evaluate the shaft resistance behaviour of a rough axially loaded pile socketed in soft rock. Geotechnical centrifuge tests were conducted at 50-g using small scale aluminium model piles fabricated with different roughness profiles. The model piles were socketed into an artificial soft rock, which consists of sand, cement, bentonite and water. Fibre Bragg grating sensors were used to measure the axial strains/loads along the piles. Results presented in this paper relate to a single tests and are used to demonstrate the viability of the approach to investigate the shaft behaviour of rock-socketed piles considering socket roughness.

Keywords: Rock-Socketed Piles, Shaft Resistance, Socket Roughness, Centrifuge Tests, Fibre Bragg Grating.

1 INTRODUCTION

Load tests and numerical modelling (Pells et al. 1980, Horvath et al. 1983, Gutiérrez-Ch et al. 2019a, 2019b) on rock-socketed piles suggested that socket roughness is an important aspect that affects the shaft resistance behaviour. Seidel and Collingwood (2001) indicated that socket roughness resulting in real projects depends mainly on the drilling tools employed, as well as the type and strength of the rock. For instance, O'Neill et al. (1996) reported that sockets drilled with an auger tool in soft rock tend to have a sinusoidal pattern, and Nam and Vipulanandan (2008) indicated that sockets drilled by core barrel are 30% rougher than those drilled with an auger tool. However, socket roughness is not usually considered in current design methods, and the estimation of shaft resistance of rock-socketed piles is commonly based on empirical correlations as a function of the uniaxial compressive strength (UCS) of the intact weaker material (rock or pile) (Rezazadeh and Eslani 2017).

This research aims to present a methodology used to study the shaft resistance response of an axially loaded rock-socketed pile considering socket roughness using a geotechnical centrifuge test.

2 MATERIALS AND METHODS

In this study, a test was conducted at 50-g using the geotechnical centrifuge facility at the University of Nottingham Centre for Geomechanics (NCG). The centrifuge has a 2 m beam radius and is capable of reaching accelerations up to 150-g. The pseudo-rock employed, the model pile and its

instrumentation, as well as the model set-up, are described next.

2.1. Pseudo rock

The effect of socket roughness on shaft resistance of rock-socketed piles is particularly significant in piles socketed in soft rocks having an intact UCS of $\sigma_c = 1 - 12$ MPa (Seidel and Collingwood 2001). However, the practicalities of preparing centrifuge models on such intact rocks is complex (Leung and Ko 1993). For this reason, an artificial soft rock was prepared by mixing sand, cement, bentonite and water with a particular proportion (see Table 1). After 44-days of normal curing, an average value of $\sigma_c = 1.14$ MPa was obtained, which was based on several cube tests.

Table 1. Pseudo rock mix proportions.

Mix proportions by percent mass (%)			
Sand	Cement	Bentonite	Water
52.3	12.2	6.5	29.0

2.2. Model pile

2.2.1 Manufacturing and instrumentation

To achieve an axial stiffness (EA ; where A is cross sectional area and E is Young's modulus) of a 0.8 m diameter concrete solid pile ($E = 30$ GPa) in prototype scale, a 15.875 mm diameter (D) model pile (model scale) with a 2.032 mm thickness ($E = 70$ GPa) was used (see Figure 1). The nominal length of the pile is 80 mm at model scale (equivalent to 4 m at prototype scale).

Also, to assess the influence of socket roughness on rock-socketed pile behavior, the model pile was machined with a sinusoidal surface (see Figure 1),

with an asperity amplitude and a wavelength of 0.8 mm and 10 mm, respectively (model scale).

To measure the axial load along the model pile, two optical fibres with corresponding fibre Bragg grating (FBG) sensors were used. Each optical fibre line has three FBG sensors (see Figure 1) bonded (via super glue and UV sensitive adhesive) to the internal surface of the aluminium model pile; these are labelled according to their distance from a 0 mm line (H) normalized by the model pile radius (i.e., H/R).

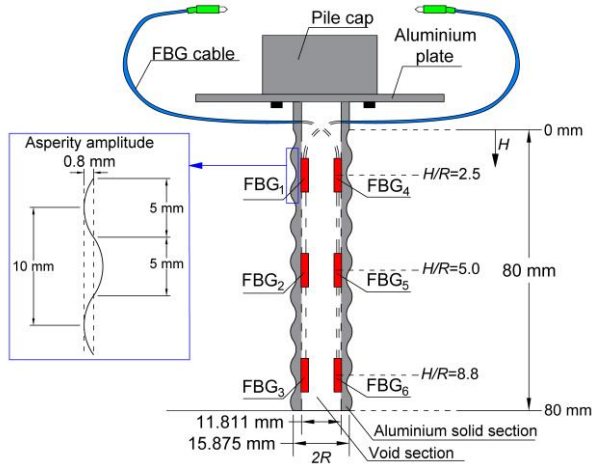


Figure 1. Aluminium model pile: schematic illustration of the geometric and instrumentation details.

2.2.2 Calibration of FBG sensors

The strain measured from FBG sensors is not necessarily equal to the strain of the aluminium pile (physical strain from the model pile is translated to the FBG via the super glue and UV sensitive adhesive), hence the FBG sensors need to be calibrated. The calibration procedures described by Song (2019) were adopted, where three uniaxial compression loading tests were carried out for each pile, so that the relationship between axial load along the pile (F_i) and shift in FBG wavelength ($\Delta\lambda_{FBG_i}$) can be obtained.

Figure 2 shows one of the calibration results. Each load increment was held for 15 s; the maximum axial load applied to the model piles was 4000 N, which is above the maximum axial load applied during the centrifuge tests (approximately 3600 N). The wavelength shift, as a function of the applied axial load, is shown in Figure 2; a linear relationship was obtained, so that the load-wavelength shift relationship can be described as:

$$F_i = K_{FBG_i} \Delta\lambda_{FBG_i} + \lambda_{OS_i} \quad (1)$$

where i is the FBG sensor number, F_i is the axial load recorded by the FBG_i sensor, K_{FBG_i} is the slope of the linear fitted line of Figure 2, $\Delta\lambda_{FBG_i}$ is

the wavelength shift for the FBG_i sensor, and λ_{OS_i} is its wavelength offset. Though there may be slight changes between the results among the calibration tests, the K_{FBG_i} is considered to be unique for each FBG sensor (FBG_i), so that its final value, employed to compute the axial load at the location of each FBG_i sensor during the centrifuge tests is taken as the average from the three calibration tests conducted for each FBG sensor.

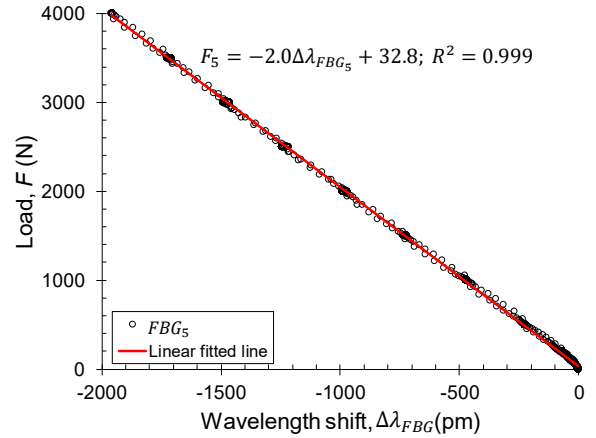


Figure 2. Example of calibration of FBG sensors conducted on the model pile for sensor FBG_5 : load-wavelength shift relationship.

2.3. Centrifuge model preparation

The centrifuge model (see Figure 3) was prepared by the following steps. A piece of soft polystyrene (length equal to the model pile diameter) was glued to the bottom of the model pile to eliminate base resistance. The pre-mixed pseudo-rock mixture was placed into a steel cylinder container, which is 20 cm in diameter and height. Then, the model pile was pushed into the mixture (just after pouring) and set to the designed position using a temporary support frame mounted to the top of the container. Finally, the container was stored and cured under high humidity condition for 44 days.

2.4. Centrifuge test

The centrifuge test was performed after 44-days of curing. The pseudo-rock container was placed on the centrifuge platform and steel plates (30 mm total thickness) were placed on the top of the pseudo-rock to induce (at 50-g) an external surcharge of 120 kPa to represent a 6 m soil stratum (with an average unit weight of 20 kN/m³), see Figure 4. Next, the loading system –i.e., the loading frame, two actuators, a load cell, and a connector– was installed and connected to the model pile. A single linear variable differential transformer (LVDT) was positioned on an aluminium plate located above the pile cap (see

Figure 4) to measure the model pile settlement. The axial force along the pile was obtained using the wavelength shift recorded at each FBG sensor. The acceleration of the centrifuge was gradually increased to 50-g and then the model pile was loaded axially with a displacement controlled procedure by the loading system (actuator rate of 0.1 mm/s).

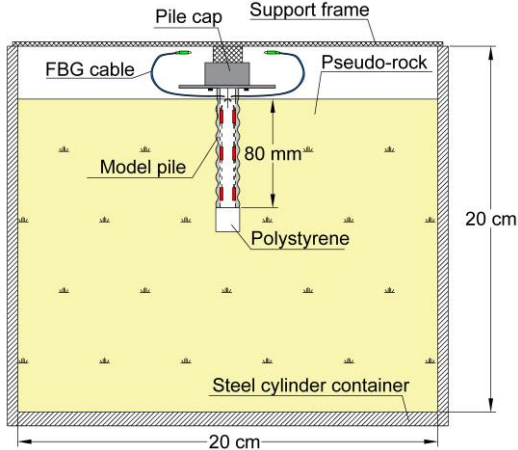


Figure 3. Drawing of the centrifuge model.

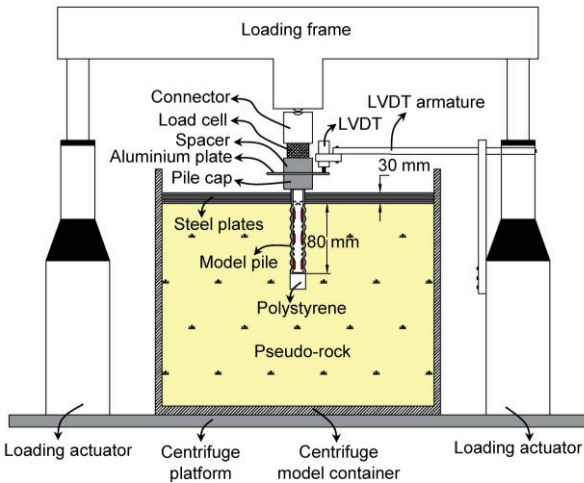


Figure 4. Centrifuge test set-up.

3 RESULTS AND DISCUSSION

3.1. Load-settlement response

The load-settlement curve from the centrifuge test conducted on a rough rock-socketed pile with the polystyrene base (i.e., considering shaft resistance only) is shown in Figure 5. The test was conducted until a limit pile head settlement (δ) of 25% of the pile diameter ($\delta/D = 25\%$) was reached. The results are presented at prototype scale.

As can be seen in Figure 5, the pile load capacity increased rapidly and almost linearly until the peak head load $F_{peak} = 8.85$ MN (and its corresponding pile head settlement, $\delta_{peak}/D = 6.6\%$) was reached. After this load threshold, a

40% gradual reduction of the pile load capacity at $\delta/D = 25\%$ is noted.

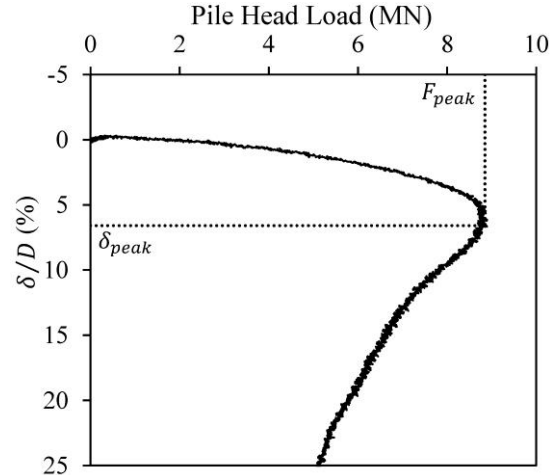


Figure 5. Load-settlement curve from the centrifuge test of a rough rock-socketed pile with a polystyrene base.

3.2. Shaft resistance-settlement response

Figure 6 shows the evolution of the mobilised average shaft resistance (f_{ave}) with settlement at different portions of the pile (referred to by the normalized depth H/R). The f_{ave} was computed as:

$$f_{ave} = \frac{F_i - F_{i+1}}{\pi D \Delta L} \quad (2)$$

where F_i and F_{i+1} are the mobilised axial loads at two consecutive locations (e.g. between the FBG sensors located at $H/R = 2.5$ and $H/R = 5.0$, see Figures 1 and 6 for reference), ΔL is the nominal length between the sensor locations, and D is the pile diameter.

Results show that the shaft resistance is first fully mobilised in the upper portion of the pile for a δ/D of 3%; as the applied load increases further, the f_{ave} decreases in the upper portion of the pile, and the full mobilization of f_{ave} in the lower portions of the pile occurs for a $\delta/D = \delta_{peak}/D$ of 6.6%. After such a threshold, a reduction of f_{ave} is noted. In addition, for lower pile head settlements ($\delta/D \leq 3\%$) much of the loads are concentrated around the front of the asperities located in the upper part of the pile; then, with increasing pile head settlement ($\delta/D > 3\%$), a damage at the rock-pile interface might occur, and the maximum values of f_{ave} shift downwards (towards the pile base), where, with further loading, a similar behaviour is observed. This experimental result is qualitatively congruous with the results of DEM^{3D} piles tests conducted on rough piles socketed in sanstone ($\sigma_c = 11.5$ MPa) by Gutiérrez-Ch et al. 2019b, in which the degradation of asperities and significant bond

breakages becomes more relevant in the front of the asperities for $\delta/D > 3\%$.

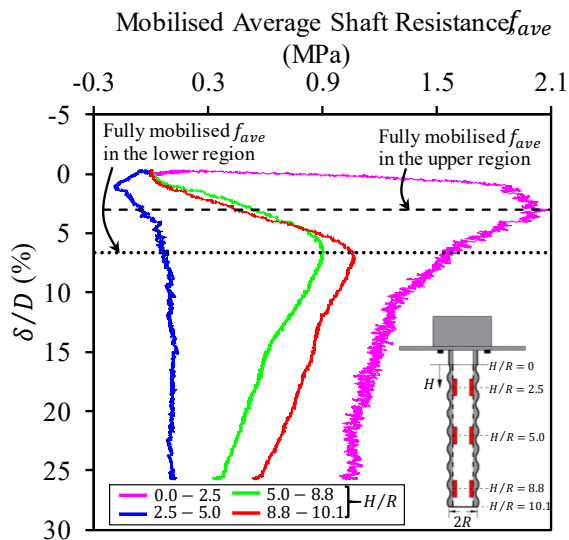


Figure 6. Mobilised average shaft resistance -settlement curves at different depths from the centrifuge test of a rough rock-socketed pile with a polystyrene base.

4 CONCLUSION

This paper presented a centrifuge test methodology to study the shaft resistance behaviour of an axially loaded rock-socketed pile considering socket roughness. To do that, an artificial soft rock made of a mixture of sand, cement, bentonite and water having $\sigma_c = 1.14$ MPa was employed. The model pile was machined from an aluminium tube with a sinusoidal surface, and instrumented with fibre Bragg grating (FBG) sensors to record the axial strains/loads along the pile. Results show that the methodology developed in this work can be employed to analyse the load- and shaft resistance-settlement response of a rock-socketed pile considering socket roughness, also providing interesting insight into the load transfer mechanisms.

5 ACKNOWLEDGEMENTS

This research was funded, in part, by the Spanish Ministry of Economy, Industry and Competitiveness under Project BIA 2015-69152-R. The first author was the recipient during 2019 of one Fellowship for PhD research provided by the José Entrecanales Ibarra Foundation. The support of both institutions is gratefully acknowledged.

6 REFERENCES

Gutiérrez-Ch, J.G., Senent, S., Melentijevic, S., and Jimenez, R. 2018. Distinct element method simulations of rock-concrete interfaces under different

boundary conditions. *Engineering Geology*, **240**: 123–139. <https://doi.org/10.1016/j.enggeo.2018.04.017>.

Gutiérrez-Ch, J.G., Melentijevic, S., Senent, S. and Jimenez, R. 2019a. DEM models to predict side shear resistance of rock-socketed piles considering socket roughness. *In Proceedings of the 53rd U.S. Rock Mechanics/Geomechanics Symposium*, New York City, New York, 23–26 June. ARMA 19–1757.

Gutiérrez-Ch, J.G., Melentijevic, S., Senent, S. and Jimenez, R. 2019b. DEM models to predict side shear resistance of rock-socketed piles considering socket roughness. *In Proceedings of the 1st Mediterranean Young Geotechnical Engineers Conference*, Mugla, Turkey, 23–24 September, pp. 47–54.

Horvath, R.G., Kenney, T.C. and Kozicki, P. 1983. Methods for improving the performance of drilled piers in weak rock. *Canadian Geotechnical Journal*, **20**(4): 758–772. <https://doi.org/10.1139/t83-081>.

Leung, C.F. and Ko, H-Y. 2001. Centrifuge model study of piles socketed in soft rock. *Japanese Society of Soil Mechanics and Foundation Engineering*, **33**(33): 88–91. https://doi.org/10.3208/sandf1972.33.3_80.

Nam, M.S. and Vipulanandan, C. 2008. Roughness and unit side resistances of drilled shafts socketed in clay shale and limestone. *Journal of Geotechnical and Geoenvironmental Engineering*, **134**(9): 1272–1279. [https://doi.org/10.1061/\(ASCE\)1090-0241\(2008\)134:9\(1272\)](https://doi.org/10.1061/(ASCE)1090-0241(2008)134:9(1272)).

O'Neill, M.W., Townsend, F.C., Hassan, K.M., Buller, A. and Chan, P. S. 1996. Load transfer for drilled shafts in intermediate geomaterials. U.S. Department of Transportation, FHWA-RD-95–172, Final Report.

Pells, P.J.N., Rowe, R.K. and Turner, R.M. 1980. An experimental investigation into shear for socketed piles in sandstone. *In Proceedings of the International Conference on Structural Foundations on Rock*, Sydney, Australia, 7-9 May 1980, pp. 291–302.

Rezazadeh, S. and Eslami, A. 2017. Empirical methods for determining shaft bearing capacity of semi-deep foundations socketed in rocks. *Journal of Rock Mechanics and Geotechnical Engineering*, **9**(6): 1140–1151. <https://doi.org/10.1016/j.jrmge.2017.06.003>.

Song, G. 2019. The use of protective structures to reduce tunnelling induced damage to buildings. Ph.D. thesis, Faculty of Engineering, University of Nottingham, UK.

Williams, A.F. 1980. The design and performance of piles socketed into weak rock. Ph.D. thesis, Monash University, Melbourne, Australia

Physical modelling of single-helix piles in sand using calibration chamber tests

Diego Moreira da Silva¹, Cristina de Hollanda Cavalcanti Tsuha¹

¹Department of Geotechnical Engineering, University of São Paulo, Brazil

Corresponding author: Cristina de Hollanda Cavalcanti Tsuha (chetsuha@sc.usp.br)

ABSTRACT: Large calibration chamber tests have been used in different studies to investigate pile performance under soil controlled conditions. For full scale field tests, pile and soil measurements are challenging and expensive; in addition, the field soil variability and the lack of information on soil characteristics are obstacles to make comparisons and evaluate geometrical effects on the pile response. Therefore, calibration chamber tests on model piles are particularly attractive to explore completely the some aspects of pile-soil interaction. The current paper presents a large calibration chamber constructed recently at the University of São Paulo (ESSC/USP) in Brazil to investigate the behaviour of helical piles in sand. The main aspects that will be studied using this equipment are: installation forces; effect of installation on the pile behaviour; pile uplift and compressive capacity; cyclic performance; effect of wing ratio and helix pitch on the pile performance and installation forces; stresses in the soil during pile installation, monotonic and cyclic loading; and effects of rotation speed and advance rate during installation. For this purpose, instrumented model piles of different configuration were fabricated. Some preliminary results of pile installation and loading tests are presented in this paper.

Keywords: Calibration Chamber; Physical Modelling; Helical Piles; Sand.

1 INTRODUCTION

Helical piles are widely used to resist tensile and compressive forces in transmission line towers, wind towers, solar panels, and other types of structures. More recently, they have been suggested for offshore applications (Byrne and Houlsby 2015, Spagnoli and Gavin 2015, Al-Baghdadi et al. 2015, Cerfontaine et al. 2019, etc.) due to the important uplift capacity provided by the anchor effect of the helix between other advantages. This type of pile is composed of one or more helical plate welded to a steel shaft. During installation, they are "screwed" into the ground by the application of torque on the shaft with a hydraulic motor (Figure 1), with a penetration rate of one pitch per revolution. The installation torque along the depth is registered during pile installation as a tool to control the pile capacity.

The current study aims to investigate the behaviour of helical piles in sand using calibration chamber modelling. In field tests, the soil conditions are normally not controlled, thus preventing the evaluation of the effects of some parameters on the problem investigated. Additionally, the soil instrumentation is not feasible in field studies, and only physical models in laboratory are able to explore completely some aspects of pile-soil response.

The performance of helical foundations have been studied using 1-g models tests by different authors (Clemence & Pepe 1984; Mooney et al. 1985; Narasimha Rao et al. 1989; Ghaly et al. 1991; etc.).

Due to some limitations of 1g-model tests (it is not adequate to study problems dependent on the confining stresses), this type of pile has also been investigated by different authors using centrifuge model tests (Levesque 2002, Tsuha 2007, Bian et al. 2008, Wang et al. 2010, Schiavon et al. 2017, Al-Baghdadi 2018).



Figure 1. Helical pile installation at the EESC-USP Campus.

Calibration chamber tests is another type of experimental technique used for tests on reduced scale models, in which the field stress condition can be reproduced in laboratory. Foray (1991) commented that this physical modelling technique can be used to study geotechnical axisymmetric

problems involving a high stress level, such as long offshore piles, anchors, nailing etc.

For calibration chamber tests, homogeneous soil samples can be prepared under different controlled boundary conditions. This physical modelling technique allows the use of sand samples under known and controlled stresses. A pressurized soil sample in a calibration chamber reproduces what occurs in a “portion” of soil at a given depth, (can simulate field overburden pressure). Therefore, tensile and compressive loading tests on a single-helix pile model in a calibration chamber can reproduce the helix bearing resistance at a particular depth in the field and the shaft resistance just above the helix, as illustrated in Figure 2.

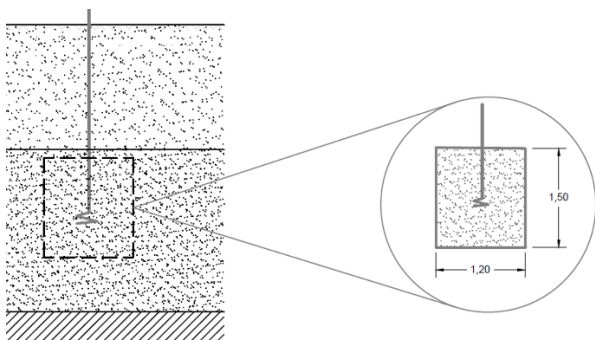


Figure 2. Simulation of the bottom section of a helical pile (Silva, 2020)

There are few studies on helical piles using calibration chamber tests. The first case is the work of Nagata & Hirata (2005). These authors performed installation and uplift tests on a helical pile model in a tank of dry sand under controlled confining pressure. These authors evaluated the shape of the failure zone and the magnitude of confining stresses action on this zone. Malik et al. (2017, 2019) investigated the end bearing capacity of a single-helix pile and the helix bending deflection in sand under controlled confining pressure. However, in these studies the pile was not installed by rotational driving reproducing the field installation procedure. Nagai et al. (2018) performed installation and uplift loading tests on a helical pile model in a calibration chamber. They tested different pile installation methods, and evaluated the helix bearing capacity under tensile loading considering the change in earth pressure at the pile tip.

The large calibration chamber of the ESSC/USP, presented in this paper, was constructed to investigate the effect of pile geometry on the installation forces, and the performance of helical piles under monotonic and cyclic tensile and compressive loading. The aim of the chamber is to simulate the field stresses condition of the surrounding soil of a helical pile in sand. For this

research, nine different instrumented model piles were fabricated to be installed and tested in dry dense sand prepared by air pluviation technique. For the tests, soil stress sensors are placed in the sand mass to measure the variation of the stresses in the soil during pile installation and under loading. Some preliminary results of this study are presented in this paper.

2 CALIBRATION CHAMBER TESTS

The EESC/USP calibration chamber is composed of: i) a steel tank with a top cover; ii) a rubber pressurised membrane; iii) air pluviation system; iv) installation and reaction structures.

2.1. EESC/USP calibration chamber

2.1.1 Steel tank

The dimensions of the calibration chamber for the study on helical foundations were calculated based on the results of numerical simulations (Silva 2020) and on the findings on boundary effects in calibration chamber tests available in the literature. The calibration chamber constructed consists of a steel tank with 25.4mm thickness, 1.50 m high and 1.20 m diameter. The bottom of the tank was installed 2 meters below the ground surface at the Experimental Foundation Site of the University of Sao Paulo at Sao Carlos, Brazil. Figure 3 shows the tank and the top cover of the chamber.



Figure 3. Steel tank and top cover.

2.1.2 Pressurised membrane

For the calibration chamber tests, a pressurised rubber membrane (Figure 4) with a central hole of 50 mm diameter (to allow the penetration of the model pile in the pressurised soil inside the chamber) is installed between the sand sample surface and the top cover to apply a controlled pressure on the soil sample in the tank. A latex rubber sheet was also placed along the rigid walls of the chamber lubricated with grease.

The upper membrane is filled with compressed air to simulate different vertical stress conditions on the

soil sample. For example, an applied pressure of 100 kPa can reproduce the helix bearing resistance of a helical pile installed at a depth of approximately 6m in dry dense sand.

2.1.3 Pile installation system

The installation system are connected to the tank cover during installation. After the soil sample preparation, the model pile is installed using a particular device to ensure a pile penetration rate into the soil sample of one pitch per revolution. As shown in Figure 5, a threaded bar (and nut) with the same pitch of the pile helix is connected to the pile shaft to control the penetration rate during installation.



Figure 4. Pressurised rubber membrane.

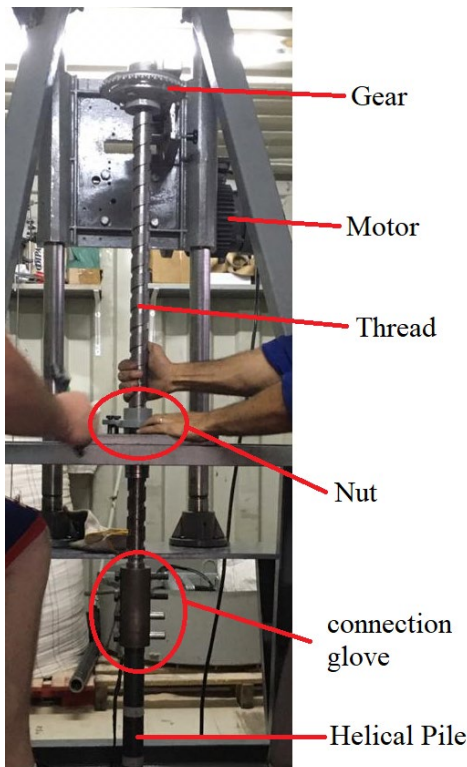


Figure 5. Model pile installation.

2.2. Experimental programme

2.2.1 Soil sample preparation

The dry sand specimens for this study are prepared in the chamber tank by air pluviation technique as illustrated in Figure 6. The characteristics of the silica sand of Analândia used in this study are presented in Table 1. The sample density shown in this table is the average value obtained from ten calibrated boxes placed in the tank at different positions during the preparation of the soil.

Table 1. Sand properties

Specific gravity of the sand	G_s	2.67
Maximum dry density (kg/m^3)	$\rho_d(\text{max})$	1794
Minimum dry density (kg/m^3)	$\rho_d(\text{min})$	1463
Sand sample average dry density	ρ_d	1784
Average grain-size (mm)	d_{50}	0.18
Coefficient of uniformity	C_u	1.73



Figure 6. Sand pluviation system.

After the chamber tank is filled, the bottom part of the model pile is placed on the soil sample before the installation of the pressurised membrane. The diameter of central hole of the membrane is smaller than the helix diameter of the model piles; therefore, the pile tip (helix) is placed under the membrane before pile installation. After that, the chamber is carefully closed.

2.2.2 Soil stress sensors

Pile-soil interactions are governed by the stress field induced by the pile installation process. Therefore, for a better understanding of the installation forces and failure mechanisms of helical piles, six soil stress sensors are placed (vertically or horizontally)

in the soil samples at different depths. These sensors are also installed to check the initial vertical stresses in the soil when the vertical pressure is applied by the rubber membrane. The stress sensors used for this study were fabricated by the Geoinstrumentos, with diameter of 20 mm and 7 mm thickness (Figure 7).



Figure 7. Soil stress sensors.

2.2.3 Helical pile models

For this research, nine different instrumented model piles (Table 2) with 1.5 m length were fabricated to be installed and tested in dry dense sand. The steel pipe (shaft) diameter of all model piles is 42.2 mm with a 9 mm-thick wall, and the thickness of the helices is 6.4 mm ($\frac{1}{4}$ ”).

Figure 8 illustrates three model piles with helix pitch of 40mm (P4, P5, and P6). The preliminary test presented in this paper was carried out on the pile model P4 (helix diameter of 84.4 mm and pitch of 40 mm).

Table 2. Dimensions of the model piles (Silva, 2020).

Type	Helix diameter D (mm)	Shaft diameter (d)	D/d ratio	Pitch (mm)
P1	84.4	42.2	2	30
P2	126.6	42.2	3	30
P3	168.8	42.2	4	30
P4	84.4	42.2	2	40
P5	126.6	42.2	3	40
P6	168.8	42.2	4	40
P7	84.4	42.2	2	50
P8	126.6	42.2	3	50
P9	168.8	42.2	4	50

Strain gages were installed at the pile surface of all model piles to measure the axial forces and installation torque acting on the shaft at 20 mm above the helix (Figure 9). For the mechanical protection of the strain gages during installation, a cold solder paste (Plasteel) was used (Figure 9b).

2.2.4 Helical pile installation

For the model pile installation, a reaction frame system (Figure 10) is connected to the top cover of the calibration chamber. An electric motor coupled laterally to a reducer apply the torque to the top of the helical pile as shown in Figure 5. The motor rotates the thread bar, which is coupled to the top of the pile with a "connection glove". When the helix reaches 1.0 m depth below the soil surface, the installation is stopped. After that, the system illustrated in Figure 10 is removed, and another reaction frame system is connected to the top cover for the pile loading tests.



Figure 8. Instrumented helical pile models with helix pitch of 40 mm (Silva, 2020)

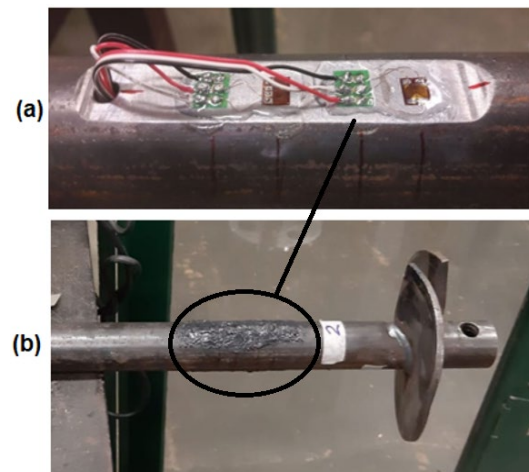


Figure 9. (a) Strain gages and (b) Mechanical protection of the strain gages.

2.2.5 Pile loading tests

For the model tests, the load is applied by a hydraulic jack attached to a test frame (for tensile and compressive loading) as illustrated in Figure 11. During the loading tests, the load at the pile head was recorded using a digital load cell, and the head displacement were measured using two supported dial gauges (Figure 11).



Figure 10. Reaction frame for pile installation.



Figure 11. Tensile and compressive loading tests.

3 RESULTS AND DISCUSSION

Some preliminary results of the first test performed using the EESC/USP calibration chamber are presented in this section. For the first test, an applied

pressure of 100 kPa was used. Figure 12 shows the results of measured torque obtained by the instrumentation installed just above the pile helix. As the bottom part of the pile is placed in the soil sample before the pile installation, the values of torque were registered after a tip depth penetration of approximately 300 mm.

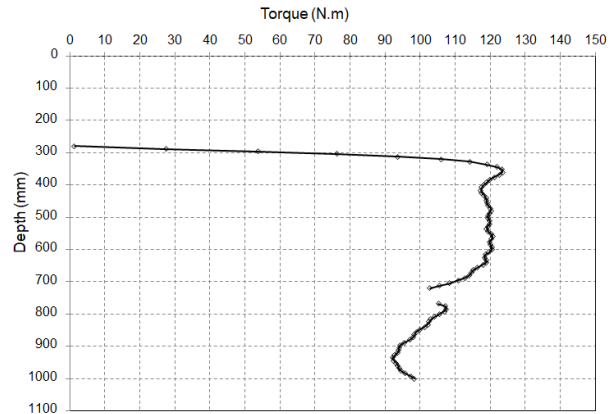


Figure 12. Installation torque measured just above the helix during the model pile installation.

Figure 12 illustrates a peak value obtained in the beginning of installation that decreases along the depth. During the model pile installation, the soil sample becomes disturbed, and the torque value is reduced during the penetration.

For this first test, a soil stress sensor registered the variation of the vertical stress in the soil at the depth of 1.25 m (the sensor was placed at 250 mm below the final embedment depth of the pile, and 300 mm distant from the pile center). The sensor results are presented in Figure 13.

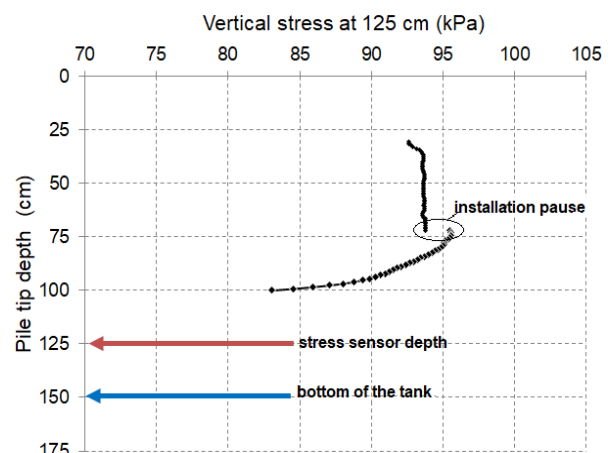


Figure 13. Variation of vertical stress measured by the sensor installed at the soil depth of 1.25m during pile installation.

The results shown in Figure 13 illustrates that before pile installation the vertical pressure at the 1.25 m was approximately 94 kPa. When the pile tip reached a depth of 0.75 m, the installation was stopped for few minutes. After the pause, the

installation starts again, and for a tip penetration between 75 cm and 100 cm (final depth) the vertical pressure at 1.25 m was reduced from around 95 kPa to 83 kPa. This observation indicates that the vertical stresses on the soil below the helix decreases when the helix approaches. These results obtained by the soil stress sensor can explain the reduction of installation torque with the depth observed in Figure 12. However, more tests are necessary to confirm this finding.

After installation, a tensile pile load test was carried out on the model pile. Figure 14 presents the vertical load x displacement curve of the uplift test. From the results of the instrumentation of the model pile just above the helix it could be separated the fraction of uplift capacity related to the helix bearing from the shaft resistance. Although the helix diameter of the pile tested has only 84.4 mm (two times the shaft diameter) the helix bearing is 88% of the total uplift capacity (Figure 14). This finding illustrates the advantage of the anchor effect of helical piles.

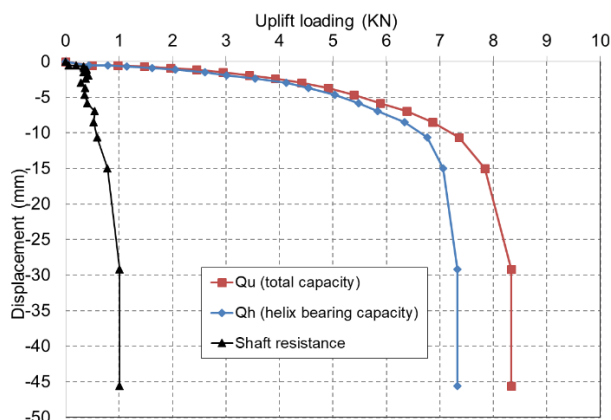


Figure 14. Uplift loading x displacement curve.

4 CONCLUSION

The current paper describes the EESC/USP calibration chamber, constructed recently at the University of São Paulo to investigate the performance of helical piles, and presents some preliminary results. The outcomes of this study should clarify some fundamental aspects for the understanding of the helical pile behaviour.

5 ACKNOWLEDGEMENTS

The authors would like to thank Vértice Engenharia, and the National Council for Scientific and Technological Development - CNPQ (Process 425770/2016-8 and 310881/2018-8), and for granting the doctoral scholarship of the first author.

6 REFERENCES

- Al-Baghdadi, T.A., Brown, M.J., Knappett, J.A., Ishikura, R. 2015. Modelling of laterally loaded screw piles with large helical plates in sand. In Meyer, V. (Ed.), *Frontiers in Offshore Geotechnics III*, Taylor & Francis Group, London, pp. 503-508.
- Al-Baghdadi, T. 2018. *Screw piles as offshore foundations: Numerical and physical modelling* (Doctoral dissertation, University of Dundee).
- Byrne, B. W., Houlby, G.T. 2015. Helical piles: An innovative foundation design option for offshore wind turbines. *Phil. Trans. R. Soc. A* **373**(2035). doi:10.1098/rsta.2014.0080.
- Cerfontaine, B., Knappett, J. A., Brown, M. J., Davidson, C., Sharif, Y. 2019. Screw pile design optimisation under tension in sand. *Proceedings of the XVII ECSMGE-2019 - Geotechnical Engineering foundation of the future*, doi: 10.32075/17ECSMGE-2019-069
- Clemence, S. P. & Pepe, F. D., Jr. 1984. Measurement of Lat-eral Stress Around Multihelix Anchors in Sand, *Geotech-nical Testing Journal* **7**(3): 145-152.
- Foray, P., 1991 "Scale and Boundary Effects on Calibration Chamber Pile Test", in *Calibration Chamber Testing*, pp. 147-160.
- Ghaly, A., Hanna, A. & Hanna, M. 1991. Uplift behavior of screw anchors in sand. I: dry sand. *Journal of Geotechnical Engineering* **117**(5): 773-793.
- Levesque, C. L. 2002. *Centrifuge modelling of helical anchors in sand*. Thesis M.Sc.E., University of New Brunswick, Canada.
- Malik, A. A., Kuwano, J., Tachibana, S., Maejima, T. 2017. End bearing capacity comparison of screw pile with straight pipe pile under similar ground conditions. *Acta Geotechnica*, **12**(2), 415-428.
- Malik, A. A., Kuwano, J., Tachibana, S., & Maejima, T. 2019. Effect of helix bending deflection on load settlement behaviour of screw pile. *Acta Geotechnica*, **14**(5), 1527-1543.
- Mooney, J.S., Adamczak, S., Clemence, S.P. 1985. Uplift capacity of helical anchors in clay and silt. In *Uplift behavior of anchor foundations in soil*: 48-72. ASCE.
- Nagai, H., Tsuchiya, T., & Shimada, M. (2018). Influence of installation method on performance of screwed pile and evaluation of pulling resistance. *Soils and Foundations*, **58**(2), 355-369.
- Nagata, M. & Hirata, H. 2005. Study on uplift resistance of screwed pile. *Nippon Steel Technical Report*, (92), 73-78.

- Narasimha Rao, S.N., Prasad, Y.V., Shetty, M.D. & Joshi, V.V. 1989. Uplift capacity of screw pile anchors. *Geotechnical Engineering* **20**(2): 139-159.
- Silva, D. M. 2020. Behaviour of helical anchors subjected to cyclic loadings. Doctoral Thesis (In preparation), São Carlos school of Engineering, University of São Paulo, São Carlos.
- Spagnoli, G., Gavin, K. 2015. Helical Piles as a Novel Foundation System for Offshore Piled Facilities. In Abu Dhabi International Petroleum Exhibition and Conference, 9-12 November, Abu Dhabi, UAE, <https://doi.org/10.2118/177604-MS>
- Schiavon J.A., Tsuha, C.H.C., Thorel, L. 2017. Cyclic and post-cyclic monotonic response of a single-helix anchor in sand. *Géotechnique Letters* **7**(1): 11-17.
- Tsuha, C.H.C. 2007. Theoretical model to control on site the uplift capacity of helical screw piles embedded in sandy soil. Ph.D. thesis, Department of Geotechnics, São Carlos School of Engineering, University of São Paulo, São Carlos, Brazil. [In Portuguese.]
- Wang, D., Merifield, R.S., Gaudin, C., Hu, Y. 2010. Centri-fuge model tests of helical anchors in clay. In Proceedings of the 7th International Conference on Physical Modelling in Geotechnics, Zurich, Switzerland, pp. 1069–1074.

Study on the installation effect of helical piles in very dense sand

José Antonio Schiavon¹, Cristina de Hollanda Cavalcanti Tsuha², Luc Thorel³

¹Civil Engineering Division, Aeronautics Institute of Technology, Brazil

²Department of Geotechnical Engineering, University of São Paulo, Brazil

³GMG Laboratory, GERS Department, Gustave Eiffel University, France

Corresponding author: José Antonio Schiavon (schiavon@ita.br)

ABSTRACT: The increasing interest on the use of helical piles to support offshore facilities has motivated the development of researches on this type of foundation. Literature presents some studies on helical piles in dense sand that disregard the effects that pile installation could cause on soil as a “wished-in-place” condition is considered. Normally this condition is adopted because of the difficulty in reproducing the pile installation according to the in-situ procedure. However, some previous studies have shown that the failure mechanism in uplift is controlled by the disturbed-non disturbed condition of the soil around the pile, mainly for dense sand condition. On the other hand, the literature also brings some studies arguing that the pile installation little influences both failure mechanism and uplift performance. Therefore, the current study uses results of centrifuge modelling to compare the monotonic uplift performance of single-helix piles in very dense sand installed via two different procedures: i) by placing the model pile during sand bed pluviation, which intends to avoid any soil disturbance (“wished-in-place” condition) and; ii) by screwing the model pile in flight with torque and downward crowd force applied simultaneously. The results show that the model pile installed in flight showed uplift capacity at least 60% greater than the “wished-in-place” model pile, also accompanied by a greater axial stiffness. The unexpected poorer performance of the “wished-in-place” model piles suggests that the model may have acted as an obstacle for the sand grains during pluviation, which resulted in density variation of the sand around the model and, consequently, provided lower uplift capacity compared to the in-flight installation case.

Keywords: Helical Piles; Sand; Soil Disturbance; Installation Procedure, Centrifuge Modelling.

1 INTRODUCTION

Because of the increasing interest on the use of helical piles in both onshore and offshore structures, many questions and issues have been raised. In this scenario, centrifuge modelling has been an important tool for the study of helical piles since it allows for parametric studies reproducing the same field of forces and mass in a full-scale structure with closely controlled test conditions (Garnier, 2001). However, reliable simulations of the pile behaviour depend on replicating the in-situ soil conditions (e.g. deposition process, stress history) and the pile installation procedure, in addition to avoiding scale effects.

Helical piles are installed by screwing it into the ground usually using a hydraulic motor attached to a backhoe loader or a rotary rig equipment. Consequently, the soil penetrated by the pile experiences displacement and shearing, which can cause changes in the soil around the pile. Based on a simulation via Discrete Element Modeling, Sharif *et al.* (2019) noted that pile installation modifies the sand density close to the pile, with the relative density (D_r) changing from 80% to 55%.

In centrifuge tests with single and multi-helix model piles in sand, Tsuha *et al.* (2012) observed that the contribution of the upper helices to the uplift

capacity is less important in dense sand than in loose sand. This finding suggests that, in addition to the interaction between helices (Hao *et al.* 2019), the difference in compactness is considerable if the dense sand is traversed by a helix one, two or three times. However, for loose sand, the penetration of the lower helix shall loosen totally the sand inside the cylinder circumscribed the helix. As a result, the sand above all the helices present equivalent sand disturbance and, consequently, similar compactness. The above observations highlight the importance of reproducing the prototype installation to replicate the disturbance caused on dense sands.

Gavin *et al.* (2014) reported full-scale load tests on single-helix piles in dense sand and analysed the results using Finite Element (FE) Modelling. Under compressive loading, the numerical simulation showed very good agreement with the experimental result in terms of load-displacement response. Under uplift loading, in contrast, the numerical simulation overpredicted both axial stiffness and uplift resistance. According to the cited authors, the parameters of sand used in the FE model derived from triaxial compression tests and, therefore, provided a very good prediction in compressive loading. In this case, the soil below the helix, which controls the pile response, is relatively unaffected



Figure 1. Helical pile models

by the installation. For the uplift case, however, the sand above the helix experience disturbance during installation. Consequently, the parameters from the triaxial tests with undisturbed samples are not suitable to be assigned for the disturbed sand above the helix.

The hypothesis by Gavin *et al.* (2014) was investigated in the study of Pérez *et al.* (2017) that showed that assigning modified values for the parameters of disturbed soil can provide good agreement with experimental results. In contrast, when the installation effect is neglected and undisturbed sand parameters are considered, the uplift capacity is overpredicted.

The testing campaign reported here was designed to evaluate the installation effect on the sand condition and, consequently, on the uplift load-displacement response of the single-helix model piles. To isolate the installation effect, the model piles were installed via two different procedures and then tested in uplift loading. At first, the model piles under “wished-in-place” condition (no installation effect) were expected to exhibit larger ultimate load compared to the model piles installed simulating the *in-situ* procedure. However, the results have shown the opposite. Therefore, the current paper aims to discuss the experimental procedure and results to contribute to future experiments.

2 MATERIALS AND METHODS

The centrifuge testing conducted for the current study was undertaken using the IFSTTAR geo-centrifuge. Different g-levels for three single-helix pile models of different sizes were used to simulate the same prototype. In addition to the comparison of two different installation procedures, the use of different model sizes aimed to ensure the non-occurrence of scale effects.

2.1. Model piles

The current tests simulated a single-helix pile prototype with a helix diameter $D = 330$ mm, a shaft diameter $d = 100$ mm, and installed with a helix depth $H = 8D$. Helix and shaft diameters were established to provide a helix-to-shaft diameter ratio (D/d) equals to 3.3, which is a common value for

helical piles used for onshore structures.

The helical pile models consist of a single helical plate welded to the tip of a round rod, both steel fabricated (Fig. 1). Table 1 presents the dimensions of the three model piles. Both pitch (p) and thickness (t_h) of the helical plates are not scaled according to the dimensions of the same prototype. The model HP1 was used in previous research conducted in the same laboratory (Tsuha, 2007), and the other two models were fabricated later for the research of which the present study is part (Schiavon, 2016).

2.2. Sand bed

The sand used in the experiments is the HN38 fraction of Hostun sand, which is a very fine and uniform silica sand extracted from deposits located in the commune of Hostun, France. Table 2 presents some characteristics of the Hostun sand. The model piles were tested in dry sand beds reconstituted by means of the raining deposition technique, in which dry sand is placed in an automatic hopper and pours through a slot to produce a uniform sand rain over a container.

Table 1. Dimensions of helical pile models.

Model pile	D (mm)	d (mm)	p (mm)	t_h (mm)
HP1	20.0	6.0	1.6	0.5
HP2	26.6	8.0	1.4	0.8
HP3	33.0	10.0	1.5	1.8

Table 2. Characteristics of HN38 Hostun sand.

Parameter	Unit	Value
Specific gravity of particles, G_s	-	2.64
Maximum dry density, $\rho_{d(max)}$	kg/m ³	1554
Minimum dry density, $\rho_{d(min)}$	kg/m ³	1186
Average grain size, d_{50}	mm	0.12
Coefficient of uniformity, C_U	-	1.97
Angle of friction*, ϕ	deg.	47

*from triaxial tests with D_r between 90% and 95% and confining stresses of 50 kPa, 100 kPa and 200 kPa.

The hopper moves into roundtrips while the sand deposits on the container bottom. Hopper horizontal speed and slot width are the parameters set to

control the drop height and the flow rate of sand. The pluviation process is known for providing homogenous specimens and good repeatability (Garnier, 2001; K us, 1992; Miura and Toki, 1982).

The final dimensions of the sand bed are 1200 mm in length, 800 mm in width and 360 mm in depth. To assess the achieved density, at least two density pots were placed on the container bottom. The average relative density (D_r) of sand beds resulting from sand raining ranged from 95% to 99%.

2.3. Installation and testing of model piles

Two different procedures were followed to install the model piles at an embedment ratio $H/D = 8$ (where H is the helix embedment depth), which is expected to provide an intermediate behaviour between shallow and deep anchor (P erez *et al.* 2017). The first procedure consisted of pausing the pluviation, positioning the model piles on the sand bed surface, and then recommencing the pluviation (Fig. 2). The use of this procedure aimed to evaluate the performance of the model piles in a sand bed unaffected by the model pile installation, which is recognised here as the “wished-in-place” (WIP) condition. Two nylon threads were used passing laterally the top of each model pile to ensure verticality. Figure 2 shows the positioning of models during the pluviation. The whole procedure is carried out at $1\times g$ outside the centrifuge.

The second procedure is similar to that reported in current authors’ previous studies (e.g. Tsuha and Aoki, 2010; Schiavon *et al.*, 2016). In this procedure, the model anchors are screwed into the sand bed similarly to field practice (SCR condition). The vertical feed rate corresponds to 1 helix pitch per revolution, with a rotating rate of 5.3 rpm (0.56 rad/s). The whole procedure is carried out under macro-gravity (in flight).

In both procedures, a minimum centre-to-centre spacing of $10D$ was kept between model piles.

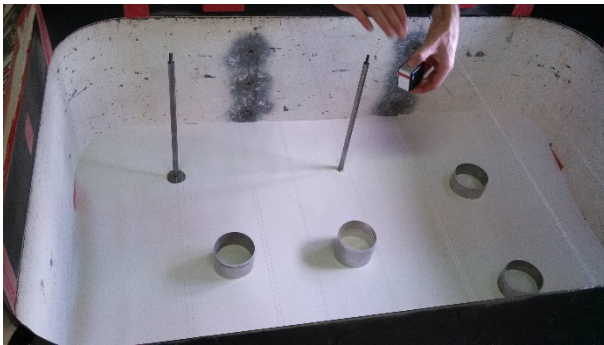


Figure 2. Sand bed preparation for WIP condition.

Before the first test in the container, three cycles of centrifugation taking three minutes each were conducted up to the maximum g-level the

container was expected to be subjected. The vertical displacement rate for pull-out tests was 0.3 mm/s at model scale.

3 RESULTS AND DISCUSSION

Figures 3 to 5 present the load-displacement response, at prototype scale, for the monotonic uplift tests with models under condition “wished-in-place” (WIP) and screwed into the sand bed in flight (SCR).

Since the use of WIP condition intended to avoid any soil disturbance caused by the model pile installation, both axial stiffness and ultimate load were expected to be larger than those obtained with the SCR condition. However, regardless the anomalous behaviour observed for the 8FH SCR test with uplift displacement between 5 and 20 mm (Fig. 4), the model piles exhibited lower stiffness for the WIP condition.

Moreover, the WIP condition resulted in significantly lower ultimate uplift load (Q_{ult}) compared to the SCR condition. The values of Q_{ult} for the WIP condition are respectively 63%, 65% and 40% lower than those of SCR condition.

Table 3 summarises the results of the monotonic uplift tests. The larger values of Q_{ult} for HP3 WIP and HP1 SCR are likely due to sand bed heterogeneity, and not necessarily scale effect since no trend with increasing size can be identified. Despite the dispersion, the results indicate a tendency of WIP condition to provide lower ultimate load and stiffness in monotonic uplift tests compared to the SCR condition.

The unexpected lower axial stiffness and ultimate load for the WIP tests may be due to possible local changes in density around the pile resulting from “umbrella” effects (Hao *et al.*, 2019). Similar effect on density is observed in the vicinity of the container walls, where the sand bed is less dense compared with the central zone of the container.

Ternet (1999) verified inhomogenous zones in the periphery of sand beds reconstituted via sand

Table 3. Results of uplift model tests (prototype scale).

Test	Cont. No.	$D_{r, avg}$ (%)	H/D	Q_{ult} (kN)	$U_{(peak)}$ (mm)
HP1 WIP	1	95	8	38.5	45.9
HP1 SCR	4	99	8	104.5	49.7
HP2 WIP	1	95	8	31.4	51.2
HP2 SCR	2	96	8	89.3	99.4
HP3 WIP	1	95	8	55.8	52.6
HP3 SCR	3	96	8	88.0	63.9

raining in containers similar to those of the current study. In addition to the action of air vortices on the falling grains, the sand deposition with reduced

kinetic energy in those zones results from the collision of grains with the container walls.

In the current work, however, no wind vortex is assumed to occur near the model piles because the tests were carried out in a zone free from boundary effects on the sand deposition. Therefore, the model piles may be acted as an obstacle for the falling grains that collide with the pile top and side.

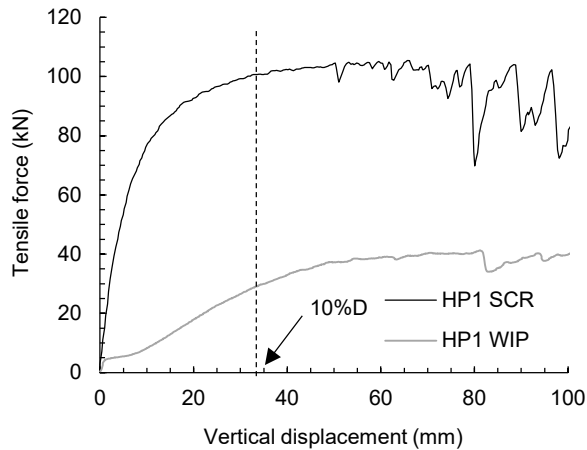


Figure 3. Load-displacement responses for HP1 model.

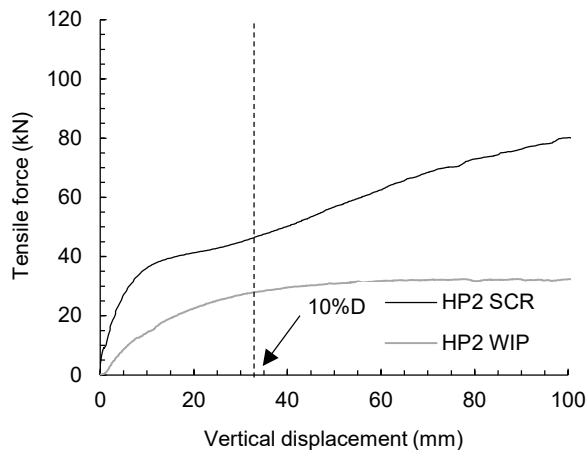


Figure 4. Load-displacement responses for HP2 model.

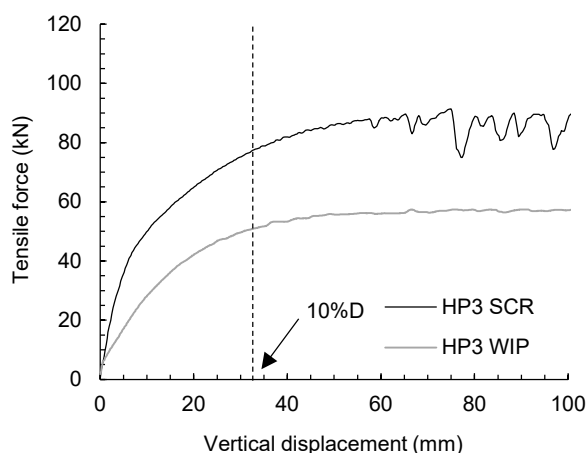


Figure 5. Load-displacement responses for HP3 model.

After collision, the sand grains lose kinetic energy and change direction. Consequently, the sand grains

are deposited in a less dense assembly than the rest of the sand bed. In addition, a small amount of sand grains can remain deposited in a loose state on top of the model pile, which can further reduce the kinetic energy of falling grains.

Figure 6 shows photos from a quick experiment conducted with fine silica sand and a threaded rod with 9.3 mm in diameter. Sand rain was simulated similarly to the procedure described in Miura and Toki (1982), but with no volume control of rain flow. The sand rain was recorded in slow motion video aiming to observe the movement of grains after colliding with the rod. The figure shows that significant change of direction occurs for the grains colliding with the rod. In addition to the loss of kinetic energy with the collision with the rod, deflected grains can strike other free falling grains (with no previous collision) and, thus, cause a chain of collision events, which will result in a broader effect of deposition with reduced energy.

For investigations considering the “wished-in-place” condition using sand pluviation for the sand bed preparation, “umbrella” effect could be minimised by dividing the pile shaft into extension segments and attaching them to the pile composition each time the sand bed height reaches the targeted location for the next segment. This procedure was conducted in the study of Hao *et al.* (2019) with single and multi-helix pile models in sand. The above-mentioned procedure can minimise but not eliminate variations on sand density, since short shaft segment extensions can also cause “umbrella” effects. Alternatively, when the sand deposition via pluviation is not a requirement for the WIP condition, the sand bed could be prepared with compaction, vibration or a combination of both.

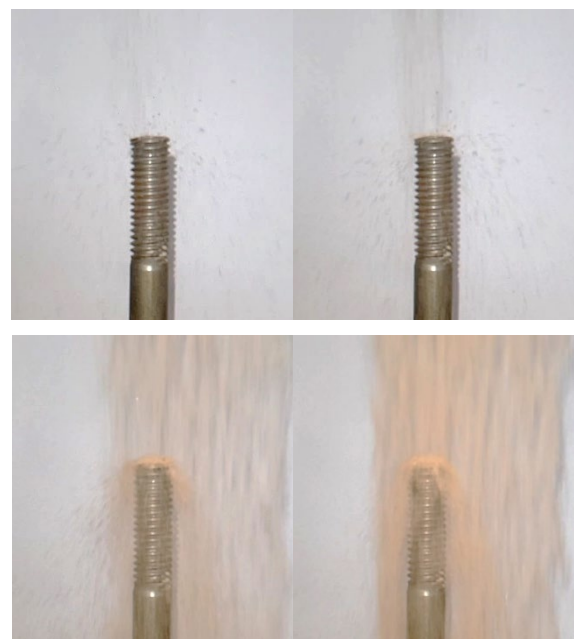


Figure 6. Pluviation of fine sand over a rod.

3.1. Comparison with numerical simulations

A Finite Element modelling in axisymmetric condition was conducted to simulate the helical pile as a “wished-in-place” element. Two different set of characteristics for the sand mass were considered in order to compare numerical and experimental results. The characteristics assigned for pile and sand are listed in Table 4.

Table 4. Sand parameters for numerical simulations.

Sand parameter	FE model 1	FE model 2
γ (kN/m ³)	15.3	15.3
E_{50}^{ref} (kPa)	5.0×10^4	2.2×10^4
E_{oed}^{ref} (kPa)	2.6×10^4	2.0×10^4
E_{ur}^{ref} (kPa)	1.0×10^5	6.0×10^4
m	0.5	0.5
ν_{ur}	0.2	0.2
p^{ref} (kPa)	100	100
K_0^{NC}	0.32	0.5
R_f	0.9	0.9
c_{ref} (kPa)	1.0	1.0
ϕ (deg.)	47	30
ψ (deg.)	17	1

where, E_{50}^{ref} = secant stiffness in standard drained triaxial test, E_{oed}^{ref} , tangent stiffness for primary oedometer loading, m = power for stress-level dependency of stiffness, E_{ur}^{ref} = unloading/reloading stiffness, ν_{ur} = Poisson's ratio for unloading-reloading, p^{ref} = reference stress for stiffnesses, K_0^{NC} = coefficient of earth pressure at rest for normal consolidation, R_f = failure ratio.

The constitutive model used for the sand was the Hardening Soil Model, HS-soil (Schanz *et al.*, 1999). The FE model 1 uses the parameters for the undisturbed HN38 Hostun sand, as listed in Table 1. The sand parameters for the FE model 2 were determined through a parametric study searching for a pile load-displacement response with reasonable agreement with those from the WIP tests. The simulation of these two conditions aimed to demonstrate the difference between the values of parameters if an undisturbed condition (FE model 1) were in fact achieved.

The pile element was modelled as linear-elastic material having Young's modulus $E = 2.0 \times 10^8$ kPa and Poisson's ratio $\nu = 0.3$. Interface elements were assigned to the pile-sand interface with interface angle of friction $\delta = 20$ deg. in both FE models.

Both sand and pile were modelled with 15-node solid elements. Meshing update technique was used to avoid excessive mesh distortion.

Figure 7 compares the experimental results in WIP condition with the numerical ones. The FE model 1 resulted an uplift resistance significantly larger than the 6 experimental tests. On the other

hand, good agreement with experimental results was obtained when the sand parameters corresponded to the constant-volume shearing condition (FE model 2), which may be compared to the loose state of sands.

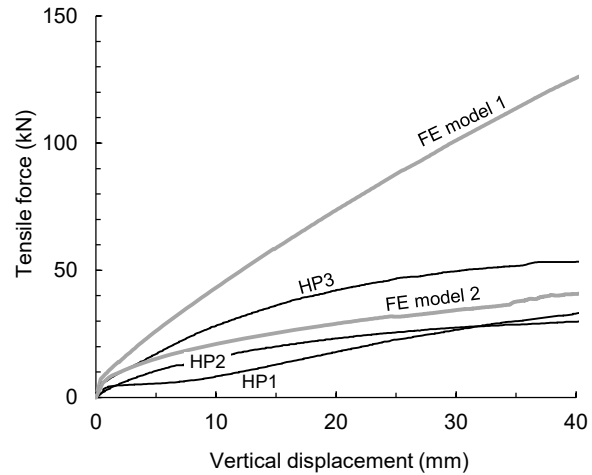


Figure 7. Load-displacement responses from numerical and experimental tests with WIP condition.

4 CONCLUSION

The current study intended to investigate the installation effects of helical pile models in very dense sand. Model piles were subjected to uplift loading in centrifuge after being installed during the sand bed preparation (“wished-in-place” condition – avoiding installation effects) or installed in flight by screwing it into the sand bed.

The pile models at “wished-in-place” condition exhibited lower ultimate uplift load, which at first could lead to the conclusion that the screwing process causes strength increase of the soil around the pile. This is not the case. The model piles positioned on the surface of the sand bed during pluviation (WIP condition) caused umbrella effects on the sand deposition around the models. As a result, local soil density variation occurred in the sand.

The findings emphasize the importance of the sample preparation to reproduce the intended test condition and, thus, avoid misinterpretation of results.

5 ACKNOWLEDGEMENTS

The authors would like to thank WEAMEC (Projects REDENV-EOL and JE-CORECT), the Pays de la Loire Region, Nantes Metropole, CARENE, Coordenação de Aperfeiçoamento de Pessoal de Nível Superior - Brazil (Finance Code 001) and USP-COFECUB Project (Grant No. UcMa 132/12) for their financial support, which enabled the study to be carried out. Special thanks go to the Gustave Eiffel University centrifuge team for their

technical support and assistance during these experimental campaigns.

6 REFERENCES

- Garnier, J. 2001. Physical models in geotechnics: state of the art and recent advances (1st Coulomb Lecture). In Proceedings of the Caquot Conference, Paris, France. Presses de l'Ecole Nationale des Ponts et Chaussées, Paris, pp. 1-59.
- Gavin, K., Doherty, P. and Tolooiyan, A. 2014. Field investigation of the axial resistance of helical piles in dense sand. *Canadian Geotechnical Journal*, **51**(11): 1343-1354.
- Hao, D., Wang, D., O'Loughlin, C.D. and Gaudin, C. 2019. Tensile monotonic capacity of helical anchors in sand: interaction between helices. *Canadian Geotechnical Journal*, **56**(10): 1534-1543.
- Küs, B. 1992. Pluviation des sables. DEA report, Université de Nantes, Nantes, France (in French).
- Miura, S. and Toki, S. 1982. A sample preparation method and its effect on static and cyclic deformation-strength properties of sand. *Soils and foundations*, **22**(1): 61-77.
- Pérez, Z.A., Schiavon, J.A., Tsuha, C.H.C., Dias, D. and Thorel, L. 2018. Numerical and experimental study on influence of installation effects on behaviour of helical anchors in very dense sand. *Canadian Geotechnical Journal*, **55**(8): 1067-1080.
- Ternet, O. 1999. Reconstitution et caractérisation des massifs de sable: application aux essais en centrifugeuse et en chambre de calibration. PhD dissertation, University of Caen, Caen, France (in French).
- Tsuha, C.H.C. 2007. Theoretical model to control on site the uplift capacity of helical screw piles embedded in sandy soil. PhD dissertation, University of São Paulo, São Carlos, Brazil (in Portuguese).
- Tsuha, C.H.C. and Aoki, N. 2010. Relationship between installation torque and uplift capacity of deep helical piles in sand. *Canadian Geotechnical Journal*, **47**(6): 635-647.
- Tsuha, C.H.C., Aoki, N., Rault, G., Thorel, L. and Garnier, J. 2012. Evaluation of the efficiencies of helical anchor plates in sand by centrifuge model tests. *Canadian Geotechnical Journal*, **49**(9): 1102-1114.
- Schanz, T., Vermeer, P.A., and Bonnier, P.G. 1999. The hardening soil model: formulation and verification. In *Beyond 2000 in computational geotechnics*. Balkema, Rotterdam, pp. 281-296.
- Schiavon, J.A. 2016. Behaviour of helical anchors subjected to cyclic loadings. PhD dissertation, University of São Paulo and LUNAM University, São Carlos, Brazil.
- Schiavon, J.A., Tsuha, C.H.C. and Thorel, L. 2016. Scale effect in centrifuge tests of helical anchors in sand. *International Journal of Physical Modelling in Geotechnics*, **16**(4): 185-196.
- Sharif, Y.U., Brown, M.J., Ciantia, M.O. et al. 2019. Numerically modelling the installation and loading of screw piles using DEM. In *1st International Symposium on Screw Piles for Energy Applications (ISSPEA 2019)*, Dundee, Scotland. University of Dundee, Dundee, pp. 101-108.

Experimental technique for creating enhanced capacity piles in a centrifuge environment

Leonardo Lalicata¹, Andrew McNamara¹ and Sarah Stallebrass¹

¹Civil Engineering, City, University of London, UK

Corresponding author: Leonardo Lalicata leonardo.lalicata@city.ac.uk

ABSTRACT: The paper describes experimental techniques developed in the geotechnical centrifuge facility at City, University of London to test bored pile foundations with profiled bores designed to increase pile capacity. Improvements were made to existing equipment to ensure accurate measurement of the load displacement response at working loads and potential errors quantified.

Keywords: Pile Foundations; Load-Displacement; Stiff Clays.

1 INTRODUCTION

Researchers at City, University of London are collaborating with Keltbray Piling, on an Innovate UK funded project to develop an enhanced capacity bored cast *in situ* pile. This research builds on work by Gorasia and McNamara (2016) which explored the enhanced capacity of bored cast *in situ* piles with discrete ribs or a rib shaped like a spiral along the length of the pile.

The research at City, University of London consists primarily of a substantial series of centrifuge model tests, 13 tests to date, exploring the influence on the load-displacement response of the piles to changes in the geometry of a novel form of profiling applied to the pile bore. These centrifuge model tests are supplemented by field trials and the results of the tests are being used to develop the profiling equipment used in the field by Keltbray Piling.

2 METHODOLOGY

There were a number of criteria that needed to be fulfilled to ensure that the programme of centrifuge testing complemented the developments and field tests undertaken by Keltbray Piling:

- Centrifuge tests should relate sufficiently closely to the field tests in terms of stress state, pile geometry and soil conditions and yet be well defined and straightforward to analyse.
- Tests should result in consistent load displacement data once allowance has been made for changes in soil properties
- It should be possible to measure displacements and loads accurately at working loads as well as when the pile reaches ultimate capacity.
- The method of profiling the pile bores should be reproducible and the geometry of the indentations representative of those used in the field.

The following sections outline how the test, model preparation equipment, displacement and load monitoring systems were developed to fulfil the above criteria.

3 THE CENTRIFUGE TEST

Bored cast *in situ* piles are commonly used foundations in London, constructed mainly in the London Clay, a stiff overconsolidated marine clay, with a casing provided to support overlying sands and gravels. They are most efficient when they do not extend into underlying unstable strata and the depth of London Clay available is often sufficient to prevent this. In the field tests piles were constructed in the London clay at Southall. Consequently, the centrifuge tests needed to simulate the construction of pile foundations in overconsolidated clay. The overlying strata would not be included in the model to simplify the analysis of the piles and ensure it was straightforward to distinguish the effect of the profiling of the bore which would not be possible in the cased sand and gravel layer. The soil used in the model was created from Speswhite Kaolin clay as discussed below.

The Geotechnical Engineering Research Group at City University makes use of an Acutronic 661 beam centrifuge, described in detail by Schofield and Taylor (1988). The model was tested at 50g so that piles representing typical diameters used in the field can be constructed at a sensible size for the purposes of model preparation. To maximise the number of piles tested a “plane strain” strongbox was used of nominal internal dimensions 550 x 200 x 375mm. The piles were bored, profiled and cast, see section 4 at 1g and the loading apparatus was then assembled on the plane strain strongbox. Constructing the piles at 1g means that the contact between the piles and the surrounding soil is optimised leading to values of the adhesion factor α typically in the region of 0.75 – 1.0 (Gorasia and McNamara, 2016). This eliminates uncertainties

that occur in the field due to the softening of the soil near the pile bore and will ensure that increases in capacity caused by profiling will be underestimated by the centrifuge tests.

Once pore pressure equilibrium was reached in flight, see below, the piles were loaded until failure at a displacement rate of 1 mm/min. Due to the high displacement rate, pile loading takes place under undrained soil conditions.

3.1. Preparation and characterisation of the model soil

The Speswhite Kaolin clay used in the tests is prepared from slurry with an initial water content of 120% which is twice the liquid limit. The slurry was created by mixing dry powder and distilled water in an industrial ribbon blade mixer.

The slurry was then carefully poured into the model container and manually stirred to expel the main air bubbles. The model container was previously coated with pump water grease to minimise skin friction. Beneath the slurry there was a filter paper and a 3 mm porous plastic sheet, with an aluminium drainage plate at the base. On top of the slurry a second filter paper and porous plastic sheet were placed and drainage was allowed through holes in the loading plate in the press. The initial slurry height (~575 mm) was much greater than the height of the strongbox (375 mm) requiring the use of an extension in the consolidation stage.

Consolidation was achieved by means of a hydraulic press over a period of 9 days including 1 day of swelling. The models were compressed to a vertical stress of 500 kPa that was then reduced to 250 kPa, inducing an in-flight over consolidation ratio (OCR) that decreases with depth. In flight, the water table was maintained at 10mm below the surface of the clay by means of a standpipe supplied continuously with water from outside the centrifuge and connected to the bottom of the model. The top surface was sealed with a synthetic rubber coating to prevent clay drying during the test. (Panchal et al., 2019; Gorasia and McNamara, 2016). This allows the clay to achieve pore pressure equilibrium with drainage to the base of the model after a period of around 44 hours in flight before the piles are loaded.

At the end of the test, the undrained shear strength was estimated from hand vane tests and water content samples. The water contents were converted to strengths using critical state theory (Wood, 2004). Soil strength measurements for the tests are given in Figure 1. The symbols in the S_u plot are the values derived from water content measurements, while the lines correspond to the hand vane results. In general, the latter give higher strengths. The

measurements are largely consistent in the tests. As might be expected, the undrained strength increases slightly with depth as water content reduces.

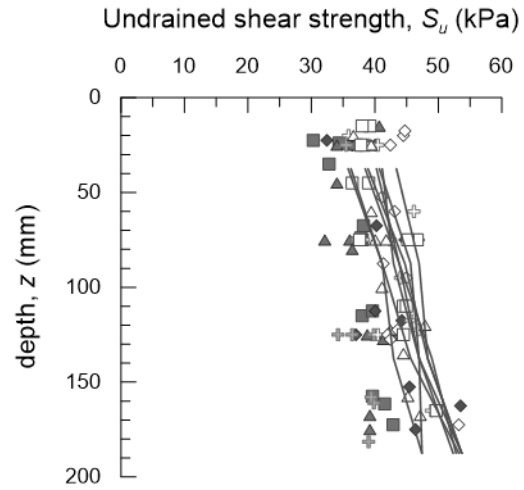


Figure 1. Undrained shear strength profiles with depth.

3.2. The experimental apparatus

For each test the soil sample provided up to four testing sites within the rectangular strong box, Figure 2. The piles are positioned at the centreline of the model, 100 mm from the sides, which is far enough to minimise boundary effects (Craig, 1995).

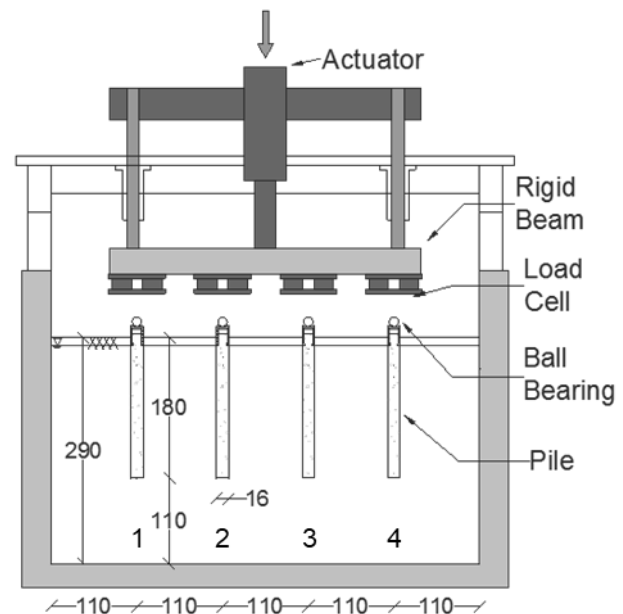


Figure 2. Model geometry.

The piles used in tests were 16 mm in diameter and 180 mm long, giving a prototype pile 800mm in diameter 9 m long. The pile length to diameter ratio is small if compared to typical piles used in the field but a reasonable compromise given the need to provide sufficient soil under the base of the piles and the limited depth of clay available. Smaller

diameter piles could have been used with a higher g level, but this would have made the profiling operation impractical. In addition, the relatively small length of the piles ensures a faster in flight consolidation prior to pile loading.

The piles, are spaced 110 mm apart and loaded simultaneously by means of a rigid beam. The apparatus is devised such that it is possible to obtain independent load and settlement data for each pile. Several pieces of apparatus were designed and developed to improve the experimental technique. These included the loading equipment, the measurements of pile displacement and the guides, jigs and impression tools needed to create the model piles, as discussed below.

4 LOAD-DISPLACEMENT MEASUREMENT

The axial load is applied from the actuator to the piles by means of a rigid reverse T-shaped beam (Taylor *et al.*, 2013). The initial concept was to measure the load whilst assuming that the loading arrangement was sufficiently stiff to ensure that the displacement applied to all piles was the same. Thus, it should have only been necessary to measure displacement on the beam. To reduce the interaction between the beam and the loaded piles the system was stiffened with two silver steel guides (16 mm in diameter) positioned at the extremes of the beam. Each guide travels through a linear bearing 100 mm long and is connected to the other guide above the plate carrying the actuator by a 40 mm thick silver steel plate, Figure 3.



Figure 3. Loading apparatus.

Although this resulted in a stiff loading system that would not deflect when loading all piles simultaneously, it was not possible to prevent some

movement of the beam if only one pile was loaded, particularly if the pile was at the end of the beam. As it was not feasible to ensure that the beam encountered all piles simultaneously the displacement of the pile heads was monitored independently.

In order to avoid any undesired eccentricity during the loading of the pile, a ball bearing laying on top of a concave plate was used to apply the load, Figure 4(a). Three load cells, sandwiched between two aluminium plates, measured the load on each pile ensuring that errors due to bending in the load cell are eliminated Figure 4(b).

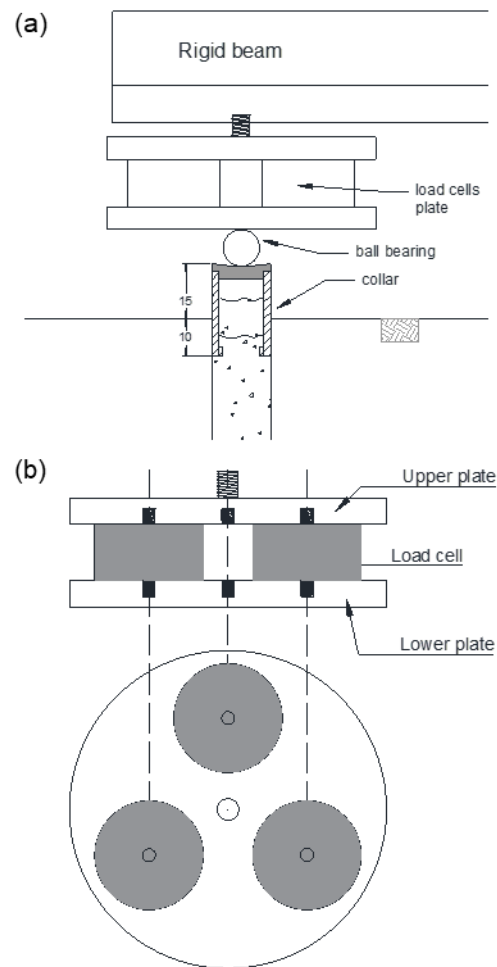


Figure 4. Load measurement system (a) vertical cross section, (b) detail of the load cells plate.

Several attempts were made to obtain reliable readings of the head displacement of the pile, the results and the consequences for the response of the pile will be discussed later in the paper. The current measuring system is sketched in Figure 5. A 2 mm thick aluminium plate, 175 mm long and 16 mm wide, is a tight fit to the pile collar and two LVDTs measure the plate displacement at its extremes. The head displacement of the pile is given by the mean value of the LVDT measurements. A 1 mm gap

between the plate and the concave dish guarantees that load and displacement are independent readings.

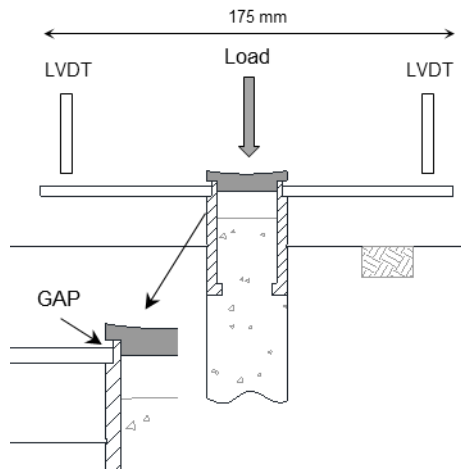


Figure 5. System for the measurement of the head displacement of the pile.

5 MODEL PILES

As noted in Section 3, the piles were cored, profiled and cast at 1g. For results to be repeatable it was key that the piles were vertical, a constant length into the clay and the profiling was precisely located and well defined.

The piles were cut using a hypodermic thin walled tube with an external diameter of 16 mm. The tube was mounted onto a brass handle to allow for easy cutting (Gorasia & McNamara, 2016). The verticality and position of the piles was achieved using the system of guides shown in Figure 6 (a). To minimise soil disturbance during boring several precautions were undertaken: the internal part of the tube was sprayed with a lubricant oil and the edge of the tube was sharpened. In addition, the boring was always undertaken in three steps of equal length.

The enhanced capacity piles were created from the plain pile bore. A custom designed tool was inserted into the guide and used to profile the pile bore Figure 6 (b). After profiling, the piles were cast using a ‘fast cast’ polyurethane resin, Sika Biresin G27 (McNamara, 2001; Gorasia and McNamara, 2016). The pot life of the resin is approximately 3 minutes. Aluminium powder was used as filler in an equal mass ratio with the two components of the resin to ensure that the pile is not buoyant. The mixture was designed to have a good fluidity to fill the profiles. Figure 7 shows some of the exhumed piles and demonstrates the success of the methodology adopted. Several uniaxial compression tests were undertaken to measure the mechanical properties of the resin when set. The

resin was found to have a Young’s Modulus equal to 1.1 GPa and a yield stress of 35 MPa. These values confirm that the pile behaves as a linear elastic material in the range of the applied loads.

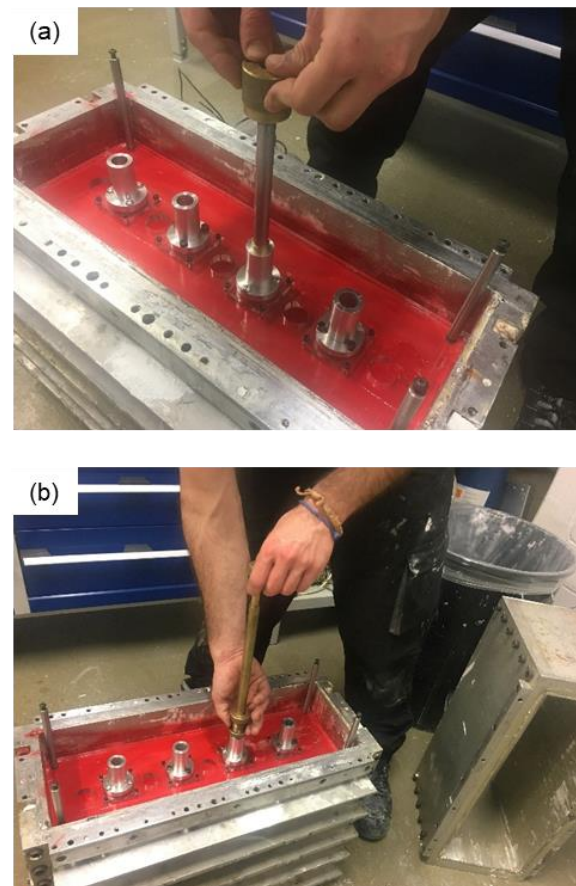


Figure 6. (a) guide for pile boring, (b) impression.



Figure 7. Exhumed model piles some with profiled bores

These values also allowed the pile-soil stiffness ratio to be estimated from standard relationships between soil stiffness and strength. For a low plasticity, heavily overconsolidated clay such as that used here, the stiffness/strength ratio is typically given by $E_u/S_u = 300$ leading to relative stiffness ratio, between pile and soil of approximately 90. Therefore, the pile is expected

behave as a compressible pile with most of the interaction concentrated in the upper part of the shaft as might be expected of a full length pile used in the field tests.

6. ANALYSIS OF RESULTS

6.1 Repeatability

Figure 8 shows data from all tests on straight-sided model piles interpreted in a consistent manner to give the ultimate capacity of the pile. These ultimate capacities have been plotted against undrained shear strength calculated using both water content measurements and vane test data. In general, the ultimate loads correlate well with undrained strengths calculated from water content data and show a slight increase in ultimate load with undrained strength as would be expected.

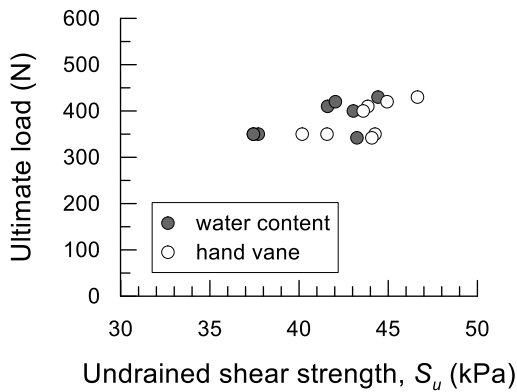


Figure 8. Ultimate load of all straight sided model piles plotted against the undrained shear strength at $z=L/2=90$ mm, where L is the length of the pile.

6.2 Pile-beam- pile response

The typical evolution with time of displacement and load for a set of four straight-sided and profiled piles are presented in Figure 9(a) and Figure 9(b) respectively. The dashed line represents the imposed displacement. For each pile, the displacement is given by the average of the LVDTs and the load is the sum of the LCs measurements. The piles are displaced over a time interval of 2.5 minutes that approximately corresponds to the accuracy of the collar installation into the bore (± 1 mm), given that the displacement rate of the beam should be 1 mm/min. Inspection of the displacements, Figure 9 (a), shows that in the early stages of loading, the pile head displacements are different from those imposed.

This is particularly true for the first two piles (4 and 1) that are at either end of the loading beam. For pile 4 the displacement curve is concave at the beginning and then, as the beam touches pile 1, the concavity changes and the trend become parallel to

that. This is likely to be related to some small ($\sim 1/400$ of rotation) rocking of the beam due to the temporary asymmetry of the loading and the relatively high stiffness of the piles. The other piles (2 and 3, in the central position) loaded last, displace with approximately the same loading rate as that imposed. That is because the external piles have “balanced” the beam by applying roughly the same reaction and because piles 2 and 3 are closer to the centre of the beam, where the effect of rocking is lower. This behaviour is not affected by the configuration of the straight-sided and profiled piles.

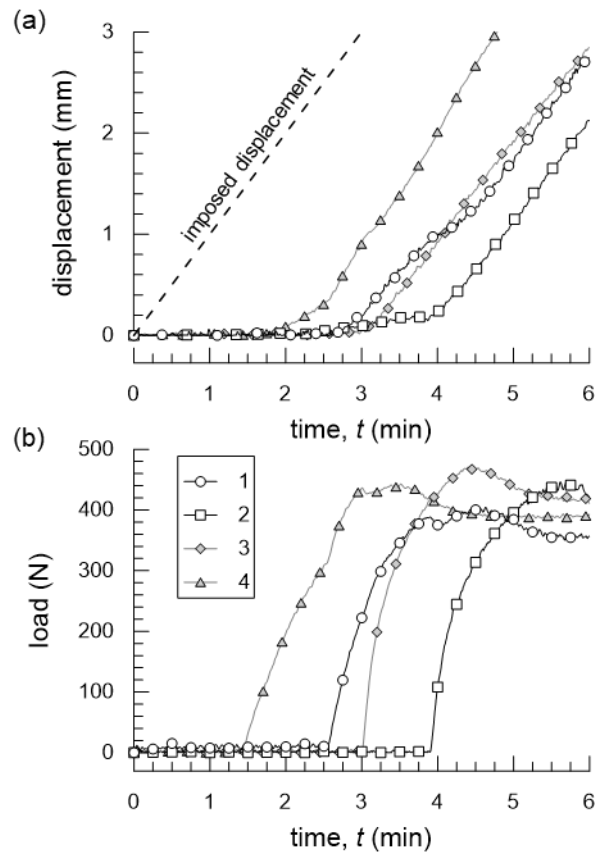


Figure 9. Evolution with time of: (a) displacements of the piles, (b) loads of the piles

The consequence of this effect is depicted in Figure 10(a) and Figure 10 (b) that show the load-settlement response for an external (1) and an internal pile (3) respectively. In each figure, the measured load-settlement curve is compared with the one that would be obtained assuming that the pile displacement was equal to that imposed. The underestimation of the initial pile stiffness in the latter case is apparent in both cases: 63% for pile 1 and 43% for pile 3. The difference reduces in the second case as the pile is loaded after piles 4 and 1 and it is closer to the centre of the beam. It is thus clear that in order to obtain reliable measurements

at low deformation levels (i.e. working load) it is critical to measure the head displacement of the pile directly. However, the value of the failure load is unaffected by errors in the displacement measurements.

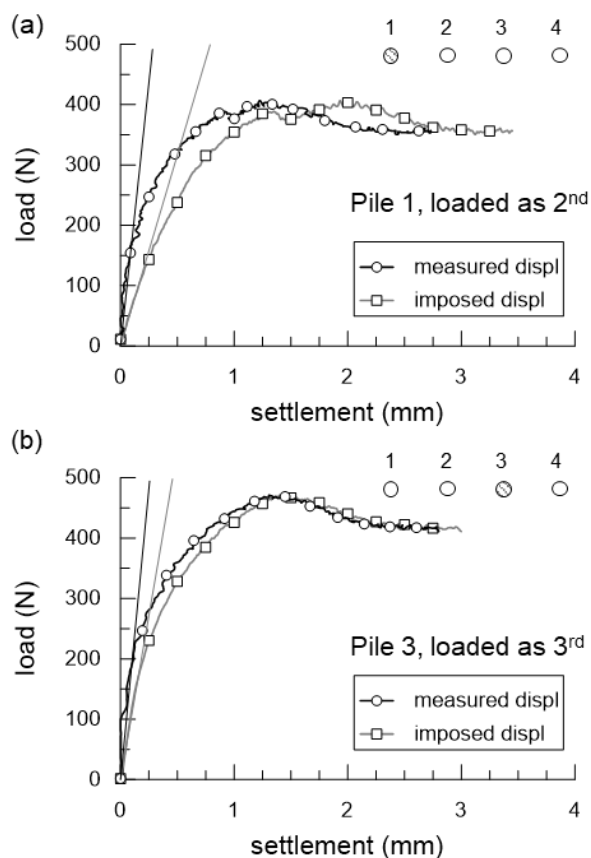


Figure 10. Direct measures of pile displacement compared with that expected from the beam movement: (a) external pile, (b) central pile.

7 CONCLUSIONS

A series of centrifuge tests have been designed to characterise the increase in pile capacity obtained by profiling the bore of a bored cast *in situ* pile. In addition to pile capacity the tests also needed to measure changes in load displacement response at working load, which required accurate measurement of both load and in particular displacement at displacements of less than 0.2mm. The aim was to produce a substantial series of tests that would form a parametric study to be compared to a limited number of field tests.

Apparatus has been developed that loads four piles always including a straight unprofiled pile for comparison. The loading system, despite being modified to improve its rigidity, did not provide a sufficiently accurate or reliable means of measuring the displacement of the pile head and consequently a system was developed to measure these

displacements separately. The consequence of measuring the pile head movements directly compared to measuring the displacement of the loading beam has been quantified.

Compromises in the modelling of the overall pile geometry have been discussed and it has been established that the soil/pile stiffness used ensures that the pile will respond as a compressible pile even though it is comparatively short. It has been shown that consistent measurements of pile capacity can be obtained if changes in undrained strength are accounted for, demonstrating that the methodology for the preparation of the soil bed and the construction of the piles provides repeatable results that can be used to generate data for a parametric study of the influence of the profiling on pile behaviour.

8 ACKNOWLEDGEMENTS

The authors would like to acknowledge the support of Innovate UK and Keltbray Piling.

9 REFERENCES

- Craig, W.H. 1995. Geotechnical centrifuges: past, present and future. In *Geotechnical Centrifuge Technology* (Taylor RN (ed.)). Blackie Academic and Professional, Glasgow, UK, ch. 1, pp. 1–19.
- Gorasia, R.J. and McNamara A.M. 2016. High-capacity ribbed pile foundations. *Proceedings of the Institution of Civil Engineers: Geotechnical Engineering*, **169**(3): 264–275.
- McNamara, A.M. 2001. *Influence of Heave Reducing Piles on Ground Movements Around Excavations*. PhD thesis, City University, London, UK.
- Panchal, J.P., McNamara, A.M., Halai, H. and Divall, S. 2019. Centrifuge modelling to determine the influence of pile stiffness on pile capacity. *Proceedings of the XVII ECSMGE-2019 Geotechnical Engineering foundation of the future*. doi: 10.32075/17ECSMGE-2019-0036.
- Schofield, A.N. and Taylor R.N. 1988. Development of standard geotechnical centrifuge operations. In *Centrifuge 88* (Corte JF (ed.)). Balkema, Rotterdam, the Netherlands, pp. 29–32.
- Taylor, R.N., Rose, A.V. and Gorasia, R.J. 2013. Pile and Pile Group Capacity: Some Findings from Centrifuge Tests. *International Journal of Geo-Engineering*, **5**(2), 5-15.
- Wood, D.M. 2004. *Geotechnical modelling*. New York: Spon Press.

Model tests of grouted piles in gravel esker and fill soils

Wik Breure¹, Anders B Lundberg¹

¹*Geotechnical Department, ELU Konsult AB, Sweden*

Corresponding author: Wik Breure (wik.breure@elu.se)

ABSTRACT: Grouted piles consist of an internal steel member used for drilling and grouting, and a grout body created during installation. The foundation method is highly efficient in permeable soils, such as the esker gravels frequently found in Sweden. During the preliminary design phase for the Slussen project in the centre of Stockholm, a series of in-situ model tests were performed and evaluated at the start of the project when grouted piles were considered as a foundation method. The objective of the model tests was to evaluate the installation procedure in the specific soil conditions, assess the load distribution and load bearing capacity during the static load tests, and the corrosion protection of the central steel member of the grouted piles. The tests were carried out at two different locations within the specific project. The challenge was to estimate and generalize the efficiency of the foundation method in the entire area. This paper discusses the in-situ model tests, especially the load test results, and elaborates on the suitability of the grouted piles for the specific project.

Keywords: Grouted Piles; Model Testing; Esker Geology.

1 INTRODUCTION

The suitability of ground engineering methods is highly depending on the local soil conditions. Figure 1 shows an idealised cross-section of the Swedish soil strata, which is dominated by soft soils deposited during the Holocene period as a result of the Weichselian glaciation. The soft clays and shallow bedrock in the Eastern part of the country permit end-bearing piles (Lundberg and Li 2015), while the shaft-bearing piles are more suitable for the deeper clay deposits in Western Sweden (Jendeby 1991).

Eskers are a particular feature of the Swedish geology, sand and gravel ridges located along subglacial rivers, in which the flow of water resulted in a soil mass with a homogenous grain size. These are highly permeable and are frequently used as groundwater reservoirs.

The traditional piling methodology using end-bearing piles in which the bearing capacity is verified by dynamic pile load tests as outlined in Andersson et al. (2016) is frequently not suitable for esker soils since the bedrock is typically located at a deeper level along the esker ridges. Application of the European continental piling methods, i.e. bored piles or continuous flight auger (CFA) piles is often not possible, due to the boulders located in the esker soil mass.

An alternative solution is the application of grouted piles. These are constructed through a casing, which is drilled through layers containing boulders. Various types of grouted piles are discussed in the scientific literature, e.g. large diameter grouted piles, e.g. Abbs et al. (1985) and Nauroy et al. (1985). The principle of grouted piles

is similar to grouted anchors: a grout mix is injected at low pressure into the ground during rotation or penetration. Laboratory tests of grouted piles in calcareous soil have been conducted by Lee and Poulos (1991), and on grouted anchors by Ostmayer and Scheele (1978). Miltenberger (2001) recommends a characteristic shaft resistance for grout anchors. However, the standard design method outlined by Miltenberger requires that the ground soil conditions are suitable for grouted anchors/piles, especially regarding the development of the grout body. In the current paper a case study of in-situ model tests in esker/fill soil layers is elaborated to assess the suitability of the method in the project specific soil strata.

2 CASE STUDY: SLUSSEN AREA IN STOCKHOLM

The geological conditions in the Slussen area result both from the natural deposition of sediments and the development of the city of Stockholm since the medieval period. The city of Stockholm was originally built on an esker ridge, extending from the South to the North of the city.

Deposition of fine sediments from the Mälaren drainage basin occurred along the original coastline before the current quays were completed: as a result, the slopes around the original coastline consisted of massive layers of gyttja and organic soil.

The city of Stockholm was founded in 1252 (Hall 2008). The urban development soon extended to the South and North of the city. The organic and inorganic waste was deposited along the coastline, consisting everything from food waste to massive boulders, as the city gradually expanded. The layers

of soft soil were covered by this mixed fill, and quays were built along the new coastline.

The Slussen area shown in Figure 2 is now undergoing an extensive reconstruction. During the project the quays are widened, and superstructures for a subway and bus terminal, and a new bridge are being built, all requiring piles for ground support.

The soil strata presents specific complications for standard foundations methods: the large boulder content in the fill makes the construction of bored

piles, such as CFA piles, tenuous, and the significant depth to the bedrock (often exceeding 50 m) makes end-bearing piles time-consuming and uneconomical.

The use of grouted piles was therefore investigated to assess the suitability of the method, and a series of model tests were performed, in which the whole installation and testing procedure was executed in-situ.

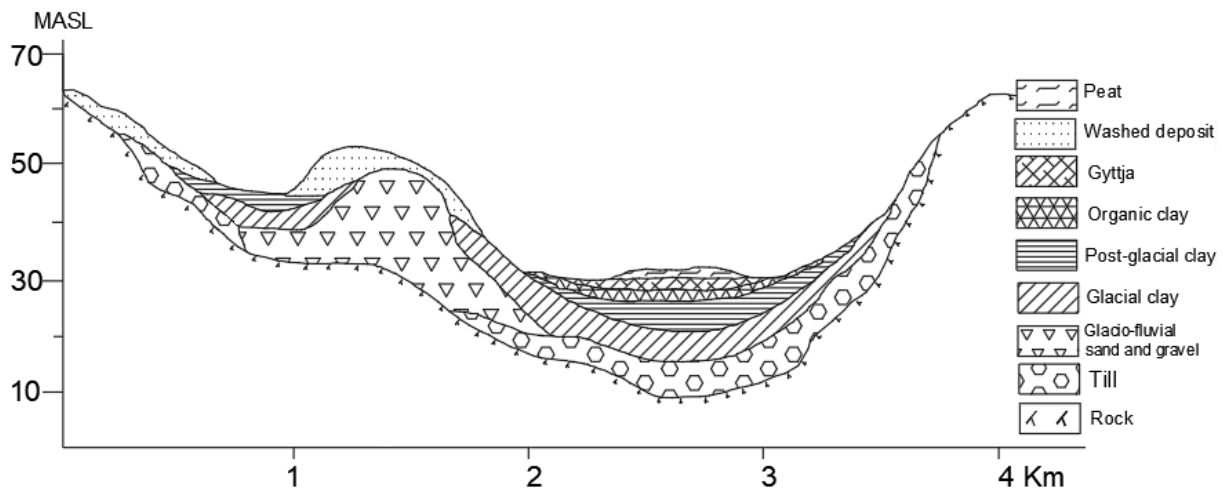


Figure 1. Idealisation of the soil strata in Sweden.

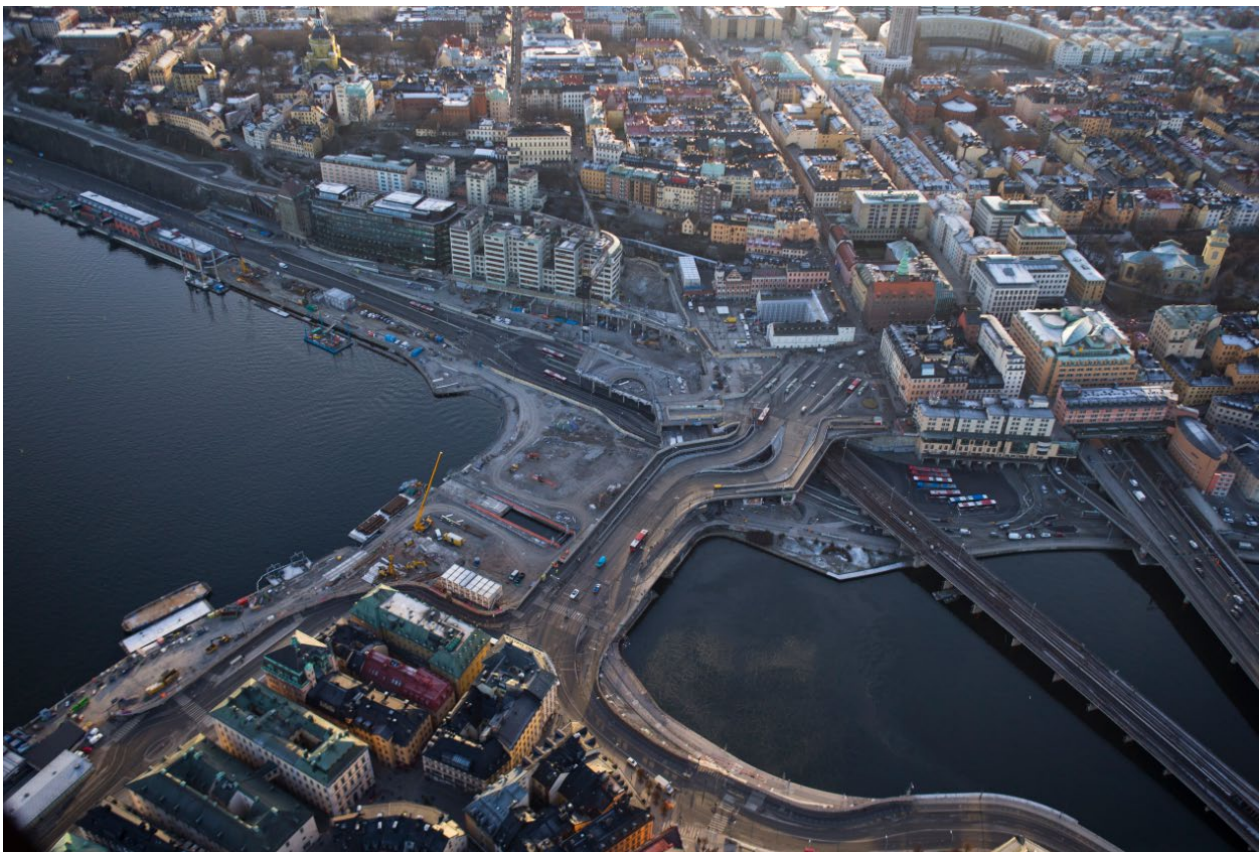


Figure 2. The Slussen area in Stockholm.

3 MODEL TESTS

3.1. Aims of the tests

The aims of the in-situ model tests were to assess the feasibility of the method with regards to:

- The construction of the piles
- Bearing capacity of the piles
- Load distribution along the piles.

The construction of the piles consisted of drilling of a casing through the fill layer, after which the pile was grouted through the casing. The high permeability of the esker material was considered a risk, since a large amount of grout would presumably be needed for the piles, resulting in environmental and economic costs. Assessment of the resulting bearing capacity from the model tests was essential, since they provided the representative shaft resistance used during pile design. The distribution of the load along the grouted piles was also of interest: the aim was to separate the casing and the grout body with a plastic tube to reduce the influence of negative skin friction if settlements would occur in the fill layer.

3.2. Model test set-up

For the model tests drilling and grouting equipment was applied for the construction and instrumentation of the nine test piles, after which compression and tension pile load tests were performed.

3.2.1 Installation

The principle of the model test piles is shown in Figure 3. Drilling was conducted from the ground surface through the fill layer. A 140 x 8 mm steel casing with a length of 21-27 m was drilled through the fill layer and terminated at the top of the esker layer. The stratification is interpreted from site investigation. At the top of the esker layer, a hollow 73 mm diameter steel pile with 53 mm internal diameter is drilled through the soil with a drill bit, which is simultaneously pumping cement grout through the soil. Before the drilling and grouting of the pile starts, a plastic pile is put on top of the hollow steel pile to separate the steel casing and the grouted pile. The grouted length varies between 4-6 m. A water-cement ratio of 0,5-0,7 is used for the grouting. Spoil was collected during drilling. Compression tests were carried out on the spoil from the grouting process with water-cement ratio of 0,5. The cube compression strength after 7 days was 39,0 MPa, after 17 days 41,5 MPa and after 29 days 48,9 MPa.

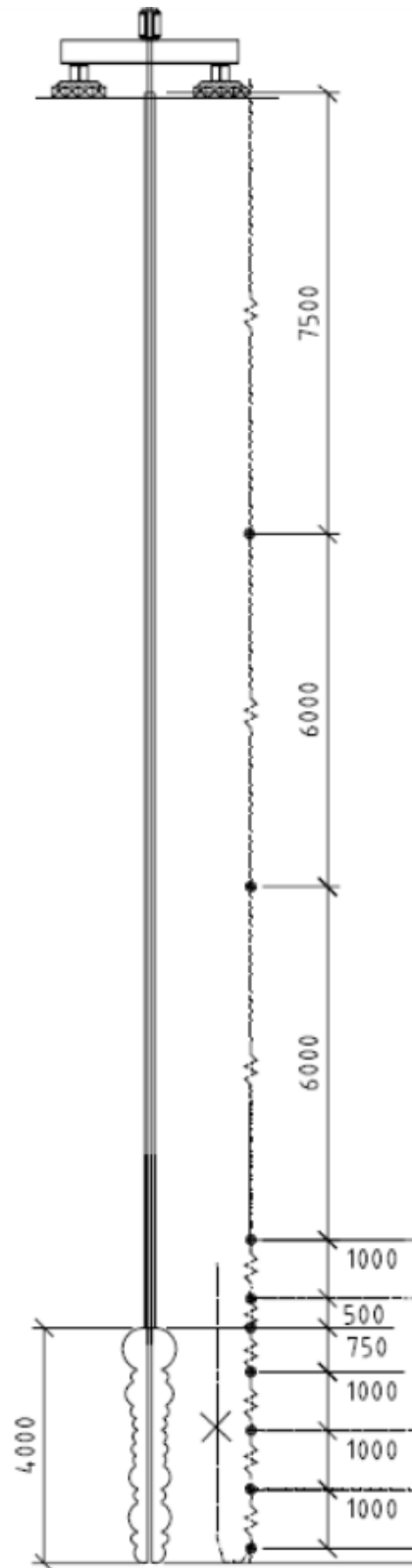


Figure 3. Schematic representation of the principle of the model pile tests, length in mm.

3.2.2 Instrumentation

The grouted pile was instrumented with strain gauges at c/c 1 m through the hollow steel pile, shown in Figure 3, as well as through the casing. A temperature sensor was installed in the middle of the

grout body to detect any anomalies during grouting. Vibrations and settlements were measured during the installation of the piles, and the impact on the ground water level was monitored during and after the tests.

3.2.3 *Compression and tension pile load tests*

Compression and tension static pile load tests were performed on the piles. A beam frame with a hydraulic apparatus was used for the test and the surrounding piles were used to mobilize the reaction for the tests. Dynamic pile load tests were subsequently executed.

4 RESULTS

4.1. *Grout flow during installation*

The grout flow showed very large variation between the piles, possibly resulting from the variation in permeability of the esker layer. The flow was at a maximum level for the piles at 21 m grouting depth, surpassing 2000 L/m. At 27 m depth the grout flow was lower, but with a maximum level of around 1400 L/m and a minimum level of 200 L/m.

4.2. *Static pile load tests*

Compressive and tension pile load tests were carried out on the piles. Figure 4 shows a representative time versus load response of a tested pile in tension. Both the total load and the load retained by the steel casing are shown in Figure 4. The steel casing ratio of the load was calculated through the measured load on the top strain gauge on the hollow steel tube compared to the total pile load in tension. Theoretically the plastic tube would permit all the load being transferred to the grout body, but a significant part of the load was retained by the steel casing through shaft friction.

Figure 4 displays a very stiff response during the initial loading stages, which is gradually transformed to a more viscous response at around 800-900 kN loads. The load ratio of the steel casing appears to reduce gradually when the load increases.

4.3. *Load distribution*

Figure 5 shows a representative obtained strain distribution along a tested pile through

measurements by the strain gauges. The strain gauges mounted on the steel casing display a relatively uniform elastic elongation of the steel casing, indicating a relatively uniform mobilization of the shaft friction along the steel casing.

The Strain measurements inside the grout body display a more gradual mobilization with less strain at the lower end of the pile.

4.4. *Dynamic pile load tests*

Dynamic pile load tests were performed on some of the grouted piles. Figure 6 shows the results of a dynamic pile load test on one pile, displaying the force and velocity multiplied by the pile impedance output. These results show a different response compared to the static pile load tests, since the reflection of the steel casing is less visible. The return signal from the grouted piles is more significant. The reason behind this could be the viscous behaviour of the plastic tube.

4.5. *Excavation of the piles*

The construction of grouted piles was also tested at another location in the area. These piles were installed by means of the described method. At a later stage during the construction of the Slussen area, these test piles were excavated, and the result of the grouting process could be examined.

Figure 7 show the grout body including the visible the intersection between the man-made fill, which is mixed with organic soil and contains boulders, and the esker gravel. This indicates that for this specific pile the steel casing ended above the intersection between the fill and esker material. The esker has a lower boulder content, but still shows a significant irregularity at the lower end of the grouted pile.

4.6. *Other measurements*

The vibration level and impact on the ground water level were also monitored during the installation of the piles and the subsequent testing activity, but these did not display any large effect compared to the background noise, which was significant, since the test was conducted in the centre of Stockholm.

Settlement measurements at the testing location showed settlements of around 6-9 mm between the piles.

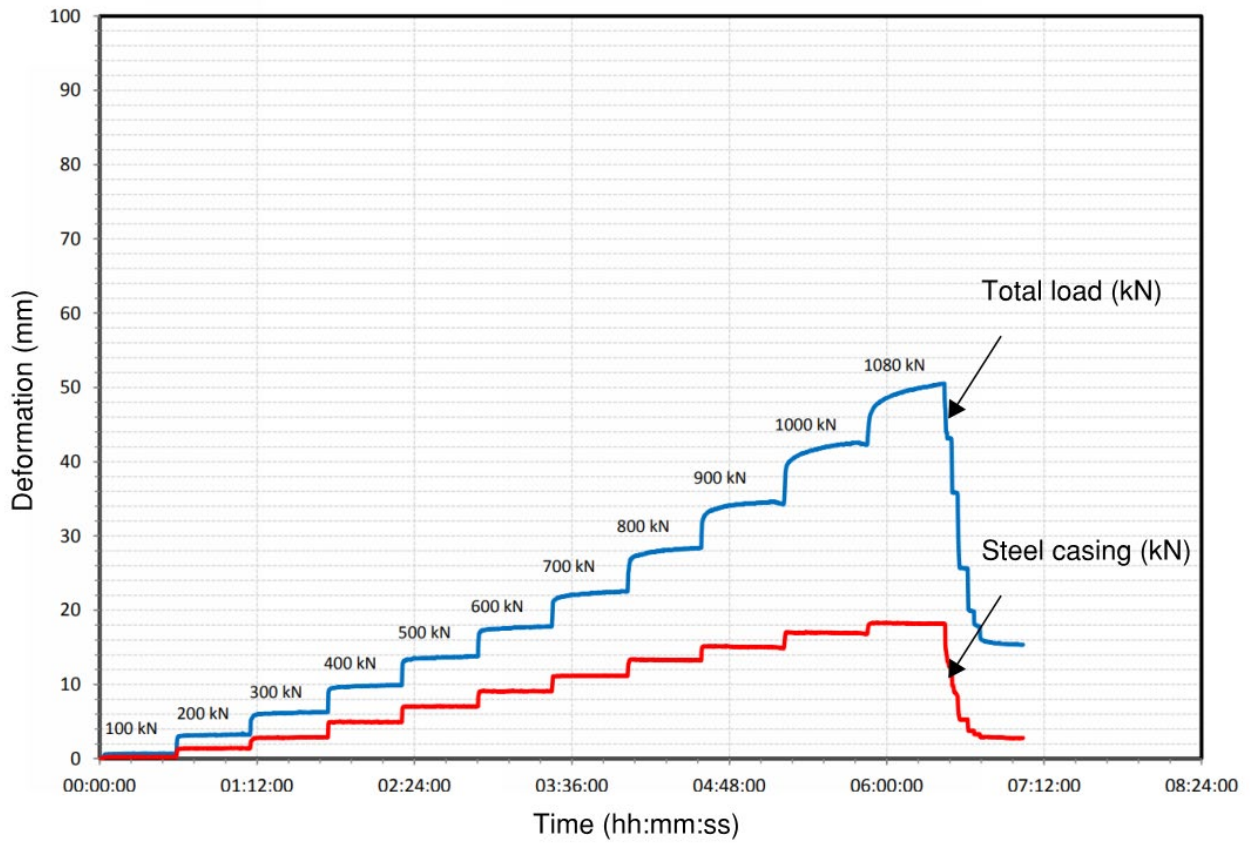


Figure 4. Representative response static pile load test.

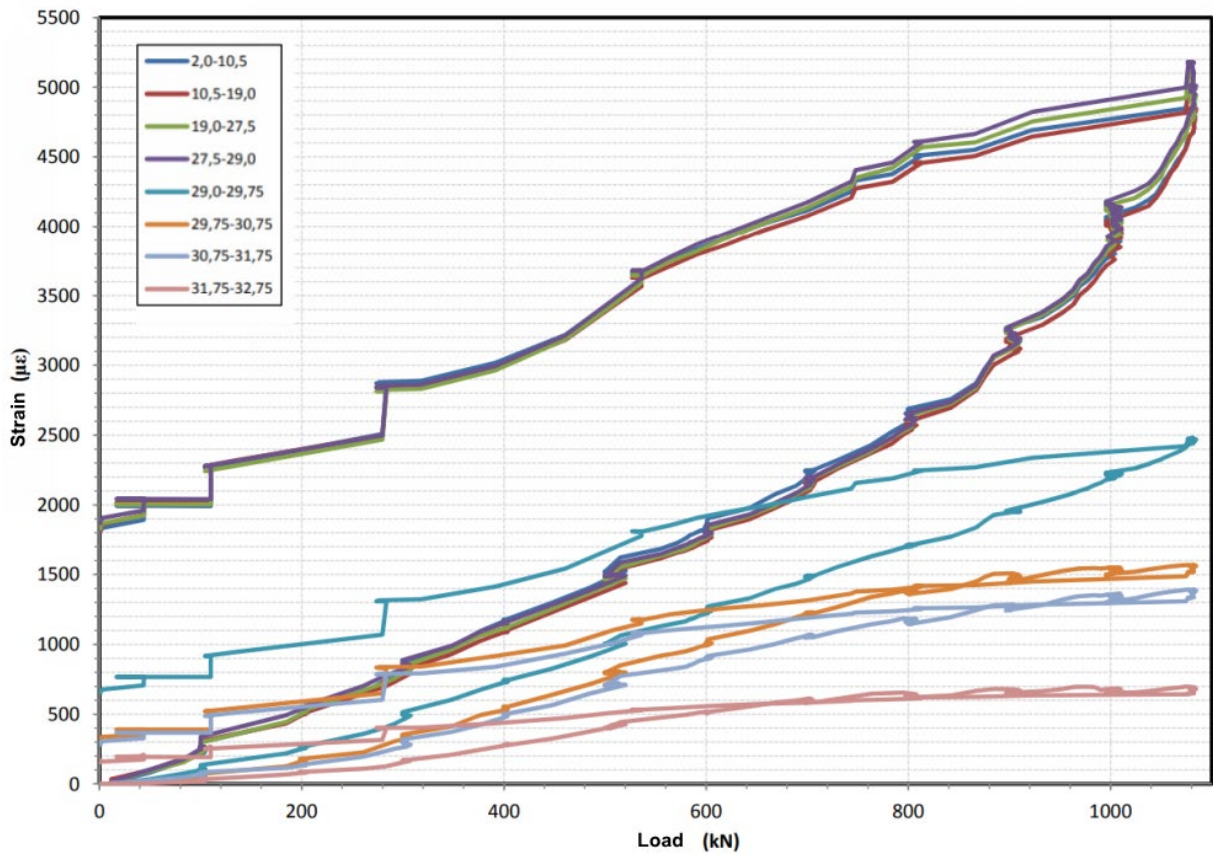


Figure 5. Representative load distribution response during static pile load tests. The legend represents the distance of the strain gauges with respect to the surface in meters.

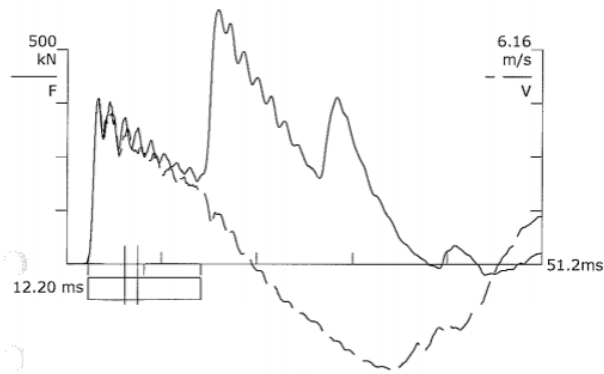


Figure 6. Response dynamic pile load test.



(a)



(b)



(c)

Figure 7. Excavated grout body.

5 CONCLUSIONS AND DISCUSSION

The in-situ tests showed that:

- The method resulted in the construction of grouted piles with an expected bearing capacity.
- The installation process resulted in excessive grout flow.
- It was not possible to separate the load between the steel casing and the grouted pile in the static pile load tests, as the results showed that a significant part of the load was retained by the steel casing through shaft friction.

Due to these reasons, the grouted pile method was not used for a large volume of piles within the Slussen project, but could still be used as an alternative for some areas, due to the minor risk of settlements and the negligible impact on vibration and ground water levels.

6 REFERENCES

- Abbs, A. F. and Needham, A. D. 1985. Grouted piles in weak carbonate rocks. In Offshore Technology Conference. Offshore Technology Conference.
- Andersson, A. Axelsson, G. and Lundberg, A.B. 2016. Reliability analysis of pile groups based on dynamic pile testing. In Nordic geotechnical conference 2016 pp. 503-512.
- Hall, T. 2008. Stockholm: the making of a metropolis. Routledge, Abingdon.
- Jendeby, L. 1991. Load transfer in friction piled foundation in soft clay. In Proc. 10th Eur. Conf. on SMFE (Vol. 1, pp. 449-452).
- Lee, C. Y. and Poulos, H. G. 1991. Tests on model instrumented grouted piles in offshore calcareous soil. Journal of geotechnical engineering, **117**(11), 1738-1753.
- Lundberg, A. B. and Li, Y. 2015. Probabilistic characterization of a soft Scandinavian clay supporting a light quay structure. Geotechnical safety and risk V. IOS Press, Amsterdam, 170-175.
- Miltenberger, M. A. 2001. Capacity design of grouted anchors. Transactions, SMiRT 16
- Nauroy, J. F. and LeTirant, P. 1985. Driven piles and drilled and grouted piles in calcareous sands. In Offshore Technology Conference. Offshore Technology Conference.
- Ostermayer, H. and Scheele, F. 1978. Research on ground anchors in non-cohesive soils. Revue Française de Géotechnique, (3), 92-97.

4. Infrastructures

Geotechnical instrumentation of an experimental embankment dam

Jasmina Toromanovic¹, Johan Lagerlund^{1,2}, Peter Viklander^{1,2,3}, Jan Laue¹

¹*Department of Civil, Environmental and Natural Resources Engineering, Luleå University of Technology, Sweden*

²*Vattenfall Research & Development, Sweden*

³*Vattenfall Vattenkraft AB, Sweden*

Corresponding author: *Jasmina Toromanovic, jasmina.toromanovic@ltu.se*

ABSTRACT: An experimental embankment dam was constructed in Älvkarleby (Sweden) in 2019, in order to allow for geotechnical experiments under realistic and, at the same time, in a controlled environment. The embankment dam is a zoned earth fill embankment dam with a central core of fine-grained till. The embankment dam is 4 m high, 20 m long with a base of 15 m, i.e. a medium scale model. The embankment dam is built in a “concrete box” and a tent has been raised over the site, which will protect from freezing temperatures and precipitation, thereby creating controlled conditions. In the paper, the construction of the embankment dam and the geotechnical instrumentation is presented. No results of the geotechnical measurements are presented, as this is an early stage of the embankment dam experiment and as data is yet to be acquired.

The geotechnical instrumentation installed are deformation measurements, pore pressure- and strain monitoring devices. All geotechnical instrumentation is placed in one section of the dam. The deformations are monitored by shape accelerometer arrays, which allows for 3D monitoring of deformations. Vibrating wire piezometers are placed in the core and downstream filter, mainly with focus on the saturation phase of the core soil. Strain measurements with fibre optics are performed in the bottom of the dam and done perpendicularly to the dam axis. The reservoir of the embankment dam will be filled during winter/spring 2020. The measurements are planned to be ongoing until summer 2021. In the end, different loading scenarios as well as grouting will be tested. Data from the geotechnical monitoring will be used as input for inverse modelling in order to back-analyse the values of material parameters. Re-calibration of the numerical models will be done in order to detect possible changes in the values of material parameters.

Keywords: Embankment Dam; Deformation; Pore Water Pressure; Vibrating wire Piezometer; Strain; Fibre Optics.

1 INTRODUCTION

In Sweden, most of the existing hydropower dams were built before the 1960s. Thus, there are a significant number of ageing structures to maintain today. As an embankment dam ages, deterioration of the structure may occur. Erosive processes both inside and outside the embankment dam may affect its performance as well as the structural stability of the dam negatively.

Erosion processes taking place on the surface of the embankment dam are easier to detect than internal erosion processes taking place inside the embankment dam. Typical damages on the surface of the embankment dam may be settlements, sinkholes and erosion of blocks from the slopes. Internal erosion processes inside the embankment dam are more difficult to detect and can go on for decades without being detected, ICOLD (2013) highlights four types of internal erosion. If erosion processes are left unattended, they may pose the embankment dam at serious risk of being damaged. Damages that could lead to collapse and in a worst-case scenario - casualties. There is a need of detecting these processes before they become critical.

Today, numerical modelling is often used as support when predicting how an embankment dam is going to behave over time. In order to do these predictions, data describing the mechanical properties of the dam are required. Sufficient data to describe the material in the different dam zones are seldom available as documentation from the construction time are lacking. As internal erosion processes takes place inside the dam, mechanical properties may also change over time. Even if data may be available, it is not necessarily that the current situation is described properly or matches today's state. Since the extraction of physical samples from embankment dam's core material may have negative consequences, it would be beneficial to develop non-destructive methods for obtaining mechanical properties. Such a non-destructive method is inverse analysis, which has been applied to embankment dams (Toromanovic et al. 2020).

In 2019, an embankment dam was constructed, as a collaboration between Vattenfall AB, Luleå University of Technology, Uppsala University, Lund University of Technology and HydroResearch AB. The scope of the project is two folded. One part is to study the mechanical behaviour of an

embankment dam during its first filling, allowing to follow the behaviour over time and thereafter to use the data in inverse analysis. Another part was to localise a number of imbedded damages within the embankment dam by geophysical methods (not reported in this paper).

Measurements will be done before, during reservoir filling as well as operation of the embankment dam. Surveillance of the mechanical behaviour of the embankment dam is performed by Luleå University of Technology.

Typical damages that could be caused by erosion processes were built in at known locations within the dam core. After the construction of the embankment dam, the built-in damages are to be found and located by a team of researchers using temperature cables, resistivity measurements and seismic methods. The locations of the damages are not known by this team, as it is a sort of blind test. Responsible for localising the damages by geophysics are Uppsala University, Lund University of Technology and HydroResearch AB.

2 THE SITE AND SUPPORTIVE STRUCTURES

The site for the test dam is in Älvkarleby, Sweden, located approximately 150 km north of Stockholm, where Vattenfall AB has its R&D laboratory. In order to build an embankment dam on dry land and have the ability to operate it as a proper embankment dam, a support structure was needed. The support structure had to be water tight and strong enough to support an embankment dam. Thus, it was constructed with reinforced concrete. Its dimensions were 20 m x 16 m and founded 4 m below the natural ground surface. The bottom concrete plate was made with glass fibre reinforcement bars, in order not to interfere with any geophysical methods, i.e. to simulate natural rock surface. The base of the support structure is leaned 1° towards the downstream side of the embankment dam where seepage water is collected. The two side walls leaned outward with a ratio of 1H:8V in order to improve the compaction of the soil materials against the abutments. An overview of the built embankment dam is shown in Figure 1.

In order to provide a controlled laboratory environment, a tent was raised over the structure, protecting the dam from precipitation and freezing temperatures. Water supply to the dam is provided from Dalälven (Dala river), which is located nearby the test site.



Figure 1. A view of the supportive concrete structure with the raised embankment dam inside.

3 THE EMBANKMENT DAM

3.1. Design

An embankment dam is a type of earthfill dam built with soil materials, i.e. gravel, sand and till and rockfill. The embankment dam is constructed with different zones. In the centre, the core is built. The core in Swedish embankment dams are most commonly built with till, which is a broadly graded type of soil commonly found in Sweden. The till has a low hydraulic conductivity when compacted well and is hydraulic barrier within the dam keeping the water in the reservoir. Outside of the core, one or several filter zones (e.g. fine and coarse filter) are built. These filter zones are built both upstream and downstream of the core to keep the core soil in place and prevent internal erosion i.e. fine grained particles from being washed out with the seepage. Filter zones are typically built with sand and/or gravel.

Outside the filters on both sides, the shoulder fill is to be found. The shoulder fill may consist of soil material ranging in size from sand to rock. The shoulder fill provides the embankment dam with structural stability.

When designing an embankment dam it is vital to choose the materials constituting each type in such way that internal erosion is prevented. If the fine-grained material is eroded from the core, its water sealant ability will be diminished. This process may damage the core soil and make the embankment dam less safe in terms of structural stability. Wherever seepage crosses a boundary from a finer to coarser grained soil, the potential exists for particles to escape from the finer soil into the coarser. By combining the particle size of each adjoining zone correctly, internal erosion may be

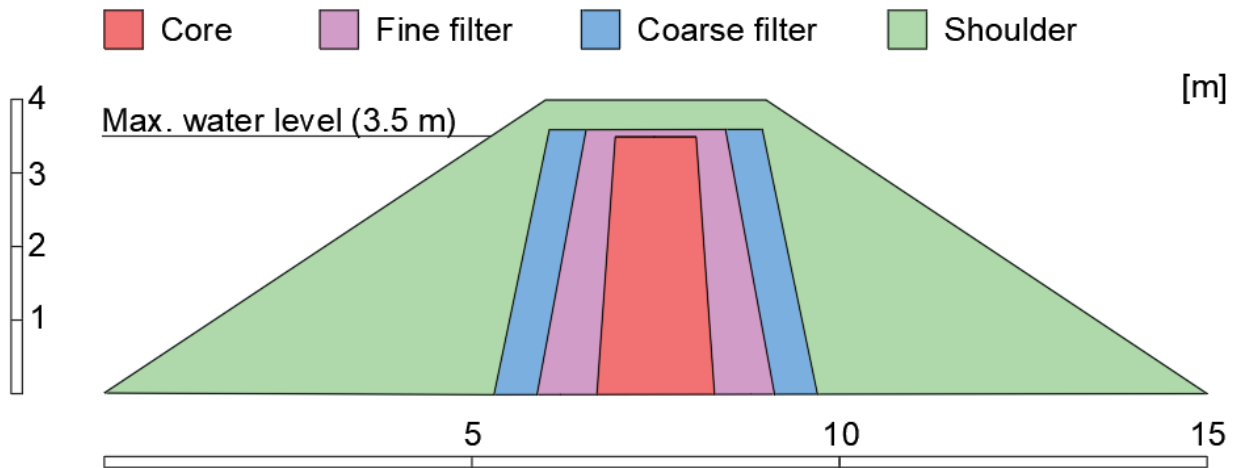


Figure 2. Section of the embankment dam.

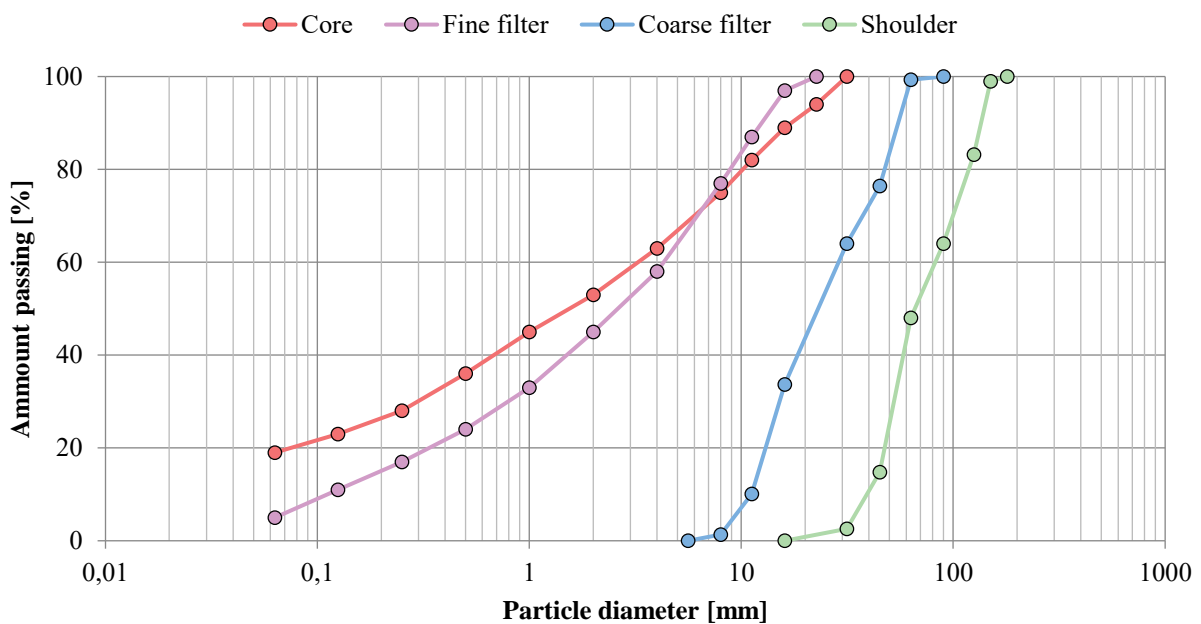


Figure 3. Particle size distributions for the materials used in the embankment dam.

Table 1. Values of material parameters in the embankment dam.

Parameter	Unit	Core	Fine filter	Coarse filter	Shoulder
Unit weight, γ	kN/m ³	22.5	19	17	18
Friction angle, φ	°	42	36	40	41
Hydraulic conductivity, k	m/s	10^{-7}	10^{-5}	10^{-2}	10^{-1}

prevented. The proper combination of particle size distribution curves is described by Terzaghi (1996).

In Sweden, the design and construction of a dam is governed by dam safety guidelines given in RIDAS (Energiföretagen, 2019). The embankment dam herein was designed to have four material zones; core, fine-, coarse filters and shoulder, Figure 2.

The core was a fine-grained till 0-32 mm with 19% content of fines and the other zones were made from crushed rock in various fractions. All particle size distributions can be found in Figure 3. These distributions are from the design stage of the

project. A total of 1500 ton of material was used in the construction of the embankment dam. An overview of some material characteristics in the dam is presented in Table 1.

3.2. Construction

It took four weeks to complete the construction of the embankment dam. The embankment dam was built in layers, by following a specific pallet plan. Each layer was 20 cm thick and was compacted before next layer was placed.

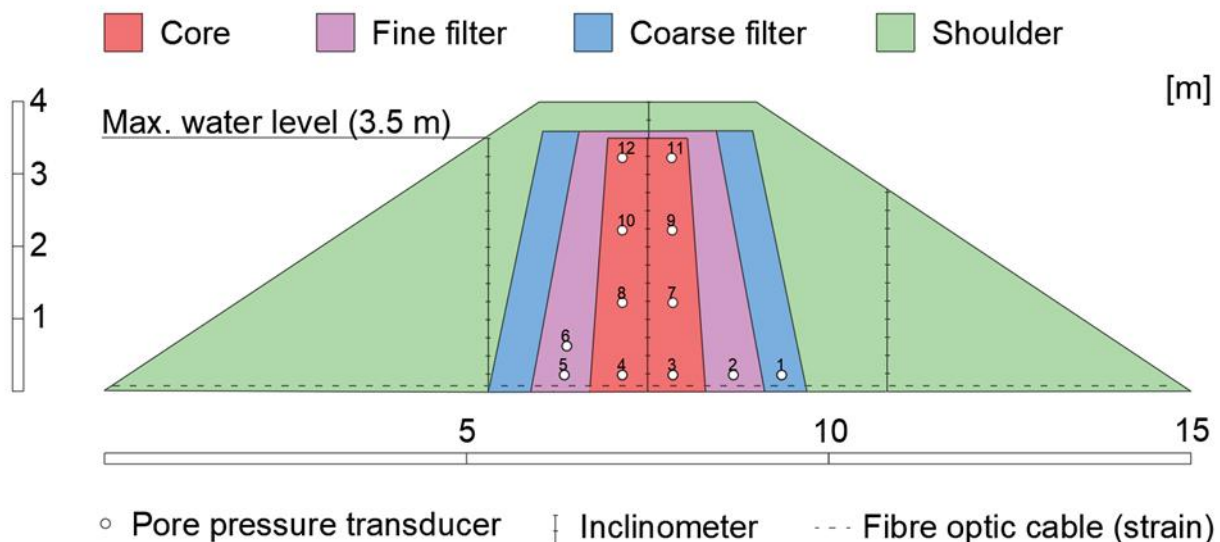


Figure 4. Geotechnical instrumentation in the dam

The sequence of construction was always to start each new layer with the core soil followed by the fine filter, coarse filter and lastly the shoulder fill and thereafter compaction was done with a vibratory rammer. The compaction was done in the same order as the materials were placed. After each layer, the compaction of the core soil was measured with balloon test. The degree of compaction was 90-95% of modified Proctor density.

At six predetermined locations, predefined damages were built into the embankment dam and their position was measured with a total station. The built-in damages are resampling defects that could be found in reality. The upstream shoulder was not compacted and the downstream shoulder was just compacted by an excavator.

Throughout the construction, measurement equipment was placed into the embankment dam. The positioning of the geophysical equipment (cables for resistivity, temperature and seismic) were placed in the fine filter. The positioning of the geotechnical measurement equipment can be seen in Figure 4. All cables from the equipment, except fibre optics, were led into a logging station.

Other measurements include the collection of seepage downstream the embankment dam. A 20 cm deep drainage ditch, running parallel to the toe of the dam, collected the leakage water and led it to a well. The embankment dam was divided into seven sections. At the drainage ditch, the seepage from each section could be measured separately by Thomson weirs.

4 GEOTECHNICAL INSTRUMENTATION

The geotechnical instrumentation was consisting of deformation-, pore pressure- and strain monitoring

devices. All instrumentation was placed in one section of the embankment dam. The location of the instrumentation is shown in Figure 4.

4.1. Deformation

The deformations in the dam were monitored by shape accelerometer arrays (SAA), which allow for deformation monitoring in x, y and z directions. The technology is based on MEMS technology (micro-electro-mechanical system). More information is found in Danisch et al. (2007). The system is able to simultaneously measure deformations (3D) as well as accelerations, based on the tilt from the gravitational direction.

The installed sensors are of type Measurand SAAV250. The rigid segments used were 0.25 m, in order to fit the scale of the project. Three inclinometers have been installed, with position and length as follows (given in Figure 4):

- Upstream, 3.5 m
- Middle, 4.0 m
- Downstream, 3.0 m

X-direction is from upstream to downstream, with just a slight deviation. This was documented and taken into consideration when performing the interpretation of movements in the dam body. The y-direction is along with the dam axis and z is down/upwards. During the construction of the dam, PipeLife tubes were installed. When installing the sensors, they were guided down in the tubes.

Continuous measurements of the deformations are on-going. The data is available online, providing the possibility to follow the development in real time. Temperatures are also measured by the devices. Measurements from finished construction until February 2020 have shown minor movements. This was expected and was mainly attributed to the

activities around the test embankment facility as levelling of the ground and setup of the tent.

4.2. Pore pressure

Vibrating wire piezometers were placed in the core and filters of the dam. The pore pressure transducers are of the type Geosense VWP-3400, with a measuring range of -70 kPa to 345 kPa. The vibrating wire within the sensor is in a closed system, which will react to the pressure changes outside the transducer. However, this also means that the measurements are affected by the atmospheric pressure and needs to be corrected due to that.

12 vibrating wire piezometers were installed during construction of the dam, where they were placed directly on a compacted layer. The placement of the piezometers was done according to Figure 4. A pore pressure transducer is shown in Figure 5.



Figure 5. Pore pressure transducer placed in the fine filter.

Continuous measurements of the pore pressure in the dam will be performed. Measurements so far have only shown that the equipment is working since water has not yet been filled in the reservoir. With time, saturation of the core soil and filters will be monitored.

4.3. Strain

Strain measurements with fibre optics are performed in the bottom of the embankment dam. The measurements are done perpendicularly to the dam axis in four sections. The application of strain measurements used here was developed in the work by Iten (2011).

Installations have been done with two fibre optic cables; one for measuring strain and one for temperature compensation. The cables have been installed in a shielded bed of sand. Since the cables are placed perpendicularly to the dam axis, the

cables have to cross all material zones. Thus, the material is varying from the fine-grained till in the core to a more boulder-sized material in the shoulder of the dam. In the area of the shoulder and filter zones, geotextile was first placed and backfilled with sand. Bentonite was used to seal the cables in the core. The cables were pre-tensioned when installed.

The fibre optic cables were installed in a loop, consisting of four sections through the dam, see Figure 6. When construction of the embankment dam was finished, the clamps providing the pre-tension were loosened, as the cables were already fixed in the material and thereby “locked” in place.



Figure 6. Installation of fibre optics cables.

Measurements will be performed at certain times, especially when there are changes in the loading scenarios as when the reservoir of the dam is to be filled. The zero-measurement readout was successful, showing that the cables were working without losses. This was conducted in end of November 2019.

5 CONTINUED MONITORING AND USE OF THE DATA

The data from the geotechnical instrumentation is mainly planned to be used in inverse modelling. Inverse modelling of the embankment dam is aiming to identify the values of the material parameters of the soil in the different zones.

With time, if changes are occurring in the embankment dam, this could be reflected in the results of the inverse analysis. The analysis could then be resulting in changes in values of material parameters with time. The amount of data to be acquired will allow for re-calibration and an upgrade of the values of the material parameters.

In reality, this amount of geotechnical instrumentation is very seldom found in existing dams. Having so many installations as in this project, gives an opportunity to determine how much instrumentation would be sufficient to perform a reliable inverse analysis. This could lead to further recommendations on how to conduct inverse analysis for other embankment dams.

6 ACKNOWLEDGEMENTS

The research presented in this paper was carried out as a part of 'Swedish Hydropower Centre – SVC'. SVC was established by the Swedish Energy Agency, Energiforsk and Svenska kraftnät together with Luleå University of Technology, KTH Royal Institute of Technology, Chalmers University of Technology and Uppsala University. Participating companies and industry associations are: Andritz Hydro, Boliden, Fortum Generation, Holmen Energi, Jämtkraft, Karlstads Energi, LKAB, Mälarenergi, Norconsult, Rainpower, Skellefteå Kraft, Sollefteåforsens, Statkraft Sverige, Sweco Energuide, Sweco Infrastructure, Tekniska verken i Linköping, Uniper, Vattenfall R&D, Vattenfall Vattenkraft, Voith Hydro, WSP Sverige, Zinkgruvan and AFRY.

The authors would furthermore like to thank Vattenfall AB for their contribution in building the test facility and to care for its proper operation. Energiforsk's Dam safety program is also acknowledged for support. Cautus Geo AS and Marmorta Engineering AG are acknowledged for the support installing the measurement system.

7 REFERENCES

- Danisch, L.A., Lowery-Simpson, M.S., and Abdoun, T. 2007. Shape-acceleration measurement device and method, US Patent US7296363 B2.
- ICOLD. 2013. Bulletin 164: Internal erosion of existing dams, levees, and dikes, and their foundations – Volume 1: Internal erosion processes and engineering assessment. ICOLD.
- Iten, M. 2011. Novel Applications of Distributed Fiber-optic Sensing in Geotechnical Engineering. ETH Zurich, Switzerland.
- Energiföretagen. 2019. RIDAS - Kraftföretagens riktlinjer för dammsäkerhet. Energiföretagen, Stockholm, Sweden. (In Swedish)
- Terzaghi, K., Peck, R., Gholamreza, M. 1996. Soil Mechanics in Engineering Practice, Third Edition. John Wiley & Sons Inc., New York, USA.
- Toromanovic, J., Mattsson, H., Knutsson, S. and Laue, J. 2020. Parameter identification for an embankment dam using noisy field data. Proceedings of the Institution of Civil Engineers - Geotechnical Engineering, Available from: <https://doi.org/10.1680/jgeen.19.00163>.

Surface wave propagation in centrifuge testing using Electromagnetic Drop-Projectile system

Vipul Kumar^{1,2}, S.P.G. Madabhushi¹

¹*Schofield Centre, Department of Engineering, University of Cambridge, UK*

²*Geotechnical Engineer, Mott MacDonald, UK*

Corresponding author: Vipul Kumar (vk337@cam.ac.uk)

ABSTRACT: Surface wave propagation can be experimentally investigated with the help of centrifuge modelling. In this paper, we discuss the development of an electromagnetic drop-projectile apparatus which will be used to generate vibrations in the soil upon impact onto a shallow foundation. This apparatus was developed as an improvement over the drop-ball apparatus developed by previous researchers. The drop projectile assembly allows to vary drop height and perform multiple drop tests during a single flight of the centrifuge package. This system can be used to generate vertical vibrations in the soil to replicate the loading pattern generated by high speed trains such as upcoming HS2 in the UK. Attenuation of accelerations in soil suggest that friction between soil particles and confining stress have a significant effect on the transmission of surface waves.

Keywords: Rayleigh Waves; Centrifuge Modelling; Drop-Projectile System; High-Speed Trains.

1 INTRODUCTION

High speed trains have emerged out as an attractive alternative for inter-city travel and commerce as compared to air transport. High speed rail networks not only tend to promote growth between their major hub cities, but they can also promote growth, act as a catalyst of socio-economic development for population centres along their routes.

European Union directive defines a high speed rail as lines which are purpose-built for train speeds equal or greater than 250 km/hr or lines which are upgraded to allow train speeds greater than 200km/hr. UK is now developing its new high speed rail network (HS2), with projected operational speed of HS2 trains is about 360 km/hr, connecting the densely populated and commercial centre of London with the other major northern cities.

Ground-borne vibrations generated by high speed trains can not only cause discomfort to the onboard passengers but the vibrations propagating within the ground can also affect railway catenary structures, adjacent buildings and any sensitive mechanical equipment which might fall within the zone of disturbance.

The main mechanism of generation of ground-borne vibrations is the wheel-axle pressure acting on the rails (Figure 1). Dynamic amplification of train-track vibrations has been a subject of theoretical research in the last century. For a non-oscillating train load moving with a constant velocity on the surface of an elastic half-space, train-track vibrations tend to amplify as the train speed approaches a certain critical velocity (Rayleigh wave velocity) of the medium supporting

railway track(s) (Fryba 1972; Kenney 1954; Krylov 1995; Payton 1967).

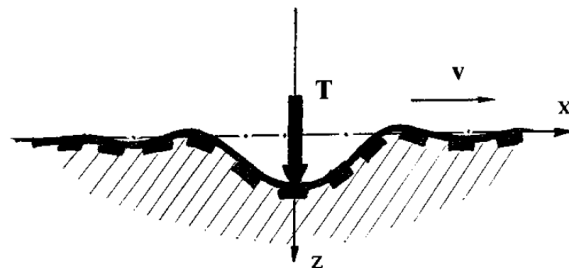


Figure 1. Generation of ground-borne vibrations due to wheel-axle load on rails (Krylov 1996)

Generally, the Rayleigh surface velocity of subgrade is in the range of 100-200 m/s and it was not possible for conventional trains to reach this critical velocity. However, it was only after 1970s that with the increasing operational train speeds, multiple instances of high dynamic train-track amplification were observed in the field where the track alignment passed over ground with low Rayleigh surface wave velocity (in the range of 40-60 m/s) consisting of soft soils such as soft silty clays, peats and organics at shallow depths (Adolfsson et al. 1999; Madshus and Kaynia 2000; Woldringh and New 1999). In these instances, high speed rail operations could only be fully resumed after undertaking ground remediation measures to stiffen the subgrade and consequently increasing the Rayleigh surface wave velocity.

Analytical solutions are generally valid only for simpler geometry and boundary conditions. A

number of researchers have used numerical methods for propagation of surface waves and vibration mitigation problems including Buonsanti et al. (2010); Correia et al. (2007); Holm et al. (2002); Banimahd et al. (2007) among others. The advantage of numerical models lie in their ability to model complex geometries such as embankments, cuttings, piled embankments etc. and wave propagation in multi-layered ground. However, the soil behaviour in most of these analyses have been limited to linear elastic and nonlinear elastic behaviour, which is not the case for soils, especially soft soils. The accuracy of numerical solutions for prediction of vibrations depend on multiple factors including constitutive model for soils, element discretisation, consideration of soil damping and simplification for vehicle-body dynamics.

Early experimental research in the form of field tests into propagation of vibrations from a stationary mechanical source and the effectiveness of vibration isolation measures were carried out by Barkan (1962) and Woods (1968) among others.

Full-scale field studies can be quite expensive and can also be limited in their flexibility to undertake parametric studies. Centrifuge modelling is an attractive alternative to develop small-scale physical models which are tested under the enhanced field of centrifugal acceleration. Centrifuge models can replicate the correct stress-strain behaviour of soil at prototype scale in the model (Madabhushi 2017). However, geotechnical centrifuge research into surface wave propagation has still remained a relatively less explored field as compared to earthquake engineering.

Luong (1996) carried out comparative centrifuge-based experiments to study the effectiveness of a stress-wave mitigation barrier subjected to impulse loading generated by explosives and a novel drop-ball apparatus. Luong (1996) concluded that the drop-ball apparatus is more convenient to set-up and the characteristics of the impulse such as frequency and amplitude, can be more easily customised than the impulse generated by blast loading. Semblat and Luong (1998) carried out further experiments using the drop-ball experiments developed for investigating surface wave propagation by Luong (1996). It was noted by the authors that the nonlinear effects near the source might affect wave propagation and limit the applicability of empirical equations of wave attenuation.

Itoh et al. (2002) further expanded on this idea by developing a multiple ball dropping system (MBDS) to simulate a moving high speed train load in centrifuge experiments. Figure 2 shows the schematic sketch of drop-ball system with two model foundations for modelling of moving point

load. The speed of moving load achieved in their centrifuge tests conducted at 50g was about 89 m/s, which was approximately half of the surface wave velocity reported by the authors. In this speed regime, the train-track (foundation) dynamic amplification effects in the experiments could be quite limited based on the data collected from case histories (Woldringh and New 1999).

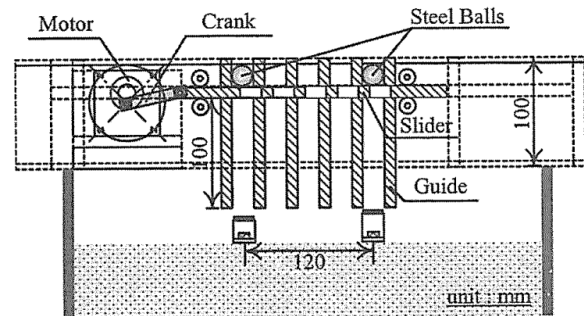


Figure 2. Schematic sketch of moving load simulator (Itoh et al. 2002)

In another set of experiments, Itoh et al. (2005) developed a vibration generator to apply harmonic loads to circular bearing plates. In contrast to the multiple ball dropping system (Itoh et al. (2002), the vibration generator applied both horizontal and vertical vibrations. Centrifuge tests performed at 50g were used to investigate the effect of epoxy poly-styrol (EPS) barrier and crumb rubber-modified asphalt (CRMA) underneath the foundation as vibration mitigation measures. The authors suggested that the performance of drop-ball system (Itoh et al. 2002) was better than the vibration generator system in terms of impact energy and mobilisation of strains within soil.

Yang et al. (2013) undertook centrifuge and numerical modelling to investigate ground-borne vibrations from surface sources. The vertical excitation was generated by an electromagnetic shaker which was driven by sinusoidal input waveform of varying frequency content. It was concluded that to calibrate the response from numerical models at surface and at depth, it is advisable to use a nonlinear stress-dependent soil stiffness rather than assuming a constant average value.

In this paper we focus on the development of modified version of drop-ball system and its application for generating surface waves in homogeneous and layered soil profiles. This paper also discusses the measurement of shear wave velocity (V_s) to characterise in-situ ground stiffness, which is not often discussed in the context of geotechnical centrifuge testing for surface wave propagation. A brief discussion of effect of soil

stiffness contrast from the preliminary analysis of surface wave propagation in soil is also presented.

2 CENTRIFUGE MODELLING

With the help of scaling laws, centrifuge experiments can be used to model correct stress-strain behaviour at a certain depth in 1g prototypes. The centrifuge tests discussed in this paper were all performed at 40g. For centrifugal acceleration of ‘Ng’, the scaling laws reproduced from Madabhushi (2017) are presented in Table 1. Two models will be discussed in this paper – Model 1 (homogeneous dry sand) and Model 3 (dense sand layer over soft clay).

Centrifuge tests reported in Section 1 were limited to homogeneous, dry sand medium. As reported in the case studies (Section 1), high dynamic train-track amplification scenarios generally occur when soft, compressible soil is present underneath the track. One of the current practices for reducing dynamic amplification of train-track vibrations is to improve the subgrade stiffness in order to increase the critical surface velocity. To investigate surface wave propagation for situations where a stiff layer overlies soft ground, Model 3 was prepared with a 47 mm thick (prototype thickness of about 1.9 m) layer of dense sand overlying soft clay.

Table 1. Centrifuge scaling laws

Parameter	Dimensions	Model/Prototype
Length	L	1/N
Velocity	LT ⁻¹	1
Acceleration	LT ⁻²	N
Strain	-	1
Stress	ML ⁻¹ T ⁻²	1
Mass	M	1/N ³
Time (dynamic)	T	1/N
Frequency	T ⁻¹	N

2.1. Equipment

The main equipment used was the 10 m beam centrifuge with a radius of 4.125 m from the centre of rotation to the top of swinging platform. The model container used in the centrifuge testing is a circular tub with an internal diameter of 850 mm and a height of 400 mm. In-situ value of small-strain stiffness of soil was evaluated by measuring the time-lag between arrival of peak shear wave amplitude between known locations of any two piezoelectric-accelerometers. The shear waves were generated with the help of Air Hammer (Figure 3), originally developed by Ghosh and Madabhushi (2002), placed near the bottom of the model container.



Figure 3. Miniature Air Hammer (Ghosh 2003)

2.2. Instruments and Data Acquisition

Piezoelectric-accelerometers of type A/23 were placed at various depths in the soil during model preparation to measure the stress-pulse generated by Air Hammer. These accelerometers were waterproofed with wax before placing them in clay. MEMS-type accelerometers of type ADXL78 with $\pm 70g$ were used to measure vertical acceleration at the source of vibration and within the soil. Previous centrifuge experiments performed by Stringer et al. (2010) showed that MEMS-type accelerometers can have a better accelerometer-soil coupling than the piezoelectric-type accelerometers.

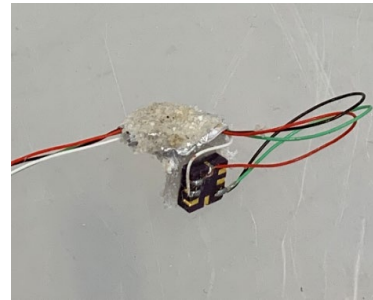


Figure 4. ADXL78 type MEMS accelerometer glued to HDPE plastic

These MEMS accelerometers have typical dimensions of 5 mm by 5mm by 2mm. These accelerometers were oriented in vertical direction by gluing them to a hand-cut piece of HDPE plastic as shown in Figure 4. Accelerometer-soil coupling was improved by gluing dry sand to the accelerometers and HDPE plastic. Electrical signals from the instruments were transmitted via junction boxes and through on-board computers on the beam computer and digitised by DASyLab data acquisition software.

2.3 Model Preparation

In the preparation of sand bed for Model 1 and Model 3, Hostun HN31 silica sand was used. The minimum (e_{min}) and maximum (e_{max}) void ratio of

Hostun sand are 0.555 and 1.01 (Mitrani 2006). The sand was poured using an automatic sand pourer designed at the Schofield Centre (Madabhushi et al. 2006) to achieve relative density of about 50% and a total thickness of 232 mm for Model 1. For Model 3, the lower clay layer was prepared by consolidating slurry made out of speswhite Kaolin powder mixed with water to 120% of its liquid limit. The slurry was consolidated to a pressure of 200 kPa under a stress-controlled consolidation rig at 1g in an 850 mm diameter circular tub. After reaching the required stress state, the tub was unloaded from the rig and the clay surface was hand-trimmed to achieve a thickness of 157 mm. Hostun HN31 sand was poured over this clay layer using automatic sand pourer to a total thickness of 47 mm and relative density of about 67%.

2.4 Vibration Generation Source

2.4.1 Piezoelectric Actuator

At first, the feasibility of a piezoelectric actuator was explored as source of generating vertical vibrations. An APA400MML amplified piezoelectric actuator (APA) was connected to an aluminium disk 30 mm in diameter and 5 mm in thickness. The actuator was controlled and driven by LA75B and LC75B supplied by Cedrat Technologies. The actuator was excited with voltage-controlled sine waves generated by a TG330 function generator with excitation frequencies in the range of 20-150 Hz.

For 1g trials, Hostun HN31 sand was poured in an 850 mm tub; piezoelectric accelerometers were placed about 15 mm below the sand surface. The piezoelectric actuator was bolted onto a gantry spanning the width of the tub to provide a rigid support. The test assembly is shown in Figure 5.

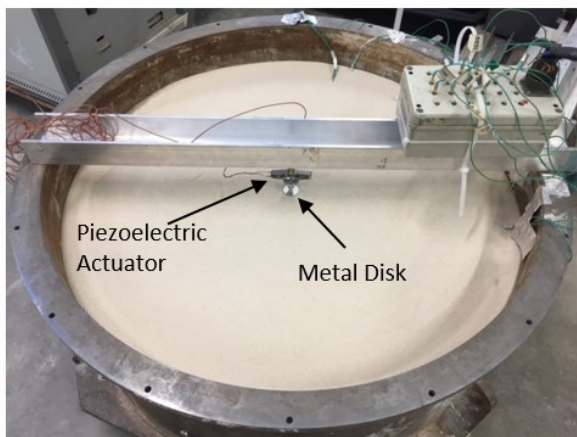


Figure 5. Test package with APA400MML actuator

A test up similar to Model 3 soil profile was run in the centrifuge with piezoelectric actuator which

yielded a poor signal-to-noise ratio and therefore, the possibility of using APA400MML piezoelectric actuator was abandoned and an alternative was developed as discussed in Section 2.4.2.

2.4.2 Drop-Projectile System

The drop-ball system of previous researchers discussed in Section 1 were limited to a single drop height. To investigate the relationship between impact load (or, drop height) and surface wave propagation, the first iteration (Figure 6) of drop-ball system was developed at the Schofield Centre. It could perform multiple drop-tests during a single flight of centrifuge package. An electromagnet of type 58-50 with 24 V DC rating supplied by SG Transmission was used to hold and pick-up a metal spherical ball of mass 34 g. The drop-height could be adjusted with the movement of a 1D linear actuator manufactured by SKF.

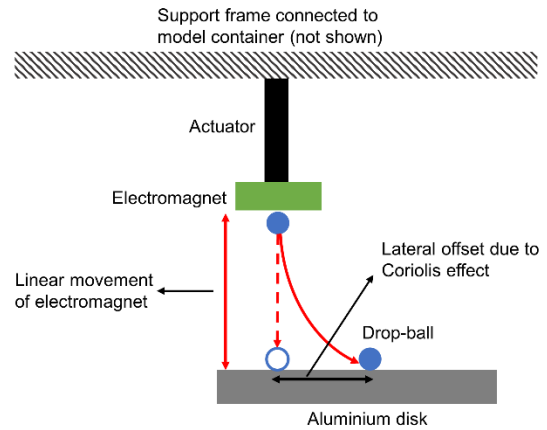


Figure 6. Schematic representation of first iteration of drop-ball system (for Model 1)

A ‘ball drop’ was performed by simply turning OFF the current to electromagnet. The impact occurred on an aluminium disk 60 mm in diameter and with an average thickness of approximately 10 mm. The disk was placed on the surface of model ground but with a lateral offset accounting for Coriolis effect on the falling spherical ball under the field of centrifugal acceleration ‘Ng’. The values of lateral offset (d_{lat}) due to Coriolis force were calculated for drop-heights (H_{cor}) of 75 mm, 100 mm and 125 mm using Equation 1 (Madabhushi 2017).

$$d_{lat} = \frac{2^{\frac{2}{\sqrt{2}}}}{3} \frac{H_{cor}^{1.5}}{4.125^{0.5}} \quad (1)$$

During the centrifuge flight of Model 1, it was found out that due to the Coriolis effect, the spherical ball would fall outside the effective diameter of the electromagnet for it to be picked up.

Therefore, for the testing of Model 3, a second iteration (Figure 7) of drop-ball system was developed to overcome these issues. To allow the movement of electromagnet within the Perspex tube, a smaller electromagnet (type 58-30) was used. A small gap was left between the end of Perspex tube and upper face of aluminium disk to vent out the air pressure (drag) which would develop in front of the projectile during its fall.

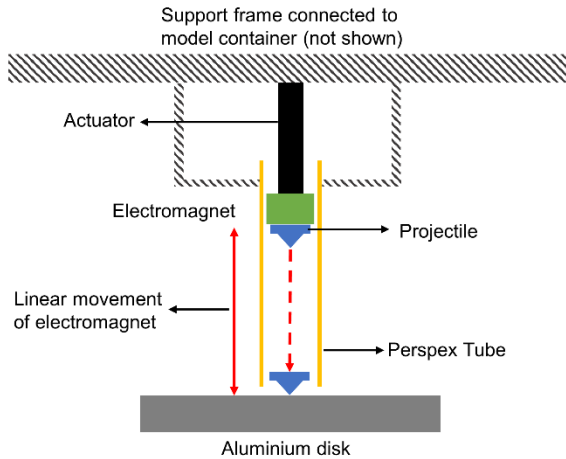


Figure 7. Schematic representation of second iteration of drop-ball system (for Model 3)

In this iteration, a Perspex guide tube was provided to channel a custom-made projectile (Figure 8). This projectile has a mass of about 34 g and a maximum diameter of 30 mm. Centrifuge experiments showed that this second iteration performed was significantly more reliable than the first iteration.



Figure 8. Custom-made projectile for second iteration of drop-ball system (Drop-Projectile System) for Model 3

2.5 Experimental Program

After loading the centrifuge package onto the beam centrifuge, it was spun upto 96 rpm to get to 40g. Figure 9 shows the assembled package of Model 3 with second iteration of drop-projectile system in the middle.

Air Hammer test was done until three clean pulses were recorded for piezoelectric-accelerometers buried throughout the model depth. Afterwards

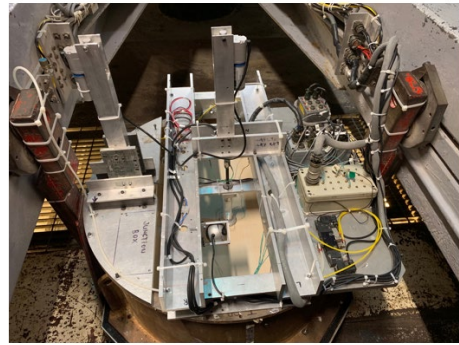


Figure 9. Assembled centrifuge package (Model 3) loaded onto the swing platform of 10 m beam centrifuge

impact tests were done using drop-ball (Model 1)/ projectile (Model 3) system. The three different drop heights were kept same between Model 1 and Model 3 for consistency. The resulting vertical accelerations were measured at the source (disk) and in soil. All signal processing operations were performed in MATLAB R2019a.

Figure 10 and Figure 11 show the sketch of instrumentation layout for Model 1 and Model 3.

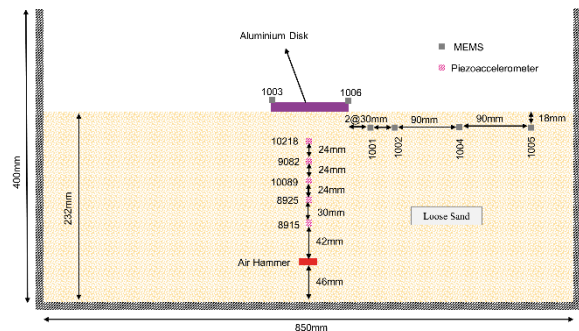


Figure 10. Sketch of instrumentation for Model 1

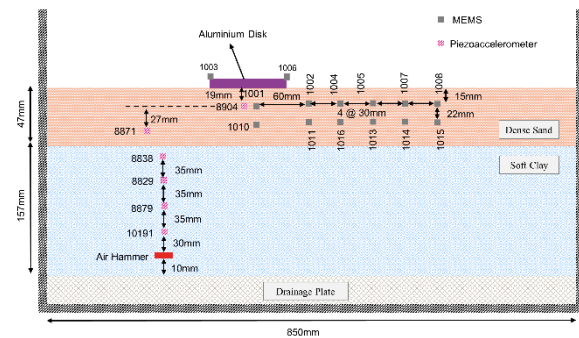


Figure 11. Sketch of instrumentation for Model 3

3 CENTRIFUGE RESULTS

3.1. Soil Stiffness (V_s)

Time-traces of vertically upwards propagating shear waves were obtained from horizontally oriented piezoelectric-accelerometers buried at different depths in model soil layer(s). The time delays in the arrival of peak pulse amplitude were used to calculate in-situ shear wave velocity profile (V_s).

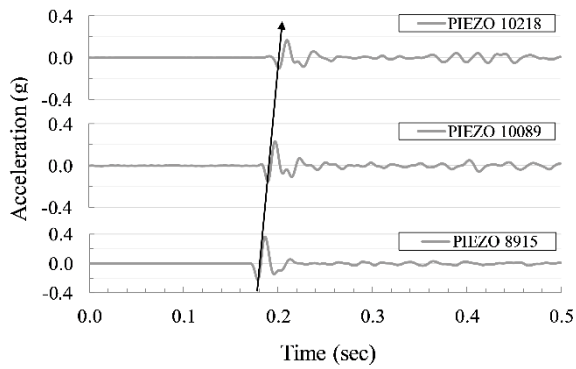


Figure 12. Acceleration time histories at prototype scale (Model 1)

Figure 12 shows the acceleration time histories at prototype scale as measured by the piezoelectric-accelerometers for a representative case (Model 1). Although the amplitude decays as the distance from the Air Hammer increases, but the waveform even near the surface was clean enough to obtain a reasonably accurate measurement of time-lag in arrival of first peak. Empirical expressions (Hardin and Drnevich 1972; Oztoprak and Bolton 2012) of small-strain shear modulus (G_0) and known values of mass density (for sand) were used to derive V_s profile as a function of depth; there is a lack of similar relationships for clays. The comparisons for Model 1 and Model 3 are presented in Figure 13 and Figure 14, respectively. It was observed that the experimental V_s profile for sands was slightly softer than the one obtained from empirical relationships. A significant V_s (soil stiffness) contrast was observed between the upper dense sand layer and lower soft clay layer for Model 3.

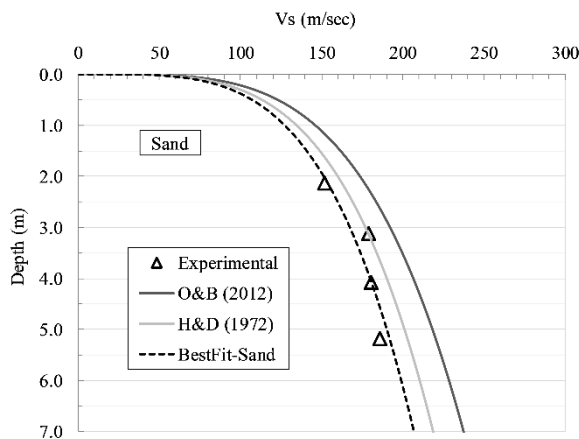


Figure 13. V_s profile at prototype scale -Model 1

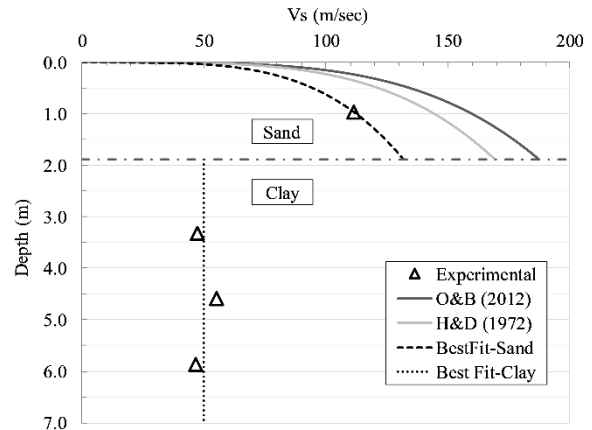


Figure 14. V_s profile at prototype scale – Model 3

3.1. Wave propagation in ground

Vertical accelerations generated due to the impact of falling ball (Model 1)/ projectile (Model 3) were measured at the source and at different locations in soil. Figure 15 shows a representative example of the vertical acceleration time histories (prototype scale) at lateral distance away from the source (shallow depth) for Model 3 generated due to the projectile falling through a drop height of 75 mm.

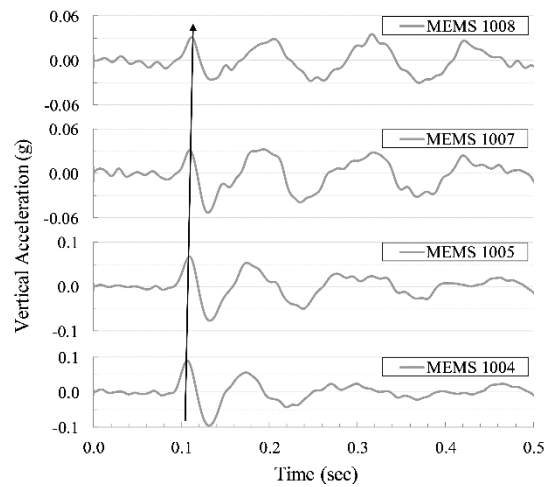


Figure 15. Vertical accelerations measured at shallow depth in soil (prototype scale) for Model 3

Attenuation of surface waves could be inferred from the decay of peak amplitude of first arrival of vertical accelerations in soil. These peak amplitudes were averaged for vertical accelerations obtained from all the three drop heights. Figure 16 shows the comparison of these averaged accelerations for

MEMS buried at shallow depth for Model 1 and Model 3 against normalised distance (d/R), where d is the magnitude of distance vector of MEMS from source of vibration and R is the inner radius of model container. The surface wave attenuation results tend to suggest that for the case of stiff soil overlying soft soil (Model 3), the stiffer layer could experience higher accelerations near the source and at shallow depths as compared to model without a significant soil stiffness contrast (Model 1).

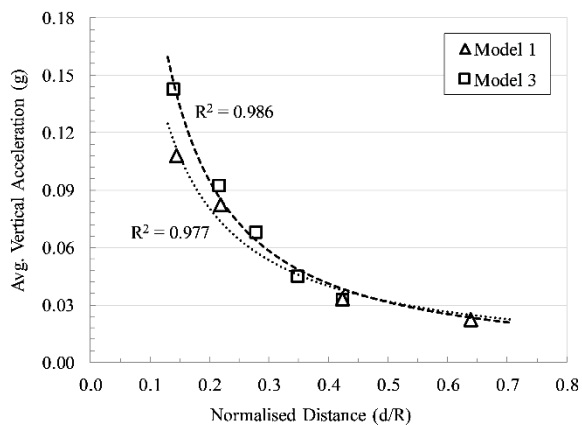


Figure 16. Comparison of averaged vertical accelerations (prototype scale) at shallow depth

For each depth location, normalised accelerations were derived wherein for a given depth, the averaged maximum acceleration at any location was normalised with respect to the first MEMS at that depth. Figure 17 shows comparison of normalised average accelerations for MEMS buried at shallow and deep depth plotted as a function of normalised distance d/R for Model 3. The results suggest that for approx. similar value of normalised distances, the MEMS at deeper depth have higher normalised amplification compared to MEMS at shallow depth, which might suggest a waveguide effect occurring within stiff sand layer due to soil stiffness contrast.

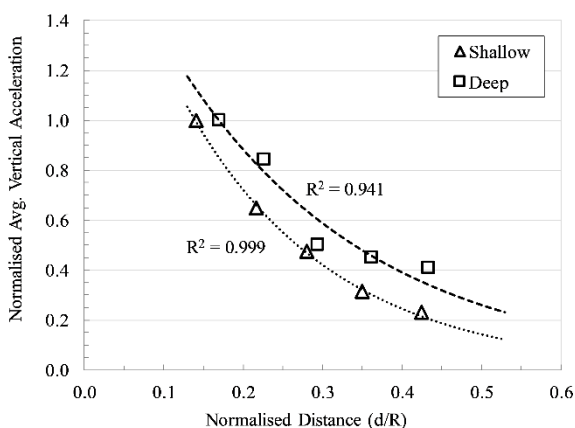


Figure 17. Comparison of normalised vertical accelerations at different depths for Model 3

4 CONCLUSIONS

This paper describes an experimental research into the generation and attenuation of surface waves in homogeneous and layered soil profiles. An electromagnetic drop-projectile was developed as an enhancement over the original drop-ball system developed by Luong (1996) to increase reliability and repeatability of experiments. Following conclusions were drawn from the centrifuge tests:

1. Air Hammer test results provided in-situ measurement of shear wave velocity (V_s) to allow for more accurate soil characterisation for wave propagation than using empirical relationships based on index properties.

2. The results suggest that regardless of the soil stiffness contrast, the impulse generated at the source has sufficiently attenuated due to geometric attenuation and frictional work between sand particles (material damping) before reaching the model container boundary.

3. Soil stiffness contrast (stiff sand over soft clay) tend to create a waveguide effect within the upper layer which tend to amplify accelerations near the source at shallow depth and also for a longer lateral distance away from the source.

5 ACKNOWLEDGEMENTS

The authors would like to acknowledge peers, technical staff at the Schofield Centre for their incredible support, meaningful discussions and sharing their experiences in overcoming the challenges. The first author would also like to thank Dr. Barnali Ghosh, Tony O'Brien, Imran Farooq for their guidance and generous grant from Mott MacDonald's Research Fund in supporting the research at Cambridge University.

6 REFERENCES

- Adolfsson, K., Andreasson, B., Bengtsson, P. E., & Zackrisson, P. 1999. High speed train X2000 on soft organic clay - measurements in Sweden. Geotechnical Engineering for Transportation Infrastructure. Proceedings of the 12th European Conference on Soil Mechanics and Geotechnical Engineering, Amsterdam, June 1999. Vol. 3.
- Banimahd, M., & Woodward, P. K. 2007. Numerical Study Of Train Speed Effect On Railway Track Response. Railway Infrastructure: Railtex - International Railway Engineering Conference, 4(1). Retrieved from <http://www.xitrack.com/paper6.pdf>
- Barkan, D. D. 1962. Dynamics of Bases and Foundations. McGraw-Hill Book Co., Inc., New York.
- Buonsanti, M., Leonardi, G., & Scopelliti, F. 2010. Analyses of ground-borne vibrations induced by high

- speed trains. 10th International Workshop on Railway Noise. Nagahama.
- Fryba, L. 1972. Vibration of Solids and Structures under Moving Loads. In *Vibration of Solids and Structures under Moving Loads* (pp. 83–93). <https://doi.org/10.1680/vosasuml.35393.0007>
- Gomes Correia, A., Cunha, J., Marcelino, J., Caldeira, L., Varandas, J., Dimitrovová, Z., Gonçalves Da Silva, M. 2007. Dynamic analysis of rail track for high speed trains. 2D approach. *Applications of Computational Mechanics in Geotechnical Engineering - Proceedings of the 5th International Workshop on Applications of Computational Mechanics in Geotechnical Engineering*.
- Ghosh, B., & Madabhushi, S. P. G. 2002. An efficient tool for measuring shear wave velocity in the centrifuge. *International Conference on Physical Modelling in Geotechnics*, 119–124. Luong, P. M. (1996). Centrifuge modelling of a seismic barrier using soil energy dissipation. *Eleventh World Conference on Earthquake Engineering*. <https://doi.org/10.13140/2.1.2613.1202>
- Ghosh, B. 2003. Behaviour of rigid foundation in layered soils during seismic liquefaction. PhD thesis, University of Cambridge.
- Hardin B.O., & Drnevich V.P. 1972. Shear modulus and damping in soils: design equations and curves. *Soil Mechanics and Foundations Division*, 98(7), 667–692.
- Holm, G., Andreasson, B., Bengtsson, P., Bodare, A., & Eriksson, H. 2002. Mitigation of Track and Ground Vibrations by High Speed Trains at Ledsgard, Sweden. Report 10. 1–60.
- Itoh, K., Koda, M., Lee, K. I., Murata, O., & Kusakabe, O. 2002. Centrifugal simulation of wave propagation using a multiple ball dropping system. *International Journal of Physical Modelling in Geotechnics*, 2(2), 33–51. <https://doi.org/10.1680/ijpimg.2002.020203>
- Itoh, K., Zeng, X., Koda, M., Murata, O., & Kusakabe, O. 2005. Centrifuge simulation of wave propagation due to vertical vibration on shallow foundations and vibration attenuation countermeasures. *JVC/Journal of Vibration and Control*. <https://doi.org/10.1177/1077546305054150>
- Kenney, J. T. 1954. Steady-state vibrations of beam on elastic foundation for moving load. *Journal of Applied Mechanics-Transactions of the ASME*, 359–364.
- Krylov, V. V. 1995. Generation of ground vibrations by superfast trains. *Applied Acoustics*, 44(2), 149–164. [https://doi.org/10.1016/0003-682X\(95\)91370-1](https://doi.org/10.1016/0003-682X(95)91370-1)
- Krylov, V. V. 1996. Vibrational impact of high-speed trains. I. Effect of track dynamics. *The Journal of the Acoustical Society of America*. <https://doi.org/10.1121/1.417123>
- Madabhushi, G. 2017. Centrifuge modelling for civil engineers. *Centrifuge Modelling for Civil Engineers*. <https://doi.org/10.1201/9781315272863>
- Madabhushi, S. P. G., Houghton, N. E., & Haigh, S. K. 2006. A new automatic sand pourer for model preparation at University of Cambridge. *Physical Modelling in Geotechnics, 6th ICPMG'06 - Proceedings of the 6th International Conference on Physical Modelling in Geotechnics*, 217–222. CRC Press.
- Madshus, C., & Kaynia, A. M. 2000. High-speed railway lines on soft ground: dynamic behaviour at critical train speed. *Journal of Sound and Vibration*. <https://doi.org/10.1006/jsvi.1999.2647>
- Mitrani, H. 2006. Liquefaction remediation techniques for existing buildings. PhD thesis, University of Cambridge.
- Oztoprak, S., & Bolton, M. D. 2012. Stiffness of sands through a laboratory test database. *Géotechnique*. <https://doi.org/10.1680/geot.10.p.078>
- Payton, R. G. 1967. Transient motion of an elastic half-space due to a moving surface line load. *International Journal of Engineering Science*, 5(1), 49–79.
- Semblat, J. F., & Luong, M. P. 1998. Wave propagation through soils in centrifuge testing. *Journal of Earthquake Engineering*, 2(1), 147–171. <https://doi.org/10.1080/13632469809350317>
- Stringer, M., Heron, C., & Madabhushi, S. 2012. Experience using MEMS-based accelerometers in dynamic testing. *Physical Modelling in Geotechnics, 7th ICPMG' 10 - Proceedings of the 7th International Conference on Physical Modelling in Geotechnics* (pp. 389–394). <https://doi.org/10.1201/b10554-61>
- Woldringh, R. F., & New, B. M. 1999. Embankment design for high speed trains on soft soils. *Geotechnical Engineering for Transportation Infrastructure. Proceedings of the 12th European Conference on Soil Mechanics and Geotechnical Engineering, Amsterdam, June 1999. Vol. 3*.
- Woods, R. D. 1968. Screening of surface waves in soils. *Journal of the Soil Mechanics and Foundations Division*, 94(4), 951–980.
- Yang, W., Hussein, M. F. M., Marshall, A. M., & Cox, C. 2013. Centrifuge and numerical modelling of ground-borne vibration from surface sources. *Soil Dynamics and Earthquake Engineering*. <https://doi.org/10.1016/j.soildyn.2012.09.003>

Centrifuge modelling of train passage over clay subgrades

Scott Robinson¹, Andrew Brennan¹, Cameron Munro¹, Peter Woodward², David Connolly², Omar Lagrouche³, Ahmet Esen³

¹Division of Civil Engineering, University of Dundee, Scotland, UK

²School of Civil Engineering, University of Leeds, England, UK

³School of the Built Environment, Heriot-Watt University, Scotland, UK

Corresponding author: Scott Robinson (s.z.robinson@dundee.ac.uk)

ABSTRACT: The modelling of large geotechnical structures on the centrifuge is now well established, but there remain technical challenges with each new application. This work arose from a larger project investigating alternative improved embankment designs. The project required full scale modelling of new embankment designs using the GRAFT II simulator at Heriot Watt University together with consideration of the large scale settlement problem over a wider area. To model foundation soil beneath the embankment required the design of a rail simulator at centrifuge scale, together with appropriate measurement techniques and appropriate modelling of useful foundation soil types. This paper therefore describes the design decisions taken to produce a centrifuge mounted rail simulator including details of modelling a translating cycling load. To measure total stress at the base of the embankment during a train passage was a key challenge faced, overcome by use of thin Singletact stress transducers. These transducers are low deflection capacitance-based force sensors that will be further discussed in the paper. In addition to the translating load and the instrumentation, the third aspect presented will be the formation and characterisation of a soft clay subgrade, required due to the nature of soils that are most of concern to UK rail industry. To accelerate consolidation without compromising the ability to achieve a clay-type mechanical response, a hybrid clay-sand-silt mixture known as KSS 541 is installed in the model container as slurry and consolidated in-flight. Experience with this material is discussed.

Keywords: Railways; Embankments; Centrifuge Modelling; Clays; Stress Measurements.

1 INTRODUCTION

This research was carried out as part of the UK EPSRC funded LOCORPS project (Lowering the Cost Of Railways using Preformed Systems), which aims to investigate and assess more efficient alternative embankment solutions for high speed rail that can be more rapidly constructed compared to conventional designs. The project consists of multiple approaches, including testing of full scale embankment sections using the GRAFT II rail test facility at Heriot-Watt University in Edinburgh, focusing on the behaviour of the embankment itself under train loading, as well as centrifuge modelling of the proposed embankment designs at the University of Dundee investigating the embankment performance on different subsoils and the interaction between them. Modelling the subsoil is difficult to achieve using full-scale testing due to the space and volume required, and is an area where centrifuge modelling is advantageous. The research investigated GRS-RW (Geosynthetic Reinforced Soil Retaining Wall) embankments (2.5 m high at prototype, see Figure 1) of the type widely used in Japan, conventional ballasted embankments (1.2 m high) and a new preformed geogrid embankment system proposed by the project (1.2 m high). Details of the scaling and miniaturisation of these

embankments will be discussed in forthcoming papers, but this involved precisely scaling model geogrid, facing walls, fill materials, model railway ballast and model track stiffnesses to ensure the miniature 1/50th scale embankments correctly replicate the behaviour of the full-size problems.



Figure 1. A section of 1/50th scale (50mm high) geosynthetic reinforced soil retaining wall (GRS-RW) embankment under construction in the centrifuge rail simulator, on a soft clay subsoil.

The centrifuge modelling aimed to investigate the embankment and subsoil settlements on both sand and soft clay, as well as how the subsoil movements affect the overlying embankments, and measuring how the train loads transfer through the track and embankment creating the resulting stress changes on the top of the subsoil. This is an area that the UK Rail Safety and Standards Board (RSSB) states is an area of poor understanding, on which there is little to no ongoing research (RSSB 2011). The focus of this paper will be the development of methods for simulating model train loading in-flight in the centrifuge, instrumenting the model embankments (including total stress measurements at the subsoil interface) and the preparation of the subsoil models used in the testing.

2 TRAIN MODELS

Before setting out the centrifuge modelling, it is important to define the train characteristics being studied. The research in this paper is based on a TGV-R train (Connolly et al. 2014), which consists of power cars weighing 68 tonnes supported by two bogies each with two axles, resulting in an axle load of 17 tonnes (34 tonnes per bogey). The passenger cars are significantly lighter, but instead share bogies at the carriage connections, resulting in a similar axle load of 16 tonnes (31 tonnes per bogey). Bogies are spaced at 14 m centre to centre on the power cars and 18.7 m on the passenger cars. The train model used in the centrifuge was based on the TGV-R power car, but due to the similarity in the axle loads between the power and passenger cars, the axle passes modelled in the centrifuge could be considered to be representative of either. This required a 1/50th scale train model (Figure 2) weighing 550 g, with model bogies (Igus WJ200QM-01 bearings) spaced at 280 mm centre to centre.



Figure 2. 1/50th scale model train used to simulate a 68 tonne TGV-R power car (550 grams, 280 mm bogey spacing).

In centrifuge modelling of high-speed rail, it is necessary to ensure that the conditions in the model are in keeping with the full size problem. Two of these considerations which arise in respect of high-speed rail are the dynamic effects from train vibrations, and also the scaling of the train velocity to match the real-world drainage conditions.

First dealing with the dynamic effects, the vibrations generated by a train whilst in motion could potentially increase the rail settlements beyond those caused only by the stress change in the embankment and subsoil due to the weight of the train. This would occur if the shear strains induced by the vibrations were greater than the elastic shear strain threshold of the subsoil, meaning that plastic deformation from the vibrations could accumulate. Connolly et al. (2014) conducted field monitoring of a high-speed rail line to measure these vibration-induced shear strains in the surrounding soil. It was found that the shear strains varied depending on the distance from the track, but that the maximum strain recorded for the case where an embankment is present was $\gamma = 5.9 \times 10^{-6}$. For clay soils, the elastic shear strain threshold is of the order of $\gamma = 1 \times 10^{-4}$ (for Kaolin, the main component of KSS 541), nearly two orders of magnitude higher than the maximum measured shear strain from vibrations. This suggests that deformations generated by the vibrations could be considered to be elastic (and recoverable) and would be unlikely to significantly affect the model embankment settlements measured during the cyclic train loadings investigated in this research, and that modelling of these dynamic effects is unnecessary. Hence the train was modelled as a smooth passing load.

Secondly, the train velocity in the field determines the drainage conditions that occur. An indication of these drainage conditions can be obtained from the train's normalised velocity (Eq. 1) where v is the train velocity, d is the representative dimension (assumed to be the track width of 2.5 m in this case) and c_v is the coefficient of consolidation ($c_v = 17.2 \text{ m}^2/\text{year}$ for KSS 541). For a full-scale train moving at 300 km/h (Connolly et al. 2014) this would correspond to $V = 3.81 \times 10^8$. A value of V greater than 10 to 30 indicates fully undrained conditions (Randolph and Gourvenec 2011) with no pore pressure dissipation during the passage of the train, hence, the normalised velocity of the model train must be greater than 30 to correctly simulate the undrained nature of the problem. The maximum actuation velocity possible with the system used was 108 m/h and considering the centrifuge scaling of the problem this means that the normalised velocity of the model train was $V = 2750$,

significantly greater than that required to correctly simulate undrained conditions.

$$V = \frac{vd}{c_v} \quad (1)$$

3 MODELLING APPROACH

Consideration was given to the loading approach adopted. Two options were possible; to model the embankment in the centrifuge as a 2D problem with a plane strain approach, or to simulate the train using a 3D approach with a moving load. Preliminary 1 g testing was undertaken to investigate the performance of a 400 mm length of 50 mm high GRS-RW embankment placed in a model container of dimensions 400 mm square and filled with 500 mm of loose HST95 sand. Uniform cyclic loading was applied to the embankment via a 50 mm wide, 400 mm long force applicator representing the width of track. The force was applied using an Instron 5985, equivalent to a uniform stress of 1 kPa across the track area. The stress was estimated based on the 34 kN bogey load being evenly distributed over the area underneath the bogey (2.5 x 3 m) giving a stress of 47 kPa, which was scaled down by $N = 50$ to account for the 1 g stress conditions in the subsoil. The embankment was subject to more than 800 cycles of loading, resulting in a final settlement of 0.22 mm (11 mm at full scale) (Figure 3).

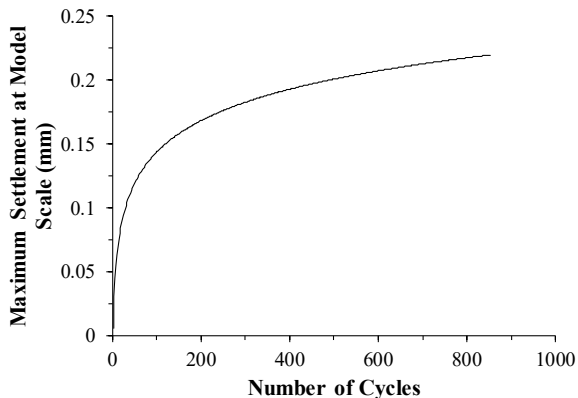


Figure 3. Maximum settlement in each cycle for a 1 g test of 1/50th scale GRS-RW embankment on loose HST95 sand.

However, the preliminary testing raised a number of issues. Firstly, the stresses (and hence also stiffnesses) in the subsoil were N times too low due to the 1 g nature of the tests, and would not be consistent with the stresses in the full scale problem. Secondly, high speed rail lines increasingly adopt high stiffness concrete slab tracks on top of the embankments, and these slab tracks act to distribute the load from the train not just laterally across the embankment, but also longitudinally along the

embankment ahead and behind each bogey. The comparatively high GRS-RW embankments would also have a similar effect. A 2D plane strain approach such as the type used in the preliminary tests would fail to capture this behaviour and mean that the stresses which reach the subsoil beneath the embankment (which are of interest in this research) would be unrealistic. To overcome these two issues, it was decided to adopt a novel approach and model the train loading and embankments using a 3D approach with a 1/50th scale model train moving along a 1 m length of model track whilst in flight at 50 g in the University of Dundee's 3 m radius beam centrifuge. To the knowledge of the authors, this is the first time that moving train loads on embankments have been tested in a centrifuge, with all previous studies using 2D plane strain methods (Zhang et al. 2018; Vorster et al. 2017; Viswanadham et al. 2012).



Figure 4. Model train and track on a model conventional ballasted embankment in the centrifuge actuation system.

This introduced further scaling requirements, such as the need to correctly scale the longitudinal bending stiffness of the track to ensure the distribution of the train load in the direction of the track is correctly modelled. Hence, the bending stiffness, EI , was scaled down by N^4 , including accounting for the differing material moduli of the steel and concrete used at full scale against the aluminium used at model scale. To achieve this, two 1.08 m long model track lengths were created, each incorporating integral low friction Igus WSQ-06-30 double bearing rails for the model train to move along (Figure 4). One length of track was scaled to match the bending stiffness of UIC60 rails typically used in combination with conventional G44 sleepers on ballasted embankments (with model sleepers also attached to match the interface with the ballast), whilst a stiffer model track was created with a bending stiffness designed to match the scaled stiffness of the concrete slab track (made up of hydraulically bonded layer (HBL), slab track and rails) used in the full scale testing (Figure 5). The

longitudinal bending stiffness of the GRS-RW track facing walls was also scaled for the same reason.

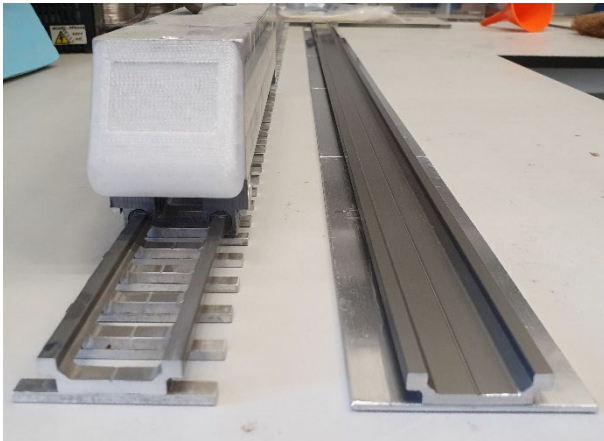


Figure 5. Comparison between the conventional UIC60 rail and sleeper model (l) and the rail and slab track model (r).

4 METHODOLOGY

4.1. Actuation system

To accommodate the track lengths required, the testing was carried out in a centrifuge strongbox with internal dimension 1500 mm long, 400 mm wide and 650 mm deep (Figure 6). A viewing chamber with a Perspex face was placed at one end of the box to allow a cross-section of the track and embankment to be viewed in-flight, which reduced the length of track and embankment to 1080 mm. The 1/50th scale train model weighing 550 g ran on the track, connecting via two 3D joints to a moving platform on an actuator attached to the top of the box such that the train was free to move vertically. Using this system, it was possible for the model train to have a travel distance of up to 600 mm which was sufficient for the train to pass and clear

an instrumented section in the middle of the track length by 150 mm and ensure the stress from the train at this point was fully relieved before the actuator reversed direction and the train passed in the opposite direction. Each cycle of the actuator resulted in the train passing this point twice, delivering four bogey passes at a speed of 30 mm/s. The cyclic testing continued for 6 hours, allowing up to 2000 bogey passes to be simulated in each centrifuge test.



Figure 6. Rail simulator and 1.5 m long strong box installed on the University of Dundee's 3 m radius beam centrifuge.

The actuation system itself consisted of a moving platform above the model running on Igus drylin WSQ-16 linear rails at each side of the box driven via a belt system by a Parvalux SD12-LWS high torque 220V DC motor (Figure 7). Displacement of the platform was measured by a Multicomp SP1-50 draw wire transducer. The system is described in detail in Robinson et al. (2019), but for this testing it was upgraded to allow programmable movement such that the cyclic testing could be automated via Labview. This was achieved by interfacing the motor's reversing DC controller with an inexpensive set point isolator, allowing the

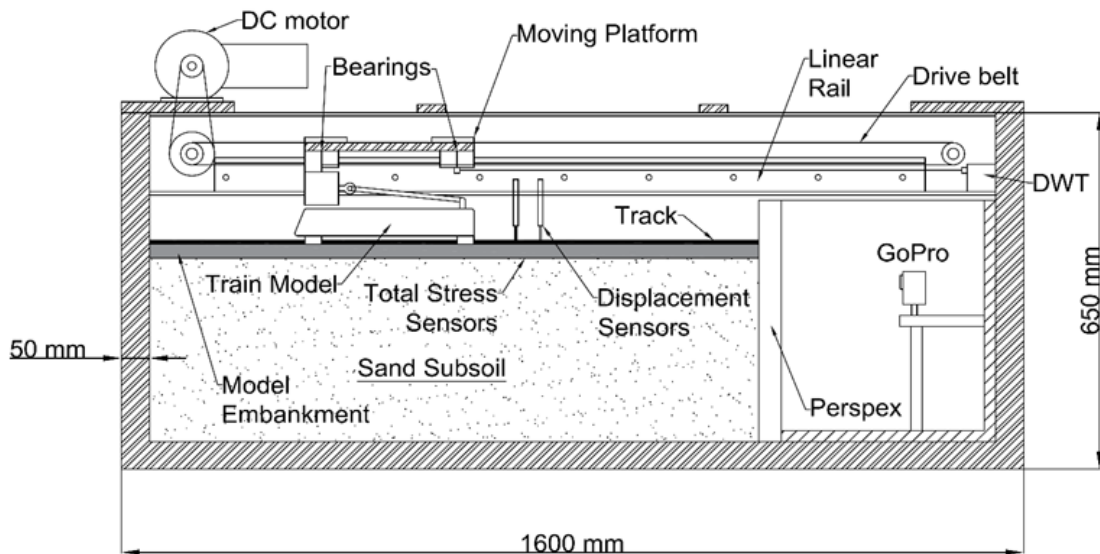


Figure 7. Schematic cross section of centrifuge rail simulator showing actuator, strong box, model and instrumentation.

motor's direction and speed to be easily controlled by a 0 to 5 V signal and an existing relay unit within the centrifuge's National Instruments CompactRIO 9047 chassis. Control signals for the motor were generated by an NI 9264 voltage output unit within the chassis, which already provides individual software programmable supply voltages for the 32 instrumentation channels on the centrifuge which pass through a custom built low-noise power conditioning unit. This allows the low current voltage signals from the NI 9264 to be used to independently power instruments with a higher current demand with a highly regulated voltage supply. By using the same CompactRIO system for both the instrument logging and the motor control signals, it was possible to implement a feedback control loop with the draw wire transducer in Labview to carry out the cyclic testing using software control.

4.2. Instrumentation

A range of instrumentation was used during the testing. Three miniature Honeywell displacement sensors were used to monitor the track, embankment and subsoil settlements at the middle of the track length, capable of measuring settlements less than 1 micron. A GoPro Hero 4 in the viewing chamber was also used for PIV analysis of a cross section of the subsoil underneath the embankment at one end of the track through a Perspex window which was fitted with markers, allowing the displacement field under the embankments to be investigated. However, the most challenging measurement was the total stress at the interface between the embankment and the subsoil. This is a key measurement in the tests as it could indicate how effective the various embankment designs were in distributing the load of the train and how the stress is transferred down through the embankment to the subsoil. Total stress measurements can be problematic to achieve, as total stress sensors can in themselves change the stress distribution in their vicinity as well as being difficult to miniaturise for use in such small models.

The total stress measurements were achieved using Singletact S8-10N capacitive force sensors, 8 mm in diameter and 350 microns thick with a sensing range of up to 200 kPa and a sensing resolution of 0.4 kPa. These operate using a stiff elastomer between two foil layers covered with a thin protective polyamide outer layer, with small changes in the thickness of the elastomer due to the applied stress causing measurable changes in the capacitance. The sensors have Singletact SE units which convert capacitance into a straightforward analogue voltage output. These differ from other

thin film pressure sensors which using printed conductive ink, which require an amount of compression ('switch-on distance') before pressure changes begin to be detected, which is unacceptable if correct in-situ stresses are to be measured. Capacitive sensors do not suffer from these issues.

If a comparatively thick sensor is stiffer (or less stiff) than the surrounding soil, then stress arching around the sensor can occur. The Singletact sensors avoid these issues due to their thin profile which minimises the volume of the inclusion used and also due to the fact that they have a stiffness which is similar to the stiffness of the surrounding materials used in the embankments and subsoil. The sensors have a Young's modulus of 7 MPa (based on manufacturer's data), which is comparable in magnitude to the stiffness of the model embankment ballast ($E_o' = 4$ to 8 MPa) and the KSS 541 subsoil ($E_o' = 2$ to 3 MPa) as well as HST95 sand ($E_o' = 5$ to 12 MPa, used in tests not described in this paper).

An array of five of these sensors (See Figure 8) were placed in the middle of the length of track ranging from the centre of the embankment to the edge, to allow a 3D model of the stress field around a bogey to be measured at the subsoil as the bogey approaches and passes the instrumentation point. The sensor electronics were coated with epoxy resin whilst the exposed edges of the sensing area were sealed with a fine layer of flexible adhesive.

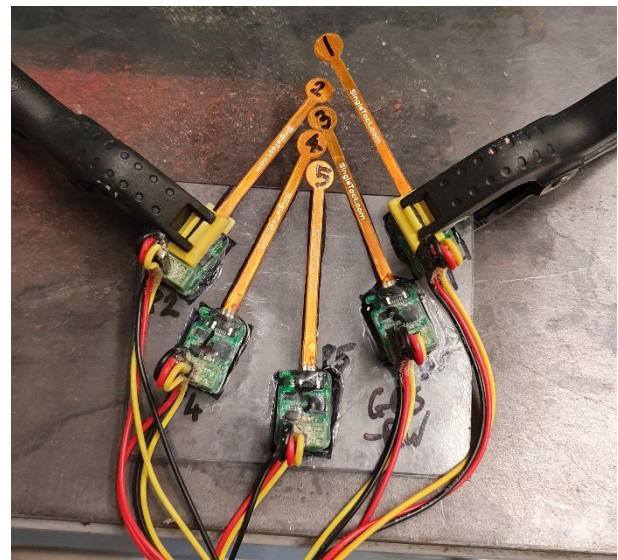


Figure 8. Array of Singletact S8-10N pressure sensors used for total stress measurement.

Figure 9 shows typical results (from the 5th and 6th train passes) from a total stress sensor located in the centre of the embankment at the ballast-subsoil interface. The change in stress generated by the passage of the individual bogies is clearly visible as four peaks in the stress measurements. The maximum change in vertical stress due to the bogey

load ranged from 13 to 22 kPa, with an average of 18 kPa. These maximum stresses were relatively constant, and showed no indication of changing with increasing cycle numbers.

Expected real-world vertical stress changes from a passenger train on the subsoil immediately beneath ballasted embankment range from 20 to 30 kPa depending on the ballast thickness (RSSB 2011). These figures are based on ballast thicknesses (including sub-ballast) ranging from 350 to 1000 mm. The ballast thickness used in this case was slightly thicker than this range at 1250 mm at prototype scale (to match other embankment weights and stresses studied in the project), which would distribute the train load over a greater area of the subsoil. Hence, the stress change for the embankment studied would be expected to be just below the lower end of the recommended range (i.e. just below 20 kPa), meaning that the average measured value of 18 kPa would be in keeping with this.

The measurements also clearly indicate that the subsoil experiences the stress change from the model train bogies approximately 220 mm (11 m at prototype) ahead of the arrival of the bogey itself. This suggests that the effect of the embankment distributing the load of the train along the length of the track is an important effect, validating the decision to adopt a 3D approach, modelling the train as a moving load.

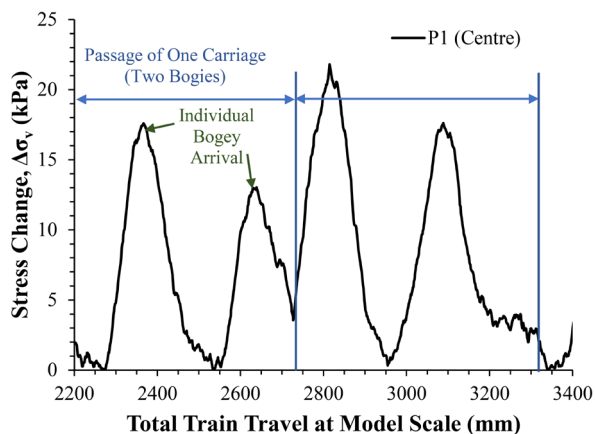


Figure 9. Typical output from a Singletact pressure sensor underneath the track (conventional ballast, 25 mm thick) for one cycle of train loading on KSS541

4.3. Subsoil preparation

The soft clay subsoil required to be consolidated in-flight from slurry. This was necessary to achieve a realistic shear strength variation with depth, as opposed to the uniform profile that would occur if a press was used to prepare the clay at 1 g. One of the primary reasons for using KSS 541 (a mixture of 50% Kaolin, 40% HST95 silica sand and 10% A50

silica silt) for the clay material was that it still provides a cohesive soil, but with less reduction in height during consolidation, as well as shorter consolidation times than pure Kaolin. The properties of KSS 541 are given in Table 1. If Kaolin had been used, it would not have been possible to have a sufficiently thick layer of clay to avoid boundary effects. The KSS 541 slurry was mixed at a moisture content of 50% and placed (400 mm deep) into the strong box on top of a 30 mm thick gravel drainage layer covered with a filter membrane and filter paper. The moisture content of the slurry was critical as it was necessary to mix it at the lowest possible moisture content which avoided air entrapment occurring, in order to minimise the height loss during consolidation. Higher moisture contents would also have risked segregation of the sand fraction in the KSS 541 during spin up. The clay was consolidated at 50 g for 3 days, with monitoring of the mass of water lost indicating this was sufficient to achieve near full consolidation. The drainage outlet location was set at 10 mm below the expected final surface level, such that the water table was held at this location, resulting in a final clay thickness of 300 mm.

Table 1. Properties of KSS 541.

Parameter	Unit	Value
Gradient of CSL, M	-	0.73
Critical friction angle, ϕ'_{crit}	°	19
Clay fraction	%	41
Plastic limit	%	18
Liquid limit	%	38
Plasticity index	%	20
Coefficient of consolidation, c_v	m ² /year	17.2

The GRS-RW embankment sections were constructed at 1g in the lab and placed onto the model. However, prior to this it was necessary to use an aluminium bar of the same area and mass as the embankment to pre-consolidate the embankment area to prevent excessive deformation during consolidation of the embankment in-situ. The aluminium preload was consolidated at 50 g for 24 hours before the actual embankment sections were installed and consolidated for a further 24 hours. Oedometer testing of KSS 541 indicated that 90% consolidation would require 12 hours, hence the 24 hour periods were selected to ensure consolidation settlements would be negligible compared to the expected embankment settlements. During testing, the exposed surfaces of the KSS 541 were covered to prevent moisture loss. The shear strength and moisture content profiles with depth for KSS 541 are shown in Figure 10, which had a final saturated unit weight of 19.1 kN/m³. Shear

strengths were measured using a Controls Testing pocket shear vane.

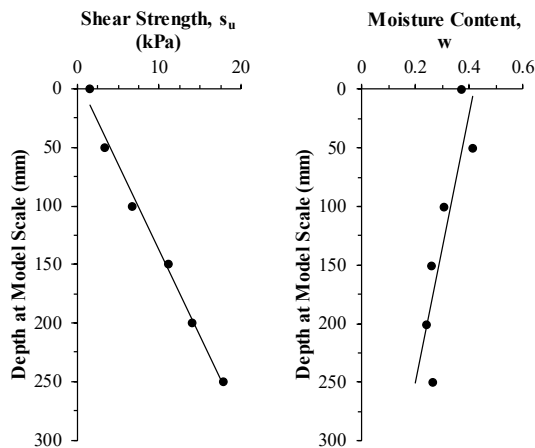


Figure 10. Shear strength and moisture content with depth variation (free field) for KSS 541 clay prepared in flight at 50g.

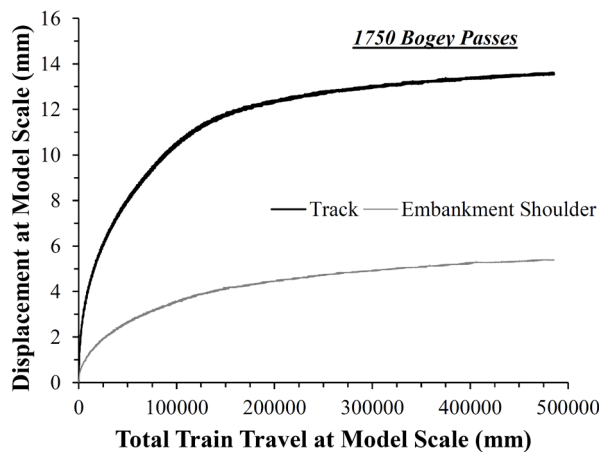


Figure 11. Model track and embankment shoulder settlements with increasing cycles of train loading for a conventional ballasted embankment (25 mm high) on KSS 541, measured at the middle of the length of track (at 50 g in the centrifuge).

Figure 11 shows the measured settlements of both the track and the embankment shoulder with the application of 1750 bogey passes for a model conventional ballasted embankment on KSS 541. The embankment shoulder settlement increases with the number of bogey passes reaching a final value of 5.39 mm (269 mm at prototype), whilst the

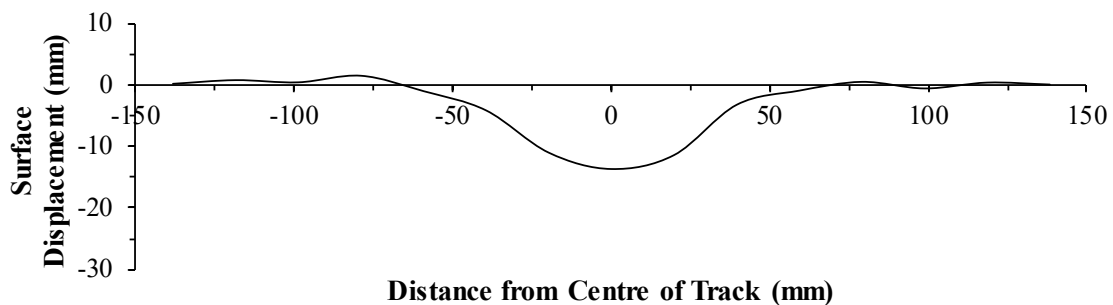


Figure 12. Variation of the subsoil surface displacement (relative to original surface levels) across the width of the model (in cross-section) after 438 bogey passes at the Perspex viewing window.

track itself reaches a significantly larger settlement of 13.52 mm (676 mm at prototype). These settlements are clearly large compared to the settlement limits on rail lines, highlighting a need for better understanding of the mechanisms behind rail embankment behaviour on soft clay soils.

The reasons for the track displacement being greater than the displacement of the embankment shoulder are clear in Figure 12, which shows the surface displacements of the subsoil for a cross-section of the model visible at the Perspex viewing chamber. The subsoil displacements are primarily focussed around the centreline of the track, reducing significantly with distance from this point and are far lower at the distance from the centreline (40 mm from centreline) at which the embankment shoulder displacements are measured. This highlights the need to study the behaviour of rail embankments considering the embankment and subsoil in combination together, rather considering the embankment alone; a task which is well suited to the use of centrifuge modelling.

5 CONCLUSIONS

A range of challenges faced during the modelling of a rail simulator for centrifuge application have been discussed. Vibrations from a moving train were considered but identified as secondary to the effects of the change in stress caused by the train load, as existing research suggests that shear strains induced by the vibrations are significantly below the elastic shear strain threshold for clays.

A 3D approach with a moving train load was chosen to ensure the true behaviour of the embankment and track combination was captured, instead of a 2D plane strain method. This required careful scaling of the track bending stiffness and a sufficiently long model container to permit a complete cycle of load for each train pass.

Total stress measurement was achieved through the use of Singletact force sensors. These produced results comparable with the stresses expected in this application. Total stresses measured during testing indicated that the model container was sufficiently

long to model the full approach and pass of a train over the instrumentation point, and that in these tests the subsoil experienced stress from the train bogey at a distance of 11 m (at prototype scale).

Preparation of a suitable soft clay subsoil was accelerated by use of a KSS 541 clay-sand-silt mixture. This soil shares cohesive mechanical behaviour with clay but has a higher coefficient of consolidation, accelerating the consolidation phase. Even so, the models required 72 hours of initial consolidation, followed by 24 hours consolidation between the construction of the embankment and the application of the rail loads. A soil with undrained shear strengths varying with depth from 2 kPa near surface to 15 kPa at 300 mm deep was achieved as a result.

6 ACKNOWLEDGEMENTS

This work was funded by the EPSRC under grants EP/N009207/1 and EP/N009215/1: LOCORPS: Lowering the cost of railways using preformed embankment systems, which is acknowledged with thanks.

7 REFERENCES

Connolly, D.P., Kouroussis, G., Woodward, P.K., Alves Costa, P., Verlinden, O. and Forde, M.C. 2014. Field testing and analysis of high speed rail vibrations. *Soil Dynamics and Earthquake Engineering*, **67**: 102-118.

Randolph, M. and Gourvenec, S. 2011. *Offshore geotechnical engineering*, Taylor and Francis, London, UK.

Robinson, S., Brown, M.J., Matsui, H., Brennan, A., Augarde, C., Coombs, W. and Cortis, M. 2019. Centrifuge testing to verify scaling of offshore pipeline ploughs. *International Journal of Physical Modelling in Geotechnics*, **19**(6): 305-317.

RSSB. 2011. Report RSSB 1386 (revised) - the effects of railway traffic on embankment stability. Rail Safety and Standards Board, London, UK. Available from <https://cdn.networkrail.co.uk/wp-content/uploads/2017/02/RSSB-report-The-effects-of-railway-traffic-on-embankment-stability.pdf> [accessed 30 January 2020].

Viswanadham, B.V.S., Das, A. and Mathur, V.K. 2012. Centrifuge model tests on rail embankments constructed with coal ash as a structural fill material. *In Proceedings of GeoCongress 2012: State of the Art and Practice in Geotechnical Engineering*, Oakland, California, USA, 25-29 March 2012. ASCE, pp. 3786-3795.

Vorster, P., Gräbe, P.J. and Jacobsz, S.W. 2017. Centrifuge modelling of railway embankments under static and cyclic loading. *Journal of the South African Institution of Civil Engineering*, **59**(3): 2-10.

Zhang, C., Jiang, G., Liu, X. and Su, L. 2018. Centrifuge modelling and analysis of ground reaction of high-speed railway embankments over medium compressibility ground. *KSCE Journal of Civil Engineering*, **22**(12): 4826-4840.

Centrifuge modelling of tunnel-soil-pile interaction considering the presence of rigid caps

Jingmin Xu¹, Andrea Franza², Alec M. Marshall¹

¹*Department of Civil Engineering, University of Nottingham, UK*

²*Canales y Puertos, Universidad Politécnica de Madrid, Spain*

Corresponding author: Jingmin Xu (jingmin.xu@nottingham.ac.uk)

ABSTRACT: Previous research on tunnelling beneath piles has assumed that caps (or other elements such as grade beams) above the pile head are elevated from the ground surface. This neglects the possible mobilisation of contact stresses beneath the foundation elements at the surface, which may occur as a result of pile settlements larger than ground surface movements caused by tunnelling. This paper presents a centrifuge study that compares the response of capped piles (where the cap is relatively stiff or rigid and is in contact with the soil) and simple piles (no cap) to tunnelling in dry silica sand. The paper includes results from 5 centrifuge tests, including both pile loading and tunnelling beneath piles. To consider a critical scenario, both simple and capped piles, subjected to a constant external load during tunnelling, are located directly above the tunnel. For strain measurement and estimation of internal forces, model piles are instrumented with fibre Bragg gratings (FBGs) along their shafts, while the external vertical and pile head settlement are also measured. The responses of simple and capped piles are compared by considering tunnelling-induced pile settlements and axial forces. Results show that simple pile settlements exceeded surface movements up to a point of pile failure (due to the loss of pile base capacity), whereas the cap restrained the pile settlement and satisfied equilibrium by mobilising the soil surface contact stresses (transferring the load from the pile to the cap). The paper highlights the role and potential benefits of considering the presence of pile caps in tunnel-pile interaction analyses.

Keywords: Tunnelling; Soil-Structure Interaction; Simple/Capped Pile; Centrifuge Modelling.

1 INTRODUCTION

Tunnelling induces stress disturbance and ground movements that can threaten existing man-made assets. In urban environments, tunnels are often excavated beneath structures with deep foundations. To prevent detrimental effects, it is important to understand the tunnel-pile interaction mechanisms.

When a pile with a relatively stiff (referred to as rigid in this paper) cap is subjected to tunnelling-induced ground movements, it is reasonable to expect the mobilization of contact stresses beneath the cap, contrary to the case of elevated caps or where no cap is present. The load carrying capacity of the cap can alter the tunnel-soil-pile interaction. Therefore, neglecting the presence or the action of pile caps results in uncertainties for risk assessment purposes. While previous experimental studies have considered the pile response to underground excavations, the presence of rigid pile caps is generally neglected (Jacobsz et al., 2004; Marshall and Mair, 2011; Ng et al., 2013; Williamson et al., 2017; Song et al., 2019), or elevated caps not in contact with the ground are assumed (Loganathan et al., 2000, 2001; Boonsiri and Takemura, 2015; Hong et al., 2015; Franza and Marshall, 2018, 2019; Chen, 2019).

In this paper, the problem is experimentally studied using elevated-gravity and reduced-scale

centrifuge models of tunnelling beneath deep foundations of two types: piles with an elevated cap or having no cap are labelled as “simple pile” (SP), whereas piles with a cap in contact with the soil are “capped pile” (CP). The paper reports the results of pile loading tests (to assess the load-settlement curve of the SP and CP cases to vertical loading) and tunnel-pile interaction tests (to compare the difference between SP and CP piles when subjected to tunnelling induced ground movements). The practical implications of neglecting the presence of the pile cap in the tunnel-pile interaction are discussed by analysing tunnelling-induced pile settlements and axial forces.

2 EXPERIMENTAL DETAILS

2.1. Experimental set up

2.1.1 Model details

The plane strain experimental package designed by Zhou (2014) for modelling a tunnel excavation process was used. It includes a strongbox, a transparent acrylic front wall, an aluminium back wall, and a flexible membrane model tunnel filled with water. The model and results presented here are described in model scale unless otherwise stated.

Tunnel volume loss was simulated by extracting water from a model tunnel with a diameter $D_t =$

90 mm. For the dry soil sample, a fine-grained silica sand known as Leighton Buzzard Fraction E was used.

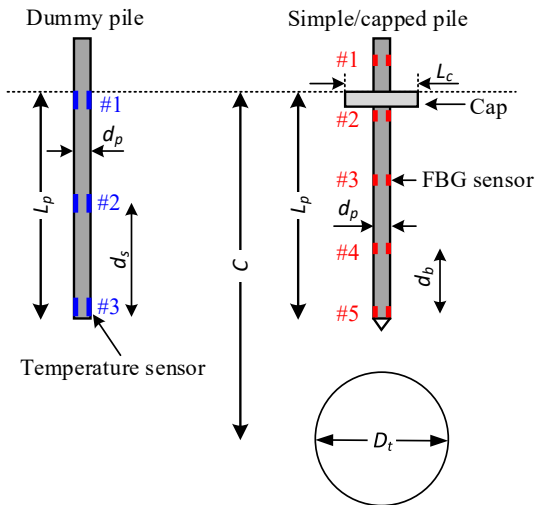


Figure 1. Experimental geometry and layout.

Figure 1 displays the test configuration for the tunnel-pile interaction tests, while pictures of the setup are shown in Figure 2. Two instrumented piles are present: a simple or capped pile located above the tunnel and a “dummy” pile for FBG temperature compensation placed 200 mm from the tunnel. In all tests, model piles were placed within in the middle of the strongbox width.

Both model piles were machined from an aluminium alloy round hollow bar (inner diameter of 10 mm, external diameter 12 mm, 200 mm long). The pile embedment length is $L_p=150$ mm with a 60° conical tip. For the capped pile, a square 10 mm thick aluminium plate was bolted to the simple pile; the cap had a side length $L_c = 48$ mm. To simulate a rough surface, a thin layer of sand was bonded to the under-side of the cap and along the pile shaft, giving a final pile diameter $d_p = 13$ mm. As shown in Figure 1, to measure the axial forces along the model piles, two fibres with 5 fibre Bragg grating (FBG) sensors (spacing of 45 mm) were glued on the opposite inner sides of the hollow bar. Importantly, the FBG positioning allowed measurement of cap, total shaft, and base loads. To compensate for the temperature change effects on the FBG measurements of the SP/CP pile, the dummy pile was instrumented with three temperature sensors (spacing of 75 mm). Axial strain was taken as the mean value between two opposing FBG sensors on the piles which was corrected for temperature based on separate tests conducted to assess the temperature-strain relationship for each FBG. Finally, axial load was obtained based on axial load calibration tests on the

piles. For further details on to the use of fibre Bragg gratings in pile testing, refer to Song et al. (2019).

The loading system developed by Song et al. (2019) was used to apply the external load on the SP/CP piles; it consists of stepper motors, gearboxes, die springs, loading bars, and associated supporting frames and connectors. A load cell (LC) and a linear variable differential transformer (LVDT) were used to measure pile head loads and vertical displacements of the SP/CP piles, as shown in Figure 2. The loading system can achieve both force control (setting a target load) and displacement control (at constant speed), using the load cell and LVDT measurements as inputs to the LabVIEW control program.

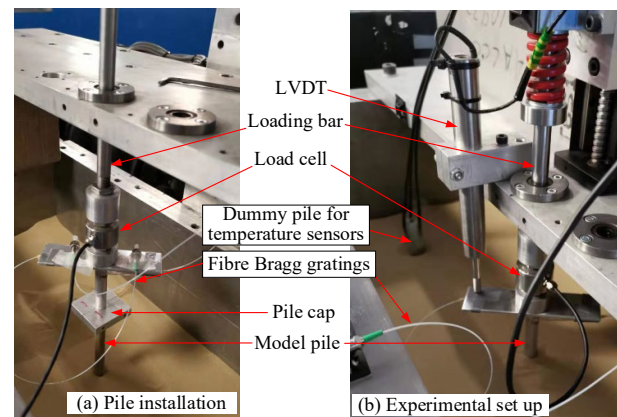


Figure 2. Pile installation and setup of a centrifuge model.

2.1.2 Testing plan

Five tests including three pile loading tests and two tunnel-pile interaction tests were performed on the University of Nottingham Centre for Geomechanics (NCG) 4-m diameter geotechnical centrifuge. Two displacement controlled loading tests were performed for the simple pile SP (to check the repeatability between tests), while one loading test was performed for the capped pile CP. A single tunnel-pile interaction (TPI) test was performed for each of the SP and CP piles, as shown in Table 1, imposing a constant external force of 400 N above the foundation. In the loading tests, the model tunnel was not included in the centrifuge container.

Table 1. Testing plan.

No.	Test type	Pile type	Load (N)
T1	Loading	Simple pile	-
T2	Loading	Simple pile	-
T3	Loading	Capped pile	-
T4	TPI	Simple pile	400
T5	TPI	Capped pile	400

Tests were performed at an acceleration of 68 times gravity (68 g) to simulate, at prototype scale,

the load-settlement response of a 10.2 m long and 0.88 m diameter pile and its response to the excavation of a 6.1 m diameter tunnel with a cover depth (C) of 12.2 m ($C/D = 2.0$), while considering the impact of a stiff square pile cap with a side length of 3.25 m. For these non-displacement simple piles, Franza and Marshall (2019) showed that there is potential for large pile settlements to be caused by tunnelling.

2.2. Testing procedure

2.2.1 Test preparation

The model preparation is summarized as follows:

- (1) With the experimental package on the centrifuge platform, the sand was manually poured into the container to achieve a loose soil sample with a relative density, I_d of approximately 30%. The repeatability of the sample preparation was demonstrated by Franza and Marshall (2018), and by repeating a loading test (presented later).
- (2) The instrumented SP/CP pile was jacked into the soil sample at 1 g (representing a non-displacement pile) with a vertical guide and rod, as shown in Figure 2(a); the LVDT and loading system were then installed.
- (3) The dummy pile instrumented with temperature sensors was pushed into the target position of the soil sample at a 1g.
- (4) The load control system was activated to add a constant external load of 5 N (based on the LC). Subsequently, the model was gradually spun to 68 g, followed by two stabilization cycles (going from 68 g to 15 g and back to 68 g), which were performed to help achieve consistency between tests by reducing localized high-stress zones within the soil.

2.2.2 Pile loading tests

After reaching the target gravity level, the load control system was switched from force- to displacement-control. Next, the pile was jacked at a rate of approximately 0.01 mm/s until a displacement of one pile diameter d_p was reached.

2.2.3 Tunnel-pile interaction tests

At the target gravity level, the external load at the pile head was increased to 400 N. Subsequently, the tunnel volume loss $V_{l,t}$ was simulated by extracting water from the model tunnel in increments of $V_{l,t}$ of 0.1%, up to a maximum $V_{l,t}$ of 3%, while keeping a constant head load. At each $V_{l,t}$ increment, digital images were taken for measurement of soil movements.

3 RESULTS AND DISCUSSION

3.1. Pile vertical loading

Figure 3 shows the load-settlement curves of both simple (SP in subplot a) and capped (CP in subplot b). Shaft, base and cap load are summarised in Figure 4 for a direct comparison. The vertical force at the pile head inferred from the load cell (LC) in Tests 1, 2, and 3 (see Table 1) are shown. On the other hand, FBG data of the axial force at locations #1-5 are plotted only for Tests 2 and 3; Test 1 results are similar to data from Test 2. Cap, shaft and base capacity can be estimated from the FBG data for both SP and CP piles. The load withstood by the cap (when present) was estimated by subtracting FBG#2 from FBG#1, the total shaft friction is given by the difference between FBG#2 and FBG#5, while FBG#5 approximated the base capacity. In this paper, the ultimate load capacity of the SP pile is defined for the displacement that mobilises the full/maximum shaft resistance ($8\% d_p$ in these tests).

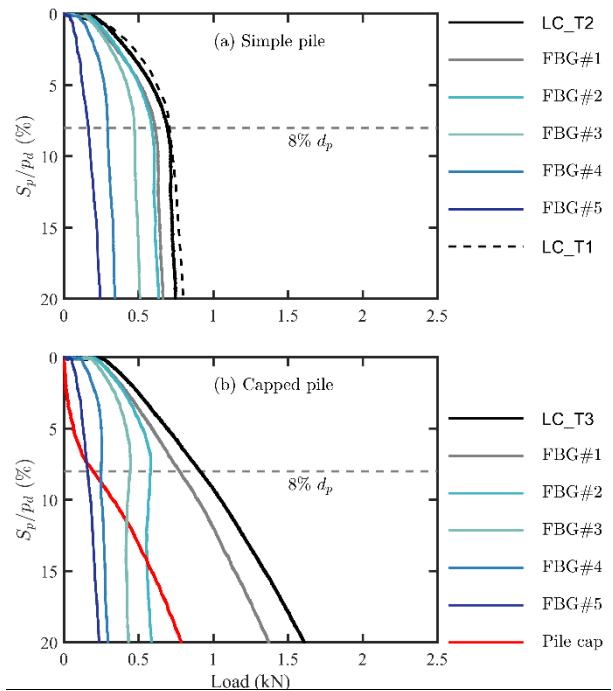


Figure 3. The response of (a) simple and (b) capped piles to vertical loading.

First, simple piles SP are considered with results in Figure 3a. Head load measured by the load cells in test 1 and 2 show good repeatability. At a displacement of $8\% d_p$, mobilising the full shaft capacity, the SP piles have an average ultimate load capacity of 705 N (with an average shaft capacity of 423 N and average base capacity of 161 N), although pile tip load marginally increases for settlements larger than $8\% d_p$. However, it should be noted that the readings from the top FBG sensor

(FBG#1) are smaller than the load measured by the load cell (LC_T2), despite being located above ground. For instance, in test 2, FBG#1 reading is 611 N while the load cell LC gives 693 N at 8% d_p . This discrepancy (in all tests) could be due to bending action transmitted to the load cells as well as incorrect temperature of the top FBG sensor of the loaded piles (FBG#1, which was above the surface, was corrected using temperature sensor #1 from the Dummy pile, which was just beneath the surface; both of these potential issues will be resolved in future tests.

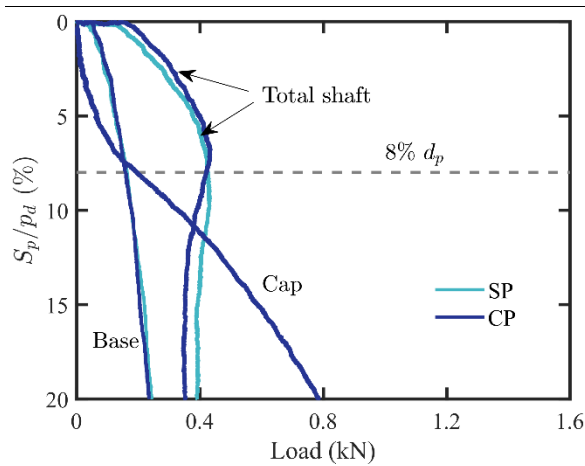


Figure 4. Pile settlements versus cap, total shaft, and base loads for vertical loading tests.

The effect of the cap in the loading test is now considered. Figure 3(b) shows that the CP pile also mobilised its shaft resistance at a displacement of approximately 8% of pile diameter. However, for a vertical displacement of $S_p = 8\sim 12\% d_p$, the cap load shows a steep rate of increase, the base load (FBG#5) was marginally affected, while the total shaft friction decreased due to the action of the cap on the underlying soil and its interaction with the pile (see Figure 4 shaft data). For large settlements $S_p > 12\% d_p$ the total load capacity of the CP pile significantly increases with settlement level due to greater cap load, dominating the overall pile response. These centrifuge results agree with Kumar and Choudhury (2018), who reported that the cap presence significantly affects the load-settlement response of CP piles both positively and negatively; the positive aspect refers to the increased load capacity and the increase of soil confining stress (caused by the compression of the cap on the soil beneath), whereas the negative aspect refers to the decreased shearing/relative displacements between the pile and surrounding soil (due to the rather uniform settlements of the soil mass beneath the cap).

Overall, with respect to the SP pile, the CP pile has the ability to resist higher loads, especially at

settlements larger than the ultimate value of 8% d_p , despite a decreased shaft friction at relatively high pile-soil settlements (see Figure 3).

3.2. Pile response to tunnelling

Results from Tests 4 and 5 for the case tunnelling beneath the SP and CP piles are summarised in Figures 5, 6, and 7. Considering an average ultimate load of 705 N from the loading tests of the simple piles, a safety factor of approximately 1.75 ($=705/400$) is obtained for SP piles. On the other hand, a safety factor of 2.3 ($=915/400$) can be associated with the CP case. Furthermore, the presence of the tunnel (which was not included in the pile loading tests) may affect the ultimate loads, leading to lower values of safety factor (Franza and Marshall, 2019). Consequently, the considered cases deal with relatively low pile safety factors.

Figure 5 presents the pile head settlements S_p and head loads (obtained from the load cells) during the simulated tunnel volume loss $V_{l,t}$, along with the centreline surface settlement of the soil U_z at the acrylic wall (130 mm from the pile; not exactly the greenfield condition but a reasonable approximation of a free field displacement), obtained using GeoPIV (White, 2003).

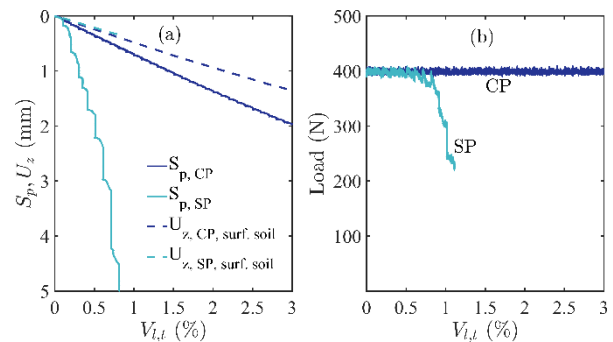


Figure 5. Pile settlements and loads against tunnel volume loss (model scale).

Figure 5(a) shows that the simple pile SP settled at a higher rate than both the CP pile and the ground surface; the SP settled 5 mm (38% d_p) at a $V_{l,t} = 0.8\%$, where the load control system could not maintain the specified load (400 N) due to the tunnelling-induced loss in the load capacity of the pile. On the other hand, the rate of settlement of the capped pile CP is nearly constant with tunnel volume loss, and slightly greater than the surface movements. At $V_{l,t} = 1.0\%$, the capped pile had an absolute settlement of 0.72 mm (5.5% d_p), which is 0.22 mm (1.7% d_p) greater than the surface soil settlement. To consider a serviceability condition, for example, at $V_{l,t} = 0.3\%$, settlements of the SP pile, CP pile and surface soil are, respectively, 1.15 (8.8% d_p), 0.22 (1.7% d_p) and 0.14 mm .

Importantly, up to large ground settlements and volume losses of $V_{l,t} = 3.0\%$, the CP had an absolute settlement of 1.97 mm (15.2% d_p) and a settlement relative to the surface of 0.52 mm (4.0% d_p). This indicates the beneficial role of the pile cap to piles directly above tunnel excavations for both low and high tunnelling-induced settlements.

To investigate the change in the pile shaft axial force during tunnelling, Figure 6 presents the pile shaft axial force obtained from the FBG sensors (FBG#2 to #5), while in Figure 7 these data are used to compare SP and CP loads at the cap (when present), shaft and base. Negative FBG data indicates that the pile underwent tensile axial forces. Comparing FBG#2 at $V_{l,t} = 0\%$ in Figure 6a and b shows that the axial forces at the top of the SP and CP piles are identical, therefore the experimental results from the two pile conditions can be directly compared.

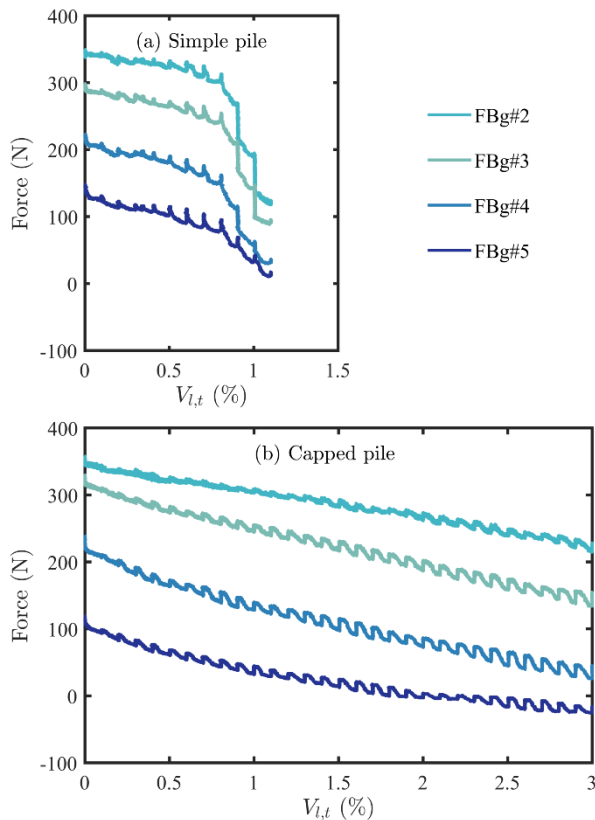


Figure 6. Pile shaft axial load against tunnel volume loss for (a) simple pile SP and (b) capped pile CP.

In the case of the simple piles SP, the service load of 400 N was taken in part by the base capacity, as shown by FBG#5 in Figure 6(a) and 7 for zero volume loss. Furthermore, Figure 6(a) for the SP pile shows that, during tunnelling, the base load (FBG#5) and compressive axial load at the bottom part of the pile (between FBG#4 and #5) decrease while the positive shaft friction of the upper section of the pile slightly increases (see the difference

between FBG#2 and #3, and the pile total shaft load in Figure 7). This means that for the SP case, due to tunnelling, both negative friction in the bottom part of the pile and base unloading developed while positive friction was mobilised in the top part. At $V_{l,t} = 0.7\sim 0.8\%$, pile base capacity was significantly reduced; pile failure is caused by the positive shaft friction in the top part of the pile not being able to withstand the external load due to the loss of base load.

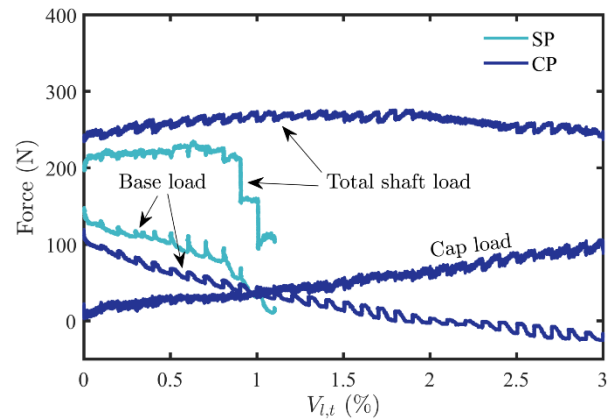


Figure 7. Pile shaft and base resistance against tunnel volume loss.

For the CP pile, first the load distribution prior to tunnelling ($V_{l,t} = 0$) in Figure 7 is described. The cap load is minimal, while the external load is supported mostly by the pile shaft (compressive force at FBG#2-4 decreasing with depth), despite a small base load being mobilised (FBG#5). Next, tunnelling effects are considered. Figure 6(b) shows that the capped pile CP could sustain the vertical load throughout the investigated tunnel volume loss (see Figure 5(b)). For the capped pile, the compressive axial force at the base (FBG#5) and along the entire shaft (FBG#2-4) decrease with $V_{l,t}$, up to the initiation of negative (tensile) axial forces near the pile base (FBG#5 is negative), which are necessarily associated with the development of negative friction. For equilibrium, the action against the external load (and negative friction, if present) was gradually transferred from the shaft and base to the pile cap (see Figure 7). Interestingly, in contrast to the SP case, the total (positive) shaft friction of the CP pile was nearly constant (slightly increased before $V_{l,t} = 1\%$ and decreased after $V_{l,t} = 2\%$), likely due the cap contact stresses increasing the soil confining pressure and balancing for the tunnelling-induced stress relief (Figure 7).

The experimental results indicate that the action of the pile cap (when in contact with the soil) can be remarkable for tunnelling beneath piles with relatively low safety factors. Interestingly, this interaction mechanism has been shown to be

effective from low up to extremely large tunnel volume losses, indicating the practical importance of this work.

4 CONCLUSIONS

This paper investigated tunnel-pile interaction through geotechnical centrifuge testing, considering the influence of a stiff pile cap on both mobilised capacity and tunnelling-induced settlements. The following conclusions can be drawn.

- (1) In the considered cases, loading test results indicate that both simple (no cap) and capped piles mobilized their shaft resistance at threshold settlements of 8% of the pile diameter d_p , while base load slightly increased for larger settlements. The cap played a significant role for pile settlements greater than the threshold displacement (mobilising the full shaft friction): it steadily increased the pile load capacity and it contributed to the decrease of shaft friction.
- (2) When the piles, which had relatively low safety factors, were subjected to tunnelling-induced ground movements, the pile with no cap experienced settlements significantly larger than the surface (from small volume losses up to pile failure), due to the loss of pile base load and positive friction near the pile base. Contrarily, for the capped pile, both losses of base and shaft load were balanced by the development of contact stresses beneath the cap (transferring the pile load to the cap); the cap was also effective at preventing pile settlements much larger than the soil surface.
- (3) Although the cap role may be negligible for the pile response to vertical loadings (before the pile shaft resistance is mobilized), when tunnelling beneath capped piles, neglecting the presence of the pile cap (if in contact with the soil) can lead to an overestimate of the pile settlement, leading to overconservative design and unnecessary mitigation measures being prescribed. However, the post-tunnelling condition of capped piles relies on the cap bearing capacity (e.g. surface excavation could be detrimental).

It should be noted that, in this work, the load cell and FBG sensor measurements did not match at the pile head. Consequently, although results describe qualitatively the soil-pile interaction and the impact of the cap, the results presented here should be considered as preliminary; further tests are ongoing to address these issues.

Future work will consider the presence of rigid caps and flexible slabs in contact with the soil (for example, piled raft foundations) when tunnelling.

5 ACKNOWLEDGEMENTS

This project has received funding from the European Union's Horizon 2020 research and innovation programme under the Marie Skłodowska-Curie grant agreement No 793715. The first author also recognizes the financial support provided by the China Scholarship Council (CSC) and the University of Nottingham, UK.

6 REFERENCES

- Boonsiri, I. and Takemura, J. 2015. Observation of Ground Movement with Existing Pile Groups Due to Tunneling in Sand Using Centrifuge Modelling. *Geotechnical and Geological Engineering*, **33**: 621-640
- Chen, S.M., Lu, H., Jiang, H.J., et al. 2019. Three-dimensional centrifuge modelling of the effects of tunnelling on vertical behaviour of pile group. *IOP Conference Series: Materials Science and Engineering*, doi:10.1088/1757899X/592/1/012125
- Franza, A. and Marshall, A.M. 2018. Centrifuge modelling study of the response of piled structure to tunnelling. *Journal of Geotechnical and Geoenvironmental Engineering*, **144**(2): 04017109.
- Franza, A. and Marshall, A.M. 2019. Centrifuge and real-time hybrid testing of tunneling beneath piles and piled buildings. *Journal of Geotechnical and Geoenvironmental Engineering*, **145**(3): 04018110.
- Hong, Y., Soomro, M. A., Ng, C. W. W. 2015. Settlement and load transfer mechanism of pile group due to side-by-side twin tunnelling. *Computers and Geotechnics*, **64**: 105-119.
- Jacobsz, S.W., Standing J.R., Mair, R.J., et al. 2004. Centrifuge modelling of tunnelling near driven piles. *Soils and Foundations*, **44**(1): 49-56.
- Kumar, A., Choudhury, D. 2018. Development of new prediction model for capacity of combined pile-raft foundations. *Computers and Geotechnics*, **97**: 62-68.
- Lee, C.J. and Chiang, K.H. 2007. Responses of single piles to tunneling-induced soil movements in sandy ground. *Canadian Geotechnical Journal*, **44**: 1224-1241
- Loganathan, N., Poulos, H.G. and Stewart, D.P. 2000. Centrifuge model testing of tunnelling-induced ground and pile deformations. *Geotechnique*, **50**(3): 283-294.
- Loganathan, N., Poulos, H.G., Xu, K.J. 2001. Ground and pile-group responses due to tunnelling. *Soils and Foundations*, **41**(1): 57-67.

- Marshall, A.M. and Mair, R.J. 2011. Tunneling beneath driven or jacked end-bearing piles in sand. *Canadian Geotechnical Journal*, **48**: 1757-1771.
- Ng, C.W.W., Lu, H., and Peng, S.Y. 2013. Three-dimensional centrifuge modelling of the effects of twin tunnelling on an existing pile. *Tunnelling and Underground Space Technology*, **35**: 189-199.
- Song, G., Marshall, A.M., and Heron, C.M. 2019. Load redistribution of piles affected by tunnelling: hybrid centrifuge tests using fibre Bragg grating. *Proceedings of the XVII ECSMGE-2019*, doi: 10.32075/17ECSMGE-2019-0236.
- Williamson, M. G., Elshafie, M. Z. E. B., Mair, R. J., & Devriendt, M. D. 2017. Open-face tunnelling effects on non-displacement piles in clay - part 1: centrifuge modelling techniques. *Géotechnique*, **67**(11): 983-1000.
- White, D., Take, W., and Bolton, M. 2003. Soil deformation measurement using particle image velocimetry (PIV) and photogrammetry. *Géotechnique*, **53**(7): 619-631
- Zhou, B. 2014. Tunnelling-induced ground displacements in sand. Ph.D. Thesis, University of Nottingham.

Centrifuge Modelling of the Reverse Faulting-Tunnel Interaction in Granular Alluvial Soil considering Tunnel Flexible Joints

Hamid Tohidifar¹, Mojtaba Moosavi¹, Mohammad Kazem Jafari¹

¹ *Geotechnical Engineering Research Center, International Institute of Earthquake Engineering and Seismology (IIEES), Iran*

Corresponding author: *Hamid Tohidifar (hamid.tohidifar@gmail.com)*

ABSTRACT: Traffic, metro and water transmission tunnels in urban areas play a crucial role in supporting the lives of the people, especially after a strong earthquake. They should maintain their stability, serviceability, and strength in such extreme events. Previous studies have shown that the Permanent Ground Deformations (PGD) due to earthquake faulting within the soil could severely damage the underground linear-structures. In this paper, the behaviour of a continuous concrete tunnel in alluvial deposit under the impact of reverse faulting has been studied. The small-scale physical modelling using the geotechnical centrifuge has been employed for this purpose. In order to reduce the damages induced by the differential fault displacements, flexible joints have been introduced in the tunnel lining. The prevalent construction-joints have been replaced by these flexible joints in this experimental work. The tunnel has been modelled using an Aluminum Tube which under 25 g centrifugal acceleration has simulated a concrete tunnel with 3m diameter. In this study, the tunnel axis and fault line were perpendicular to each other. The displacement of a 60° bedrock reverse fault and propagation of the shear bands within the upper soil layer has impacted the embedded tunnel. Results have shown that the presence of the transverse flexible joints could reduce the resistance of the tunnel against surface faulting displacements. Furthermore, they make the tunnel's behaviour more consistent with the soil deformations. In this respect, these joints decrease the damages that may occur in the tunnel lining. Three mechanisms, including rigid rotation, rigid movement, and locking, have been formed in the tunnel segments after the fault offset.

Keywords: Geotechnical Centrifuge; Tunnel; Fault Rupture; Alluvium; Flexible Joint.

1 INTRODUCTION

Natural hazards like earthquakes, landslides, or volcanoes are dangerous phenomena in the world that threaten the lives of humans around the world. Amongst these geohazards, earthquakes are more important because they occur several hundred times a day in different locations worldwide. Therefore, different human-made structures are influenced by this type of extreme events and might be damaged due to its related mechanisms.

Underground structures such as pipelines or tunnels, which serve as significant lifelines in modern societies, are more prone to the earthquake damages owing to their long-linear configuration. Hashash et al. (2001) have indicated that two different mechanisms affect the tunnels during the earthquakes. These are (1) ground shaking, and (2) ground failure. The former mechanism refers to the ground deformations due to the seismic waves propagation within the earth's crust. The second mechanism points out to the Permanent Ground Deformations (PGD) because of the earthquake displacements. These displacements could come from seismic-shaking or earthquake-faulting.

The earthquake-faulting was one of the main causes of the tunnels deformations and collapses

during past earthquakes (Brown et al., 1981). Although different researchers have studied the effect of the fault movement on the tunnel behaviour (Brown et al., 1981; Burrige et al., 1989; Cai et al., 2019; Russo et al., 2002; Wang et al., 2012), but most of the studies were in the rock media with strike-slip faults. There is limited evidence in the literature regarding the effects of faults on alluvial tunnels (Burrige et al., 1989; Cai et al., 2019; Kiani et al., 2016; Lin et al., 2007).

Moreover, when it is not possible to avoid the construction of tunnels through the active fault regions, a fault crossing strategy is required to reduce the tunnel damages (Hashash et al., 2001). There are very few published results about the feasible strategies to mitigate the influence of the faults on the tunnels (Romero and Caulfield, 2012; Russo et al., 2002; Shahidi and Vafaeian, 2005; Wang et al., 2012). Table 1 shows the strategies that have been employed in past practical works to reduce fault rupture effects on tunnels. The majority of these fault crossing techniques have focused, again, on strike-slip faulting within the rock media. Therefore, more research is needed to understand the interaction of a tunnel constructed in soft grounds (or alluvial deposits) and subjected to the surface dip-slip faulting.

The purpose of this work is to present the results of an experimental centrifuge study on a model tunnel subjected to the displacement of a 60° reverse fault. The surrounding medium was sandy soil, and articulated crossing method has been used against fault offset.

Table 1. Different available strategies to mitigate tunnel damages across active fault zones (Power et al., 2006; Wang et al., 2012).

Strategy	Description
Over-excavation	Enlarging the tunnel cross-section.
Articulated Design	Ductile joints increase the longitudinal flexibility of the tunnel.
Grouting technique	Increase the ductility of fault zone by grouting.
Isolation technique	An enlarged primary liner is surrounding smaller inner liner with injected frangible materials in between them.

2 MATERIALS AND METHODS

The centrifuge modelling of the fault-tunnel interaction has been conducted at the Geotechnical Centrifuge Facility of the Advanced Soil Mechanics Laboratory of the International Institute of Earthquake Engineering and Seismology (IIEES). The IIEES's centrifuge machine is an Actidyn C67-2 model with 3.5m beam radius (Figure 1). It can accelerate a payload equal to 1.5 Tons up to 100g or 0.5 Tons up to 130g. Its swinging basket dimensions are 100cm × 80cm × 80cm (length × width × height).



Figure 1: Geotechnical centrifuge of the International Institute of Earthquake Engineering and Seismology (IIEES).

The centrifugal acceleration in the centrifuge test has been set to be 25 g. Therefore, according to the principles of similitude in centrifuge and Ng space (Wood, 2004), the ratio between linear dimensions in prototype and model scales was N=25.

The definition of the problem studied in this paper is schematically illustrated in Figure 2. Three

different longitudinal segments of a tunnel are shown in this figure. Reverse faulting with a dip-angle equal to 60° and 3.5 cm vertical offset (0.875 m in prototype scale) has been applied in the hanging-wall side. The relative angle between the fault line and tunnel axis was 90°.

The alluvium material in centrifuge test was Firoozkough Sand No.161 which its properties are presented in Table 2 (Ahmadi et al., 2018). The total depth of the soil layer was 28cm in model scale. It is equivalent to 7m of alluvium deposit in prototype scale. The relative density of the soil was $D_r=65\%$, which shows medium dense sand. This density obtained using the wet tamping technique and under-compaction method.

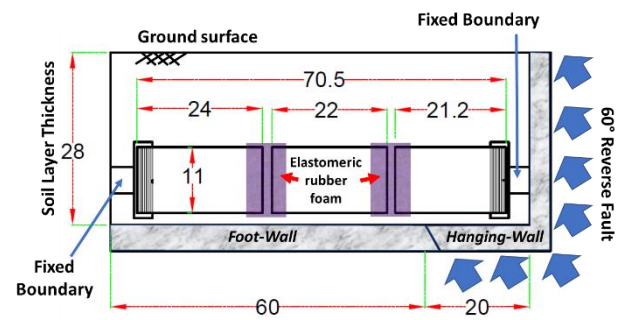


Figure 2: Problem schematic definition (all dimensions in cm).

Table 2: Physical and mechanical characteristics of the Firoozkough sand No.161.

USCS	G _s	W _c (%)	D ₅₀ (mm)	e _{min}	e _{max}	φ (°)
SP	2.65	3	0.27	0.548	0.943	37

2.1 Tunnel properties

A circular concrete tunnel in prototype scale was simulated with Aluminium material in the centrifuge. The tunnel geometrical and mechanical properties in both prototype and model scales are presented in Table 3. The tunnel's embedment depth to diameter ratio is 1.625 which demonstrate a shallow excavated tunnel in soft soil stratum. This tunnel could be an urban facility underground lifeline. It has been shown in Figure 2 that three segments of a tunnel were modelled in this study. These segments simulated cast-in-place concrete lining in continuous tunnels. However, instead of the transverse expansion or construction joints that are common in practice in 6 to 12m longitudinal spacing (Halvorsen et al., 1995), flexible joints with low shear and bending rigidities have been used here. To this purpose, two elastomeric-rubber-foam tubes with 10 cm length have been placed over the two transverse gaps in Figure 2. The extremely lower young's modulus ($E \approx 3\text{MPa}$) of these elastomers compared to the Aluminium one ($E=70\text{GPa}$) have simulated two flexible joints along

the tunnel axis. These sleeve-like elastomers have also prevented the entrance of the sand into the tunnel.

Because of the dimensional limitations of the model container, fixed boundary conditions at vertical plates of foot-wall and hanging-wall sides have been implemented (Figure 2). In this study, it is more desired to survey the performance of the middle segment deformations against the surface faulting. Therefore, the left and right tunnel segments behaviour were not important.

Table 3: Tunnel properties in prototype and model scales.

	Prototype	Model
Material	Concrete	Aluminium
E (GPa)	35	70
Diameter (m)	3	0.12
Lining thickness (cm)	30	0.6
EI (MN.m ²)	72700	0.19
Tunnel Length (m)	17.6	0.705
Embedment Depth (m)	4.875	0.195

2.2 Fault simulator box

A split box for simulation of the surface faulting within the alluvium strata has been designed and manufactured by authors for Geotechnical Centrifuge of IIEES. This fault simulator has the capability to model both normal and reverse faults with 60 degrees dipping-angle and maximum vertical offset of 50mm in the hanging-wall side. The simulator also has the feasibility to simulate different dipping-angles by substituting the backward guider wedges with other desired fault angles. A hydraulic jack, connected to the vertical plate of the hanging-wall side, has provided the required force for the fault displacement. The internal dimensions of the box's soil container are 800mm×700mm×580mm (length×width×height).

Moreover, particular components and details were also attached to the box's walls to model the boundary conditions with desired flexibility. These components could model the fixed, free, or semi-flexible boundaries for the buried linear-structures like tunnels or pipes.

3 RESULTS AND DISCUSSION

The propagation of shear bands within the soil layer after the 3.5 cm vertical and 2 cm horizontal reverse fault displacements has been illustrated in Figure 3. It is evident in this figure that the ground displacements and shear bands influenced the segments No.1 and 2. Segment No.2 could freely rotate and move between segments No.1 and 3. A longitudinal section of the tunnel deformation is

shown in Figure 4. This figure shows explicitly that due to the surface faulting, the deformational mechanisms of segment No.2 were rigid displacement and rotation. The rotation angle was 3.5 degrees counter-clockwise with 2 cm horizontal displacement to the left.

The displacement of the reverse fault has caused the flexible-joints gaps between the consecutive segments, to be closed (Compare Figure 3 with Figure 4). Therefore, after the simultaneous rotation and displacement in segment No.2, a locking mechanism will happen. In this third mechanism, the tunnel segments will go partially inside each other (Figure 4). The amount of the tunnel segments displacement, rotation, and the location of the locking mechanisms, are dependent on some parameters. These are the extent of fault offset, fault angle, and the tunnel segments' diameters and lengths.

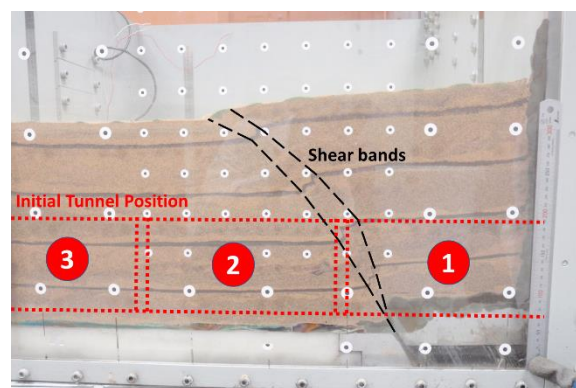


Figure 3: Reverse fault rupture propagation with 60° dipping-angle and developed shear bands.

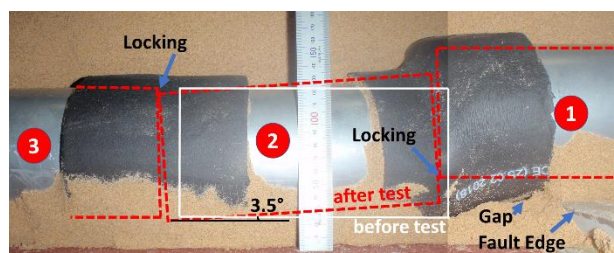


Figure 4: Tunnel's segments deformation after fault's 3.5 cm vertical and 2.0 cm horizontal displacements.

Due to the usage of aluminium tube for modelling of a concrete tunnel, segments in the centrifuge test have not shown any failure or collapse. Nevertheless, the segments qualitatively displayed the dominant deformational mechanisms in the tunnel after the fault rupture. According to Power et al. (2006), because the distribution of the fault displacements in the soft soils occur in relatively extensive zones, using the articulation method with flexible joints is more desired. If concrete sections have enough strength and stability against the imposed soil stresses, and flexible joints do not fail

during the large fault displacements, then the failure mode of the tunnel would be due to the locking mechanism.

Figure 4 also shows that a gap has been formed in the right side of the picture, just in the location that shear bands (Figure 3) have reached the bottom of segment No.1. This gap has shaped due to the hanging-wall movements and the stationary shape of the foot-wall. The tunnel in this portion acted as a shield and has not allowed the upper soil grains to fill the underlying gap. Therefore, zero soil pressure was available in this section.

4 CONCLUSION

This paper has argued that how is the deformational mechanisms of a continuous concrete tunnel with flexible joints during the reverse surface faulting.

For accommodation of the tunnel behaviour with fault displacements, the construction joints of the tunnel have been replaced with flexible joints in this study. The flexible joints have been simulated with elastomeric-rubber-foam in geotechnical centrifuge test. Using these ductile joints, the tunnel could distort into an S-shape in the fault zone with lower probable damages.

Three mechanisms have been obtained for tunnel after the centrifuge test. They were rigid rotation, rigid movement, and locking mechanisms. The first two mechanisms occurred simultaneously during the fault movement. The latter mechanism could be happened due to the large displacements of the reverse fault, along with closing the flexible joints gap. If concrete tunnel cross-sections have enough strength against the induced earth stresses, the failure of the tunnel would be due to the locking mechanism of adjacent segments. This, in turn, shows that in the designing process of flexible joints, the suitable gap-space should be obtained based on three parameters. These parameters are probable maximum fault displacement, tunnel segment length, and tunnel diameter.

5 ACKNOWLEDGEMENTS

The authors wish to express their thanks for the financial support of the International Institute of Earthquake Engineering and Seismology (IIEES), under project number 6137. The authors also acknowledge Mr Kamran Shirazian for the support in carrying out the geotechnical centrifuge test.

6 REFERENCES

Ahmadi, M., Moosavi, M., Jafari, M.K., 2018. Experimental investigation of reverse fault rupture propagation through wet granular soil. *Engineering Geology* **239**, 229-240.

Brown, I., Brekke, T., Korbin, G., 1981. Behavior of the Bay Area Rapid Transit Tunnels through the Hayward Fault. Final Report to the US Department of Transportation. Report No. UMTA-CA-06-0120-81-1.

Burridge, P.B., Scott, R.F., Hall, J.F., 1989. Centrifuge study of faulting effects on tunnel. *Journal of geotechnical engineering* **115**, 949-967.

Cai, Q., Peng, J., Ng, C.W., Shi, J., Chen, X., 2019. Centrifuge and numerical modelling of tunnel intersected by normal fault rupture in sand. *Computers and Geotechnics* **111**, 137-146.

Halvorsen, G.T., Poston, R.W., Barlow, P., Fowler, D.W., Palmbaum, H.M., Barth, F.G., Gergely, P., Pashina, K.A., Bishara, A.G., Hansen, W., 1995. Joints in concrete construction.

Hashash, Y.M., Hook, J.J., Schmidt, B., John, I., Yao, C., 2001. Seismic design and analysis of underground structures. *Tunnelling and Underground Space Technology* **16**, 247-293.

Kiani, M., Akhlaghi, T., Ghalandarzadeh, A., 2016. Experimental modeling of segmental shallow tunnels in alluvial affected by normal faults. *Tunnelling and Underground Space Technology* **51**, 108-119.

Lin, M.-L., Chung, C.-F., Jeng, F.-S., Yao, T.-C., 2007. The deformation of overburden soil induced by thrust faulting and its impact on underground tunnels. *Engineering geology* **92**, 110-132.

Power, M., Fishman, K.L., Makdisi, F., Musser, S., Richards Jr, R., Youd, T.L., 2006. Seismic retrofitting manual for highway structures: Part 2-retaining structures, slopes, tunnels, culverts and roadways. Technical Report MCEER-06-SP11, MCEER, University at Buffalo, The State University of New York.

Romero, V., Caulfield, R., 2012. Improving the Seismic Resilience of Lifeline Tunnels, NZSEE Annual Technical Conference, Christchurch, New Zealand.

Russo, M., Germani, G., Amberg, W., 2002. Design and construction of large tunnel through active faults: a recent application, Proceedings International Conference of Tunneling and Underground Space Use, Istanbul.

Shahidi, A., Vafaeian, M., 2005. Analysis of longitudinal profile of the tunnels in the active faulted zone and designing the flexible lining (for Koohrang-III tunnel). *Tunnelling and underground space technology* **20**, 213-221.

Wang, Z., Zhang, Z., Gao, B., 2012. Seismic behavior of the tunnel across active fault, The 15th world conference on earthquake engineering, Lisbon, Portugal, Sept, pp. 24-28.

Wood, D.M., 2004. *Geotechnical Modelling*. Spoon Press.

Soil Improvement of a Subway Station Excavated by an Earth Pressure Balance Machine

Mohammad Zamani Ahmad Mahmoudi.¹, Ali Entezari Zarandi², Milad Naghibi³, Ali Azad⁴

¹*Kavoshgaran Consultant Engineers, Senior Consultant, Iran*

²*Institut national de la Recherche Scientifique, Postdoctoral Research Fellow, Canada*

³*The Wellington Institute of Technology, Academic Staff Member, New Zealand*

⁴*Shahrood University of Technology, PhD candidate in Mining Engineering Faculty, Iran*

Corresponding author: Mohammad Zamani Ahmad Mahmoudi (miszamani@gmail.com)

ABSTRACT: In this research, the soil stability around U7 station of Tehran Subway was physically and numerically investigated using a miniature tunnel-boring machine (TBM) and FLAC^{3D} finite difference program, respectively. The results demonstrated that instability occurs around launch portal and thus, an appropriate soil improvement technique should be adopted. After comparing the possible techniques, usage of fore pole umbrella above the tunnel and installation of fiberglass nails at tunnel face were chosen and utilized. Finally, the number, length, diameter and strength features of fore poles and fiberglass nails were determined through sensibility analysis and numerical modelling.

Keywords: Soil improvement; EPB; Modelling; Plastic Concrete; Fiberglass nails.

1 INTRODUCTION

In urban areas, the construction of subway stations is conducted in two ways: in the first method, the tunnel is excavated and then stations will be constructed. In the second method, stations are already constructed and then the tunnel is excavated all over the designed route by Tunnel Boring Machine (TBM). An exemplary of later method is a special supportive station constructed before TBM arrival. This type of stations are commonly constructed in the middle of subway routes and its main purpose is that, in the rest of subway route, transportation of precast concrete segments and emission of excavated soil to out carries out from this site rather than the first station in where TBM was already set up. The supportive stations have two portals: the reception portal that TBM pierces it and enters to the station; the launch portal that TBM penetrates to soil through it and continues the excavation of remainder part of tunnel route. Support members of stations are usually diaphragm walls, nails, shotcrete and steel struts that are installed inside the station space.

When the TBM arrives near the reception portal and enters through it, the support elements of wall such as nails, shotcrete and steel struts are influenced by cutter-head pressure of TBM and may fail that can bring about to instability of wall. Moreover, when excavation process is restarted at the launch portal and TBM penetrated into the soil, the risk of soil instability and damage to the support elements are highly expected. Financial cost and time delays due to rehabilitation may be up to several times more than primary costs of stabilizing the reception and launch portals ground.

In order to avoid instability in the reception and launch portals, the necessary measurements must be taken; Hence at the first phase, an appropriate system must be selected to stabilize the soil behind Tunnel Eye. The Tunnel Eye is defined as a part of diaphragm wall that is located directly in front of cutter-head. A soft Eye is a wall type that can be excavated and penetrated by the TBM; for example: frozen ground, glass fibre bar reinforced concrete, soilcrete and non-reinforced concrete. A hard Eye cannot be excavated and penetrated by the TBM and other equipment is need to remove it. Hard Eyes include: steel bar reinforced concrete, steel sheet piling and concrete with unconfined compressive strength exceeding cutter-head capability.

In second phase, geometric details and resistance features of this system is designed so that it must be economical and meet the possible instability of two portals. The Engineering design of the Tunnel Eye features has a crucial role in preventing of instability occurrence in both portals.

2 LITERATURE REVIEW

Two papers that specifically focused on launch and reception portals challenges with tunnel boring machines (TBMs) have been published by Richards et al. (1996) and Dean et al. (2006). Richards et al. provided a detailed discussion of launch and reception challenges for pressurized face tunnelling with precast concrete segment linings. The paper summarized experience on Cairo Metro Line 2 and other global experience on eleven major projects. Dean et al. also provided a detailed discussion of launch and reception challenges for pressurized face tunnelling with precast concrete segment linings

and relates experience on several recent North American projects. Schürch and Jost (2006) discussed GFRP soft Eyes within slurry diaphragm walls for TBM launch and reception with references to projects in Australia, Singapore, and Switzerland. In 2008, Steven et al. gathered prior studies about reception and launch portals challenges at different subway projects excavated by Earth Pressure Balance (EPB) machines and presented feasible solution methods to stabilizing the portals.

According to prior studies, Portal challenges and the cost of mitigating depend on combinations of the many factors such as ground type, strength, permeability, TBM type, initial lining method, station ground support method, Tunnel Eye type and specially groundwater pressure. Risks are higher with increased groundwater heads; Excessive groundwater inflows might flood the station and TBM, damage to contractor's equipment and adjacent property, collapse of the station ground support system and cause drawdown settlement. Solving this problem, a mechanical seal to resist against water pressure should be designed and assembled at Tunnel Eye. In addition, the stabilizing systems should then be designed and constructed to avoid lost ground problems, delays and costs.

3 PROJECT DESCRIPTION

3.1. U7 Station and Tehran Subway Details

Tehran Subway is a rapid transit system serving the public transportation in Tehran, the capital city of Iran. Four lines (lines 1, 2, 4 and 5) of the subway are operational while two lines (lines 3 and 7) are still under construction. The Line 7 includes 27 kilometres of tunnel with internal diameter of 9.165 m excavated by an EPB machine.

EPB technology is fundamentally based on the use of excavated soil in an excavation chamber to support the ground. During the excavation, the soil is extruded through the openings of the cutter head and into a screw conveyor situated within the EPB. By balancing the thrust speed of the EPB and the rotation of the screw conveyor, it is possible to utilize the excavated material within the screw conveyor to establish a controlled volume and controlled face support pressure. EPB machine excavates as it drives forward then erects a precast concrete segmental ring in its rear shield that seals against the previous ring. The TBM then drives forward again off the newly installed segment ring. The detailed properties of the EPB Machine and precast concrete segments used in line 7 Tehran Subway project are presented in Table 1.

The line 7 of subway begins in the north from Yousef Abad and end at Takhti Stadium in the south-east of Tehran city. The line is included

northern-southern and eastern-westerner parts. Both two parts have a particular supportive station in middle: U7 station in the middle of northern-southern part and G7 station in the middle of northern-southern part. In this research the study area is U7 station that is located in south of Goftogo Park and on the edge of Chamran Highway. The construction of northern-southern part of line 7 started by EPB breaking in at Navab shaft (March 2012). Simultaneously, the construction of U7 station was begun.

Table 1. Properties of EPB and precast segments

Property	Unit	Quantity
Outer Diameter	m	9.165
Shield diameter	m	9.126
Shield length	m	10
Excavation step length	m	1.5
Precast segment length	m	1.5

The U7 station was 800 m long with the width of 100 m. The ground overburden above the tunnel varies from 15 to 20 meters. The construction of the station was begun from surface to final floor approximately 36 meters below ground level. First, holes bored on the boundaries of the station box and then reinforced concrete piles with diameter of 1 m steel pipe were taken as retaining structures. The whole number of piles at perimeter of station was 88 and the interval between those centres was 2.6 meter. The excavation operation of station box was divided into six levels and 5 struts rows. After removing the soil in level 1, the support elements such as shotcrete, nails and direct and diagonal steel struts were installed. Then these operations were repeated for next levels until the whole box of station was constructed and supported. The inner view of U7 station after construction is shown in Figure 1.

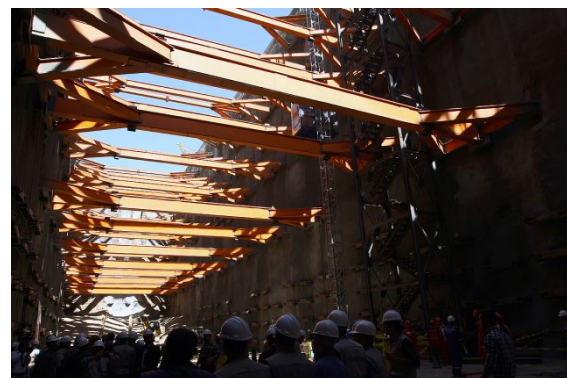


Figure 1. U7 station inner view after construction

3.2. Geotechnical and geological properties

According to engineering geological survey report, the soil profile throughout U7 station comprises two

layers; the first layer is upper layer with average thickness of 4 m, containing rubbles, stone, etc. The second layer is a mix of very dense gravel soils that continue to depth of 50 m. No exploration holes met underground water in U7 station ground until depth of 55 meter. If underground water existed, the cost of ground improvement to achieve the desired permeability reduction and suitable strength would exceed. The moisture of in-situ soil was reported 10%. The Geotechnical properties of these layers collected from the samples of boreholes at U7 Station are summarized in Table 2.

Table 2. Soil properties at U7 station site

Parameter	Unit	Upper layer	gravel mix
Depth	m	0-4	4-50
Young's modulus, E	MPa	0.025	0.090
Poisson's ratio, ν	-	0.2	0.3
Cohesion, C	MPa	0.015	0.010
Density, ρ	Kg/m ³	1700	2200
Friction angle, ϕ	Degrees	30	34

4 PROBLEMS

4.1. Problems at Reception portal

Figure 2 illustrates the EPB excavation near reception portal. As EPB approaches to the wall station, it's necessary to reduce the face pressure to approximately zero value in front of shotcrete. After cutting the shotcrete by equipment inside the station, the EPB can enter the station safely. If analytical assessments or numerical modelling results show any instability at the reception portal, then the necessary measurements include ground improvement methods must be adopted and used. Crossing of EPB at reception portal needs less measurements than launch portal. In case of launch portal, at first the shotcrete must be cut and then EPB slowly penetrates to soil; this act may cause instability of the soil behind the shotcrete. In U7 station, the problems including instability of face and deviation of cutter head did not exist at reception portal but a mechanical seal was needed to isolate tail-gap grout.

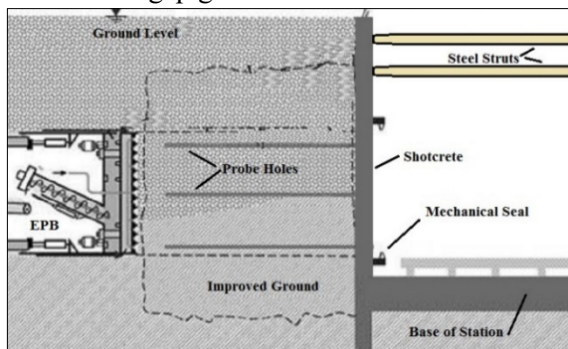


Figure 2. EPB machine near the reception portal

4.2. Problems at Launch portal

Figure 3 illustrates an EPB machine that has penetrated from the station into the improved ground behind the launch portal. After cutting the shotcrete, the primary challenge for EPB launch is to achieve face stability until at least the cutter-head can be advanced past a suitable internal mechanical seal and the excavation chamber may be filled and brought to the necessary pressure for ground control. After the EPB and at least one full segment ring have past the mechanical seal, the tail gap can be thoroughly grouted. When EPB passes the improvement zone and enters the soil, the necessary face pressure is prepared from muck in chamber.

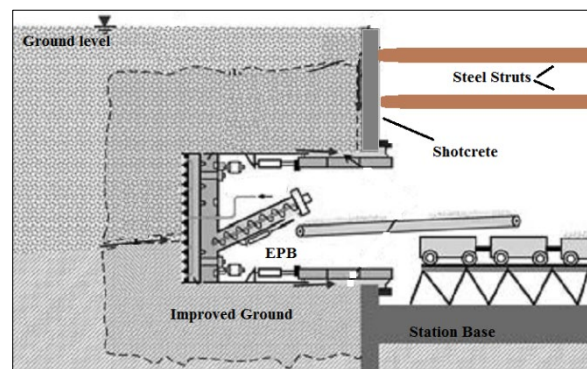


Figure 3. EPB machine penetrating into the launch portal

The main problems in the launch portals are explained at below.

4.2.1 Soil instability after cutting shotcrete

The first step is cutting shotcrete that acts as the soil support member and exists directly in the front of cutter head at the launch portal. At this moment, if the soil behind of the removed shotcrete was instable and flowed into the station, there would not be balancing force to prevent of soil instability. In case of U7 Station, by physical and numerical modelling, it was found that after cutting the shotcrete at Tunnel Eye, the soil behind the launch portal is instable. The main methods to meet this problem are:

- 1) Use of grouting methods as jet grouting, penetration grouting and chemical grouting; these techniques improve the soil properties like cohesion and inner friction angle. This method is used when underground water exists because it may flow to station and cause soil instability. In case of U7 station not only the length of grouting holes would exceed than 35 meters and so it had huge operational costs but the interference of grouting equipment and steel struts caused many problems.
- 2) Soil replacement with stronger materials like plastic concrete; in this technique, many holes are

bored from ground surface to remove the soil behind the shotcrete and simultaneously are filled with plastic concrete. The cement and bentonite increase the strength and deformation plasticity of plastic concrete. Use of plastic concrete needs many laboratory tests to achieve the suitable mix in regard to uniaxial compress strength and allowable settlement of plastic concrete. The uniaxial compress strength of plastic concrete must be less than cutting tools of the EPB. Preventing the deviation from main route, the plastic concrete settlement must be in allowable ranges. Since a certain method to calculate uniaxial compress strength and allowable settlement according to amount of cement, bentonite and water portion don't exist, determination of mix layout is expensive and time-consuming.

3) Supporting the soil by installation of fiberglass bolts at Tunnel Eye; in this method, fiberglass bolts are installed into pre-drilled holes and then cement is grouted into them. Axial behaviour of FG bolts is the main property that increases the soil strength. This behaviour is due to remarkable tensile strength and large axial stiffness of FG bolts. This method was decided to support of the soil at U7 station.

4.2.2 Soil instability after tunnel excavation

When EPB starts to excavate the soil, the excavation chamber is vacant and the face pressure to support the soil does not exist yet. Thus, it is quite vital that the soil behind the launch portal must be stable in the several meters behind the launch portal until the excavation chamber is filled with muck. By physical modelling of tunnel excavation by EPB at launch portal of U7 Station, it was found out that FG bolts cannot ensure the soil stability when the chamber is empty. So the roof umbrella method (pipe roof method) was decided as an auxiliary method to minimize the soil displacements near the launch portal. This pipes act like beams and bear the weight of overburden ground. Geometric details and resistive features of FG bolts and roof pipes were designed and obtained by sensitivity and parametric analysis in FLAC^{3D} program.

4.2.3 Cutter-head deviation from main route

Main factor in preventing the cutter-head deviation is operator's skill to use properly the trust force and excavation parameters based on ground properties. Two methods is usually adopted to preventing of the cutter head deviation:

1) Excavation manually of a little length of tunnel; in this method, first several meter of soil is excavated by labours and then EPB machine pursues excavation in this pre-excavated route.

2) use of "start ring" in front of Tunnel Eye; this method often is a preferred option against prior method because in addition to control of excavation route and preventing of cutter head deviation, it makes the grouting operation behind the first segment ring much easier.

4.2.4 Grouting behind the first segment

This problem is composed two challenges: instability of the soil above the first segment and grout scape. In case of U7 station. To ensure the stability of the soil above the first segment, it was decided to excavate first 3 meters (two segments that each of them had 1.5 m length) of the tunnel manually.

To solve the second challenge, a mechanical seal was provided to isolate the tail-gap grout for completion of the first segments.

5 PHYSICAL AND NUMERICAL MODELLING

5.1. Modelling of U7 station

For constructing the U7 station, the reinforced concrete piles as retaining wall was installed before the excavation start. First, a vibro-hammer drove a casing into the pre-determined piles position and then the soil within the casing removed by auger. Then a crane put the steel cages in the boreholes and concrete was poured into the boreholes to form the piles. Then the vibro-hammer extracted the casing from the ground. This work repeated for 88 piles around the station.

Then soil was excavated to the first level and steel struts were installed. Then, mesh-reinforced shotcrete and steel nails were used to support the station walls before the excavation would proceed the lower level. The soil excavated to the second level and prior steps were repeated. This process was progressed until the excavation reached to final depth. Finally, reinforced concrete slab or base slab was constructed.

Five rows of struts were installed. Due to increasing of soil lateral pressure with depth, the lower steel struts had larger section than upper ones.

In this research, the U7 station construction and then tunnel excavation by EPB machine, were physically and numerically modelled using a miniature tunnel boring machine (TBM) and FLAC^{3D} finite difference program, respectively. The miniature TBM was constructed to simulate the process of tunnelling. The main box was a 300×800×800 mm stainless steel box with soil and the displacement measurement system (Figure 4).

The shield was made up of three tubes, a stainless steel tube with a cutting-head for soil excavation,

the middle tube as the tunnel lining and finally, a steel pipe for simulating the tail void formation. The driving part consisted of two engines; the first for advancement of the shield and the second, for driving the cutter. The machine was used in a centrifuge under appropriate range of acceleration.

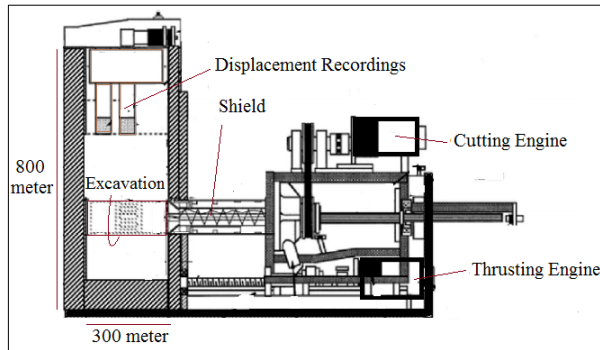


Figure 4. Layout of physical model of TBM and soil Box

FLAC^{3D} program is widely used for deformation and stress analysis around underground structures. In this present study, the main aim is to probe the displacements and stresses around the reception and launch portals when tunnel is excavated by EPB. The explicit, Lagrangian, calculation scheme and the mixed-discretization zoning technique used in FLAC^{3D} ensure that plastic collapse and flow are modelled accurately. Because no matrices are formed, large three-dimensional calculations can be made without huge memory requirements (FLAC^{3D} manual).

To emit the boundary conditions effect and demonstrate the real behaviour of portals when are affected by tunnel excavation, several grid of U7 station was built according to real conditions. Eventually the most suitable mesh was decided. The size of grid dimensions were 40 m length, 30 m width and 50 m height. The centre of coordinates of grid was on tunnel axial at exactly in centre of tunnel Eye. The U7 Station and Tunnel geometries, soil properties, boundary conditions and in-situ stresses were applied to the model. The Mohr-Coulomb criterion was considered for geo-mechanical behaviour of soil. The steel struts, nails and shotcrete were modelled as beam, cable and shell elements in FLAC^{3D} program. Features of shotcrete and nails have been presented in tables 3 and 4. For steel struts the steel properties were used.

Table 3. Properties of shotcrete

Parameter	Unit	Quantity
Thickness	m	0.25
Young's modulus, E	GPa	21
Poisson's ratio, ν	-	0.25
Density, ρ	Kg/m ³	2400

Table 4. Properties of nails

Parameter	Unit	Quantity
Section area	mm ²	800
Tensile strength	MPa	0.22
Cohesion, C	MPa	4.4
Friction angle, ϕ	Degrees	25

Next, the each level inside the station was removed and simultaneously support members were installed.

5.2. Modelling of tunnel exaction at reception portal

Physical modelling at reception portal indicated stability of the wall. No instability was occurred and the miniature machine could enter into the station without any collapse. Numerically, to excavate the tunnel, the EPB features and concrete segment characteristics were. To achieve the real EPB's face pressure, the tunnel excavated with several face pressures. Eventually the value of 50Kpa was decided for EPB's face pressure. Also, the grout pressure behind segments, that is effective in decreasing soil convergences, was decided equal to face pressure plus 150 Kpa.

First, the soil displacements were assigned to zero value to investigate the effect of tunnel excavation by EPB. Then tunnel was bored. Figure 5 shows that when cutter-head (white mesh) reaches the 12 m behind the reception portal, the prior plastic zone (that was made in station construction phase) is combined with plastic zone that caused by tunnel excavation. The maximum horizontal displacement of reception portal was 5 mm in this time.

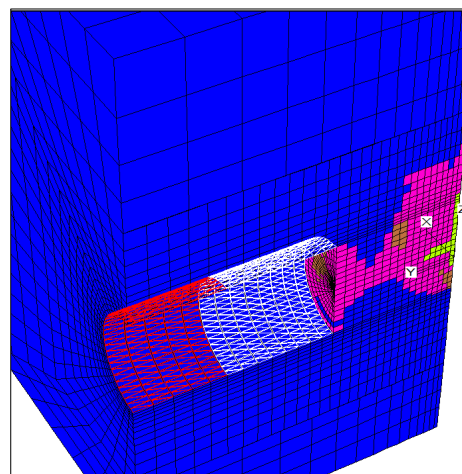


Figure 5. Combination of plastic zone around reception portal

After excavation of whole tunnel and installation the final segment, the shotcrete was cut and no signs of instability were found. Therefore, reception portal was stable and EPB machine successfully crossed it. Same with numerical modelling, the EPB

crossed at the reception portal without any instability occurrence of soil on 12 March 2018 (Figure 6).



Figure 6. EPB break out at reception portal without instability

5.3. Modelling of tunnel excavation at launch portal

After crossing the miniature machine at reception portal, the necessary measurements were taken to continue the tunnel boring from the launch portal. Therefore the shotcrete was cut and the machine was placed at front of wall. Through physical modelling, the soil behind the launch portal was unstable after cutting the shotcrete. The numerical results confirmed the findings obtained from physical modelling.

5.3.1 Choosing the stabilizing system

In order to improve the resistance and permeability of the soil behind the launch portals, methods as dewatering, ground freezing, grouting techniques, plastic concrete, fore pole umbrella and fiberglass nails are commonly used. According to geological and geotechnical conditions, financial analysis and technical restrictions, the execution of fore pole umbrella at tunnel crown and installation of fiberglass nails at the tunnel face had been chosen. This technique is quite appropriate for soils that the peril of underground water flow does not exist when the excavation of tunnel is started.

Fore pole umbrella includes several poles carried out above the tunnel crown to sustain the overburden pressure and control the displacements caused by tunnel excavation. When the excavation of station reaches tunnel's crown level, the fore pole s are bored. Then a steel bar is placed in each pole and the spout is closed with a bonnet. Finally the grout is pumped into the overall length of the pole.

Cohesion and frictional angle of grout cause to increase the shear strength of soil and decrease the extent of plastic zone as soon as excavation is started. Most important role of fore pole umbrella is maintaining the stability of work face when

excavation is carried out without EPB's pressure. In addition, to insure the stability of work face after cutting the shotcrete, fiberglass nails are installed at the tunnel section. The fiberglass pipes have become popular due to their cost-effectiveness, and some technical advantages such as high axial strength while relatively brittle in the transverse direction hence easily breakable during excavation. This technique is often combined with fore pole umbrella to eliminate the entirely unsupported spans in weak grounds.

5.3.2 Geometry and resistive features of stabilizing system

After cutting the shotcrete, three main zone with highest displacements towards inner space of station appeared. The shape of these zones was similar to ellipse and their extent increase from tunnel centre to out (Figure 7).

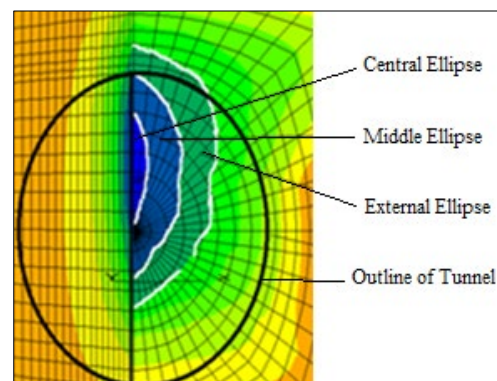


Figure 7. Three zones with highest displacements

The principal criterion in determining the geometry and resistive features of fiberglass nails is preventing the expanding of these unstable zones. If the nails' position is properly designed, it will need minimum number of nails.

5.3.3 Safety factor of launch portal's stability

To design the fore poles and fiberglass nails, different arrays of both systems were modelled above tunnel and in three critical ellipses, respectively. In each case, the maximum of soil displacements and the maximum of tensile stress in fiberglass nails were recorded. The safety factor of launch portal's stability is equal to portion of allowable tensile strength to maximum of tensile stress that was existed in fiberglass nails.

Due to difference between tensile stresses in distinct nails, it is necessary to consider the maximum and minimum of tensile stresses in the nails. One of the best guides on determination of walls safety factor in civil projects has been published by Shaw-shong in 2005. According to

Showshong, the minimum of safety factor for urban underground subway walls supported by nails is equal to 2.

Since the excavation of first 3 m of tunnel is manually done, three safety factors were recorded in models: the safety factor of portal stability in cutting of shotcrete phase, in excavation phase of first 1.5 m of tunnel length (equal to length of first precast concrete segment) and finally in excavation phase of second 1.5 m of tunnel length (equal to length of second precast concrete segment).

According to the geometry and numbers of fore poles and fiberglass nails in each displacement ellipse, many different arrays of them were modelled and their safety factors were recorded. In each case, upon to maximum of tensile stresses in the fiberglass nails, the safety factor of launch portal has been calculated. The stabilizing system must have at least safety factor of 2 in cutting of shotcrete phase. In all models the fiberglass nails had 10 m length with diameter of 10 mm and an allowable tensile strength equal to 688 N/mm². The length of 10 meter has been decided upon the plastic zone extent in the soil behind the Tunnel Eye.

Eventually, With regards to this point that the portal stabilizing system must be safe and economic, a layout that is showed in Figure 8, was decided as the best design. This layout with the minimum of fore poles at tunnel crown and fiberglass nails in tunnel face, ensures the safety factor of 2. After deciding this layout as the proposal design, the numerical modelling of tunnel excavation was executed that was a stable process without any collapse and instability.

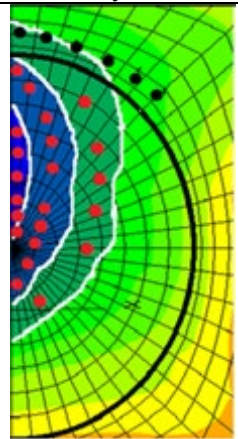
Layout	Description
	<ul style="list-style-type: none"> -6 fore poles at 0.5 m above the tunnel - 6 fiberglass nails in central ellipse - 10 fiberglass nails in middle ellipse - 6 fiberglass nails in external ellipse - Maximum of displacement in tunnel face: 2.5 cm -Safety factor: 2.4

Figure 8. The layout of treatment system at tunnel eye

5.3.4 Sensibility analysis

Sensibility analysis is necessary for assessment of geometric features effect of fore poles and fiberglass nails on the launch portal stability. So it was done by changing the geometric features of

stabilizing system consist of length and diameter of fore poles and fiberglass nails.

5.3.5 Effect of length and diameter of fore poles

The primary length of fore poles in the Figure 8 was 15 meter; According to Figure 9, increasing of length for values more than 15 meter has not a remarkable influence on safety factor of launch portal. Increasing of poles length causes to increasing of safety factor of both shotcrete cut and excavation of first 1.5 meter phases but it has not any effect on safety factor of excavation of second 1.5 meter of tunnel.

Similar to length, increasing of diameter causes to increasing of safety factor of both shotcrete cut and excavation of first 1.5 meter phases but it has not any effect on safety factor of excavation of second 1.5 meter (Figure 10).

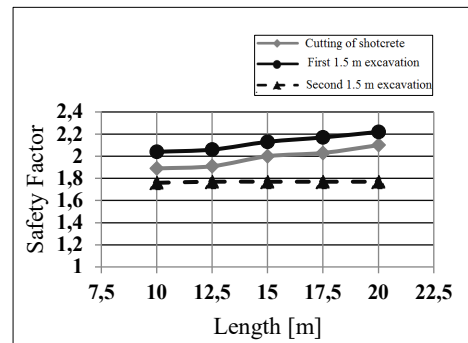


Figure 9. Effect of fore pole length on three safety factors

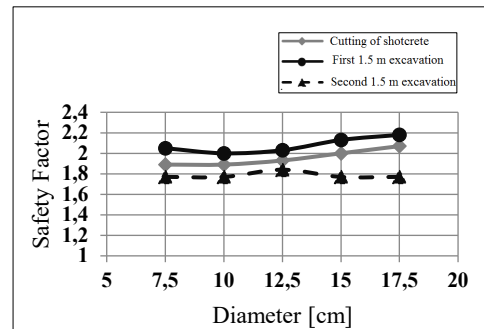


Figure 10. Effect of fore pole diameter on three safety factors

5.3.4 Effect of length and diameter of fiberglass nails

The primary length of fiberglass nails in the Figure 8 was 10 meter; According to Figure 11, effect of changing in fiberglass nails length has two part.

The first part is related to lengths less than 8 meter. In this case, the length of fiberglass nails is less than plastic zone length (10 meter) behind the tunnel Eye. If fiberglass nails length be less than 5.7 meter, the collapse of tunnel face will definitely occur in the excavation of second 1.5 meter phase. In addition, for fiberglass nails between 5.7 m and 8

m, the safety factor of cutting of shotcrete and excavation of first 1.5 meter phases decrease while the safety factor of excavation of second 1.5 meter phase rapidly increases.

The second part occurred when the length is more than 10 meter. In this case, the length of fiberglass nails is more than plastic zone length behind the tunnel Eye. According to Figure 11, increasing in length of fiberglass nails causes to increase the safety factor of cutting of shotcrete and excavation of first 1.5 meter phases but it has not any effect on safety factor of excavation of second 1.5 meter.

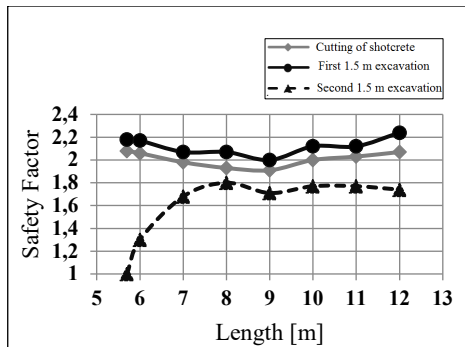


Figure 11. Effect of fiberglass length on three safety factors

The primary diameter of fiberglass nails in the Figure 8 was 10 mm; According to factory brochures, the change in fiberglass nails diameter causes to change in their tensile strength and axial stiffness. Increasing in diameter causes to decrease the tensile strength and increase the axial stiffness. The axial stiffness of nails is equal to multiply its section area by its axial deformability module. So in addition to change in nails diameter, their tensile strength and axial stiffness change too. In according to Figure 12, increasing in diameter of fiberglass nails causes to increase the safety factor of shotcrete cutting phase remarkably but has less effect in excavation of first and second 1.5 m safety factors.

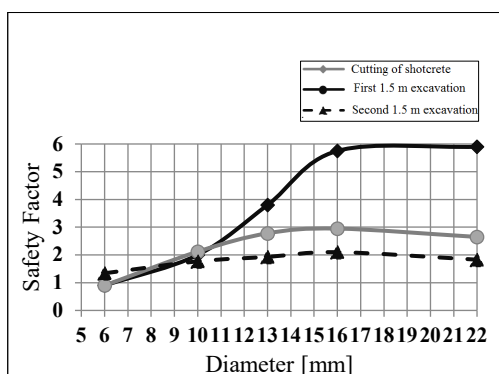


Figure 12. Effect of fiberglass diameter on three safety factors

6 RESULTS AND DISCUSSION

The results of modelling indicated that after the construction of U7 station, a plastic zone with 10 m

length is extended around the both reception and launch portals. Although the reception portal is stable and safe, that dangerous zone will subject the soil of launch portal to instability in primary phases of excavation the tunnel. The tunnel face instability in cutting of shotcrete phase is reduced by installation of fiberglass nails. Additionally, the face instability after start the excavation of tunnel, executed without EPB pressure, is omitted by installation of fore poles.

7 CONCLUSION

The length of fiberglass nails has a remarkable influence on the face stability in excavation of second 1.5 m phase. If the length is less than 5.7 m, the safety factor of this phase will be less than 1 and soil instability definitely occur. The length of fiberglass nails must be at least 10 m.

Increasing of fore pole length and diameter causes to slowly increasing of safety factors of both shotcrete cutting and excavation of first 1.5 meter phases but it has not any effect on safety factor of excavation of second 1.5 meter. Increasing grout cohesion and tensile strength causes to increasing of all safety factors remarkably.

8 ACKNOWLEDGEMENTS

Experimental studies, were supported by Tehran Subway Organization grant.

9 REFERENCES

- Dean, A., and Young, D. J. 2006. A Framework for Design of Tunnel Eyes. Proceedings 19th Canadian Tunnelling Conference, 17-20 September 2006, Vancouver, Canada.
- Richards, D. P., Burchell, A. J., Campo, D. W. and Raymond, P. 1996. Review of break-in and breakout concepts for tunnel boring shields in saturated soft ground. Geotechnical engineering international resources centre, 6(2): 79-98.
- Schürch, M. and Jost, P. 2006. GFRP Soft-Eye for TBM Breakthrough: Possibilities with a Modern Construction Material. International Symposium on Underground Excavation and Tunnelling, 2-4 February 2006, Bangkok, Thailand.
- Shaw-Shong, L. 2005. Soil nailing for slope strengthening. Geotechnical Engineering, Gue & Partners Sdn Bhd, Kuala Lumpur, Malaysia, 30-31 May, p. 1-9.
- Steven, W. H., & Andrew, J. F. 2008. Mitigating Tunnel Launch and Reception Challenges. The 11th international conference of IACMAG, 19-24 June, Torino, Italy.

Performance of Geogrid reinforced soil walls with low permeable backfill: Centrifuge Study

B.V.S. Viswanadham¹, Midhula Jayanandan², Dipankana Bhattacharjee³, Prince Kumar⁴

¹Dept. of Civil Engineering, Professor, Indian Institute of Technology Bombay, India

²Dept. of Civil Engineering, Research Scholar, Indian Institute of Technology Bombay, India

³Dept. of Civil Engineering, Formerly Research Scholar, Indian Institute of Technology Bombay, India (Currently Assistant Professor, IEST, Shibpur)

⁴Dept. of Civil Engineering, Former Postgraduate Student, Indian Institute of Technology Bombay, India

Corresponding author: B.V.S. Viswanadham (viswam@civil.iitb.ac.in)

ABSTRACT: The objective of the present study is to assess the performance geogrid reinforced soil walls with low permeable backfill subjected to rainfall in a large beam centrifuge facility available at IIT Bombay. The model low-permeable soil containing 20% fines was formulated by blending locally available fine sand and commercially available kaolin in the ratio of 4:1 by dry weight. A model hybrid geosynthetic was prepared by combining reinforcing geogrids with drainage non-woven geotextile in an integral manner. Subsequently, a robust rainfall simulating system was used for inducing rainfall at high gravities by applying relevant scaling laws related to rainfall modelling in a geotechnical centrifuge at 40 gravities. Results of two centrifuge tests soil walls of 10 m height, one with the conventional geogrid reinforcement layers and other with hybrid geosynthetic reinforcement layers, were reported and tested. The surface settlements, movements along the wall face and pore water pressure profiles developed during rainfall were monitored with the help of data recorded by pore pressure transducers during centrifuge tests, and by performing image analysis. Furthermore, displacement contours experienced by geosynthetic layers with the progress of rainfall. The results showcased the effectiveness of hybrid geosynthetic layers in reducing crest settlements and wall face movements during rainfall by providing necessary reinforcement action coupled with in-plane drainage. The adoption of this technique helps in using locally available low-permeable backfills in reinforced soil wall construction.

Keywords: Hybrid Geosynthetics; Low Permeable Soils; Reinforced Soil Walls; Rainfall; Centrifuge Modelling.

1 INTRODUCTION

There is a steady increase in the frequency of rainfall-triggered retaining wall and slope failures around the world, coincident with the effects of climate change. Many cases of such failures have been reported in retaining walls, excavated slopes and road subgrades due to rainwater infiltration. The instability arises due to the inefficiency of the soil to dissipate the excess pore water pressure generated within the reinforced retaining walls and slopes during rainfall due to its low permeability. While Koerner et al. (1998) recommends a backfill material which is completely devoid of fines, AASHTO (2009) and FHWA (Berg et al. 2009) mandate the use of backfill materials with less than 15% of fines passing 0.075 mm sieve and with plasticity index less than or equal to six. A recent report by NCMA recommends soils having less than 35% fines and MORTH (Ministry of Road Transport and Highway, Govt. of India) restricts the fines to 15%. Similarly, the boundary of poor drainage material is defined by Casagrande with a value of 10^{-6} m/s for the saturated coefficient of permeability (Holtz and Kovacs 1981). However, due to the unavailability and high cost implications of such good quality soils, poorly draining/low

permeable native soils with high fines content are heavily used. Such soils are typically characterized by their low peak shear resistance, loss of shear strength on wetting, poor drainage characteristics and volume changes and creep potential. The problems associated with the low-permeable backfill soils have been studied by various researchers like Christopher et al. (1998), Christopher and Stuglis (2005), Koerner and Koerner (2011) and Koerner and Koerner (2018).

Marginal soils with low hydraulic conductivity build up excess pore water pressure during rainfall due to its inability to drain water quickly and cause failure of geostructures. Hence, application of structural mitigation measures is important. In the present study, a nonwoven geotextile bonded to a geogrid will be used, wherein the geotextile component provides in-plane drainage while the geogrid provides tensile reinforcement.

A few full scale tests/ field tests were carried out to address the effect of climatic events such as rainfall on geostructures (Stuglis 2010, Portelinha and Bueno 2012, Portelinha et al. 2013). Similarly, Garcia et al. (2007), Olivares et al. (2009), Lee et al. (2011), Portelinha and Bueno 2013 and Yoo and Jang (2013) have simulated rainfall through small-

scale physical model tests. While full scale studies are time consuming and cost intensive, small scale physical model tests fail to replicate actual stress conditions and are usually considered to have limited scope while simulating rainfall events. Centrifuge based physical model studies, which ensure the most precise replication of field conditions, have been employed in a very limited number of works to study the effect of rainfall on retaining walls. Craig et al. (1991), Ling et al. (2009), Tamate et al. (2010), Tristancho et al (2012), Ling and Ling (2012), Portelinha et al. (2013) and Yoo and Jang (2013) have simulated rainfall conditions in centrifuge at enhanced gravity conditions to assess the response of reinforced slopes. However, the existing rainfall simulators produced only uniform intensity of rainfall. Scaling down of rain droplets into mist size to reduce impact pressure was explored by few researchers like Ling et al. (2010), Tamate et al. (2010), Tristancho et al (2012). The rainfall simulator used in the present study designed based on the Modified Mariotte's principle overcomes all the above discussed drawbacks. Details of the custom-designed in-flight rainfall simulator are explained in (Bhattacharjee and Viswanadham 2017, 2019). Researchers have explored the behaviour of geosynthetic reinforced soil slopes (Raisinghani and Viswanadham (2011) and walls with rigid facing under seepage conditions (Viswanadham et al. (2017), Razeghi et al. (2019), Mamaghanian et al. (2018, 2019) with varying drainage means including geocomposite layers, sand chimney drains, geotextile chimney drains etc. However, hybrid geosynthetics (combination of non-woven geotextile and geogrid) which have the dual functionality of in-plane drainage and reinforcing capability, especially in low permeable marginal soils, were incorporated only by a few researchers like Raisinghani and Viswanadham (2011) and Bhattacharjee and Viswanadham (2017, 2018, 2019), Mamaghanian et al. (2019) and Razeghi et al. (2019). In this study, two centrifuge tests are compared to understand the improvement in behaviour of a rigid facing reinforced wall with low permeable backfill soils subjected to rainfall when geogrid reinforcements are replaced with dual functional hybrid geosynthetics.

2 CENTRIFUGE MODEL TESTS

2.1. Model Materials

2.1.1 Model Soil

A locally available fine sand (SP as per USCS) and commercially available kaolin (CL as per USCS) were blended in a proportion of 4:1 (sand : kaolin) by dry weight, which resulted in a model soil with

finer percentage equal to 20%, close to the mandated value of 15% suggested by AASHTO and FHWA in construction of reinforced soil structures. In addition, the coefficient of permeability of the blended soil was observed to be 1.54×10^{-6} m/sec by conducting falling head test on moist-compacted soil samples placed at γ_{dmax} and OMC. The properties of model soil are summarized in Table 1.

Table 1 Properties of model soil

Soil properties	Unit	Values
Specific gravity, G_s		2.62
<i>Particle size distribution</i>		
Sand [>0.075 mm - < 4.75 mm]	%	80
Silt [>0.002 mm - < 0.075 mm]	%	10
Clay [< 0.002 mm]	%	10
<i>Atterberg limits</i>		
Liquid limit, LL	%	11.86
Plastic limit, PL	%	9.78
Plasticity index, PI	%	2.08
Soil classification (USCS)		SM
<i>Compaction characteristics</i> ^a		
Maximum dry unit weight, γ_{dmax}	kN/m ³	18.75
Optimum moisture content, OMC	%	9
<i>Permeability</i> ^b		
Coefficient of permeability, k	m/s	1.54×10^{-6}
<i>Shear strength parameters</i> ^c		
Cohesion, c'	kPa	7
Angle of internal friction, ϕ'	°	33

^a: Standard Proctor compaction; ^b: Falling head tests performed on moist-compacted soil sample at γ_{dmax} and OMC; ^c: CU triaxial tests conducted on moist-compacted soil samples at γ_{dmax} and OMC.

2.1.2 Model Reinforcement

A number of geosynthetic samples were tested to determine the tensile load-strain characteristics, transmissivity properties and soil-geosynthetic interaction properties. Finally, a model geogrid sample (G1) and a model geotextile sample (N1) were chosen as parent materials to develop the model hybrid geosynthetic, referred to as G1N1, by satisfying the scaling considerations. G1 exhibited an ultimate tensile load (T_{gu}) of 0.93 kN/m and ultimate tensile strain (ϵ_{gu}) of 18.9% along the machine direction for the wide-width tensile tests (as per ASTM D4595-2010). N1 has a much lower peak tensile load load of 0.25 kN/m in the machine direction at an ultimate strain value of 9.89%.G1 was scaled based on tensile load-strain and interface characteristics criteria to represent bandwidth of commercially available prototype woven geogrids.[Viswanadham and König (2004), Izawa and Kuwano (2010) and Balakrishnan and Viswanadham (2017)]. Identical percentage open area of 97.4% was ensured for both model and prototype geogrids to avoid danger of losing contact between soil-geogrid-soil and to prevent scale effects.The hybrid geosynthetic (G1N1) has an ultimate tensile load of 1.01 kN/m and an ultimate tensile strain of 18.3%. The radial transmissivity

was obtained at a normal stress of 20 kPa as $1.85 \times 10^{-6} \text{ m}^2/\text{s}$. The 4.5 m radius large beam centrifuge facility at IIT Bombay was used to perform centrifuge tests. The specifications of the centrifuge are given in Chandrasekaran (2001).

2.1.3 Model Facing

Facing is one of the most integral components of a reinforced soil wall system and provides protection against backfill sloughing and erosion. Rigid facings are usually preferred over a flexible facing due to their ability to reduce deformations and due to ease in transferring reinforcement loads. In this study, a precast concrete panel was selected as the prototype wall facing. The prerequisites for modelling the facing panel are that it should have low water absorption, light weight and high stiffness. For model facing panels, Eq. (1) gives the thickness as well as the type of the facing material required in centrifuge model tests.

$$(t_f)_m = \frac{(t_f)_p}{N} \left[\frac{(E_f)_p}{(E_f)_m} \right]^{\frac{1}{3}} \quad (1)$$

where, t_f is the thickness of the wall facing, E_f is the elastic modulus of the facing material, N is the gravity level and m , p represents model and prototype dimensions respectively.

Facing element is made from a marine plywood sheet. Three layers of 3 mm thick marine plywood sheets are joined together using a special wood glue to get 10 mm (model dimension) thick facing panel. Facing element consists of six panels, connecting six layers of reinforcements adopted in centrifuge model with a vertical spacing of 40 mm (model dimensions). The facing panels are aligned to provide a batter of 6° with vertical and the bottom most panel will be connected to an acrylic block to simulate a strip foundation levelling pad block in the field. Foundation block will be placed 25 mm below the base layer to attain a rigid toe condition and to create an embedment of 1 m in prototype dimensions. The geogrid-facing connection should be a hinged type connection and for this purpose, a stainless steel rod of 2.2 mm diameter and 198 mm length was used to attach to the panel with the help of two screws at both side of the panel.

2.2. Model Test Package

Figure 1 shows the view of model test package mounted on the swing basket of centrifuge. The internal dimensions of model container used are 760 mm in length, 200 mm in width and 410 mm in height. The front wall of this container was made of 100 mm thick transparent Perspex sheet for viewing front elevation of the model during the flight. The other three rigid walls are of mild steel plates. Four

permanent markers with horizontal and vertical distances of 350 mm and 200 mm respectively between them were used to trace the movement of discrete markers glued to geogrid layers and facing panels during the test. To achieve plane strain condition, the inner side of Perspex glass of the front and the rear wall was lubricated and then covered with flexible polyethylene sheet strips of 100 mm width which reduces friction.

The geogrid reinforced soil wall models were instrumented with three miniature Pore water Pressure Transducers (PPTs) placed along the base layer at a distance of 25 mm (PPT3), 125 mm (PPT2) and 225 mm (PPT1) from the seepage tank. Seepage tank was placed towards left hand side of model container to commence flow of water into the base layer to simulate an initial ground water table up to the base of model reinforced soil walls. The seepage tank wall in contact with the soil was provided with perforated holes having a non-woven geotextile covering in order to prevent migration of soil particles into the tank.

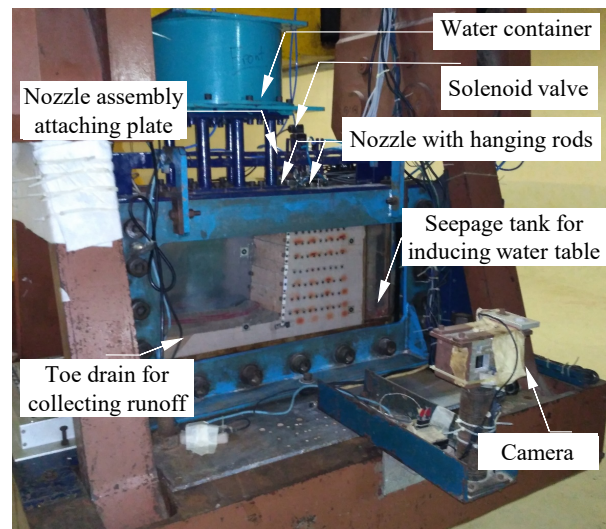


Figure 1. View of model test package mounted on the swing basket of centrifuge

The same model soil was utilized for base layer as well as for the reinforced wall portion. First of all, the base was placed up to the level of foundation block. Then an acrylic block of length 200 mm, width 50 mm and height 20 mm was placed at the specified position. After that, a temporary wooden frame was used to achieve facing inclination of 84° with horizontal. The first facing panel was placed in the groove in the foundation block and construction of base layer was proceeded up to 40 mm from container base. Subsequently, the wall was constructed in seven soil layers compacted at OMC and γ_{dmax} , with vertical spacing of 40 mm except at bottom and top layers (thickness of 30 mm each).

Plastic markers were used to obtain displacement field and strain along geogrid layers by tracing their coordinates in images taken during various stages of the test. Red food dye was placed on top of each layer to trace water flow within the wall. The temporary support was removed and a soil layer of 25 mm thickness was placed in front of the wall to complete the base layer and to reach an embedment depth of 25 mm (i.e. 1 m in prototype dimensions) for the wall toe. PPT readings were regularly recorded using data acquisition system to the right of the basket.

2.3. Test Programme

The wall height, H , was equal to 250 mm, simulating a wall with 10 m height in prototype dimensions. Wall face inclination, (β) , was equal to 84° with horizontal. Six layers of geosynthetic reinforcements of length of 200 mm ($0.8H$) were provided in the model walls with a vertical spacing of 40 mm ($S_v/H = 0.160$). The present study includes centrifuge tests on two models namely RSW1 and RSW2. Model RSW1 was reinforced with six layers of model geogrid G1. Model RSW2 was reinforced with six layers of hybrid geosynthetic layers derived from non-woven geotextile N1 and woven geogrid G1. The initial ground water level was maintained to coincide with the base layer. The centrifuge was rotated at constant angular velocity of 92 rpm (revolutions per minute) to attain 40g, after which the water pressure (regulated by valve P1) and air pressure (regulated by valve P2) were set at desired values as per calibration to simulate rainfall intensity of 15 mm/h. As pressure values became constant, the solenoid valve installed in the path of pressurized water flow from the overhead water tank was activated remotely to start the rainfall onto the soil wall and was continued until wall failure occurred or equilibrium conditions were achieved in terms of pore water pressure development and wall deformations. The rainfall was stopped by switching off the solenoid valve.

3 RESULTS AND DISCUSSION

The surface settlements measured along the wall crest, lateral displacements along the soil wall face and strains in geosynthetic reinforcement layers with progress of rainfall were determined by performing image analysis on photographs captured in-flight during centrifuge testing using an on-board digital camera, while the positive pore water pressures generated during rainfall were measured using pore pressure transducers (PPTs) placed within the wall model.

The deformation stages of the two centrifuge models RSW1 and RSW2 are given in Figure 2 and Figure 3 respectively, thus indicating excessive deformation in wall reinforced with geogrid layers (G1) alone.

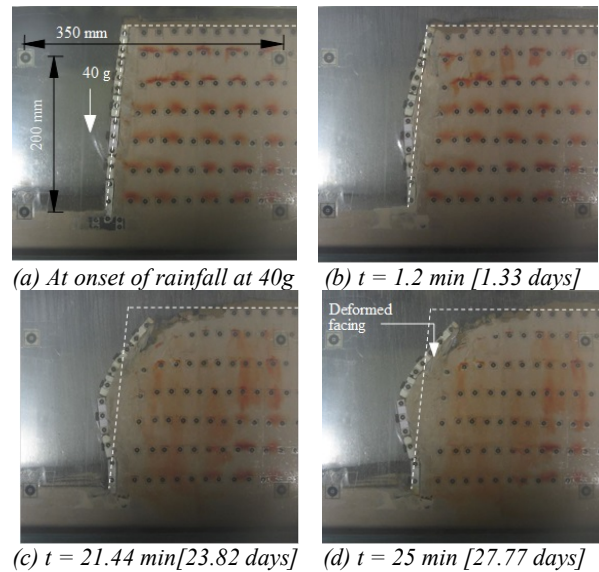


Figure 2. Deformation stages of Model RSW1 [G1, $n_g = 6$; $S_v = 1.6$ m; $I = 15$ mm/h] at various stages during rainfall

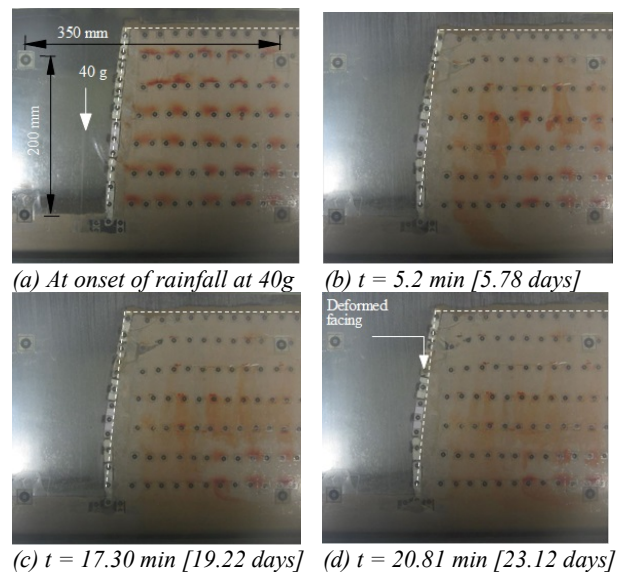
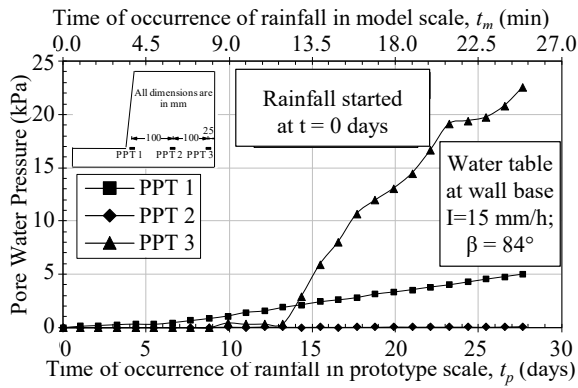


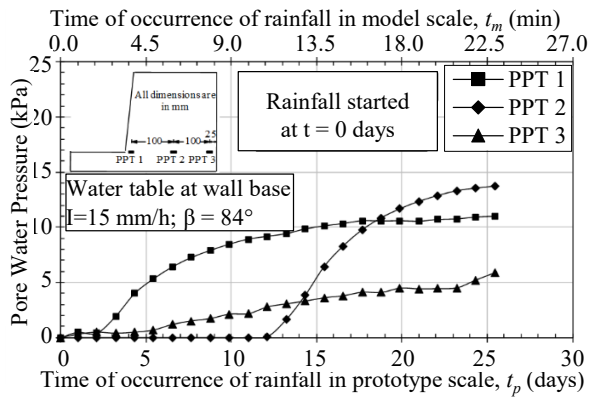
Figure 3. Deformation stages of Model RSW2 [G1N1, $n_{hg} = 6$; $S_v = 1.6$ m; $I = 15$ mm/h] at various stages during rainfall

3.1. Pore water pressure development during rainfall

Figures 4(a) and 4(b) depict the pore water pressure variations with time for the three PPTs measured within the geosynthetic reinforced soil wall models RSW1, and RSW2 respectively under a moderate prototype rainfall intensity of 15 mm/h.

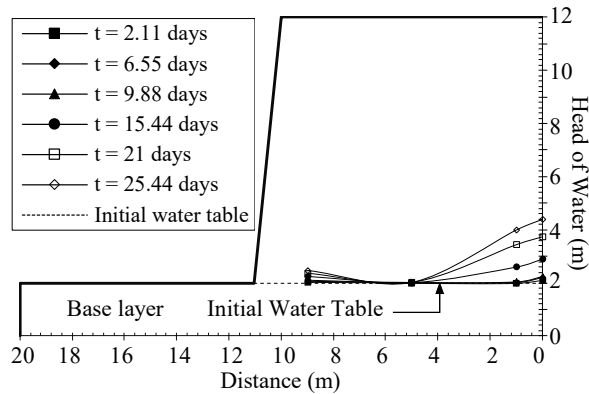


(a) Model RSW1 [G1, ng = 6; Sv = 1.6 m; I = 15 mm/h]

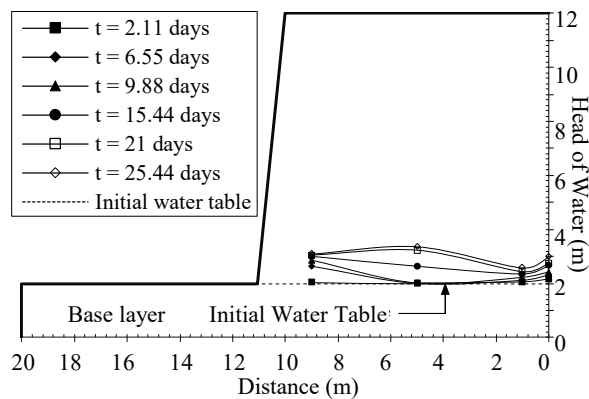


(b) Model RSW2 [G1N1, nhg = 6; Sv = 1.6 m; I = 15 mm/h]

Figure 4. Variation of positive pore water pressure with progress of rainfall



(a) Model RSW1



(b) Model RSW2

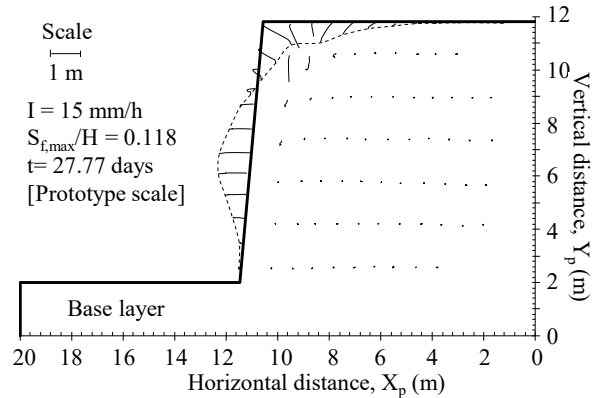
Figure 5. Development of phreatic surfaces with rainfall within reinforced soil walls

The pore pressure readings thus obtained were used to determine the development of phreatic surfaces within the soil wall models with the progress of rainfall. Figure 5(a) and Figure 5(b) present the phreatic surfaces developed for different time intervals during rainfall for the soil wall models RSW1 and RSW2 respectively. The phreatic surfaces of hybrid geosynthetic reinforced wall Model RSW2 indicate lower phreatic level with rainfall as compared to Model RSW1, thereby highlighting the necessity of inclusion of suitable drainage layers within the reinforced wall. Also, it can be observed that irrespective of rainfall intensity and wall inclination, the water head recorded by the PPTs increased rapidly with time away from the toe.

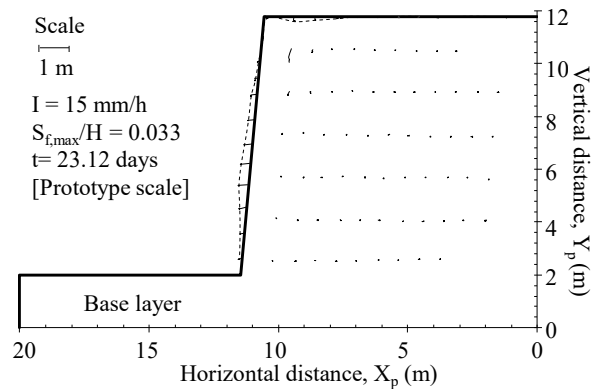
In general, it can be observed that irrespective of rainfall intensity and wall inclination, the water head recorded by the PPTs increased rapidly with time away from the toe, towards the wall face for the entire duration of rainfall.

3.2. Displacement vectors obtained in model soil walls

The face movements and surface settlements experienced by the model soil walls during rainfall were analyzed in terms of displacement vectors plotted on the original wall profile, obtained by tracking the L-shaped plastic markers in horizontal and vertical direction for each selected image.



(a) Model RSW1



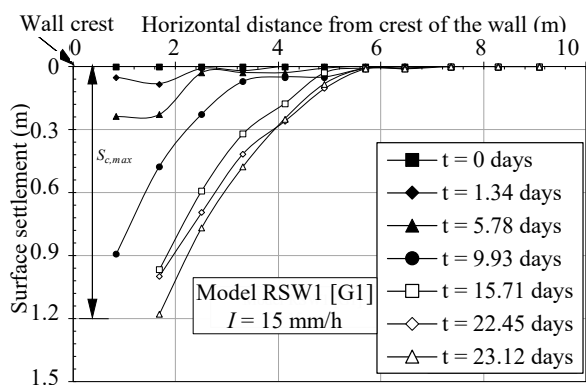
(b) Model RSW2

Figure 6. Displacement vectors of reinforced soil walls subjected to rainfall

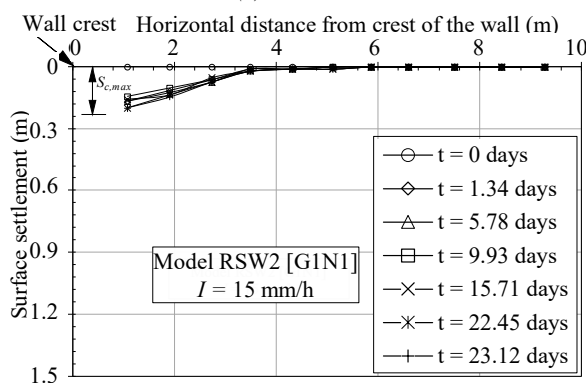
Figures 6(a) and 6(b) show the normalized maximum face movement ($S_{f,max}/H$) and corresponding penultimate stage of each centrifuge test in addition to the displacement vectors obtained for models RSW1 and RSW2 respectively. Model RSW2 experienced lesser distress as compared to Model RSW1. The displacement vectors for Model RSW1 clearly depict formation of a global failure surface with the weakest zone clearly being the wall facing and crest region of the soil wall, due to drop in soil matric suction as the wetting front descends gradually.

3.3. Surface settlements induced during rainfall

The settlement values obtained from image analysis are plotted against horizontal distance measured from the crest of the wall in prototype dimensions, corresponding to various intervals of time with the progress of rainfall. The variation of surface settlement with horizontal distance from the crest of the soil wall for the geogrid (G1) reinforced Model RSW1 subjected to 15 mm/h rainfall depicts a steadily increasing trend with rainfall duration (Figure 7a). The final crest settlement at the onset of failure at the end of 25 min (27.8 days) was about 1.2 m.



(a) Model RSW1



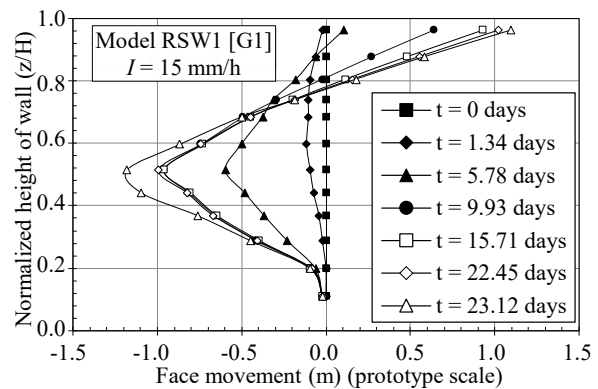
(b) Model RSW2

Figure 7. Surface settlements at various stages of rainfall for reinforced soil walls

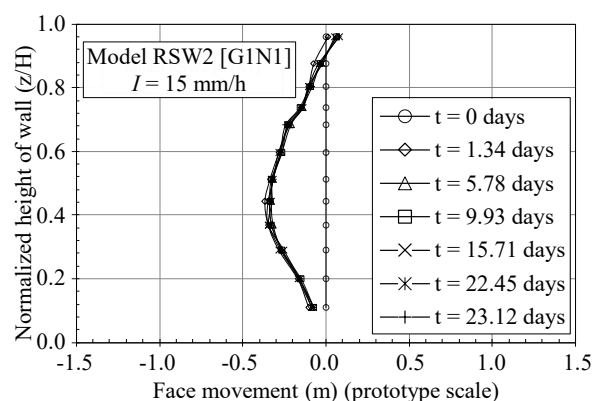
As observed from Figure 7(b), the maximum surface settlement at the penultimate stage of test corresponding to 20.81 min (23.12 days) of rainfall in Model RSW2 was 0.197 m, which is still substantial in magnitude, which is about 0.019 times wall height

3.4. Displacements along the wall face during rainfall

Figures 8(a) and 8(b) present the displacements observed along the model wall facing at various time intervals, until failure occurred, or equilibrium conditions were achieved. The face movements were plotted in prototype scale against normalized height of the wall (z/H), based on co-ordinates of L-shaped inclined plastic markers stuck at the wall facing. The maximum face movement in Model RSW1 was about 1.2 m in prototype scale at the end of 25 min (27.8 days) as against a maximum of 0.34 m only in Model RSW2 at the end of 20.81 min (23.1 days) of rainfall.



(a) Model RSW1



(b) Model RSW2

Figure 8. Face movements observed during rainfall in reinforced soil walls

4 CONCLUSIONS

In the present study, the potential of hybrid geosynthetic layers was assessed for improving the performance of soil walls with marginal backfill

subjected to rainfall. A total of two centrifuge model tests were conducted and based on analysis and interpretation of the test results, the following inferences can be drawn:

- i. The pore water pressure values recorded indicated that the geogrid (G1) reinforced soil wall registered increasing phreatic levels during rainfall with a maximum normalized value of 0.105 near the backfill side, thus indicating build-up of positive pore water pressures within the soil wall constructed with low permeable backfill soil owing to absence of drainage elements. In comparison, lower values of pore water pressures were observed in the hybrid geosynthetic (G1N1) reinforced soil wall model, with a maximum normalized value of about 0.033, potentially attributed to the freely draining conditions provided by geotextiles.
- ii. The geogrid (G1) reinforced wall showed a gradual increase in surface settlements with rainfall of 15 mm/h, resulting in wall instability and face deformations with maximum settlement value as high as 1.18 m in prototype dimensions. In comparison, the model reinforced with hybrid geosynthetic layers (G1N1) was stable throughout the rainfall event and recorded reduced crest settlements of 0.197 m in prototype dimensions, demonstrating benefits of coupling drainage and reinforcement functions offered by geogrid and non-woven geotextile respectively for improving the performance of soil walls with marginal backfill when subjected to rainfall.
- iii. The deformations observed at the wall facing reduced by ~72% within the hybrid geosynthetic reinforced wall (G1N1) compared to the geogrid (G1) reinforced soil wall, which indicates the effectiveness of hybrid geosynthetic layers as possible inclusions in improving performance of soil walls with marginal backfill under rainwater infiltration.

Further studies are warranted by investigating the effect of rainfall intensity, rainfall duration, wall inclination, location of initial water table and vertical spacing of hybrid geosynthetic layers placed within the wall cross-section.

5 ACKNOWLEDGEMENTS

The authors would like to acknowledge the staff and team members of the National Geotechnical Centrifuge Facility (NGCF) in IIT Bombay for their active cooperation and for extending all support throughout the present study.

6 REFERENCES

- AASHTO 2009. Standard specifications for highway bridges. American Association of State Highway and Transportation Officials. Washington D.C. USA.
- ASTM-D4595, 2011. Standard Test Method for Tensile Properties of Geotextiles by the Wide-width Strip Method. ASTM International, West Conshohocken, PA, USA.
- Balakrishnan, S, Viswanadham, B. V. S. 2019. Centrifuge model studies on the performance of soil walls reinforced with sand-cushioned geogrid layers. *Geotextiles and Geomembranes*. **47**(6):803-814.
- Berg, R. R., Christopher, B. R. and Samtani, N. C. 2009. Design and Construction of Mechanically Stabilized Earth Walls and Reinforced Soil Slopes. FHWA/NHI-10-024 Report. National Highway Institute, Washington, DC, 1:306.
- Bhattacharjee, D. and Viswanadham, B.V.S. 2017, Design and Performance of an Inflight Rainfall Simulator in a Geotechnical Centrifuge, (ISSN: 0149-6115, 5-year Impact Factor: 1.318), American Society for Testing and Materials (ASTM), United States, **41**(1): 72-91.
- Bhattacharjee, D. and Viswanadham, B.V.S. 2018. Effect of Geocomposite Layers on Slope Stability Under Rainfall Condition. *Indian Geotech J.*, **48**(2):316-326.
- Bhattacharjee, D., and Viswanadham, B. V. S. 2019. Centrifuge Model Studies on Performance of Hybrid Geosynthetic--Reinforced Slopes with Poorly Draining Soil Subjected to Rainfall. *Journal of Geotechnical and Geoenvironmental Engineering*, ASCE.**45**(12).
- Bui Van, D., Chinkulkijniwat, A., Horpibulsuk, S., Yubonchit, S., Limrat, I., Arulrajah, A., Jothityangkoon, C. 2017. Steady flow in mechanically stabilised earth walls using marginal soils with geocomposites. *Geosynth. Intl.* **24** (6): 590-606.
- Christopher, B. R., Zornberg, J. G and Mitchell, J. K. 1998. Design guidance for reinforced soil structures with marginal soil backfills. In: Proceedings of the Sixth International Conference on Geosynthetics, Atlanta, Georgia **2**(6): 797-804.
- Christopher, B. R. and Stuglis, R. S. 2005. Low permeable backfill soils in geosynthetic reinforced soil wall: State of the Practice in North America, In: Proceedings of North American Geosynthetics Conference (NAGS), GRI-19, Cooperative Conference Proceedings, Las Vegas, Nevada, USA, 16.
- Chandrasekaran, V. 2001. Numerical and centrifuge modelling in soil structure interaction. *Indian Geotechnical J.*, **31**(1):30-59.

- Craig, W. H., Bujang, B. K. H., and Merrifield, C. M. 1991. Simulation of Climatic Conditions in Centrifuge Model Tests, *Geotechnical Testing Journal*, ASTM, **14**(4), 406-412.
- Garcia, E. F., Gallage, C. P., K., and Uchimura, T., 2007, Function of permeable geosynthetics in unsaturated embankments subjected to rainfall infiltration, *Geosynthetics International*, **14**(2): 89-99
- Holtz, R. D. and Kovacs, W. D. 1981. *An Introduction to Geotechnical Engineering*, Prentice-Hall, Englewood Cliffs, N.J, ISBN- 0-13- 484394-0.
- Izawa, J., Kuwano, J. 2010. Centrifuge modeling of geogrid reinforced soil walls subjected to pseudo-static loading. *Int. J. Phys. Model. Geotech*, **10**(6): 1-18.
- Koerner, R. M. and Koerner, G. R. 2011. The importance of drainage control for geosynthetic reinforced mechanically stabilized earth wall. *Journal of GeoEngineering*, **6**(1): 3-13.
- Koerner, R. M., Koerner, G. R. 2018. An extended data base and recommendations regarding 320 failed geosynthetic reinforced mechanically stabilized earth (MSE) walls. *Geotextiles and Geomembranes* **46** (10): 904-912.
- Lee, L. M., Kassim, A., and Gofar, N., 2011. Performances of Two Instrumented Laboratory Models for the Study of Rainfall Infiltration into Unsaturated Soils” *Eng. Geol.*, Vol. **117**(1-2):78-89.
- Ling, H. I., Wu, M. H., Leshchinsky, D and Leshchinsky, B. 2009. Centrifuge Modeling of Slope Instability, *J. Geotech. Geoenviron. Eng.*, ASCE, **135**(6): 758-767.
- Ling, H and Ling, H. I., 2012. Centrifuge Model Simulations of Rainfall-Induced Slope Instability, *J. Geotech. Geoenviron. Eng.*, ASCE, **138**(9): 1151-1157.
- Mamaghanian, J., Razeghi, H. R., Viswanadham, B. V. S, Manikumar, C. H. S. G. 2018. Behaviour of geogrid reinforced soil walls with marginal backfills with and without chimney drain in a geotechnical centrifuge. *Proceedings of the 9th International Conference on Physical Modelling in Geotechnics*. 17-20 July 2018, University of London, In: McNamara, A, Divall, S, Goodey R, Taylor N, Stallebrass S, Panchal, J (Eds). Taylor & Francis Group (Pubs.), London, ISBN 978-1-138-34422-8. **1**. pp.1211-1216.
- Mamaghanian, J., Viswanadham, B. V. S., Razeghi, H. R. 2019. Centrifuge model studies on geocomposite reinforced soil walls subjected to seepage. *Geosynthetics International*. **26**(4). 371-387.
- National Concrete Masonry Association. 1997. *Design Manual for Segmental Retaining Walls*, Second edition, Second printing, J. Collin (Editor), Herndon, Virginia.
- Olivares, L., Damiano, E., Greco, R., Zeni, L., Picarelli, L., Minardo, A., Guida, A., and Bernini, R., 2009. An Instrumented Flume to Investigate the Mechanics of Rainfall-Induced Landslides in Unsaturated Granular Soil. *Geotech. Test. J.* **32**(2): 108-118.
- Porbaha, A., Goodings, D.J., 1996. Centrifuge modeling of geotextile-reinforced cohesive soil retaining walls. *J. Geotech. Eng, ASCE*, **122**(10): 840-848.
- Portelinha, F, H, M., Bueno, B, S., Zornberg, J. G., 2012. Performance of geotextile reinforced soil wall in unsaturated poorly draining backfill soil conditions, In: *Proceedings of 5th European Geosynthetics Congress, Soil Improvement and Reinforcement*, **5**: 455- 465.
- Portelinha, F.H.M., Bueno, B.S., Zornberg, J.G. 2013. Performance of nonwoven geotextile-reinforced walls under wetting conditions: laboratory and field investigations, *Geosynth. Int*, **20**(2): 90-104.
- Raisinghani, D. V., Viswanadham, B. V. S. 2011. Centrifuge model study on low permeable slope reinforced by hybrid geosynthetics. *Geotextiles and Geomembranes*, **29**(6): 567-580.
- Razeghi, H. R., Viswanadham, B. V. S, Mamaghanian, J. 2019. Centrifuge and numerical model studies on the behavior of geogrid reinforced soil walls with marginal backfills with and without geocomposite layers. *Geotextiles and Geomembranes*. **47**(5):671-684
- Stuglis, R.P. 2010. Fullscale MSE test walls. In: *Proc., GRI-19 Conference, Las Vegas*. GII Publication, Folsom, PA, USA.
- Tamate, S., Suemasa, N., and Katada, T. 2010. Simulating Shallow Failure in Slopes Due to Heavy Precipitation. presented at the 7th International Conference in Physical Modelling in Geotechnics, Zurich, Switzerland, CRC Press, Boca Raton, FL.
- Tristancho, J., Caicedo, B., Thorel, L., and Obregon, N. 2012. Climatic Chamber with Centrifuge to Simulate Different Weather Conditions, *Geotech. Test. J.* **35**(1): 159-171.
- Viswanadham, B, V, S and König, D. 2004. Studies on scaling and instrumentation of a Geogrid. *Geotext. Geomembr.* **22**(5): 307-328.
- Viswanadham, B. V. S., Razeghi, H. R., Mamaghanian, J., Manikumar, C. H. S. G. 2017. Centrifuge model study on geogrid reinforced soil walls with marginal backfills with and without chimney sand drain. *Geotextiles and Geomembranes*. **45**(5): 430-446.
- Yoo, C., Jang, D, W. 2013, Geosynthetic reinforced soil wall performance under heavy rainfall. In: *Delage, P., Desrues, J., Frank, R., Puech, A., Schlosser, F. (Eds.), Proceedings of the 18th International Conference on Soil Mechanics and Geotechnical Engineering, Paris*, pp. 2131-2134.

Centrifuge model studies on geogrid and hybrid geosynthetic reinforced slopes subjected to rainfall

Dipankana Bhattacharjee¹, B.V.S Viswanadham²

¹*Department of Civil Engineering, Indian Institute of Engineering Science and Technology, Shibpur, Howrah - 711103, Assistant Professor, India*

²*Department of Civil Engineering, Indian Institute of Technology, Bombay, Powai, Mumbai - 400076, Professor, India*

Corresponding author: B.V.S Viswanadham (viswam@civil.iitb.ac.in)

ABSTRACT: The objective of the study is to investigate the effect of inclusion of two varieties of geosynthetic material, referred to as geogrids and hybrid geosynthetics on the seepage, deformation and stability aspects of slopes subjected to rainfall. Geogrids function as reinforcing elements within slopes, whereas hybrid geosynthetics integrate the drainage potential of non-woven geotextile with the reinforcing property of woven geogrid. Centrifuge-based physical modelling was adopted in this study at 30 gravities using the 4.5 m radius beam centrifuge facility available at IIT Bombay, India. The model slope corresponded to a prototype height of 7.2 m and a crest width of 7.5 m, and was constructed with silty sand having 20% fines content and a saturated permeability of 1.54×10^{-6} m/s. Rainfall was simulated using a custom-designed rainfall simulating assembly, capable of replicating fine mist at high gravities with intensities varying from 2 mm/h – 80 mm/h. The response of slope models reinforced with geogrid and hybrid geosynthetic inclusions was monitored for a prototype rainfall intensity of 20 mm/h. It was observed that the geogrid reinforced slope experienced considerable deformations and increasing phreatic levels with rainfall due to insufficient drainage, accompanied with geogrid straining in the range of 48%. The inclusion of hybrid geosynthetics resulted in reduction of pore water pressures by almost 40%, and the crest settlements and slope face movements were reduced by 86% and 82% respectively. Further, negligible straining in the order of 8% was observed in the hybrid geosynthetic layers at the end of rainfall event. The above study thus highlights the importance of coupling reinforcement and drainage functions in the form of hybrid geosynthetics within slopes subjected to rainfall.

Keywords: Slope Stability; Rainfall; Centrifuge Modelling; Geogrid; Hybrid Geosynthetic.

1 INTRODUCTION

Instability of soil slopes and retaining walls followed by catastrophic landslides is a common problem in many parts of the world, and cause thousands of deaths and severe infrastructural damage each year. Although some failures may occur due to construction activities, many cases of failure have been reported in natural soil walls, excavated slopes and road subgrades simply due to rainwater infiltrating in an otherwise stable soil structure. As per the International Disaster Database (EM-DAT), incidences of slope failures due to hydro-meteorological disasters depict a rapidly increasing trend over the years, and have increased by almost 70% on an average over the last decade. The mechanism that leads to slope failure is that the negative pore water pressure starts decreasing when water infiltrates the unsaturated soil. This results in build-up of positive seepage forces, leading to excessive deformations, and in some cases, structural collapse. An effective technique of providing stability of earth structures against rainwater infiltration is through the inclusion of stiff and durable geosynthetics [Koerner (2012)].

The present study explores the possibility of mitigating rainfall induced slope instability through provision of two varieties of geosynthetic material, referred to as geogrids and hybrid geosynthetics. Under the impact of load, strains in the soil mass induce strains in the geogrids, which in turn, generate tensile loads within these reinforcements. Geogrids thus function as reinforcing elements within slopes, whereas hybrid geosynthetics function as composite materials by integrating the drainage potential of non-woven geotextile with the reinforcing property of woven geogrid.

Centrifuge-based physical modelling technique has been adopted in this study to replicate identical stress-strain response in model and prototype slopes subjected to rainfall. Rainfall was simulated using a custom-designed actuator, capable of replicating fine mist at high gravities with intensities varying from 2 mm/h – 80 mm/h. The model silty sand slope tested in centrifuge corresponded to a prototype height of 7.2 m and a crest width of 7.5 m. The response of geogrid and hybrid geosynthetic reinforced slopes was monitored in centrifuge for a prototype rainfall intensity of 20 mm/h.

2 MATERIALS AND METHODS

Small-scale physical modelling of engineered earth structures is widely adopted to provide insight into field performance. However, the stress levels of models scaled down under normal gravity condition are much smaller than that of prototype structures existent in the field. Although full-scale physical modelling can account for these complexities, it is expensive and time-consuming, and difficult to replicate with natural hazards like flooding and rainfall. In such situations, geotechnical centrifuge modelling can be used as an effective tool [Schofield (1980), Taylor (1995)] to investigate the behaviour of earth structures as scaled-down models at high-gravity environment. Accordingly, a robust rainfall simulator was developed for studying the response of geosynthetic reinforced slopes based on the principle of centrifuge modelling. Details of rainfall simulator, scale factors, model materials and test procedure are discussed in subsequent sections.

2.1. Scale factors

Rainfall is characterized primarily by its intensity, duration, and frequency, and can be scaled at high gravities based on scaling factors derived for time and water flow under transient unsaturated conditions. The scaling laws briefly discussed below are derived based on Dell'Avanzi et al. (2004) and Bhattacharjee and Viswanadham (2018a). Let the notations p and m denote respectively the prototype and centrifuge model at $1/N$ scale, where N corresponds to the geometric scale factor or gravity level. The intensity (r) and duration (t) of rainfall are scaled in centrifuge as per Eq. (1) and Eq. (2) respectively. Additionally, the droplet size should be reduced at high gravities to ensure formation of mist, and occurrence of equivalent impact pressure on model ground surface as that experienced by prototype.

$$r_m = N r_p \quad (1)$$

$$t_p = N^2 t_m \quad (2)$$

Further, standard scaling relationships have been employed in this study to link the behaviour of model geosynthetics with commercially available prototypes. The parent geotextile component of hybrid geosynthetic was scaled based on identical transmissivity requirements outlined in Raisinghani and Viswanadham (2011), whereas the parent geogrid was modelled based on scaling considerations proposed by Viswanadham and König (2004). Table 1 summarizes the relevant scaling laws adopted during centrifuge modelling.

2.2. Model soil and geosynthetic materials

The problem of rainfall induced slope instability aggravates if the fill material has low permeability. Design issues include drainage, deformations and reinforcement pull-out. Hence, there arise the necessity to investigate the behaviour of slopes constructed with low-permeable fill material under rainwater infiltration. Accordingly, the model soil used in slope preparation was formulated in the laboratory by blending sand and kaolin the ratio of 4:1 by dry weight. The model silty sand has percentage of fines equal to 20% and a saturated permeability (k_{sat}) of 1.54×10^{-6} m/s, thereby representing the properties of locally available marginal soils. The ultimate tensile capacity (T_{gu}) and ultimate tensile strain (ε_{gu}) of model geogrid (G1) and hybrid geosynthetic (G1N1) were evaluated as per the wide-width tensile test procedure outlined in ASTM D 4595 (2005). Further, the drainage potential of hybrid geosynthetic was ascertained based on radial flow principle outlined in ASTM D 6574 (2006). The properties of model geosynthetics as determined in the laboratory are presented in Table 2.

Table 1. Scale factors adopted in present study

Parameter	Unit	Scale factor
^a Unit weight of soil (γ)	kN/m ³	N
Pore water pressure (u)	kPa	1
Suction (ψ)	kPa	1
Tensile load (T_g)	kN/m	1/N
Transmissivity of geotextile (θ)	m ² /s	1
Percentage open area (f)	%	1
Strain (ε)	%	1
Duration of rainfall (t)	h	1/N ²
Rainfall intensity (r)	mm/h	N

N: Gravity level; ^a $\gamma_m/\gamma_p = N$; m = model; p = prototype

Table 2. Properties of model geosynthetic materials

Property	Geogrid	Geocomposite
Peak tensile load, T_{gu} (kN/m)		
Wide-width	0.93	1.01
Zero-span	1.05	1.09
Peak tensile strain, ε_{gu} (%)		
Wide-width	18.9	18.3
Zero-span	52.5	52.7
Secant modulus at 5% strain, J_g (kN/m)		
Wide-width	7.76	8.24
Zero-span	6.01	7.60
Transmissivity ($\times 10^{-6}$), θ_g (m ² /s)	0.07	1.35

2.3. Rainfall Simulator

Reproducing rainfall in a geotechnical centrifuge is possible using a set of nozzles [Kimura et al. (1991)]. The nozzles used in the present study (Figure 1) are specialized full cone air-atomizing brass nozzles, capable of producing rainfall in the form of fine mist at high gravities by internal collision of pressurized air and pressurized water. The nozzles are capable of producing fine mist at a uniform rate in-flight condition for intensities ranging from 2 mm/h to as high as 80 mm/h.

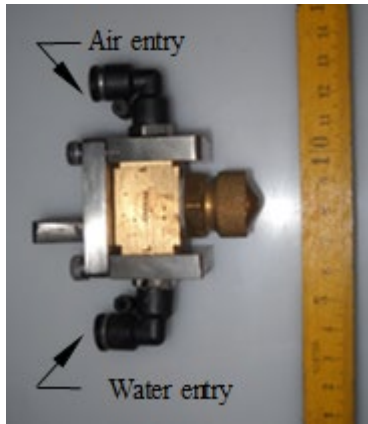


Figure 1. Air-atomizing nozzle used in the study.

Apart from spray nozzles, the rainfall simulating assembly consist of nozzle hanging rods, nozzle assembly attaching plate, a water container assembly with support system and additional components involving a solenoid valve, a seepage tank and run-off collector. The water container used for supplying pressurized water to nozzles is designed to act like a Modified Mariotte's tube, capable of maintaining a constant head of water with progress of rainfall at high gravities. Further, while designing the simulator, side slots were provided at regular intervals along the entire length of nozzle assembly attaching plate. This enabled horizontal shift in position of the nozzles, depending upon direction of centrifugal rotation to nullify effects arising due to Coriolis force at high gravity.

2.4. Model preparation and Test procedure

From here onwards, the values are mentioned in model dimensions, with corresponding prototypes within parenthesis. Centrifuge modelling was performed at 30 gravities on a representative silty sand slope of 240 mm (7.2 m) height, 60 mm (1.8 m) base layer and 2V:1H inclination, having a crest width of 250 mm (7.5 m). Tests were conducted using the 4.5 m radius beam centrifuge facility available at IIT Bombay, INDIA. A set of four nozzles were placed at the slope crest, while another four were placed at the inclined face. The response of geosynthetic reinforced slope models was

monitored for a prototype rainfall intensity of 20 mm/h, which corresponds to a heavy rainfall event as per standard global thresholds of Llasat (2001). An initial water table was simulated in model slopes up to the base before the onset of rainfall using the perforated seepage tank mentioned previously. The slopes were instrumented with four pore pressure transducers (PPTs) placed above the base layer at distances of 20 mm (PPT4), 125 mm (PPT3), 250 mm (PPT2) and 350 mm (PPT1) from the perforated face of seepage tank in model dimensions. Further, L-shaped plastic markers made from thin transparency sheets of 20 mm x 10 mm dimensions were embedded within the slope front elevation to track slope displacements with progress of rainfall. Additional L-shaped plastic markers were glued on to the slope face to facilitate computation of slope face movements with rainfall. The model geogrid and hybrid geosynthetic (G1N1) were cut to a total length of $(L_A + L_F + L_R)$ and to a width of 200 mm. The anchorage length (L_A) was equivalent to 0.25 times the model slope height H , L_F represented the length along the slope face and the reinforcement length (L_R) was $0.85H$. The various stages involved in model preparation are discussed elaborately in Bhattacharjee and Viswanadham (2018b).

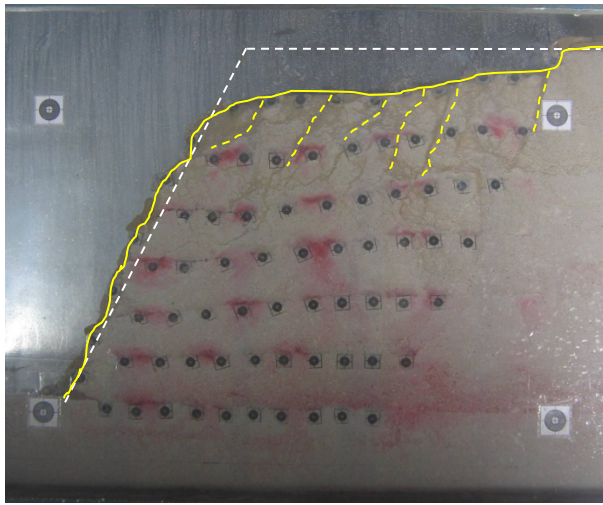
3 RESULTS AND DISCUSSION

The surface settlements, slope face movements, reinforcement strains and pore water pressures developed during rainfall were investigated in the study based on data recorded by pore water pressure transducers and through image analysis of selected images captured during centrifuge tests. The results of two centrifuge model tests (T1 and T2) are discussed, wherein Model T1 and Model T2 correspond to slopes reinforced with six layers of geogrid (G1) hybrid geosynthetic (G1N1) respectively. The results are presented in this study up to a point of time beyond which the observed slope deformations and recorded pore water pressure values depicted negligible variations with progress of rainfall. The above duration has been referred to as the ultimate stage of centrifuge test (Table 3) during rainfall simulation in centrifuge.

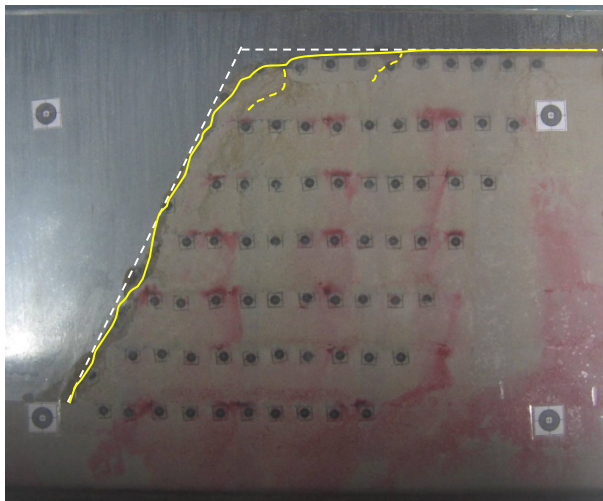
3.1. Deformed slope profile

The geogrid (G1) reinforced slope (Model T1) was observed to experience excessive deformations until a time period of 35 min (22 days) from the onset of rainfall, which has been referred to as the ultimate stage of test. Model T2 reinforced with hybrid geosynthetic layers (G1N1) was found to be stable under 20 mm/h rainfall, and experienced minor slope movements close to the slope face up to 38 min (23.5 days) of rainfall [ultimate stage].The

deformed profiles of Model T1 and Model T2 captured at respective ultimate stages of 35 min (22 days) and 38 min (23.5 days) are presented in Figure 2(a)-2(b) respectively.



(a) Front-elevation of geogrid reinforced slope [Model T1; $t = 22$ days]



(b) Front-elevation of geocomposite reinforced slope [Model T2; $t = 23.5$ days]

Figure 2. Front-elevation of reinforced slope models

3.2. Crest settlements and face movements

The crest settlements and face movements within slopes reinforced with geogrid (G1) and hybrid geosynthetic inclusions (G1N1) were obtained by image analysis. The resultant plots shown in Figure 3 and Figure 4 respectively indicate that the peak vertical and horizontal displacements are substantial in the geogrid reinforced slope (Model T1). The magnitudes are found to be in the order of about 33.3 mm (1.0 m) and 43.7 mm (1.31 m) respectively for Model T1. In comparison, the peak vertical and

horizontal displacements registered in the geocomposite reinforced slope (Model T2) are found to be in the range of 7 mm (0.210 m) and 13.33 mm (0.40 m) respectively.

3.3. Reinforcement strains

The corresponding strains generated in geogrid (G1) and geocomposite (G1N1) reinforcement layers under 20 mm/h rainfall are presented in Figure 5 at respective ultimate stage of tests. Figure 5 indicates considerable straining of geogrids throughout the reinforced zone. The maximum value of strain among the peak strains mobilized in individual reinforcement layers was identified as the maximum peak strain value ($\epsilon_{p,max}$), which was evaluated as 48% for Model T1 (G1). However, negligible straining in the order of 8% was observed in hybrid geosynthetic layers (G1N1) in case of Model T2 at the end of rainfall event.

3.4. Pore water pressure profile

The pore water pressure profiles of geogrid (G1) reinforced slope (Model T1) and geocomposite (G1N1) reinforced slope (Model T2) captured through pore pressure transducers are shown in Figure 6. The pore water pressure values measured by PPT3 ($u_{PPT3}/\gamma H$) have been normalized with respect to the unit weight of model soil (γ) multiplied by the slope height (H), and are expressed in prototype dimensions, starting from the time of occurrence of rainfall. As evident from the development of pore pressure values with rainfall shown in Figure 6, the pore water pressures in hybrid geosynthetic reinforced slope (Model T2) got reduced by almost 40% as compared to the geogrid reinforced slope (Model T1). The above is attributed to the permeable geotextile component of hybrid geosynthetic, which provided alternate drainage paths for the infiltrating rainwater. The primary findings derived from the study, as discussed above, are summarized in Table 3.

Table 3. Summary of centrifuge test results

Parameter investigated	Test T1	Test T2
	[G1]	[G1N1]
^a Time, t (days)	22.0	23.5
^b Crest settlement, $S_{c,max}/H$	0.14	0.03
^b Slope face movement, $S_{f,max}/H$	0.18	0.06
^b Pore water pressure, $u_{max}/\gamma H$	0.51	0.21
Peak reinforcement strain, $\epsilon_{p,max}$ (%)	48	8

^aTime in prototype scale (ultimate stage of centrifuge test); ^bNormalized maximum values.

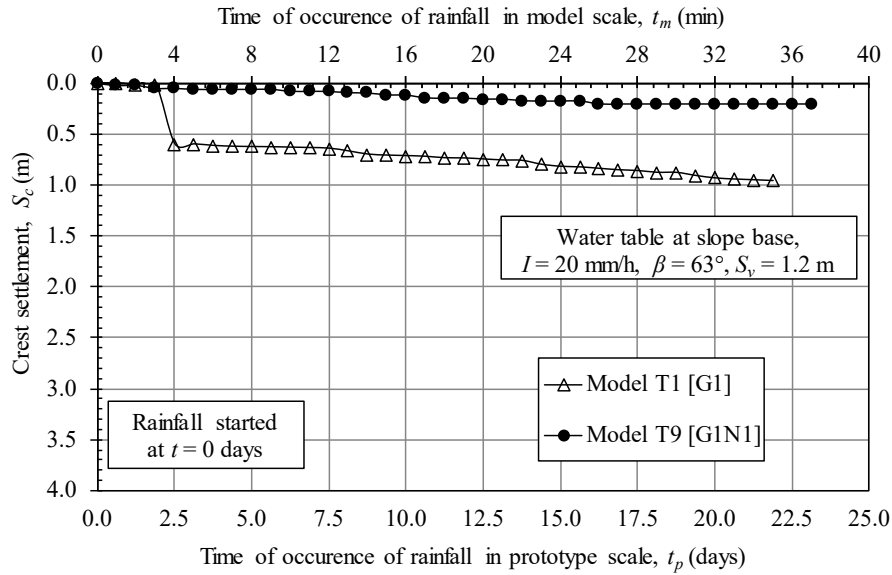


Figure 3. Crest settlement of reinforced slopes with progress of rainfall

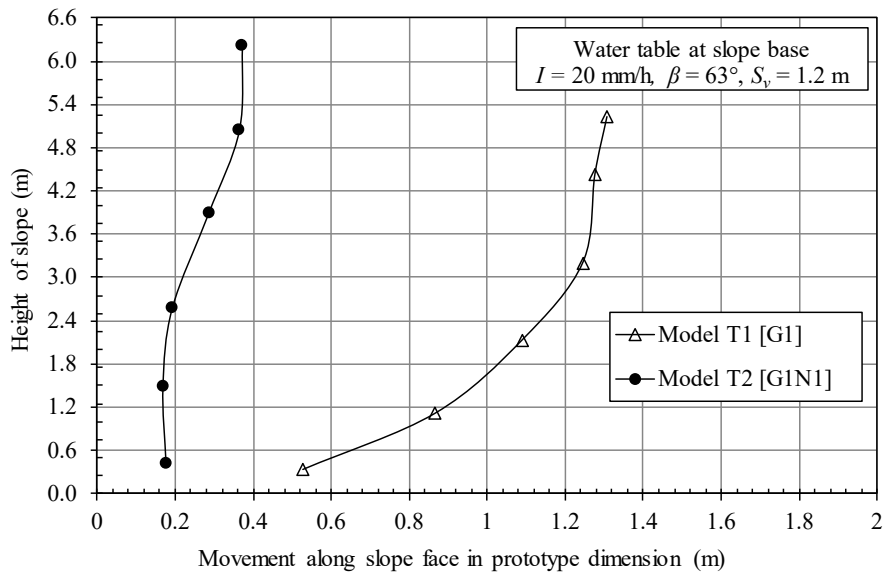


Figure 4. Face movements of reinforced slopes with progress of rainfall

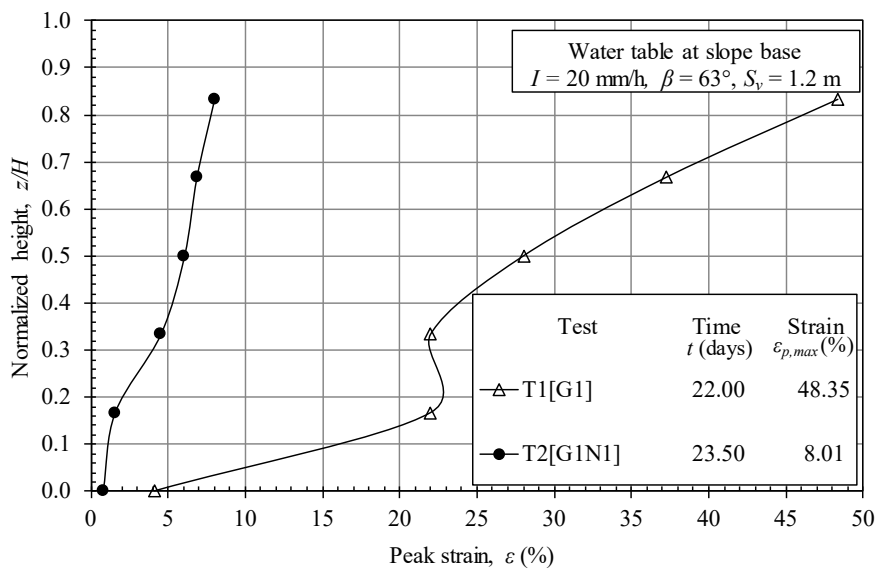


Figure 5. Reinforcement strains at ultimate stage of test

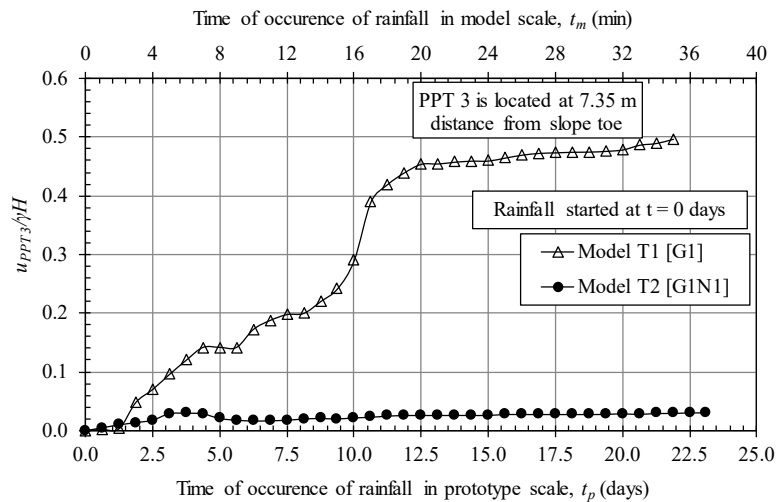


Figure 6. Pore water pressure development in reinforced slopes with progress of rainfall

4 CONCLUSIONS

In the present study, the effect of inclusion of two varieties of geosynthetic material, referred to as geogrids and hybrid geosynthetics on the seepage, deformation and stability aspects of slopes subjected to rainfall are investigated through centrifuge-based physical modelling technique. Rainfall was simulated using a custom-designed rainfall simulating assembly, and the response of slope models was monitored for a prototype rainfall intensity of 20 mm/h. The geogrid reinforced slope was observed to experience considerable deformations and increasing phreatic levels with rainfall due to insufficient drainage, accompanied with geogrid straining in the range of 48%. In comparison, the crest settlements and slope face movements were less by 86% and 82% respectively in the hybrid geosynthetic reinforced slopes, along with 40% reduction in phreatic levels at the slope base. Moreover, negligible peak strains of the order of 8% were registered along hybrid geosynthetics throughout the rainfall event. The above observations highlight the importance of coupling reinforcement and drainage functions within low-permeability soil slopes subjected to rainfall.

5 ACKNOWLEDGEMENTS

The authors thank the staff at National Geotechnical Centrifuge Facility, IIT Bombay, India, for their support throughout the present study.

6 REFERENCES

ASTM D 4595 2005. Standard test method for tensile properties of geotextile by wide-width strip method, American Society for Testing and Materials, U.S.A.

ASTM D 6574 2006. Standard test method for determining the (in-plane) hydraulic transmissivity of

a geosynthetic by radial flow, American Society for Testing and Materials, Pennsylvania, U.S.A.

- Bhattacharjee, D., Viswanadham, B.V.S. 2018a. Design and Performance of an In-flight Rainfall Simulator in a Geotechnical Centrifuge. *Geotechnical Testing Journal*, ASTM, **41**(1): 72-91.
- Bhattacharjee D., Viswanadham B.V.S. 2018b. Effect of geocomposite layers on slope stability under rainfall condition. *Indian Geotechnical Jr.*, **48**(2): 316-326.
- Dell'Avanzi, E., Zornberg, J. G., Cabral, A. R. 2004. Suction Profiles and Scale Factors for Unsaturated Flow Under Increased Gravitational Field. *Soils and Foundations*, **44**(3): 79-89.
- Kimura, T., Takemura, J., Suemasa, N., Hirooka, A. 1991. Failure of fills due to rain fall. *In Proceedings of Centrifuge 91*, H. Y. Ko and F. G. McLean (Eds.), A.A. Balkema (Pub.), pp. 509-516.
- Koerner, R. M. 2012. *Designing with Geosynthetics*, 6th edition, Xlibris Publishing.
- Llasat, M. C. 2001. An objective classification of rainfall events on the basis of their convective features. *International Jr. of Climatology*, **21**(1): 1385-1400.
- Raisinghani, D.V., Viswanadham, B.V.S. 2011. Centrifuge model study on low permeable slope reinforced by hybrid geosynthetics. *Geotextiles and Geomembranes*, **29**(6): 567-580.
- Schofield, A. N. 1980. Cambridge geotechnical operations. *Geotechnique*, **30**(3): 227- 268.
- Taylor, R. N. 1995. *Centrifuges in modelling: principles and scale effects*, Geotechnical Centrifuge Technology, Blackie Academic and Professional, U.K.
- Viswanadham, B. V. S., König, D. 2004. Studies on scaling and instrumentation of a geogrid. *Geotextiles and Geomembranes*, **22**(5): 307-328.

Effect of fiber soil reinforcement on the bearing capacity of a surface strip foundation

Maria Diakoumi¹, Kevin Stone¹, David Roddy²

¹ Civil Engineering, University of Brighton, Brighton, U.K.

² Amey, Kettering, U.K.

Corresponding author: Maria Diakoumi (m.diakoumi@brighton.ac.uk)

ABSTRACT: The use of randomly distributed fibers as a means of reinforcing the soil matrix has attracted increasing attention in geotechnical engineering in recent years. Fiber soil reinforcement can be employed in current practice to strengthen poor quality soil around foundations and/or limit excessive settlements. This study presents an experimental investigation of the effect of discrete and randomly distributed fiber reinforcement on the bearing capacity of a shallow foundation. To this aim, a series of centrifuge tests were undertaken on a surface strip footing assuming plane strain conditions. The results are presented through plots of bearing pressure versus settlement ratio. The inclusion of fiber reinforcement was found to improve the foundation's bearing capacity, reduce settlements significantly and increase the stiffness of the reinforced soil-foundation system.

Keywords: Fiber Reinforcement; Reinforced Soil; Bearing Capacity; Footings/Foundations; Settlement.

1 INTRODUCTION

Several methods and techniques have been explored with the aim to improve the bearing capacity and limit the settlements of a shallow foundation resting on poor quality soil. The use of randomly distributed synthetic or natural fibers as a means of reinforcing the soil matrix is a relatively new soil improvement technique that has attracted increasing attention in geotechnical engineering in recent years; this is due to its cost effectiveness, reliability and bulk availability of fibers.

Numerous published experimental studies (Gray and Ohashi, 1983; Freitag, 1986, Gray and Al-Refeai, 1986; Maher and Gray 1990, Al-Refeai, 1991; Fatani et al 1991; Maher and Ho, 1994; Ranjan et al., 1994; Michalowski and Zhao, 1996; Michalowski and J. Čermák, 2002; Yetimoglu and Salbas, 2003) that involved the conduction of direct shear, triaxial or unconfined compression tests have shown that the inclusion of randomly distributed discrete fibers can increase the soil's peak strength and stiffness and reduce the post peak shear strength loss. The beneficial effect of the fiber reinforcement on the soil has been shown to depend on the type, length, aspect ratio (length to diameter), modulus of elasticity, concentration and orientation of the fibers in the soil matrix as well as the soil's grain size and shape, density and confining stresses. The fiber orientation is considered an important parameter (Jewell and Wroth, 1987; Palmeira and Milligan, 1989). Random distribution of fibers within the soil matrix is usually preferred since it presents the advantage of strength isotropy and avoidance of the development of a potential weak plane parallel to

the reinforcement orientation (Maher and Gray 1990).

A number of studies have focused on the effect of fiber soil reinforcement on the soil's loading capacity and settlement characteristics. Consoli et al. (2003) conducted a series of plate load tests on silty sand reinforced with fibers at high bearing pressures and found that the fiber reinforced soil exhibited a significantly stiffer response compared to unreinforced soil. Consoli (2009) conducted further plate load tests on sand reinforced with 0.5% by weight long polypropylene fibers at different relative densities. The results showed higher bearing capacity and overall stiffness for all tests with these effects being more pronounced at higher values of relative density. This beneficial effect was attributed to a reduction in dilation due to the inclusion of fibers in the soil matrix. Kumar and Kaur (2012) presented results of plate load tests on poorly graded sand reinforced with different concentrations of randomly distributed fibers and different depths overlying an unreinforced soil layer. A substantial increase in the ultimate bearing capacity was found; the beneficial effect of the fiber reinforcement was more pronounced at a relative density of 55% compared to a respective value of 25%. Kumar et al (2011) presented results of small scale 1g tests and numerical modelling on the bearing capacity of a strip footing founded on a layer of sand reinforced with 1% randomly distributed synthetic fibers for different depths of the reinforced layer. The results showed a significant increase in the ultimate bearing capacity for depths of the reinforced layer equal to two times the footing's width, (B).

The published studies presented above have investigated the effect of reinforcing the soil with randomly distributed discrete fibers on its load bearing capacity for a specific concentration and length of fiber reinforcement. Therefore, the effect of varying the fiber concentration or length on the load bearing capacity in the case of a strip footing has not been explored widely. Clearly, the improvement in the bearing capacity can be more realistically assessed under higher values of stresses that correspond to field conditions. To achieve a realistic simulation of soil stresses, small scale physical modelling facilitated by a geotechnical centrifuge is ideally suited. This study presents a series of centrifuge tests on a surface strip footing founded on a two layer-soil; the top layer is reinforced with randomly distributed fibers extending to a depth equal to 3B, where B is the footing's width, and the bottom layer is kept unreinforced for all tests. The effect of two different fiber lengths and three different fiber percentage concentrations on the response of the footing under applied load is explored.

2 MATERIALS AND METHODS

2.1. Experimental programme

The tests undertaken in this study and presented herein are summarised in Table 1 below. Table 1 lists five tests which were conducted in a geotechnical balanced beam centrifuge at an enhanced acceleration level of 20 gravities (20g) to investigate the influence of the length and concentration of fiber reinforcement on the bearing capacity of a surface strip footing assuming plane strain conditions. The first test investigated the behaviour of a strip footing founded on unreinforced dry sand and the results were used for comparison with subsequent tests (numbered 2 to 5 in Table 1) in which two soil layers were introduced below the footing: i) a layer of fiber reinforced sand below the footing and ii) a layer of unreinforced sand directly below the reinforced soil layer. The depth of the fiber reinforced soil layer was selected equal to three times the footing's width, B, to ensure that the failure plane is well within the reinforced soil zone. The second layer of unreinforced dry sand had a depth of 6.3B. Two fiber cut lengths of 6mm and 19mm were tested. The fibers were mixed randomly with the soil at different percentage concentrations as listed in Table 1.

Table 1. Summary of centrifuge tests at 20g

Test No	Depth of fiber reinforced layer	Fiber length (mm)	Fiber concentration (%)
1	0	-	0
2	3B	6	0.2
3	3B	6	0.45
4	3B	6	0.85
5	3B	19	0.2

2.2. Material and equipment

The sand used for the tests is dry, poorly graded, Fraction C (300-600 microns) silica sand of rounded and sub-rounded particle shape with 98% silica content supplied by David Ball Limited. The sand has a specific gravity of 2.67, maximum and minimum void ratios of 1.06 and 0.61 respectively and a critical state angle of friction ϕ_{crit} of 31° . The fibers used as reinforcement are synthetic polyolefin fibers with a ridged, rough surface and two different cut lengths of 6mm and 19mm respectively; the fibers' physical and engineering properties are given in Table 2. The model strip footing was manufactured from aluminium with dimensions 90mm (length) x 15mm (width) x 9mm (depth) and can be seen in Figure 1. A recess was drilled on the top surface of the footing to ensure that the vertical load is applied at its centre. A layer of sandpaper was attached to the bottom surface of the footing to increase the friction in the interface between the soil and the foundation.

All the tests were carried out in the balanced beam geotechnical centrifuge at the University of Brighton. This machine is manufactured by Thomas Broadbent & Sons Ltd. and is a 6 g-tonne machine (20kg payload to 300g) with a radius of 760mm. The tests were conducted in a rectangular steel strongbox of internal dimensions 300mm (length), 100mm (width) and 180mm (depth). The strongbox was equipped with clear, acrylic panels placed on the long sides of the box that allowed the sample to be observed during testing. The strongbox was placed in a cradle which was then mounted on the centrifuge arm. A two degree of freedom actuator was then mounted on the cradle; the actuator in the vertical direction has a capacity of 2 kN and was used in the tests presented herein.

Table 2. Physical and engineering properties of the synthetic fibers used in the tests

Property	Fiber
Type	Synthetic polyolefin
Fiber length 1	6mm
Fiber length 2	19mm
Diameter	0.5mm
Specific gravity	0.91
Tensile strength	590 N/mm ²
Modulus of elasticity	>11 GPa

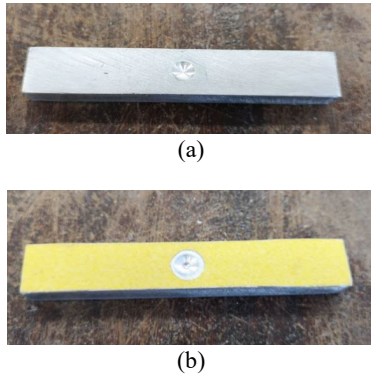


Figure 1. Aluminium model footing tested in the centrifuge: a) top surface b) bottom surface

2.3. Model preparation and test procedures

The unreinforced soil sample used in test 1 (see Table 1) was placed in the rectangular steel strongbox and was vibrated to the target density via means of a vibrating table. The unreinforced soil specimen had a bulk density of 1575 kg/m³ and a sample height of 140mm. The soil sample in tests 2 to 5 consisted of two soil layers; the bottom soil layer was unreinforced, had a depth of 6.3B (95mm), and its target bulk density was achieved via vibration. The second soil layer was placed directly on top of the unreinforced soil layer and beneath the model footing; this layer had a depth of 3B (45mm) and was reinforced with randomly distributed fibers with the lengths and percentage concentrations listed in Table 1. The fibers were mixed with the soil manually to ensure random distribution and orientation and they were placed in the strongbox in three layers using dry tamping to achieve the required density. The average concentration of fibers, f_c , in the reinforced soil specimen was calculated as a percentage of the dry weight of the sand:

$$f_c = W_f / W_s \times 100\% \quad (1)$$

where W_f is the weight of fibers and W_s is the weight of dry sand. The weight concentration was used as a useful guide for the mixing stage, but actually the fiber concentration was calculated by setting the void ratio of the reinforced soil specimen equal to the respective value of the unreinforced specimen. To achieve the target void ratio, it was assumed that the fibers' volume, V_f , is part of the solid particles' volume V_s ; this is expressed with Equation 2:

$$e = \frac{V_v}{V_s} = \frac{V_v}{V_s + V_f} \quad (2)$$

where V_v is the volume of the voids. This method of determining the mixing quantities of fiber reinforcement is commonly used in previous studies (e.g. Michalowski and Zhao, 1996).

The friction between the soil and the acrylic panels of the strongbox was considered negligible since the panels appeared in good condition with no obvious signs of abrasion. The model footing was placed on the soil surface and then a two degree of freedom actuator was mounted on the strongbox. Loads were applied via the vertical actuator so its piston rod was lowered to the top of the centre (see recess in Fig. 1) of the footing; a miniature load cell was attached to the actuator to measure the applied load and the footing's settlement was determined from the vertical displacement of the actuator. Two Linear Variable Differential Transformers (LVDT) were positioned on the footing at a distance of 15mm from each edge to measure any potential rotation. The model and actuator were set-up on the laboratory bench and then loaded onto the centrifuge. The actuator was connected to the power and control system; the actuator and measuring gauges were controlled by the in-flight computer which was remotely connected to a desktop computer.

All tests were conducted at an acceleration level of 20g. Once the model had achieved the target test acceleration the actuator was run at a velocity of 3 mm/minute for all tests and data from the load cell and actuator encoders were recorded continuously until the end of each test. Figure 2 shows a view of the assembled model package post testing. At the end of each test, the fibers were removed from the soil matrix and were inspected.

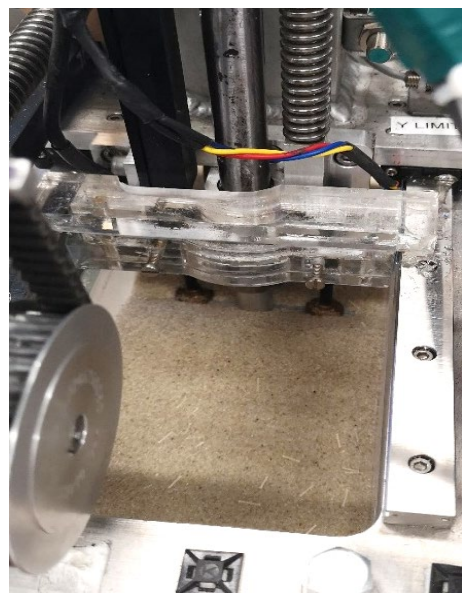


Figure 2. Centrifuge model package assembled (photo taken post-testing)

3 RESULTS AND DISCUSSION

The experimental results are presented through plots of applied bearing pressure versus percentage values of settlement ratio, s/B , where s is the measured settlement and B is the footing's width, in order to investigate the behaviour of a strip footing resting on soil reinforced with different fiber concentrations and lengths. Figure 3 presents the results for fiber lengths of 6mm for different fiber percentage concentrations, namely 0%, 0.20%, 0.45% and 0.85%. Figure 4 shows the results for 19mm long fibers at 0% and 0.2% fiber concentrations. The results derived for the case of unreinforced sand consisting of one uniform soil layer are included in Figures 3 and 4 for comparison.

All the plots presented in Figures 3 and 4 demonstrate a distinct peak value of applied bearing pressure which is assumed to correspond to the ultimate bearing capacity. For values beyond the peak, the bearing pressure appears to gradually reduce but it is still considerably higher than that for unreinforced sand (fiber concentration equal to 0%).

It is apparent from Figures 3 and 4 that the inclusion of a fiber reinforced soil layer directly below the footing increases the bearing pressure at any settlement level and reduces the settlement at any of the values of pressure applied in the experiments presented herein. It can also be observed that increasing the fiber percentage concentration will result in an increase in the capacity of the soil to carry the applied pressure at the same level of settlement and a reduction in the settlement compared to the case of unreinforced soil. The increase in the bearing capacity can be attributed to the mobilisation of additional frictional resistance between the sand grains and fibers. It should be noted that for pre-peak values of bearing pressure, the stiffness of the soil-footing when a reinforced soil layer is included directly beneath the footing is greater than that of the unreinforced soil.

Figure 5 shows the results for unreinforced and reinforced soil with 0.2% fiber concentration for two fiber lengths, 6mm and 19mm for comparison. From Figure 5, it is obvious that the increase in fiber length from 6mm to 19mm results in an increase in the ultimate bearing capacity of the foundation. Specifically, the ultimate bearing capacity in the case of 19mm fiber length at 0.2% concentration is 1.3 times the respective value in the case of 6mm fiber length.

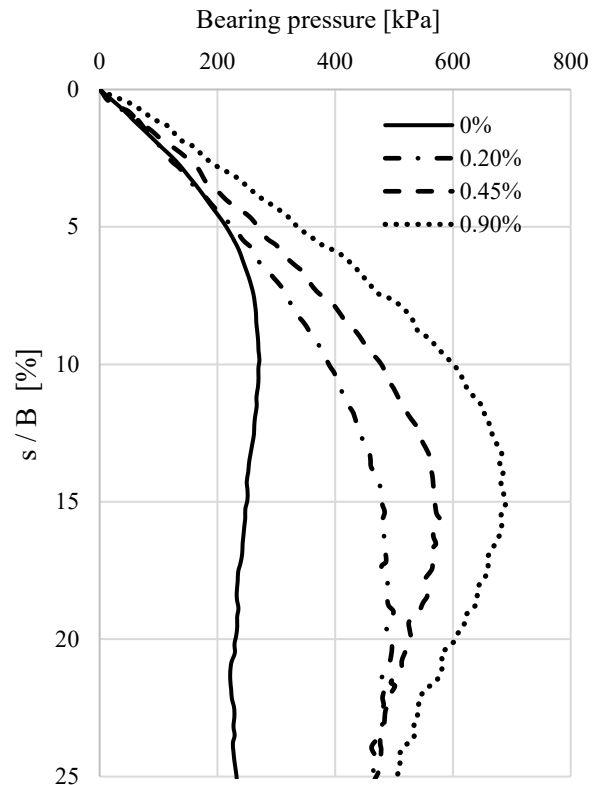


Figure 3. Results for 6mm fiber length

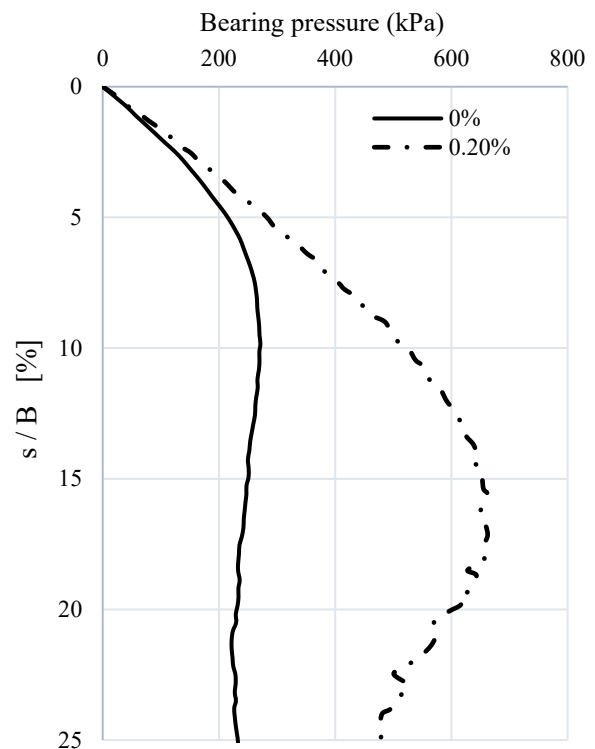


Figure 4. Results for 19mm fiber length

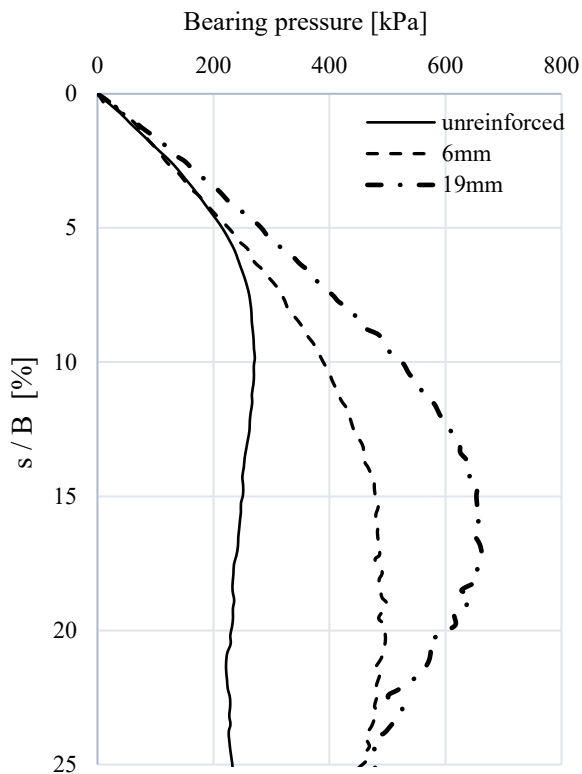


Figure 5. Results for unreinforced and reinforced soil with 0.2% fiber concentration for two fiber lengths, 6mm and 19mm.

Table 3 lists the ultimate (peak) bearing capacity for each fiber percentage concentration and length and the percentage values of the settlement ratio (s/B) that correspond to the peak values recorded. It is common in the available literature on reinforced soil to use the bearing capacity ratio to quantify the beneficial effect of the inclusion of reinforcement in the soil matrix and it is thus useful to adopt it for the results presented herein. The bearing capacity ratio (BCR) is defined in this study as the ultimate (peak) bearing capacity of the fiber reinforced soil to the ultimate bearing capacity (peak) of unreinforced soil; the values of BCR for the fiber lengths and percentage concentrations tested are listed in Table 3.

From Table 3, the increase in the ultimate bearing capacity of the soil which has been reinforced with 6mm long fibers is between 1.8 to 2.5 times the respective value of the unreinforced soil layer. For the 6mm fiber lengths, the relationship between fiber concentration and BCR appears to be non-linear since an increase in fiber concentration from 0% to 0.2% results in a greater increase in BCR compared to an increase in fiber concentration from 0.2% to 0.45% or 0.85%. From Figures 3 and 4 and Table 3, it is apparent that for both fiber lengths, the ultimate bearing capacity is reached at greater settlement ratios in the case of fiber reinforced soil

compared to the case of unreinforced soil. As the fiber concentration increases, the values of settlement required to reach the ultimate bearing capacity reduce. It is also noticed that the reinforced soil samples can sustain greater values of bearing pressure at large post-peak displacements. At the end of each test the fibers were removed from the soil matrix and were checked; this inspection did not reveal fiber elongation but a small amount of the 19mm long fibers appeared to be slightly bent.

Table 3. Summary of results from all tests

Fiber length (mm)	Fiber concentration (%)	Ultimate bearing capacity (kPa)	Settlement ratio (s/B) at max pressure (%)	BCR
-	0	271.4	9.83	1
6	0.20	498.9	19.03	1.8
6	0.45	578.8	15.72	2.1
6	0.85	686.2	13.86	2.5
19	0.20	662.4	15.6	2.4

4 CONCLUSIONS

This paper has presented a set of experimental results derived from centrifuge tests to investigate the bearing capacity of a strip foundation resting on soil reinforced with synthetic rigid fibers of two different lengths and three different percentage concentrations. The results were compared with those derived for a case of unreinforced soil. The inclusion of fiber reinforcement improved the foundation's bearing capacity and reduced the settlement significantly. The improvement in the ultimate bearing capacity of the reinforced soil compared to the respective value of the unreinforced soil was expressed by the bearing capacity ratio (BCR). For the fiber length and concentrations tested in this study the bearing capacity ratio (BCR) varied from 1.8 to 2.4 times. For pre-peak values of bearing pressure, the stiffness of the soil-foundation is greater in the case of fiber reinforced soil compared to unreinforced soil. As the fiber concentration increases, the values of settlement required to reach the ultimate bearing capacity reduce. The reinforced soil samples were found to sustain greater values of bearing pressure at large post-peak displacements compared to unreinforced soil.

5 ACKNOWLEDGEMENTS

The authors would like to express their gratitude to Mr David Harker for his assistance in conduction of the centrifuge tests and fabrication of equipment.

6 REFERENCES

- Al-Refeai, T.O. 1991. Behaviour of granular soils reinforced with discrete randomly oriented inclusions. *Geotextiles and Geomembranes*, **10** (4): 319-333.
- Consoli, N. C., Casagrande, M. D. T., Prietto, P. D. M. & Thome, A. 2003a. Plate load test on fibre-reinforced soil. *Journal of Geotechnical and Geoenvironmental Engineering*, ASCE **129** (10): 951–955.
- Consoli, N. C., Casagrande, M. D. T., Thome, A. Rosa, F.D. and Fahey, M. 2009. Effect of Relative Density On Plate Loading Tests on Fibre Reinforced Sand. *Geotechnique* **59** (5): 471–476.
- Fatani, M.N., Bauer, G.E. and Al-Joulani N. 1991. Reinforcing soil with aligned and randomly oriented metallic fibers. *Geotechnical Testing Journal*, **14** (1): 78-87.
- Freitag, D.R. 1986. Soil randomly reinforced with fibers. *Journal of Geotechnical Engineering*, ASCE, **112** (8): 823- 826.
- Gray, D.H. and Al-Refeai, T. 1986. Behavior of fabric-versus fiber-reinforced sand. *Journal of Geotechnical Engineering*, ASCE **112** (8): 804-820.
- Gray, D. H., and Ohashi, H. 1983. Mechanics of Fiber Reinforcement in Sand. *Journal of Geotechnical Engineering* **109** (3): 335–353.
- Jewell, R.A. and Wroth, C.P. 1987. Direct shear tests on reinforced sand. *Geotechnique* **37** (1): 53–68.
- Kumar, A., Bhatia, R., and Walia, B.S. 2011. An experimental study on the load vertical settlement behavior of a fiber-reinforced sand bed. *International Journal of Geotechnical Engineering*, **5** (3): 353- 360.
- Kumar, A. and Kaur, A. 2012. Model tests of square footing resting on fiber reinforced sand bed. *Geosynthetics International*, **19** (5): 385-392.
- Maher, M. H., and Gray, D.H. 1990. Static Response of Sands Reinforced with Randomly Distributed Fibers. *Journal of Geotechnical Engineering* **116** (11): 1661–1677.
- Maher, M. H., and Y. C. Ho. 1993. Behaviour of Fiber Reinforced Cemented Sand under Static and Cyclic Loads. *Geotechnical Testing Journal* **16** (3): 330–338.
- Michalowski, R.L. and Zhao, A. 1996. Failure of fiber-reinforced granular soils. *Journal of Geotechnical Engineering*, ASCE **122** (3): 226–234.
- Michalowski, R.L. and Cermak, J. 2002. Strength anisotropy of fiber-reinforced sand. *Computers and Geotechnics*, **29**: 279–299.
- Palmeira, E.M. and Milligan, G.W.E. 1989. Large scale direct shear tests on reinforced soil. *Soils and foundations*, **29** (1): 18–30.
- Ranjan, G., Vasan, R. M. and Charan, H. D. 1994. Behaviour of Plastic-Fibre-Reinforced Sand. *Geotextiles and Geomembranes*, **13** (8): 555–565.
- Yetimoglu, T. and Salbas, O. 2003. A study on shear strength of sands reinforced with randomly distributed discrete fibers. *Geotextiles and Geomembranes*, **21** (2): 103-110.

5. Offshore geotechnics

Centrifuge tests of monopile foundations under one-way cyclic lateral loading

Kunkun Cheng¹, Charles M. Heron¹, Luke J. Prendergast¹, Alec M. Marshall¹

¹ *Department of Civil Engineering, University of Nottingham, UK*

Corresponding author: Charles M. Heron (charles.heron@nottingham.ac.uk)

ABSTRACT: Monopile foundations are commonly used for offshore wind turbines due to their ease of construction and comparatively low cost. These foundations are subjected to various loads from wind, currents, waves and superstructure self-weight, resulting in a combination of cyclic lateral loads and vertical dead loads. To ensure an offshore wind turbine meets serviceability requirements throughout the entire life cycle, it is important to understand the behaviour of monopile foundations under this cyclic lateral loading. A programme of centrifuge testing is ongoing at the University of Nottingham to investigate the pile-soil interaction of monopiles subjected to large numbers of lateral cyclic loads. A newly developed load control apparatus capable of applying both one-way and two-way cyclic lateral loads to a model pile is employed to investigate foundation response under a large number of load cycles (greater than 50,000) and a sample of the analyses is presented in this paper. The accumulation of lateral displacement and the change in pile-soil interaction secant stiffness is discussed. The results may help enhance the understanding of monopile foundation response to large numbers of cyclic lateral loads.

Keywords: Centrifuge; Monopile Foundations; Cyclic Loading.

1 INTRODUCTION

Wind energy has attracted growing interest due to increasing global energy demands, and the requirement to adopt renewable energy systems, leading to an emphasis on the development of offshore wind turbines (OWTs). Monopile foundations have been widely adopted for supporting OWTs due to their relative ease of construction and installation. OWT foundations are subjected to cyclic loading from a large number of load cycles over their lifetime due to a combination of wind, currents and waves. However, the existing design codes for OWT foundations (API 2007 and DNV 2016) are based on a limited number of load cycles, which results in uncertainty about the safety and projected lifespan of OWTs.

A variety of research has been conducted to investigate the response of monopile foundations under cyclic loading. LeBlanc et al. (2010) performed a series of tests on stiff piles subjected to tens of thousands of lateral load cycles in drained sand at 1-gravity (1-g) and presented a model for predicting the pile rotation and pile stiffness under long-term cyclic loading. The model took into account the number of cycles, characteristics of cyclic loading and sand relative density. Albiker et al. (2017) also carried out 1-g model tests on stiff piles to investigate the soil relative density and characteristics of cyclic loading on the accumulation of pile displacement, with results generally being in agreement with those from LeBlanc et al. (2010). However, it was suggested that the sand relative density has limited influence on the displacement accumulation. Arshad and

O’Kelly (2017) conducted a series of 1-g cyclic loading experiments with 6000 load cycles on a rigid pile instrumented with 8 strain gauges to study the effect of cyclic loading characteristics and the evolution of lateral soil resistance profiles. It was suggested that a logarithmic model between number of cycles and pile rotation yielded the best fit to the experimental data. In terms of lateral soil resistance, the authors suggested bending moment data should be fitted with a fourth order polynomial function and highlighted the sensitivity of results to the adopted polynomial function. The above small-scale 1-g tests commonly employed sands with low values of relative density in an attempt to represent the behavior of full-scale systems with soil of a higher density, however this approach does impose uncertainties caused by the stress dissimilarity between the model and full-scale scenarios.

An alternative to 1-g testing is geotechnical centrifuge modelling, wherein stress similarity between a small-scale model and a full-scale prototype is achieved by increasing gravitational acceleration within the model, thereby achieving a better simulation of the full-scale behavior of soil-pile systems. Klinkvort and Hededal (2012) performed 12 centrifuge tests on monopiles in sand to investigate the effects of cyclic lateral loading characteristics on the change of pile stiffness and accumulation of pile head displacements. Empirical models relating the characteristics of cyclic loading to pile head displacement and cyclic secant stiffness were presented. It was suggested that one-way cyclic loading is more critical than two-way loading, which contradicts LeBlanc et al. (2010).

Bayton et al. (2018) introduced a new method to predict the rotation of a pile under cyclic lateral loading. The method predicts pile rotation diagrammatically using a cyclic accumulation contour diagram established based on experimental centrifuge tests. The diagram is essentially a database of experimental test results, which were based on a specific system (i.e. one type of sand, relative density, pile and load eccentricity).

In terms of loading system, mechanical gear driven devices have been widely adopted to impose cyclic loads on piles in 1-g tests (LeBlanc et al., 2010; Arshad and O’Kelly, 2017; Albiker et al., 2017). These loading systems have the ability to apply large numbers of cyclic loads with varying load magnitude and frequency. Actuator loading systems including servo and pneumatic systems have been deployed in centrifuge tests (Li et al., 2010; Bayton et al., 2018). However, these loading systems cannot achieve high loading frequencies at the load levels needed to replicate full-scale OWT monopiles.

This paper describes the development of a new mechanical system for centrifuge testing that is capable of applying the large number of lateral loading cycles needed to replicate the long term life-cycle response of OWT monopiles. The paper provides a description of the experimental components, including a model monopile instrumented with fibre Bragg grating (FBG) strain sensors, the associated control systems, and results from an experiment to illustrate the tested soil-pile interaction behavior.

2 KIT DEVELOPMENT

2.1. General layout of load-control cyclic loading system

Figure 1 (a) and (b) show the components of the newly developed system at the University of Nottingham Centre for Geomechanics (NCG) used for applying load-control cyclic loads to a model pile. The pile and sand are contained in a steel tank with an inner diameter of 0.49m and overall depth of 0.5m. A cap is rigidly attached to the top of the pile and connected by steel cables and pulleys to a dead weight one side of the pile and the loading system on the other side. The loading system is comprised of a mass block sitting on a pin-supported plate equipped with a carriage system and an AKM 32E motor in conjunction with a 21.5:1 gearbox. The movement of the mass block is controlled by the rotation of the AKM motor through a circular disc and connection rod. The AKM motor and gearbox are secured on a gantry and a conveyance system which is controlled by a

separate stepper motor and gearbox system. In order to apply cyclic loads to the pile, the AKM motor is operated to drive the circular disc in a rotary motion and hence generate a periodic movement of the mass block. This movement of the mass block results in a varying force which is transferred to the pile through the attached cable. The difference between forces in the cables attached to the dead weight and the loading system provides the resultant force applied to the pile. The movement range of the mass block is determined by the diameter of the circular disc. The centre point of movement of the mass block is determined by the location of the AKM motor gantry, which is adjusted by the stepper motor; this location controls the “bias” of the applied pile load (i.e. varying from 1-way to 2-way loading).

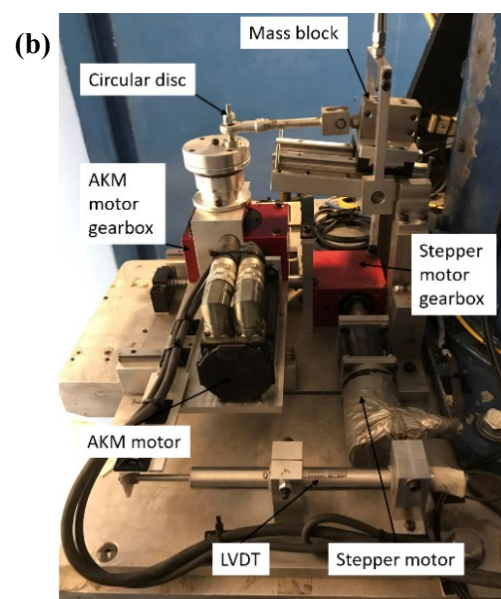
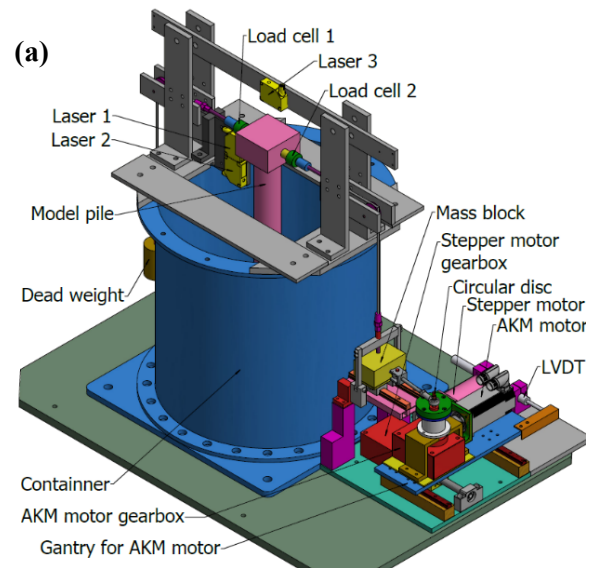


Figure 1. Newly developed load-control cyclic loading system for piles: (a) schematic drawing, and (b) image.

2.2. Loading principle

The motivation of the system development was for an experimental methodology that could generate load-controlled cyclic loads in the centrifuge in a way that would allow relatively high loading frequencies to be achieved alongside load magnitudes that are representative of OWT monopile foundations. The developed system is capable of (i) applying relatively large loads by changing the weights of the mass block and dead weight, and (ii) varying the loading frequency by increasing the AKM motor speed (current motor/gearbox system can reach 4Hz pile loading; higher frequencies can be achieved by altering the motor/gearbox). Figure 2 shows a schematic of the loading system. Since pile head displacement during tests are small, the plate containing mass M_2 can be considered horizontal, and it is assumed that the mass block is at a constant g-level (which varies with distance from the central axis of the centrifuge). Force F_2 resulting from the mass block and force F_1 from the dead weight are calculated by Eq. 1-3; the resultant force on the pile ΔF is given by Eq. 4.

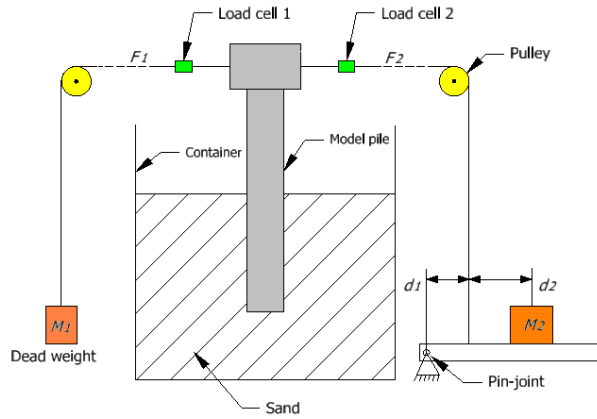


Figure 2. Schematic of pile loading system.

$$F_1 = NM_1 g \quad (1)$$

$$F_2 d_1 = NM_2 g(d_1 + d_2) + NM_{plate} g d_1 \quad (2)$$

$$F_2 = NM_2 g \left(1 + \frac{d_2}{d_1}\right) + NM_{plate} g \quad (3)$$

$$\Delta F = F_2 - F_1 \quad (4)$$

where N is the centrifuge scaling factor (i.e. N times gravity g), M_{plate} is the mass of the plate supporting mass M_2 , d_1 is the distance from the pin support to the cable attaching the plate to the pile (constant), d_2 is the horizontal distance from the centre of mass M_2 to the plate-cable attachment position (varies), and mass M_1 is the dead weight. The balance position (i.e. $\Delta F = 0$) of the mass block is calculated by Eq. 5:

$$d_{2,balance} = \left(\frac{M_1 - M_{plate}}{M_2} - 1\right) d_1 \quad (5)$$

For specific values of M_1 and M_2 , $d_{2,balance}$ is fixed. Through the movement of the mass block M_2 relative to this position, the kit can apply both one-way and two-way cyclic loading. The amplitude of ΔF can be controlled by changing the weight of the mass block. Hence, the kit is capable of producing cyclic loads with different characteristics.

2.3. Control program

The control program, written in LabVIEW, regulates the position of the AKM motor gantry. This control program operates in two different stages. The first stage ensures that forces F_1 and F_2 on each side of the pile remain balanced during changes in gravity level (g-level) as the centrifuge is spun up (any imbalance of these forces could cause movement of the pile during spin-up, disturbing the soil sample and adversely influencing test results). The stepper motor control system reads in values of F_1 and F_2 and automatically adjusts the position of the gantry to achieve a balance in the forces (within a tolerance of 30N). The second stage occurs when the target g-level is reached and the system is ready for cyclic loading of the pile under a prescribed loading condition (e.g. one-way or two-way loading). In this stage, the stepper motor is temporarily stopped and the AKM motor is set to spin at a given speed. The stepper motor control is then enabled to adjust the position of the AKM motor gantry to achieve the desired cyclic loading characteristic. To apply cyclic loading, the mass block is always first positioned to the balance point determined by M_1 and M_2 . All the instruments were logged at 250Hz in the test.

3 CASE STUDY: ONE-WAY CYCLIC LOADING TEST

A one-way cyclic loading test was conducted to evaluate the performance of the new system. The loading frequency was specified to be 3Hz with a load amplitude of 500N (2MN at prototype scale given the applied scaling factor of $N=63$). A total of 70,000 load cycles were applied to the pile.

3.1. Model pile

The model pile was made of aluminium with properties shown in Table 1. The bottom of the pile was sealed with a cap, making it a closed-ended hollow pile. A mass of 2kg was mounted on the top of the pile to simulate the dead-weight of a superstructure. The pile was instrumented with 7 evenly distributed FBG strain sensors from 20mm

to 320mm at 50mm intervals relative to the pile bottom.

Table 1. Properties of model pile.

Parameter	Unit	Pile
Pile length, L	mm	500
Wall thickness, t	mm	3
Outer diameter, d	mm	60
Young's modulus, E ,	GPa	69
Moment of inertia, I ,	m^4	$2.2E-7$
Flexural stiffness, EI	MNm^2	0.015
Cross section area, A	m^2	$0.5E-3$

3.2. Soil preparation

The sand used for this test was Congleton silica sand (HST95) from Bent Farm in Congleton, Cheshire (UK). The properties of the sand were evaluated by the Norwegian Geotechnical Institute (NGI) and are presented in Table 2. In this study, the ratio between the pile diameter and the average grain size is 333, which avoids scaling issues according to Garnier et al. (2007). The air pluviation method was utilized to prepare the sand sample. Sand was first air-pluviated into the centrifuge container to form a 150mm thick layer. The model pile was then placed on the sand and secured by a temporary frame. After the placement of the pile, the sand was poured into the container to achieve a 300mm embedded depth. This process represents a 'wished-in-place' closed-ended pile and avoids the disturbance caused by installation effects. All tests were performed in dry dense sand with a relative density of 90%.

Table 2. Properties of HST95 Congleton sand.

Parameter	Unit	Sand
Specific gravity of particles, G_s	-	2.63
Minimum void ratio, e_{min}	-	0.494
Maximum void ratio, e_{max}	-	0.765
Average grain size, d_{50}	mm	0.17
Coefficient of uniformity	mm	1.9

3.3 Experimental setup

Figure 3 shows a sketch of the test setup. The load eccentricity and embedment depth for the test were 200mm and 300mm, respectively. Laser sensors (Baumer OADM 20I6460/S14F) were utilised to measure pile displacements. The sensing range of the lasers can be adjusted to a narrower range to improve accuracy. As shown in Figure 6, laser 1 and laser 2 were located on the side of the pile at

different heights in order to evaluate pile rotation. Laser 3 was mounted above the pile to monitor the vertical displacement of the pile during testing.

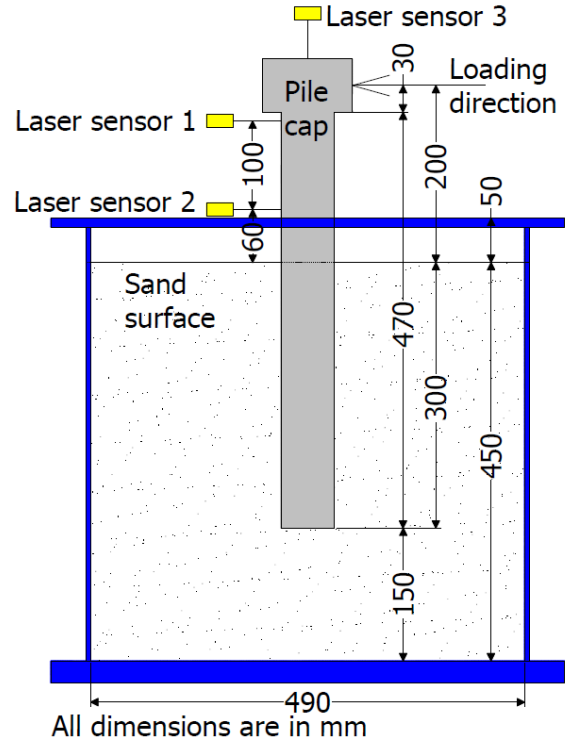


Figure 3. Experimental setup.

4 DEMONSTRATION OF SYSTEM PERFORMANCE

This section provides an overview of the data obtained from the cyclic loading tests. All results are provided in model scale unless otherwise stated.

4.1 Spin-up and stabilisation cycles

Figure 4 shows forces F_1 and F_2 measured during centrifuge spin-up to 63g and the subsequent 3 stabilisation cycles (from 63g-10g-63g) prior to cyclic loading of the pile. The stabilisation cycles are undertaken to encourage a uniform stress distribution within the soil body and improve repeatability between tests. The difference between F_1 and F_2 (i.e. the resultant force ΔF applied to the pile) was generally controlled to less than 25N, preventing any significant disturbance to the soil. Upon reaching 40g during the initial spin-up, there was a peak of about 60N, which is believed to be due to some reorientation of the sliding mass system caused by stretching of the cables; the force balance control system quickly corrected for this.

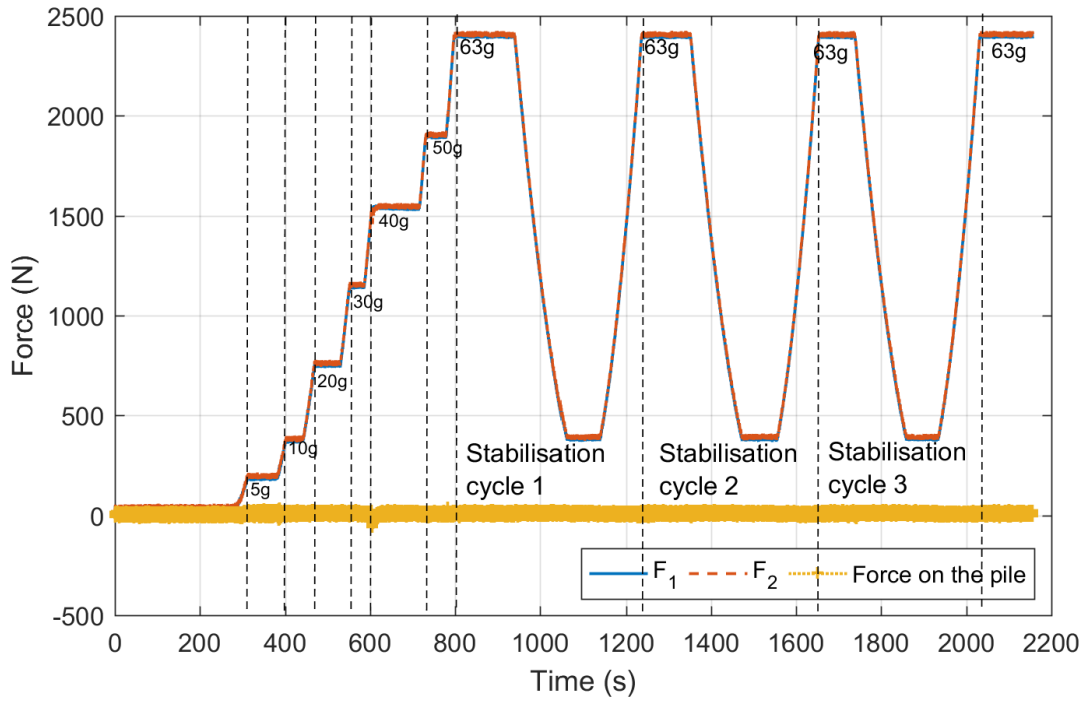


Figure 4. Measured forces F_1 and F_2 during centrifuge spin-up and stabilisation cycles.

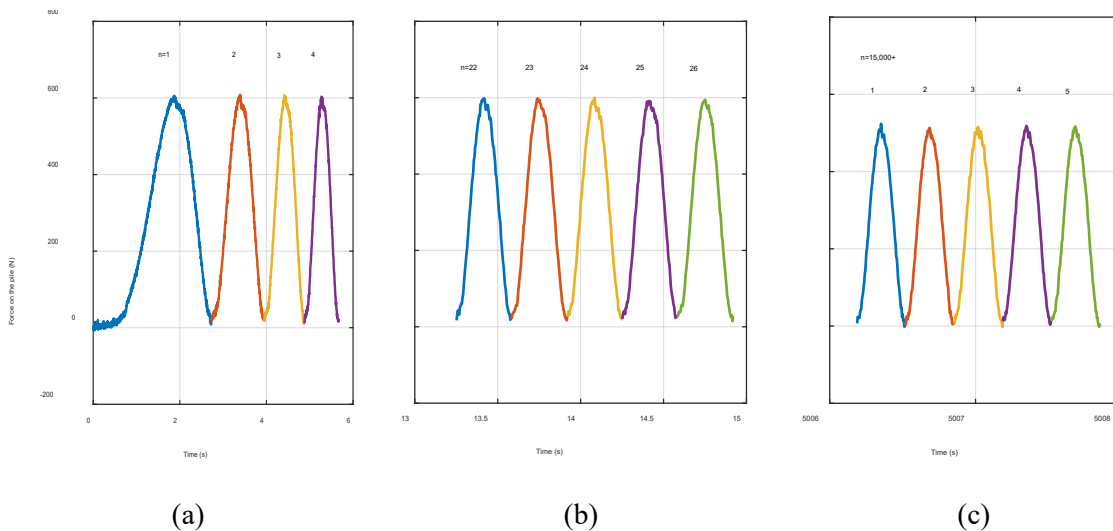


Figure 5. Resultant force on the pile for cycles: (a) $n=1, 2, 3$ and 4 ; (b) $n=22, 23, 24, 25$ and 26 ; (c) $n=15001, 15002, 15003, 15004$ and 15005 .

4.2 Cyclic loading

Figure 5 presents the resultant force applied to the pile for different cycle numbers, given by n . The specified loading frequency of 3Hz was reached after 22 cycles. The system requires a certain number of cycles to converge on the specified load amplitude (500N for this test); the load overshoot to 600N and then steadily decreased to 500N after cycle number 500, where it was subsequently maintained.

4.3 Load-displacement curve

Loads versus pile horizontal displacement curves are shown in Figure 6 for different cycle numbers. Figure 6(a) presents load-displacement data for

cycle number $n=1, 2, 3, 10$ and 100 where the pile is subjected to forces ranging from 0 to 600N. Figure 6(b) highlights representative cycles when the loads stabilized in the 0 to 500N range. From Figure 6(a), it is clear that residual displacement after each cycle accumulates but that maximum pile displacement remains approximately constant. After 400 cycles the pile's residual displacement fluctuates around 0.32mm; the maximum displacement decreases steadily with subsequent load number up to $n=70,000$, which suggests the sand experiences densification. Figure 7(a) and (b) show the moment, which is the product of the lateral force and the load eccentricity, against pile rotation for cycles before and after $n=400$, respectively. The pile rotation is calculated using readings from laser

1 and laser 2 and the pile above the sand is assumed to be undeformed.

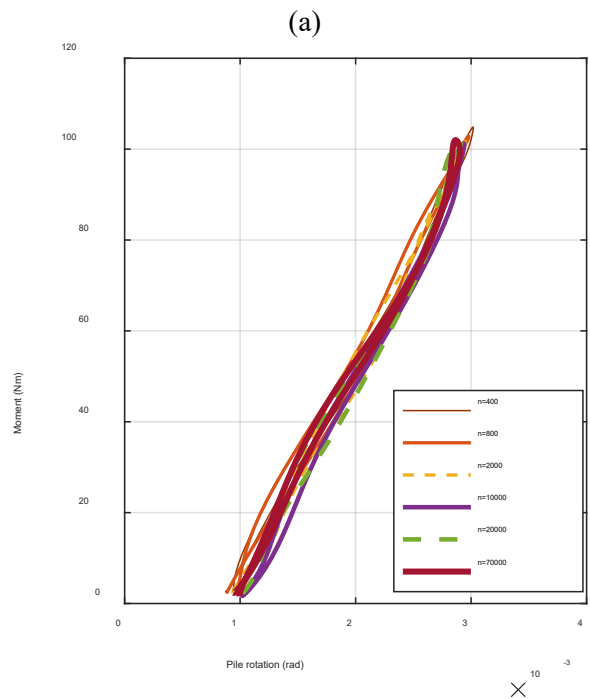
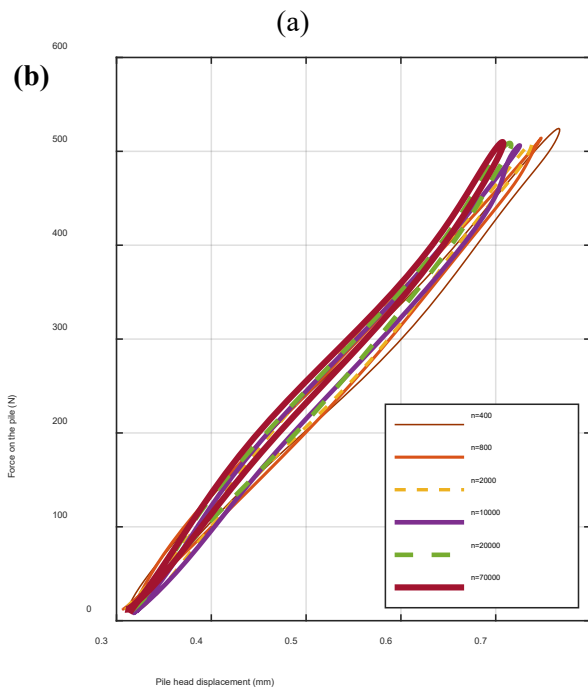
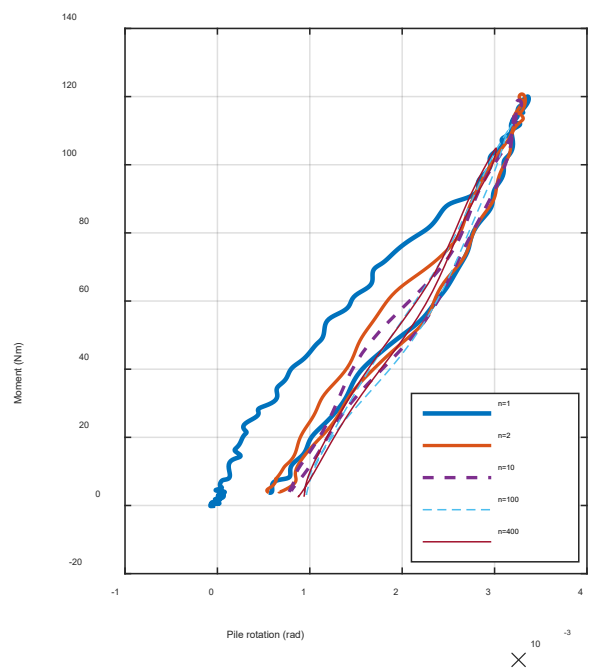
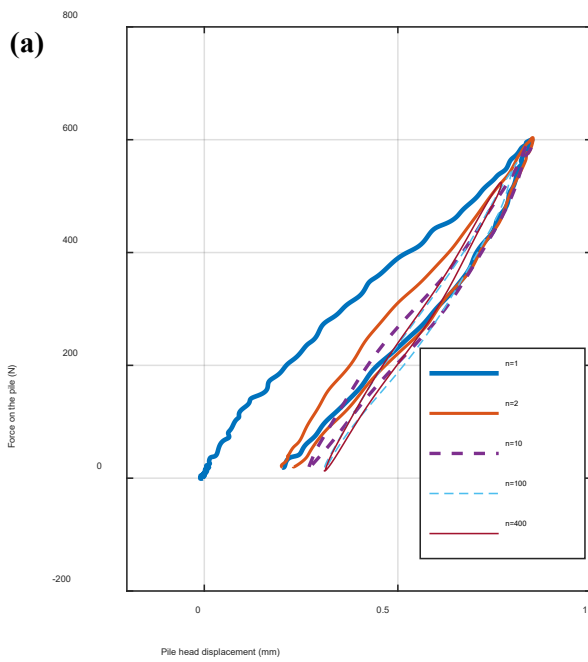


Figure 6. Force versus pile horizontal displacement for cycles: (a) $n=1, 2, 10, 100$ and 400 ; (b) $n=400, 800, 2000, 10000, 20000,$ and 70000 .

Figure 7. Moment versus pile rotation for cycles: (a) $n=1, 2, 10, 100$ and 400 , (b) $n=400, 800, 2000, 10000, 20000,$ and 70000 .

4.4 Stiffness variation

Figure 8 shows the secant stiffness against number of cycles. Stiffness was calculated by curve-fitting the load and displacement hysteresis loop for each cycle using linear regression. This was undertaken to minimise the effect of signal noise in the data which has more of an effect when selecting the peaks/troughs of individual hysteresis loops. Figure 8 shows that stiffness increased rapidly at the beginning of the test from 600N/mm at the first cycle to 1150N/mm at the 150th cycle. Stiffness subsequently increased slowly with additional cycle number, with some fluctuations, which is consistent with observations by Klinkvort and Hededal (2012). Figure 8 also presents the enclosed area of moment-rotation curves for each cycle. The enclosed area is representative of the energy dissipated by the pile-soil system. As shown in Figure 8, the enclosed area continues to decrease with increasing load cycle.

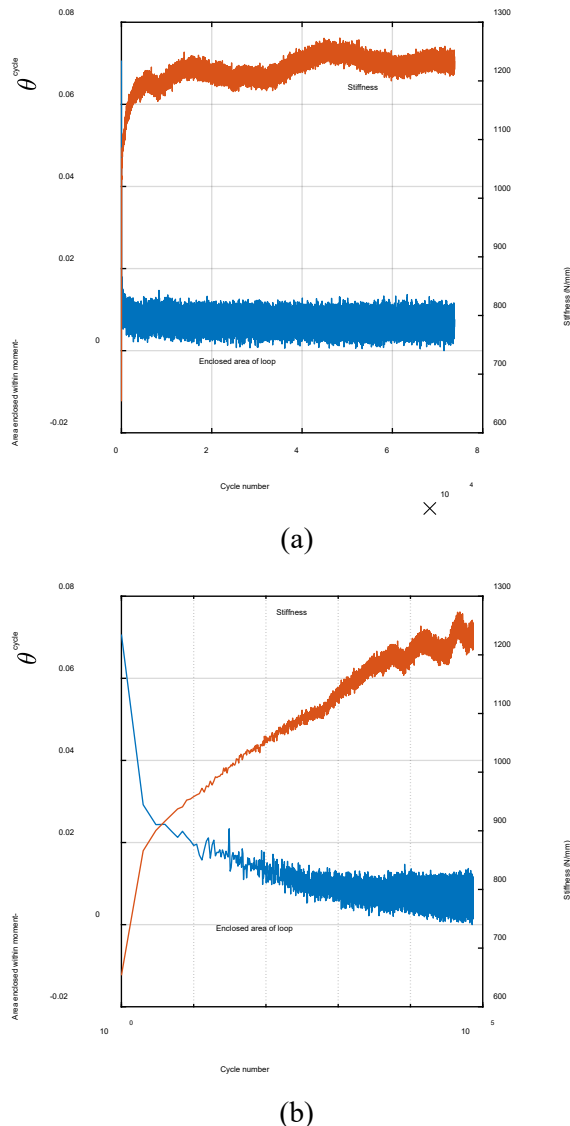


Figure 8. Secant stiffness and area enclosed within moment-rotation cycle versus cycle number: (a) cycle number in linear scale; (b) cycle number in log scale.

4.5 Loading rate effect

To evaluate the potential effect of loading rate, after completing 70,000 cycles, the test was paused and the loading frequency was varied between 4Hz and 2Hz. Figure 9(a) presents the stiffness variation for the different loading frequencies and shows that the stiffness remained relatively constant across the tested range of frequencies. As shown in Figure 9(b), the loading frequency had a limited effect on the obtained load-displacement loop.

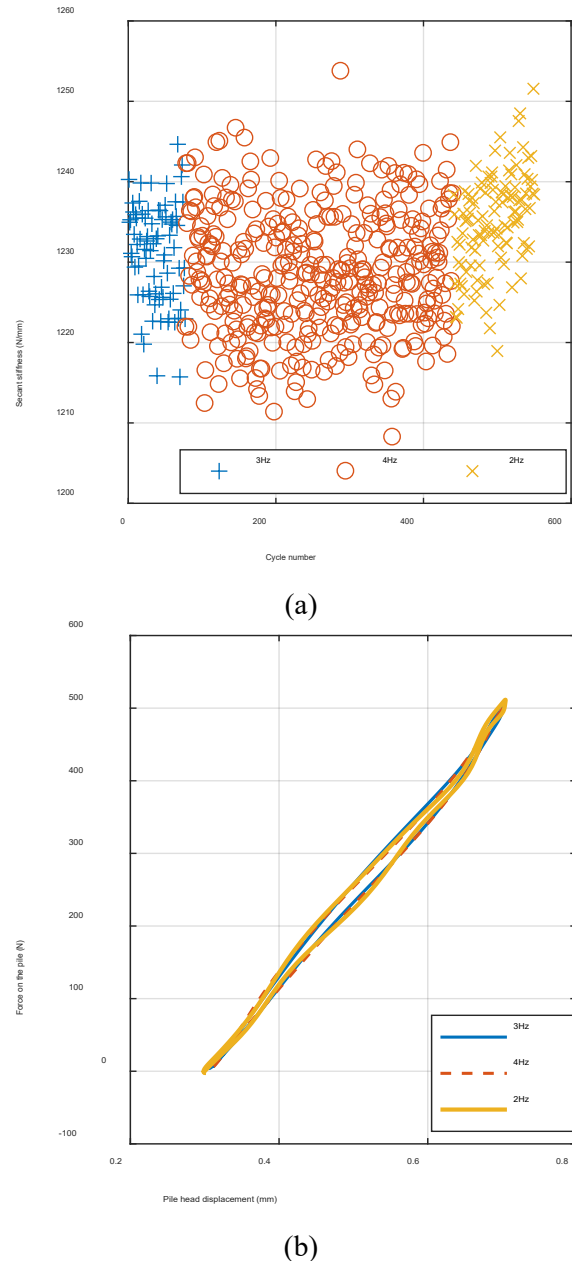


Figure 9. (a) Stiffness for different loading frequency; (b) force versus pile head displacement for different loading frequency.

5 CONCLUSIONS

This paper described a newly developed centrifuge testing apparatus for applying large numbers of cyclic loads and presented preliminary results

related to the response of OWT monopile foundations. Results were provided to demonstrate the successful operation of the experimental system, including balancing the resultant force applied to the pile during centrifuge spin-up to limit disturbance to the pile, and imposing a specified loading rate and amplitude (3Hz and 500N were demonstrated in this paper). The system can be adjusted to achieve different cyclic loading characteristics, ranging from one-way to two-way loading and with different load amplitudes. The current system has ability to apply a relatively large number of load cycles at a frequency of up to 4Hz; modifications to the motor and gearbox will allow future applications at higher frequencies. Data from a one-way cyclic load test were provided and showed a general increase in secant stiffness with load cycle, with some fluctuation, suggesting the sand was continually densifying with load cycle. In addition, it was shown that variation of loading frequency between 2Hz and 4Hz had a limited effect on the load-displacement curve and secant stiffness evolution in the dry sand tests conducted.

6 REFERENCE

- Albiker, J., Arshad, M., Frick, D., and Flindt, F. 2017. 1g Model Tests on the Displacement Accumulation of Large-Diameter Piles Under Cyclic Lateral Loading. *Geotechnical Testing Journal*, **40**(2):173–184.
- API 2007. Recommended Practice for Planning, Designing and Constructing Fixed Offshore Platforms Working Stress Design. *Api Recommended Practice*, 24-WSD (December 2000):242.
- Arshad, M. and O’Kelly, B. C. 2017. Model Studies on Monopile Behavior under Long-Term Repeated Lateral Loading. *International Journal of Geomechanics*, **17**(1).
- Bayton, S. M., Black, J. A., and Klinkvort, R. T. 2018. Centrifuge modelling of long term cyclic lateral loading on monopiles. *Physical Modelling in Geotechnics*, **2**:689–694.
- DNV 2016. DNVGL-ST-0126: Support structures for wind turbines. *Dnv Gl As*.
- Klinkvort, R. T. and Hededal, O. 2012. Lateral response of monopile supporting an offshore wind turbine. *Proceedings of the Institution of Civil Engineers - Geotechnical Engineering*, **166**(2):147–158.
- LeBlanc, C., Byrne, B. W., and Houlsby, G. T. 2010. Response of stiff piles in sand to long-term cyclic lateral loading. *Gotechnique*, **60**(2):79–90.
- Li, Z., Haigh, S. K., and Bolton, M. D. 2010. Centrifuge modelling of mono-pile under cyclic lateral loads. *7th International Conference on Physical Modelling in Geotechnics*, **2**:965–970.
- Garnier, J., Gaudin, C., Springman, S. M., Culligan, P. J., Goodings, D., Konig, D., and Thorel, L. 2007. Catalogue of scaling laws and similitude questions in geotechnical centrifuge modelling. *International Journal of Physical Modelling in Geotechnics*, **7**(3), 1–23.

Use of optical fibres to measure pore water pressure development during impact pile driving: a geotechnical centrifuge study

Amin Askarinejad¹, Tristan O. Quinten^{1,2}, Mario Alvarez Grima³, Cornelis van 't Hof³, Ken Gavin¹

¹ Faculty of Civil Engineering and Geosciences, Delft University of Technology, the Netherlands

² DEME group, Belgium

³ Royal IHC-MTI, Delft, the Netherlands

Corresponding author: Amin Askarinejad (A.Askarinejad@tudelft.nl)

ABSTRACT: Pile driveability is affected by, amongst other factors, the pore pressure changes in the vicinity of the pile. However, accurate quantification of the generated pore pressure in the soil layer during impact pile driving is a challenging task, especially in the small-scale models. An electro-mechanical miniature impact pile driver has been designed and constructed for the geo-centrifuge at TU Delft. This hammer has been used to study the pore pressure generations at various radial distances from the pile. An optical fibre capable of measuring pore pressure changes was installed on the outer skin of the model pile to monitor the pore pressure generation at the pile-soil interface. This data is complemented by standard miniature pore pressure transducers embedded in the soil mass that allow the radial distribution of excess pore pressure to be measured. The details of instrumentation, installation, performance and the results of this novel sensor are presented and discussed in this paper.

Keywords: Pore Water Pressure; Impact Pile Driving; Optical Fibres; Geotechnical Centrifuge; Small-Scale Physical Model.

1 INTRODUCTION

The vast majority of substructures for offshore wind turbines require the installation of one (monopile) or multiple open-ended steel piles. These offshore piles are mostly installed using costly operations involving large hydraulic hammers. Prior to installation, drivability analyses are commissioned which determine the required hammer capacity. Several full-scale experiments have demonstrated that modification of driving parameters, specifically: (I) hammer weight; (II) driving frequency; (III) falling height/impact velocity; can improve pile installation time. Not all of the physical processes leading to the improved impact pile driving efficiencies are yet fully understood. However, it is hypothesised that the generation and dissipation of pore water pressure in the vicinity of the pile has potentially a major effect on the driveability. A miniature pile driving hammer has been developed to conduct impact pile driving on small scale models in the centrifuge in this study. The details of the hammer and instrumentation are discussed. Moreover, the results of pore pressure measurements at various radial distances from the model pile are presented.

2 MINIATURE IMPACT PILE DRIVER

The miniature hammer developed at the Geo-Engineering section of TU Delft was designed

based on the specifications of IHC Hydro-hammers S200, S280 and S500 with a blow rate of 45 blows per minute. Considering the scaling requirements for the energy flux of the hammers an electro-mechanical lift system was adapted which is composed of a 1.2 kW electric brushless motor, a flywheel that picks up the ram mass at its lowest point and releases it at a predefined point, and a set of gears. The gear system ensures that the motor can operate at maximum efficiency while keeping the flywheel at the correct speed for pile driving (Van Zeben et al., 2018, Azua et al., 2018 and Azua et al., 2019).

A modular system was utilised for the ram mass to provide flexibility in augments of the required mass. The ram mass is composed of a central bearing, which facilitates a smooth fall of the mass on to the pile head, a top cap and a connecting arm to be picked up by the fly wheel (Figure 1). The mass of the top cap can be altered and makes it possible to change the blow energy in between tests and also accommodate different masses for future research without the necessity of major alternations. The fall height is determined by several factors and can be varied from 25 to 55 mm resulting in an impact speed on the anvil up to 6.3 m/s at 50g

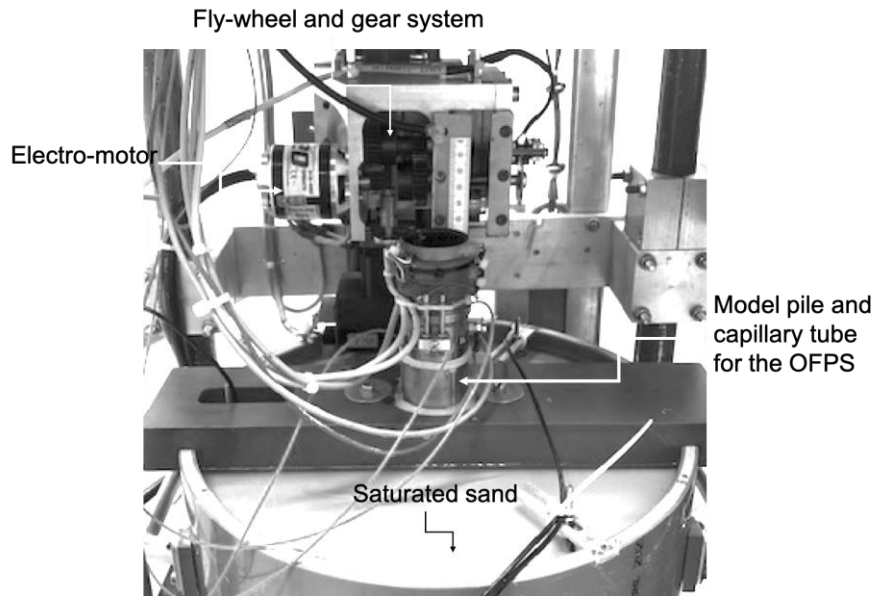


Figure 1 Test setup, model pile and capillary tube

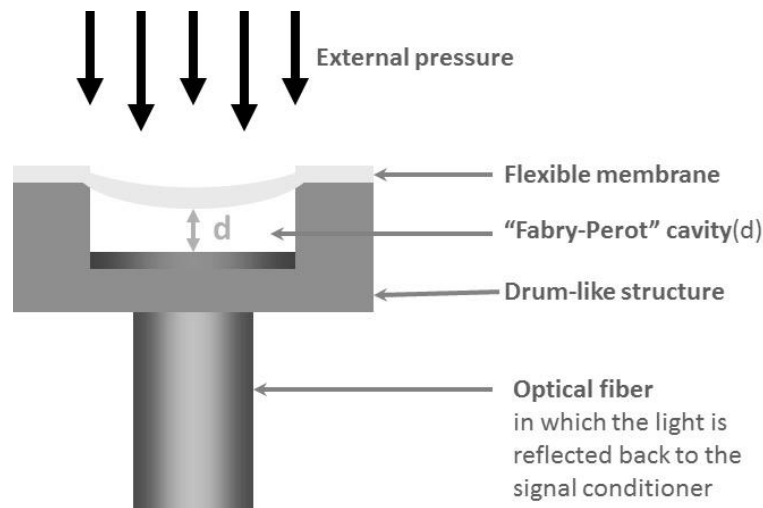


Figure 2 Pressure optical fibres (after Pinet 2009)

3 OPTICAL FIBRES TO MEASURE PORE PRESSURE

Optical fibres were installed at the interface of the pile and the soil and were housed by capillary tubes (with inner diameter of 0.8 mm). The capillary tubes were embedded into the outer periphery of the model piles. The pore pressure sensor is produced by FISO and is made of a *Micro-Opto Mechanical System* (MOMS) bonded to the tip of a fibre optic (Pinet 2009). This system is composed of a deformable membrane (mechanical part) which is assembled over a cylindrical cavity. The membrane deflects towards the base of the cavity when external fluid pressure is applied and this results in a decrease in the length of the sensing cavity (Figure 2). By filling the capillaries with silicon oil, and

subsequently closing them off at the top with a water-resistant silicon adhesive, a closed chamber is obtained in which pressure fluctuations along the shaft can be monitored. At the bottom of the capillary, a small slit (behind which a filter is installed), allows for the transmittance of pressure from the pore fluid at the interface to the sensor. An advantage of this installation method is that the sensors follow the movement of the pile. In total three optical fibre pressure sensors (OFPS) were used, which were installed at different distances with respect to the tip of the pile. The results of the OFPS2 installed at a distance of 0.7D from the pile tip are presented in this paper (D = 42 mm: pile diameter) the initial embedment of the sensor before pile driving is about 2D from the soil surface.

4 STATIC PORE PRESSURE SENSORS

To capture the development of excess pore fluid pressure during the driving operation, static pore fluid pressure sensors (SPS) are installed in the soil layer at various radial distances from the pile and three different depths from the soil surface. The results of deepest sensor which is installed at about 2D from the soil surface and a radial distance of 0.3D from the pile are presented in this paper.

5 SAMPLE PREPARATION

Circular strongboxes with diameter of 315 mm and an inner effective height of 175 mm were used. The soil samples were prepared using submerged pluviation and subsequent densification to a relative density of 80%. Fine uniform silica sand with a D_{50} of 110 micrometers and internal friction angle of 34 degrees was used (Table 1). In order to scale the pore pressure generation and dissipation correctly in the centrifuge model the permeability of the soil has been reduced (Askarinejad et al., 2014) by saturating the samples with a viscous fluid with dynamic viscosity of 50 cSt.

Table 1 Properties of silica sand (De Jager et al. 2017, Maghsoudloo et al. 2017)

Parameter	Silica sand
Maximum void ratio	0.86
Minimum void ratio	0.625
c_u	1.38
D_{50}	0.110 mm
c_c	1.05
Friction angle (ϕ_{cv})	34°
Permeability	8.41E-4 m/sec
Specific Gravity (-)	2.65

6 TEST RESULTS

The results of the pore pressure measurements as a function of the model time and centrifugal

acceleration are presented in Figure 3. Both conventional and optical fibre pressure sensors were installed at similar depth with respect to the soil surface (~2D). Both sensors measure an increase in the hydro-static pressure due to the increase of centrifugal acceleration. A very good agreement is seen between the two measurements. Moreover, the decrease in the centrifugal acceleration and its effect on the hydrostatic pore pressures is very well captured by both sensors.

The optical fibre sensor shows higher values of pore pressure after installation compared to pre-installation measurements. This increase in hydrostatic pore pressure indicates the added embedment of the pile. Whereas, the static PPT measures equal values before and long after the hammering. The area confined by the rectangular zone in Figure 3 shows the time span of pile driving and the details of the measurements in terms of excess pore pressure (EPP) development are shown in Figure 4. Optical sensor which is installed at the interface of the dense sand and the driven pile has measured the accumulation of negative pressures over a set of consecutive blows. At its peak, the under-pressure is about 5 kPa, equivalent to a decrease of about 10% with respect to hydrostatic conditions. Hence, it is cautiously stated that for dense sand samples as used for this research, the accumulation of positive excess pore water pressures in the vicinity of the pile is non-existent. Hence, a state of soil liquefaction seems to be ruled out in this zone. However, the limited resolution of data logging rate inhibits the further exploration pore pressure generation at the soil-pile interface. On the contrary, the pore pressure transducer installed with a radial distance of about 0.3D measures 30% increase in the pore pressure with respect to the initial hydrostatic values pre-installation.

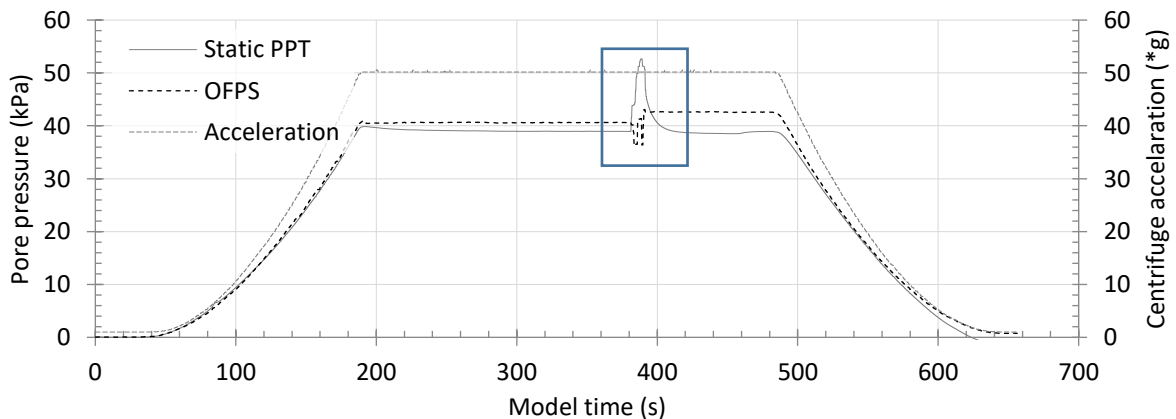


Figure 3 Results of pore pressure measurements as a function of model time. The rectangle shows the time span of pile driving.

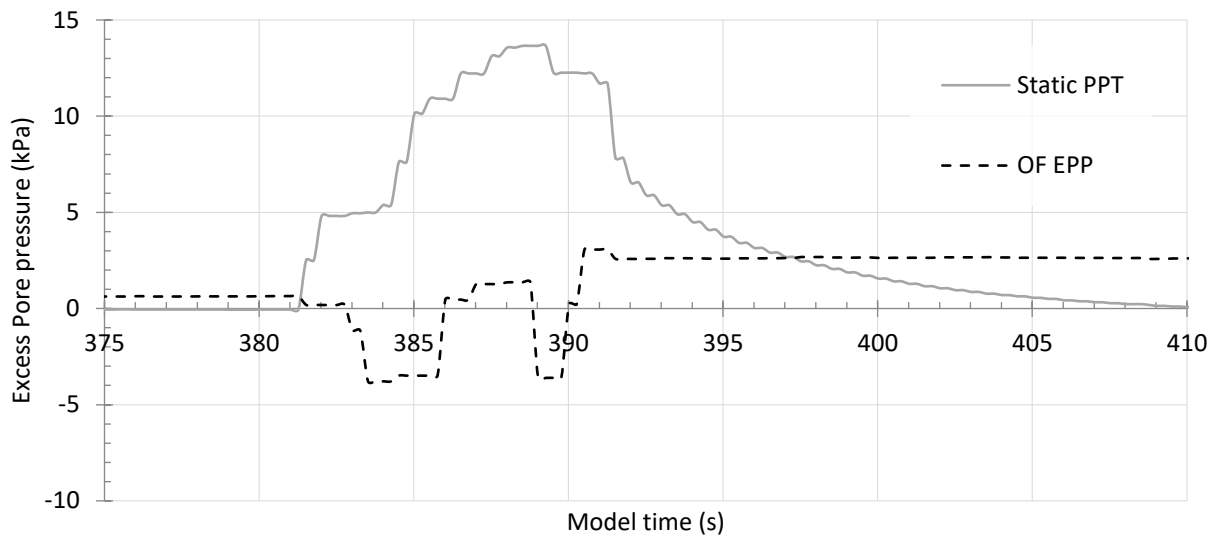


Figure 4 Development of excess pore pressure in the vicinity of the pile.

7 CONCLUSIONS

In this paper, the usage of optical fibre pressure sensors for centrifuge models of offshore mono-pile driving is described. From practical point of view, it could be concluded that the largest challenge lies in the area of sensor fixation and the saturation of the capillary tubes, which might tend to leak oil during the experiments. Moreover, it was observed that it would be beneficial to increase the measurement frequency of these sensors. However, it should be noted that the intrinsic data logging rate of the system used in this study is limited to 125 Hz. The results of pore pressure measurements yield valuable insights with regard to processes during impact pile driving. Slight negative development of excess pore pressures was detected at the interface of the dense sand and the pile. Whereas, at larger radial distances from the pile, the global trend of measurements demonstrates a rather uniform increase of the pore pressure with respect to hydrostatic conditions in the soil body surrounding the pile.

8 REFERENCES

Askarinejad, A., Beck, A. and Springman, S.M., 2015. Scaling law of static liquefaction mechanism in geocentrifuge and corresponding hydromechanical characterization of an unsaturated silty sand having a

viscous pore fluid. *Canadian Geotechnical Journal*, **52**(6), pp.708-720

Azúa-González, C.X., van Zebena, J.C.B., Grimab, M.A., van't Hof, C. and Askarinejada, A., 2019. Dynamic FE analysis of Soft Boundary (SB) effects on impact pile driving response in centrifuge tests. *Proceedings of the XVII ECSMGE-2019*. doi: 10.32075/17ECSMGE-2019-0821

De Jager, R.R., Maghsoudloo, A., Askarinejad, A. and Molenkamp, F., 2017. Preliminary results of instrumented laboratory flow slides. *Procedia Engineering*, **175**, pp.212-219

Maghsoudloo, A., Galavi, V., Hicks, M.A. and Askarinejad, A. 2017, September. Finite element simulation of static liquefaction of submerged sand slopes using a multi-laminate model. In *19th International Conference on Soil Mechanics and Geotechnical Engineering (Vol. 2, pp. 801-804)*.

Pinet, É., 2009. Fabry-Pérot fiber-optic sensors for physical parameters measurement in challenging conditions. *Journal of sensors* (2). <https://doi.org/10.1155/2009/720980>

Van Zeben, J.C.B., Azúa-González, C.X., Alvarez Grima, M., van't Hof, C. and Askarinejad, A. 2018, July. Design and performance of an electro-mechanical pile driving hammer for geo-centrifuge. In *Proc. Int. Conf. Phys. Mod. Geotech. (ICPMG 2018)* (pp. 469-473).

The modelling of piles under multidirectional loading

Christophe Gaudin¹, Conleth O’Loughlin, Manuel Herduin

¹ Centre for Offshore Foundation Systems, The University of Western Australia, Australia

Corresponding author: Christophe Gaudin (christophe.gaudin@uwa.edu.au)

ABSTRACT: Offshore foundations are typically designed to resist mooring loads coming from a single direction. This paper provides some insights into the geotechnical challenges associated with anchor sharing (i.e. where mooring loads are coming from multiple directions to a single anchor) for Offshore Renewable Energy (ORE) applications. This is relevant to arrays of floating renewable energy devices (waves or wind), when multiple devices are anchored to a single foundation to generate economies of scale. The paper presents the modelling methodology and the results of centrifuge tests investigating the behaviour and performance of a rigid pile subjected to cyclic multidirectional loading regimes, as identified from hydrodynamics analyses. Results highlight the importance of the magnitude of the vertical resultant of the different loadings, as well as the variation of direction of the horizontal resultant.

Keywords: Pile, Centrifuge Modelling, Multidirectional Loading, Offshore Renewables

1 BACKGROUND

Offshore renewable energy is rapidly evolving as one of the highest potential sources of clean energy. Fixed offshore wind has experienced rapid development (+30% per year between 2010 and 2018, with a total capacity of 19 GW, IEA 2019), and has absorbed most of the research attention over the last decade. More recently, floating technology has been increasingly considered to support the growth in demand for renewable energy. This is the case for wind, to access higher and more consistent wind resources, but also for wave and tidal, two technologies still in their infancies but with very large potential.

Renewable energy generation from floating systems has been proven, and includes for example: (i) the Hywind spar floating wind turbine, which has been in operation in 198 m of water off the southwest coast of Norway since 2009, (ii) the WindFloat semi-submersible floating wind turbine that has been tested in 40-50 m water depths off the coast of Portugal since 2011, (iii) the Ocean Power Technology floating wave energy device, which has been tested off the coasts of Hawaii, USA and Scotland in water depths of up to 30 m since 2005, and (iv) the Perth Wave Energy Project from Carnegie Wave Energy, with three 240 kW wave energy converters (WECs) operating over 12 months offshore Garden Island in Western Australia.

Floating technology for offshore renewables still presents several significant challenges. It requires reliable and economical anchoring systems that can perform in the type of seabed sediments encountered on the continental shelf, where marine renewables are expected to operate. Anchoring systems can contribute up to 22% of the total

installed cost of an offshore wind turbine (Willow & Valpy, 2011), and up to 30% of the total installed cost of a wave energy converter (Martinelli et al., 2012). This is one order of magnitude higher than for oil and gas structures (Kost et al., 2013), and contributes significantly to the high levelised cost of offshore wind and wave energy. For marine renewable energy to be commercially affordable and competitive, a significant paradigm shift is required both in foundation technology and in foundation design.

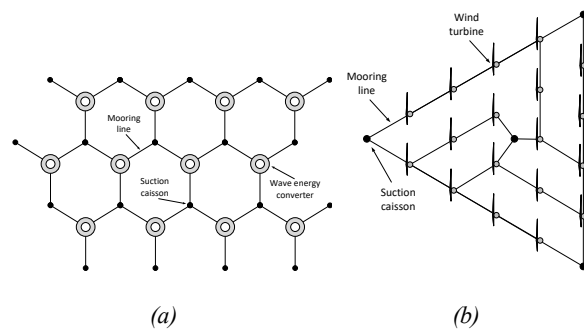


Figure 1. Example array of: (a) WECs and (b) floating wind turbines sharing anchoring points. Regardless of the pattern of the array, the number of mooring points reduces linearly with the number of mooring lines connected to it.

One of these paradigm shifts, either for wave energy converters or floating wind turbines, is the sharing of foundation between multiple devices when assembled in an array (Karimirad et al., 2014) to significantly reduce the foundation engineering costs. Different array patterns can be considered as a function of the power output and shadowing effects between devices (see Child & Venugopal, 2010), as presented in Figure 1. But in all cases, the number of foundations can be reduced significantly, such that for instance, in a three mooring point

absorber in a honeycomb pattern (Figure 1a), 20 devices can be anchored by 30 foundations, instead of 60 (see Figure 2).

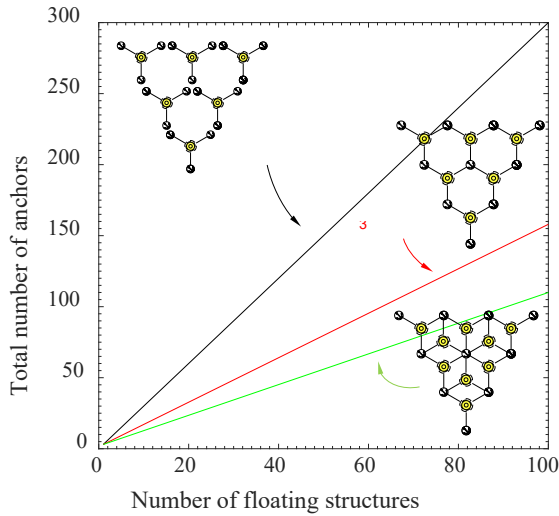


Figure 2. Example of the benefit of anchor sharing for arrays of renewable energy devices. A floating device is typically anchored by three mooring points. By sharing these mooring points between devices, it is possible to reduce significantly the number of mooring points and hence foundations, reducing the cost of foundation engineering (installation and infrastructure). The benefit increases with the number of mooring lines on each mooring points, but also the complexity of the loading applied to the foundation.

A direct consequence of the foundation sharing strategy is the complexity of the loading regime on the foundation that can come from multiple directions (Figure 2). Depending on the wave spectra and period, and the spacing of the floating devices, the foundation can be subjected to loads coming from different directions that can be in phase (resulting in alternate loading along each of the mooring lines) or out of phase. This complex multi-directional loading mode is fundamentally different from typical design considerations for floating oil and gas facilities, on which most of the design methodologies are based.

This paper reports some of the outcomes obtained from a research project undertaken to characterise the response of rigid piles under multidirectional loading. The first stage of the project entailed defining precisely the loading regimes experienced by the foundation as a function of the pattern of the array and the wave characteristics. This was undertaken through a comprehensive hydrodynamic analysis, validated by in-situ measurements, with the main conclusions presented in the next section. The second stage involved a series of centrifuge tests modelling the identified loading regimes and investigating the response of a rigid pile embedded in sand. This paper presents a limited number of results, showcasing the modelling techniques used

and highlighting some critical aspects of the pile response.

2 HYDRODYNAMIC ANALYSIS

2.1. Numerical analysis

The characteristics of the multidirectional loading acting on a foundation are complex. Each load does not act independently of the other, but as a function of the pattern of the array, the direction and period of the waves and the spacing between the floating bodies, and the resultant of these loads follows specific patterns defined by these input characteristics.

Before engaging in a complex centrifuge programme, it is necessary to identify clearly the range of loading regimes that are applied on a multi-moored foundation, to be able to identify which of these regimes are detrimental for the foundation performance, and hence inform the optimal array pattern and dimensions. To that end, a comprehensive numerical analysis was undertaken with Orcaflex.

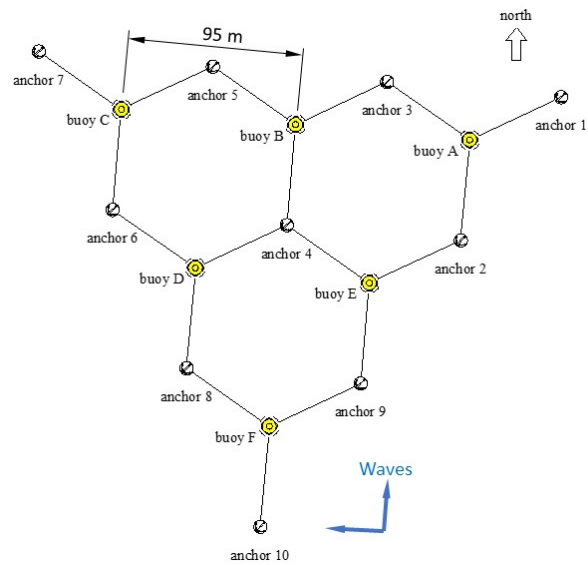


Figure 3. Case investigated via Orcaflex analysis to identify multidirectional loading regimes on anchoring points. The array consists of 6 floating bodies, with spacing of 95 m, in mean water depth of 27 m. 6 sea states were considered, corresponding to field measurements made in Falmouth Bay, UK, and provided by the University of Exeter. The wave direction ranged from 86° to 179° , while the wave period ranged from 6.5 to 8.2 s and the significant wave height from 0.19 to 2.31 m. The analysis provided load regimes on each mooring line as a function of the sea state considered. Details of the Orcaflex analysis, including all hydrodynamic parameters, are presented in Herduin (2019).

The Orcaflex analysis was first validated against field data from a 3-point mooring floating structure, mimicking the dynamic response of a scaled point absorber in real open ocean conditions, and provided by the University of Exeter (Herduin,

2019). The analysis was subsequently extended to an array of floating bodies at the sea surface, arranged in a honeycomb pattern and attached to 3 mooring points. Each mooring point is connected to 2 (at the edge of the array) or 3 (inside the array) catenary mooring lines (Figure 3). The array was subjected to 6 different sea states (established from the field measurements provided by University of Exeter), which varied the direction and period of the wave, and its significant wave height.

An example of the results is provided in Figure 4, which represents the time series of the load resultant and its variation in direction. These two parameters are important to define the loading regimes. Across varying sea states, both the load resultant and its direction may vary significantly in magnitude, or only very slightly, with fundamentally different consequences on the anchor behaviour and performance.

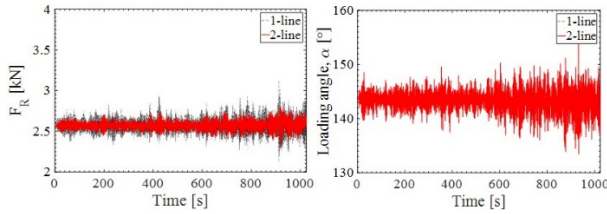


Figure 4. Example results from the Orcaflex analysis. The figure relates to anchor 2 in Figure 3, with two loading directions spaced by 120° . It presents the time series of the force resultant F_R , the magnitude of which ranges from 2.2 to 3.2 kN, with a resultant loading direction in the horizontal plane α_R varying between 133° and 156° .

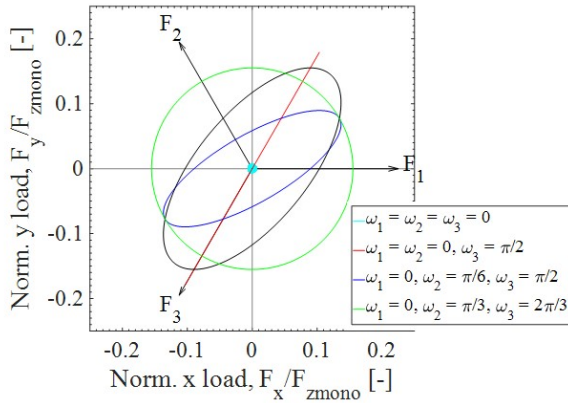


Figure 5. Example resultant load path in the horizontal plane for three loading directions spaced at 120° . The input on each line is established from a regular sinusoidal wave, with the direction of the wave and the distance between floating bodies resulting in a phase angle between the loads on each line varying from 0 to $2\pi/3$. The load path varies from a single line across the horizontal plane, indicating a large variation in magnitude but no variation in direction, to a circle, indicating a large variation in direction and no variation in magnitude. This variation in loading regime results in different foundation behaviour, as identified by the centrifuge testing campaign.

Orcaflex analyses are demanding and time consuming. Based on the numerical analysis, an analytical model was developed that enables rapid identification of the various loading regimes (see Herdouin, 2019 for full details). The analytical model is a simplification of the real conditions, assuming only regular waves, but it provides results that are close enough to those generated by the Orcaflex analysis to be able to identify families of loading regimes. An example of output from the analytical model is presented in Figure 5 for the three loading direction case. The model also defines the vertical resultant, which is an important parameter of the foundation behaviour as discussed later in the paper.

3 CENTRIFUGE MODELLING

3.1. Models and experimental setup

Tests were performed in the 10 m diameter 240 g-tonne beam centrifuge (Gaudin et al., 2018) at the University of Western Australia. Sand samples were reconstituted in a square strongbox, with breadth 1 m and depth 0.5 m.

The model piles are close-ended short rigid piles with diameter $D = 23$ mm and length $L = 155$ mm ($L/D = 6.7$). They were manufactured from a hollow piece of aluminium and closed by screw caps at either end. A drainage hole in the pile allowed the pile to fill with water prior to the testing to avoid unrealistic buoyancy. The fine silica sand used for the sample was glued to the outer shaft of the pile to create a fully rough interface (Figure 6).

Commercial fine silica sand, with main characteristics summarised in Table 1, was used to create two soil samples using dry pluviation. The sand was from a constant drop height to ensure that the relative density remained constant with depth. Pluviation was continued until a sample 150 mm high was achieved, at which point the model piles were suspended in the strong box from a customised mesh, with the piles bases resting on the surface of the sand. Pluviation was then resumed, such that the piles were effectively pre-embedded in the sample. The final sample height was 305 mm, with a pile embedment length of 155 mm (i.e. the full pile length). Following pluviation, the samples were saturated with water from the base of the sample.

The two samples were characterised through in-flight cone penetrometer tests (CPTs) performed before and after the pile tests, using a cone 7 mm in diameter. Tests were performed at 1 mm/s (under drained conditions) to a target depth of 180 mm. Results (not presented in this paper for brevity) indicated a good homogeneity and consistency

within and between samples. The relative density, estimated from the empirical relationship proposed by Jamiolkowski et al. (2003), was 82% for Sample 1 and 85% for Sample 2.

Table 1. UWA fine silica sand properties after Chow et al. 2019. Peak and residual friction angles are established from drained direct shear tests at a relative density of 88-98% and vertical stresses in the range of 21-400 kPa.

Property	
Sample relative density D_r	85%
Specific gravity, G_s	2.65
Maximum void ratios, e_{max}	0.78
Minimum void ratios, e_{min}	0.49
Average particle size, D_{50}	0.19 mm
Peak friction angle, $\phi_{p(DS)}$	40.1°
Residual friction angle, $\phi_{r(DS)}$	33.1°

Significant efforts were devoted to the design of the centrifuge setup to enable application of loading from 2 or 3 directions in the horizontal plane, and at varying angles from the horizontal in the vertical plane (see Figure 6). The setup consists of a platform assembled around 2 I-beams, onto which 3 linear electric actuators are attached vertically, allowing for loading along three lines connected between each actuator and the pile head. A bottom plate located under the platform and featuring multiple pulleys allowed the load inclination (to the horizontal) to be varied in the range 10 to 60 degrees, and the load direction to be along three directions with spacing of 30, 60, 90, 120 and 180 degrees in the horizontal plane.

Three in-line load cells, each with a measurement range of 2 kN, were located on each loading line, while linear displacement transducers (LDTs) were mounted on each actuator to measure displacement along the loading direction. A 3D-printed support was fixed on the pile head (see Figure 4) to host two accelerometers to measure the pile rotations in two orthogonal directions (ω_x, ω_y) using the methodology developed by Beemer et al. (2018). Three additional LDTs were connected to a bar sitting on top of the 3D-printed support to measure horizontal ($\delta x, \delta y$) and vertical (δz) displacements.

The three linear actuators were controlled by the Package Actuator Control System 2nd version (PACS2), developed in-house at UWA. It provides the user with four Proportional Integral Derivative (PID) controller channels, which can be set up individually in either displacement or load-control, and synchronised using a built-in waveform and sequence generator. This feature is particularly critical to model accurately the load regime generated by given wave conditions. All data were acquired at a sampling rate of 10 Hz using the

DigiDAQ system developed in-house at UWA (Gaudin et al, 2009).

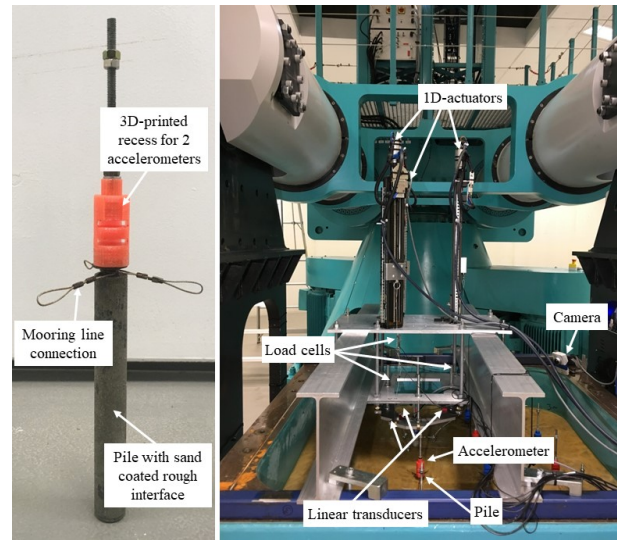


Figure 6. Model pile and centrifuge setup. Adjustment of the bottom plane enables variation of the loading angle from the vertical and the direction of loading in the horizontal plane, while instrumentation measures the load and displacement on each mooring line, the rotation of the pile (through accelerometers) the horizontal displacement of the pile in two directions and its vertical displacement. The combination of the line displacement, horizontal displacement and pile rotation gives the complete motion of the pile in the 6 degrees of freedom.

The centrifuge setup is shown schematically in Figure 7 with all the relevant dimensions.

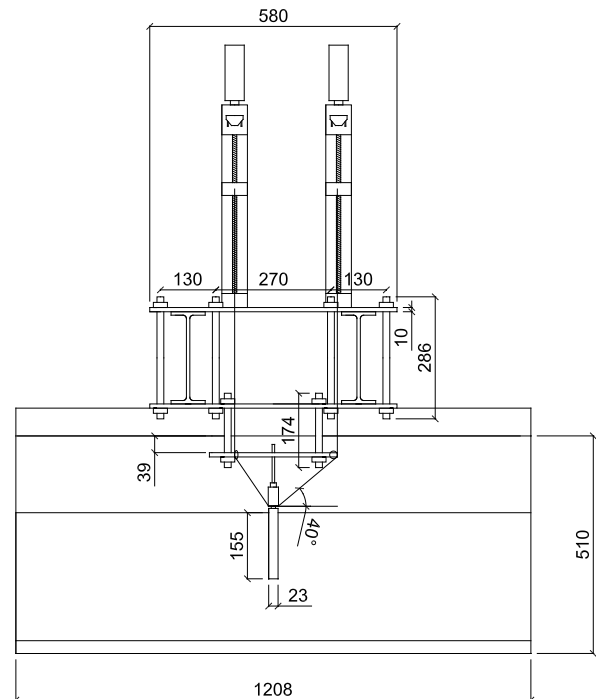


Figure 7. Centrifuge setup with main dimensions. The loading rig can be displaced as a single block to load up to 16 piles in the 1 × 1 m sample, while maintaining a spacing between piles and boundaries of at least 4D.

4.2 Testing programme and procedure

A total of 24 tests were performed in this research programme, with 3 reported in this paper. The programme included unidirectional monotonic vertical and inclined (40°) tests used as reference for ultimate capacity, and multidirectional cyclic sinusoidal tests in 2 and 3 directions with two different types of loading regimes. The first type, defined as alternate loading, involved loading in 2 or 3 directions one after another. While this does not model specific wave regimes, it does provide insights on the effect of multidirectional loading on the pile performance. The second type, defined as out of phase loading, aims at replicating loading regimes as defined by the hydrodynamic analysis.

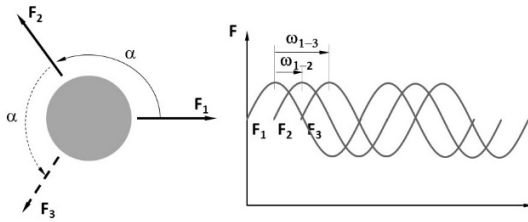


Figure 8. Multidirectional cyclic loading tests includes loading along 2 or three directions, with spacing α in the horizontal plane varying as 60, 90, 120, 180 and 180 degrees. During phase loading, the phase angle between the two or three sinusoidal loading signals varies as $\pi/9$, $\pi/6$, $\pi/4$, $\pi/3$, $7\pi/18$ and $\pi/2$. The resulting loading path in the horizontal plane encompasses all the loading regimes identified in the hydrodynamic analysis.

Figure 8 presents the different parameters that were varied during the multidirectional cyclic tests, while Figure 9 presents the details of the 3 tests reported here, with parameters listed in Table 2.

For all tests, the magnitude of the load was set as a ratio of the ultimate capacity established from the unidirectional monotonic inclined loading tests, F_{mono} . The load was increased by increments of 0.25 or $0.05F_{mono}$, with number of cycles varying from 50 to 100 depending on the displacement response during the tests.

Table 2. Summary of the multidirectional cyclic tests tests reported in the paper

Test ID	Test type	α ($^\circ$)	ω_{1-2} ($^\circ$)	ω_{1-3} ($^\circ$)
cyc_04_1	A-2L	120	-	-
cyc_06_1	A-3L	120	-	-
cyc_06_2	P-3L	120	$\pi/6$	$\pi/2$

The test procedure involved an important step prior to the start of the test in order to calibrate PACS2. For PACS2 to be able to apply synchronised loading in three directions, it was necessary to slightly pre-tension each line equally.

This was undertaken simultaneously on all lines. The pre-tension applied was very small ($\sim 0.05F_{mono}$) to avoid any significant vertical (in the case of the 2 and 3 loading lines case) and horizontal (in the case of the 2 loading line case) displacements.

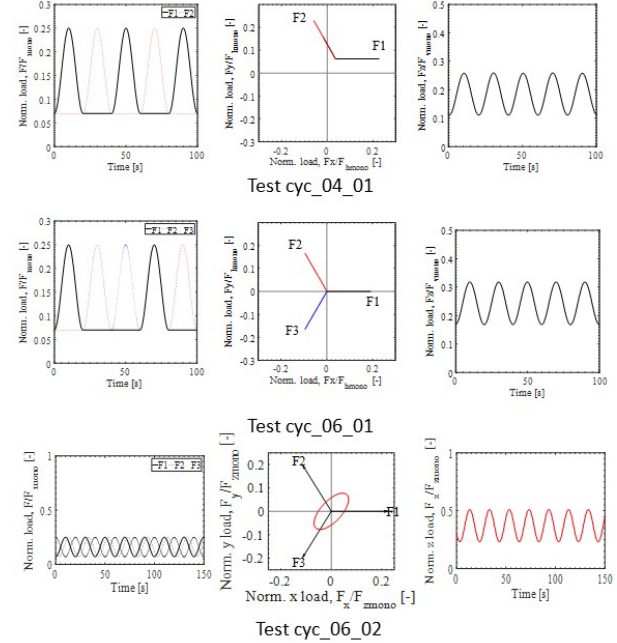


Figure 9. Loading regimes for the 3 multidirectional cyclic tests reported in this paper. The figures on the right shows the load applied along loading lines as a ratio of the ultimate unidirectional monotonic capacity. Test cyc_04_01 and cyc-06-01 are 2 directions and 3 directions alternate loading tests, where the loads were applied one after another. Test cyc_06_02 is a phase loading test, with the phase angle between the second and third loading being $\pi/6$ and $\pi/2$, respectively. The resulting loading path in the horizontal plane is presented in the middle figure and represent an ellipsoid. For the three tests, the figures on the left shows the trace of the vertical resultant. Note that in some cases (for tests not reported here), the vertical resultant may be a monotonic load. This has consequences on the performance of the pile.

4.3 Test results and discussion

Results for the three tests reported in this paper are presented in Figures 10, 11 and 12, respectively. The figures include (i) the load displacement curves along the loading lines, (ii) the accumulation of displacement with number of cycles along the loading lines, (iii) the resultant vertical load displacement curve, and (iv) the 3D motion of the pile in x, y, z space. The figures need to be examined with respect to the load regimes presented in Figure 7 and notably the resultant vertical load input.

For all three tests, failure occurred under vertical motion, with the pile being pulled out of the soil. The kinematics of the pile is however strongly influenced by the load path followed, and notably the vertical resultant. Under the first packet of cycles (at $0.25F_{mono}$), horizontal displacements are

$<0.1D$ and of the same amplitude as the vertical displacement for both test *cyc_04_01* (2 loading directions) and test *cyc_06_01* (3 loading directions). Test *cyc_04_01* is able to sustain $0.25F_{mono}$, as well as a higher $0.5F_{mono}$, before failing at $0.75F_{mono}$, at which point horizontal and vertical displacements are still of the same magnitude ($0.6D$ - $0.8D$). In contrast, test *cyc_06_01* is unable to sustain $0.25F_{mono}$ for more than 45 cycles. Failure occurs rapidly, essentially through an acceleration of the accumulation of vertical displacement ($0.5D$), while horizontal displacement remains limited to $0.1D$. The different behaviour in the two tests cannot be attributed to the different multidirectional loading regimes, but is most likely explained by the

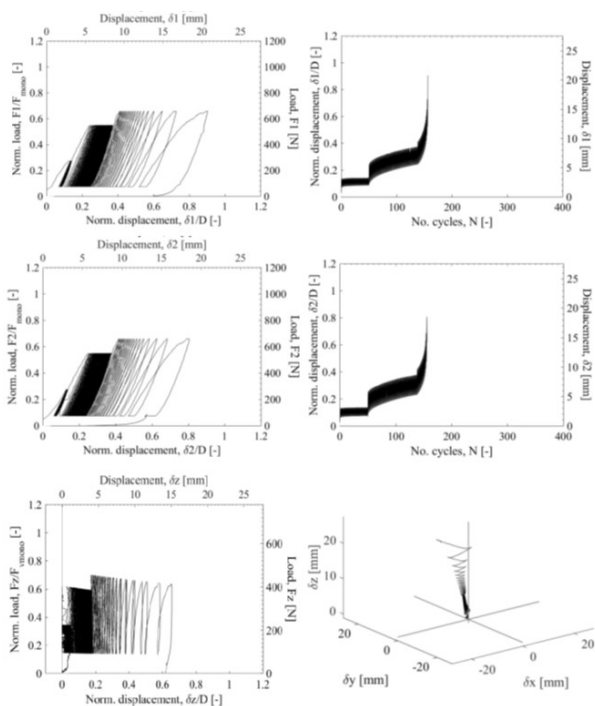


Figure 10. Results of test *cyc_04_01*. It is an alternate two lines loading test. The test was conducted with 3 increasing cyclic packets, 50 cycles at $0.25F_{mono}$, 100 cycles at $0.5F_{mono}$ and 18 cycles at $0.6F_{mono}$ as failure was reached. Displacement along the two loading lines show similarities, with no accumulated displacements over the first packet, a more significant accumulation over the second packet, and an acceleration over the third, leading to failure. Displacement reached at failure is $0.9D$ along the first direction of loading and $0.8D$ along the second direction, showing a dissymmetry of motion and the preponderance of the first loading direction on the pile behaviour. The bottom right plot shows the evolution of the vertical resultant with vertical displacement. The trend is identical to that along the two loading lines, with accumulated vertical displacement reaching $0.65D$ at failure. The bottom left plots shows the 3D pile motion in x , y , and z space, and confirms the observation made from the previous plots. Failure is reached by the pile being pulled out of the ground, while experiencing horizontal displacements of similar magnitude as the vertical displacements, with a slight dissymmetry towards the first direction of loading (the resultant horizontal displacement is not along the resultant load, but slightly biased towards the first direction of loading).

difference in peak vertical resultant load, as illustrated in Figure 9. For test *cyc_04_01*, the vertical load resultant peaks at $0.25F_{mono}$, while it peaks at $0.3F_{mono}$ for test *cyc_06_01*. This slight difference may be sufficient to explain the predominance of vertical failure for test *cyc_06_01*. This is discussed in more details later in the paper.

Comparison of test *cyc_06_01* and *cyc_06_02* provides insights into the effect of alternate and out of phase loadings on the pile behaviour. For the latter case, the pile experiences an ellipsoid motion, with horizontal and vertical displacement of very limited amplitude ($<0.05D$) within the first packet of cycles, increasing to $0.1D$ over the second packet, before reaching 0.15 - $0.25D$ in the horizontal plane and $0.5D$ in the vertical plane at failure over the third packet. Interestingly, the peak vertical resultant for test *cyc_06_01* is $0.5F_{mono}$ for the first

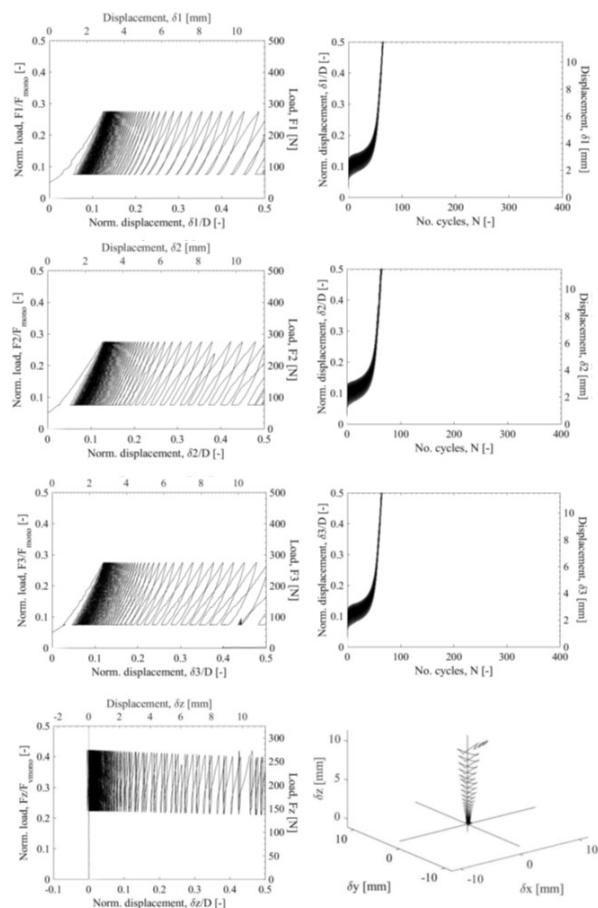


Figure 11. Results of test *cyc_06_01*. It is an alternate 3 lines loading test. 80 cycles at $0.25F_{mono}$ were performed and led to failure. The accumulation of displacement along the three loading lines are identical, with a significant acceleration of displacement after about 45 cycles. As seen on the 3D pile motion, horizontal displacements are $<0.1D$ at failure, while the vertical displacement goes beyond $0.5D$, indicating that failure is essential a shearing failure at the pile soil interface. Closer examination of the pile displacements on the horizontal plane (figure not shown here) indicates that pile drifted rapidly towards the 3rd loading direction as the vertical displacement accelerated.

packet of cycles, i.e. higher than for test cyc_04_01, which experienced failure after only 45 cycles. In this case, the multidirectional loading regime is the main contributor to failure, with alternate loading, generating abrupt loading reversal and higher vertical resistance degradation.

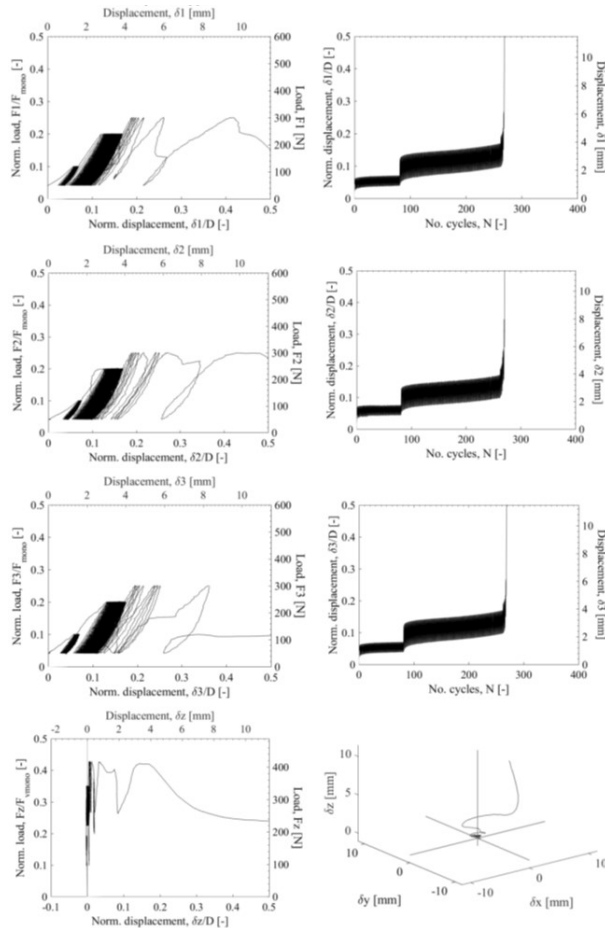


Figure 12. Results of test cyc_06_02. It is a 3 lines phase loading test. The testing sequence included 90 cycles at $0.05F_{mono}$, 170 cycles at $0.15F_{mono}$, and 10 cycles at $0.2F_{mono}$ at which point failure was reached. Load displacement curves along the three loading direction indicate no accumulated displacement over the first packet of cycles, a moderate accumulation of displacement over the second packet (about $0.04D$ over 170 cycles), and a very large acceleration of accumulation of displacement, leading to failure after less than 10 cycles in the third packet. Examination of the 3D displacement motion, and displacements on the horizontal plane indicates that the pile experienced an ellipsoid motion around its centre, with its major axis oriented 90° from the major axis of the ellipsoid load path defined in Figure 7. Displacements were of very limited amplitude in the x , y and z directions ($<0.05D$). Upon application of the third packet, the orientation of the ellipsoid remained unchanged, but displacement increased significantly in amplitude, reaching $0.15D$ in the x direction, $0.25D$ in the y direction and over $0.5D$ in the z direction. Failure occurs with the pile being pulled out of the ground with significant horizontal displacements.

These 3 tests illustrate that the pile performance is affected by multidirectional loading, but that the parameters governing failure, whether the change in loading direction, or the magnitude of the vertical

component, depend essentially on the nature of the multidirectional loading, alternate or out of phase, which itself is governed by the wave characteristics and the geometry of the array.

In all cases, the piles fail by being pulled out from the soil, at vertical peak load not exceeding 0.5 times the monotonic vertical capacity. Such reduction cannot be only explained by cyclic friction degradation at the interface from ϕ_p to ϕ . Additional mechanisms must take place and they include (i) a reduction of the stress state around the pile from K_0 conditions to K_a conditions, as the pile is loaded in multiple directions and the soil in the vicinity moves to active state, and (ii) a reduction of the soil density in the vicinity of the pile. In all cases, the horizontal displacements prior to failure were in the range 0.05 - $0.1D$ leading to strain levels in the soil that are expected to be of the order of 5 - 10% . At these strain levels the density is reduced significantly, as observed from direct shear tests reported by Chow et al. (2019). Further analysis is required to understand how each of these factors contribute to the degradation of pile performance under multidirectional loading.

6 CONCLUSIONS

Centrifuge tests were performed to investigate the performance of piles under multidirectional loading, as relevant for anchor sharing within arrays of floating renewable energy devices (wind turbines or wave energy converters). The load paths experienced by the piles were identified from numerical hydrodynamic analyses. 3 tests are reported in this paper that illustrate the reduction in pile capacity due to multidirectional loading. In all cases, the pile fails by being pulled out vertically of the soil, while experiencing horizontal displacements, of a magnitude that was a function of the type of multidirectional loading experienced. Failure occurs at resultant vertical peak loads lower than 0.5 times the monotonic vertical capacity. This reduction of vertical capacity is likely to be due to a combination of cyclic friction degradation, change of stress state and reduction of density around the pile due to the multidirectional loading. The contribution of each of these factors, as a function of the type of multidirectional loading (alternate or out of phase) and the magnitude the cyclic vertical resultant requires further analysis.

7 ACKNOWLEDGEMENTS

The research presented in this paper was supported by the Australian Research Council Discovery Project programme DP35402000, the Lloyd's Register Foundation (LRF) Centre of Excellence in Offshore Foundation Engineering and the Western

Australian State Government via the Wave Energy Research Centre. In-situ wave and hydrodynamic data were provided by the Renewable Energy Research Group of the University of Exeter. Their contribution is gratefully acknowledged.

8 REFERENCES

- Beemer, R.D., Murali, M., Aubeny, C.P., and Biscontin, G. 2018. Use of a MEMS accelerometer to measure orientation in a geotechnical centrifuge. *International Journal of Physical Modelling in Geotechnics*. **15**(5): 253-265.
- Child, B. F. M. and Venugopal, V., 2010. Optimal configurations of wave energy device arrays. *Ocean Eng.*, **37**(16): 1402–1417.
- Chow, S., Roy, A., Herduin, M., Heins, H., King, L., Bienen, B., O’Loughlin, C.D., Gaudin, C., Cassidy, M.J. 2018. Characterisation of UWA superfine silica sand. GEO report 18844. Centre for Offshore Foundation Systems, The University of Western Australia
- Gaudin, C., O’Loughlin, C.D., Breen, J. 2018. Commissioning of a 240 g-tonne geotechnical centrifuge at the University of Western Australia. *Proceedings of the 9th International Conference on Physical Modelling in Geotechnics*, London, UK.
- Gaudin, C., White, D.J., Boylan, N., Breen, J., Brown, T.A., De Catania, S., Hortin, P. 2009. A wireless data acquisition system for centrifuge model testing. *Measurement Science and Technology*. **20**: 095709.
- Herduin, M. 2019. Multidirectional loading on shared anchors for offshore renewable energy: definition and preliminary investigation into soil behaviour and anchor performance. PhD Thesis, the University of Western Australia.
- IEA 2019. Offshore wind outlook 2019. World energy outlook special report. Technology report 2019.
- Jamiolkowski, M., Presti, D.C.F. Lo, and Manassero, M. 2003. Evaluation of relative density and shear strength of sands from CPT and DMT. *ASCE Geotechnical Special Publication*. **119**: 201–238.
- Karimirad, M., Koushan, K., Weller, S.D., Hardwick, J., Johanning, L., 2014. Applicability of offshore mooring and foundation technologies for marine renewable energy (MRE) device arrays. *Proc. 1st International Conference on Renewable Energies Offshore*, Lisbon, Portugal.
- Kost, C., Mayer, N.J., Thomsen, J., Hartmann, N., Senkpiel, C., Philipps, S., Nold, S., Lude, S., Saad, N., Schlegl, T., 2013. Levelized Cost of Electricity. PV and CPV in Comparison to Other Technologies. *Proc. 29th International Photovoltaic Solar Energy Conference*, Amsterdam, The Netherlands.
- Martinelli, L., Ruol, P., Coretelazzo, G., 2012. On mooring design of wave energy converters: The Seabreath application. *Proceedings of the 33rd International Conference on Coastal Engineering*, Santander, Spain.
- Willow, C., and Valpy, B. 2011. Wave and tidal energy in the UK, state of the industry report. *Renewable UK*.

Suction caisson response under tensile and compressional vertical cyclic loading in sand over clay

Marc Stapelfeldt¹, Jürgen Grabe¹

¹ *Institute of Geotechnical Engineering and Construction Management, Hamburg University of Technology, Germany*

Corresponding author: Marc Stapelfeldt (marc.stapelfeldt@tuhh.de)

ABSTRACT: Offshore wind turbines supported by suction caisson jackets transfer the loading to the foundation primarily through a vertical push-pull mechanism. This leads to the foundation performance under vertical cyclic loading being a critical design aspect. Recent research of suction caissons under cyclic vertical loading into tension in uniform soil profiles has revealed the complexity of the load transfer mechanisms and the importance of understanding the soil permeability and shear strength governing the in-service foundation performance. Soil stratification, with clay and sand layers, adds further complexity. Numerical modelling of the suction caisson under vertical cyclic loading is complex, challenging and the consideration of individual aspects may not necessarily be required. Simplified numerical models, once validated, can provide insights into key aspects of the load bearing behaviour. However, the identification of those aspects and the validation of a numerical model requires an experimental database that does not exist to date. The current paucity of data of suction caisson in-service performance in sand over clay under loading conditions relevant to offshore wind turbines calls for physical evidence to be gathered. This is addressed here through centrifuge tests on vertical cyclic loading, which unravel the actual impact of tensile loads below and above the recommended design capacities. The vertical cyclic loading test results indicate that not just the development of suction pressure inside the caisson foundation, but also the interplay between tension and compression have a significant effect on the overall response of suction caissons under cyclic vertical loading in sand over clay.

Keywords: Offshore Wind Turbine; Suction Caisson; Layered Soil; Cyclic Loading; Numerical Modelling; Centrifuge Modelling.

1 INTRODUCTION

Offshore wind farm locations are moving from shallow water depths towards deeper water. This development often implies sea beds characterised by clay and layered soils rather than sand. Suction caisson jackets are a suitable foundation system for offshore wind turbines (OWTs) in such conditions (Tjelta, 2015). OWT supporting jackets are typically equipped with three or four suction caissons (also called suction buckets). The aspect ratio of length L to diameter D usually ranges between $L/D = 0.5$ and $L/D = 1$. Steel suction caissons for OWTs are relatively thin-walled (Tjelta et al., 1990; Masui et al., 2001), with wall thicknesses t ranging from $t \approx D/150$ to $t \approx D/250$. OWTs are significantly lighter than most other offshore platforms. Wind and wave action transferred to the individual footings is primarily withstood by a vertical push-pull mechanism. Hence, the windward caisson is subjected to vertical cyclic loading, which might extend into tension (Bienen et al, 2018a,b).

The behaviour of suction caissons embedded in layered soil profiles under vertical cyclic loading – particularly in sand over clay (SoC) – is not fully understood. Experimental data and a numerical

model that is validated through those can provide valuable insights into the suction caisson performance. This approach is taken here. This paper aims to investigate suction caisson performance under vertical cyclic loading in SoC through complementary centrifuge tests and numerical analyses.

Investigations in sand showed that the average load has a major influence on the response under vertical cyclic load (Bienen et al, 2018a,b). Similar behaviour might be present in layered soil profiles, such as SoC. Hence, two different average loads are considered in order to provide insights into the interplay between tension and compression.

2 METHODS

2.1. Numerical simulations

The numerical simulations were performed with Abaqus/Standard 2018. Undrained caisson response is expected in SoC due to the low effective permeability of the clay main layer. This also holds for the sand part of the soil plug, because it is hydraulically encapsulated inside the caisson skirt. The free top layer is not expected to be subject to considerable soil state changes besides the frictional

interaction with the caisson skirt. Hence, undrained one-phase numerical analyses are conducted.

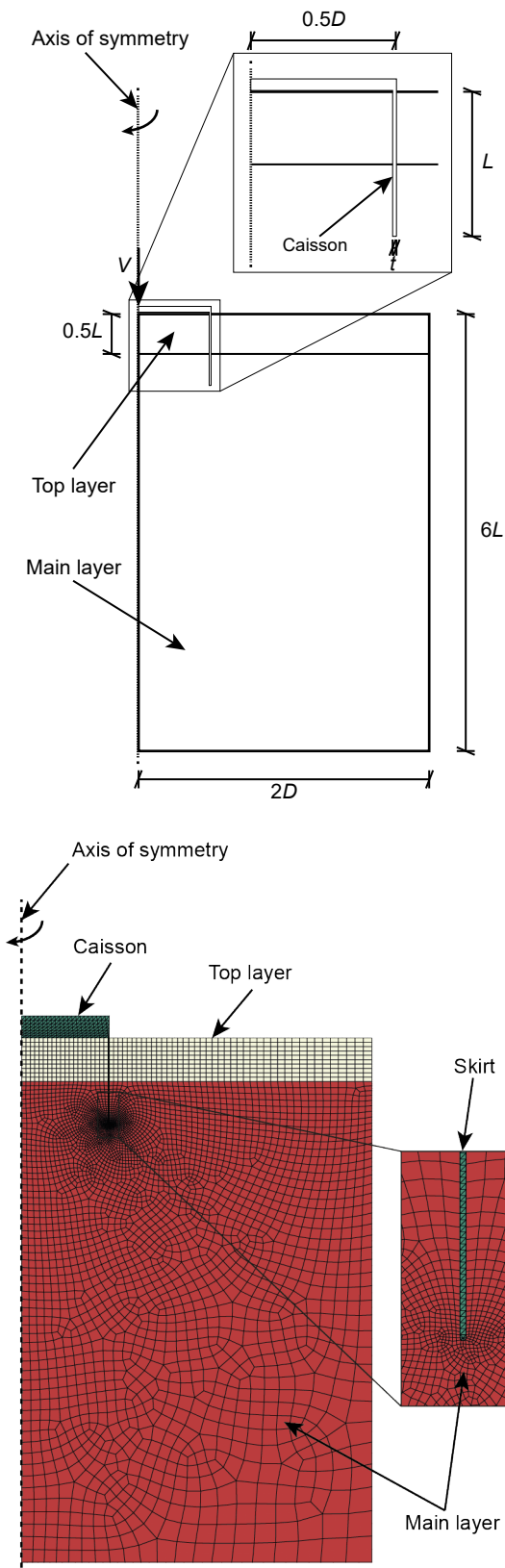


Figure 1. Dimensions (a) and discretization (b) of the numerical model utilised for FEM analyses of the suction caisson response to vertical cyclic loading in a layered soil.

The utilised model geometry is shown in Figure 1. The given dimensions were found to minimise boundary effects in the numerical simulations. The two-dimensional axisymmetric model geometry was meshed with high order rectangular elements (CAX8). The suction caisson was modelled as a rigid body meshed with triangular elements (CAX6). A half-circular shaped skirt tip was found to reduce artificial stress peaks in that area. The discretisation of the computational mesh is shown in Figure 1b.

Horizontal displacements were prevented at the axis of symmetry and outside vertical edge of the model geometry, while vertical displacements were permitted. The base featured zero vertical displacements boundary conditions. The displacements at the soil surface were free. The vertical load V was applied to the centre of the caisson (see Figure 1a).

The parameters required for the utilised constitutive models are summarised in Table 1. The top layer consists of dense fine silica sand and the kaolin clay main layer is considerably overconsolidated. The parameters found suitable for fine silica sand are determined under consideration of the laboratory test discussed in Tran (2005), Pucker et al. (2013), and Chow et al. (2018). The laboratory experiment results discussed in Qui (2012) and Mašín (2019) form the basis of the determination of the parameters for kaolin clay listed in Table 1.

Table 1. Model parameters for FEM simulations featuring silica sand and kaolin clay (Pucker et al., 2013, Chow et al., 2018).

Parameter	Unit	FSS	KC
Undrained shear strength s_u	kPa	-	25
Young's modulus E	MPa	60	1.2
Poisson's ratio ν	-	0.475	0.475
Specific weight soil γ'	kN/m ³	10.5	7.1

FSS = fine silica sand; KC = Kaolin clay

The soil-structure interaction is modelled through hard normal contact. Separation of the contact surfaces is prevented. Tangential friction is modelled by means of the Coulomb friction model utilising a frictional coefficient of $\mu_s = 0.15$ in sand and $\mu_c = 0.4$ in clay, a shear stress limit of $\tau_{max,s} = 12$ kPa and $\tau_{max,c} = 20$ kPa and an elastic slip limit of $\gamma_i = 0.005$.

The simulations are conducted according to the following procedure: First, the vertical and horizontal stresses are initialised by applying a K_0 initial condition. A minimum load is applied at the caisson in order to minimise the effect on the K_0 soil state. The installation process is neglected. Load

controlled caisson cyclic loading commences once stable K_0 conditions are reached. The loading amplitudes are given in Table 2 (see section 2.2.3).

2.2. Centrifuge tests

The experiments are performed at 100g in the Acutronic Model 661 centrifuge (Randolph et al., 1991; Randolph and Gaudin, 2017) at the University of Western Australia. The presented test results from part from a comprehensive series of centrifuge test discussed in Stapelfeldt et al. (2020b).

2.2.1 Soil sample and fluid preparation

Overconsolidated stiff clay and dense sand were used in the centrifuge tests. The layered soil sample with a thickness of the top layer of 20 mm was prepared to create realistic conditions for sites that allow the utilisation of suction caisson foundations. The clay was prepared from slurry at a water content of approximately 120 %, mixed under vacuum, filled in a strong box and consolidated in a hydraulic press under a maximum vertical pressure of $\sigma_v = 350$ kPa. The height of this clay layer was approximately 140 mm.

The sand top layer was prepared by pluviation of dry sand into the strongbox from a height of approximately 1.2 m by means of an automatic pluviator. The sand layer was vacuum levelled to a target total sample height of 160 mm above the base of the strongbox. The sand layer was saturated from the layer boundary through tubes – one located in each corner of the strongbox. A total sample height of at least $4L$ was targeted in order to minimise boundary effects (Tran and Randolph, 2008). The sand unit weight was determined from weight and volume measurements. The sand relative density was thus determined to be $D_r \approx 83$ %.

Under consideration of scaling laws governing the suction caisson response, the viscosity η of the sand top layer pore fluid was increased from approximately $\eta_w = 1$ cSt for water to a target value of $\eta = 100$ cSt (Taylor, 2011). Hereby an effective permeability of the sand layer – i. e. $k_f \approx 1 \cdot 10^{-4}$ m/s – at 100g was targeted, which is representative of typical North Sea sands (Tan and Scott, 1985). The viscosity was increased through the addition of methyl cellulose ether (DOW, 2002). The targeted pore fluid viscosity is confirmed by measurements. The clay layer was water saturated.

The targeted soil sample characteristics were confirmed through in-flight cone penetration and T-bar tests conducted before and after the suction caisson tests. A T-bar test was also conducted immediately after the clay consolidation in order to verify the targeted undrained shear strength of $s_u \approx 25$ kPa. The centrifuge soil sample

characterisation test results are presented and discussed in detail in Stapelfeldt et al. (2020b).

2.2.2 Caisson model, test arrangement and instrumentation

The tests were performed with the same centrifuge arrangement as utilised by Stapelfeldt et al. (2020a,b). The anodised aluminium model caisson has a diameter of $D = 80$ mm and a skirt length of $L = 40$ mm, which when tested at 100g represents a diameter $D = 8$ m and a skirt length of $L = 4$ m in prototype scale. The skirt wall thickness is $t = 0.5$ mm, which corresponds to a prototype wall thickness of $t = 50$ mm.

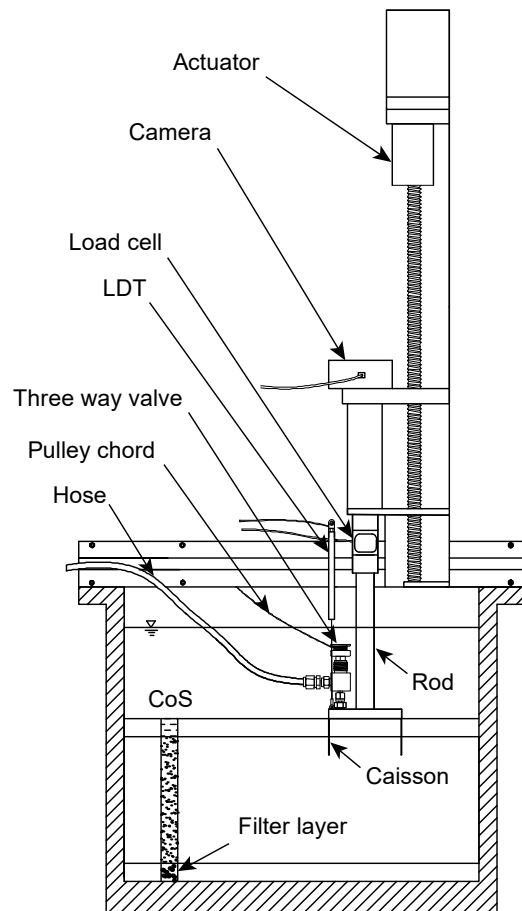


Figure 2. Centrifuge test set-up for cyclic loading model test in layered soil.

The model caisson has been equipped with two total pressure transducers (TTP) – one at the lid invert and another one at the top of the lid, and a pore pressure transducer (PPT) at the lid invert. The caisson model shown in Fig. 2 is connected to a load cell with a maximum capacity of 3 kN by means of a rigid rod. This assembly is carried by an actuator, which is mounted on top of the strongbox. The three-way valve on the caisson lid was operated by an electric winch and was able to vent to ambient, to connect the caisson to the syringe pump (House,

2002) and to be sealed. The fluid table was at least $h_w = 100$ mm above the soil surface to ensure that the model caisson including the three-way valve were submerged to minimise changes in buoyancy during the installation. The self-weight and the cyclic loading of the model caisson were applied with the actuator, which was controlled through a feedback loop from the load cell. The displacement of the caisson was recorded by means of a linear displacement transducer (LDT) that was independently mounted.

2.2.3 Testing procedure

The model caisson was installed in-flight through self-weight penetration and subsequent suction installation. The self-weight was applied with the actuator. The syringe pump provided suction pressure through the three-way-valve. Once the installation was completed, a static vertical pressure of $V/A = 116$ kPa representing the full self-weight of the OWT was applied. This load was maintained until the internal excess pore pressure dissipated, which was monitored by the pore pressure transducer at the lid invert. Unloading to the low magnitude compressive average load (see Table 2) including another waiting period simulated a reduction of the vertical load on the critical windward caisson due to wind and wave loading, before the cyclic loading amplitude was applied.

Table 2. Load cases (LCs) and specifications of the four cyclic loading sequences (LSQs).

LSQ	Cycles	Load LC 20	Load LC 21
-	n	V/A	V/A
-	-	kPa	kPa
1	1000 (18)	8 ± 16	32 ± 24
2	100 (5)	8 ± 30	32 ± 54
3	10 (3)	8 ± 60	32 ± 84
4	1 (1)	8 ± 90	32 ± 114

Number of cycles for FEM analysis in brackets

3 RESULTS AND DISCUSSION

The experimental and numerical results are presented in non-dimensional form, unless stated otherwise. Positive values indicate compression and downward displacements, whereas negative values represent tension and upward displacements.

3.1. Numerical simulations

The presented numerical model is utilised in order to investigate the response of a suction caisson foundation subjected to vertical cyclic loading. The two applied load cases (LCs) featured cyclic vertical loading to the same minimum vertical load, which

is tensile in each cycle, except the first loading sequence (LSQ 1) of LC 21. The average stresses differ: An increased compressive average stress is applied in LC 21. The calculated displacement response of the suction caisson model is presented in Figure 3.

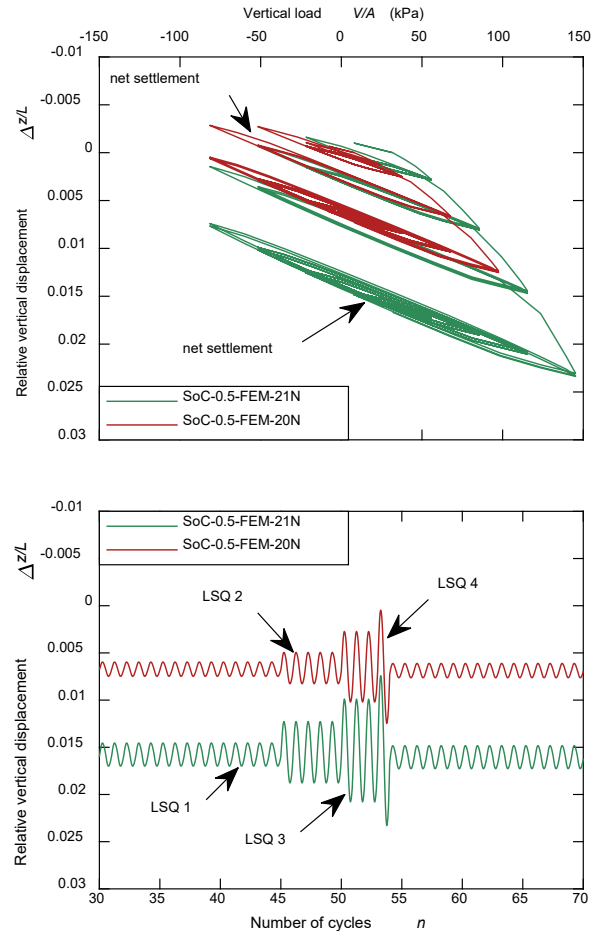


Figure 3 Calculated normalised vertical displacements during vertical cyclic loading.

The calculated vertical displacements show net settlements in both LCs. The shift of the average load towards compression yields increased net settlements in LC 21. The calculated net settlements always occur during the first cycle of LSQ within the first loading package –i. e. every time a new maximum compressive load is reached. Figure 3b indicates that almost elastic behaviour results from the application of the second loading package. This is consistent due to the utilisation of the elastic-plastic constitutive model, which is a fundamental simplification. Hence, a more advanced constitutive model is required. However, determining a suitable constitutive model requires fundamental knowledge of the underlying load transfer mechanisms, which currently does not exist. Hence, the performance of experiments is required in order to evaluate and improve the validity of numerical simulations.

3.2. Centrifuge tests

The centrifuge results presented in Figure 4 reveal that LC 21 results in increased relative vertical displacement amplitudes compared to LC 20. This is consistent, because larger cyclic loading amplitudes are required to reach the same tensile peak load starting from an increased compressive average load. Furthermore, the results obtained from test SoC-0.5-150J-21 visualise the occurrence of net settlement in response to load sequences that feature significant excursions into tension. The results of test SoC-0.5-125SI-20 show minor net uplift. This holds for each of the three loading packages evaluated in Figure 4a.

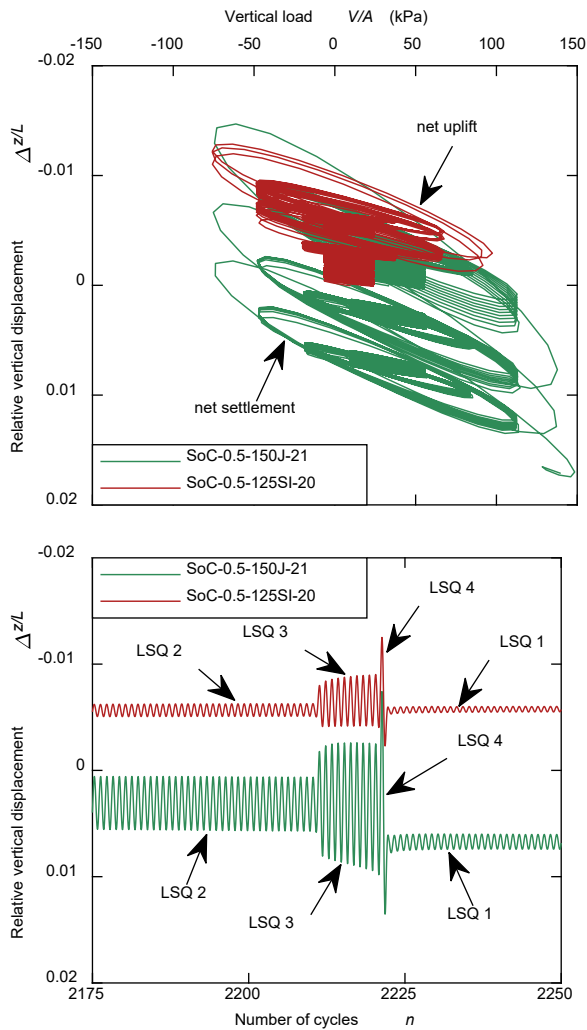


Figure 4 History of the normalised relative vertical displacements during three cyclic loading packages (a) and during load package two (b) in centrifuge tests.

The data shown in Figure 5 indicates that compressive loads are transferred by the skirt friction, tip resistance and the lid similarly in LC 20 and LC 21. Figure 5 also shows that the estimated sum of the skirt and the tip resistance $(V/A)_{S+T} \approx 74$ kPa is arguably fully mobilised in

LC 21. Consequently, considerable net settlements result instead of minimal net uplift, which occurs in test LC 20 (see Figure 5b).

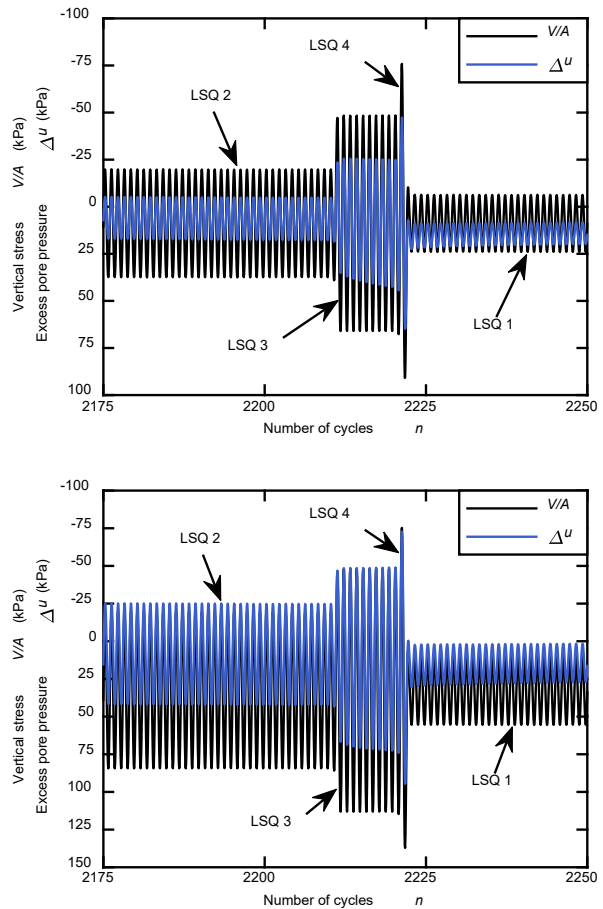


Figure 5 History of vertical stresses and excess pore pressures at the lid invert during SoC-0.5-125SI-20 (a) and SoC-0.5-150J-21 (b).

The transfer mechanisms in tension differs in the centrifuge experiments: Tensile loads are completely transferred through suction pressure at the lid invert in LC 21 (Figure 5a). In contrast, tensile loads are carried by a combination of skirt friction and suction pressure in test SoC-0.5-125SI-20 (Figure 5b). Excess pore pressures, which are present in compression, dissipate before tensile loading commences at an increased average vertical stress in LC 21. Internal suction pressure develops immediately – i. e. before the skirt friction is mobilised – and provides sufficient resistance. Excess pore pressures only partially dissipate before tensile loading is reached, if low compressive loads are present in LC 20. Hence, internal suction pressure mobilisation is postponed in this case and a considerable portion of the tensile load is transferred by the skirt resistance. The results presented in Figure 4b indicate that this leads to increased uplift, if the applied tensile load exceeds the skirt resistance considerably in LSQ 3 and 4.

Thus, the presented results suggest that the average compressive load determines whether cyclic loading with similar excursions into tension leads to net uplift or net settlement.

3.3. Evaluation of the numerical analyses

The comparison between Figure 3 and 4 shows that the calculated displacements amplitudes are within a similar magnitude with the centrifuge test results. However, the net displacement response differs considerably: The numerical model yields plastic and therefore irreversible soil deformations as soon as the shear strength is exceeded locally. A recovery of the soil shear strength or a certain residual soil strength is not considered in the utilised constitutive model. This is certainly different from the behaviour observed in the centrifuge experiments: Effects resulting from repetitive loading occurring during LSQ 3 (Figure 4b) are not considered. These effects are considered in advanced constitutive models – e. g. the ISA plasticity-based model for clay discussed in Fuentes et al. (2018).

The experimental results show an accumulation of displacements that is accompanied by an increasing amplitude, which appears to reach a certain maximum in tension (LC 20), but continues until the end of LSQ 3 in compression (LC 21). Hence, the experimental results indicate that the utilisation of an advanced constitutive model like the ISA plasticity-based model for clay is required in order to improve numerical investigations. However, the ISA plasticity-based model for clay is still under development and remains unavailable for further investigations on the response of suction caissons subjected to vertical cyclic loading.

4 CONCLUSIONS

Numerical investigation of suction caissons embedded in sand over clay and the performance of centrifuge tests featuring vertical cyclic loading into tension support the following findings:

Numerical methods are capable of the simulation of suction caissons subjected to vertical cyclic loading in general. The comparison to experimental results shows that advanced constitutive models that include hardening and account for cyclic loading effects are required in order to obtain appropriate results.

The pivotal mechanisms underlying the vertical cyclic load transfer mechanisms in sand over clay are pointed out through the centrifuge test results. Hence, the presented experiments form a basis for future developments of numerical models.

The centrifuge test results furthermore show that the average compressive load determines whether

net settlements or net uplift results from vertical cyclic loading featuring significant excursions into tension. This is crucial for the in-service performance of offshore wind turbines with low magnitude compressive loading determining the response of the windward caisson foundation.

5 ACKNOWLEDGEMENTS

The centrifuge experiments were performed at the National Geotechnical Centrifuge Facility (NGCF) in Perth, Western Australia, and in cooperation between the Hamburg University of Technology (TUHH) and the Centre for Offshore Foundation Systems (COFS) at the University of Western Australia (UWA).

We acknowledge the support from the Deutsche Forschungsgemeinschaft (DFG) for our research project GR 1024/26-2 “Sauginstallation Maritimer Strukturen” (SIMS). This work forms part of the activities of the Centre for Offshore Foundation Systems (COFS), which is currently supported as a Centre of Excellence by the Lloyd’s Register Foundation. Lloyd’s Register Foundation helps to protect life and property by supporting engineering-related education, public engagement and the application of research. This support is gratefully acknowledged.

6 REFERENCES

- Bienen, B., Klinkvort, R.T., O’Loughlin, C.D., Zhu, F. and Byrne, B.W., 2018a. Suction caissons in dense sand, part I: Installation, limiting capacity and drainage. *Géotechnique*, **68**(11): 937-952. doi:10.1680/jgeot.16.P.281.
- Bienen, B., Klinkvort, R.T., O’Loughlin, C.D., Zhu, F. and Byrne, B.W., 2018b. Suction caissons in dense sand, part II: Vertical cyclic loading into tension. *Géotechnique* **68**(11), 953-967. doi:10.1680/jgeot.16.P.282.
- Chow, S.H., O’Loughlin, C.D., Gaudin, C., and Lieng, J.T., 2018. Drained monotonic and cyclic capacity of a dynamically installed plate anchor in sand. *Ocean Engineering* **148**, pp. 588-601. doi:10.1016/j.oceaneng.2017.11.051.
- DOW, 2002. Methocel Cellulose Ethers: Technical handbook, United States of America.
- Fuentes, W., Tafili, M., and Triantafyllidis, T., 2018. An ISA-plasticity-based model for viscous and non-viscous clays. In: *Acta Geotechnica* **13.2**, p. 367-386. doi:10.1007/s11440-017-0548-y.
- House, A.R., 2002. Suction Caisson Foundations for Buoyant Offshore Facilities, PhD thesis, The University of Western Australia, Perth, Australia.

- Masín, D., 2019. Modelling of Soil Behaviour with Hypoplasticity: Another Approach to Soil Constitutive Modelling, Springer Series in Geomechanics and Geoengineering, Springer International Publishing. doi:10.1007/978-3-030-03976-9.
- Masui, N., Yoneda, H., Zenda, Y., Ito, M., Iida, Y. and Hermstad, J., 2001. Installation of offshore concrete structure with skirt foundation. In Proceedings of the 11th International on Offshore and Polar Engineering Conference, pp. 626-630.
- Pucker, T., Bienen, B., and Henke, S., 2013. CPT based prediction of foundation penetration in siliceous sand. *Applied Ocean Research*, 41, pp. 9-18, doi:10.1016/j.apor.2013.01.005.
- Qui, G., 2012. Coupled Eulerian Lagrangian Simulations of Selected Soil-Structure Interaction Problems, PhD thesis, Hamburg University of Technology, Hamburg, Germany.
- Stapelfeldt, M., Bienen, B. and Grabe, J. 2020a. The influence of the drainage regime on the installation and the response to vertical cyclic loading of suction caissons in dense sand". *Ocean Engineering* 0(0), pp. 1-29. (under review).
- Stapelfeldt, M., Bienen, B. and Grabe, J. 2020b. The influence low permeability layers on the installation and the response to vertical cyclic loading of suction caissons. *Journal of Geotechnical and Geoenvironmental Engineering* 0(0), pp. 1-20. (under review).
- Tan, T.S. and Scott, R.F., 1985. Centrifuge scaling considerations for fluid-particle systems: Centrifuge scaling considerations for fluid-particle systems. *Géotechnique* 35(4), 461-470. doi:10.1680/geot.1985.35.4.461.
- Taylor, R.N., 2011. *Geotechnical centrifuge technology*. Taylor & Francis, London.
- Tjelta, T.I., 2015. The suction foundation technology, Meyer, V. (Ed.), In *Frontiers in Offshore Geotechnics III*. Balkema, pp. 85-93. doi:10.1201/b18442-6.
- Tjelta, T.I., Aas, P.M., Hermstad, J., and Andenaes, E. 1990. The skirt piled Gullfaks C platform installation, In *Offshore Technology Conference 1990*, pp. 453-462. doi:10.4043/6473-MS.
- Tran, M.N., 2005. Installation of Suction Caissons in Dense Sand and the Influence of Silt and Cemented Layers, PhD thesis, The University of Sydney, Sydney, Australia.
- Tran, M.N. and Randolph, M.F., 2008. Variation of suction pressure during caisson installation in sand. *Géotechnique* 58(1), 1-11. doi:10.1680/geot.2008.58.1.1.

Centrifuge Modelling of Suction Caissons Subjected to Cyclic Loading in Tension

Yuen Zhang¹, Kamaleshwar Sudhakaran^{1,2}, Amin Askarinejad¹

¹ Faculty of Civil Engineering and Geosciences, Delft University of Technology, the Netherlands

² Heerema Marine Contractors, the Netherlands

Corresponding author: Amin Askarinejad (A.Askarinejad@tudelft.nl)

ABSTRACT: Wind is a major source of renewable energy in Northern Europe. Suction caissons are increasingly considered as an alternative foundation solution for offshore wind turbines (OWT) in the last two decades because of various advantages such as low installation noise, low cost, ease of installation and removal as well as high bearing capacity under extreme environmental conditions (Hung et al., 2018; Jin et al., 2012). For a jacket structure installed on three suction caissons, the response of the foundation under cyclic vertical loading in tension is of primary interest in geotechnical design. In practice, horizontal loads induced by wind and waves are relatively large in comparison to the self-weight of the jacket structure. This leads to relatively large overturning moments and large pull-out loads on the windward leg of the tripod jacket structure. During this study, a series of centrifuge tests has been conducted to investigate the response of suction caissons to two types of vertical cyclic loading, i.e. one-way and two-way asymmetric loading. Test results in terms of cumulative settlement response of the caisson along with damping and stiffness behaviour are analysed.

Keywords: Suction Caissons; Cyclic Loading; Storm Loading; Unloading Stiffness.

1 INTRODUCTION

As countries around the world are in a clean energy race, various renewable energy sources are harvested to meet the energy needs. In Western Europe, wind is the primary source of renewable energy. To meet the energy demand, higher capacity wind turbines are being installed in deeper waters. In deep waters, monopile foundations are uneconomic and ineffective due to its inability to withstand large overturning moments. Thus, multi-caisson foundations are preferred in deeper waters (Bo Ibsen et al., 2005).

Typically jacket or tripod structures are preferred as multi-footing foundation and these foundations are supported by either piles or suction caissons. Suction caissons are preferred due to the ease of installation and removal. Installation of suction caisson takes place in two phases. First phase is the self-weight penetration phase (SWP), where the caisson is allowed to penetrate the soil under its own weight. In the second phase, penetration is achieved using suction, which creates a differential force on caisson lid resulting in downward movement. During the second phase, seepage flow occurs, and this helps in reducing the soil resistance at the tip of the caisson (Houlsby and Byrne, 2005). Prediction models are also available to predict the self-weight penetration depth and suction required for penetration. Different prediction methods use different set of parameters for the calculation. Senders and Randolph method uses the cone penetration resistance data to predict the suction required for installation (Senders &

Randolph, 2009). It is a straight forward and accurate method as very few parameters are needed for the calculation. Houlsby and Byrne (Houlsby and Byrne, 2005) prediction model follows a beta approach and is used widely when CPT data for the site or sample is not available. However, estimation of key input parameters such as N_q , N_γ and pore pressure factor creates uncertainty in the calculation for prediction

Suction caissons had been used in the foundation for oil and gas platforms in deep waters due to their economic advantages over traditional pile driving in deep waters (Houlsby and Byrne, 2005). Due to the very high vertical load provided by the platform, overturning moments are negligible in the oil rigs. In case of an offshore wind turbine (OWT), since the structures are relatively light, horizontal loads and overturning moments are larger than the vertical loads (Houlsby and Byrne, 2000). The large overturning moments are balanced using a ‘push-pull’ system (**Figure 1**), where when the windward caisson experiences tension, the movement is compensated by the other two leeward caissons. Due to the strict permanent rotational limit of 0.25° in serviceability conditions for OWTs, ‘pull behaviour’ or tensile capacity plays a major role in the design of an OWT (Peire et al., 2009).

Various investigations have been done in laboratory conditions and enhanced acceleration levels in centrifuge to study the tensile response of suction caissons (Kelly, Houlsby, & Byrne, 2006; Kim, Lee, & Kim, 2016). Response of suction

caissons under cyclic loading in sand depends mainly on the drainage conditions. Drainage conditions depend on several factors such as density, permeability of sand and frequency of the applied cyclic loads. In an offshore scenario, a partially drained condition is usually witnessed. Thus, a wide knowledge on the settlement and stiffness response of caisson under various drainage conditions is necessary, as OWTs are designed as a soft-stiff system. Bienen et al. (Bienen et al., 2018a) have conducted several tests in almost undrained condition in sand. They observed that foundation stiffness changed when the loading changed from compression to tension, which indicates that serviceability under tensile loading is vital for the design of foundation. Undrained behaviour will only occur locally or when the frequency of the load cycle is very high.

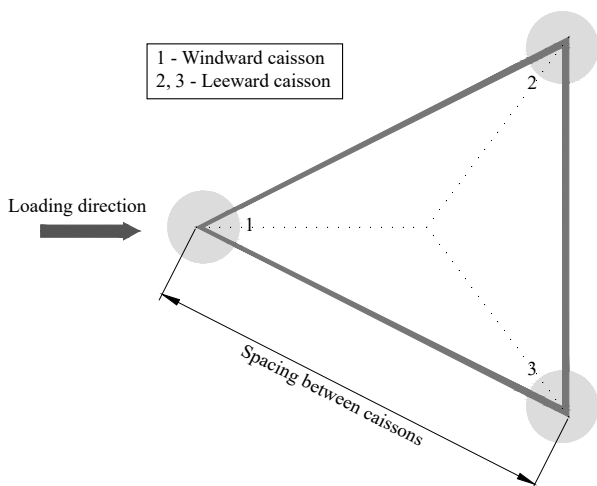


Figure 1. 'Push-Pull' behaviour of offshore tripod foundation

In this paper, installation of caisson is done at laboratory conditions and effect of installation method is studied. Extraction of caisson is also done in a very slow manner to obtain the drained tensile capacity of the caisson. Loading scenario is designed based on the drained tensile capacity of the caisson. The main goal of this paper is to study the drained response of suction caisson under one-way and two-way asymmetric loading.

2 EXPERIMENTAL METHODS

All the tests are done in the geo-centrifuge at Delft University of Technology. Installation of suction caisson is made possible using an apparatus developed in-house which constitutes of a strong box, reservoir, pressure sensors and appliances for the application of suction.

2.1 Model suction caisson

Cyclic loading tests are done at an acceleration level of 100g. To study the worst-case scenario of a caisson in tension, an embedment ratio (L/D) of 0.5 is used, where diameter of model caisson (D) is 60 mm and skirt length (L) is 30 mm equivalent to prototype diameter of 6 m and skirt length of 3 m. The model caisson has a thickness of 1 mm (skirt and lid) and is fabricated out of brass. A fine filter layer with a thickness of 0.5 mm is placed inside the caisson beneath the lid to avoid damage to the pore water pressure sensor and to prevent sand outflow during suction application.

Both phases of the installation of suction caissons (SWP and SAP) are simulated in these tests. The caisson lid has two openings for water outlet during each phase. The SWP outlet is closed after self-weight installation is completed and the SAP outlet is connected to the pump or reservoir to facilitate suction during the main phase of installation using suction application. Two pore pressure transducers are mounted on top of the caisson lid to measure the water pressure both outside and inside the caisson (Figure 2).

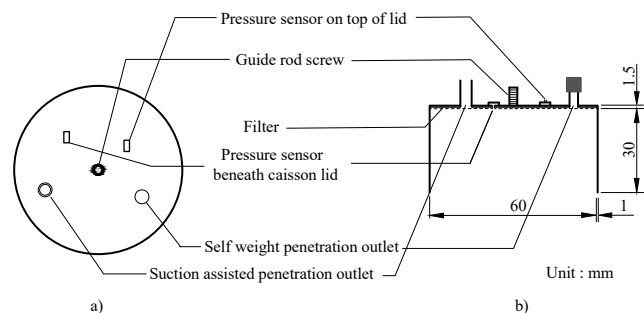


Figure 2. Schematics of instrumented suction caisson a) Top view b) Side view

2.2 Installation of suction caissons

Two setups are designed for the application of suction during installation. The first setup uses gravity flow to apply suction during suction assisted penetration phase (Figure 3). Gravity flow is established through the head difference between strong box (h_1) and the reservoir (h_2). Using a pressure sensor at the bottom of the reservoir, flow rate can be measured. A very low flow rate of 7.52 ml/sec is attained during this set-up. All the pipe connections are kept beneath the water level in the strong box to avoid air bubbles. Flow is controlled using a pneumatic valve which is operated remotely.

In the second installation setup, a gear wheel pump is used to apply the necessary suction (Figure 4). Flow rate in this setup is controlled with the help of a needle valve manually.

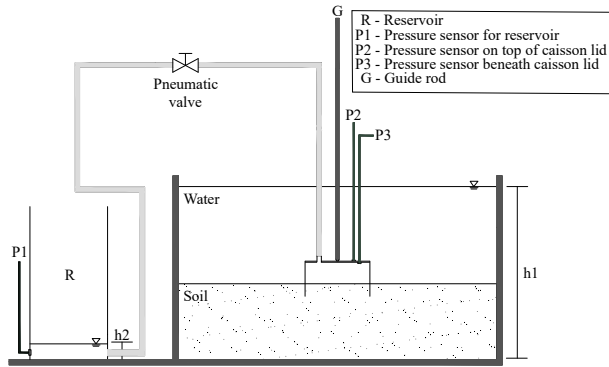


Figure 3. Setup for installation using gravity flow

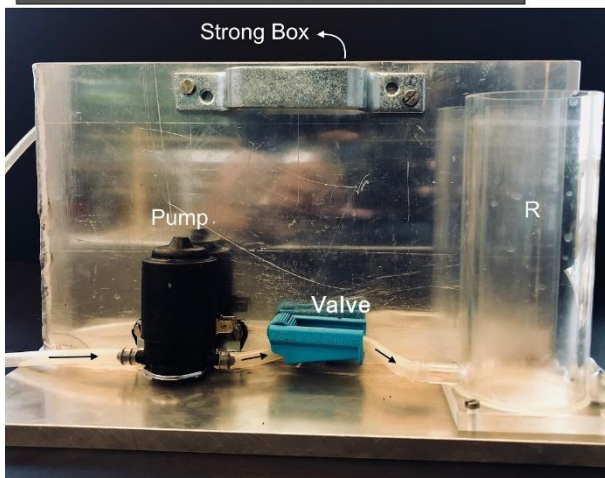
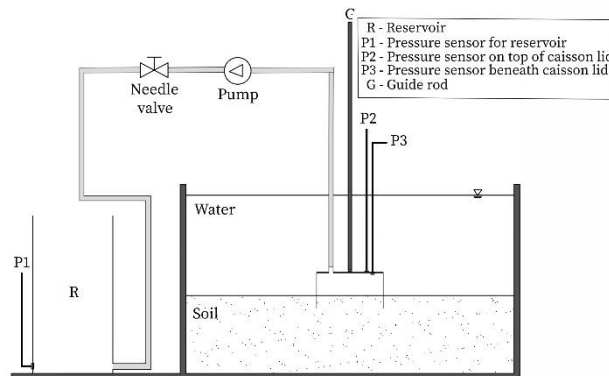


Figure 4. Setup for installation using pump

In order to avoid tilting of suction caisson during installation, a guiding system is introduced for both setups. It comprised of a guide rod and a few guide screws. Guide rod is a cylindrical steel rod connected to the caisson. Strain gauges are mounted on the actuator to measure the load applied during cyclic loading and extraction phase. The vertical displacement of caisson during installation and cyclic loading tests are measured using a linear variable displacement transducer (LVDT), which is connected to the other end of guide rod.

2.3 Soil description and sample preparation

Medium sized silica sand is used to in this research. Geotechnical properties of silica sand types are obtained from laboratory tests (Table 1). Soil profile characteristic is illustrated (Figure 5).

Table 1. Properties of silica sand (De Jager et al., 2017)

Parameter	Silica sand
Maximum void ratio	0.86
Minimum void ratio	0.625
c_u	1.38
D_{50}	0.39 mm
c_c	1.05
Friction angle (ϕ_{cv})	34.1°
Cohesion	0 kPa
Permeability	8.41E-4 m/sec
Specific Gravity (-)	2.65

In this paper, de-aired water is used as a pore fluid for preparing the samples in order to study an almost drained behaviour of sand. Homogeneous sand samples are prepared using dry pluviation technique. First, dry silica sand is pluviated into the strong box filled with water, and vibration is applied during this process to obtain a dense sample. Once the sand reached a depth of 20 mm, further densification is done by dropping the sample onto the floor from a height of 5 mm. This process is repeated till the desired sample height is achieved. After the desired height is reached, vibration is applied for a period of 15 minutes. This created a sample with a relative density of $75 \pm 2\%$.

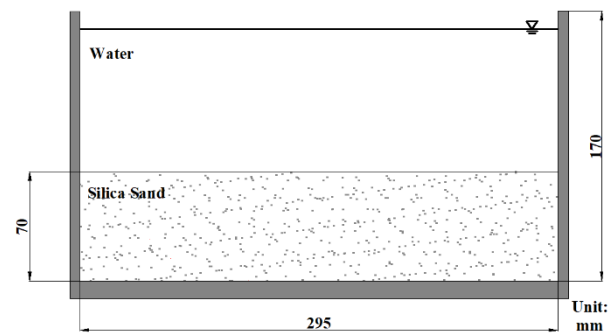


Figure 5. Soil profile characteristic in homogeneous sand

2.4. Test procedure

For all the tests, installation of suction caisson is conducted at 1g laboratory conditions. The installation is followed by cyclic loading tests or extraction tests which are performed at 100g. A detailed procedure of the entire process is given below:

- Saturated sand sample prepared in the strong box is placed in the centrifuge carrier which is fitted with a loading actuator.

Table 2. Overview of all the centrifuge cyclic loading tests

Test mode	Soil type	Average vertical load (kN)	Max. compressive load (kN)	Max. tensile load (kN)	Initial cycle No.	Final cycle No.	Load frequency (at model scale)
One-way	Homogeneous	250	500	0	0	310	0.028
Two-way	Homogeneous	-100	500	-700	0	150	
		-175	500	-850	151	250	
		-300	500	-1100	251	310	

(b) Caisson is slowly and completely submerged into the de-aired water in a diagonal manner to get rid of any air bubbles underneath the caisson lid. The SWP valve is open during this process. Caisson is then fixed to the guide rod before placing it gently on the soil surface.

(c) Using the loading actuator, self-weight installation is done to a depth of 10 mm using the actuator with a displacement rate of 0.05 mm/sec. During this phase, the SWP outlet is kept open. Once self-weight installation is done, SWP outlet is sealed.

(d) Suction assisted penetration is conducted by applying suction either using a pump or with the help of gravity flow up to a depth that the inner side of caisson lid came in contact with the soil surface. This is realised when there is a sudden spike in the pressure sensor reading underneath the caisson lid and no displacement in LVDT is recorded.

(e) Once installation is complete, centrifuge is spun to 100g, and cyclic loads are applied in a load-controlled manner. Maximum and minimum amplitudes, along with the number of cycles are pre-designed.

(f) Extraction of the caisson is also done at 100g after all the tests using the loading actuator. It is performed at a very slow rate of 0.001 mm/sec to determine the drained tensile capacity of the caisson.

A very low frequency of 0.028 Hz (at model scale) is used in this research for all the tests. This led to the drainage conditions being predominantly drained, which is determined using pore pressure measurements beneath the caisson. Drained tensile capacity of almost 1700 kN in prototype scale is obtained from all the extraction tests.

Compressive load amplitude is fixed based on the buckling capacity of the guide rod, using which load is applied on the caisson. Since compressive loads are not the main concern in this paper, higher compressive loads are not used and 500 kN is fixed as maximum compressive amplitude in one-way

compressive loading and two-way asymmetric storm loading. Bienen et al. observed that significant uplift of the caisson is witnessed when tensile loads exceed 30~50% of the drained tensile capacity (Bienen et al., 2018b). Thus, 30% of the drained tensile capacity (500 kN) is fixed as maximum tensile amplitude in serviceability limit state. For two-way asymmetric storm loading, tensile loads of more than 50% of the drained tensile capacity is used. Details of each test and amplitudes in prototype scale are provided (Table 2). The loading history curve is presented in Figure .

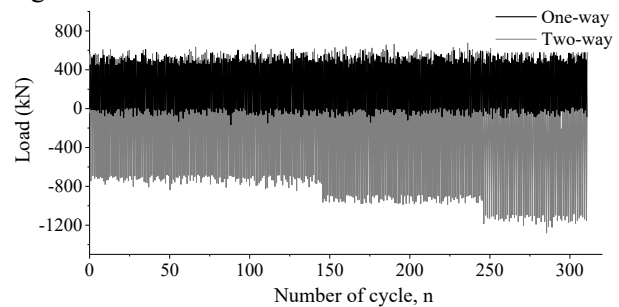


Figure 6. Loading history corresponding to cyclic load packets

3 RESULTS AND DISCUSSION

3.1. Installation response

In offshore suction caisson installation, a pump is always used for pumping water out of the caisson. In laboratory conditions, various methods are available for the application of suction required for installation. Figure 6 compares the results obtained from installation done using pump and gravity flow. Although the overall flow rate of gravity flow is low, initial flow rate in gravity flow is 25.17 ml/sec, which is higher than the rate obtained in slow installation using pump. Thus, suction required for the onset of seepage is higher in gravity flow than the suction required in slow installation. Therefore, as in the previous case, required suction increases with increase in penetration depth. Thus, it can be concluded that the method of suction does not affect the installation process as long as the necessary suction is applied.

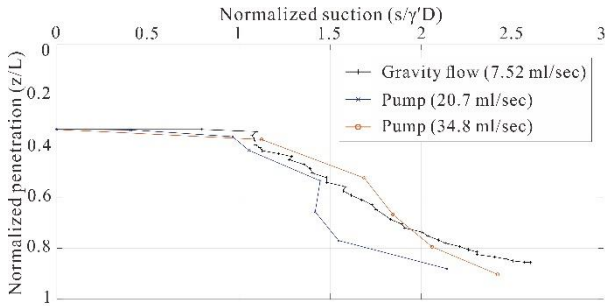


Figure 6. Normalized suction pressure acquired against the normalized depth for the two installation methods

3.2. Vertical displacement

Under one-way compressive loading, no significant settlement of the caisson is witnessed as the compressive load applied was much smaller compared to the bearing capacity of the foundation (for this case the estimate is in excess of 1.5 MPa). Under two-way asymmetric loading, compressive amplitude load is kept constant at 500 kN and the tensile load amplitude is increased. When tensile loads are applied to the caisson, resistance to the uplift of caisson is generated by the internal and external skin friction. Uplift of caisson causes shearing of sand at the caisson-sand interface, which further leads to loosening or restructuring of sand. Thus, in the next compressive cycle, significant settlement of caisson is witnessed. When the maximum tensile load is less than or equal to 50% of the drained tensile capacity (850 kN), caisson uplifted up to 10 mm. Whereas, when the tensile load exceeds 50% of the drained tensile capacity (1100 kN), larger uplift of caisson is witnessed, and the uplift increases by a factor of 2 (Figure 8). In all the results, positive denotes settlement and negative denotes uplift of the caisson.

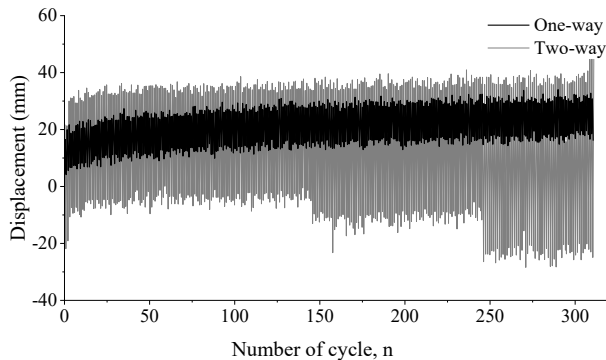


Figure 8. Displacement behaviour under cyclic load packets

3.3. Unloading stiffness

The unloading stiffness is by obtaining a slope between the maximum load point of the previous cycle and the minimum load point of the next cycle as shown in Figure 9.

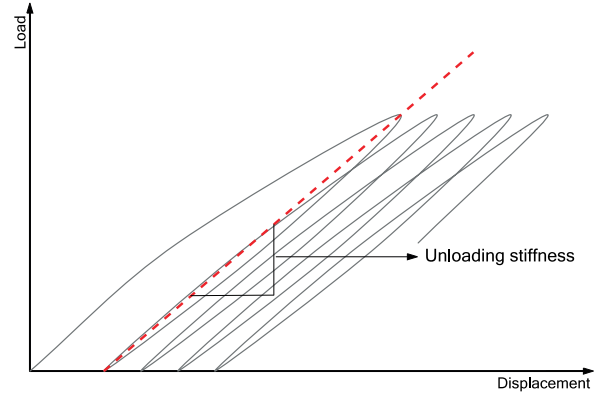


Figure 9. Load-displacement curves for the definition of unloading stiffness

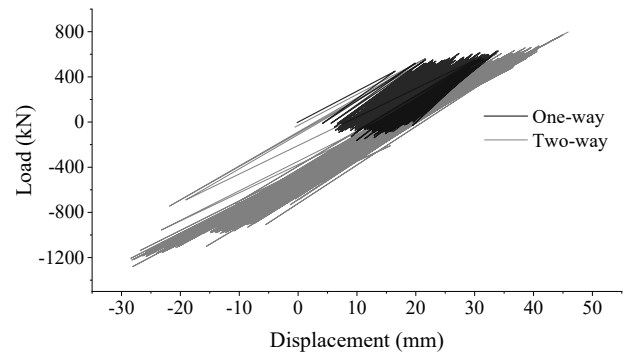


Figure 10. Displacement behaviour under cyclic loading (prototype scale)

The normalized stiffness of the caisson is obtained as shown in Figure 11. K_1 is the reference unloading stiffness for the first loading circle, and K_u is the unloading stiffness for each loading circle. For one-way compressive loading, the unloading stiffness remains constant during the entire loading duration. However, for two-way asymmetric loading, the unloading stiffness decreases with a decreasing average load in general. Within each cyclic amplitude packet, there is a slight increase in the unloading stiffness. When the average load decreases, the stiffness behaviour shifts to a lower magnitude instantly and remains constant or shows a slight increase in that packet. It can be noted that, at 250 cycles, there is a tremendous drop in the stiffness. This is attributed to the introduction of tensile load which is higher than 50% of the drained tensile capacity.

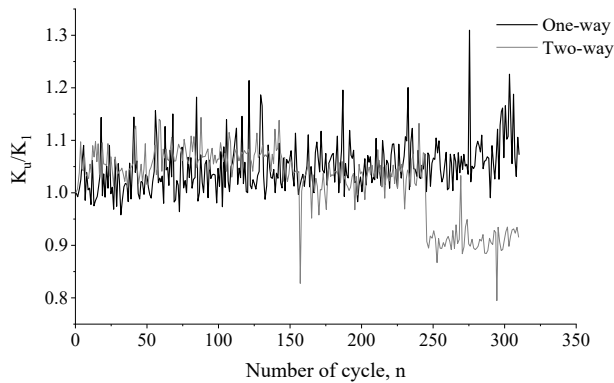


Figure 11. Unloading stiffness behaviour under cyclic loading

4 CONCLUSIONS

The results of an experimental study on cyclic loading of suction caisson foundations in homogenous sand have been described. The main results can be summarised as follows:

(a) Although suction installation in a real scenario is done only using a pump, various methods are available for the application of suction at laboratory scale. It is noted that change in the installation method has no significant effect on the installation process, as long as sufficient flow rate is obtained.

(b) Tensile loads lead to an increase in the settlement of the suction caisson compared to the settlement under one-way compressive load. Also, unloading stiffness decreases with a decreasing average load and further remains either constant or increased slightly throughout each cyclic load packet.

(c) Significant uplift of caisson is witnessed when the tensile load amplitude equals to 50% of the drained tensile capacity after which, double the amount of uplift displacement is observed when tensile load is larger than 50% of the tensile capacity. Stiffness of the caisson instantly decreased with increasing tensile load.

(d) To understand the role of pore pressure in the response of the foundation, further centrifuge tests can be done with samples prepared using viscous fluid to study the undrained or partially drained behaviour of sand.

5 ACKNOWLEDGEMENTS

This work is funded by the Section of Geo-Engineering, Delft University of Technology. One

author has been funded by the China Scholarship Council (CSC).

6 REFERENCES

- Bienen, B., Klinkvort, R.T., O’Loughlin, C.D., Zhu, F., Byrne, B.W., 2018a. Suction caissons in dense sand, part I: Installation, limiting capacity and drainage. *Geotechnique* **68**, 937–952. <https://doi.org/10.1680/jgeot.16.P.281>
- Bienen, B., Klinkvort, R.T., O’Loughlin, C.D., Zhu, F., Byrne, B.W., 2018b. Suction caissons in dense sand, part II: vertical cyclic loading into tension. *Géotechnique* **68**, 953–967. <https://doi.org/10.1680/jgeot.16.P.282>
- Bo Ibsen, L., Houlsby, G., Byrne, B., 2005. Suction caissons for wind turbines, in: *Frontiers in Offshore Geotechnics*. Taylor & Francis, p. 1110. <https://doi.org/10.1201/NOE0415390637.ch4>
- De Jager, R.R., Maghsoudloo, A., Askarnejad, A., Molenkamp, F., 2017. Preliminary Results of Instrumented Laboratory Flow Slides. *Procedia Engineering* **175**, 212–219. <https://doi.org/10.1016/j.proeng.2017.01.012>
- Houlsby, G.T., Byrne, B.W., 2005. Design procedures for installation of suction caissons in sand. *Proceedings of the Institution of Civil Engineers: Geotechnical Engineering* **158**, 135–144. <https://doi.org/10.1680/geng.2005.158.3.135>
- Houlsby, G.T., Byrne, B.W., 2000. Suction Caisson Foundations for Offshore Wind Turbines and Anemometer Masts. *Wind Engineering* **24**, 249–255. <https://doi.org/10.1260/0309524001495611>
- Hung, L.C., Lee, S.H., Vicent, S., Kim, S.R., 2018. An experimental investigation of the cyclic response of bucket foundations in soft clay under one-way cyclic horizontal loads. *Applied Ocean Research* **71**, 59–68. <https://doi.org/10.1016/j.apor.2017.11.010>
- Jin, S.C., Zhang, Y.T., Wu, Q.H., 2012. A Study on the Failure Mechanism of Suction Caisson under Vertical Load. *Applied Mechanics and Materials* **256–259**, 1985–1989. <https://doi.org/10.4028/www.scientific.net/AMM.256-259.1985>
- Peire, K., Nonneman, H., Bosschem, E., 2009. Gravity Base Foundations for the Thornton Bank Offshore Wind Farm. *Terra et Aqua* **115**, 19–29.

An investigation into the performance of helical piles with fins under lateral loading

Kevin Stone¹, Maria Diakoumi¹, Oliver Jeffcock¹

¹*Civil Engineering, University of Brighton, Brighton, U.K.*

Corresponding author: Kevin Stone (kevin.stone@brighton.ac.uk)

ABSTRACT: Helical or screw piles have been used extensively with applications in a variety of geotechnical foundations with renewed interest in their potential for offshore applications. This paper presents a study of the performance of a helical pile with enhanced lateral capacity provided by fins ('screwfin' pile). It is proposed the installation process of the screw pile is utilised to embed the fins into the soil. In the model tests undertaken in this study the installation of the model piles is carried out prior to conducting centrifuge tests on the lateral capacity of the pile. Consequently, full-installation effects are not modelled, although there will be disturbance to the soil from the installation procedure carried out prior to testing. These tests therefore investigate primarily the post-installation performance of model screw piles with fins.

Keywords: Helical Piles; Screw Piles; Offshore Foundations; Lateral Capacity.

1 INTRODUCTION

This paper presents a centrifuge model study of the performance of a helical or screw pile with enhanced lateral capacity provided by fins (screwfin pile). The screw pile potential for the Offshore Wind industry is currently the focus of recent research, see for example Al-Baghdadi et. al. (2015), Davisson et. al. (2018), Richards et. al. (2018). A potential disadvantage of a conventional screw pile is the small cross section of the shaft. Since the pile is installed by rotation, then the smaller the pile shaft the less the shear resistance developed as the shaft rotates against the soil during installation which would result in less installation torque and associated equipment. However, the small shaft diameter means that the installed screw pile is unable to develop any significant lateral resistance. To overcome this limitation commercial systems have been developed to retro-fit screw piles with a system of fins or other enhancements to provide additional lateral resistance (Stone and Diakoumi, 2019).

The screwfin pile is designed, that as the screw pile penetrates the soil the pile shaft engages and drags into the soil a set of fins to a predetermined embedment depth. The fins are not rotated during installation and are installed as part of the screw pile installation and not retrospectively. The screwfin pile is designed so that the fins are not rotated during installation. The fins are not rotated during installation. An example of the installation process is illustrated schematically in Figure 1. However, it is also noted that the fins could be installed by jacking against the tensile capacity of the installed screw pile.

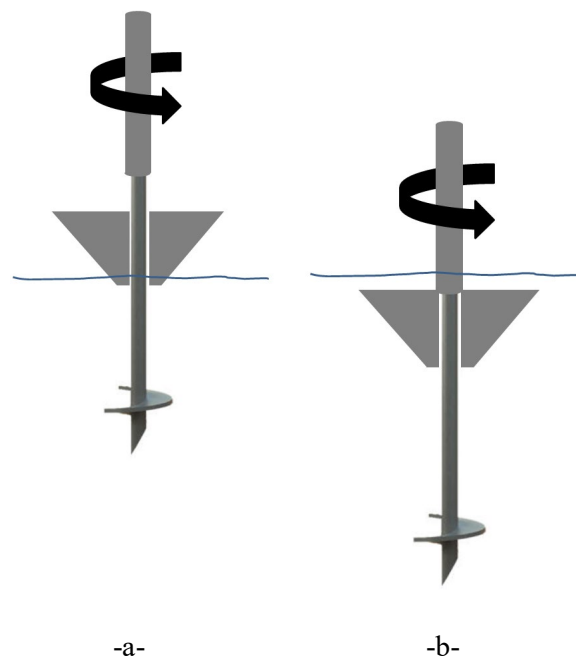


Figure 1. (a) Rotation of shaft and auger embeds the pile and (b) engagement of shaft collar embeds fin on continued installation of pile.

The screwfin pile once installed is likely to behave in a similar manner to a finned-pile, a system which has been reasonably well reported in the literature. Early studies using tapered fins reported by Lee and Gilbert (1980) followed by later research has clearly demonstrated the enhancement of pile lateral capacity through the use of fins under both monotonic and cyclic loading, see for example (Sayles et al 2018, Bienen et al 2012, Duhrkop et al 2010, Nasr 2014, Rudolph & Grabe 2013, Duhrkop & Grabe 2008, Peng 2006, DTI 2006, Peng et al

2010). Several of these studies focused on the geometrical arrangement of the fins, (Sayles et al 2018, Peng 2006), in terms of length and projection from the pile shaft.

These studies have generally concluded that piles with fins can provide a considerably higher lateral resistance and stiffer behaviour than straight shafted piles. A simple approach to the design of a finned pile is to consider the lateral load development as the sum of the lateral capacity of the pile plus an additional contribution from the fin in terms of passive soil resistance and to a lesser extent possible shear stress developed on the fin surface. The extent of these contributions will be a function of the fin geometry and its location on the pile. For example, a centrifuge model study reported by Sayles et. al. (2018) on monotonic lateral load performance of fin piles in dry sand, investigated only the effect of the fin length on the pile performance, and whilst there is not complete agreement in the literature, it is generally observed that the relationship between lateral load and fin length tends to decrease linearly up to a fin to pile length ratio of about 0.3, after which the efficiency reduces.

2 MATERIALS AND MODEL PREPARATION

The sand used for the model tests was uniformly graded Fraction C (300-600 micron) silica sand supplied by David Ball Limited. The sand has maximum and minimum void ratios of 1.06 and 0.61 respectively, with a critical state angle of friction ϕ_{crit} of 31° . The models were prepared through a combination of dry pluviation and vibration using a vibrating table. This method produced consistent soil specimens with a bulk density of 1725kg/m^3 .

2.1. Model Piles

All the model pile shafts were formed from a solid 9.5mm diameter aluminium rod. The auger flights were made from aluminium plate curved into a helical shape and then glued onto a circular section which can be screwed into the pile tip. For the screwfin pile, the pile shaft is reduced to a 4mm diameter section and passed through a hollow section of 9.5mm rod with the fin attached to this section. Above this section the shaft widens to form a shoulder. As the main shaft rotates and embeds itself into the soil the shoulder of the shaft extending contacts the finned section and pulls it into the soil as the pile continues to embed itself, refer to Figure 1. Consequently, the fins are installed as part of the screw pile installation and not retrospectively.

Figure 2 shows the model screwfin pile used in the centrifuge tests.

2.2. Centrifuge Test Package

The tests were carried out on the balanced beam geotechnical centrifuge at the University of Brighton. This machine is manufactured by Thomas Broadbent & Sons Ltd. and is a 6 g-tonne machine (20kg payload to 300g) with a 750mm radius. The tests were conducted in a rectangular steel strongbox with dimensions 300mm (length), 155mm (width) and 180mm (depth). The steel strongbox was placed in a cradle which was then mounted on the centrifuge arm. A two degree of freedom actuator is then mounted on the cradle. Lateral loading is applied to the pile through the use of a rod push mechanism attached to the horizontal actuator as shown in Figure 4. The rod is attached to a load cell fixed to the actuator traveller plate. The horizontal displacement at the point of loading is determined from the horizontal displacement of the actuator, and is also measured via a Linear Variable Differential Transformer (LVDT) which is attached to the pile at the point of loading.



Figure 2. Photograph of model screwfin pile. The fins are free to rotate on the pile shaft and are pushed into the soil by the widened section of shaft.

The model screw pile and screwfin piles were installed into the soil approximately 55mm from the edge of the container. A special former was utilised to allow the pile to rotate and embed itself without the fins rotating and hence overly disturbing the soil. Installation was undertaken by hand prior to mounting the actuator onto the strong box. Great

care was taken during installation to ensure verticality of the model piles and since the pile is displaced away from the tub walls and towards the centre of the sample, boundary effects are not considered significant. The tests listed in Table 1 were conducted at an acceleration level of 25g to investigate performance of a screwfin pile over that of a monopile or simple screw pile. The pile embedment depth was maintained for all the tests at 90mm and the load was applied at an elevation of 32mm above the soil surface.

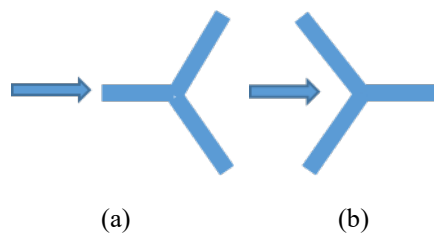


Figure 3a) Open fin arrangement and b) closed fin arrangement; the arrow indicates the direction of the screwfin pile movement.

Table 1. Summary of centrifuge tests at 25g

Test ID	Pile type	Shaft Diameter D (mm)	Embedded Length L (mm)
MP	Pile only	9.5	90
SP	Screwpile only	9.5	90
SFP90OV	Screwfin open	9.5	90
SFP90CO	Screwfin closed	9.5	90
SFP110OV	Screwfin open	9.5	110
SFP110CV	Screwfin closed	9.5	110

2.2.1 Centrifuge Test Procedure

After the model and actuator assemblage have been set-up on the laboratory bench the package was then loaded onto the centrifuge. The actuator was connected to the power and control system and a digital video camera was mounted on the top of the cradle to observe the model during the test, refer to Figure 4. All the tests were conducted at an acceleration level of 25g.

Once the model had achieved the target test acceleration the actuator was run at a velocity of 3 mm/minute and data from the load cell and actuator encoders were recorded continuously until the end of the test.

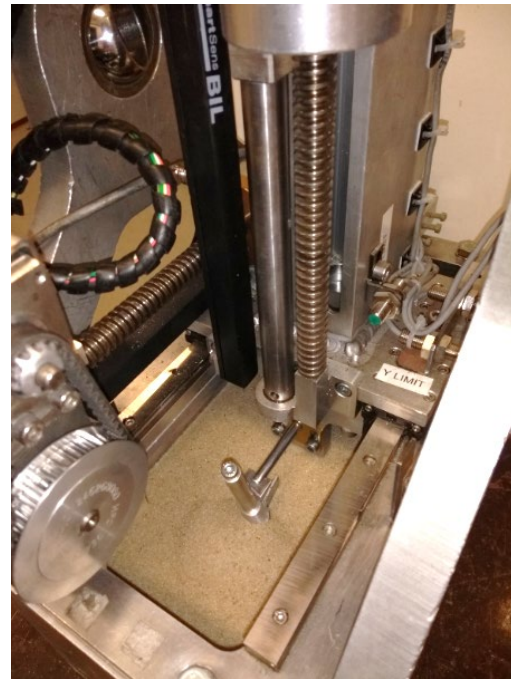


Figure 4. Model package (post-test).

3 RESULTS AND DISCUSSION

The experimental results are presented through plots of lateral load versus lateral displacement measured at the point of load application. Figure 5 presents a summary of the centrifuge model tests where the response of the monopile (MP) and simple screw pile (SP) is compared to the lateral response of the screwfin pile (SFP) for two different orientations of the fin arrangement. The two fin orientations to the direction of movement were with the fins forming either an open or closed ‘V’ in the direction of movement into the soil, refer to Figure 3. These fin orientations are denoted respectively OV and CV representing either the open or closed arrangement.

The results presented in Figure 5 indicate that the addition of the auger plate provides some enhancement of the lateral capacity of the pile which can be associated with the bearing resistance of the auger which is analogous to a buried horizontal plate fixed to the pile shaft. For the pile to rotate in the vertical plane the plate must also rotate in the horizontal plane and thus develops a resisting moment and point of fixity to the pile. It is thus apparent that this additional resistance would be a function of the plate diameter (auger diameter) and its location (depth) on the shaft. For all the tests reported herein the same configuration was used with regard to screwplate size and location.

For the screwfin pile tests with the 90mm long embedment (from base of pile to rear of fins) an additional increase in lateral capacity is observed. It is interesting to note that the load-displacement plots for these tests are very similar and suggests that the orientation of the fins to the direction of travel does not have a significant effect. However comparison between the 90mm and 110mm embedment lengths as shown in Figure 6 suggests that for this case the closed V arrangement provides a greater lateral resistance than the open V configuration. The reasons for this are not entirely clear and more experimental work is required to verify this result.

With regard to the performance of the system at serviceability loads the data has been plotted up to 4mm of lateral displacement to observe the performance at smaller displacements. Referring to Figure 7 it is apparent that the lateral stiffness of the monopile is initially enhanced by the presence of the screw plate and then further enhanced by the action of the fins. For all the screwfin pile tests relatively similar initial lateral stiffness responses are observed although it is generally observed that the longer 110mm embedment does provide an enhanced stiffness over the 90mm depth of embedment.

The results presented herein represent an initial set of experimental results as a ‘proof of concept’ study of screwfin piles.

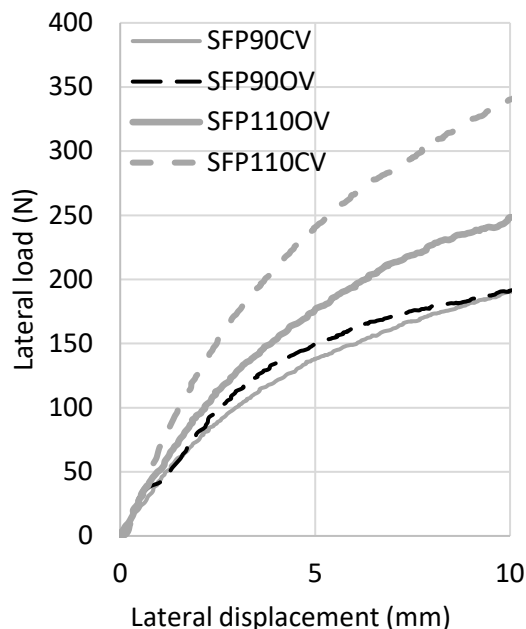


Figure 6. Lateral load versus displacement plots for 90mm and 100mm embedded screwfin piles.

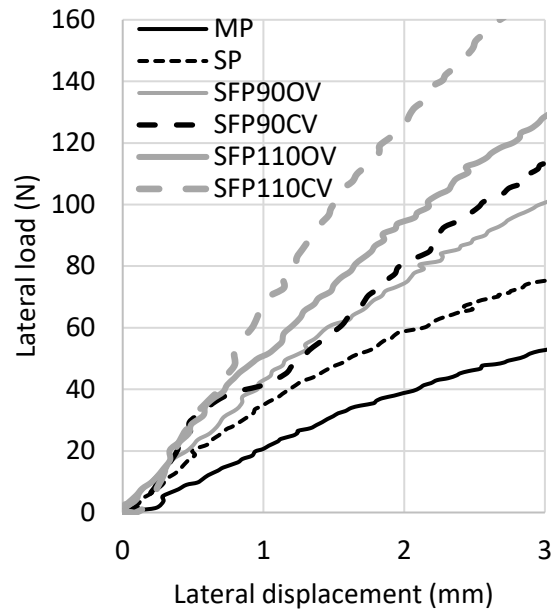


Figure 7. Initial lateral load versus displacement plots.

The results and observations are consistent with those associated with the response of piles with fins or wings. Therefore, once the screwfin pile is installed, it can be treated as a finned pile. There are also other issues that would require to be addressed which are beyond the scope of this study, for example the disturbance of the soil resulting from the installation process, and the optimisation of fin geometry to allow them to be carried into the soil by the action of the screw pile installation.

4 CONCLUSIONS

Based on the relatively limited information presented, it can nevertheless be concluded that a ‘finned’ screw pile (screwfin pile) where the installation process of the screw pile is utilised to install a set of fins integral with the pile shaft, can significantly improve the lateral capacity of the screw pile. It is apparent that there remains much to investigate with regard to the application of the system and in particular the limitations based on the ability to actually install the system and the effects of the installation process on the ground properties and lateral performance. Considerably more research is required to investigate these issues and determine the viability of the system.

5 ACKNOWLEDGEMENTS

The authors would like to thank Mr. David Harker for fabricating the models and assisting in running the centrifuge.

6 REFERENCES

- Al-Baghdadi, T., Brown, M.J., Knappett, J. A. & Ishikura, R. 2015. Modelling of laterally loaded screw piles with large helical plates in sand. *In* Proceedings of the 3rd International Symposium on Frontiers in Offshore Geotechnics, Oslo, Norway, 10-12 June 2015. Taylor & Francis Group, London, pp. 503-508.
- Bienen B, Dührkop J, Grabe J, Randolph MF, White D. 2012. Response of piles with wings to monotonic and cyclic lateral loading in sand. *Journal of Geotechnical and Geoenvironmental Engineering* **138**(3): 364-375.
- Davidson, C., Al-Baghdadi, T., Brown, M.J., Knappett, J., Brennan, Augarde, C.E., A., Wang, L., Coombs, W.M., Richards, D. & Blake, A. & Ball, J. 2018. A modified CPT based installation torque prediction for large screw piles in sand. *In* Proceedings of the 4th International Symposium on Cone Penetration Testing, 21-22 June 2018, Delft, Netherlands, pp. 255-261.
- Davidson, C., Al-Baghdadi, T., Brown, M.J., Knappett, J., Brennan, Augarde, C.E., A., Wang, L., Coombs, W.M., Richards, D. & Blake, A. 2018. Centrifuge modelling of optimised screw piles for offshore wind energy foundations. *In* Proceedings of the 9th International Conference on Physical Modelling in Geotechnics, London, U.K., 17-20 July 2018. Taylor Francis Group, London, pp. 695-700.
- Department of Trade and Industry (DTI). 2006. "Finpile Project: Final Report," London: Department of Trade and Industry.
- Duhrkop, J. & Grabe, J. 2008. Laterally Loaded Piles with Bulge. *Journal of Offshore Mechanics and Arctic Engineering*, **130**(4): 041602.
- Duhrkop, J., Grabe, J., Bienen, B., White, D. & Randolph, M. 2010. Centrifuge experiments on laterally loaded piles with wings. *In* Proceedings of the 7th International Conference on Physical Modelling in Geotechnics, Zurich, Switzerland, 28 June-1 July 2010. Taylor & Francis Group, London pp. 919-924
- Lee, P.Y. and Gilbert, L. W. 1980. The Behaviour of Steel Rocket Shaped Pile. *In* Proceedings of Symposium of Deep Foundations. Atlanta, U.S.A., October, 1979, ASCE, New York, pp. 253-273.
- Nasr, A. 2014. Experimental and theoretical studies of laterally loaded finned piles in sand. *Canadian Geotechnical Journal*, **51**(4):381-393.
- Peng, J. 2006. Behaviour of Finned Piles in Sand under Lateral Loading. PhD thesis. Newcastle University, U.K., 2006
- Peng, J., Rouainia, M. and Clarke, B. G. 2010. Finite element analysis of laterally loaded fin piles, *Computers and Structures*. **88**(21-22): pp. 1239–1247.
- Richards, D.J, Blake, A.P., White, D.J, Bittar, E.M, & Lehane, B.M. 2018. Field tests assessing the installation performance of screw pile geometries optimised for offshore wind applications. *In* Proceedings of the 1st International Symposium on Screw Piles for Energy Applications, Dundee, United Kingdom, 27-28 May 2019, pp. 47-54.
- Rudolph C. & Grabe J. 2013. Laterally loaded piles with wings: In situ testing with cyclic loading from varying directions. *In* Proceedings of the ASME 32nd International Conference on Ocean, Offshore and Arctic Engineering, Nantes, France, 9-14 June 2013. ASME, New York, pp.
- Sayles S., Stone K.J., Diakoumi M. and Richards D. 2018. Centrifuge model testing of Fin Piles in sand . *In* Proceedings of the 9th International Conference on Physical Modelling in Geotechnics, City University London, U.K., 17-20 July 2018. Taylor Francis Group, London.
- Stone K.J. & Diakoumi M. (2019) Performance of screw piles enhanced for lateral load capacity. *In* Proceedings of the XVII European Conference on Soil Mechanics and Geotechnical Engineering, Reykjavik, Iceland, 1-6 September 2019, pp. 551-556.

Pile test database on centrifuged models: tension loading for floating wind turbine anchor

Luc Thorel¹, Ismat El Haffar^{1,2}, Matthieu Blanc¹

¹ GERS-GMG, Univ. Gustave Eiffel, IFSTTAR, F-44344 Bouguenais, France

² Fugro GeoConsulting, Bruxelles, Belgique

Corresponding author: Luc Thorel (luc.thorel@ifsttar.fr)

ABSTRACT: The memory of series of centrifuge tests performed in Nantes is being to come accessible through an open database. The main parameters of the database (piles-anchors in sand) which includes 190 tests on small-scale centrifuged models of piles subjected to tension loading are presented: density, saturation, installation, embedment and loadings (monotonic, cyclic or combined).

Keywords: Close-Ended Pile; Helical Pile; Tension; Sand; Centrifuge Models.

1 INTRODUCTION

As part of the energy transition and the development of marine renewable energies, the Ifsttar began in 2017, in response to a call for proposals from the Weamec, the REDENV-EOL research programme, which deals with the Reduction of the Environmental Impact of Floating Wind Turbine anchored with Pile Foundations. The idea here is to reduce the length of the anchor lines, favouring the tension lines that make the anchor pile work in traction, mobilizing the vertical resistance of the pile-soil interaction.

190 tensile tests on close-ended cylindrical piles or helical piles have been carried out and grouped in a database, which is presented here. Four smooth piles (Figure 1) installed in flight at 100g in Fontainebleau Sand NE34, dense or loose, dry or saturated, are then subjected to vertical tension. Five single helix helical piles (Figure 1) of different diameter are installed in flight by screw driving at 10 different relative depths, in Hostun sand HN38, dense or loose, dry or saturated. The installation forces are measured. The helical piles are subjected to monotonous, cyclic or even monotone post-cyclic loads. All these tests are grouped in a database whose detailed characteristics are presented here.

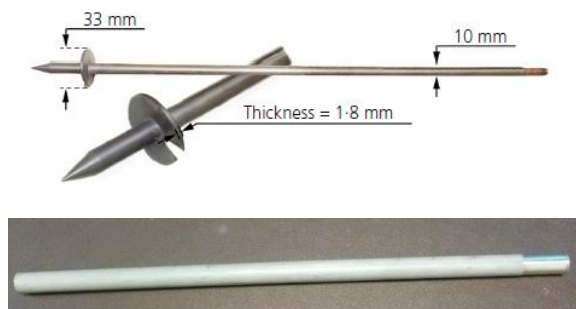


Figure 1 Model piles. Example of single helical steel helical pile (left, Schiavon et al. 2018) and closed cylindrical aluminum pile ($D=18\text{mm}$, length 250mm, El Haffar, 2018).

2 MATERIALS

The experiments were conducted in the geotechnical centrifuge of the Univ. Gustave Eiffel. These are models of smooth piles installed in sand that is usually very dense, in flight (that is, under conditions of stress similar to those observed in real size), and then subjected to a coaxial tensile load. Figure 2 shows the example of a test on a closed cylindrical pile ($D=18\text{mm}$) in saturated dense sand, including the driving phase (with a hydraulic jack in flight) and then the loading phase in tension. The procedure is detailed in El Haffar et al. (2017).

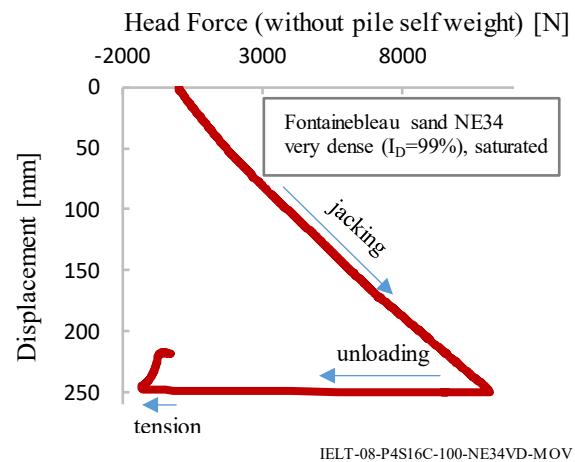


Figure 2 Displacement stress curve (model sizes) of a closed cylindrical smooth pile installed in very dense saturated sand and then loaded in traction ($D=18\text{mm}$, according to El Haffar, 2018).

For helical piles, the procedure, described by Schiavon et al. (2018), includes a controlled pole movement and rotation installation phase, followed by monotonous or cyclic loading phases (Figure 3).

Table 1 presents the parameters of geometry, scale (a scale model 1/N is tested under a centrifugal acceleration of N times the acceleration of earth gravity), and loading applied. Some tests were carried out in dry sand and others in saturated sand.

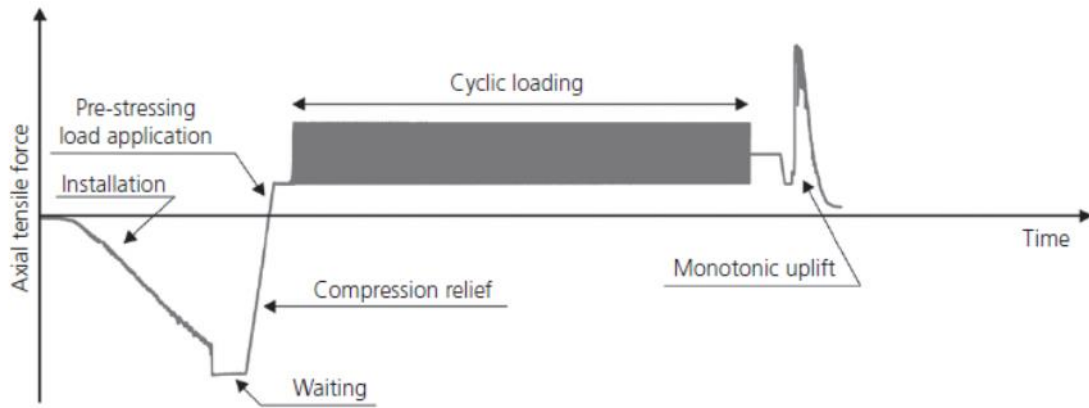


Figure 3 Example of the evolution of axial force versus time of a helical pile test, including installation, cyclic loading, and post-cyclic monotone phases (Schiavon et al., 2018).

Table 1 Distribution of geometries, densities and loading types of the 190 tests.

Pile			Scale	Sand	Number of tests		Loading				
Type	D [mm]	Relative depth z/D			dry	saturated	m	c	m-c	m-c-pc	c-pc
Close ended	12	20.83	1/100	NE34	1 MD	1+1 MD	3	0	0	0	0
	14	17.86	1/100	NE34	1+1 MD	1+1 MD	4	0	0	0	0
	16	15.63	1/100	NE34	1+1 MD	1+1 MD	4	0	0	0	0
	18	13.89	1/100	NE34	1+1 MD	1+1 MD	4	0	0	0	0
Mono-helix d=10mm	40	6	1/10	HN38	4	9	0	0	0	6	7
	33	6 - 7.4 - 7.8 - 8	1/10	HN38	20	41	5	10	1	7	38
	25	6 - 8 - 9.6 - 10 - 12 - 14	1/10	HN38	12	36	3	0	1	17	27
	18	6 - 8 - 10 - 10.5 - 13.3	1/10	HN38	15	17	10	0	7	11	4
	13	6 - 8 - 18.5	1/10	HN38	5	3	4	0	3	1	0
Mono-helix instrumented d=10mm	33	7.4	1/10	HN38	13	0	0	0	0	0	13

MD : medium dense / D : helix or cylindrical pile diameter / d : diameter of the helical pile's shaft
m : monotonic initial / c : cyclic / pc : monotonic post-cyclic

The helix geometry is specified in Table 2 (Schiavon, 2018). The relative depth of the tip of the closed cylindrical piles takes four different values shown in a balanced way, while 11 helix depths have been tested, four of them representing almost the entire population (Figure 4). The relative depths tested make it possible to scan several configurations, but also, for some of them to test different combinations and loading intensities.

Table 2 Helical pile's geometry

Helical pile	D/d	D (mm)	d (mm)	t _h (mm)	φ _h (°)
HA13	1.3	13	10	1.0	6
HA18	1.8	18	10	1.0	6
HA25	2.5	25	10	1.5	6
HA33	3.3	33	10	1.5	6
HA40	4.0	40	10	2.0	6

D : Helix's diameter / d : shaft's diameter / t_h : Helix's thickness / φ_h : Helix's angle

4 DATABASE STRUCTURE AND NUMERICAL DATA

The structuring of the base (Figure 7) uses other files containing detailed information which are not in the data file *stricto sensu*, such as the characteristics of the soil used, the nature of the experimental campaign, the properties of the pile, the experimental assembly or loading conditions.

The file of each test follows a particular organization, starting with its name, which follows a specific nomenclature (Figure 8). The termination depends on the type of software used to edit the data (e.g. .txt or .xls). Each file contains in the first column the time, then in the other columns the recorded data.

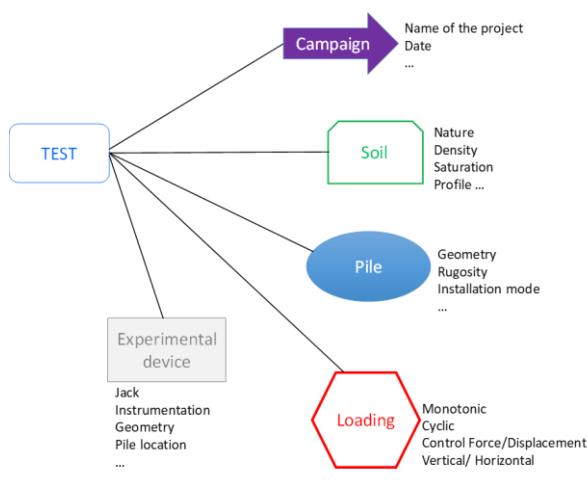


Figure 7 Database structure

□	First name's initial
□□□	Name's initial of the researcher
-	
□□	N° container
-	
□□□□□□	Type of pile
-	
□□□	g-level
-	
□□□□□□	Soil
-	
□□□	Loading

Figure 8 Nomenclature of the files' name. Each rectangle □ corresponds to a character

The file corresponding to the test presented on figure 2 is named IELT-08-P4S16C-100-NE34VD-MOV corresponding to the following informations:

- **Ismat EL Haffar** Thèse
- Container (or strongbox) n°**08**
- Pile n°**P4**, Smooth, **16mm** in diameter, Closed at the tip

- Centrifuge acceleration of **100g** corresponding to a test at scale 1/100
- Fontainebleau sand **NE34 Very Dense**
- **Monotonic Vertical Loading**

The data for each test of the database will be recorded in a « dataverse » system, with a free access for tests already published, and identified with a DOI number: https://research-data.iftstar.fr/dataverse/piles-anchors_in_sand.

5 CONCLUSIONS

An overview of a new database of experiments carried out in the geotechnical centrifuge of the Université Gustave Eiffel, Campus de Nantes, has been presented here. All the tests carried out relate to traction loading. This base includes closed cylindrical piles under monotonous load and monohelical piles under monotonous or cyclic loads. All model piles are installed in macro gravity.

6 ACKNOWLEDGEMENTS

The authors would like to thank WEAMEC (Projects REDENV-EOL and JE-CORECT), the Pays de la Loire Region, Nantes Metropole and CARENE for their financial support, which enabled the study to be carried out. Special thanks go to the Gustave Eiffel University centrifuge team for their technical support and assistance during these experimental campaigns.

7 REFERENCES

- El Haffar I., Blanc M., Thorel L. 2017. Impact of pile installation method on the axial capacity in sand. *Géotechnique Letters*, 7, 260-265. <http://dx.doi.org/10.1680/jgele.17.00036>
- El Haffar 2018. Physical Modelling and study of the behavior of deep foundations of offshore wind turbines. PhD thesis Univ. Bretagne Loire, Sciences pour l'Ingénieur.
- Schiavon J.A., Tsuha C., Neel A., Thorel L. 2018. Centrifuge modelling of a helical anchor under different cyclic loading conditions in sand. *International journal on physical modelling in geotechnics*; **19**(2): 72–88. <https://doi.org/10.1680/jphmg.17.00054>
- Schiavon J.A. 2018. Effect of the helix-to-shaft diameter ratio on the behaviour of single-helix anchors subjected to cyclic loading. Scientific mission report. IFSTTAR-USP Partenariat structurant international HELICAL PILE. 108p.

6. Extended abstracts

Experimental study of the interaction of shallow foundations with an emerging strike-slip fault rupture

Athanasios Agalianos¹, Evangelia Korre², Tarek H. Abdoun², Ioannis Anastasopoulos¹

¹Institute of Geotechnical Engineering, ETH Zurich, Switzerland

²Dept. of Civil and Environmental Engineering, Rensselaer Polytechnic Institute, Troy, NY, USA

Corresponding author: Athanasios Agalianos (agaliana@ethz.ch)

Keywords: Strike-Slip Fault; Shallow Foundations; Centrifuge Testing; Fault-Rupture-Soil-Foundation Interaction.

1 INTRODUCTION

Several case histories of structures such as buildings, bridges, dams, tunnels, or pipelines subjected to tectonic deformation have been recorded during past seismic events, most commonly associated with severe damage or collapse. Nevertheless, there have been also cases of satisfactory performance. Foundation continuity and rigidity have been shown to play a crucial role in the survival of structures, while diversion of the fault rupture is possible due to the presence of a heavily loaded structure lying on compliant soil.

Several researchers have studied experimentally the interaction of propagating dip-slip fault ruptures with foundation–structure systems. A significant amount of centrifuge model tests has been performed, focusing on the interaction with shallow foundations (Bransby et al. 2008), embedded caisson foundations (Loli et al. 2012) and piled foundations (Cai and Ng 2016). With respect to strike-slip faulting, most studies have examined the response of buried pipelines subjected to earthquake faulting (Abdoun et al. 2009). Aiming to bridge the apparent gap in the literature, this paper studies experimentally the interaction of slab foundations with emerging strike–slip faults on dense sand.

2 EXPERIMENTAL SETUP

Five centrifuge model tests were conducted at the Rensselaer Polytechnic Institute (RPI) geotechnical centrifuge facility, utilizing a 3-section split container (Figure 1). The latter is capable of reproducing 2 parallel strike-slip fault ruptures simultaneously, resulting in testing of 10 different prototype problems. All centrifuge tests were performed at 75g centrifugal acceleration. Dry Nevada 120 sand was used, which was deposited in the split container using the air pluviation method. In this way, a uniform 7.5 m (in prototype scale) thick sand layer of dense sand ($D_r \approx 85\%$) was achieved. The middle section of the split container was then subjected in a quasi-static manner to a total horizontal displacement of 1.5 m (prototype scale) with respect to the two stationary edge sections.

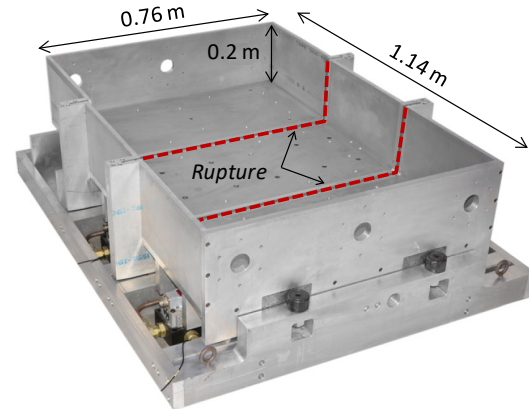


Figure 1. 3-section split container at RPI centrifuge lab.

Initially, the free-field fault rupture propagation through the dense sand layer was examined (in the absence of the footings) and used as reference case. Subsequently, 2 footings were placed at the ground surface to examine their interaction with the outcropping faults. The parameters that were parametrically varied in this study to examine their effect on the system response were: (a) the relative footing location with respect to the fault trace; (b) the foundation surcharge load; (c) the foundation aspect ratio; and (d) the foundation stiffness. A schematic illustration of the conducted centrifuge tests is shown in Figure 2, while the key parameters of each test are collected in Table 1.

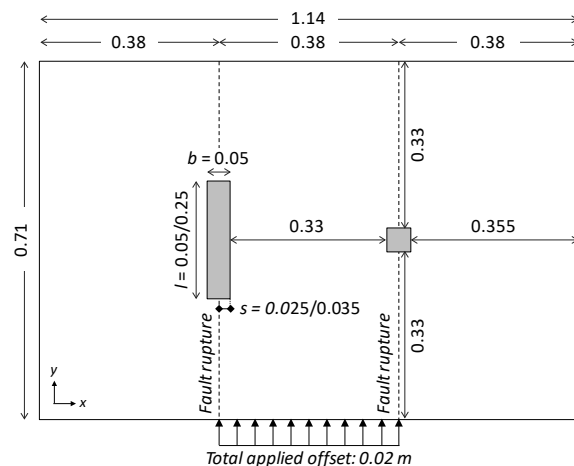


Figure 2. Schematic illustration of the centrifuge tests.

Table 1. Key foundation parameters of the 4 centrifuge tests.

Test	1	2	3	4
Fault location, s/b (-)	0.5	0.7	0.5	0.7
Surcharge load, q (kPa)	27/105	27/105	21/98	21/94
Aspect ratio, b/l (-)	1	1	0.2	1
Stiffness (-)	Rigid	Rigid	Rigid	Flexible

3 KEY RESULTS AND DISCUSSION

Regarding the deformation field at the ground surface under free-field conditions derived from image analysis (not presented herein), there is diffusion of the fault-induced deformations, without evidence of significant strain localization at the 2 fault rupture locations. As also confirmed through Finite Element analyses, the surface deformation field due to an emerging strike-slip fault depends strongly on the test boundary conditions. The interface friction at the base and sides of the split-box can alter significantly the results. In general, rough base and side interfaces lead to more realistic results, with vertical propagation of the fault rupture and development of a shear band parallel to the fault trace due to strain localization of dense sand.

The fault rupture-soil-foundation interaction (FR-SFI) tests revealed the existence of two distinct kinematic mechanisms (Figure 3): a rotational, where the foundation rotation around the vertical z axis θ_z increases proportionally to the fault offset h ; and a translational, where θ_z stops increasing and the foundation either displaces horizontally parallel to the fault trace or remains almost stationary, depending on whether most of its footprint lies on the moving or the stationary block.

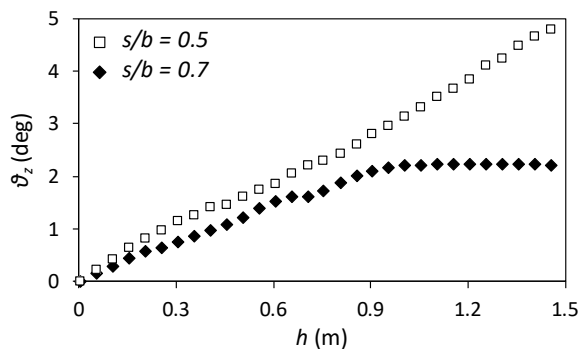


Figure 3. Foundation rotation θ_z as function of fault offset h .

The rotational mechanism develops when the fault rupture emerges vertically at the ground surface, as observed in the test where the square footings ($b/l = 1$) were centrally placed relative to the free-field fault trace ($s/b = 0.5$). In contrast, the translational mechanism develops when the fault rupture deviates from its free-field trace. This was observed for the

test where the square footings were positioned with an eccentricity with respect to the fault parallel axis ($s/b = 0.7$) and for the test with the longer footings ($b/l = 0.2$). In both cases the rotational resistance of the practically rigid footings was large enough to facilitate the diversion of the fault rupture, which always follows the minimum energy path. Each mechanism leads to different foundation distress (not shown herein).

An additional test was then conducted, considering two idealized flexible foundations (by cutting them in multiple small pieces), to examine the influence of foundation rigidity. The flexible square footings were placed eccentrically with respect to the fault parallel axis ($s/b = 0.7$). As opposed to the corresponding rigid foundations test, where fault diversion was observed, in this case the fault rupture propagated through the foundations. This confirmed the importance of foundation rigidity, which affects its rotational resistance.

4 CONCLUSIONS

The present study examined experimentally the interaction of slab foundations with an emerging strike-slip fault. The split container boundary conditions was shown to affect significantly the strike-slip fault rupture propagation under free-field conditions. Regarding the FR-SFI tests, the system response was mainly controlled by the foundation, acting as a kinematic constraint, with the surcharge load playing a secondary role. Such investigations provide useful insights on the response of surface foundations subjected to strike-slip faulting, facilitating thus the development of appropriate design methods against large tectonic deformations.

5 REFERENCES

- Abdoun, T.H., Ha, D., O'Rourke, M.J., Symans, M.D., O'Rourke, T.D., Palmer, M.C., Stewart, H.E. 2009. Factors influencing the behavior of buried pipelines subjected to earthquake faulting. *Soil Dynamics and Earthquake Engineering*, **29**(3): 415-427.
- Bransby, M.F., Davies, M.C.R. and El Nahas, A. 2008. Centrifuge modelling of normal fault-foundation interaction. *Bulletin of Earthquake Eng*, **6**(4): 585-605.
- Cai, Q.P. and Ng, C.W.W. 2016. Centrifuge Modeling of Pile-Sand Interaction Induced by Normal Faulting. *Journal of Geotechnical and Geoenvironmental Engineering*, **142**(10): 04016046.
- Loli, M., Bransby, M.F., Anastasopoulos, I., Gazetas, G. 2012. Interaction of Caisson Foundations with a Seismically Rupturing Normal Fault: Centrifuge Testing versus Numerical Simulation. *Géotechnique*, **62**(1): 29-43.

Investigation of the dynamic behavior of gravity-type quay wall under saturated condition

Yeon-Sam Kim¹, Kil-Wan Ko¹, Dong-Soo Kim¹

¹Department of Civil and Environmental Engineering, Korea Advanced Institute of Science and Technology, Corresponding author: Dong-Soo Kim (dskim@kaist.ac.kr)

Keywords: Quay wall; Soil-Structure Interaction; Saturation System; Liquefaction.

1 INTRODUCTION

After the port of Kobe was severely damaged during the 1995 Kobe Earthquake, interest in the behavior of the port structures has increased (Inagaki et al. 1996). Damages of port and harbor structures were observed during 2017 Pohang earthquake. Therefore, an increased need for evaluation of the dynamic behavior of the port and harbor structures has arisen in Korea. Since one of the most common type of port and harbor structures in Korea is a gravity-type quay wall, this study focused on the quay wall. Complex interaction between water, soil, and quay wall results in the dynamic response of the soil-structure system, so that a dynamic centrifuge test is one of the most useful method (Lee 2005). To evaluate its complicated dynamic behavior, dynamic centrifuge test was performed under fully saturated soil. The objective of this study is to evaluate the dynamic behavior of a gravity-type quay wall under a strong earthquake. Liquefaction occurrence, permanent settlement caused by soil-structure interaction will be evaluated and the sliding mechanism of the quay wall will be investigated throughout the dynamic centrifuge test.

2 CENTRIFUGE TESTING PROGRAM

Dynamic centrifuge test was conducted at the KOCED Geotechnical Centrifuge Testing Center at KAIST. The centrifugal acceleration was 60 g-level. Further descriptions and test results are expressed in prototype scale.

2.1. Testing model

2.1.1 Ground modeling

The testing model was constructed in a rigid model container. Silica sand (SP) was used to construct the whole testing model. Sand pluviation method was used to achieve a target relative density of 50 %.

Physical properties of the silica sand are presented in Table 1.

Table 1. Physical properties of the silica sand

Property	Value
Maximum unit weight, γ_{max} (t/m ³)	1.645
Minimum unit weight, γ_{min} (t/m ³)	1.244
Specific gravity, G_s	2.65
Coefficient of curvature, C_c	1.11
Uniformity coefficient, C_u	1.96

2.1.2 Structure modeling

The gravity-type quay wall was modelled in a cuboid shape to simplify its shape. The dimension and weight of the structure was determined to achieve k_h value of 0.13, based on the design standard provided by the Korean Ministry of Oceans and Fisheries (2014).

2.2. Model saturation

After preparing a dry testing model, viscous fluid which is a mixture of methylcellulose and water was used to saturate the model. 2 % mass ratio of water and methylcellulose was used to achieve a target viscosity of 60 cSt, according to the scaling law. The degree of saturation of the testing model was over than 99 % by applying Okamura method (Okamura and Inoue 2014).

2.3. Dynamic loading

To investigate a dynamic behavior of the quay wall, a strong 2 Hz sinusoidal wave was applied to the testing model, which had a duration of 15 seconds and 0.3 g of peak acceleration at bedrock.

3 RESULTS AND DISCUSSION

The testing results will be described in three parts: liquefaction, settlement, and sliding behavior of the quay wall.

3.1. Liquefaction

Excess pore water pressure time history at the top layer of far-field is shown in Figure 1. In the upper layer of far-field backfill soil, liquefaction was observed. Maximum value of excess pore water pressure remained for about 75 seconds. Total dissipation time was about 8 minutes. Minus peaks were observed in acceleration records.

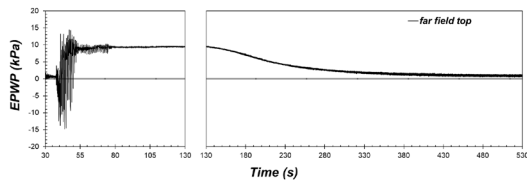


Figure 1. Excess pore water pressure time history at the top layer of far-field soil.

3.2. Soil settlement

In near-field, the interaction between the quay wall and backfill soil played an important role of causing soil settlement. Figure. 2 shows the interaction between near-field soil and quay wall resulting in soil settlement. When the displacement time histories of quay wall and near-field soil were out of phase, soil and the quay wall repetitively moved against and towards each other. During the repetitive interaction, excess pore water pressure value fluctuated, making water to move inside and to be pushed out. This interaction resulted in the cumulative settlement of near-field ground.

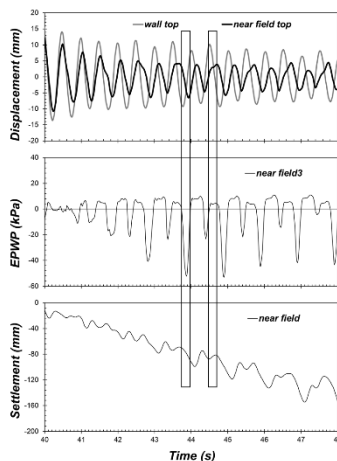


Figure 2. Interaction between near-field soil and quay wall resulting in soil settlement.

3.3. Sliding failure

Figure. 3 shows acceleration time histories of the bedrock and quay wall, with its cumulative displacement records. Sliding of the quay wall occurred with 45 cm displacement, which lead to failure. The acceleration of quay wall stopped after the end of the shake, even though the excess pore

water pressure remained its positive value. Consequently, inertial force of quay wall, which was generated by the dynamic loading, governed the failure.

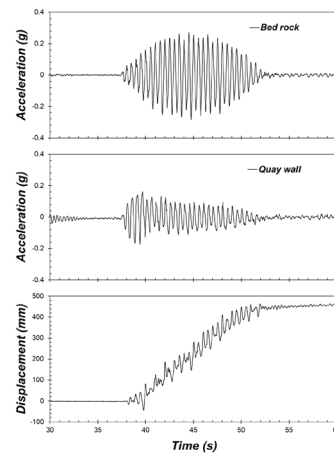


Figure 3. Acceleration time histories of bedrock and quay wall with its cumulative displacement.

4 CONCLUSION

In this paper, dynamic behavior of quay wall was evaluated by the centrifuge test. Important findings in this study are summarized as follow.

- (1) Liquefaction occurred only in the upper layer of far-field backfill soil.
- (2) Settlement in the near-field ground was due to the interaction between water, soil, and quay wall structure.
- (3) Sliding failure of the quay wall was mainly due to the inertial force of quay wall.

5 ACKNOWLEDGEMENTS

This research was supported by a grant (18CTAP-B139287-02) from Technology Advancement Research Program (TARP) funded by Land, Infrastructure and Transport of Korean government.

6 REFERENCES

- Inagaki H, Iai S, Sugano T, Yamazaki H, and Inatomi T. 1996. Performance of caisson type quay walls at Kobe Port, Soils and Foundations, Special Issue, pp. 119-136.
- Lee, C. J. 2005. Centrifuge modeling of the behavior of caisson-type quay walls during earthquakes. Soil Dynamics and Earthquake Engineering, **25**(2), 117-131.
- Okamura, M., & Inoue, T. 2012. Preparation of fully saturated models for liquefaction study. International Journal of Physical Modelling in Geotechnics, **12**(1), 39-46.

Design of a Miniature Cone Penetrometer for the Geotechnical Centrifuge of Delft University of Technology

Dirk de Lange^{1,2}, Siavash Honardar¹, Amin Askarinejad¹

¹*Geo-engineering, Delft University of Technology, The Netherlands*

²*Geo-engineering, Deltares, The Netherlands*

Corresponding author: Dirk de Lange (Dirk.deLange@deltares.nl)

Keywords: Miniature Cone Penetrometer; Design Considerations; Geotechnical Centrifuge.

1 INTRODUCTION

Cone penetration testing (CPT) has proven to be one of the most significant forms of in-situ geotechnical site investigation techniques. Different types of cone penetrometers have been designed. It has been recognized that several factors affect the measurements conducted by a CPT (Lunne et al, 1997). The most general resultant measures from a CPT test consist of the cone resistance q_c , the sleeve friction f_s , and often the pore pressure u . Even though CPTs are one of the most effective geotechnical investigation techniques, it is undeniable that correlation of certain properties based on measurements obtained through CPT testing, relies on a series of empirical factors that are derived through calibration and experimentation (Gui & Bolton, 1998). The use of miniature CPTs in small scale physical models can be helpful in a better interpretation of experimental results and relating measurements to full scale prototypes.

The objective of this paper is to illustrate the main steps taken in designing a miniature penetrometer for a geotechnical centrifuge. The geotechnical centrifuge of Delft University of Technology (DUT) and the available actuator define physical boundary conditions which should be respected in the design. Boundary conditions and boundary effects act as limiting features and create constraints to the application of a standard cone penetrometer.

2 BOUNDARY CONDITIONS

Consideration of boundaries and physical specifications of the test apparatus is crucial. Firstly, the inner width or diameter of the sample container is a limiting factor as the rigid boundary walls may affect the readings from a CPT. Research has shown that the ratio of container width (B) to CPT diameter (D) should exceed a minimum measure of 40 in order to negate all boundary effects. ($D / B \geq 40$) (Gui & Bolton, 1998). This ratio was derived through tests conducted on sand samples with a density index varying between 74% and 81%. It has been recognized by the authors that such a ratio will be clearly dependent on the relative density of the

samples. Considering such a limiting ratio, the design proposal depends heavily on the dimensions of the testing containers and the centrifuge platform. Two types of containers are taken into consideration with an inner width or diameter of 150 and 300 mm, respectively.

Another factor that is considered is the actuator and loading frame utilized in the DUT centrifuge. The current maximum loading range of this actuator is approximately 3.5 kN and the maximum displacement rate is 0.1 mm/s.

3 GRAIN SIZE EFFECTS

Another issue is the grain size of the testing material. Results from various experimental studies suggest requirements for the CPT diameter (B) to median grain size (d_{50}) ratio. Research has shown that for CPTs measuring only the cone resistance, a minimum B/ d_{50} ratio of 20 is required (Gui & Bolton, 1998). If the device is to measure sleeve friction as well as cone resistance, a minimum ratio of 28 is required (Fioravante, 2002).

4 CONSIDERATIONS AND DESIGNS

Designs of various standard and miniature cone penetrometers were reviewed in order to derive a basis for the proposal of a new design. The obtained insight was then considered with regard to the aforementioned boundary conditions. The ratio of container width to CPT diameter was a defining factor resulting in a maximum probe diameter of 4 mm for the container of 150 mm width and a maximum CPT diameter of 7.5 for the container with 300 mm diameter. For each of the two proposed dimensions, different load cells needed to be designed.

The design of the loadcells revolved around the measurement of a minimum threshold of 500 microstrains by the strain gauges of each loadcell. Three categories of cone resistances were defined: (I) 0.5 – 2 MPa, (II) 5 – 25 MPa and (III) 30 – 70 MPa. Based on the ranges defined in these categories, the geometry of the load cell unit and the material type

was chosen so that it would register the minimum threshold strain.

The first penetrometer design is illustrated in Figure 1 (left). This design is 7.5 mm in diameter, and consists of a hollow tube load cell with a diameter of 4 mm and a wall thickness of 0.125 mm. This penetrometer is capable of measuring both the cone resistance and the sleeve friction. The hollow chamber outlined at the cone creates opportunity for the usage of pore-pressure transducers if need be. This device can be used for soil samples of a maximum average grain size of 270 μm .

Figure 1 (right) illustrates the second design with a diameter of 4 mm. This device consists of a modular load cell with a tube diameter of 2.5 mm and a wall thickness of 0.1 mm. This design utilizes bolt strain gauges which are inserted and glued inside the load cell chamber. This device is only capable of measuring the cone resistance (q_c) of a sample. This penetrometer is to be used in any soil sample with a maximum average grain size of 200 μm .

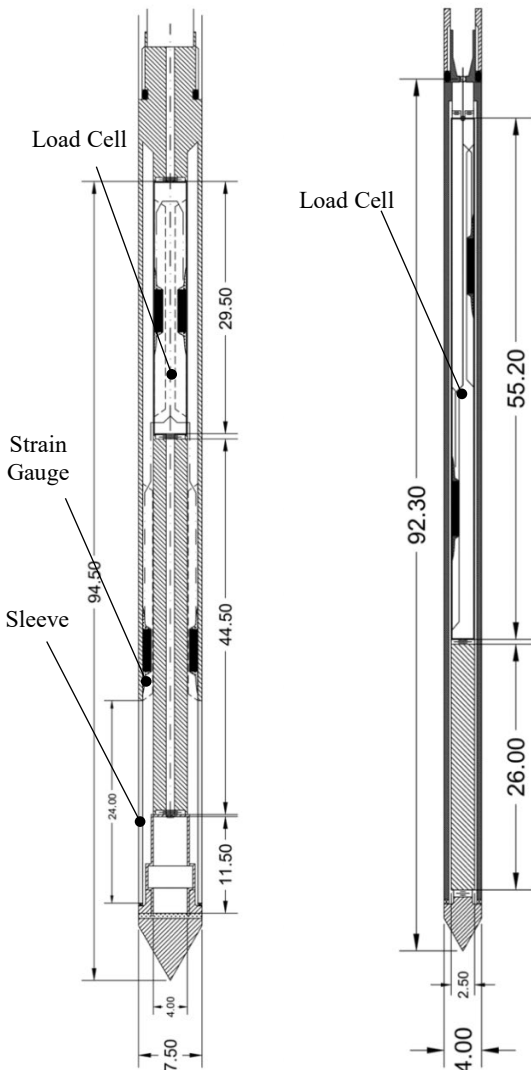


Figure 1. 7.5 mm \varnothing design (left) and 4.0 mm \varnothing design (right)

Another option that is considered is the usage of a bending load cell for the second design and the replacement of the load cell with a hollow tube. This tube extends and is attached to the load cell mounted on the loading frame. This allows for more accurate measurements and simplicity during the design and manufacturing processes. This design also enables the users to conduct measurements in soft soils with lower cone resistance values. An illustration of this design is illustrated in Figure 2.

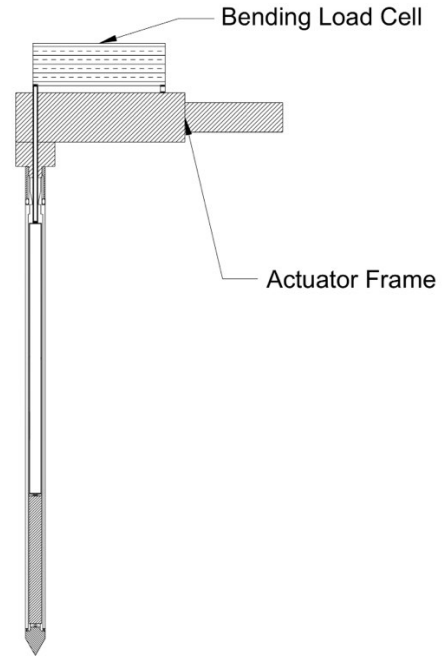


Figure 2. Bending load cell option

5 CONCLUSIONS

It has been concluded that an extended inner tube, connected to the cone, attached to a load cell, which mounted on the loading frame is the most feasible option, since the boundary conditions only allow cone diameters up to 7.5 mm.

6 ACKNOWLEDGEMENTS

The authors would like to acknowledge Karel Heller and Kees van Beek for their practical input.

7 REFERENCES

- Fioravante, V. 2002. On the shaft friction modelling of non-displacement piles in sand. *Soils and Foundations*, 42, 23–33. doi:10.3208/sandf.42.2 23
- Gui, M., and Bolton, M.D. 1998. Geometry and scale effects in CPT and pile design. Proc. 1st International Conference of Site Characterisation 1063-1068.
- Lunne, T., Robertson, P., and Powell, J. 1997. Cone penetration testing in geotechnical practice (1st ed.). Blackie Academic and Professional, London, England.

Behaviour of prefabricated concrete screw piles under axial loading

André Arnold¹, Amin Askarinejad²

¹Lucerne University of Applied Sciences and Arts, Engineering and Architecture, Institute of Civil Engineering, Switzerland

²TU Delft, Geo-Engineering Section, The Netherlands

Corresponding author: André Arnold (andre.arnold@hslu.ch)

Keywords: Concrete Screw Piles, Loading Behaviour, Centrifuge Modelling.

1 INTRODUCTION

A newly developed prefabricated concrete screw pile system (Figure 1) is being used in Switzerland for a wide range of applications such as pile foundations for masonry buildings and offshore test-foundations for the cable car project across Lake Zurich (Arnold et al. to be published 2020). Static and dynamic load tests on the piles have shown that the shaft resistance of the piles is higher compared to conventional displacement piles, whereas the exact loading behaviour of this screw pile system is mostly unknown due to the new screw geometry. Therefore, the screw piles have been investigated preliminary with the use of centrifuge model tests in the beam centrifuge at TU Delft (Allersma 1994; Li et al. 2020). The testing procedure in the centrifuge and first results on the loading behaviour are presented in this contribution.



Figure 1. Prefabricated concrete screw piles “KIDRILL” for the test foundation of the cable car project across Lake Zurich. Pile-sections length 8.0 m.

2 CENTRIFUGE MODELLING

The model piles were made using advanced 3D printing techniques. Vingerling Clay K122, described in Hiemstra and Rijdsdijk (2003), available in blocks has been used for the soil model (Fig. 2). Its strength and stiffness have been investigated using geotechnical standard tests such as Oedometer-, Direct Shear-, Vane Shear- and Triaxial tests. A list of approximate soil parameters is given in Table 1. The outer diameter of the 3D printed model screw piles is 5.5 mm (equivalent to 550 mm at prototype scale). The centrifuge tests were conducted at 100g.

Table 1. Soil parameters of Vingerling Clay

Parameter	Unit	
Unit weight, γ	kN/m ³	19.5
Water content, w	%	29
Pre-consolidation stress, σ'_0	kN/m ²	100
Friction angle, ϕ'_{crit}	°	24-26
Undrained shear strength, s_u	kN/m ²	35-37
Water permeability, k	m/s	$7 \cdot 10^{-11}$
Degree of Saturation, S_r	%	96

2.1. Testing procedure

A screw model pile and a conventional smooth model pile both with an outer diameter of 5.5 mm have been placed in the same clay block to directly compare the loading behaviour of the two pile systems in the same soil model. The model piles have been installed at 1g conditions.

The soil model including the two model piles has been consolidated at 100g for approximately 40 min to ensure dissipation of excess pore water pressures. Both piles have been tested axially at a constant axial settlement-rate of 0.005 mm/s. This settlement-rate is lower than recommended by Knappett and Craig (2012) who recommended a rate of 0.0083 – 0.03 mm/s. The centrifuge needed to be stopped in between the two pile tests to reposition the actuator. The soil model was again consolidated at 100g for at least 5 minutes before the second pile test has been conducted.



Figure 2. Vingerling Clay-block after centrifuge test: Backwards: smooth pile; in front: screw pile with screw profile visible in the pile-soil interface. Model width: 133 mm; model length: 200mm; model depth: 120 mm; pile-embedment depth: 80 mm.

3 RESULTS AND DISCUSSION

The load-settlement-curves of both model piles are given in Fig. 3. The screw pile can sustain a prototype axial load of approx. 390 kN at an axial settlement of approx. 60 mm. Whereas, the smooth pile can sustain a prototype axial load of approx. 270 kN at an axial settlement of approx. 26 mm. The ultimate limit state of the screw pile is approx. 40 % higher than the ultimate limit state of the smooth pile in the two given tests. The settlement at ultimate limit state of the screw pile fits well to $0.1 \cdot D$, which would be 55 mm. The smooth pile reaches its ultimate limit state earlier at approx. $0.05 \cdot D$.

The curves do also show, that for small settlements both pile systems show the same stiffness as a load-transferring system, whereas the smooth pile seems to reach its ultimate limit state more or less suddenly by reaching the maximum axial load without any hardening effects. One could say that the pile system seems to have an elastic, perfectly plastic behaviour. The screw pile shows not only a greater ultimate limit state but also some hardening with a distinct decrease of stiffness before reaching the ultimate limit state.

4 CONCLUSION

The two tests, among more tests in this series, show that the screw pile can sustain larger axial load than a smooth pile with the same outer diameter. The loading behaviour of the screw pile is more robust

in terms of some hardening effects with a more gradual decrease of stiffness compared to the smooth pile, which tend to suddenly reach the ultimate limit state showing an elastic – perfectly plastic behaviour. The tests given here allow for a comparison of two different pile systems in the same soil model. More centrifuge tests would be needed to investigate the loading behaviour of the screw piles in more detail.

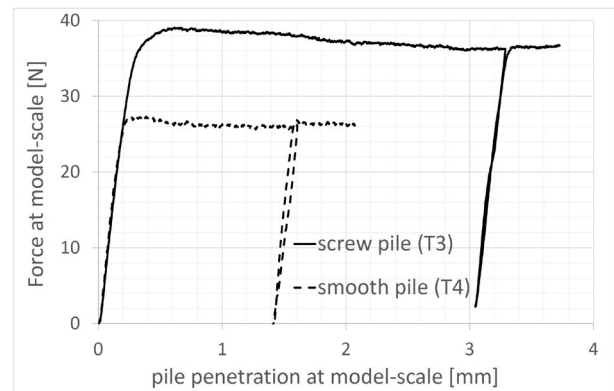


Figure 3. Load-settlement curves of the screw- and smooth piles tested in the same Vingerling-Clay soil model.

5 ACKNOWLEDGEMENTS

We are most grateful to Alphabeton AG, Switzerland, KIBAG AG, Switzerland and Innosuisse, which funded the research project and section of Geo-Engineering at TU Delft, which partly funded the centrifuge model tests.

6 REFERENCES

- Allersma, H.G.B. 1994. The University of Delft geotechnical centrifuge. *In* Centrifuge '94: Proceedings of the International Conference (Leung, C.F. and Lee, F.H. (eds)), Balkema, Rotterdam, the Netherlands, pp. 47-52.
- Arnold, A., Espinosa, T., Felder, H.P., Zürcher, E. and Askarinejad, A. to be published 2020. Seilbahnstützen-Fundamente für die ZüriBahn. In 35. Christian Veder Kolloquium Graz, Austria, 16–17 April 2020.
- Hiemstra, J.F. and Rijdsdijk, K.F. 2003. Observing artificially induced strain: implications for subglacial deformation. *Journal of Quaternary Science*, **18**(5): 373-383. doi: 10.1002/jqs.769.
- Knappett, J.A. and Craig, R.F. 2012. *Craig's Soil Mechanics*. Spon Press, an imprint of Taylor & Francis, London and New York.
- Li, Q., Prendergast, L., Askarinejad, A., Chortis, G. and Gavin, K. 2020. Centrifuge Modeling of the Impact of Local and Global Scour Erosion on the Monotonic Lateral Response of a Monopile in Sand. *Geotechnical Testing Journal* (in-press). doi:10.1520/GTJ20180322.

Validation of ESB Box and Estimation of Shear Wave Velocity in Partially Saturated Soil

Yoon-Ah Kim¹, Hae-In Lee², Satish Manandhar¹, Dong-Soo Kim¹

¹ Department of Civil and Environmental Engineering, Korea Advanced Institute of Science and Technology (KAIST), Korea

²The 4th R&D Institute, Agency for Defense Development, Korea

Corresponding author: Dong-Soo Kim (dongsookim@kaist.ac.kr)

Keywords: Dynamic Centrifuge Test; ESB Box; Shear Wave Velocity; Partially Saturated Soil.

1 INTRODUCTION

In this study, dynamic centrifuge tests were conducted to simulate and verify the 1D site response analysis of level-ground during earthquakes. The dynamic centrifuge test was performed using a uniform layer of partially saturated sand model inside an equivalent shear beam (ESB) box, which is known to minimize the boundary effect during earthquake shaking (Lee et al., 2012). Strata was used as the program for performing the 1D site response analysis, and the V_S profile obtained from the bender elements (BE) placed at different depths during the centrifuge test was set as an input parameter to Strata. Then ratio of response spectra (RRS), ratio of response spectra at the sand surface and of the input motion, obtained from the centrifuge test and strata were compared. In RRS from the centrifuge test, greatest amplification occurred at 0.5 second, while the RRS from Strata showed largest amplification at around 0.75 second. This discrepancy could be due to two main reasons; boundary effect from the container box and incorrect estimation of V_S from BE test in the centrifuge test. Therefore, validation of the ESB box used in the centrifuge test was done, and the V_S was obtained by other various methods.

2 EXPERIMENTAL CONFIGURATIONS

The geotechnical centrifuge facility and the ESB box at KAIST were used to perform the tests. The ESB Box was initially filled with landfill soil from Ulsan, and it is classified as silty-sand (SM). The water content of the soil was 11%, and it was compacted with to a relative density of 40%. As the results from the centrifuge test and Strata results differed significantly, performance of ESB was revalidated.

Lee et al. (2012) validated the performance of KAIST ESB box by shaking an empty ESB box, a fully-filled ESB box, and a partially-filled ESB box in 20g and 40g centrifugal acceleration levels. Since the ESB box have aged for over 8 years, the initial performance of the ESB box may have deteriorated.

Following the procedure from Lee et al. (2012), the empty ESB box was shaken again to see if the natural frequency of the box has changed over the years. A summary of centrifuge tests cases are shown in *Table 1*.

Table 1. Summary of centrifuge test cases (in prototype scale)

Test Cases	g-level (g)	Input Signals	Max. input acceleration (g)
Filled ESB	50	sweep, resweep, artificial, sine 3Hz,	0.022-0.076
Empty ESB	20, 40	sweep, resweep, artificial	0.041-0.241

3 METHODS AND RESULTS

3.1. Validation of ESB Box

According to the RRS of the empty ESB box (ratio of response spectra at the top and the bottom of the box), the natural period of the empty ESB box was estimated to be 0.17 ~ 0.18 s at 20g and 0.3 ~ 0.4 s at 40g. According to Lee et al. (2012), the natural period of the ESB box was 0.2 second at 20 g and 0.4 second at 40 g. Hence, it can be inferred that the ESB box has become stiffer. However, these changes in the natural period of the empty ESB box did not appear to have a significant impact on the performance of the filled ESB box during shakings, because the accelerometers placed at the same height (centre of the box and near the box wall) in the soil model have the same response. This means there were almost no boundary effect.

3.2. Estimation of Shear Wave Velocity

In Section 3.1, it was shown that the performance of the ESB box was intact, so it is necessary to check the reliability of V_S obtained by the BE test. Therefore, the V_S was calculated by using other methods.

3.2.1 Method 1: Resonant Column Test

The soil samples used in the resonant column test (RC test) were the same as the soil used in the

centrifuge test, and were performed under three initial confining pressures; 60 kPa, 120 kPa, and 240 kPa. The V_S can be obtained by using Equation 1, and V_S profile is shown in *Figure 1*.

$$V_S = \sqrt{G_{max}/\rho} \quad (1)$$

3.2.2 Method 2: Stress-Strain Loop

The shear modulus (G) can be determined using the density of the soil and the V_S . The V_S of the ground can thus be calculated from the shear modulus obtained from the acceleration responses at different depths. The shear modulus is equal to the slope of the stress-strain loop, and a method for calculating the shear stress and the shear strain using the acceleration time history is described in Zeghal et al (2018). V_S from stress-strain loop is shown in *Figure 1*. The reason for the V_S obtained by the stress-strain loop being smaller than the V_S from the RC test is because of higher shear strain in centrifuge test than the RC test.

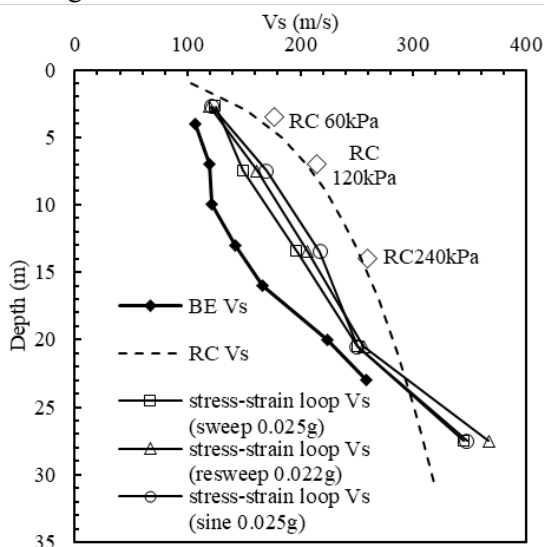


Figure 1. V_S profiles from BE test, RC test, stress-strain loops. The dashed line is a fitted line of data points at three confining pressures.

3.2.3 Method 3: Amplification Function

The shape of the amplification function is determined by the shear wave velocity and the damping ratio of the ground. In centrifuge tests, the amplification ratio can be obtained by Fourier transform of the acceleration time history. As shown in *Figure 2*, the best-fit function was obtained by fitting the amplification ratio with an amplification function. The V_S and damping ratio obtained from the amplification function is the average V_S and damping ratio of the ground (Conti et al. 2012). The estimated average V_S is 249.7 m/s, which is very close to the average value of 248.7 m/s obtained from the RC test. However, when using the

amplification function, there is a disadvantage that only the average V_S of the entire soil model is obtained, not the V_S of each layer of the model.

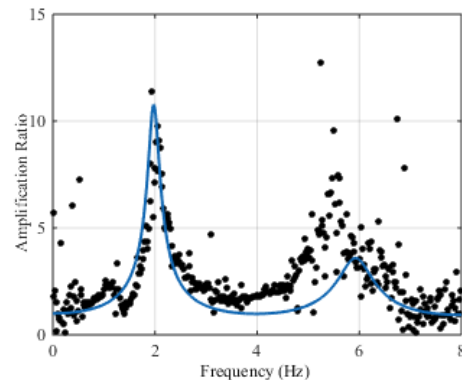


Figure 2. Line: fitted amplification function, dots: amplification ratio from the centrifuge test

4 CONCLUSIONS

In this study, the performance of the ESB box after a period of 8 years was revalidated and the shear wave velocity of unsaturated soil was estimated by various methods. The ESB box became a little stiffer, but the performance during the centrifuge test was intact. By comparing the V_S obtained from the BE test, the RC test, stress-strain loops, and amplification functions, it was found that the BE test underestimates V_S in partially saturated soil. Therefore, it is suggested to estimate the shear wave velocity of the model using stress-strain loops or amplification functions or the RC test rather than using the BE test if unsaturated soil is used in centrifuge model tests.

5 ACKNOWLEDGEMENTS

This research was supported by a grant (18CTAP-B139287-02) from Technology Advancement Research Program (TARP) funded by Land, Infrastructure and Transport of Korean government.

6 REFERENCES

- Lee, S.H., Choo, Y.W., Kim, D.S. 2013. Performance of equivalent shear beam (ESB) model container for dynamic geotechnical centrifuge tests. *Journal of Soil Dynamics and Earthquake Engineering*, **44**(2013): 102–114.
- Conti, R., Viggiani, M.B.G. 2012. Evaluation of Soil Dynamic Properties in Centrifuge Tests. *Jr. Geo. and Geoenv. Eng.*, **138**(7): 850-859.
- Zeghal M, Goswami N, Kutter B, Manzari MT, Abdoun T, Arduino P, et al. 2018. Stress-strain response of the LEAP-2015 centrifuge tests and numerical predictions. *J Journal of Soil Dynamics and Earthquake Engineering*, **113**(2018): 804-818.

Retrofit, redesign, and restructuring of a large geotechnical centrifuge research center

April J. Bowman¹, Anthony F. Tessari¹, Christopher Price¹

¹Centrifuge Research Center, Engineer, Research & Development Center, United States Corps of Engineers, USA
Corresponding author: April J. Bowman (april.j.bowman@erdc.dren.mil)

Keywords: Centrifuge; Business practices; US Army Corps of Engineers.

1 INTRODUCTION

The US Army Corps of Engineers (USACE) Engineer Research and Development Center (ERDC) solves the United States' most challenging problems in civil and military engineering, geospatial sciences, water resources, and environmental sciences for the US Army, Department of Defense, government agencies, and other research institutions. With seven laboratories and multiple field sites, over 2,100 employees with incredible breadth and depth in science and engineering knowledge, and a US\$2 billion research program means the ERDC's capabilities are far-reaching. Research and development is conducted in five primary business areas.

- Engineered Resilient Systems
- Geospatial Research and Engineering
- Military Engineering
- Environmental Quality and Installations
- Water Resources

The US Army Centrifuge Research Center (CRC), located at the ERDC's Geotechnical and Structures Laboratory (GSL) in Vicksburg, Mississippi, provides researchers an economical approach for evaluating alternative designs, investigating

complex problem areas, and validating numerical methods with instrumented physical models. The Centrifuge Research Center (CRC) was originally commissioned for operation in 1995 (Schofield and Steedman 1992) and was designed and built by Actidyn Systems of Elancourt, France. The original price of construction for the facility was approximately US\$15M. Estimated cost of construction in 2020 dollars is about US\$26M. The CRC represents a significant investment by the ERDC into a highly specialized and unique scientific capability. Efforts to modernize the centrifuge and support facilities, and updates to the business model are ongoing.

2 RETROFIT AND REDESIGN

The implementation of major procedural and technological advances in a centrifuge research center presents a significant challenge, especially if enacted all at once, and raises an interesting question, "how does one revitalize the infrastructure and research objectives of an entire centrifuge operation?" This is the challenge currently facing the Centrifuge Research Center.

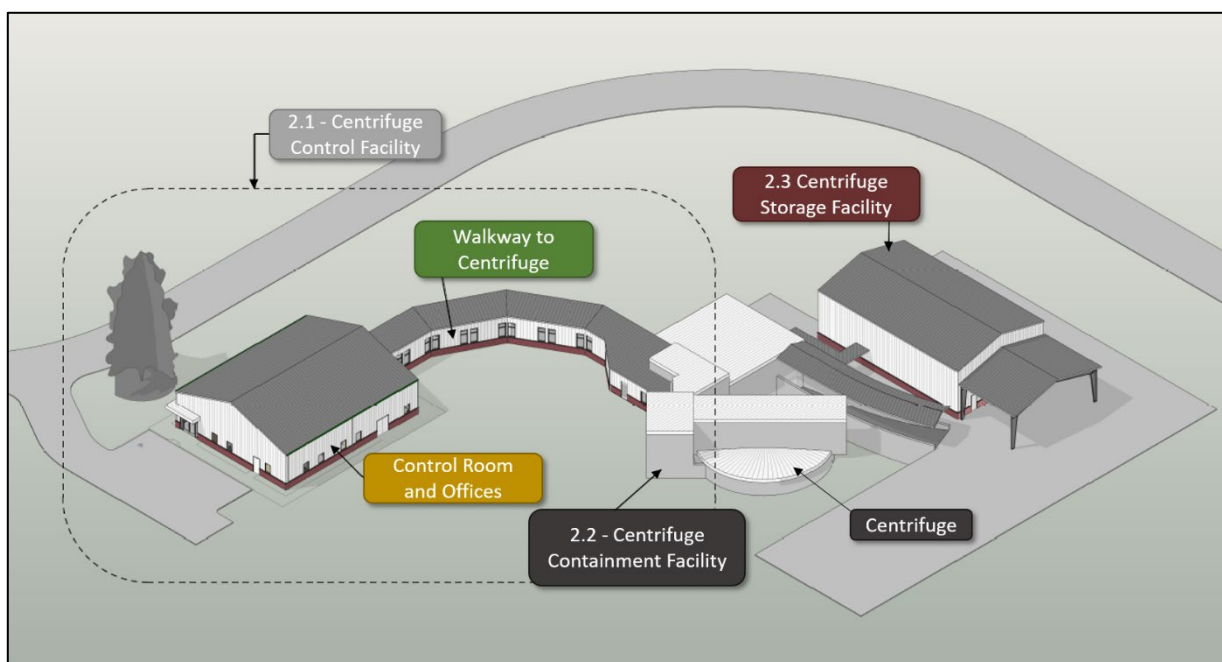


Figure 1. Facilities associated with the ERDC's Centrifuge Research Center

The first step has been to upgrade the existing infrastructure and testing capabilities followed by a program of new construction. Approximately US\$5.3M has been invested into this modernization effort with an additional US\$5.2M projected to complete all phases. Figure 1 shows the new CRC complex with indicators of how this investment will be phased.

2.1. Phase 1: Upgrade existing Centrifuge Control Facility

The original control facility was built in 1989 and modified in 1993 to support centrifuge operations. Demolition and renovation of this facility started in November of 2019 with scheduled completion in October 2020. The new building will have 10 offices for centrifuge personnel and visiting scholars, a state-of-the-art control room, and a secure conference room capable of supporting classified briefings, training, and test protocols. Data transfers between office work stations, the control room, and the centrifuge will be conducted over a stand-alone fiber-optic network system. Additionally, the existing walkway connecting this facility and the centrifuge will be enclosed and house historical exhibits chronicling the ERDC’s 25 year history with the centrifuge including our work with blast effects (Charlie et al. 2005) and on the New Orleans Levees following Hurricane Katrina (Ubilla et al. 2008).

2.2. Phase 2: Centrifuge Upgrades

At the time of its commissioning the CRC was the only centrifuge facility in the world that could accommodate large model sizes and high g-levels. Presently, only the Deltares GeoCentrifuge in Delft, Netherlands matches the U.S. Army centrifuge in size and power. Table 1 outlines some of the key specifications of the ERDC centrifuge.

Table 1. The ERDC’s Centrifuge Specifications

Parameter	Unit	Specifications
Payload	tons	8.8
Platform Dimensions (l x w x h)	m	1.4x1.4x1.8
Arm Radius	m	6.5
Max g-force	g	350

To continue to carry out fundamental research in geotechnical and structural engineering several upgrades to the centrifuge itself and its equipment are ongoing. In addition to infrastructure improvements to the facility, centrifuge upgrades include

- Replacement of variable frequency drive cabinets, fluid rotary joint, optical rotary joint, and aerodynamic cowlings,
- Upgrading the self-balancing system and data acquisition system, and the 1-D shaker control systems to accommodate waveform generation, and
- Development and implementation of novel instrumentation including fibre-optics.

2.3. Phase 3: Centrifuge Storage Facility

In 2022, a new 298 sq. m. storage facility is planned to house large items supporting centrifuge operations. In addition to warehouse-type shelving, this facility will house the ERDC’s large scale consolidometer for clay model preparation.

3 RESTRUCTURING

The facility has a long tradition of working with other Army Corps of Engineers Districts in addition to other government and civilian institutions. The business plan is being restructured to allow flexibility to venture outside this sphere and engage with academic and civilian institutions, both US-based and international. Further, the business model is being modified to reflect recent upgrades in capabilities and captive markets in the centrifuge modelling arena. Many high-performing facilities around the world have carved out productive niche markets based on their production, capabilities, reputation, and geographic location. The facility is similarly tailoring their approach to generate new strategic collaborations in what it has identified as underserved markets that align with key capabilities of the centrifuge and the ERDC. The CRC is actively seeking to increase engagement with the international physical modelling community and to forge mutually-beneficial partnerships that increase research output in vital areas, support graduate students, and increase visibility of said research efforts through widespread dissemination of results.

4 REFERENCES

Charlie, W.A., Dowden, N.A., Villano, E.J., Veyera, G.E. and Doehring, D.O., 2005. Blast-induced stress wave propagation and attenuation: centrifuge model versus prototype tests. *Geo. Test. Jr.*, **28**(2): 207-216.

Schofield, A., and Steedman, R. 1992. Development of a WES Centrifuge. Report No. 26-02-R-004.

Ubilla, J., Abdoun, T., Sasanakul, I., Sharp, M., Steedman, S., Vanadit-Ellis, W. and Zimmie, T., 2008. New Orleans levee system performance during hurricane Katrina: London Avenue and Orleans canal south. *Jr. Geo. Geoenv. Eng.*, **134**(5): 668-680.

Using Fibre Bragg Grating sensors to estimate the horizontal monopile behaviour in centrifuge

Matthieu Blanc¹, Zhong-Sen Li², Luc Thorel¹

¹*Geomaterial and Geotechnical modelling laboratory, University Gustave Eiffel, France*

²*Department of Civil Engineering, Aalto University, Finland*

Corresponding author: Matthieu Blanc (matthieu.blanc@univ-eiffel.fr)

Keywords: Monopile; Horizontal Loading; Fibre Bragg Grating Sensors; Sand.

1 INTRODUCTION

In the literature, reduced-scale centrifuge tests have been used to characterise the response of pile or monopile under horizontal loads (e.g. Verdure et al. 2003; Rosquoet et al. 2007; Li et al. 2010; Klinkvort and Hededal 2014; Klinkvort et al. 2019; Choo and Kim 2015; Truong et al. 2018). Through carrying out centrifuge tests, researchers were able to test monopiles as large as 50 mm in diameter (e.g. Klinkvort et al. 2019).

The present study is part of the SOLCYP+ project, which is an extension of the SOLCYP project (Puech and Garnier 2017). The main objective was to experimentally investigate the response of the model piles under horizontal load in geotechnical centrifuge and then to extrapolate the prototype pile behaviour. Fibre Bragg Grating sensors (FBGS) were used to measure the local strains and to determine the moment profile of the pile (Li et al., 2020).

2 MODEL PILE

In previous centrifuge tests, piles were instrumented with strain gages glued on the external pile shaft (Roesquoët et al. 2007) or even inside the tube (El Haffar 2018), with the connection wires embedded inside the tube. These methods, however, alter the pile dimension and surface roughness and as a result may lead to erroneous measurements. To accurately model the monopile behaviour, the pile must be open-ended with sand inside the pile (i.e. in-situ situation). For this purpose, the model monopile in this study has been instrumented with Fibre Bragg Grating sensors (FBGs).

The model monopile is an open-ended aluminium 2017A tube with the external diameter $D = 50$ mm, the embedded length $L = 450$ mm, the load eccentricity, $le = 500$ mm and the wall thickness $t = 2.5$ mm.

Two semi-cylindrical grooves, diametrically opposed and with a radius of 0.5 mm, have been machined along the pile shaft in its embedded part. In this way, the depth of the grooves is 0.5 mm, i.e. 1/5 of the wall thickness.

Two identical optical fibres with a diameter of 180 μm are glued in the two grooves. On each fibre, 10 Fibre Bragg Grating sensors (FBGs) have been manufactured every $D/2$ (i.e. 25 mm) from the ground level to the pile base. These FBGs are protected by a Teflon tube of 200 μm in diameter. These FBGs measure the external deformations at 10 different cross sections of the pile and then, after calibration, give the bending moments of the pile at these levels.

3 EXPERIMENTAL SET-UP

Concerning the pile installation, the instrumented model pile was pushed into the sand at 1g level by a hydraulic jack. The jacking speed was 1 mm/s and the attained depth is 450 mm, i.e., 9D. The sand level inside the pile was checked and there was no plug generated.

After pile installation, an electric actuator was mounted on two supporting beams that perpendicularly placed on the longitudinal edges of the strongbox (Figure 1).

Centrifuge test was performed at 100g level. Horizontal load was applied through the centre of the cross section by pushing the steel rod that crosses the monopile perpendicularly to the instrumentation plan. The loading point situates at 500 mm (i.e. 10D) above the ground level. The loading was displacement-controlled with a rate of

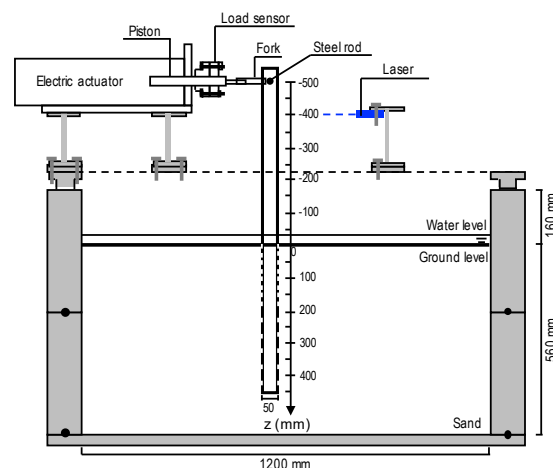


Figure 1. Schematic drawing of the horizontal loading system in the centrifuge at 100g.

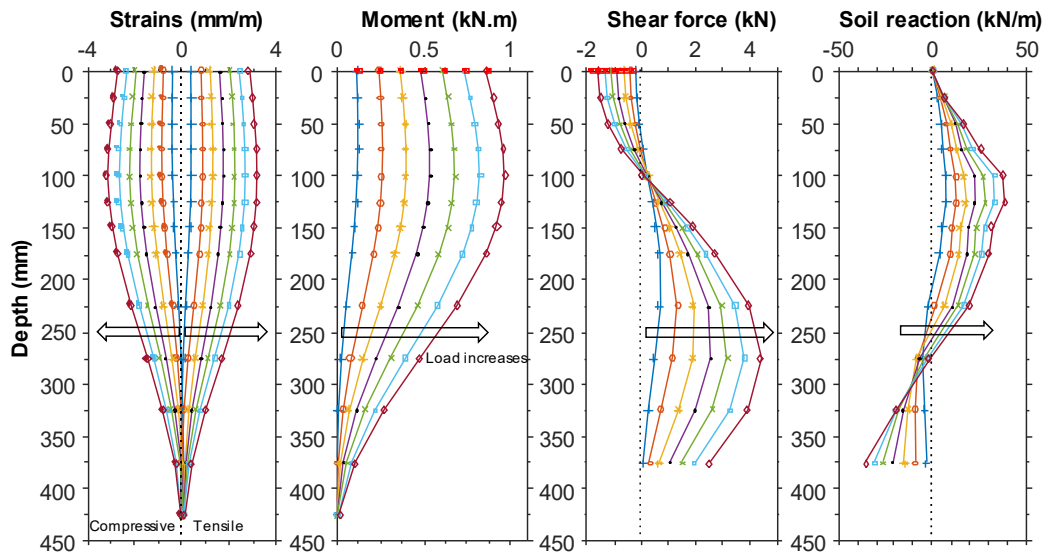


Figure 2. Profile of (a) the measured strains, (b) the bending moment, (c) the shear force and (d) the soil reaction (i.e., the distributed load) for seven horizontal loads (every 0.25 kN until 1.75 kN).

1 mm/s at the actuator level and terminates at 50 mm (i.e. 1D). The measurements of the FBGS, the laser and force transducer were recorded and registered every 0.02 second (i.e., 50 Hz).

4 CONCLUSION

The experimental results (Figure 2) show that:

- All the 26 FBGS survived in the 100g centrifuge test.
- At the ground level, the moments determined by FBGS are in accordance with the moments calculated from the transversal force;
- Shear forces at the ground level are slightly larger than the applied transversal forces. Such difference mainly results from the difficulty of the accurate derivation operation at the ground level.
- The pile local behaviour is characterized: under the effect of the increasing horizontal load, pile rotates at the depth 210 - 275 mm (i.e., 4.2 - 5.5D) below the ground level. Due to the large embedment depth, the pile deflection below the rotation centre was close to zero. The P-y curves at different depths were also determined.

5 ACKNOWLEDGEMENTS

This work benefited from France Energies Marines and State finance managed by the National Research Agency under the Investments for the Future program bearing the reference SOLCYP+ ANR-10-IEED-0006-18. Assistancess from the technical staffs of the centrifuge group are acknowledged.

6 REFERENCES

Choo, Y.W., Kim, D. 2015. Experimental Development of the p-y Relationship for Large-Diameter Offshore

Monopiles in Sands: Centrifuge Tests. *J. Geotech. Geoenviron. Eng.*, **142**(1), 04015058.

El Haffar, I. 2018. Physical modelling and study of the behaviour of deep foundations of offshore wind turbines in sand (Doctoral dissertation, IFSTTAR).

Klinkvort, R.T., Hededal, O. 2014. Effect of load eccentricity and stress level on monopile support for offshore wind turbines. *Can. Geotech. J.*, **51**(9), 966-974.

Klinkvort, R.T., Britta Bienen B., Fan, S., Black, J., Bayton, S., Thorel, L., Blanc, M., Madabhushi, G., Haigh, S., Broad, T., Zania, V., Askarinejad, A., Li, Q., Kim, D. S., Park, S. 2019. Centrifuge modelling considerations of laterally loaded monopiles in sand. *Géotechnique* (submitted).

Li, Z.S., Blanc, M., Thorel, L. 2020. Using FBGS to estimate the horizontal response of a monopile in geotechnical centrifuge. *Int. J. Phys. Model Geo.* <https://doi.org/10.1680/jphmg.19.00022>.

Puech, A. and Garnier, J. 2017. Design of piles under cyclic loading: SOLCYP recommendations. Wiley-ISTE, 454 pages.

Rosquoet, F., Thorel, L., Garnier, J., and Canepa, Y. 2007. Lateral cyclic loading of sand-installed piles. *Soils and Foundations*, **47**(5), 821-832.

Truong, P., Lehane, B.M., Zania, V., and Klinkvort, R. T. 2018. Empirical approach based on centrifuge testing for cyclic deformations of laterally loaded piles in sand. *Géotechnique*, **69**(2), 133-145.

Verdure, L., Garnier, J., and Levacher, D. 2003. Lateral cyclic loading of single piles in sand. *Int. J. Phys. Model Geo.*, **3**(3), 17-28.

High density soil instrumentation for a thermal pile test

Anders Bergström¹, Saqib Javed^{2,3}, Jelke Dijkstra²

¹Infrastructure, NCC, Sweden

²Architecture and Civil Engineering, Chalmers University of Technology, Sweden

³Building and Environmental Technology, Lund University, Sweden

Corresponding author: Jelke Dijkstra (jelke.dijkstra@chalmers.se)

Keywords: Field Test; Thermal Piles; Sensitive Clay; Instrumentation.

1 INTRODUCTION

Whilst physical modelling at 1-g and N-g in the laboratory has proven to be a very effective tool for systematic quantification of the response of deep foundations in various soils (e.g. Leung et al. 2004, Lehane and White 2005) including thermal piles (Stewart and McCartney 2013, Ng et al. 2014, Yavari et al. 2016), there are scaling mechanisms remaining. The scaling issues are most pronounced in case creep is considered, i.e., one of the governing mechanisms that does not scale at elevated acceleration levels (Taylor 1995). In the case considered here, the high sensitivity of the clay cannot be easily replicated in the laboratory.

The project sets out to investigate the impact of thermal loading on the long-term soil response of a floating pile in sensitive clay by performing a scaled in-situ test at a well characterised and densely instrumented test site with sensitive clay. For a full overview of the test setup and results, see Bergström et al. (2020)

2 DESIGN CONSIDERATIONS

2.1. Thermo-mechanical design

The design approach of the instrumented field test on a 28 m long floating pile in sensitive clay fitted with a heat exchanger followed the following guiding design principles:

- 1) The mechanical and thermal boundary conditions should reflect those of a loaded floating thermal pile in soft soil.
- 2) The soil response during heating and cooling needs to be captured with high spatial and temporal resolution.

These requirements led to a long small diameter slender steel tubular pile. The small diameter and steel section reduced the total test duration for thermal loading, whilst the long pile length still accessed the deep soil layers between 7 and 28 m. Furthermore, the long-term mechanical load remained manageable at 80-90 kN and the thermal capacity of the mobile heat exchanger system.

2.2. Soil instrumentation

The number of instruments used in a full-scale field test is often rather limited. This not only is a cost consideration, as instruments are often lost during the test, it is also related to the discipline specific background. Most field instrumentation is designed by geotechnical engineers with a focus on assessing the occurrence of well-established mechanisms (Dunncliff 2012). Hence, only few instruments at carefully chosen locations are sufficient. In contrast this particular project aimed to provide a detailed monitoring of the soil surrounding the pile during thermal loading.

A combination of manual measurements with classic extensometers using a bellow-hose (Bozozuk and Fellenius 1978) and 17 retrievable piezometers (Torstensson 1984) have been used. The standpipes and the filter tips of the BAT® system were made out of plastic, to minimise thermal conduction paths from the instrumentation. A Sensornet fibre based Distributed Temperature Sensing (DTS) system was used to measure the temperatures in the heat exchanger system and on the outer pile wall.

The installation of the plastic standpipes proved to be challenging, even in the slightly over-consolidated deposit of soft sensitive clay. The soil at the site has a linear increasing undrained shear strength profile: 15 kPa below the dry crust near the surface and 50 kPa at the depth of the pile base.

3 RESULTS

After pile installation, load application of the Thermal Response Test (TRT) is performed, during which the distribution of excess pore water pressures and temperature in the soil is assessed.

The results of 17 pore water pressure and temperature sensors are spatially integrated by interpolating the point measurement on an unstructured mesh for several instances in time. This in turn allows to process full-field information of pore water pressures and temperature fields in a 'virtual' cross-section of ca. 7 m width and 21 m height. Figure. 1 & 2 show an example result for

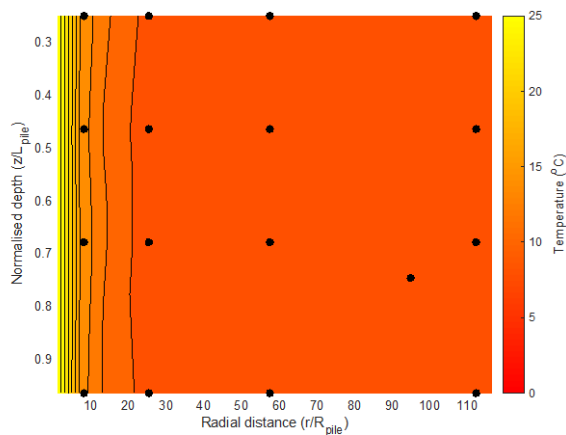


Figure 1. Temperature field in the soil after 504 hrs of heating from the thermal pile. The black dots denote the location of the sensors. $L_{pile} = 28$ m; $R_{pile} = 0.0575$ m.

respectively the temperature and excess pore water pressures at the end of the TRT test. Despite the reasonably small number of measurement points the uniform heating of the thermal pile and the excess pore water pressures it triggers can be captured with high fidelity. One of the main findings is the relatively benign magnitude of excess pore water pressures (Δu) during heating. $\Delta u = \pm 3$ kPa after 20 days of heating and cooling respectively. The temperature for the 50W/m heat exchanger pile reached in excess of 25 °C at the pile wall, quickly reducing to 13 at $8.5R_{pile}$ distance.

4 CONCLUSION

The densely instrumented field test enabled new insights in the spatial and temporal evolution of the pore water pressure and temperature fields. The thermo-mechanical design and instrumentation plan were developed with a physical modelling approach in mind. The first-time combination of plastic filter tips and standpipes and retrievable BAT probes proved to be attainable in soft clays.

5 ACKNOWLEDGEMENTS

The Authors are grateful for the excellent support from the research engineers Håkan Larsson and Aaro Pirhonen at Chalmers. The financial support from SBUF (grant no. 12904), FORMAS (grant no. 243-2013-771), Swedish Energy Agency (grant no. P37307-1), NCC, Hercules and Chalmers University of Technology is gratefully acknowledged. SAB/Ruukki kindly donated the steel piles used in this research project.

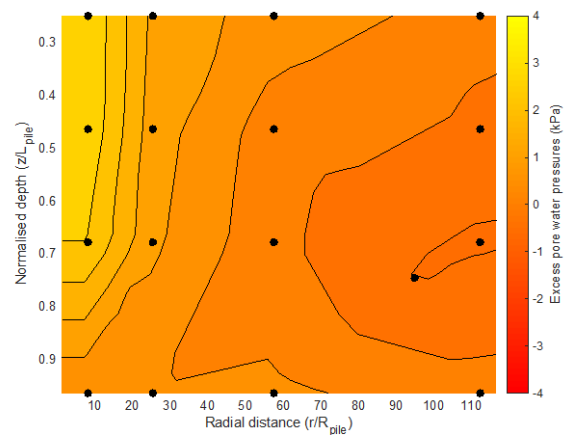


Figure 2. Excess pore pressure field in the soil after 504 hrs of heating from the thermal pile. The black dots denote the location of the sensors. $L_{pile} = 28$ m; $R_{pile} = 0.0575$ m.

6 REFERENCES

- Bergström, A., Javed, S. & Dijkstra, J. 2020. Field test of a floating thermal pile in sensitive clay. *Géotechnique*, ahead of print: doi.org/10.1680/jgeot.19.P.094
- Bozozuk, M., & Fellenius, B. H. 1979. The bellow-hose settlement gauge. *Canadian Geotechnical Journal*, **16**(1), 233-235.
- Dunnicliff, J. 2012. Chapter 95 Types of geotechnical instrumentation and their usage. *In ICE manual of geotechnical engineering* (pp. 1379-1403). Thomas Telford Ltd.
- Lehane, B. M., & White, D. J. 2005. Lateral stress changes and shaft friction for model displacement piles in sand. *Can. Geot. Journal*, **42**(4), 1039-1052.
- Leung, C. F., Liao, B. K., Chow, Y. K., Shen, R. F., & Kog, Y. C. (2004). Behavior of pile subject to negative skin friction and axial load. *Soils and Foundations*, **44**(6), 17-26.
- Ng, C. W. W., Shi, C., Gunawan, A., & Laloui, L. 2014. Centrifuge modelling of energy piles subjected to heating and cooling cycles in clay. *Géotechnique letters*, **4**(4), 310-316.
- Stewart, M. A., & McCartney, J. S. 2013. Centrifuge modeling of soil-structure interaction in energy foundations. *Journal of Geot. and Geoenvironmental Engineering*, **140**(4), 04013044.
- Torstensson, B.A. (1984). A new system for ground water monitoring. *Groundwater Monitoring & Remediation*, **4**(4), 131-138.
- Yavari, N., Tang, A. M., Pereira, J. M., & Hassen, G. (2014). Experimental study on the mechanical behaviour of a heat exchanger pile using physical modelling. *Acta Geotechnica*, **9**(3), 385-398.

Physical Modelling of Geotechnical structure subjected to Hydraulic Scour

Liam Jones¹, Ioannis Anastasopoulos¹

¹Institute for Geotechnics, ETH Zürich, Switzerland
Corresponding author: Liam Jones (jonesli@ethz.ch)

Keywords: Scour; PIV; Tsunami; Flooding.

1 INTRODUCTION

Increases in the frequency of freak weather events, rising sea levels and aging infrastructure are speculated to increase the demands on coastal or near-water infrastructure (Steffen, Hunter and Hughes, 2014). In order to make sure that these structures are adequate, and in order to construct so-called “resilient” societies, we must first understand how structures behave during these events. Scouring is the process of removal of soil by a flow of water, and is often seen at the bases of submerged bridge piers and other foundation structures placed within flowing water. Scour is known to significantly alter the geometry of foundation soil systems, possibly affecting their performance (Yilmaz, Banerjee and Johnson, 2016). There exists much physical experimental data which is used to predict various scour for various configurations (eg. Richardson & Davis, 1995). However, there is considerably less knowledge of how the process of scouring affects the performance of real structures.

2 MATERIALS AND METHODS

In order to shed some new light on these problems; a new physical experimental apparatus is under development at ETH Zürich. Consisting of a “Miniaturised Tidal Generator” (MTG), this set-up aims to combine geotechnical physical modelling with the ability to model a wide range of hydraulic events such as Tsunamis and flooding (Jones and Anastasopoulos, 2018, 2019). A simple experiment, consisting of a 50mm by 50mm aluminium “breakwater” placed on a pluviated layer of 50mm of cohesionless marine sand ($D_r = 65\%$) (“Perth Sand”), was constructed inside the MTG (Figure 1). This structure was then subjected to a “Tsunami-like” pulse wave, period 10s, and maximum amplitude of 20mm, targeting a model scale of $N = 100$. The resulting failure is then recorded with high speed photography, through the Perspex side of the model box. The camera used is a Mikrotron Cube 7, shooting at 300fps. Images are then processed using the particle image velocimetry method (PIV) using the code GeoPIV_RG (Stanier *et al.*, 2016).

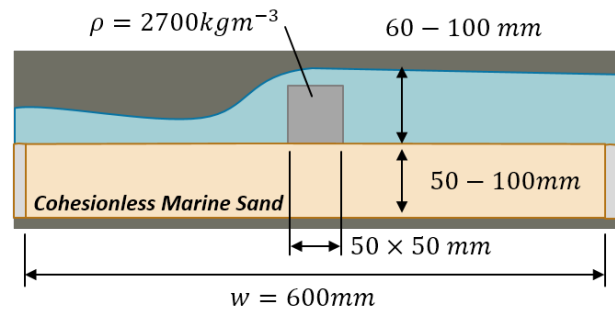


Figure 1. Planar model dimensions, the incoming wave travels from right to left.

3 RESULTS AND DISCUSSION

Initially, as the breakwater is overtopped, scouring occurs and rapidly begins to create a hole of increasing depth (Figure 2). During this phase the block exhibits some small (apparently negative, clockwise) rotation, towards the wave. At some time (A), the scour depth appears to reach a steady state, and almost immediately we begin to see the block rotating anticlockwise.

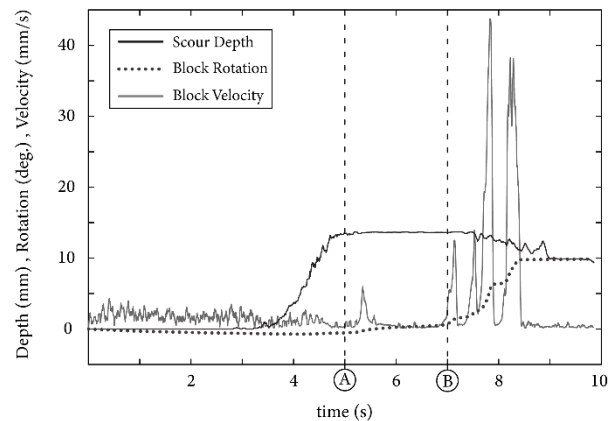


Figure 2. Plot showing the evolution of scour depth, breakwater rotation and breakwater velocity with time.

The third phase (beginning point B) shows how as the block begins to undergo significant movement (rotation), and the scour hole begins to re-fill (the scour depth decreases). Here, we see large spikes in the velocity of the block while the structure is sliding over the soil, rather than simply moving in response to soil loss. Important observations can be made by viewing the strain-field within the soil

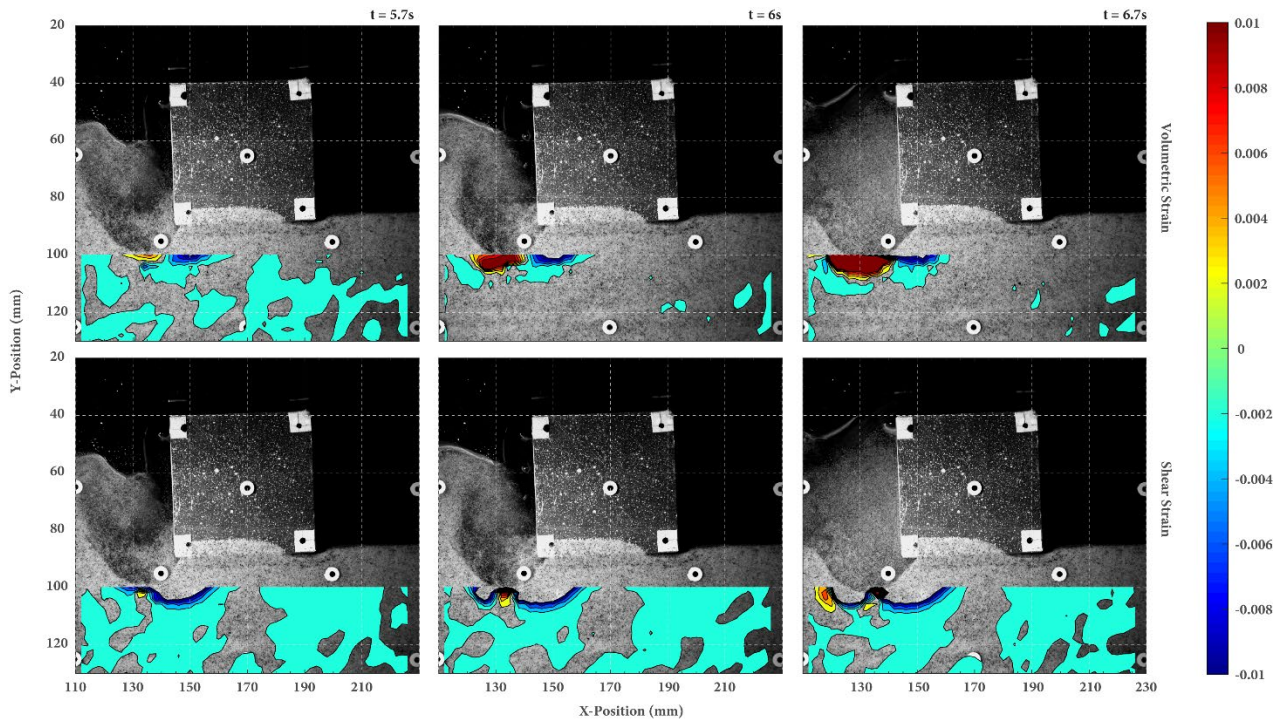


Figure 3. Computed strain field within the soil from PIV analysis using GeoPIV_RG, volumetric (top) and shear (Bottom)

(Figure 3). Generally, a trend can be seen where the soil in the immediate vicinity of the scour hole develops shear and volumetric strains. Interestingly, the soil on the breakwater side appears to loosen. Shear planes, in the form of a partial slip surface can also be seen forming under the foundation before we observe significant rotation. These shear planes may be the source of the apparent loosening observed, caused by soil dilation.

4 CONCLUSION

Although only one short test has been presented here, some important observations can already be made about such soil-structure-hydraulic systems. Firstly, after observing the complex, multi-phase deformation/failure behaviour it seems unlikely that the response of such systems can be captured by applying an equivalent static force to a simple block foundation as is often used in practice (Chock, 2016). Secondly, even if the scoured geometry of the soil could be approximated and simulated, the changes in soil state, as well as the interaction between scour evolution and block rotation, mean that using approximate scour geometries for such systems may not yield satisfactory results. Further questions include: how can we first explain, and further predict what is happening within the body of the soil in terms of changes in state (loosening), and what is the effect of this observed re-filling. Lastly, one critical question that must be addressed is: how much of this observed behaviour is a function of boundary conditions i.e. what is the influence of

stress similitude on such problems (especially to the observed loosening). These questions are the subject of ongoing work; adapting the entire scheme to the new ETH IGT Geotechnical Centrifuge.

5 REFERENCES

- Chock, G. Y. K. 2016. Design for Tsunami Loads and Effects in the ASCE 7-16 Standard, JoSE (ASCE), **142**(11), p. 04016093. doi: 10.1061/(asce)st.1943-541x.0001565.
- Jones, L. and Anastasopoulos, I. 2018. Development of an Apparatus for the Simulation of Coastal Structures Subjected to Tsunami, 16ECEE.
- Jones, L. and Anastasopoulos, I. 2019. Design and Characterisation of a 1-g Testing Apparatus for Simulating the interaction between Tsunamis and Geotechnical Systems, ICONHIC 2019.
- Richardson, E. V and Davis, S. R. 1995. Evaluating scour at bridges - Third edition.
- Stanier, S. A. et al. 2016. Improved image-based deformation measurement for geotechnical applications, Canadian Geotechnical Journal, **53**(5), pp. 727-739. doi: 10.1139/cgj-2015-0253.
- Steffen, W., Hunter, J. and Hughes, L. 2014. Counting the Costs : Climate Change and Coastal Flooding.
- Yilmaz, T., Banerjee, S. and Johnson, P. A. 2016. Performance of Two Real-Life California Bridges under Regional Natural Hazards, JoBE, **21**(3), p. 04015063. doi: 10.1061/(ASCE)BE.1943-5592.0000827.

Distribution of temperature in culverts in cold climate

Karina Tommik¹, Jan Laue¹, Sven Knutsson¹, Nina Lintzén¹

¹Department of Civil, Environmental and Natural resources Engineering, Luleå University of Technology, Sweden

Keywords: Culvert, Frost Heave, Cold Climate, Convective Heat Transfer.

1 INTRODUCTION

Frost heave and thaw settlement in roads and railways is a persistent problem in cold climates leading to degradation of the road structure over time. The presence of a culvert in the road structure changes the temperature distribution in that particular area considerably, as cold air is allowed to pass through the structure. Therefore the frost depth around the culvert is increased compared to the rest of the road. If frost susceptible soil is present under the road or railway structure, this might lead to a larger frost heave in areas of culverts.

The temperature inside the culvert usually is either considered equal to the ambient outside temperature or a function of it (Hua et al. 2014). There are no studies incorporating temperature change along the axis of the culvert or the distribution inside the culvert and the factors affecting it.

Considering the placement of the culvert in the embankment, it is reasonable to assume that there will be airflow through the culvert if the ends are unobstructed. There are two factors contributing to the air flow. Firstly, stack effect that causes air to flow from higher pressure area to lower pressure area. Stack effect will be present if the culvert is inclined and there is a temperature difference between the ends of the culvert. Secondly, air flow inside the culvert will be caused by wind (Zeng et al. 2017). Increased cooling effect due to air flow has previously been studied in relation to road construction on permafrost, where it has been noted that frost depth under air ducts placed in road embankments increases during cold periods (Coulombe et al. 2012).

Presence of air flow inside the culvert indicates that the heat transfer mechanism is convection. Therefore, heat transfer between the culvert and the soil will be governed by temperature and air velocity inside the culvert as well as the thermal properties of soil. Additional factors contributing to the temperature distribution are solar radiation, snow cover, geometry and material of the culvert.

Developing a model that describes temperature distribution inside a culvert accurately will result in a higher degree of precision when estimating frost

depth and consequently predicting road damages that occur around culverts.

2 METHOD

As measurements in the field provide insight into the topic, it has to be studied in ideal conditions to investigate the various contributing parameters separately under defined conditions. Thus, laboratory investigations will be used to better understand the temperature distribution inside culverts.

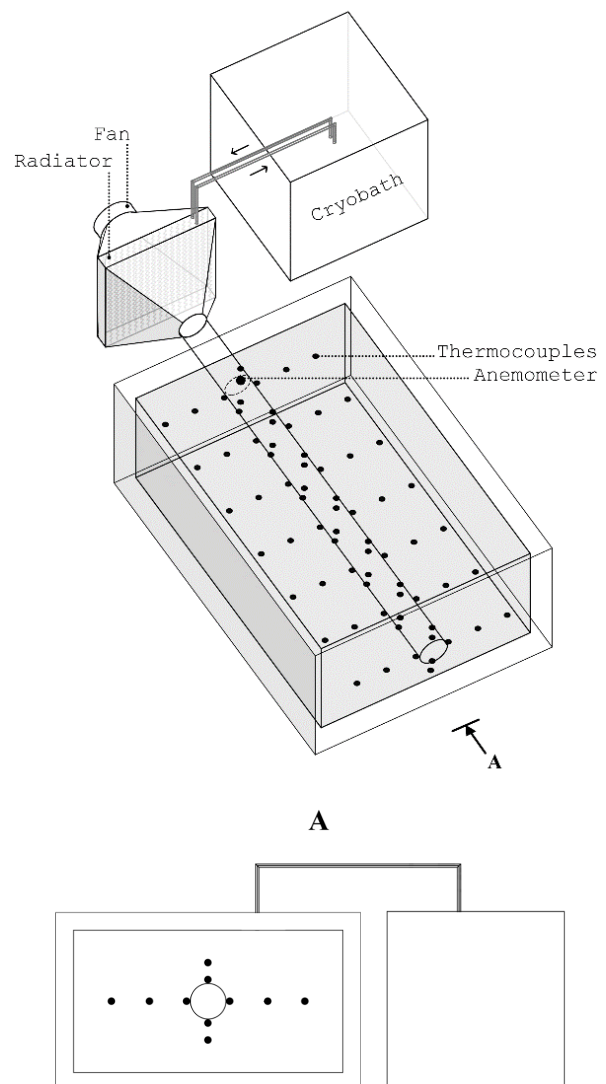


Figure 1. Schematic of the experiment setup

In order to investigate the effect of air velocity and temperature on the temperature distribution inside the culvert, a simplified model is constructed. This first laboratory investigation allows control of environmental factors in order to focus on the convection process.

A schematic setup of the experiment can be seen in Figure 1. The experiment setup is constructed inside an insulated pallet with dimensions of 116x76x29 cm (length:width:height). Homogenous dry sand with known thermal properties is used as the soil surrounding a steel corrugated pipe with a diameter of 10cm. Homogeneity of the sand will allow for a simplified verification of the model using analytical methods. The steel pipe has a high thermal conductivity which will allow for faster heat transfer between air and soil. The corrugated surface of the pipe will introduce some turbulence to the model in order to compensate for the reduced diameter of the pipe compared to an actual outdoor culvert. A fan with adjustable rotation speed is used to push air through a radiator unit and further into the steel pipe. The air velocity can be regulated by altering the rotational speed of the fan. A radiator connected to a cryobath is used to cool the air. A large surface area of the radiator allows for rapid cooling of the air while cryobath allows for simple temperature adjustments. Thermocouples are embedded into the soil around the pipe as well as placed inside the pipe as it is arranged in the field. A thermal anemometer is placed at the inlet of the pipe to verify the air velocity at the entrance. The experiment is conducted in a temperature controlled room to maintain a constant temperature of the inlet air.

Experiments will be performed with different air velocities and temperatures. Between each test soil and the pipe temperature will be allowed to return to initial conditions at room temperature. Recorded temperatures inside and around the pipe will be used to estimate the effect of air velocity on the temperature distribution inside the experiment setup in the direction of air flow.

3 DISCUSSION

Implementation of the experiment described above will aid in describing convective heat transfer in soil. The results of the experiment along with field

measurements of actual culverts will be used as basis for developing of a numerical model describing the temperature distribution in full-scale culverts and subsequently the distribution in the surrounding soil. The purpose of the experiments is to identify to what extent the heat extraction rate will increase with increasing air velocity. The more heat extracted per unit of time, the greater the temperature change in the soil will be. A larger heat extraction rate in situ would lead to increased frost depth and thus possible frost heave.

It is also of interest how the temperature distribution changes along the longitudinal axis of the pipe. Temperature differences along the axis of a culvert would lead to varying frost depth under the length of the culvert which in turn could lead to uneven frost heave in the perpendicular cross-section of the road.

Additional studies looking into thermal properties of potential culvert materials as well as insulating properties of snow cover and solar radiation will have to be performed and taken into account when addressing temperature distribution in culverts.

The initial laboratory experiment described above will serve as initial basis for development of a numerical study and future field tests. The experiment will determine the effect of air velocity on heat transfer within culverts thus aiding in estimation of frost depth around culverts.

4 REFERENCES

- Coulombe, S., Fortier, D., Stephani, E. 2012. Using air convection ducts to control permafrost degradation under road infrastructure: Beaver Creek experiment site, Yukon, Canada. *In* Proceedings of the Cold Regions Engineering 2012: Sustainable Infrastructure Development in a Changing Cold Environment, Quebec City, Canada, 19-22 August 2012. American Society of Engineers (ASCE), pp. 21-31
- Hua, L., Fujun, N., Yonghong, N., Xifebg, Y. 2014. Study on thermal regime of roadbed-culvert transition section along a high speed railway in seasonally frozen ground. *Cold Regions Science and Technology*, **106-107**: 216-231
- Zeng, Y., Liu, K., Zhou, X., Fan, L. 2017. Tunnel Temperature fields analysis under the couple effect of convection-conduction in cold regions. *Applied Thermal Engineering*, **120**: 378-392

Geosynthetic reinforcement in lightly piled embankments: Laboratory model development

Per Gunnvard¹, Jan Laue¹, Qi Jia¹

¹Department of Civil, Environmental and Natural Resources Engineering, Luleå University of Technology, Luleå
Corresponding author: Per Gunnvard (per.gunnvard@ltu.se)

Keywords: Piled Embankment, Geosynthetics, Arching, Beam Theory, Catenary Theory

1 INTRODUCTION

This contribution describes part of a study with the aim of optimising the use of geosynthetic reinforcement (GR) in the method of geosynthetic reinforced pile-supported embankments (GRPSE) with timber piles, also called light embankment piling (Gunnvard et al. 2017). GRPSE is an effective foundation method, which utilises arching (Terzaghi 1943) and membrane effect (Villard et al. 2000) to transfer the embankment weight and traffic load onto the piles instead of the soft subsoil. Light embankment piling used in Sweden is a low-cost alternative to GRPSE with steel or concrete piles, as the material and transport cost of timber often is far less. More importantly, timber piling allows for a solution with lower carbon footprint than concrete or steel piling.

The use of timber piles and the exclusion of pile caps in lightly piled embankments result in a design with very low pile coverage ratio, which could lead to punching failure and unwanted settlements. To counter this, the lightly piled embankment should, according to Swedish standard TK Geo 13 (STA 2016), be reinforced with two layers of GR (Case 3 in Figure 1) and the centre-to-centre pile spacing (s) is limited to $0.8 \leq s \leq 1.2\text{m}$. This requires a lot of timber piles and GR. A layer of dense soil is added on top of the pile heads in order to distribute the load better and to keep the soil around the timber piles fully saturated, as the timber will otherwise rot over time. The layer thicknesses t_1 , t_2 and t_3 are the minimum possible from practical point of view but means that the height of the arch above the GR (h') is less than half the arch height (h) for the beam theory design if $s \leq 1.2\text{m}$, assuming semi-circular arch formation. Satibi (2009) showed using numerical modelling that the GR layers need to be placed within the lower half of the arch height ($h' \geq h/2$) to efficiently reduce subsoil settlements (d). Thus, it needs to be evaluated whether increasing s or adjusting the placement and stiffness of the two GR layers is the most resource efficient or if a single GR layer (Case 2 in Figure 1) could improve enough, as well as if an exclusion of GR entirely (Case 1 in Figure 1) could yield a more resource

efficient design. Based on this, a more detailed analysis in which the development of the arches and the need and placement of the GR will be studied physically and numerically.

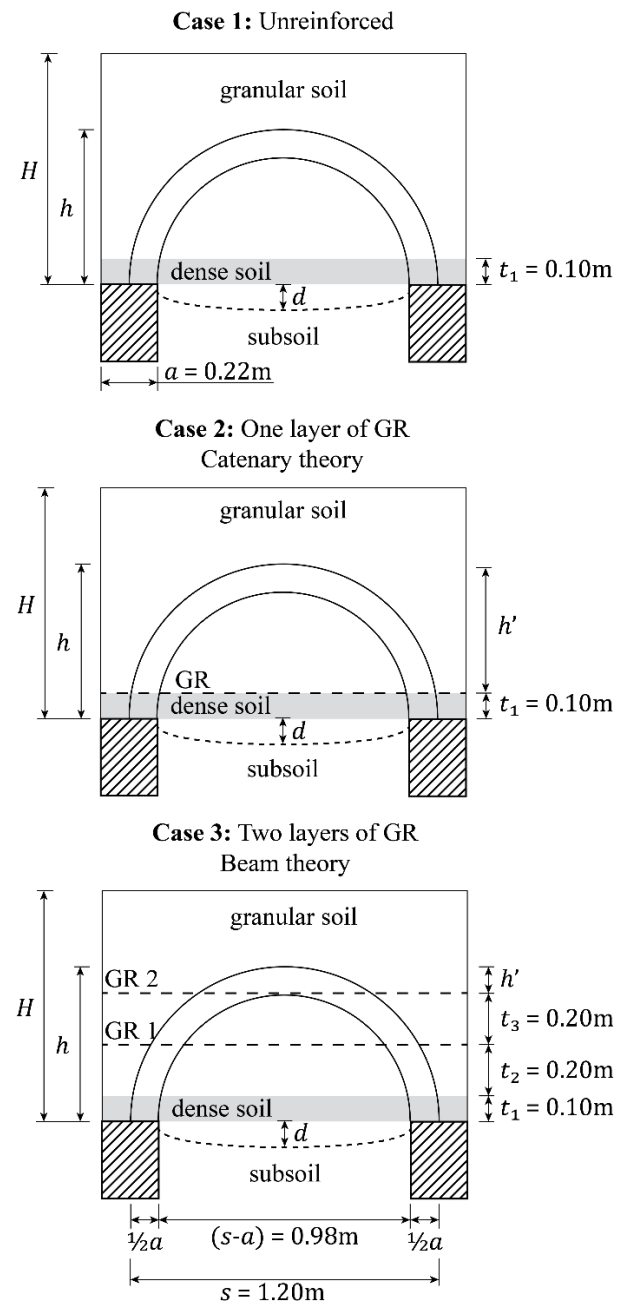


Figure 1. Illustration of a semi-circular arch formation between two piles in relation to the three different cases of geosynthetic reinforcement (GR). Dimensions in case 3 are according to TK Geo 13 (STA 2016) with $s = 1.2\text{m}$.

The aim of the analyses also includes the potential of reducing the minimum embankment height (H) and increasing the maximum allowed s above 1.2m for lightly piled embankments in TK Geo 13, further saving resources.

2 LABORATORY MODEL

A 1-g physical experiment in scale 1:1 or 1:2 will be developed at Luleå University of Technology to study the load distribution between two adjacent piles while simulating the cross section of an embankment and load transfer platform. The test setup is the part of the pile-supported embankment shared by two adjacent piles with centre-to-centre pile spacing s (see Figure 1). The width of the model is $s + a$, where a is the equivalent square width of a 0.25m diameter timber pile, and the height from the pile heads equals H . Plane strain is chosen to enable optical measurements of soil and GR displacements using Particle Image Velocimetry (PIV), captured through sheets of plexiglass on either side of the model setup, drawing inspiration from the trapdoor geotechnical centrifuge tests by da Silva et al. (2016) and Rui et al. (2016). This would allow the observation of formation of arches in real time while measuring pile loads as well as deformation (settlements) between the piles. It will also allow observation of the development of voids below the GR (or the dense soil). Traffic load will be added via a hydraulic piston from the top.

The setup of the physical experiment will be based on the current design criteria in TK Geo 13 for lightly piled embankments, i.e. Case 3, as well as Case 1 and 2 in Figure 1. Only the upper-most part of the piles will be included and made from steel to exclude the stiffness of the timber. The subsoil will be modelled as a cushion filled with water, where the subsoil settlements are controlled via drainage during the test through a tap (van Eekelen et al. 2012). Load cells will be placed on the two piles to measure arching and the GR strain will be measured by fibre optics (Briançon & Simon, 2012) or PIV analysis.

3 OUTLOOK

The analyses of the physical modelling and complementary numerical modelling will allow the revision of the design criteria in TK Geo 13 for lightly piled embankments. A relationship will be developed between H , clear spacing between piles ($s - a$) and GR placement and stiffness. The results will improve timber piling as an environmental and cost-efficient alternative in GRPSE design. However, the results are applicable on general

GRPSE design as the piles will be modelled as short rigid blocks.

4 ACKNOWLEDGEMENTS

This study has been supported by the Swedish transport administration (STA) and the Swedish joint research program for road and railway geotechnology Branschsamverkan i grunden (BIG). The authors would like to express their gratitude for the financial support.

5 REFERENCES

- Briançon, L., and Simon, B. 2012. Performance of pile-supported embankment over soft soil: Full-scale experiment. *Journal of Geotechnical and Geoenvironmental Engineering*, **138**(4): 551–561. doi.org/10.1061/(ASCE)GT.1943-5606.0000561.
- da Silva, T. S., Elshafie, M. Z. E. B., and Madabhushi, G. S. P. 2016. Physical modelling of geosynthetic-reinforced soils spanning voids. *In Proceedings of the 6th European Geosynthetics Congress, Ljubljana, 25-28 September 2016. Turkish chapter of IGS, Istanbul*, pp.774–781.
- Gunnvard, P., Mattsson, H., and Laue, J. 2017. Numerical analysis of the mechanical behaviour of light embankment piling. *In Proceedings of the 19thICSMGE, Seoul 17-22 September 2017. Korean Geotechnical Society, Seoul*, pp.749–752.
- Rui, R., van Tol, F., Xia, X.-L., van Eekelen, S., Hu, G., and Xia, Y.-y. 2016. Evolution of soil arching; 2D DEM simulations. *Computers and Geotechnics*, **73**: 199–209. doi.org/10.1016/j.compgeo.2015.12.006.
- Satibi, S. 2009. Numerical analysis and design criteria of embankments on floating piles. *Mitteilung 62, Institute of Geotechnical Engineering, University of Stuttgart, Stuttgart*.
- STA. 2016. Trafikverkets tekniska krav för geokonstruktioner - TK Geo 13 (TDOK 2013:0667), Swedish Transport Administration (STA), Borlänge, Sweden. (In Swedish)
- Terzaghi, K. 1943. *Theoretical Soil Mechanics*. In Karl Terzaghi. John Wiley & Sons.
- van Eekelen, S. J. M., Bezuijen, A., Lodder, H. J., and van Tol, A. F. 2012. Model experiments on piled embankments. Part I. Geotextiles and Geomembranes, **32**: 69–81. doi.org/10.1016/j.geotexmem.2011.11.002.
- Villard, P., Gourc, J. P., and Giraud, H. 2000. A geosynthetic reinforcement solution to prevent the formation of localized sinkholes. *Canadian Geotechnical Journal*, **37**: 987–999. doi.org/10.1139/cgj-37-5-987.

Co-seismic response of a mat-founded structure on deposits with silty-sand layers.

April J. Bowman¹, Orestis Adamidis², Shideh Dashti³, Ioannis Anastasopoulos²

¹Centrifuge Research Center, Engineer, Research & Development Center, United States Corps of Engineers, USA

²Institute for Geotechnical Engineering, ETH Zurich, Switzerland

³College of Engineering and Applied Science, University of Colorado Boulder, USA

Corresponding author: April J. Bowman (april.j.bowman@erdc.dren.mil)

Keywords: Silty-Sand; Liquefaction; Centrifuge; Settlement; Rotation.

1 INTRODUCTION

Deposits of loose, non-plastic silt and silty-sand liquefied during the 1999 Kocaeli earthquakes and the 2010-2011 Canterbury earthquake sequence, causing significant damage to structures with shallow foundations and their connected lifelines (e.g. Bray et al., 2004; Cubrinovski et al., 2011).

Both in Adapazari and in Christchurch, discrepancies between liquefaction triggering criteria and field observations existed, which were attributed to the influence of fine grained soils (Sancio et al. 2002; Beyzaei et al. 2018). Element tests performed on high-quality extraction samples showed that the content of clay and the stratigraphy must be taken into account for the evaluation of liquefaction triggering. In Adapazari, a set of updated criteria was developed to account for the influence of fines (Bol et al. 2008). In Christchurch, extensive testing showed that the key problem in evaluating the influence of fines is their effect on both density and penetration resistance. This double effect can be reconciled by using appropriate density measures for comparison (Cubrinovski et al. 2010).

Despite significant advances in our understanding of the influence of fines on the element response of saturated granular soils, uncertainty remains regarding boundary-value problems involving soil-structure interaction, which include layers of such intermediate materials (Sancio et al. 2002). In order to investigate this problem, three dynamic centrifuge experiments were performed, modelling a mat-founded, single-degree-of-freedom structure resting on a soil profile that included a layer of loose, saturated silty-sand, whose fines content was altered for each experiment. The goal was to investigate which density measure method might be appropriate for the silty-sand layers, in order to generate an equivalent response for the structures.

2 MATERIALS AND METHODS

Three centrifuge experiments were performed at the University of Colorado Boulder, examining the

response of a mat-founded structure. A sketch of the models is given in Figure 1. The soil layers were prepared by dry pluviation into a flexible-shear-beam container, using an automated sand-pourer described by Kirkwood and Dashti (2018a). The same soil profile was used in each model consisting of a lower 10m-thick dense, made of clean, Ottawa sand ($D_r = 90\%$), a 6m-thick layer of liquefiable silty-sand whose properties varied for each test as described in Table 1, and a 2m-thick surface crust layer of dense Monterey sand ($D_r = 90\%$). Three levels of non-plastic fines content were examined, 0%, 5%, and 15%. In all cases, the relative density was kept nearly the same, calculated using the relevant maximum and minimum void ratio for each layer. Soil parameters for the lower layer and the surface layer can be found in Kirkwood and Dashti (2018b). The structure examined was placed at the centre of the model, as shown in Figure 1, and was instrumented using LVDTs and MEMS accelerometers.

Table 1. Material parameters for the liquefiable layers of silty-sand used in each test.

Parameter	Unit	Test 5	Test 3	Test 4
Fines content, f_c	%	0	5	15
Relative density, D_r	%	40	36	42
Minimum void ratio, e_{min}	-	0.530	0.420	0.216
Maximum void ratio, e_{max}	-	0.810	0.700	0.697
Mean grain size, d_{50}	mm	0.18	0.22	0.21

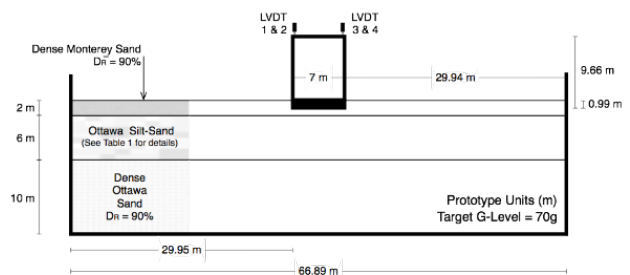


Figure 1. Layout of centrifuge models. Dimensions in prototype scale.

The models were saturated using a pore fluid whose viscosity was appropriate (Adamidis and Madabhushi, 2015). A centrifugal acceleration of 70g was used. A major 1-D horizontal earthquake motion was applied, called “Kobe-L”, full details of which can be found in Kirkwood and Dashti (2018b).

3 RESULTS AND DISCUSSION

Figure 2 displays the combined results from LVDTs 1 through 4 positioned on the top four corners of the structure (Figure 1) for settlement, plotted versus rotation, which was calculated using results from MEMS accelerometers for the high-frequency rotation component and LVDTs for the low frequency rotation trend. The strong pulses in the earthquake led to significant settlement and rotations. Settlement of more than 0.35 m was accumulated at the end of the earthquake for all three experiments. However, not much residual rotation was recorded at the end of the excitation, for any of the three experiments. In Test 3, where fines content, $FC = 5\%$, a re-centering response was observed towards the end of shaking.

Overall, the settlement-rotation response was remarkably similar for all tests, showing that relative density, calculated using the relevant values of e_{\min} and e_{\max} for each layer, is a good indicator of equivalency in terms of structural response, when considering layers with increasing fines content.

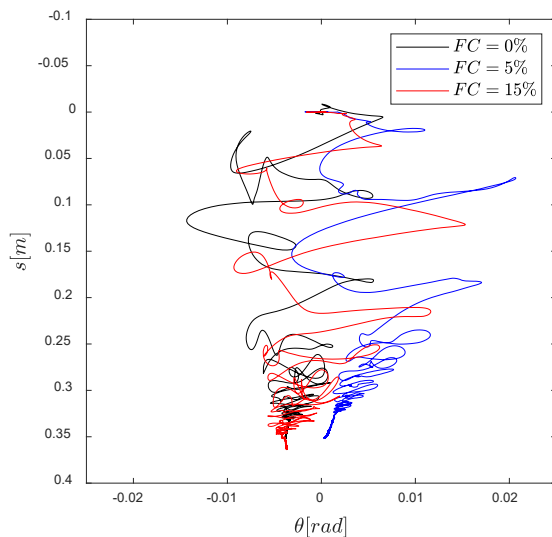


Figure 2. Rotations and settlements of structure during the earthquake.

4 CONCLUSIONS

Three dynamic centrifuge experiments were presented, examining the response of a mat-founded structure resting on a saturated soil profile that includes a layer of silty-sand. A different level of

non-plastic fines content was examined in each test: 0%, 5%, and 15%. In all cases, the relative density was kept about the same, calculated using the relevant maximum and minimum void ratio. A similar relative density led to a similar structural response in terms of settlement and rotation, irrespective of the increase in fines, up to $FC = 15\%$.

5 REFERENCES

- Adamidis, O. and Madabhushi, G.S.P., 2015. Use of viscous pore fluids in dynamic centrifuge modelling. *International Journal of Physical Modelling in Geotechnics*, **15**(3), 141-149.
- Beyzaei, C.Z., Bray, J.D., Cubrinovski, M., Riemer, M. and Stringer, M., 2018. Laboratory-based characterization of shallow silty soils in southwest Christchurch. *Soil Dynamics and Earthquake Engineering*, 110, pp.93-109.
- Bol, E., Önalp, A., Arel, E., Sert, S. and Özocak, A., 2010. Liquefaction of silts: the Adapazari criteria. *Bulletin of Earthquake Engineering*, **8**(4): 859-873.
- Bray, J. D., Sancio, R. B., Durgunoglu, T., Onalp, A., Youd, T. L., Stewart, J. P., Seed, R. B., Cetin, O. K., Bol, E., Baturay, M. B., Christensen, C., and Karadayilar, T., 2004. Subsurface Characterization at Ground Failure Sites in Adapazari, Turkey. *Journal of Geotechnical and Geoenvironmental Engineering*, **130**(7): 673–685.
- Cubrinovski, M., Bray, J. D., Taylor, M., Giorgini, S., Bradley, B., Wotherspoon, L., and Zupan, J. 2011. Soil Liquefaction Effects in the Central Business District during the February 2011 Christchurch Earthquake. *Seismological Research Letters*, **82**(6): 893–904.
- Cubrinovski, M., Rees, S. and Bowman, E., 2010. Effects of non-plastic fines on liquefaction resistance of sandy soils. In *Earthquake Engineering in Europe (125-144)*. Springer, Dordrecht.
- Kirkwood, P. and Dashti, S., 2018a. A centrifuge study of seismic structure-soil-structure interaction on liquefiable ground and implications for design in dense urban areas. *Earthquake Spectra*, **34**(3), 1113-1134.
- Kirkwood, P. and Dashti, S., 2018b. Considerations for the Mitigation of Earthquake-Induced Soil Liquefaction in Urban Environments. *Journal of Geotechnical and Geoenvironmental Engineering*, **144**(10).
- Sancio, R.B., Bray, J.D., Stewart, J.P., Youd, T.L., Durgunoğlu, H.T., Önalp, A., Seed, R.B., Christensen, C., Baturay, M.B. and Karadayilar, T., 2002. Correlation between ground failure and soil conditions in Adapazari, Turkey. *Soil Dynamics and Earthquake Engineering*, **22**(9-12): 1093-1102.

Author Index

- Abdoun T. H. 281
 Abrashitov A. 95
 Adamidis O. 303
 Agalianos A. 281
 Alén C. 103
 Anastasopoulos I. 281, 297, 303
 Arbanas Ž. 115
 Arnold A. 287
 Askarinejad A. 243, 263, 285, 287
 Azad A. 205

 Bergström A. 295
 Bezuijen A. 75
 Bhattacharjee D. 213, 221
 Blanc M. 89, 275, 293
 Bowman A. J. 291, 303
 Brennan A. 185
 Breure W. 163

 Casini F. 49
 Čeh N. 115
 Cheng Kunkun 235
 Christensen M. S. 9
 Coelho P. 31
 Connolly D. 185

 Dashti S. 303
 de Lange D. 65, 75, 133, 285
 de Sauvage J. 3
 Desideri A. 49
 Diakoumi M. 227, 269
 Dijkstra J. 103, 295
 Divall S. 25
 Dubreucq T. 3

 Escoffier S. 39
 Esen A. 185

 Franza A. 193

 Gaudin C. 247
 Gavin K. 243
 Goodey R. 25
 Gorlov A. 95
 Grabe J. 255
 Grima M. A. 243
 Gunnvard P. 301
 Gutiérrez-Ch J. G. 139

 Haffar El I. 275
 Haigh S. 31

 Hashemi M. A. 109
 Henke S. 125
 Herduin M. 247
 Heron C. M. 57, 109, 139, 235
 Honardar S. 285

 Jafari M. K. 201
 Jagodnik V. 115
 Javed S. 295
 Jayanandan M. 213
 Jeffcock O. 269
 Jensen M. R. 17
 Jia Qi 301
 Jimenez R. 139
 Jones L. 297

 Kim Dong-Soo 283, 289
 Kim Yeon-Sam 283
 Kim Yoon-Ah 289
 Knutsson S. 299
 Ko Kil-Wan 283
 Korre E. 281
 Kumar P. 213
 Kumar V. 177
 Kundu S. 43

 Lagerlund J. 171
 Lagrouche O. 185
 Lalicata L. M. 25, 49, 157
 Laue J. 171, 299, 301
 Lee Hae-In 289
 Lehane B. M. 17
 Li Zheng 39
 Li Zhong-Sen 293
 Lintzén N. 299
 Lundberg A. B. 163

 Maatouk S. 89
 Madabhushi S. P. G. 31, 177
 Mahmoudi M. Z. A. 205
 Manandhar S. 289
 Marques A. 31
 Marshall A. M. 109, 139, 193, 235
 McNamara A. 157
 Moosavi M. 201
 Munro C. 185

 Naghibi M. 205

 O'Loughlin C. 247

 Pajalić S. 115
 Peranić J. 115
 Pettey A. 57
 Prendergast L. J. 235
 Price C. 291
 Prodan M. V. 115

 Quinten T. O. 243

 Ritchie. E. 25
 Robinson S. 185
 Rocchi I. 9
 Roddy D. 227
 Rotisciani G. M. 49

 Savin A. 95
 Schiavon J. A. 151
 Sidrakov A. 95
 Silva da D. M. 143
 Song Geyang 139
 Stallebrass S. 157
 Stapelfeldt M. 255
 Stone K. 227, 269
 Støren A. 83
 Sturm H. 83
 Sudhakaran K. 263

 Terwindt J. 65, 75, 133
 Tessari A. F. 291
 Thorel L. 49, 89, 151, 275, 293
 Tohidifar H. 201
 Tommik K. 299
 Toromanovic J. 171
 Tsuha C. H. C. 143, 151

 van der Star W. 65
 van't Hof C. 243
 Viklander P. 171
 Viswanadham B. V. S. 43, 213, 221

 Woodward P. 185

 Xu Jingmin 109, 193

 Yannie J. 103

 Zania V. 9, 17
 Zarandi A. E. 205
 Zaytsev A. 95
 Zhang Yuen 263
 Zwaan R. 75

